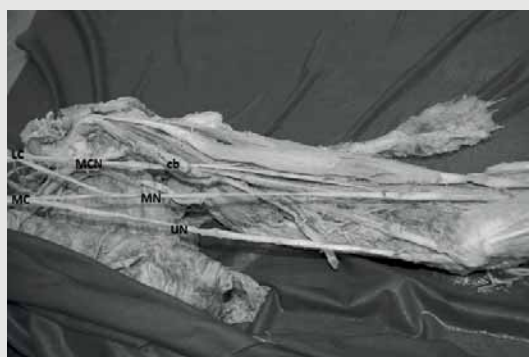


ISSN 0015-5659
eISSN 1644-3284
Impact Factor: 1.195

POLISH ANATOMICAL SOCIETY

FOLIA MORPHOLOGICA



Vol. 82 2023 No. 1


VIA MEDICA

https://journals.viamedica.pl/folia_morphologica

FOLIA MORPHOLOGICA

An international multidisciplinary journal devoted to fundamental research in the morphological sciences

Official Journal of the Polish Anatomical Society

(a Constituent Member of European Federation for Experimental Morphology — EFEM)

EDITOR-IN-CHIEF

Janusz Moryś

Department of Normal Anatomy,
Pomeranian Medical University, Szczecin, Poland

https://journals.viamedica.pl/folia_morphologica

*See our website for information on manuscript status, aims and scope,
instructions for authors as well as editorial board.*

Folia Morphologica

Publishing, Subscription and Advertising Office:

VM Media Group sp. z o.o., Grupa Via Medica

ul. Świątokrzyska 73, 80–180 Gdańsk, Poland

tel. (+48 58) 320 94 94, fax (+48 58) 320 94 60

Managing editor

Joanna Niezgodna

e-mail: fm.journals@viamedica.pl

Cover designer

Sylvia Scisłowska

The journal is published at: https://journals.viamedica.pl/folia_morphologica in one volume per year consisting of four numbers.

Subscription rates: Paper subscription, 4 issues incl. package and postage institutional — 140 euro. The above prices are inclusive of regular postage costs. Payment should be made to: VM Media Group sp. z o.o., Grupa Via Medica, BNP Paribas Bank Polska SA account number: 15 1600 1303 0004 1007 1035 9021; SWIFT: PPABPLPK. Single issues, subscriptions orders and requests for sample copies should be send to e-mail: prenumerata@viamedica.pl. Electronic orders option available at: https://journals.viamedica.pl/folia_morphologica. The publisher must be notified of a cancellation of access to electronic version not later than two months before the end of a calendar year. After that date electronic access will be automatically prolonged for another year.

Advertising. For details on media opportunities within this electronic version of journal please contact the advertising sales department, ul. Świątokrzyska 73, 80–180 Gdańsk, Poland, tel: (+48 58) 320 94 94, e-mail: viamedica@viamedica.pl

The editors accept no responsibility for advertisement contents.

Folia Morphologica is the official journal of the Polish Anatomical Society. For information about the Society, please contact: Prof. Janusz Moryś, Department of Normal Anatomy, Pomeranian Medical University, Al. Powstańców Wielkopolskich 72, 70–111 Szczecin, Poland, tel. (+48 91) 466 15 43, e-mail: jmorys@pum.edu.pl

All rights reserved, including translation into foreign languages. No part of this periodical, either text or illustration, may be used in any form whatsoever. It is particularly forbidden for any part of this material to be copied or translated into a mechanical or electronic language and also to be recorded in whatever form, stored in any kind of retrieval system or transmitted, whether in an electronic or mechanical form or with the aid of photocopying, microfilm, recording, scanning or in any other form, without the prior written permission of the publisher. The rights of the publisher are protected by national copyright laws and by international conventions, and their violation will be punishable by penal sanctions.

Editorial policies and author guidelines are published on journal website: https://journals.viamedica.pl/folia_morphologica

Legal note: https://journals.viamedica.pl/folia_morphologica/about/legalNote

Folia Morphologica is indexed by: BIOSIS Previews, CAS, CINAHL, CrossRef, Dental Abstracts, EBSCO, Elsevier BIOBASE, EMBIOLOGY, FMJ, Google Scholar, Index Copernicus (159.83), Index Medicus/MEDLINE, Index Scholar, Polish Ministry of Education and Science (70), NCBI/National Center for Biotechnology Information, Polish Medical Bibliography, Scopus, SJR, Thomson Reuters, Thomson Scientific Products — Biological Abstracts, Ulrich's Periodicals Directory, Veterinary Bulletin, WorldCat and Zoological Record. Position in Index Copernicus ranking systems is available at: www.indexcopernicus.com. Current Impact Factor of Folia Morphologica (2021) is 1.195.



FOLIA MORPHOLOGICA

Editor-in-Chief
JANUSZ MORYŚ

Department of Normal Anatomy, Pomeranian Medical University
Al. Powstańców Wielkopolskich 72, 70-111 Szczecin, Poland
tel. (+48 91) 466 15 43, e-mail: jmorys@pum.edu.pl

EDITORIAL ADVISORY BOARD

Rafael BOSCOLO-BERTO, *Department of Neuroscience, University of Padova, Italy*

Franciszek BURDAN, *Experimental Teratology Unit of the Human Anatomy Department, Medical University of Lublin, Poland*

Małgorzata BRUSKA, *Department of Anatomy, University Medical School, Poznań, Poland*

Mafalda CACCIOTTOLO, *USC Leonard Davis School of Gerontology, University of Southern California, Los Angeles, United States*

Stephen W. CARMICHAEL, *Department of Anatomy, Mayo Clinic, Rochester, United States*

Bogdan CISZEK, *Department of Human Anatomy, Medical University of Warsaw, Poland*

Om Prakash CHOUDHARY, *Department of Veterinary Anatomy, Guru Angad Dev Veterinary and Animal Sciences University, Bathinda, Punjab, India*

Carla D'AGOSTINO, *Neuromuscular Center, University of Southern California, Los Angeles, CA, United States*

Halina DOBRZYŃSKI, *Cardiovascular Sciences, Faculty of Biology, Medicine and Health, University of Manchester, United Kingdom*

Zygmund Antoni DOMAGAŁA, *Department of Anatomy, Medical University of Wrocław, Poland*

Rastislav DRUGA, *Department of Functional Anatomy, 2nd Medical Faculty Charles University, Prague, Czech Republic*

Sergio Domenico GADAU, *Department of Veterinary Medicine, University of Sassari, Italy*

Marek GRZYBIAK, *Elblag University of Humanities and Economics, Elblag, Poland*

Hans Jorgen GUNDERSEN, *Stereological Research Laboratory, University of Aarhus, Denmark*

Kazimierz JĘDRZEJEWSKI, *Department of Anatomy, Medical University of Łódź, Poland*

Leszek KACZMAREK, *Department of Molecular Cell Neurobiology, Nencki Institute, Warsaw, Poland*

Ilona KLEJBOR, *Department of Anatomy, Jan Kochanowski University of Kielce, Poland*

Zbigniew KMIEĆ, *Department of Histology, Medical University of Gdańsk, Poland*

Henryk KOBRYŃ, *Department of Morphological Sciences, Warsaw, Agricultural University, Poland*

Przemysław KOWIAŃSKI, *Department of Human Anatomy and Physiology, Pomeranian University in Słupsk, Poland*

Marios LOUKAS, *Department of Anatomical Sciences, School of Medicine, St. George's University, Grenada, West Indies*

Andrzej ŁUKASZYK, *Department of Histology and Embryology, University Medical School, Poznań, Poland*

Alexander J. McDONALD, *Department of Cell Biology and Neuroscience, USC School of Medicine, Columbia, United States*

Stanisław MOSKALEWSKI, *Department of Histology and Embryology, Medical University of Warsaw, Poland*

Łukasz OLEWNIK, *Department of Normal and Clinical Anatomy, Medical University of Łódź, Poland*

Orlando PACIELLO, *Dipartimento di Patologia e Sanità animale, Univesita degli Studi di Napoli Federico II, Napoli, Italy*

Asla PITKÄNEN, *Department of Neurobiology, A.I. Virtanen Institute, University of Kuopio, Finland*

Michał POLGUJ, *Department of Angiology, Medical University of Łódź, Poland*

Marcin SADOWSKI, *Department of Anatomy, Jan Kochanowski University of Kielce, Poland*

Michał K. STACHOWIAK, *Department of Molecular and Structural Neurobiology and Gene Therapy, State University of New York, Buffalo, United States*

Paweł SYSA, *Department of Histology and Embryology, Warsaw University of Life Sciences, Poland*

Michał SZPINDA, *Department of Anatomy, Nicolaus Copernicus University in Toruń, Collegium Medicum in Bydgoszcz, Poland*

Edyta SZUROWSKA, *2nd Department of Radiology, Medical University, Gdańsk, Poland*

Jean-Pierre TIMMERMANS, *Laboratory of Cell Biology and Histology/Central Core Facility for Microscopic Imaging, Department of Veterinary Sciences, University of Antwerp, Belgium*

Mirosław TOPOL, *Department of Angiology, Medical University of Łódź, Poland*

Mehmet Cudi TUNCER, *Department of Anatomy, University of Dicle, Medical School, Diyarbakir, Turkey*

Krzysztof TURLEJSKI, *Department of Biochemistry and Cell Biology, Cardinal Stefan Wyszyński University, Warsaw, Poland*

Jiro USUKURA, *Structural Biology Research Center, Nagoya, Japan*

Jerzy WALOCHA, *Department of Anatomy, Jagiellonian University, Collegium Medicum, Kraków, Poland*

Mark J. WEST, *Department of Neurobiology, Institute of Anatomy, Aarhus University, Denmark*

Sławomir WÓJCİK, *Department of Anatomy and Neurobiology, Medical University of Gdańsk, Poland*

Maciej ZABEL, *Collegium Medicum University of Zielona Gora, Poland*

Marco ZEDDA, *Department of Veterinary Medicine, University of Sassari, Italy*

How to write an umbrella review? A step-by-step tutorial with tips and tricks

M. Bonczar^{1*}, P. Ostrowski^{1*}, A.V. D’Antoni², R.S. Tubbs^{3, 4}, J. Iwanaga^{3, 4}, S.K. Ghosh⁵, I. Klejbor⁶, M. Kuniewicz¹, J. Walocha¹, J. Moryś⁷, M. Koziej¹

¹Department of Anatomy, Jagiellonian University Medical College, Krakow, Poland

²Division of Anatomy, Department of Radiology, Weill Cornell Medicine, New York, NY, United States

³Department of Neurosurgery, Tulane Centre for Clinical Neurosciences, Tulane University School of Medicine, New Orleans, LA, United States

⁴Department of Neurology, Tulane Centre for Clinical Neurosciences, Tulane University School of Medicine, New Orleans, LA, United States

⁵Department of Anatomy, All India Institute of Medical Sciences, Phulwarisharif, Patna, India

⁶Department of Anatomy, Collegium Medicum, Jan Kochanowski University, Kielce, Poland

⁷Department of Normal Anatomy, Pomeranian Medical University, Szczecin, Poland

[Received: 25 October 2022; Accepted: 30 November 2022; Early publication date: 22 December 2022]

The number of meta-analyses (MA) and systematic reviews (SR) on various medical issues has increased during the last two decades. The MA and SR results may differ from one another due to a number of factors such as inaccurate or diverse searches through the databases, discrepancies in the extraction process or in statistical analysis, among others. Some results may even contradict one another, resulting in confusion among readers. Umbrella reviews (UR) have allowed the collection of all available data on a medical issue into one concise study, making it the source of evidence-based medical knowledge to the highest degree. Furthermore, UR can resolve those problems by collecting all data and taking into account both MA and SR, making it the superior tool for physicians. Although the pros of UR are clear and the overall popularity of these types of study has increased tremendously, there is no available step-by-step guide on how to conduct one. Therefore, the objective of the present study was to provide researchers with a detailed tutorial on how to conduct an UR. UR represent the next major step in the advancement of evidence-based medicine, with great practical potential for physicians looking for the most up-to-date data on their topic of interest. We hope that our step-by-step guide may be a useful tool for researchers conducting UR in the future. (Folia Morphol 2023; 82, 1: 1–6)

Key words: umbrella review, evidence based medicine (EBM), meta-analysis, systematic review

INTRODUCTION

The number of meta-analyses (MA) and systematic reviews (SR) on various medical issues has in-

creased during the last two decades. These types of studies were the best sources of up-to-date and evidence-based information on certain topics for med-

Address for correspondence: Dr. M. Koziej, Department of Anatomy, Jagiellonian University Medical College, ul. Mikołaja Kopernika 12, 33–332 Kraków, Poland, e-mail: mateusz.koziej@gmail.com

*Equal contribution

This article is available in open access under Creative Common Attribution-Non-Commercial-No Derivatives 4.0 International (CC BY-NC-ND 4.0) license, allowing to download articles and share them with others as long as they credit the authors and the publisher, but without permission to change them in any way or use them commercially.

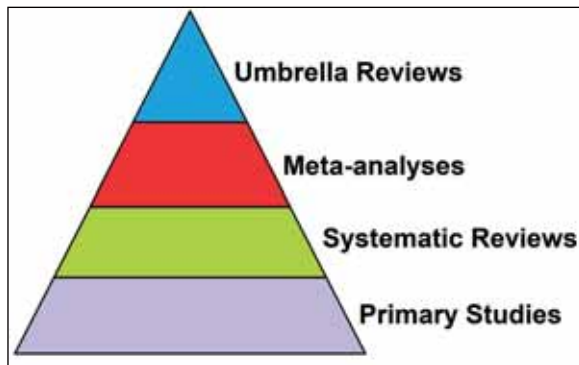


Figure 1. The evidence-based medicine pyramid.

ical professionals. The MA allowed us to make sense of numerous and often contrasting findings about different medical issues, pushing our knowledge forward. However, with the increased number of MA and SR, medical professionals can feel overwhelmed when looking for evidence-based knowledge on their topic of interest. Gathering more precise and significant statistical conclusions is the basis of scientific development.

Umbrella reviews (UR) have allowed the collection of all available data on a medical issue into one concise study, making it the source of evidence-based medical knowledge to the highest degree (Fig. 1). They are reviews based on previous MA and SR, presenting all available data on a specific topic in the literature. Therefore, the popularity of UR has increased significantly in recent years. The difference in methodology between MA and SR can present different conclusions about the same topic, which may give an incorrect clinical picture of the issue at hand. The MA and SR results may differ from one another due to a number of factors such as inaccurate or diverse searches through the databases, discrepancies in the extraction process or in statistical analysis, among others. Some results may even contradict one another, resulting in confusion among readers. UR can resolve those problems by collecting all data and taking into account both MA and SR, making it the superior tool for physicians. Although the pros of UR are clear and the overall popularity of these types of study has increased tremendously, there is no available step-by-step guide on how to conduct one. Therefore, the objective of the present study was to provide researchers with a detailed tutorial on how to conduct an UR. Lastly, we will also discuss the potential limitations associated with UR.

HOW TO PREPARE AN UMBRELLA REVIEW?

Planning and establishing goals

The initial step of creating an UR, and probably the most crucial one, is a precise and accurate establishment of the aim of the study. Additionally, it is essential to understand the sense, importance, and overall assumptions of the UR. The goal of UR is to gather and summarise the available data in the literature and/or to standardise inaccuracies. The MA and SR results may differ from one another due to a number of factors such as inaccurate or diverse searches through the databases, discrepancies in the extraction process or in statistical analysis, among others. Additionally, some MA and SR may be related to the same topics from different points of view. Therefore, UR are created in order to gather, summarise, and/or idealistically standardise the results and dispel the doubts in the literature. Additionally, UR minimise the time that is needed to be spent on the recognition in the literature by the physician, which is purely beneficial for the clinical practice. Therefore, by creating the UR it is aimed to gather all MA and SR regarding the studied topic. At the beginning, we highly recommend doing an initial recognition in the literature, especially with respect to the overall number and availability of SR and MA for the proposed topic. There are no contradictions for the use of a search filter, especially the one regarding the type of study, as it is only the first, initial search, only to recognise whether the topic is suitable for further investigation. It is critical to evaluate whether the found SR and MA concern the same or at least related topics. Additionally, cohesion of the methodologies among the said studies and mutually exclusive results increase the relevance and need for such UR. This step is essential, as the creation of an UR is only possible if there are enough appropriate studies and data in the literature on a specific research issue. Therefore, initial estimates of the number of SR and MA on the topic studied allow evaluation of the risk of incomplete, unsuccessful, or impossible research.

Systematic search

After the initial evaluation of the topic, it is time to perform a systematic search through the databases. Therefore, the search phrases have to be established, preferably with the usage of the Boolean technique. The Boolean technique is based on mathematical logic. Between each of the phrases we can add one of

three conjunctions: 'AND', 'OR' and 'NOR'. Using the conjunction 'AND' will result in the appearance of only studies that refer to all those phrases simultaneously. Using the conjunction 'OR' will result in the appearance of studies that are related to at least one of the phrases. Using the 'NOR' conjunction will result in the appearance of all studies related to the initial phrase (the one used before the 'NOR' conjunction) but with the omission of all studies related to the other phrase (the one used after the 'NOR' conjunction). It is possible to use brackets to create multilevel, complicated search phrases (example: (((Phrase1 OR Phrase2 OR Phrase3 OR Phrase 4) AND (Phrase5 OR Phrase6)) NOR (Phrase6 OR Phrase7))). For the UR, we recommend for the search phrases to be as wide as possible in order to minimise the chances of losing any relevant study. We recommend applying as many synonyms for each phrase when using the 'OR' conjunction. In addition, it is beneficial to add as many abbreviations as possible commonly used in clinical practice or the literature on the studied topic. It is also beneficial to use all historical eponyms in the researched issue. The given topic might have been studied for a long time before modern nomenclature. We strongly advise against using the 'NOR' conjunction, as it greatly increases the chances of an unsuccessful search or missing some of the potentially relevant studies. We advise against applying phrases that refer to 'meta-analysis' or 'systematic review' (example: (Phrase1 OR Phrase2) AND (Meta OR Meta-analysis OR Systematic OR Systematic Review)). Additionally, it is possible to use quotation marks (example: 'Phrase1' OR Phrase2) in order to search only for the particular word used as a phrase, without its varieties; however, we strongly advise against using this function in systematic searches. Graphical illustration of the Boolean conjunctions and their influence on the searched phrases is presented on Figure 2.

After the establishment of the search phrases, the search can be conducted through the databases. We recommend searching through as many databases as possible, especially the main ones such as PubMed, Embase, Web of Science, Scopus, Google Scholar and Cochrane Library, as it maximises the chances of gathering all relevant studies. In some of the databases, the search phrases will need to be adjusted for the specific search coding systems used on those sites. We strongly advise against the usage of filters at this stage of the process. The aim of this part of the study is to collect all MA and SR regarding the

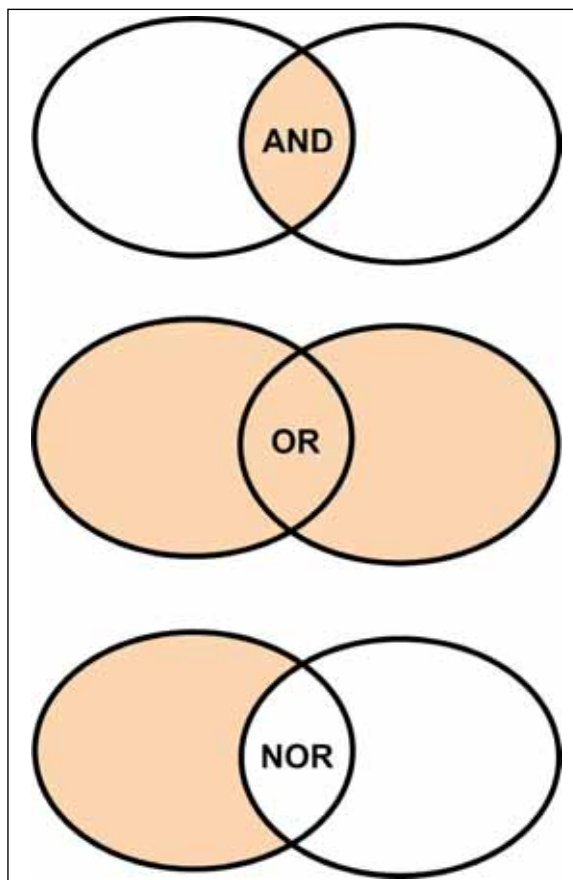


Figure 2. Scheme, illustrating the Boolean conjunctions and their influence on the searched phrases.

topic researched. It is acceptable to create UR regarding only MA, with omission of the SR; however, we recommend gathering both types of studies. During the search, determining the relevance and reference to the topic of the study should be done in the first step by evaluating the title and abstract and by reading the article in the second step. Studies in foreign languages should be evaluated only by reviewers who speak fluently the said language. Clearly, irrelevant research should not be screened for further evaluation. It is also recommended for the search to be done twice by two independent reviewers. Afterwards at the final step of the search, we recommend performing a manual search through the references of the submitted studies to find more research which may not have been found by the database's algorithms.

Furthermore, all submitted studies should be evaluated. For this purpose, inclusion and exclusion criteria should be established. This should be the final point of clarification of the detailed aim and topic of the study, as the submitted studies must have results in at least one identical category so they

can be compared with each other. We recommend excluding studies that are burdened with strong bias. There are not many tools created for the evaluation of bias and the evaluation of quality in MA and SR. However, there are many detailed and specific tools for the evaluation and assessment of primary studies that are used in the process of conducting MA and SR. We recommend the MeaSurement Tool to Assess Systematic Reviews 2 (AMSTAR 2) [6], the ROBIS tool [7] for the quality assessment. It is also beneficial to use more dedicated tools, such as AQUA or CATAM, for anatomical MA [1, 2]. We recommend using these tools, as there is a high similarity between MA, SR, and UR in methodology. Irrelevant, biased, low-quality, and duplicated research should be deleted.

Double extraction and statistical dilemma

Later, after the systematic search has been completed, the extraction process must be performed. During this part, it is aimed to extract and gather all possible data, both quantitative and qualitative, from the qualified studies. It is crucial to perform this part with great care and precision. We strongly suggest performing the extraction twice by two independent researchers. During this part of the process of creating MA and SR, the authors gather all extractable data from the primary studies. The UR is a relatively new type of review study, and its statistical results are based on the results of the MA, which are based on the results of the primary studies. It comes down to the statistical dilemma of whether it is acceptable to establish new results taking into consideration only the results of the MA. During our experience, we agreed that statistical analysis should be done based on the results of the primary studies and only compared to the results of the MA. The MA results may differ from one another due to different searches within the different sets of databases. However, some of the studies may have been included in more than one MA. Therefore, we strongly suggest performing a double extraction to prevent multiplied use of the results from the primary studies in the new results. All discrepancies need to be discussed and resolved to create a one-consistent version. The first part of the double extraction should be performed on the MA and SR. All qualitative and quantifiable data should be collected. Subsequently, the data for statistical analysis should be extracted from the primary studies. In order to perform this part, the authors must eval-

uate the studies on which each of the MA performed its statistics. We recommend searching through the reference lists of the MA as all primary studies should have been reported there. It is essential to extract data from primary studies to prevent multiplication of the results. Data from MA and UR should be gathered in separate tables in order to avoid unnecessary confusion. The aim should be to collect all relevant data from qualified studies. Qualitative results, for example, the year when the study was conducted, the continent and country in which the study has been performed, studied groups, the methodology of the study (for example: cadaveric study, intraoperative observations, study based on the computed tomography results, comparison of the surgical techniques, comparison of the groups using different methods, etc.) and more. Quantitative results are all numeric data obtained during the study by the researchers. These are strongly varied depending on the purpose of the said study. However, all quantitative results should be presented using mathematical tools like means, medians, risk ratios, odds ratios, pooled prevalences, percentages, standard deviations, etc. It is essential for those data to be properly interpreted and understood by the researcher so they can be grouped and qualified as analogical ones. Incorrect extraction leads to incorrect statistical analysis, resulting in false conclusions.

Statistical analysis

Statistical analysis of the UR should be performed based on the results of the primary studies instead of the results of the MA. It is crucial to properly collect and group the extracted data and establish an accurate method of analysis. For UR regarding the results from SR in which MA were not performed, we recommend using the Summary of Finding table to present the data in clear format [3, 5].

At the beginning of the statistical analysis of the UR, we recommend evaluating the types of outcomes in the submitted MA. From a mathematical point of view, we can output data in numerous ways. However, we recommend presenting the newly established UR results in the same way that the authors of the MA presented the analogous results in their study. This will allow us to compare the new results with those from MA and potentially resolve the contradictions occurring in the literature. Additionally, it will minimise the potential confusion associated with numer-

ous mathematical and statistical methods in which the same topic is discussed. We strongly recommend providing possibly the most accurate results but, simultaneously, presenting them in a simple way. This will allow clinicians to understand the mathematics behind the conclusions. Establishing the way in which it is preferred to present the results allows us to properly choose statistical tools.

Authors creating UR will most commonly find three types of outcomes in MA: (1) comparisons of risks between cohorts, presented as risk ratios, odds ratios, hazard ratios, etc., (2) proportions or prevalences, and (3) means. Independently, heterogeneity among the gathered data has to be assessed, preferentially using both the chi-squared test and the I-squared statistic. For the chi-squared test, the p-value of Cochran's Q should be reported, with a value of < 0.10 considered to indicate statistically significant heterogeneity between studies [3, 4]. The I-squared statistic, an overall measure of heterogeneity, should be reported with its 95% confidence interval. The I-squared statistic should be interpreted as follows: 0% to 40% might not be important; 30% to 60% may represent moderate heterogeneity; 50% to 90% may represent substantial heterogeneity; and 75% to 100% may represent considerable heterogeneity, according to the guidelines in the current version of the Cochrane Handbook of Systematic Reviews of Interventions [3, 4]. This will allow authors to choose either fixed- or random-effects models. Mostly, the data will be heterogeneous; therefore, the random-effects model will be used much more commonly rather than the fixed-effects model. Unlike a fixed-effects model which assumes that the differences between the results of studies are due solely to chance, a random-effects model assumes that the effects being estimated in the different studies are not identical [3, 4].

To establish new risks (1) we recommend using the Comprehensive Meta-analysis 3.0 (Biostat Inc., Englewood, NJ, USA) tool. It is a highly efficient, accurate and user-friendly tool with numerous tutorials and examples implemented in it. Additionally, it allows one to choose an outcome type after the insertion of group sizes and number of positive outcomes in each group (or more if needed for specific type of outcome). Therefore, we can decide whether to present new outcomes such as risk ratios, odds ratios, hazard ratios, or others. Additionally, both fixed- and random-effects models can be assessed depending

on heterogeneity of data. For proportions and prevalences (2) we recommend using MetaXL (EpiGear International Pty Ltd., Wilston, Queensland, Australia), which is a highly efficient plug-in for Microsoft Excel. To establish pooled prevalences, one will need to implement the quantity of the study group and the number of individuals who present such variation. Evaluation of means (3) is only possible when, in addition to the mean itself, the authors extracted data such as standard deviations, interquartile range, standard error, or any other results that mathematically reflect the diversity of data. For this purpose, we recommend using Comprehensive Meta-analysis V3 tool (Biostat Inc., Englewood, NJ, USA) tool, analogously to the establishment of risks (1). We recommend presenting the data gathered in tables and figures (graphs, forest plots, etc.), rather than in a descriptive form, as it is much more reader-friendly.

Writing the manuscript

When writing the manuscript, we would like to recommend following a structure similar to that of MA, that is, separate sections for the introduction, materials and methods, results, and discussion. The manuscript should be concise, but comprehensive, covering the wholesome of the studied topic. Using simple language and avoidance of sublime phrases or complicated statistical descriptions (if not needed) could also be beneficial, as it would be more understandable for a wider group of readers.

The introduction should contain general information about the research at hand, why it is important, and how it impacts what we know now. It should also cover topics and definitions that have to be introduced in order for the reader to understand the full content of the study. Finally, the introduction should explain how the paper at hand will fill a missing piece of information in the literature.

Materials and methods should present the search strategy, that is, how the data were searched from the literature. Later, one has to explain the process of assessing the eligibility of the searched studies and the extraction techniques used. Subsequently, the methodological quality of all MA submitted must be assessed. Finally, the authors need to describe how the statistical analysis was performed. If any other steps were taken, in order to prepare the UR, the authors must state them in this chapter. There are no standardized, dedicated checklists or guidelines on what to include in the manuscript of an UR. However,

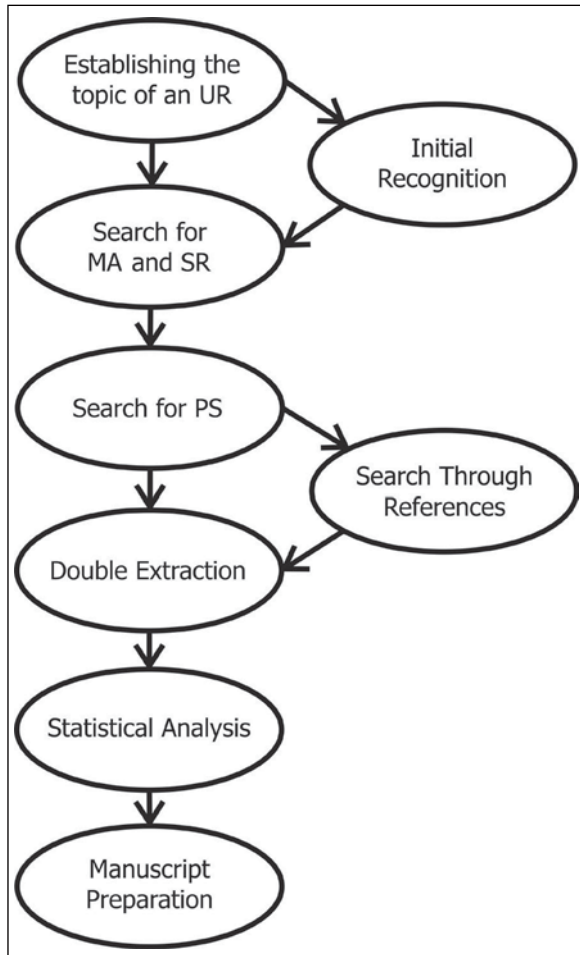


Figure 3. A simplified step-by-step diagram of how to prepare an umbrella review (UR); MA — meta-analyses; SR — systematic reviews; PS — primary studies.

we recommend using the PRISMA and MOOSE guidelines, which are implicitly designed for MA and SR.

The results should be concisely presented in the 'Results' section. For readability, all results should be categorized into sub-paragraphs and briefly presented. We recommend presenting the results as simply as possible, without paying attention, for example, to repeated words. This section should be the essence of the results, deprived of any stylistic additives which may cause potential confusion or misunderstanding. More in-depth data should be presented in additional tables and/or figures.

The 'Discussion' section should present the clinical significance of the results obtained from the UR. Comparing the results with data from other MA or SR may be beneficial, as it may show the possible discrepancies and contradictory results on the topic at hand. The discussion should also address the prac-

tical implications of the gathered data and potentially suggest the direction for further research. Lastly, it is crucial to acknowledge the limitations of the study, as UR are only as good as the submitted studies. A simplified step-by-step diagram of how to prepare an umbrella review can be found in Figure 3.

CONCLUSIONS

Umbrella reviews represent the next major step in the advancement of evidence-based medicine, with great practical potential for physicians looking for the most up-to-date data on their topic of interest. We hope that our step-by-step guide may be a useful tool for researchers conducting UR in the future.

Funding

Doctor Mateusz Koziej was supported by the Foundation for Polish Science (FNP). The funders had no role in the study's design, data collection and analysis, decision to publish, or preparation of the manuscript.

Conflict of interest: None declared

REFERENCES

1. D'Antoni AV, Tubbs RS, Patti AC, et al. The critical appraisal tool for anatomical meta-analysis: a framework for critically appraising anatomical meta-analyses. *Clin Anat.* 2022; 35(3): 323–331, doi: [10.1002/ca.23833](https://doi.org/10.1002/ca.23833), indexed in Pubmed: [35015336](https://pubmed.ncbi.nlm.nih.gov/35015336/).
2. Henry BM, Tomaszewski KA, Ramakrishnan PK, et al. Development of the anatomical quality assessment (AQUA) tool for the quality assessment of anatomical studies included in meta-analyses and systematic reviews. *Clin Anat.* 2017; 30(1): 6–13, doi: [10.1002/ca.22799](https://doi.org/10.1002/ca.22799), indexed in Pubmed: [27718281](https://pubmed.ncbi.nlm.nih.gov/27718281/).
3. Henry BM, Tomaszewski KA, Walocha JA. Methods of evidence-based anatomy: a guide to conducting systematic reviews and meta-analysis of anatomical studies. *Ann Anat.* 2016; 205: 16–21, doi: [10.1016/j.aanat.2015.12.002](https://doi.org/10.1016/j.aanat.2015.12.002), indexed in Pubmed: [26844627](https://pubmed.ncbi.nlm.nih.gov/26844627/).
4. Higgins JPT, Thomas J, Chandler J. (eds). *Cochrane Handbook for Systematic Reviews of Interventions*. Wiley 2019.
5. Langendam MW, Akl EA, Dahm P, et al. Assessing and presenting summaries of evidence in Cochrane Reviews. *Syst Rev.* 2013; 2: 81, doi: [10.1186/2046-4053-2-81](https://doi.org/10.1186/2046-4053-2-81), indexed in Pubmed: [24059250](https://pubmed.ncbi.nlm.nih.gov/24059250/).
6. Shea BJ, Reeves BC, Wells G, et al. AMSTAR 2: a critical appraisal tool for systematic reviews that include randomised or non-randomised studies of healthcare interventions, or both. *BMJ.* 2017; 358: j4008, doi: [10.1136/bmj.j4008](https://doi.org/10.1136/bmj.j4008), indexed in Pubmed: [28935701](https://pubmed.ncbi.nlm.nih.gov/28935701/).
7. Whiting P, Savović J, Higgins JPT, et al. ROBIS: A new tool to assess risk of bias in systematic reviews was developed. *J Clin Epidemiol.* 2016; 69(9): 225–234, doi: [10.1016/j.jclinepi.2015.06.005](https://doi.org/10.1016/j.jclinepi.2015.06.005), indexed in Pubmed: [26092286](https://pubmed.ncbi.nlm.nih.gov/26092286/).

Anatomy of the occipital lobe using lateral and posterior approaches: a neuroanatomical study with a neurosurgical perspective on intraoperative brain mapping

T.A. Dziedzic¹ , A. Bala^{1, 2}, A. Balasa¹, A. Olejnik^{1, 2}, A. Marchel¹

¹Department of Neurosurgery, Medical University of Warsaw, Poland

²Faculty of Psychology, University of Warsaw, Poland

[Received: 1 November 2021; Accepted: 29 December 2021; Early publication date: 31 December 2021]

Background: A major concern of occipital lobe surgery is the risk of visual field deficits. Extending anatomical occipital lobectomy to the functional requires awake conditions because the anterior resection border comprises language-, motor- and visuospatial function-related areas within the temporal and parietal lobes. This study investigated the lateral and posterior perspectives of the occipital lobe anatomy when approaching intraaxial occipital lobe lesions.

Materials and methods: Ten adult cadaveric cerebral hemispheres were dissected after being prepared following the concept described by Klingler for the first time.

Results: The occipital lobe was located posteriorly to the parietotemporal line. Within the occipital lobe, the occipital horn of the lateral ventricle represented the only anatomical landmark. Laterally, optic radiation was identified as a part of the sagittal stratum. None of the intraoperatively identifiable tracts was found medial to the occipital horn. Language- and motor-related areas were identified anteriorly and should be actively identified when lobectomy based on function is planned. Subcortically, from a posterior perspective, the anterolateral border constituted the arcuate fascicle/superior longitudinal fascicle complex and was anteromedial to the thalamocortical tract. Remaining posterior to the line connecting the preoccipital notch with the superior Rolandic point avoided the cortical and white matter tracts related to language, motor and visuospatial function.

Conclusions: Knowledge of occipital lobe anatomy and surrounding structures is essential to preoperatively assess the risk of the procedure and proper consultation of a patient in terms of the extent of resection, primarily concerning visual field deficits. (Folia Morphol 2023; 82, 1: 7–16)

Key words: white matter dissection, glioma, awake mapping, lobectomy, tractography, neurosurgery

INTRODUCTION

Intraaxial occipital lobe lesions can be approached under awake conditions from the lateral or poste-

rior trajectory [5, 21, 29]. Using both approaches, selective lesionectomy and anatomical or functional occipital lobectomy can be performed. The approach

Address for correspondence: Dr. T.A. Dziedzic, Department of Neurosurgery, Medical University of Warsaw, ul. Banacha 1a, 02–097 Warszawa, Poland, e-mail: tdziedzic@wum.edu.pl

This article is available in open access under Creative Common Attribution-Non-Commercial-No Derivatives 4.0 International (CC BY-NC-ND 4.0) license, allowing to download articles and share them with others as long as they credit the authors and the publisher, but without permission to change them in any way or use them commercially.

is chosen based on the lesion's anatomical localization, presumed neuropathological type, preoperative visual field deficit, and the aim of surgery. The lateral trajectory is reserved for lesions lateral to the sagittal stratum (SS) or, in gliomas, where oncological benefit outweighs the cost of permanent hemianopsia, and lobectomy is planned. According to Viegas and Duffau [29], the neurooncological benefit from occipital lobectomy outweighs the permanent side effects of postoperative hemianopsia and should be performed even for low-grade glioma with a longer life expectancy. When optic radiation preservation is expected — for example, when driving abilities are crucial for patients — Nguyen et al. [21] found it useful to leave part of the tumour behind. Thus, the resection border is based on awake intraoperative mapping until quadrantanopsia appears, a condition that is asymptomatic in the long term compared with always symptomatic homonymous hemianopsia [5]. For lesions medial to the SS without coexisting hemianopsia, the posterior approach is more suitable. If the lesion extends beyond the occipital lobe or functional resection is planned, the anatomical resection is extended to the functional boundaries within the parietal and temporal lobes. The anterior extent of functional resection is identified based on cortical and subcortical mapping for language, sensorimotor and visuospatial function [5, 29]. Preoperative planning, intraoperative decision-making processes and the application of brain mapping require an anatomical background. We performed an anatomical study regarding occipital lobe surgery using the lateral and posterior approaches. We described the main anatomical cranial, cortical and subcortical landmarks that are crucial during these procedures. Despite mentioned anatomical aspects of the surgical planning a meticulous study of preoperative imaging in terms of anatomy of the dural sinuses, the cerebral veins and cerebral arteries is mandatory [23]. The patency, size, dominance, and localisation of the superior sagittal sinus, the transverse sinus, the sinus confluence and the vein of Labbe should be taken into consideration when planning craniotomy as they state for medial and inferior borders of the craniotomy [24]. After anatomical disconnection of the occipital lobe from the rest of the hemisphere and before removal of the separated lobe care should be taken of the draining veins especially at proximity to the confluence of sinuses. Rupture of these veins in proximity to the sinus may cause a significant bleeding which

can be troublesome in managing. The main arterial vessels are found on the mesial surface of the occipital lobe in proximity to the calcarine fissure where the distal branches of the posterior cerebral artery are identified. When lobectomy is performed care must be taken for proper identification, coagulation, and finally safe division of these arteries. This study also discusses the strategy for intraoperative cortical and white matter mapping under awake conditions.

MATERIALS AND METHODS

Ten adult cadaveric cerebral hemispheres were prepared following the concept described by Klingler for the first time [see 19, 31, 34]. The specimens were fixed with 4% formalin for at least 4 weeks. The dry brain was placed on the tray inside the freezer with the temperature set at -15 degrees Celsius and then was frozen for 2 weeks. To preserve the sample, a 4% formalin solution was used. Details of the preservation technique were described previously [11]. The cortical surface was assessed using the naked eye (Fig. 1). Next, white matter dissection was performed from the lateral to the midline using microscopic magnification and microsurgical tools to expose the white matter tracts and ventricular system within the occipital lobe. We then assessed anatomical correlation of the cortical regions and white matter tracts within the occipital lobe, particularly regarding the sensorimotor, visuospatial and language cortical and subcortical regions. The findings were correlated with the craniometric points and represented a surgical perspective of lateral and posterior approaches. For the lateral approach, the head was rotated laterally; for the posterior approach, the head was positioned neutrally, simulating a semi-sitting position, which provides comfort for sophisticated visual field testing (Fig. 2) [14, 24]. Measurements were made using an electric digital calliper, a protractor and a measuring tape. A digital camera (NikonD7200 with a Nikon DX 35 mm lens; 1:1.8G) was used for image documentation. The study was approved by the Bioethics Committee of our University (approval number: AKBE/126/2019).

RESULTS

Occipital lobe sulci and gyri (Figs. 1, 2)

The preoccipital notch was located 50.5 (ranging from 45 to 58) mm from the occipital pole along the base of the hemisphere, while the parietooccipital sulcus was 50.7 (ranging from 39 to 62) mm along the superior margin of the hemisphere. The

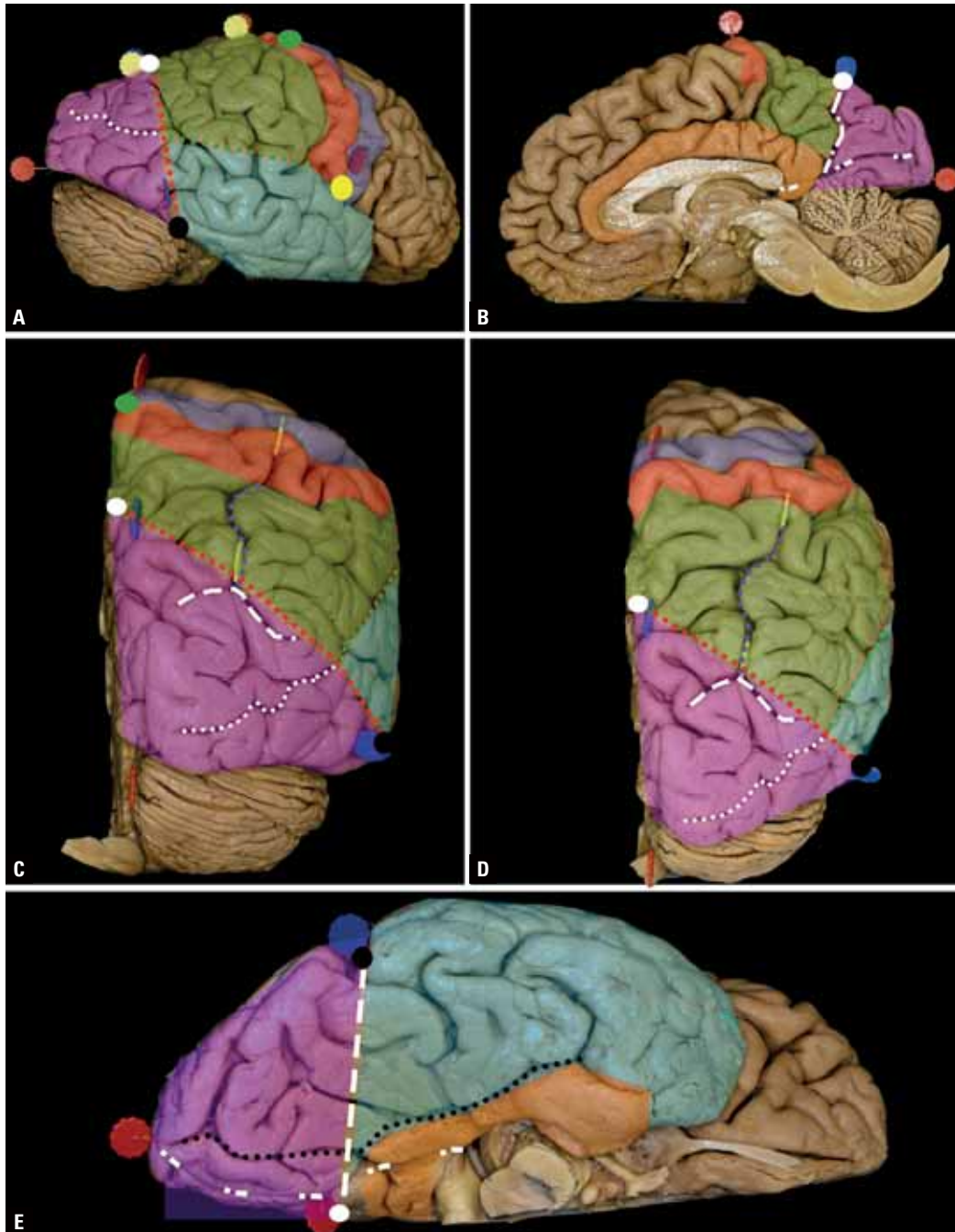


Figure 1. Cortical anatomy of the occipital lobe and surrounding structures; **A.** The occipital lobe (purple) is located behind the parietotemporal line (red dots), which connects the preoccipital notch (black dot) with the parietooccipital sulcus (white dot). Within the occipital lobe, the lateral occipital sulcus (white dots), which is an extension of the superior temporal sulcus, is observed on the lateral surface. Anteriorly and superiorly, the parietal lobe (green) and temporal lobe inferiorly (light blue) are identified. Both are separated by occipitotemporal lines (green dots). Anterior to the parietal lobe, the postcentral (red) and precentral (blue) gyri are identified, which are separated by the central sulcus. The inferior end of the central sulcus is called the inferior Rolandic point (yellow dot), while the superior end is called the superior Rolandic point (green dot); **B.** On the medial surface, the anterior border of the occipital lobe comprises the parietooccipital sulcus (white dotted rectangular line) and extends inferiorly beyond the calcarine sulcus (white square rectangular line). Anteriorly, where the parietooccipital and calcarine sulci join the isthmus of gyrus cinguli is identified. The mesial part of the hemisphere between the base and calcarine sulcus is formed by the lingula and between the calcarine and parietooccipital sulcus by the cuneus. Anteriorly, within the parietal lobe, the precuneus (green) and paracentral lobule (red) are identified; **C, D.** Posteriorly, in addition to previously described structures, the transverse occipital sulcus (white rectangle line) is visualised at the level of the intraparietal sulcus (purple dots), which becomes a very short segment (in this example) of the intraoccipital sulcus; **E.** Basal view of the hemisphere. The occipital lobe is located posteriorly to the imaginary temporoparietal line connecting the preoccipital notch and inferior extension of the parietooccipital sulcus. The basal surface of the occipital lobe is formed by the occipitotemporal gyrus and basal surface of the lingula, separated by the collateral sulcus (black dots). Anteriorly, the parahippocampal gyrus (orange) and lateral surface (light blue) of the temporal lobe are identified.

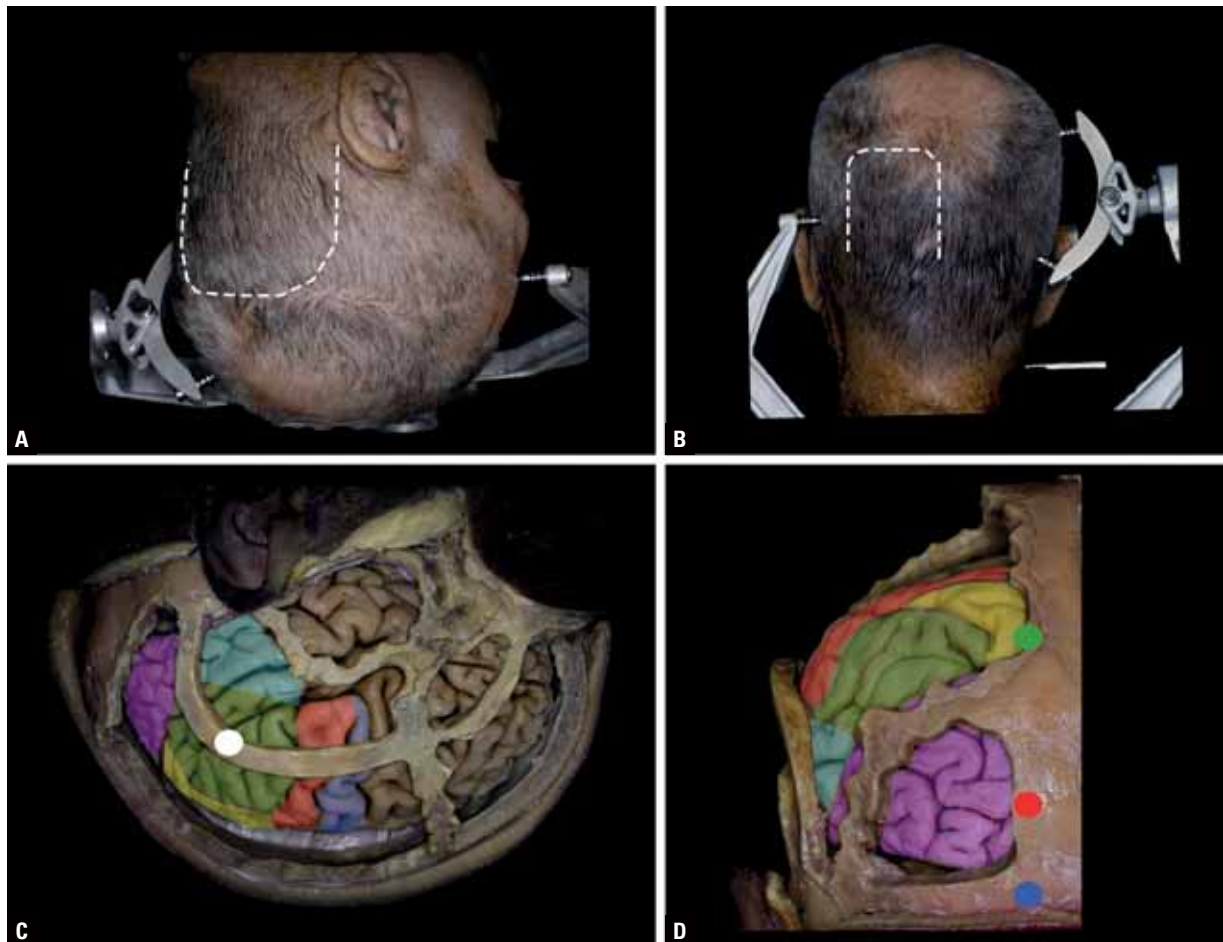


Figure 2. Surgical perspective of the occipital lobe anatomy; **A.** For tumours located lateral to the sagittal stratum (SS) and occipital horn of the lateral ventricle or when lobectomy is planned, the long axis of the head is rotated to the contralateral side, as parallel to the floor as possible. A u-shaped skin incision (white rectangle) is preferred, with the base on the transverse sinus posterior to the ear posteriorly close to the midline; **B.** For tumours located medial to the SS and lateral ventricle or when the aim of surgery is to preserve the visual fields and intraoperative testing is required, a semi-sitting position with the head in the neutral position is applied. The size of the skin incision, which is usually u-shaped with the base on the transverse sinus, is determined. Depending on the lesion location and aim of surgery, the incision can be extended superiorly as much as needed; **C.** The lateral perspective of the occipital lobe (purple) in relation to the craniometric points, with a marked superior parietal lobule (yellow), inferior parietal lobule (green) and posterior aspect of the lateral surface of the temporal lobe (light blue). When functional occipital lobectomy is planned, the previous (panel A) skin incision must be extended anteriorly to visualise the postcentral gyrus, posterior part of the superior temporal gyrus and supramarginal gyrus. From a craniometric perspective, the most prominent point of the parietal tuberosity (Euryon) (white dot) corresponds to the superior-posterior aspect of the supramarginal gyrus; **D.** Posterior perspective of the occipital lobe in relation to the craniometric points. The parietooccipital sulcus, which represents the anterior border of the occipital lobe, is the point where the lambdoid suture joins the intraparietal suture (green dot). This point is identified approximately 6 cm above the inion (blue dot); with an additional 4 cm, the postcentral sulcus is anterior to which the primary sensory cortex (red) is identified. The most prominent point of the occipital lobe (opistocranium) (red dot) is related to the calcarine sulcus on the medial surface of the hemisphere and is approximately 1 cm above the inion [14, 24].

parietotemporal line had a length of 73 (ranging from 66 to 85) mm and was at 58.1 (ranging from 46 to 65) degrees with the base of the hemisphere and at 67 (ranging from 63 to 79) degrees with the interhemispheric fissure (IHF). The occipitotemporal line started 33.1 (ranging from 23 to 43) mm along the parietotemporal line and had an average length of 44.4 (ranging from 32 to 75) mm. From its Sylvian end, the inferior Rolandic point was an addition-

al 14.4 (ranging from 8 to 23) mm anteriorly. The intraparietal sulcus (the supero-posterior border of the angular gyrus) was identified along the parietotemporal line 52.4 (ranging from 35 to 72) mm from the base of the hemisphere and 24.9 (ranging from 16 to 29) mm from the IHF. The line connecting the preoccipital notch with the superior Rolandic point (SRP) demarked the motor cortex and most of the sensory cortex anteriorly. This line had a length of

46.0 (ranging from 37 to 52) mm and was 67 (ranging from 63 to 79) degrees with the parietotemporal line.

On the medial surface of the hemisphere, the calcarine fissure was identified at 8.5 (ranging from 6 to 13) mm, parietooccipital sulcus at 50.7 (ranging from 39 to 62) mm and SRP at 96.2 (ranging from 85 to 107) mm along the superior margin of the hemisphere from the base of the hemisphere. The calcarine-parietooccipital sulci junction was located 37.3 (ranging from 26 to 43) mm along the calcarine sulcus and 26.0 (ranging from 23 to 31) mm along the parietooccipital sulcus. Along the base of the occipital lobe, the most anterior point of the calcarine sulcus was identified at 58.1 (mean: 47 to 65) mm, just below the splenium of the corpus callosum. The parietooccipital sulcus was identified at 74.8 (ranging from 60 to 90) degrees with the superior margin of the hemisphere. On the medial surface, the resection trajectory was the end of the calcarine sulcus (through the precuneus), and this trajectory was 101.7 (ranging from 85 to 122) degrees with the superior margin of the hemisphere and identified at 41.5 (ranging from 36 to 44) mm.

The anterior border of the basal surface of the occipital lobe is formed by the oblique line connecting the end of the calcarine sulcus with the preoccipital notch. The width of the occipital lobe measured along the anterior border of the occipital lobe was 45 (ranging from 32 to 52) mm. The anterior border of the occipital lobe from the occipital pole runs from 50.5 (ranging from 45 to 58) mm laterally to 56.6 (ranging from 42 to 65) mm medially. This trajectory of the resection is at approximately 103.5 (ranging from 95 to 112) degrees to the lateral brain surface. When lobectomy targets the parietooccipital sulcus, approximately 67 (ranging from 65 to 70) degrees should be aimed in relation to the inferior border of the hemisphere.

White matter dissection

Lateral approach (Figs. 2, 3)

The arcuate fasciculus/superior longitudinal fasciculus (AF/SLF) complex was located anteriorly to the parietotemporal and preoccipital SRP lines. The shortest distance from the parietotemporal line to the AF/SLF complex was observed in the basal aspect of the hemisphere, close to the preoccipital notch. Superiorly, the distance was extended. The top of the vertical ramus of the AF/SLF complex was located approximately 17.3 (ranging from 13 to 23) mm anterior to the parietotemporal line, and this point is located 33.5 (ranging from 31 to 35) mm

above the preoccipital notch and 37.0 (ranging from 30 to 43) mm below the parietooccipital sulcus along the parietotemporal line. At the same level as the AF/SLF complex, the vertical occipital fascicle (VOF) was identified behind the parietotemporal lobe also running in the inferior to superior direction. Medial to the VOF and posterior to the AF/SLF complex, the long white matter tract running in the anterior-posterior direction was the SS identified at 22.8 (ranging from 19 to 29) mm from the cortex. Passing the SS, which has a width of 9.8 (ranging from 6 to 13) mm, opened the lateral ventricle. The tip of the occipital horn was located 3.8 (ranging from 0 to 8) mm posterior to the parietotemporal line. It is located 24.0 (ranging from 16 to 27) mm above the base of the occipital lobe and 32.4 (ranging from 29 to 35) mm in depth from the cortical surface. The medial surface of the hemisphere was an additional 25.8 (ranging from 23 to 31) mm from the occipital horn.

Posterior approach (Figs. 2, 4)

The occipital horn from the posterior approach was identified along the line parallel to the base of the occipital lobe, at the level of the calcarine sulcus at an angle of 31.8 (ranging from 25 to 37) degrees from the IHF at a depth of 39.0 (ranging from 34 to 44) mm. The vertical ramus of the AF/SLF complex was identified lateral to the occipital horn at a depth of 53.3 (ranging from 51 to 57) mm along the previous trajectory. This depth was an additional approximately 15 mm from the tip of the occipital horn. The AF/SLF complex was identified just lateral to the lateral ventricle and medial to the lateral surface of the hemisphere at 55.8 (ranging between 53 and 60) degrees in relation to the IHF. The mean height of the base of the occipital lobe below the occipital horn was 24.0 (ranging from 16 to 27) mm. The genu and superior short segment of the vertical ramus of the AF/SLF complex above the roof of the occipital horn were identified. The occipital horn of the lateral ventricle was identified from the superior end of the parietooccipital sulcus at 36.8 (ranging from 35 to 39) mm in the direction of approximately 49 (ranging from 46 to 53) degrees lateral and 87.5 (ranging from 80 to 90) degrees in relation to the brain surface in the anterior-posterior direction. The same point was identified 29.8 (ranging from 26 to 37) mm from the IHF at the level of the parietooccipital sulcus perpendicular to the IHF and at a depth of approximately 29.0 (ranging from 28 to 32) mm.

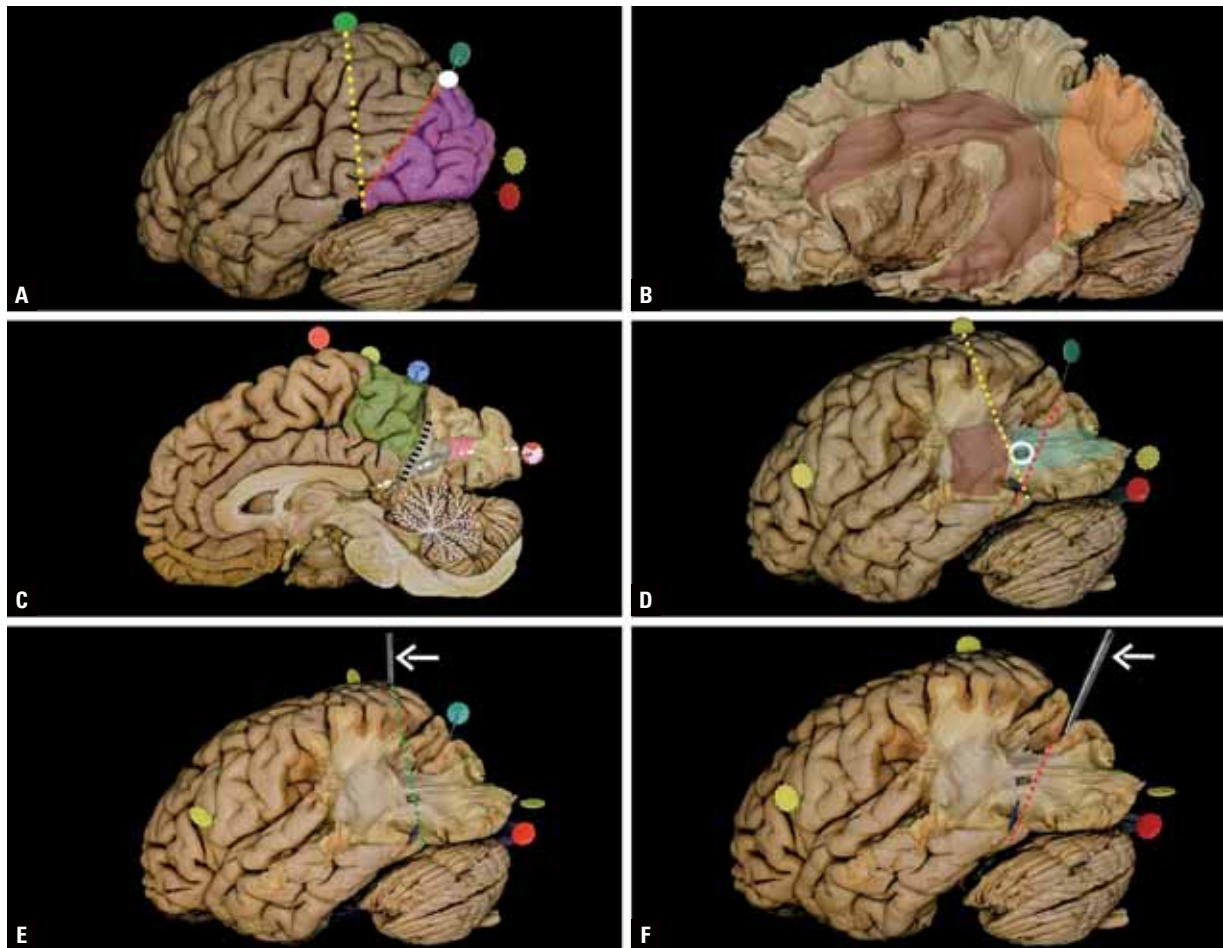


Figure 3. Lateral perspective of the approach to the occipital lobe; **A.** The occipital lobe (purple) is located behind the parietotemporal line (red dots), which is an artificial line marked at two ends by the parietooccipital sulcus (white dot) and preoccipital notch (black dot). Surgically, a line (yellow dots) should be set connecting the preoccipital notch with the superior Rolandic point (SRP) (green dot). This line allows us to stay posteriorly to the posterior segment of the superior temporal gyrus; to the motor cortex, most of the sensory cortex, and subcortically, this line is tangential to the arcuate fasciculus/superior longitudinal fasciculus (AF/SLF) complex; **B.** Laterally, most of the superficial layer of white matter fibres identified after u-fibre removal is formed by the AF/SLF complex (burgundy) and vertical occipital fasciculus (VOF) (orange); **C.** When occipital lobectomy is performed, the sledge runner fasciculus (black dots) and stratum calcarinum (pink) on the medial surface of the hemisphere are also resected. The stratum calcarinum is a white matter tract oriented vertically that connects two banks of the calcarine fissure (white square rectangular line). The sludge runner fascicle has an oblique trajectory and follows the trajectory of the parietooccipital sulcus, which separates the precuneus (green) from the occipital lobe; **D.** The only anatomical landmark that can be identified when occipital lobectomy is performed is the occipital horn (white circle) of the lateral ventricle. It is covered from lateral to medial by the u-fibres, VOF (orange on panel B) and sagittal stratum (SS) (light blue). Anterior to the parietotemporal line at the level of the VOF, lateral to the SS, the vertical ramus of the AF/SLF complex is identified. The line (yellow dots) connecting the preoccipital notch with the SRP is tangential to the most posterior aspect of the AF/SLF complex; **E.** The marker (white arrow) is placed at the end of the calcarine sulcus, just behind the splenium of the corpus callosum. The line (green dots) marks the trajectory of the extended occipital lobectomy (beyond the anatomical borders), which also involves the parietal lobe. This line is posterior to the line connecting the preoccipital notch with the SRP; thus, it is also located posteriorly to the AF/SLF complex; **F.** The marker (white arrow) is placed along the parietooccipital sulcus of the medial surface of the hemisphere. The trajectory of the anatomical occipital lobectomy follows the parietotemporal line.

DISCUSSION

We aimed to present the cortical and white matter anatomies related to occipital lobe surgery in terms of lesionectomies and occipital lobectomies. Gliomas limited exclusively to the occipital lobe have been reported rarely in the literature [7, 18, 29]. Depending on their lesion type, localisation, and the aim of surgery, occipital lobectomy or selective lesionectomy

can be performed. Awake craniotomy with intraoperative brain mapping and neuropsychological assessment in selected cases allows avoidance of optic radiation injury or extension of the anatomical occipital lobectomy to the functional lobectomy; this strategy likely plays an important role in occipital gliomas regarding the oncological outcome [21, 29]. The gyral and sulcal patterns of the occipital lobe

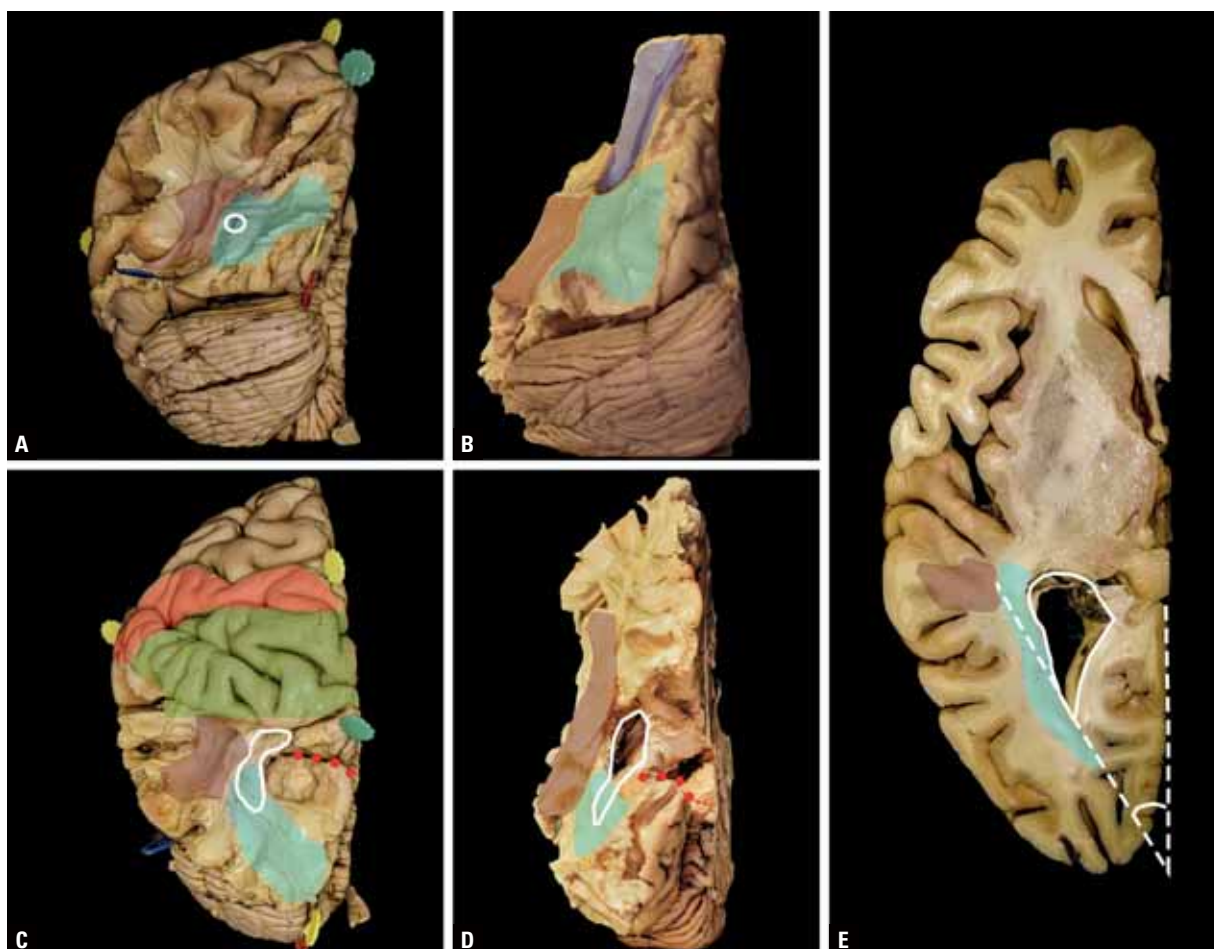


Figure 4. Posterior perspective of the approach to the occipital lobe; **A, B.** The posterior perspective of the white matter tracts within the occipital lobe. The occipital horn (white circle) is located medially to the sagittal stratum (SS) and arcuate fasciculus/superior longitudinal fasciculus (AF/SLF) complex (burgundy). The occipital horn of the lateral ventricle is the only anatomical landmark within the occipital lobe. The anterior-lateral border of the resection comprises the AF/SLF complex (burgundy). The thalamocortical tract anterior-medial to the AF/SLF complex (blue) is identified; **C, D.** Posterior-superior perspective of the white matter tracts within the occipital lobe. Medial to the SS (light blue) and lateral ventricle (white continuous line) despite the sledge runner fascicle running along the parietooccipital sulcus (red dots), no other white matter tracts are identified whose function can be tested intraoperatively. The anatomical resection of the occipital lobe can be extended anteriorly to the parietal lobe (green) up to the primary sensory cortex within the postcentral gyrus (red); **E.** Axial cut of the left hemisphere at the level of the occipital horn (white continuous line). The occipital horn (continuous white line) is identified at approximately 30 degrees (dashed line) with the interhemispheric fissure. The white matter tracts related to permanent neurological deficits of language, motor and visuospatial function are identified anteriorly. Lateral to the occipital horn, the SS (light blue) and AF/SLF complex (burgundy), which represent the anterior-lateral border of the resection, are identified.

show the greatest variabilities of all the lobes, and intraoperative identification of the specific gyri may be troublesome [1, 17, 23]. Identifying the preoccipital notch, parietooccipital sulcus, calcarine sulcus and SRP based on preoperative imaging may help a surgeon plan and perform occipital lobe surgery by setting artificial guiding lines. Anatomically, the anterior anatomical border of the occipital resection is based on the parietotemporal line. By definition, the parietotemporal line connects the preoccipital notch with the preoccipital sulcus, which are both located approximately 5 cm along the inferior and superior margins of the hemisphere. This line is approximately

7 cm long; at the preoccipital notch, it can be established at an angle of approximately 60 degrees with the base of the hemisphere and at 70 degrees with the IHF. In cases when preservation of the visual fields is expected or the aim of surgery is to extend the anatomical resection to the functional borders, brain mapping under awake conditions is required. To maximise the safety of awake brain mapping, stimulation of the sensorimotor cortex should be initiated to set the lowest parameters of the stimulation for the rest of the procedure [3, 9]. Laterally, the motor cortex and most of the primary sensory cortex, despite the short superior segment, were located anteriorly to

the artificial line between the preoccipital notch and SRP. This line is identified at approximately 70 degrees with the parietotemporal line. Subcortically, staying posterior to this line avoids the AF/SLF complex. The inferior Rolandic point, where the cortical motor and sensory representations of the face are expected, was identified 6 cm anterior to the parietotemporal line along the parietooccipital line (4.5 cm) and posterior part of the Sylvian fissure (1.5 cm). The intraoperative stimulation of the primary sensory cortex under awake conditions results in different types of sensory sensations, primarily tingling or numbness in the contralateral part of the body [3]. Using the posterior approach to identify the sensorimotor cortex, a craniotomy must be performed approximately 9 cm above the base of the occipital lobe within the parietal region [14, 24]. On the dominant hemisphere at the cortical level, the language cortical site, called Wernicke's area, represents the anterior border of the functional resection. Originally, this area was defined as the posterior part of the superior temporal gyrus; however, but based on intraoperative brain mapping, nearby regions with the inferior parietal lobule should also be considered [27]. Stimulation of these areas elicits anomia and paraphasias. Stimulation of basal occipitotemporal regions results in reading disorders or, in rare cases, music performance [10, 29]. The superior-posterior border of the inferior parietal lobule was located approximately 5 cm superior along the parietotemporal line from the preoccipital notch and 2.5 cm from the parietooccipital sulcus. The primary visual cortex around the calcarine sulcus is localised within the occipital lobe; injury to this region results in homonymous hemianopsia. Posteriorly, the primary visual cortex was located approximately 8 mm superior to the base of the hemisphere along the superior margin. It runs anteriorly almost parallel to the base of the hemisphere with a slight upward angle. Up to the junction with the parietooccipital sulcus, it is approximately 3.5 cm long; in total, it is 6 cm long to just below the splenium of the corpus callosum. The same point from the parietooccipital sulcus was located approximately 2.5 cm along the trajectory at approximately 65 degrees with the superior margin. When lobectomy up to the end of the calcarine (passing through the precuneus) is the goal, the trajectory must be performed at approximately 100 degrees and is reached at approximately 4.0 cm.

The anterior functional borders of the resection within the white matter regardless of the side are

the AF/SLF complex, cortico-spinal, or thalamo-cortical tracts. When the dominant hemisphere AF/SLF complex is stimulated, language deficits, such as phonemic paraphasias, are mainly observed [12, 15, 32]. In the nondominant hemisphere, the AF/SLF is related to visuospatial function, and its stimulation elicits rightward deviation during the line bisection test [2]. Laterally, the base of the vertical ramus of the AF/SLF complex was identified just in front of the preoccipital notch. Superiorly, this distance extended to approximately 2.0 cm from the parietotemporal line at the top of the vertical ramus of the SLF/AF complex. Stimulation of the most superficial layer of white matter posteriorly to the AF/SLF complex, just under the short u-fibres, may elicit pure alexia on the dominant side, a phenomenon that is related to VOF localisation [22, 33]. The AF/SLF complex represents the lateral limit posteriorly, while the thalamo-cortical tract represents the medial limit of the resection anteriorly; while the occipital horn is in the middle, between both. The anterior border of the resection was located approximately 5.5 cm from the occipital pole and 1.5 cm anteriorly to the tip of the occipital horn, which was identified at approximately 4.0 cm. The type of approach for selective lesionectomy within the occipital lobe is based mainly on the relationship of the lesion to the sagittal stratum. Within the sagittal stratum, three main functional bundles are identified: the inferior fronto-occipital fasciculus (IFOF), inferior longitudinal fasciculus and optic radiation [4, 6, 20]. Identification of the specific tracts within the sagittal stratum can be performed only based on intraoperative awake brain mapping [30]. When stimulating dominant IFOF, semantic paraphasias were observed while the non-dominant IFOF was tested in non-verbal semantic processing and face-based mentalising. Stimulation of the dominant inferior longitudinal fasciculus results in reading impairment and visual agnosia, is related primarily to visuospatial processing and plays a main role in face recognition and visual memory [12]. For both hemispheres, when visual field deficit testing is performed, the patient is instructed to note any loss of vision or blurriness, shadowing, or flashing lights during stimulation when optic radiation is mapped [8, 13]. This procedure aims to avoid hemianopsia, while quadrantanopsia is neglected by the patient in most cases [25]. The extent of resection in terms of visual field deficit should be discussed preoperatively with the patient and family to define the acceptable deficit in terms of oncologico-functional

balance [26]. When performing occipital lobectomy, the sledge runner fasciculus on the medial surface of the hemisphere should be considered [16, 28]. The result of intraoperative stimulation of this fascicle is not well known, but its function is related to spatial navigation and visuospatial imaging. Functional lobectomy is limited by intraoperative mapping, which cannot be assessed in anatomical studies. Additionally, the physical parameters of cadaveric brain tissue may not exactly present an intraoperative brain structure; for example, the size of the ventricles on cadavers, because of the lack of cerebrospinal fluid, cannot be correlated with the size in living patients. Because of the limited number of specimens used in the study, readers should carefully consider our results because we could not describe all possible variants of the anatomy. Additionally, the anatomical relationship between the structures in patients with tumours may be disturbed by the tumour mass or during tumour removal because of brain shifts.

CONCLUSIONS

Proper anatomical definition of a tumour within the occipital lobe, particularly in relation to the SS, is crucial for proper planning of lesionectomy. When occipital lobectomy is planned, a discussion about the oncological-functional balance with the patient is required. Despite optic radiation and the primary visual cortex within the occipital lobe, the functional limitation of the resection is based on direct cortical and subcortical brain mapping on the anterior border of the resection. The anterior border of the resection governs language, motor and visuospatial functions. The decision concerning the lateral or posterior approach is based mainly on the type of intraoperative brain mapping.

Acknowledgements

The authors wish to sincerely thank those who donated their bodies to science so that anatomical research could be performed.










Conflict of interest: None declared

REFERENCES

- Alves RV, Ribas GC, Párraga RG, et al. The occipital lobe convexity sulci and gyri. *J Neurosurg.* 2012; 116(5): 1014–1023, doi: [10.3171/2012.1.JNS11978](https://doi.org/10.3171/2012.1.JNS11978), indexed in Pubmed: [22339163](https://pubmed.ncbi.nlm.nih.gov/22339163/).
- Bartolomeo P, Thiebaut de Schotten M, Duffau H. Mapping of visuospatial functions during brain surgery: a new tool to prevent unilateral spatial neglect. *Neurosurgery.* 2007; 61(6): E1340, doi: [10.1227/01.neu.0000306126.46657.79](https://doi.org/10.1227/01.neu.0000306126.46657.79), indexed in Pubmed: [18162882](https://pubmed.ncbi.nlm.nih.gov/18162882/).
- Berger MS, Hadjipanayis CG. Surgery of intrinsic cerebral tumors. *Neurosurgery.* 2007; 61(1 Suppl): 279–304, doi: [10.1227/01.NEU.0000255489.88321.18](https://doi.org/10.1227/01.NEU.0000255489.88321.18), indexed in Pubmed: [18813160](https://pubmed.ncbi.nlm.nih.gov/18813160/).
- Chan-Seng E, Moritz-Gasser S, Duffau H. Awake mapping for low-grade gliomas involving the left sagittal stratum: anatomofunctional and surgical considerations. *J Neurosurg.* 2014; 120(5): 1069–1077, doi: [10.3171/2014.1.JNS132015](https://doi.org/10.3171/2014.1.JNS132015), indexed in Pubmed: [24484222](https://pubmed.ncbi.nlm.nih.gov/24484222/).
- Conner AK, Baker CM, Briggs RG, et al. A technique for resecting occipital pole gliomas using a keyhole lobectomy. *World Neurosurg.* 2017; 106: 707–714, doi: [10.1016/j.wneu.2017.06.181](https://doi.org/10.1016/j.wneu.2017.06.181), indexed in Pubmed: [28705703](https://pubmed.ncbi.nlm.nih.gov/28705703/).
- Di Carlo DT, Benedetto N, Duffau H, et al. Microsurgical anatomy of the sagittal stratum. *Acta Neurochir (Wien).* 2019; 161(11): 2319–2327, doi: [10.1007/s00701-019-04019-8](https://doi.org/10.1007/s00701-019-04019-8), indexed in Pubmed: [31363919](https://pubmed.ncbi.nlm.nih.gov/31363919/).
- Mandonnet E, Capelle L, Duffau H, et al. Preferential brain locations of low-grade gliomas. *Cancer.* 2004; 100(12): 2622–2626, doi: [10.1002/cncr.20297](https://doi.org/10.1002/cncr.20297), indexed in Pubmed: [15197805](https://pubmed.ncbi.nlm.nih.gov/15197805/).
- Duffau H, Velut S, Mitchell MC, et al. Intra-operative mapping of the subcortical visual pathways using direct electrical stimulations. *Acta Neurochir (Wien).* 2004; 146(3): 265–9; discussion 269, doi: [10.1007/s00701-003-0199-7](https://doi.org/10.1007/s00701-003-0199-7), indexed in Pubmed: [15015049](https://pubmed.ncbi.nlm.nih.gov/15015049/).
- Dziejdz T, Bernstein M. Awake craniotomy for brain tumor: indications, technique and benefits. *Expert Rev Neurother.* 2014; 14(12): 1405–1415, doi: [10.1586/14737175.2014.979793](https://doi.org/10.1586/14737175.2014.979793), indexed in Pubmed: [25413123](https://pubmed.ncbi.nlm.nih.gov/25413123/).
- Dziejdz TA, Bala A, Podgórska A, et al. Awake intraoperative mapping to identify cortical regions related to music performance: Technical note. *J Clin Neurosci.* 2021; 83: 64–67, doi: [10.1016/j.jocn.2020.11.027](https://doi.org/10.1016/j.jocn.2020.11.027), indexed in Pubmed: [33317886](https://pubmed.ncbi.nlm.nih.gov/33317886/).
- Dziejdz TA, Balasa A, Jeżewski MP, et al. White matter dissection with the Klingler technique: a literature review. *Brain Struct Funct.* 2021; 226(1): 13–47, doi: [10.1007/s00429-020-02157-9](https://doi.org/10.1007/s00429-020-02157-9), indexed in Pubmed: [33165658](https://pubmed.ncbi.nlm.nih.gov/33165658/).
- Fernández Coello A, Moritz-Gasser S, Martino J, et al. Selection of intraoperative tasks for awake mapping based on relationships between tumor location and functional networks. *J Neurosurg.* 2013; 119(6): 1380–1394, doi: [10.3171/2013.6.JNS122470](https://doi.org/10.3171/2013.6.JNS122470), indexed in Pubmed: [24053503](https://pubmed.ncbi.nlm.nih.gov/24053503/).
- Gras-Combe G, Moritz-Gasser S, Herbet G, et al. Intraoperative subcortical electrical mapping of optic radiations in awake surgery for glioma involving visual pathways. *J Neurosurg.* 2012; 117(3): 466–473, doi: [10.3171/2012.6.JNS111981](https://doi.org/10.3171/2012.6.JNS111981), indexed in Pubmed: [22794319](https://pubmed.ncbi.nlm.nih.gov/22794319/).
- Kendir S, Acar HI, Comert A, et al. Window anatomy for neurosurgical approaches. Laboratory investigation. *J Neurosurg.* 2009; 111(2): 365–370, doi: [10.3171/2008.10.JNS08159](https://doi.org/10.3171/2008.10.JNS08159), indexed in Pubmed: [19361260](https://pubmed.ncbi.nlm.nih.gov/19361260/).
- Komaitis S, Skandalakis GP, Kalyvas AV, et al. Dorsal component of the superior longitudinal fasciculus revisited:

- novel insights from a focused fiber dissection study. *J Neurosurg.* 2019; 132(4): 1265–1278, doi: [10.3171/2018.11.JNS182908](https://doi.org/10.3171/2018.11.JNS182908), indexed in Pubmed: [30835690](https://pubmed.ncbi.nlm.nih.gov/30835690/).
16. Koutsarnakis C, Kalyvas AV, Skandalakis GP, et al. Sledge runner fasciculus: anatomic architecture and tractographic morphology. *Brain Struct Funct.* 2019; 224(3): 1051–1066, doi: [10.1007/s00429-018-01822-4](https://doi.org/10.1007/s00429-018-01822-4), indexed in Pubmed: [30607495](https://pubmed.ncbi.nlm.nih.gov/30607495/).
 17. Koutsarnakis C, Komaitis S, Drosos E, et al. Mapping the superficial morphology of the occipital lobe: proposal of a universal nomenclature for clinical and anatomical use. *Neurosurg Rev.* 2021; 44(1): 335–350, doi: [10.1007/s10143-019-01212-2](https://doi.org/10.1007/s10143-019-01212-2), indexed in Pubmed: [31758336](https://pubmed.ncbi.nlm.nih.gov/31758336/).
 18. Larjavaara S, Mäntylä R, Salminen T, et al. Incidence of gliomas by anatomic location. *Neuro Oncol.* 2007; 9(3): 319–325, doi: [10.1215/15228517-2007-016](https://doi.org/10.1215/15228517-2007-016), indexed in Pubmed: [17522333](https://pubmed.ncbi.nlm.nih.gov/17522333/).
 19. Ludwig EKJ. *Atlas cerebri humani.* S Karger Basel, New York 1956.
 20. Maldonado IL, Destrieux C, Ribas EC, et al. Composition and organization of the sagittal stratum in the human brain: a fiber dissection study. *J Neurosurg.* 2021 [Epub ahead of print]: 1–9, doi: [10.3171/2020.7.JNS192846](https://doi.org/10.3171/2020.7.JNS192846), indexed in Pubmed: [33418529](https://pubmed.ncbi.nlm.nih.gov/33418529/).
 21. Nguyen HS, Sundaram SV, Mosier KM, et al. A method to map the visual cortex during an awake craniotomy. *J Neurosurg.* 2011; 114(4): 922–926, doi: [10.3171/2010.11.JNS101293](https://doi.org/10.3171/2010.11.JNS101293), indexed in Pubmed: [21235311](https://pubmed.ncbi.nlm.nih.gov/21235311/).
 22. Panesar SS, Belo JT, Yeh FC, et al. Structure, asymmetry, and connectivity of the human temporo-parietal aslant and vertical occipital fasciculi. *Brain Struct Funct.* 2019; 224(2): 907–923, doi: [10.1007/s00429-018-1812-0](https://doi.org/10.1007/s00429-018-1812-0), indexed in Pubmed: [30542766](https://pubmed.ncbi.nlm.nih.gov/30542766/).
 23. Rhoton A. *The cerebrum.* Anatomy. Neurosurgery. 2007; 61(1): SHC-37, doi: [10.1227/01.neu.0000255490.88321.ce](https://doi.org/10.1227/01.neu.0000255490.88321.ce).
 24. Ribas G, Yasuda A, Ribas E, et al. Surgical anatomy of microneurosurgical sulcal key points. *Operative Neurosurgery.* 2006; 59(suppl_4): ONS-177–ONS-211, doi: [10.1227/01.neu.0000240682.28616.b2](https://doi.org/10.1227/01.neu.0000240682.28616.b2).
 25. Sarubbo S, De Benedictis A, Milani P, et al. The course and the anatomic-functional relationships of the optic radiation: a combined study with ‘post mortem’ dissections and ‘in vivo’ direct electrical mapping. *J Anat.* 2015; 226(1): 47–59, doi: [10.1111/joa.12254](https://doi.org/10.1111/joa.12254), indexed in Pubmed: [25402811](https://pubmed.ncbi.nlm.nih.gov/25402811/).
 26. Tanaka T, Takei J, Teshigawara A, et al. Avoidance and improvement in visual field defect after surgery for metastatic brain tumors in the parietal and the occipital lobe. *World Neurosurg.* 2021; 155: e847–e857, doi: [10.1016/j.wneu.2021.09.029](https://doi.org/10.1016/j.wneu.2021.09.029), indexed in Pubmed: [34530147](https://pubmed.ncbi.nlm.nih.gov/34530147/).
 27. Vanacôr CN, Isolan GR, Yu YH, et al. Microsurgical anatomy of language. *Clin Anat.* 2021; 34(1): 154–168, doi: [10.1002/ca.23681](https://doi.org/10.1002/ca.23681), indexed in Pubmed: [32918507](https://pubmed.ncbi.nlm.nih.gov/32918507/).
 28. Vergani F, Mahmood S, Morris CM, et al. Intralobar fibres of the occipital lobe: a post mortem dissection study. *Cortex.* 2014; 56: 145–156, doi: [10.1016/j.cortex.2014.03.002](https://doi.org/10.1016/j.cortex.2014.03.002), indexed in Pubmed: [24768339](https://pubmed.ncbi.nlm.nih.gov/24768339/).
 29. Viegas C, Moritz-Gasser S, Rigau V, et al. Occipital WHO grade II gliomas: oncological, surgical and functional considerations. *Acta Neurochir (Wien).* 2011; 153(10): 1907–1917, doi: [10.1007/s00701-011-1125-z](https://doi.org/10.1007/s00701-011-1125-z), indexed in Pubmed: [21842441](https://pubmed.ncbi.nlm.nih.gov/21842441/).
 30. Wolfson R, Soni N, Shah AH, et al. The role of awake craniotomy in reducing intraoperative visual field deficits during tumor surgery. *Asian J Neurosurg.* 2015; 10(3): 139–144, doi: [10.4103/1793-5482.161189](https://doi.org/10.4103/1793-5482.161189), indexed in Pubmed: [26396597](https://pubmed.ncbi.nlm.nih.gov/26396597/).
 31. Wysiadecki G, Clarke E, Polguj M, et al. Klingler’s method of brain dissection: review of the technique including its usefulness in practical neuroanatomy teaching, neurosurgery and neuroimaging. *Folia Morphol.* 2019; 78(3): 455–466, doi: [10.5603/FM.a2018.0113](https://doi.org/10.5603/FM.a2018.0113), indexed in Pubmed: [30536356](https://pubmed.ncbi.nlm.nih.gov/30536356/).
 32. Wysiadecki G, Mazurek A, Walocha J, et al. Revisiting the morphology and classification of the paracingulate gyrus with commentaries on ambiguous cases. *Brain Sci.* 2021; 11(7), doi: [10.3390/brainsci11070872](https://doi.org/10.3390/brainsci11070872), indexed in Pubmed: [34210078](https://pubmed.ncbi.nlm.nih.gov/34210078/).
 33. Yeatman JD, Weiner KS, Pestilli F, et al. The vertical occipital fasciculus: a century of controversy resolved by in vivo measurements. *Proc Natl Acad Sci U S A.* 2014; 111(48): E5214–E5223, doi: [10.1073/pnas.1418503111](https://doi.org/10.1073/pnas.1418503111), indexed in Pubmed: [25404310](https://pubmed.ncbi.nlm.nih.gov/25404310/).
 34. Zemmoura I, Blanchard E, Raynal PI, et al. How Klingler’s dissection permits exploration of brain structural connectivity? An electron microscopy study of human white matter. *Brain Struct Funct.* 2016; 221(5): 2477–2486, doi: [10.1007/s00429-015-1050-7](https://doi.org/10.1007/s00429-015-1050-7), indexed in Pubmed: [25905864](https://pubmed.ncbi.nlm.nih.gov/25905864/).

Safety window for the transsphenoidal approach for pituitary tumours: a computed tomographic angiography study

F.J. Arrambide-Garza^{1*} , P.P. Zarate-Garza^{1*} , K. Aguilar-Morales¹ ,
I.S. Villarreal-del-Bosque² , A. Quiroga-Garza¹ , A. Gómez-Sánchez¹ ,
R. Pinales-Razo² , R.E. Elizondo-Omaña¹ , S. Guzmán-López¹ 

¹Universidad Autónoma de Nuevo León, School of Medicine, Human Anatomy Department, Monterrey, Nuevo León, México

²Universidad Autónoma de Nuevo León, University Hospital “Dr. José Eleuterio González”, Radiology and Imaging Department, Monterrey, Nuevo León, México

[Received: 7 October 2021; Accepted: 5 November 2021; Early publication date: 16 November 2021]

Background: The aims are to evaluate the morphometry of the sellar region and propose a safety window on the floor of the sella turcica for the transsphenoidal approach in a Hispanic population.

Materials and methods: We retrospectively analysed 150 computed tomographic angiography sellar region images from asymptomatic patients. The images were evaluated intraobservatory by an expert radiologist. We measured: intercarotid distance of cavernous segment; depth of sella turcica; skull base angle; anterior distance, the distance between anterior spinal nasal and floor of the sella turcica; posterior distance, the distance between anterior spinal nasal and posterior wall of the sella turcica; anterior surgical angle, formed between the floor of the nostril and superior limit of the anterior wall of the sella turcica; and posterior angle, formed between the floor of the nostril and the inferior limit of the posterior wall of the sella turcica.

Results: Safety window was based on two measures: the intercarotid distance and depth. The mean of the safety window is 151.13 mm² and 147.60 mm² for men and women, respectively. The intercarotid distance was 17.83 mm. The depth of the sella turcica was 8.46 mm. The skull base angle was 112.13 grades. The anterior distance was 76.34 mm. The posterior distance was 87.59 mm. The anterior surgical angle was 32.76 grades. The posterior surgical angle was 87.59 grades. *Conclusions:* The surgical approach space is smaller in females. It could signifi- cate a more complicated surgery in this population. Anatomical understanding could reduce complications in hospitals without a neuronavigation system. (Folia Morphol 2023; 82, 1: 17–23)

Key words: computed tomographic, internal carotid artery, safety window, sella turcica, transsphenoidal surgery

Address for correspondence: S. Guzmán-López, MD, PhD or R.E. Elizondo-Omaña, MD, PhD, Human Anatomy Department, Faculty of Medicine and University Hospital “Dr. José Eleuterio González”, Universidad Autónoma de Nuevo León (UANL), Monterrey, Nuevo León, México, tel: +52 (81)83-29-41-71, e-mails: dr.santos.anato@gmail.com or rod_omana@yahoo.com

*Both authors participated equally in the study, and both should be considered in the position of first author.

This article is available in open access under Creative Common Attribution-Non-Commercial-No Derivatives 4.0 International (CC BY-NC-ND 4.0) license, allowing to download articles and share them with others as long as they credit the authors and the publisher, but without permission to change them in any way or use them commercially.

INTRODUCTION

The pituitary gland is a structure located in the middle cranial fossa, inside in the sella turcica [14, 15]. It is conformed by the tuberculum sellae, the hypophyseal fossa, and the dorsum sellae [10, 24]. It is reported that 19% of central nervous system tumours originate in the sellar region and pituitary adenomas are the most common tumours in this region [3]. The general prevalence of pituitary adenomas is 16.7% [11]. These tumours are classified as microadenomas when their size is less than 10 mm, and as macroadenomas when their size is greater than 10 mm [12, 19, 20]. Treatment options include endoscopic endonasal transsphenoidal surgery (EETS), which is reserved mainly for patients whose symptoms are associated with tumour size, tumour invasion to adjacent structures, and tumours that do not respond to drug treatment [8, 23].

Endoscopic endonasal transsphenoidal surgery is divided into nasal, sphenoidal, and sellar phases. The opening of the sellar floor and the resection of the tumour is performed in the sellar phase. It is a challenging procedure due to the complexity of the anatomical region and the limited surgical area [1, 5]. Common complications include intercavernous sinus bleeding and internal carotid artery (ICA) laceration [6, 9, 13]. Part of the ICA is located inside the cavernous venous sinus until it passes through the dura mater that forms the roof of the venous sinus [7, 28]. A thorough understanding of the nasal cavity and middle cranial fossa is needed to improve patient safety during these procedures. This study aims to evaluate the morphometry of the region and propose a safety window on the floor of the sella turcica.

MATERIALS AND METHODS

An observational, cross-sectional, retrospective and descriptive study was performed. Computed tomographic angiography (CTA) studies were obtained from the database of the Radiology and Imaging Department of the University Hospital between April 2015 and July 2018. Sampling was done in consecutive cases. Studies from Hispanic patients from north-east of México with an age between 18 and 86 who underwent a head and neck CTA indicated by their treating physician. We categorised the population into groups according to their sex. Those patients with sellar or parasellar disease, central nervous system vascular disease, previous cranial surgery, or

other central nervous system diseases that may alter anatomy, were excluded. Studies with abnormalities or artefacts were eliminated.

Study technique

We used a 64-slice computed tomography (General Electric CT99 Light Speed VCT), Software 12HW14.6, using the following parameters: rotation of 0.4 s helical acquisition, coverage of detectors of 20 mm, 120 kV, 400 more, cutting thickness of 0.625 mm, Pitch of 0.53:1 mm/rot, and field of view from 22 to 23 cm. All the imaging data was uploaded to the Carestream Vue PACS and analysed in coronal and sagittal planes for the following parameters (Fig. 1):

- intercarotid distance: the smallest distance between medial walls of the cavernous segment of ICA;
- depth of sella turcica: the greatest distance between the floor and a perpendicular line connecting the tuberculum and dorsum;
- skull base angle: the angle formed between the planum clival and the clivus;
- anterior surgical angle: the angle formed between the floor of the nostril and the superior limit of the anterior wall of the sella turcica;
- posterior surgical angle: the angle formed between the floor of the nostril and the inferior limit of the posterior wall of the sella turcica;
- anterior distance: the distance between the anterior nasal spine and the midpoint of the anterior wall of the sella turcica;
- posterior distance: the distance between the anterior nasal spine and the superior border of the posterior wall of the sella turcica;
- safety window of the sella turcica: an area based on intercarotid distance and depth of sella turcica.

All parameters were measured twice by a head and neck expert radiologist using a 5 stage zoom and recorded in a database using millimetres with two decimal unit precision. We considered measurements of the intercarotid distance of cavernous segment, skull base angle, and depth of sella turcica from other published papers. All authors agreed to use bone and vascular landmarks to determine the safety window, such as sphenoid bone and ICA. We used a sagittal and coronal plane for all measurements. The first sagittal plane was aligned with the anterior nasal spine, to include all structures within the same plane. The coronal plane was used to measure the smallest distance between the medial walls of the cavernous

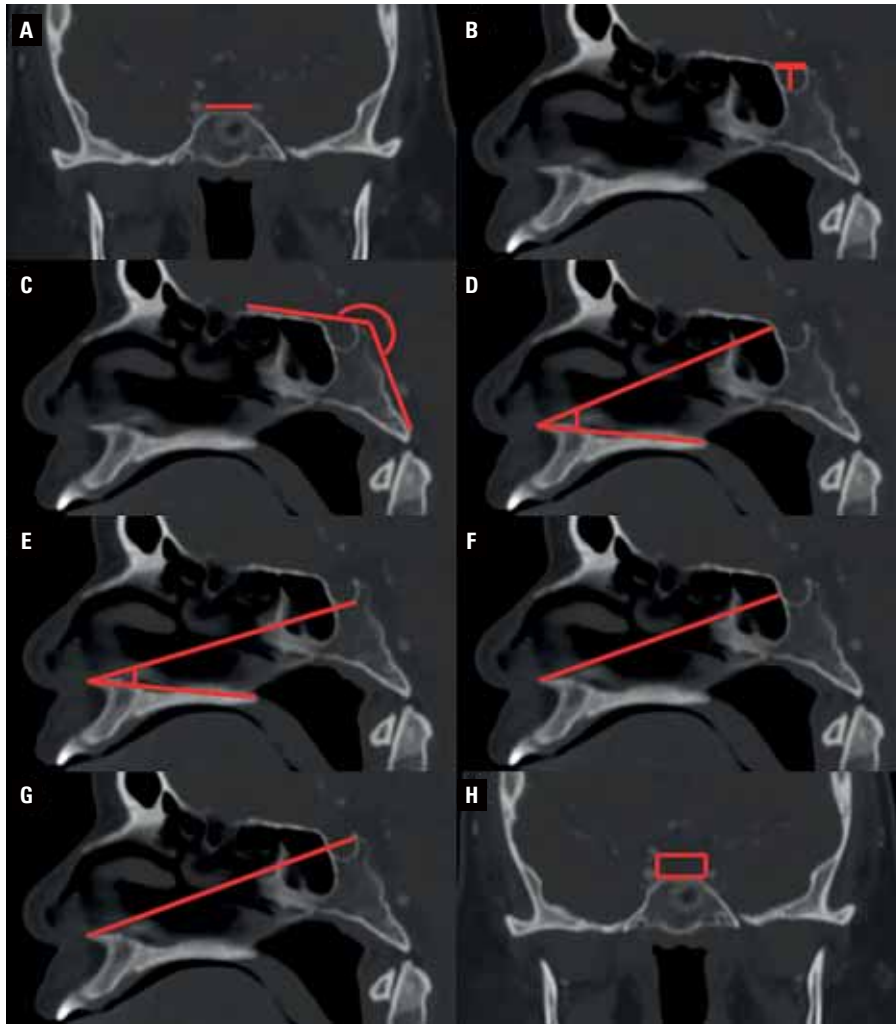


Figure 1. Parameters analysed in coronal and sagittal planes in the sellar region; **A.** Coronal plane in the sellar region. The intercarotid distance is defined as the smallest distance between the inner walls of the cavernous segment of the internal carotid artery; **B–G.** Sagittal plane aligned with the anterior nasal spine. **B.** Sagittal plane. Depth of sella turcica: the greatest distance between the floor and a perpendicular line connecting the tuberculum and dorsum; **C.** Sagittal plane. Skull base angle: the angle formed between the planum clivale and the clivus; **D.** Sagittal plane. Anterior surgical angle: the angle formed between the floor of the nostril and upper limit of the anterior wall of the sella turcica; **E.** Sagittal plane. Posterior surgical angle: the angle formed between the floor of the nostril and the lower limit of the posterior wall of the sella turcica; **F.** Shows the anterior surgical distance: the distance between the anterior nasal spine and the anterior wall of the sella turcica; **G.** Sagittal plane. Posterior surgical distance: the distance between the anterior nasal spine and the upper border of the posterior wall of the sella turcica; **H.** Coronal plane. Safety window on the floor of the sella turcica.

segment of ICA. Once the planes were established, the measurements were manually plotted and adjusted for accuracy by an expert radiologist. All variables were measured, and the process blinded when repeated in the same patient to establish satisfactory intraobserver variability ($\kappa > 0.80$).

Statistical analysis

The database was analysed using the SPSS Version 24.0 programme for Windows 10 (IBM, Armonk, NY, USA). The normality test was performed using the Kolmogorov-Smirnov test. The mean and

standard deviation for each parameter was determined independently. A t Student test was used to determine the statistical significance for the parametric data between men vs. women, and Pearson's ρ correlation test for age and each variable. Mann-Whitney U and Kruskal-Wallis were performed for the nonparametric data. The p-value of 0.05 was set for statistical significance. Subsequent statistical tests were performed on age subcategorisations or classification by skull base angle categorisation using ANOVA test with post hoc adjusted with Tukey and Bonferroni.

Table 1. Measurements for both sexes

Measurement	General (n = 150)	Males (n = 77)	Females (n = 73)	P-value
Intercarotid distance [mm]	17.83 ± 4.28	18.81 ± 4.29	16.75 ± 4.11	0.003*
Depth of sella turcica [mm]	8.46 ± 1.34	8.05 ± 1.19	8.85 ± 1.44	< 0.001*
Anterior angle approach [°]	32.76 ± 2.95	32.47 ± 2.80	33.04 ± 3.20	0.244
Posterior angle approach [°]	25.13 ± 3.09	25.40 ± 2.83	24.84 ± 3.36	0.265
Skull base angle [°]	112.13 ± 7.68	111.74 ± 7.18	112.58 ± 8.19	0.507
Anterior distance [mm]	76.34 ± 5.27	79.52 ± 4.52	72.99 ± 3.82	< 0.001*
Posterior distance [mm]	87.59 ± 5.21	90.43 ± 4.97	84.55 ± 3.48	< 0.001*
Area [mm ²]	149.36 ± 38.90	151.13 ± 36.96	147.60 ± 41.06	0.581

Data are shown as mean ± standard deviation. *Statistical significance

Ethical considerations

This study was previously reviewed and approved by the University's Ethics and Research Committees with the registration number AH19-00002 on April 25, 2019, making sure it adheres to the Helsinki declaration and national and international standards of research. The authors declare no financial or commercial gain for the realisation of this study. Also, the authors declare no conflict of interest. None of the imaging studies were performed for the purposes of this study.

RESULTS

We retrospectively reviewed 150 head and neck CTA with a mean age of 53.51 ± 15.9 (range 18–86 years). The sample was stratified by gender with 77 (51.3%) men with a mean age of 53.21 ± 15.2 years, and 73 (48.7%) women with a mean age of 53.85 ± 16.69.

Descriptive statistics are shown in Table 1. Significant differences between sexes were found in the intercarotid distance, depth, and the anterior and posterior distances. All distances were smaller in women, except for the depth.

Statistical tests were performed for comparison between subcategorised age groups divided into ranks by decades however no statistical significance was found among the groups. Correlation tests were performed by Pearson correlation coefficient finding the following values: intercarotid distance –0.136, the height of the sella turcica 0.122, anterior surgical angle 0.127, posterior surgical angle 0.089, skull base angle –0.140, anterior distance –0.52, posterior distance –0.004, and area –0.028.

Skull base angle

Subcategorisation was performed at the skull base angle. These were divided into horizontal (> 121°) with 24 (15.6) patients, normal (120–105°)

with 106 (70.6%) patients, and vertical (< 104°) with 20 (13.3%) patients without statistical difference between them.

DISCUSSION

Endoscopic endonasal transsphenoidal surgery has been developed in the last 10 years, currently improving outcomes due to a better understanding of the local anatomy, and technological and surgical advancement. A clear example is the neuronavigation system. It consists of a set of computer-assisted technologies to guide the surgeon within the skull, providing the best surgical planning/safety, and decreasing trans-operating complications. The use of this system is recommended in all neurosurgical approaches. The image-guided neurosurgery is used to perform tumour resection, treatment of vascular disease, epilepsy surgery, and biopsies. During the surgery, the neuronavigation system permits a precise localisation of the region of interest and it also allows the visualisation of the instrument movements inside the skull. It helps to determine the difference between the healthy brain and the pathologic process that could be undifferentiated in a macroscopic view [29]. Although the neuronavigation improves the neurosurgical performance, anatomical knowledge is still essential for a precise surgery.

Intercarotid distance and depth of the sella turcica determines a corridor for the EETS and others skull base surgeries. Different methods have been used for estimate it, these variables may be measured using CTA as a reproducible method. Our findings show differences between sexes in the intercarotid distance, depth, anterior and posterior distance. This data suggests a smaller space for women during the surgical approach. Moreover, all these findings are of importance due to differences with other pop-

Table 2. Comparative with other studies

Measurement	Arrambide-Garza et al. (2020)	Nunes et al. (2015)	Mascarella et al. (2015)	Shrestha et al. (2018)
Country	México	Brazil	Canada	Nepal
Imaging study	CTA	MRI	CTA	Radiograph
Sample size	150	20	34	40
Intercarotid distance [mm]	17.83 ± 4.28	19.41 ± 3.00	17.3 ± 0.8	ND
Depth [mm]	8.46 ± 1.34	ND	ND	6.40 ± 0.92
Anterior angle approach [°]	32.76 ± 2.95	ND	ND	ND
Posterior angle approach [°]	25.13 ± 3.09	ND	ND	ND
Anterior distance [mm]	76.34 ± 5.27	ND	ND	ND
Posterior distance [mm]	87.59 ± 5.21	ND	ND	ND
Area [mm ²]	149.36 ± 38.90	ND	ND	ND

Data are shown as mean ± standard deviation. CTA — computed tomographic angiography; MRI — magnetic resonance imaging; ND — not described

Table 3. Classification of planum-clival angle type and comparative with another study

Measurement	Arrambide-Garza et al. (2020)	Alkherayf et al. (2015)
Country	México	Canada
Sample size	150	89
Skull base angle type A	25 (15.6%)	15 (17%)
Skull base angle type B	106 (70.6%)	61 (69%)
Skull base angle type C	20 (13.3%)	13 (15%)

ulations (Tables 2, 3). Implementing these findings improve the knowledge of base skull anatomy and could help in the planning of transsphenoidal surgery in those hospitals where a neuronavigation system is not available.

Relevance for the surgical practice

The sellar region is limited from above by the circle of Willis and chiasm, laterally by cavernous sinuses, and posteriorly by the brainstem, basilar artery, and its branches [25]. EETS can be divided into three phases, nasal, sphenoidal, and sellar, each one with possible complications. In most cases, the surgeon performs the surgery only with anatomical orientation, therefore, we considered the following information is useful to increase the anatomic understanding for each phase.

Nasal and sphenoidal phase. The nasal phase consists of advancing with the endoscope through the floor of the nostril towards the choana; subsequently, the ethmoidal recess is identified, and the posterior portion of the nasal septum is removed. In the sphenoidal phase, the anterior wall of the sphenoidal sinus is removed. Within the sphenoidal sinus,

the floor of the sella turcica should be delimited, including the sphenoidal plane, clivus, the protrusions of both carotid arteries, and the prominence of the optic nerves [4].

Landmarks have been reported to orient the surgical intranasal trajectory. Misalignment during the trajectory could increase the length of the procedure that could lead to a more difficult surgical approach [2]. Alkherayf et al. [2] described a classification of the skull base angle that recommends the head position during the EETS that determines a direct surgical intranasal trajectory. The angle was classified into three types: a) > 121° is related with a horizontally oriented sella, requiring 10 or 20 degrees of neck flexion; b) 105–120° requiring neutral head position for a standard sphenoidectomy; and c) < 104° associated with a vertical oriented sella, this type requires 10 or 20 degrees of neck extension. The skull base angle (Fig. 1C) in our study reveals that type B (105–120°) is the most common (70.6%), requiring neutral head positioning with the standard sphenoidectomy, similar data as Alkherayf et al. [2] in the Canadian population (Table 3). This would permit an adequate surgical exposure and a better tumour resection. Although this classification does not supplant the image guidance, it is a practical orientation method for neurosurgeons [2].

The sellar region is limited by a small space. We propose the anterior and posterior surgical angles that correspond to the anterior and posterior limits of the sella turcica in a sagittal plane (Fig. 1D, E) to determine the angle approach in the surgery and limit the space of the sellar region, therefore, the surgeon would not reach the anterior or posterior cranial fossa. The superior limit of the anterior aspect

of the sella turcica, and the inferior limit of the dorsum sellae, respectively. Our results show an anterior surgical angle of $32.47 \pm 2.80^\circ$ and posterior surgical angle of $25.40 \pm 2.83^\circ$ for males, with a range of motion of 7.02 degrees. In females, the anterior and posterior angles approach were $33.04 \pm 3.19^\circ$ and $24.84 \pm 3.36^\circ$, respectively, with a range of motion of 8.2 degrees. We do not obtain statistical differences between sexes.

We also propose the anterior distance which oriented the interval between the sphenoid bone and the anterior nasal spine. We obtain statistical differences in the anterior distance between sexes (Fig. 1F) is 79.52 mm in males, and 72.99 mm in females. Exist roughly 10 mm of difference between sexes to reach the sellar region that suggest a more distance in males and it could help in surgical planning.

Sellar phase. The surgeon opens the sellar floor and the resection of the tumour is performed [4]. The most important complication in this phase is the intrasellar haemorrhage due to a laceration of the ICA, which can potentially result in death [26]. We described a safety window based on two measures: the intercarotid distance and depth.

Lin et al. [16] determined a correlation between the intercarotid distance in the cavernous segment and non-functional pituitary macroadenomas treated with EETS, as these modify the position of non-bone structures. Our findings are from healthy patients, therefore, can be only applied in microadenomas due to the anatomy is respected. We report a mean intercarotid distance (Fig. 1A) in the sellar region of 17.83 mm, similar data as Mascarella et al. [17] who reported a mean of 17.3 mm using CTA in a Canadian population (Table 2). However, Nunes et al. [21] reported a larger mean of 19.41 mm in the Brazilian population using enhanced-magnetic resonance imaging (Table 2). These differences could be related to the method used to measure the intercarotid distance and ethnic differences among the population.

We did not obtain a statistical difference between sexes in the depth of the sella turcica but, we measured roughly 1 cm of difference, in males 8.05 mm and 8.85 mm in women. This data determines the range motion in a vertical plane within sella turcica, a higher height in females could be an advantage during EETS. The mean depth of the sella turcica of our study (Fig. 1B) was 8.46 ± 1.34 mm, larger than the reported 6.40 ± 1.21 by Shrestha et al. [26] in the Nepal population. This extra 25% of depth in our population,

allows the surgeon more space for the incision and a possible advantage in the performing of the procedure. These differences between the populations are attributed to genetics and environmental factors.

The safety window on the floor of the sella turcica is 151.13 ± 36.96 mm² and 147.60 ± 41.06 mm² for males and females, respectively (Fig. 1H). The intercarotid distance has an important role in EETS, it determines the space for the surgery. We obtain statistical differences in the intercarotid distance between sexes, 18.81 mm in males and 16.75 mm in females. It is also important to consider gender, as women tend to have a higher prevalence of adenomas and smaller distances and areas, the surgical approach could be more difficult in females than males [18].

We can find the thalamoperforating arteries posterior to the sellar region. These arteries supply irrigation to the midbrain and thalamus [22, 27, 30] and are a potential complication when the tumour is being removed. To avoid these arteries, we propose an anatomic reference, the posterior distance that is the distance to reach the dorsum sellae from the anterior nasal spine (Fig. 1G). We obtained statistical differences between sexes in the posterior distance, the mean is 90.43 ± 4.97 mm in men and 84.55 ± 3.48 mm in women.

Strengths and limitations

Our study provides useful information for a better anatomical understanding of the nasal fossa and middle cranial fossa. Nonetheless, there are some limitations. Some of the measurements have not been validated by other studies, such as anterior and posterior approach angles, safety window, anterior and posterior distances. The measurements obtained by imaging are constant with bone structures, which may not be the case in the patient's anatomy due to soft tissue. The patients' anthropometric characteristics were not included in the analysis. The study population only includes Hispanic patients, therefore, further data is needed to compare results with other populations. Morphometric parameters reported are from normal sellar anatomy. Patients that require a transsphenoidal approach to the sellar region may present distorted anatomy due to large tumours like pituitary macroadenomas, therefore results are most useful to guide surgeons in smaller pathologies, such as pituitary microadenomas. Future studies could analyse differences between patients with sellar and parasellar tumours, to compare with a control group.

CONCLUSIONS

The differences in the variables measured between sexes are important due to greater difficulty in the female population because the surgical approach space is smaller and a higher prevalence of pituitary adenomas. Understanding the morphometrical variations of the sella turcica improves the anatomical knowledge for radiologists and neurosurgeons in preoperative planning.

Acknowledgements




We thank all authors for revision and writing assistance. Further, we thank Alejandro Quiroga Garza for providing language help and guidance in the writing process.

Conflict of interest: None declared

REFERENCES

- Ajler P, Hem S, Goldschmidt E, et al. [Endoscopic transnasal surgery for pituitary adenomas]. *Surg Neurol Int.* 2012; 3(Suppl 6): S389–S394, doi: [10.4103/2152-7806.104403](https://doi.org/10.4103/2152-7806.104403), indexed in Pubmed: [23596553](https://pubmed.ncbi.nlm.nih.gov/23596553/).
- Alkherayf F, Edem I, Ouattara JM, et al. Planum-Clival angle classification: a novel preoperative evaluation for sellar/parasellar surgery. *J Neurol Surg B Skull Base.* 2015; 76(4): 316–322, doi: [10.1055/s-0035-1549002](https://doi.org/10.1055/s-0035-1549002), indexed in Pubmed: [26225323](https://pubmed.ncbi.nlm.nih.gov/26225323/).
- Anaya-Delgado G, de Juambelz-Cisneros PP, Fernández-Alvarado B, et al. [Prevalence of central nervous system tumours and histological identification in the operated patient: 20 years of experience]. *Cir Cir.* 2016; 84(6): 447–453, doi: [10.1016/j.circir.2016.01.004](https://doi.org/10.1016/j.circir.2016.01.004), indexed in Pubmed: [27094784](https://pubmed.ncbi.nlm.nih.gov/27094784/).
- Cappabianca P, Cavallo L, de Divitiis E. Endoscopic endonasal transsphenoidal surgery. *Neurosurgery.* 2004; 55(4): 933–941, doi: [10.1227/01.neu.0000137330.02549.0d](https://doi.org/10.1227/01.neu.0000137330.02549.0d).
- Cavallo LM, Somma T, Solari D, et al. Endoscopic endonasal transsphenoidal surgery: history and evolution. *World Neurosurg.* 2019; 127: 686–694, doi: [10.1016/j.wneu.2019.03.048](https://doi.org/10.1016/j.wneu.2019.03.048), indexed in Pubmed: [31266131](https://pubmed.ncbi.nlm.nih.gov/31266131/).
- Charalampaki P, Ayyad A, Kockro RA, et al. Surgical complications after endoscopic transsphenoidal pituitary surgery. *J Clin Neurosci.* 2009; 16(6): 786–789, doi: [10.1016/j.jocn.2008.09.002](https://doi.org/10.1016/j.jocn.2008.09.002), indexed in Pubmed: [19289287](https://pubmed.ncbi.nlm.nih.gov/19289287/).
- Chin OY, Ghosh R, Fang CH, et al. Internal carotid artery injury in endoscopic endonasal surgery: A systematic review. *Laryngoscope.* 2016; 126(3): 582–590, doi: [10.1002/lary.25748](https://doi.org/10.1002/lary.25748), indexed in Pubmed: [26525334](https://pubmed.ncbi.nlm.nih.gov/26525334/).
- Christian E, Harris B, Wrobel B, et al. Endoscopic endonasal transsphenoidal surgery: implementation of an operative and perioperative checklist. *Neurosurg Focus.* 2014; 37(4): E1, doi: [10.3171/2014.7.FOCUS14360](https://doi.org/10.3171/2014.7.FOCUS14360), indexed in Pubmed: [25270128](https://pubmed.ncbi.nlm.nih.gov/25270128/).
- Deng X, Chen S, Bai Ya, et al. Vascular complications of intercavernous sinuses during transsphenoidal surgery: an anatomical analysis based on autopsy and magnetic resonance venography. *PLoS One.* 2015; 10(12): e0144771, doi: [10.1371/journal.pone.0144771](https://doi.org/10.1371/journal.pone.0144771), indexed in Pubmed: [26658152](https://pubmed.ncbi.nlm.nih.gov/26658152/).
- Di Iorgi N, Morana G, Gallizia AL, et al. Pituitary gland imaging and outcome. *Endocr Dev.* 2012; 23: 16–29, doi: [10.1159/000341736](https://doi.org/10.1159/000341736), indexed in Pubmed: [23182817](https://pubmed.ncbi.nlm.nih.gov/23182817/).
- Ezzat S, Asa SL, Couldwell WT, et al. The prevalence of pituitary adenomas: a systematic review. *Cancer.* 2004; 101(3): 613–619, doi: [10.1002/cncr.20412](https://doi.org/10.1002/cncr.20412), indexed in Pubmed: [15274075](https://pubmed.ncbi.nlm.nih.gov/15274075/).
- Go JL, Rajamohan AG. Imaging of the Sella and Parasellar Region. *Radiol Clin North Am.* 2017; 55(1): 83–101, doi: [10.1016/j.rcl.2016.09.002](https://doi.org/10.1016/j.rcl.2016.09.002), indexed in Pubmed: [27890190](https://pubmed.ncbi.nlm.nih.gov/27890190/).
- Hofstetter CP, Shin BJ, Mubita L, et al. Endoscopic endonasal transsphenoidal surgery for functional pituitary adenomas. *Neurosurg Focus.* 2011; 30(4): E10, doi: [10.3171/2011.1.FOCUS10317](https://doi.org/10.3171/2011.1.FOCUS10317), indexed in Pubmed: [21456921](https://pubmed.ncbi.nlm.nih.gov/21456921/).
- Hong GK, Payne SC, Jane JA. Anatomy, physiology, and laboratory evaluation of the pituitary gland. *Otolaryngol Clin North Am.* 2016; 49(1): 21–32, doi: [10.1016/j.otc.2015.09.002](https://doi.org/10.1016/j.otc.2015.09.002), indexed in Pubmed: [26614827](https://pubmed.ncbi.nlm.nih.gov/26614827/).
- Korkmaz M, Yildirim AE, Osun A, et al. Endoscopic endonasal transsphenoidal pituitary surgery: experience of 80 cases. *Turk Neurosurg.* 2015; 25(6): 883–887, doi: [10.5137/1019-5149.JTN.10495-14.2](https://doi.org/10.5137/1019-5149.JTN.10495-14.2), indexed in Pubmed: [26617137](https://pubmed.ncbi.nlm.nih.gov/26617137/).
- Lin BJ, Chung TT, Lin MC, et al. Quantitative analysis of anatomical relationship between cavernous segment internal carotid artery and pituitary macroadenoma. *Medicine (Baltimore).* 2016; 95(41): e5027, doi: [10.1097/MD.0000000000005027](https://doi.org/10.1097/MD.0000000000005027), indexed in Pubmed: [27741111](https://pubmed.ncbi.nlm.nih.gov/27741111/).
- Mascarella MA, Forghani R, Di Maio S, et al. Indicators of a reduced intercarotid artery distance in patients undergoing endoscopic transsphenoidal surgery. *J Neurol Surg B Skull Base.* 2015; 76(3): 195–201, doi: [10.1055/s-0034-1396601](https://doi.org/10.1055/s-0034-1396601), indexed in Pubmed: [26225301](https://pubmed.ncbi.nlm.nih.gov/26225301/).
- McDowell BD, Wallace RB, Carnahan RM, et al. Demographic differences in incidence for pituitary adenoma. *Pituitary.* 2011; 14(1): 23–30, doi: [10.1007/s11102-010-0253-4](https://doi.org/10.1007/s11102-010-0253-4), indexed in Pubmed: [20809113](https://pubmed.ncbi.nlm.nih.gov/20809113/).
- Mercado M, Melgar V, Salame L, et al. Clinically non-functioning pituitary adenomas: Pathogenic, diagnostic and therapeutic aspects. *Endocrinol Diabetes Nutr.* 2017; 64(7): 384–395, doi: [10.1016/j.endinu.2017.05.009](https://doi.org/10.1016/j.endinu.2017.05.009), indexed in Pubmed: [28745610](https://pubmed.ncbi.nlm.nih.gov/28745610/).
- Molitch ME. Diagnosis and treatment of pituitary adenomas: a review. *JAMA.* 2017; 317(5): 516–524, doi: [10.1001/jama.2016.19699](https://doi.org/10.1001/jama.2016.19699), indexed in Pubmed: [28170483](https://pubmed.ncbi.nlm.nih.gov/28170483/).
- Nunes CF, Cabral GA, Mello Junior JO, et al. Pituitary macroadenoma: analysis of intercarotid artery distance compared to controls. *Arq Neuropsiquiatr.* 2016; 74(5): 396–404, doi: [10.1590/0004-282X20160046](https://doi.org/10.1590/0004-282X20160046), indexed in Pubmed: [27191236](https://pubmed.ncbi.nlm.nih.gov/27191236/).
- Park SQ, Bae HG, Yoon SM, et al. Morphological characteristics of the thalamoperforating arteries. *J Korean Neurosurg Soc.* 2010; 47(1): 36–41, doi: [10.3340/jkns.2010.47.1.36](https://doi.org/10.3340/jkns.2010.47.1.36), indexed in Pubmed: [20157376](https://pubmed.ncbi.nlm.nih.gov/20157376/).
- Pinar E, Yuceer N, Imre A, et al. Endoscopic endonasal transsphenoidal surgery for pituitary adenomas. *J Craniofac Surg.* 2015; 26(1): 201–205, doi: [10.1097/SCS.0000000000001240](https://doi.org/10.1097/SCS.0000000000001240), indexed in Pubmed: [25469897](https://pubmed.ncbi.nlm.nih.gov/25469897/).
- Rajaratnam S. Pituitary gland imaging. *Indian J Endocrinol Metab.* 2013; 17(Suppl 1): S100–S101, doi: [10.4103/2230-8210.119516](https://doi.org/10.4103/2230-8210.119516), indexed in Pubmed: [24251122](https://pubmed.ncbi.nlm.nih.gov/24251122/).
- Rhoton A. The sellar region. *Neurosurgery.* 2002; 51(suppl 4): S1-335-S1-374, doi: [10.1097/00006123-200210001-00009](https://doi.org/10.1097/00006123-200210001-00009).
- Shrestha GK, Pokharel PR, Gyawali R, et al. The morphology and bridging of the sella turcica in adult orthodontic patients. *BMC Oral Health.* 2018; 18(1): 45, doi: [10.1186/s12903-018-0499-1](https://doi.org/10.1186/s12903-018-0499-1), indexed in Pubmed: [29548316](https://pubmed.ncbi.nlm.nih.gov/29548316/).
- Uz A. Variations in the origin of the thalamoperforating arteries. *J Clin Neurosci.* 2007; 14(2): 134–137, doi: [10.1016/j.jocn.2006.01.047](https://doi.org/10.1016/j.jocn.2006.01.047), indexed in Pubmed: [17113294](https://pubmed.ncbi.nlm.nih.gov/17113294/).
- Vijaywargiya M, Deopujari R, Athavale SA. Anatomical study of petrous and cavernous parts of internal carotid artery. *Anat Cell Biol.* 2017; 50(3): 163–170, doi: [10.5115/acb.2017.50.3.163](https://doi.org/10.5115/acb.2017.50.3.163), indexed in Pubmed: [29043093](https://pubmed.ncbi.nlm.nih.gov/29043093/).
- Wang EW, Gardner PA, Zanation AM. International consensus statement on endoscopic skull-base surgery: executive summary. *Int Forum Allergy Rhinol.* 2019; 9(5): S127–S144, doi: [10.1002/alr.22327](https://doi.org/10.1002/alr.22327), indexed in Pubmed: [30957956](https://pubmed.ncbi.nlm.nih.gov/30957956/).
- Weidenbecher M, Huk WJ, Iro H. Internal carotid artery injury during functional endoscopic sinus surgery and its management. *Eur Arch Otorhinolaryngol.* 2005; 262(8): 640–645, doi: [10.1007/s00405-004-0888-8](https://doi.org/10.1007/s00405-004-0888-8), indexed in Pubmed: [15657746](https://pubmed.ncbi.nlm.nih.gov/15657746/).

Circle of Willis: anatomical variations of configuration. A magnetic resonance angiography study

M. Enyedi^{1, 2}, C. Scheau³, R.O. Baz⁴, A.C. Didilescu⁵

¹Department of Anatomy, Carol Davila University of Medicine and Pharmacy, Bucharest, Romania

²“Victor Babes” Centre for Diagnosis and Treatment, Bucharest, Romania

³Department of Physiology, Carol Davila University of Medicine and Pharmacy, Bucharest, Romania

⁴Department of Radiology, County Clinical Emergency Hospital, Constanța, Romania

⁵Department of Embryology, Faculty of Dental Medicine, Carol Davila University of Medicine and Pharmacy, Bucharest, Romania

[Received: 4 October 2021; Accepted: 30 November 2021; Early publication date: 15 December 2021]

Background: The main scope of this paper is to investigate the prevalence of the anatomical variants of the circle of Willis (CoW) in the Romanian population through magnetic resonance angiography.

Materials and methods: Magnetic resonance angiography images were obtained for 126 individuals and the configurations of the anterior and posterior CoW were identified, and classified. The prevalence of each variant and the number of complete anterior or posterior parts of the circle were determined.

Results: A classical configuration of the CoW was found in 39 (30.9%) cases. The most common posterior variation was the unilateral absence of a posterior communicating artery ($n = 28$) while in the anterior circle it was the unilateral absence of the precommunicating segment of an anterior cerebral artery ($n = 17$). A complete entire CoW was found in 63 cases, while the anterior and posterior parts yielded complete configurations in 108 and 73 cases, respectively. Eight cases did not present complete configurations. A foetal posterior communicating artery was identified unilaterally in 14 cases and bilaterally in 6 cases.

Conclusions: Unilateral variations were the most common changes found in CoW configuration. The correct assessment of the CoW configuration may prove useful in the planning and follow-up of brain surgery and interventional procedures, as well as in estimating the prognosis of patients suffering from stroke or other related cerebral vascular events. (Folia Morphol 2023; 82, 1: 24–29)

Key words: circle of Willis, anatomic variation, magnetic resonance angiography

INTRODUCTION

The circle of Willis (CoW) is defined as the ring-shaped vascular structure situated at the base of the brain, where the anterior (internal carotid) and

posterior (vertebral) circulations converge. It is named after the anatomist Thomas Willis who vastly contributed to its understanding, and is also called the

Address for correspondence: C. Scheau, MD, PhD, 8 Eroii Sanitari Blvd., 5th district, 050474, Bucharest, Romania, tel: +40213103722, e-mail: cristian.scheau@umfcd.ro

This article is available in open access under Creative Common Attribution-Non-Commercial-No Derivatives 4.0 International (CC BY-NC-ND 4.0) license, allowing to download articles and share them with others as long as they credit the authors and the publisher, but without permission to change them in any way or use them commercially.

cerebral arterial circle, the Willis polygon, and the loop of Willis [22].

One of the most important functions of the CoW is to sustain the blood flow through its network of anastomoses, in case of disturbances involving one of its branches [11]. When certain conditions are met, the particular configuration of the CoW provides a fail-safe, maintaining the brain tissue vascularisation by rerouting the cerebral haemodynamics [1]. However, in the case of an anatomical variant of the CoW that yields an incomplete circle, the compensatory capacity is lost, and severe flow hindering in either internal carotid or vertebral artery leads to ischaemia and potentially exitus [2]. Thus, knowledge of the configuration of the CoW is extremely important in patients undergoing cerebral vascular surgery where one of the branches may be involved, as well as in patients with chronic vascular diseases leading to occlusions.

Studies on various world populations cite an incidence between 16.6% and 85.4% for the “classical” configuration of the CoW [12, 21, 23–25]. Significant differences between populations of various races were noted, and genetic and environmental factors were considered as elements that may influence the development of the CoW [10, 16, 21, 23, 24]. This paper aims to investigate the anatomical variants of the CoW and to compare their prevalence to the available literature studies. To our knowledge, this is the first report on the CoW configurations in a Romanian cohort.

MATERIALS AND METHODS

Study design

We designed a retrospective cohort study that included all patients that were submitted to cerebral magnetic resonance angiography (MRA) in a defined period of time, recording the configurations of the CoW in all examinations.

The imaging studies were performed in the “Victor Babes” Centre for Diagnosis and Treatment, Bucharest, Romania, between 01.05.2019 and 30.09.2019. All cerebral investigations that included the MRA sequence were considered. The data is stored in the local picture archiving and communication system, for an indefinite period of time. No follow-up was performed.

All configurations of the anterior and posterior parts of the CoW were recorded and classified based on the model of distribution proposed by Chen et al. [6] which proposes 10 anterior and 10 posterior

patterns of the circle. According to this classification, the following aspects are mentionable: unilateral fetal origin of the posterior cerebral artery (fPCA) corresponds to posterior circle variants B, F, G and H, while the bilateral fPCA is found in variants C, I and J; also, a complete anterior circle is observed in variants A through F, while the posterior circle is complete in variants A through C; a complete entire circle requires concurring complete anterior and posterior circles. The imaging assessment regarded the topography, relative diameter and morphology of the internal carotid arteries (ICA), anterior, middle and posterior cerebral arteries (ACA, MCA and PCA, respectively), as well as the anterior and posterior communicating arteries (ACoA and PCoA). Other measured variables were the patients’ ages and gender.

Participants

The study population consisted of 126 patients (53 male, 73 female), aged between 1 and 93 years (mean age of 36 ± 24 years), that underwent cerebral MRA in our clinic for developmental delay (for the 14 patients aged 1 to 5 years old) or non-specific neurological symptoms including headache, dizziness, nausea, and anxiety. Patients with prior brain surgery or interventional procedures were excluded.

Informed consent for the imaging investigation, as well as for the processing and presenting of data, was obtained from all patients or guardians, respectively. The study was approved by the institutional ethics committee (registration no.: 1523/02.04.2020) and was performed in accordance with the Declaration of Helsinki and its later amendments.

Image acquisition

The images were acquired on a Siemens MAGNETOM Avanto 1.5 Tesla using the dedicated 12 element Head Matrix coil. The MRA protocol employed in all cases relied on the three-dimensional-time-of-flight (3D-TOF) imaging method (repetition time: 25 ms, echo time: 7 ms, resolution of $0.7 \times 0.7 \times 0.7$ mm with a 180×180 mm field of view). The imaging interpretation was performed on a dedicated workstation and the CoW variants were recorded for each patient, for the anterior and posterior components. An arterial vessel was deemed absent when it was not visualised and hypoplastic when its diameter was smaller than 0.8 mm. The 3D-TOF sequence was repeated when motion or other artefacts occurred in order to obtain a satisfactory image quality. There

was no need to exclude investigations due to motion or metallic artefacts, thus the study size included all investigations available in the three months of recruiting.

Ethics approval and consent to participate

Institutional Ethics Committee approval was obtained (id no: 1523/02.04.2020).

All patients (or caregivers, or guardians when applicable) gave their informed consent to be submitted to the investigation and for their data to be processed and used in research purposes.

Statistical methods

Data distributions were expressed as means, standard deviations and percentages. Possible associations between gender and variant types were tested using Pearson χ^2 test. Fisher's exact test was used when the expected frequency in any cell was less than 5. The level of significance was set at 0.05. We performed statistical analyses using Stata/IC 16 (StataCorp).

RESULTS

The prevalence of the CoW anatomic variants is presented in Tables 1 and 2, for the anterior and posterior parts, respectively. While the model used for classification yields 10 possible variants for each of the two parts of the CoW, we only encountered 8 variants in the anterior (A through H), and 6 variants in the posterior CoW (A through F); example cases of all identified anterior and posterior configurations are presented in Figure 1.

A classical configuration of the CoW was found in 39 (30.9%) cases. The most common variation from the classical configurations was the unilateral absence of one of the posterior communicating arteries ($n = 28$), which was also the most frequent variation of the posterior circle. The most common variation in the anterior part of the CoW was the unilateral absence of the precommunicating segment of an anterior cerebral artery ($n = 17$).

A statistical association between the female gender and the presence of a bilateral fPCA (posterior CoW variant C) was identified ($p = 0.039$).

The prevalence of the complete anterior, posterior and entire CoW is presented in Table 3. A complete structure of the entire CoW was found in 63 cases, while the anterior and posterior parts yielded complete configurations in 108 and 73 cases, respectively.

Table 1. The prevalence of the anatomic variants of the anterior circle of Willis in relation to patient gender

Group	Variant type (%)							
	A	B	C	D	E	F	G	H
Males	64.2%	0	9.4%	0	1.9%	9.4%	5.7%	13.2%
Females	68.5%	2.8%	6.9%	1.4%	1.4%	5.5%	2.7%	13.7%
Total	66.7%	1.6%	7.9%	0.8%	1.6%	7.1%	4%	13.5%

Table 2. The prevalence of the anatomic variants of the posterior circle of Willis in relation to patient gender

Group	Variant type (%)					
	A	B	C	D	E	F
Males	52.8%	7.6%	0	24.5%	11.3%	1.9%
Females	39.7%	8.2%	8.2%*	20.6%	19.2%	4.1%
Total	45.2%	7.9%	4.8%	22.2%	15.9%	3.2%

* $p = 0.039$, Fisher's exact test

Eight (6.4%) cases did not present complete configurations neither in anterior, nor in posterior CoW. Among them, 50% were males.

The bilateral fPCA presence was identified in a total of 6 cases, while a unilateral fPCA was detected in 14 cases. The gender-relative prevalence for the adult and fetal configurations of the CoW is depicted in Table 4.

No incidental aneurysms were identified in the CoW vessels in the study group.

DISCUSSION

Despite diverse classifications of the CoW variations are available, the present study relied on the one proposed by Chen et al. [6], which we found to be the most simple and intuitive, while also addressing the complexity and clinical relevance of the different configurations [6, 9, 13, 15, 17]. Moreover, the existence of multiple similar papers that have adopted this method in various populations was encouraging in regard to presenting data in a manner that allows for comparison in future studies. Out of the 20 total possible configurations of the CoW, we identified only the first 8 for the anterior, and first 6 for the posterior circle, respectively. A scarcity of these unidentified variants was cited in other similar studies with comparable study population size [25].

The possibility of a correlation between the configuration of the CoW and the type of ethnic or racial group is a recurring conception and was one of the fundamental grounds for our paper, alongside the



Figure 1. A collection of maximum intensity projection images of three-dimensional-time-of-flight acquisitions from 7 cases from the study group (labelled a through f). The anatomic variants of the anterior (yellow) and posterior (green) circle of Willis (CoW) are represented with arrows, except for the type A configuration, which is identified in the anterior (e) and posterior (d') components, respectively. For the anterior CoW, the anatomic variants depicted are, as follows: duplication of the anterior communicating arteries (ACoA) in the axial plane in images f' and detailed in f'' (arrow and arrowhead); medial artery of the corpus callosum originating in the ACoA (b); fusion of post-communicating anterior cerebral artery (ACAs) (c'); common trunk for post-communicating ACAs (g); double trunk of middle cerebral artery (d); absent ACoA (b); hypoplastic precommunicating ACA (a). In the posterior CoW we identified: unilateral posterior cerebral artery (fPCA) (a'), bilateral fPCA (f, f'), unilateral absent posterior communicating artery (PCoA) (e), bilateral absent PCoA (c), unilateral fetal type PCA with absent pre-communicating segment (g).

paucity of reports regarding the configuration of the CoW in the Romanian population [9]. However, we did not perform a thorough comparison to reports from other populations, as it did not fall within the scope of our study, and we consider that a structured/

/systematic review is more appropriate in order to draw relevant conclusions on this topic.

The development of the CoW in the embryo occurs in two stages: vasculogenesis and angiogenesis; the events occurring in the embryological state can lead

Table 3. The prevalence of the complete anterior, posterior and entire circle of Willis (CoW) in relation to patient gender

Group	Complete anterior CoW (%)	Complete posterior CoW (%)	Complete entire CoW (%)
Males	84.9%	60.4%	52.8%
Females	86.3%	56.2%	47.9%
Total	85.7%	57.9%	50%

Table 4. The prevalence of the adult and fetal circle of Willis (CoW) in relation to patient gender

Group	Adult CoW (%)	Fetal unilateral CoW (%)	Fetal total (uni + bilateral) CoW (%)
Males	88.7%	9.4%	9.4%
Females	79.5%	12.3%	20.6%
Total	83.3%	11.1%	15.9%

to either anomalies of normal arteries or the persistence of embryonic arteries or anastomoses [20].

A "classical" configuration with a complete entire circle and "standard" configuration of distribution and size of the arteries contributing to the CoW was found in 30.9% of cases, which is within the range of most similar studies [23, 25]. The most common variation from the classical aspect was identified as the unilateral absence of one of the posterior communicating arteries (22.2%) in the posterior CoW, while in the anterior circle, the second most common configuration after the classical pattern was the unilateral absence of the precommunicating segment of an anterior cerebral artery (13.5%).

The complete entire circle was identified in 50% of subjects, which is analogous to other similar studies, despite some reports that cite a very high prevalence of up to 99.4% complete circles [3, 14]. Eight (6.4%) cases presented an incomplete anterior and posterior circle, which may represent a risk factor for a cardiovascular event, as this condition was linked to poorer prognosis and higher severity of strokes [27]. A complete CoW was found to be not only a protective factor in stroke, but also a predictor of a more favourable clinical outcome in stroke, with less haemorrhage transformation [26].

A bilateral fPCA was identified statistically significant more common in women than in men; however, the correlation may be incidental and relevance of this finding should be validated in larger studies.

Adult type circulation was found in 105 (83.3%) patients, with fetal circulation identified unilaterally in 11.1% of cases, and bilaterally in 5.6% of cases,

a finding that is congruent with literature studies [15, 19, 24]. In the evaluation of adult vs. fetal type circulation, that relies on deciding whether the posterior communicating artery is larger than the precommunicating segment of the posterior cerebral artery, some studies cite a third variant called transitional, where the two arteries are identical in size; however, we did not take this option into consideration, as we considered that it can introduce bias due to the limits in accurately comparing the vessel diameters, where the imaging plane, resolution and scale, blood flow, and imaging software may influence the measurements.

Differences in prevalence of CoW configuration were noted between imaging and autopsy studies [16]. Possible contributing factors are, among others, the cutoff size value for considering a vessel hypoplastic, flow turbulences and artefacts that may impede correct assessment on imaging studies, and operator-dependent limits in the cadaveric dissection.

This study has limitations, the most important being the study population size, that may not accurately describe the distribution of the CoW configuration in the general population. Imaging artefacts may hinder the correct assigning of the variants; however, no such distortions were identified. Nevertheless, while MRA is a very competent method in evaluating the CoW configuration and the patency of any of its branches and has undergone significant technical improvements over the recent years, conventional angiography is still regarded by some authors as the gold standard in specific cases [7, 8].

The adequate imaging analysis of vessel morphology may uncover the presence of inflammatory or tumoural lesions and may contribute to a superior understanding of vascular dynamics, greatly impacting the management of selected patients [4, 5, 18].

CONCLUSIONS

To our knowledge, this is the first paper that assesses the configuration variants of the CoW through MRA in our country. The findings may prove useful in the planning and follow-up of brain surgery and interventional procedures, as well as in estimating the prognosis of patients suffering from stroke or other related cerebral vascular events.

Conflict of interest: None declared

REFERENCES

1. AbuRahma AF, Mousa AY, Stone PA, et al. Correlation of intraoperative collateral perfusion pressure during carotid

- endarterectomy and status of the contralateral carotid artery and collateral cerebral blood flow. *Ann Vasc Surg.* 2011; 25(6): 830–836, doi: [10.1016/j.avsg.2011.04.002](https://doi.org/10.1016/j.avsg.2011.04.002), indexed in Pubmed: [21680143](https://pubmed.ncbi.nlm.nih.gov/21680143/).
2. Alastruey J, Parker KH, Peiró J, et al. Modelling the circle of Willis to assess the effects of anatomical variations and occlusions on cerebral flows. *J Biomech.* 2007; 40(8): 1794–1805, doi: [10.1016/j.jbiomech.2006.07.008](https://doi.org/10.1016/j.jbiomech.2006.07.008), indexed in Pubmed: [17045276](https://pubmed.ncbi.nlm.nih.gov/17045276/).
 3. Alpers BJ, Berry RG, Paddison RM. Anatomical studies of the circle of Willis in normal brain. *AMA Arch Neurol Psychiatry.* 1959; 81(4): 409–418, doi: [10.1001/archneurpsyc.1959.02340160007002](https://doi.org/10.1001/archneurpsyc.1959.02340160007002), indexed in Pubmed: [13636509](https://pubmed.ncbi.nlm.nih.gov/13636509/).
 4. Baz RA, Scheau C, Niscoveanu C, et al. Morphometry of the entire internal carotid artery on CT angiography. *Medicina (Kaunas).* 2021; 57(8), doi: [10.3390/medicina57080832](https://doi.org/10.3390/medicina57080832), indexed in Pubmed: [34441039](https://pubmed.ncbi.nlm.nih.gov/34441039/).
 5. Baz RA, Scheau C, Sârbu N, et al. Carotid paragangliomas: case report and imaging review. *Folia Morphol.* 2021; 80(3): 699–706, doi: [10.5603/FM.a2020.0078](https://doi.org/10.5603/FM.a2020.0078), indexed in Pubmed: [32710793](https://pubmed.ncbi.nlm.nih.gov/32710793/).
 6. Chen HW, Yen PS, Lee CC, et al. Magnetic resonance angiographic evaluation of circle of Willis in general population: A morphologic study in 507 cases. *Chin J Radiol.* 2004; 29: 223–229.
 7. Cuong NN, Luu VD, Tuan TA, et al. Conventional digital subtractional vs non-invasive MR angiography in the assessment of brain arteriovenous malformation. *Clin Neurol Neurosurg.* 2018; 169: 29–33, doi: [10.1016/j.clineuro.2018.03.022](https://doi.org/10.1016/j.clineuro.2018.03.022), indexed in Pubmed: [29604508](https://pubmed.ncbi.nlm.nih.gov/29604508/).
 8. D'Arco F, D'Amico A, Caranci F, et al. Cerebrovascular stenosis in neurofibromatosis type 1 and utility of magnetic resonance angiography: our experience and literature review. *Radiol Med.* 2014; 119(6): 415–421, doi: [10.1007/s11547-013-0358-8](https://doi.org/10.1007/s11547-013-0358-8), indexed in Pubmed: [24297593](https://pubmed.ncbi.nlm.nih.gov/24297593/).
 9. Eftekhari B, Dadmehr M, Ansari S, et al. Are the distributions of variations of circle of Willis different in different populations? Results of an anatomical study and review of literature. *BMC Neurol.* 2006; 6: 22, doi: [10.1186/1471-2377-6-22](https://doi.org/10.1186/1471-2377-6-22), indexed in Pubmed: [16796761](https://pubmed.ncbi.nlm.nih.gov/16796761/).
 10. Forgo B, Tarnoki AD, Tarnoki DL, et al. Investigation of circle of Willis variants and hemodynamic parameters in twins using transcranial color-coded Doppler sonography. *Int J Cardiovasc Imaging.* 2018; 34(9): 1419–1427, doi: [10.1007/s10554-018-1359-4](https://doi.org/10.1007/s10554-018-1359-4), indexed in Pubmed: [29675634](https://pubmed.ncbi.nlm.nih.gov/29675634/).
 11. Jahed M, Ghalichi F, Farhoudi M. Comparison of blood velocity between transcranial Doppler and numerical method in the patient-specific circle of Willis with aneurysm. *Biomed Mater Eng.* 2019; 30(4): 427–438, doi: [10.3233/BME-191064](https://doi.org/10.3233/BME-191064), indexed in Pubmed: [31561321](https://pubmed.ncbi.nlm.nih.gov/31561321/).
 12. Jalali Kondori B, Azemati F, Dadsereht S. Magnetic resonance angiographic study of anatomic variations of the circle of willis in a population in Tehran. *Arch Iran Med.* 2017; 20(4): 235–239, doi: [0172004/aim.009](https://doi.org/0172004/aim.009), indexed in Pubmed: [28412828](https://pubmed.ncbi.nlm.nih.gov/28412828/).
 13. Jin ZN, Dong WT, Cai XW, et al. CTA characteristics of the circle of Willis and intracranial aneurysm in a Chinese crowd with family history of stroke. *Biomed Res Int.* 2016; 2016: 1743794, doi: [10.1155/2016/1743794](https://doi.org/10.1155/2016/1743794), indexed in Pubmed: [26881211](https://pubmed.ncbi.nlm.nih.gov/26881211/).
 14. Kapoor K, Singh B, Dewan LI. Variations in the configuration of the circle of Willis. *Anat Sci Int.* 2008; 83(2): 96–106, doi: [10.1111/j.1447-073X.2007.00216.x](https://doi.org/10.1111/j.1447-073X.2007.00216.x), indexed in Pubmed: [18507619](https://pubmed.ncbi.nlm.nih.gov/18507619/).
 15. Karatas A, Coban G, Cinar C, et al. Assessment of the circle of Willis with cranial tomography angiography. *Med Sci Monit.* 2015; 21: 2647–2652, doi: [10.12659/MSM.894322](https://doi.org/10.12659/MSM.894322), indexed in Pubmed: [26343887](https://pubmed.ncbi.nlm.nih.gov/26343887/).
 16. Klimek-Piotrowska W, Kopeć M, Kochana M, et al. Configurations of the circle of Willis: a computed tomography angiography based study on a Polish population. *Folia Morphol.* 2013; 72(4): 293–299, doi: [10.5603/fm.2013.0049](https://doi.org/10.5603/fm.2013.0049), indexed in Pubmed: [24402749](https://pubmed.ncbi.nlm.nih.gov/24402749/).
 17. Klimek-Piotrowska W, Rybicka M, Wojnarska A, et al. A multitude of variations in the configuration of the circle of Willis: an autopsy study. *Anat Sci Int.* 2016; 91(4): 325–333, doi: [10.1007/s12565-015-0301-2](https://doi.org/10.1007/s12565-015-0301-2), indexed in Pubmed: [26439730](https://pubmed.ncbi.nlm.nih.gov/26439730/).
 18. Low A, Mak E, Rowe JB, et al. Inflammation and cerebral small vessel disease: a systematic review. *Ageing Res Rev.* 2019; 53: 100916, doi: [10.1016/j.arr.2019.100916](https://doi.org/10.1016/j.arr.2019.100916), indexed in Pubmed: [31181331](https://pubmed.ncbi.nlm.nih.gov/31181331/).
 19. Machasio RM, Nyabanda R, Mutala TM. Proportion of variant anatomy of the circle of Willis and association with vascular anomalies on cerebral CT angiography. *Radiol Res Pract.* 2019; 2019: 6380801, doi: [10.1155/2019/6380801](https://doi.org/10.1155/2019/6380801), indexed in Pubmed: [31316832](https://pubmed.ncbi.nlm.nih.gov/31316832/).
 20. Menshawi K, Mohr JP, Gutierrez J. A functional perspective on the embryology and anatomy of the cerebral blood supply. *J Stroke.* 2015; 17(2): 144–158, doi: [10.5853/jos.2015.17.2.144](https://doi.org/10.5853/jos.2015.17.2.144), indexed in Pubmed: [26060802](https://pubmed.ncbi.nlm.nih.gov/26060802/).
 21. Naveen SR, Bhat V, Karthik GA. Magnetic resonance angiographic evaluation of circle of Willis: A morphologic study in a tertiary hospital set up. *Ann Indian Acad Neurol.* 2015; 18(4): 391–397, doi: [10.4103/0972-2327.165453](https://doi.org/10.4103/0972-2327.165453), indexed in Pubmed: [26713008](https://pubmed.ncbi.nlm.nih.gov/26713008/).
 22. Rengachary SS, Xavier A, Manjila S, et al. The legendary contributions of Thomas Willis (1621-1675): the arterial circle and beyond. *J Neurosurg.* 2008; 109(4): 765–775, doi: [10.3171/JNS/2008/109/10/0765](https://doi.org/10.3171/JNS/2008/109/10/0765), indexed in Pubmed: [18826368](https://pubmed.ncbi.nlm.nih.gov/18826368/).
 23. Siddiqi H, Tahir M, Lone KP. Variations in cerebral arterial circle of Willis in adult Pakistani population. *J Coll Physicians Surg Pak.* 2013; 23(9): 615–619, doi: [09.2013/jcsp.615619](https://doi.org/09.2013/jcsp.615619), indexed in Pubmed: [24034183](https://pubmed.ncbi.nlm.nih.gov/24034183/).
 24. Yeniçeri İÖ, Çullu N, Deveer M, et al. Circle of Willis variations and artery diameter measurements in the Turkish population. *Folia Morphol.* 2017; 76(3): 420–425, doi: [10.5603/FM.a2017.0004](https://doi.org/10.5603/FM.a2017.0004), indexed in Pubmed: [28150270](https://pubmed.ncbi.nlm.nih.gov/28150270/).
 25. Zaki SM, Shaaban MH, Abd Al Galeel WA, et al. Configuration of the circle of Willis and its two parts among Egyptian: a magnetic resonance angiographic study. *Folia Morphol.* 2019; 78(4): 703–709, doi: [10.5603/FM.a2019.0015](https://doi.org/10.5603/FM.a2019.0015), indexed in Pubmed: [30761512](https://pubmed.ncbi.nlm.nih.gov/30761512/).
 26. Zhao H, Wang B, Xu G, et al. Collateral grade of the Willis' circle predicts outcomes of acute intracranial internal carotid artery occlusion before thrombectomy. *Brain Behav.* 2019; 9(12): e01452, doi: [10.1002/brb3.1452](https://doi.org/10.1002/brb3.1452), indexed in Pubmed: [31696661](https://pubmed.ncbi.nlm.nih.gov/31696661/).
 27. Zhou H, Sun J, Ji X, et al. Correlation between the integrity of the circle of Willis and the severity of initial noncardiac cerebral infarction and clinical prognosis. *Medicine.* 2016; 95(10): e2892, doi: [10.1097/MD.0000000000002892](https://doi.org/10.1097/MD.0000000000002892), indexed in Pubmed: [26962785](https://pubmed.ncbi.nlm.nih.gov/26962785/).

Performance of rupture-related morphological parameters in posterior communicating artery aneurysms with fetal-type variant

S. Chen^{1*}, C. Li^{3*}, C. Karmonik⁴, Y. Cheng¹, N. Lv²

¹Shanghai Interventional Medical Device Engineering Technology Research Centre, University of Shanghai for Science and Technology, Shanghai, China

²Department of Neurosurgery, Changhai Hospital, Second Military Medical University, Shanghai, China

³Department of Geriatrics, Dongying New District Hospital, Dongying, China

⁴MRI Core, Houston Methodist Research Institute, Houston, Texas, United States

[Received: 12 October 2021; Accepted: 5 November 2021; Early publication date: 9 November 2021]

Background: The aim of the study was to investigate the impact of fetal-type posterior cerebral artery (fPCA) variant on morphological parameters of posterior communicating artery (PComA) aneurysms for rupture risk assessment.

Materials and methods: A total of 98 PComA aneurysms (62 ruptured and 36 unruptured) in 98 consecutive patients were reviewed. Morphological parameters were calculated including aneurysm size, aspect ratio (AR), size ratio (SR), dome-to-neck ratio, bottleneck factor and inflow angle. Performances of morphological parameters to discriminate rupture status were compared between aneurysms with or without fPCA.

Results: Fetal-type posterior cerebral artery variant was determined in 39 (39.8%, 25 ruptured and 14 unruptured) lesions. The ruptured group revealed a significantly larger size ($p = 0.004$), AR ($p = 0.003$), SR ($p = 0.001$), and inflow angle ($p < 0.001$). For the aneurysms without fPCA, all morphological parameters were significantly different between ruptured and unruptured aneurysms ($p < 0.05$); for the aneurysms with fPCA, only inflow angle ($p = 0.001$) was significantly related with the rupture status. Multivariate analysis showed that SR ($p = 0.035$ and $p = 0.011$) and inflow angle ($p = 0.001$ and $p = 0.028$) were independent rupture risk factors for the total cohort and the aneurysms without fPCA; while only inflow angle ($p = 0.004$) revealed to be independently related with rupture status of aneurysms without fPCA.

Conclusions: The performances of morphological parameters to discriminate rupture status were different between PComA aneurysms with and without fPCA variants. Inflow angle might be a reliable predictor for rupture risk of PComA aneurysms. (Folia Morphol 2023; 82, 1: 30–36)

Key words: intracranial aneurysm, rupture, morphology

Address for correspondence: Dr. N. Lv, Department of Neurosurgery, Changhai Hospital, 168 Changhai Road, Shanghai, China, 200433, tel: +86 21-31161784, fax: +86 21-31161784, e-mail: lvnan2008@163.com

*S. Chen and C. Li contributed equally to this work and should be considered as co-first authors.

This article is available in open access under Creative Common Attribution-Non-Commercial-No Derivatives 4.0 International (CC BY-NC-ND 4.0) license, allowing to download articles and share them with others as long as they credit the authors and the publisher, but without permission to change them in any way or use them commercially.

INTRODUCTION

Advances in neuroimaging techniques are leading to an increasing number of incidentally detected unruptured intracranial aneurysms (IAs) [1, 2]. Despite the adverse consequences of morbidity and mortality of subarachnoid haemorrhage (SAH) caused by a ruptured IA, the annual incidence rate of such an event is comparable to or even lower than the risk of preventive treatment [18]. Therefore, it is important to identify risk factors for rupture so that treatment strategies for the individualised patient may be optimised.

Accounting for 15–25% of all IAs, posterior communicating artery (PComA) aneurysms are one of the most frequent occurring types and have larger rupture risk than aneurysms of other segments of the internal carotid artery (ICA) [3]. Several location-specific studies on PComA aneurysms suggest that the morphology of the aneurysm and its involved arteries may serve as a potential discriminant for rupture status [8, 10]. Several anatomic vascular variants of the ICA-PComA bifurcation exist at this location [16]. Morphological parameters calculated based on the size or direction of aneurysmal sac and its parent arteries only may not consider the influence of these vascular variants. This might partially explain why even location-specific studies considering vessel wall characteristics and peri-aneurysmal environment did not achieve consensus conclusions [8, 10].

Fetal-type posterior cerebral artery (fPCA) is one of the most frequent types of vascular variants of the ICA-PComA bifurcation, occurring in 4–29% of the population [5, 16]. To maintain adequate blood flow in the posterior circulation, PComAs with fPCA variants tend to have a larger diameter and different angulations, which might cause distinctive morphological features of aneurysms originated from this kind of ICA-PComA bifurcation. In this study, we reviewed the morphological parameters of PComA aneurysms with and without fPCA, to investigate the impact of this variant on rupture risk assessment of PComA aneurysms.

MATERIALS AND METHODS

This retrospective study was approved by our institutional review board, and the requirement for informed consent was waived. The patients' information was anonymised and de-identified before analysis.

Patients

We retrospectively reviewed 163 consecutive patients with diagnosed PComA aneurysms between January 2015 and December 2016 at our institution. The PComA aneurysms were determined and measured using three-dimensional rotational angiography (3DRA). Only aneurysms that involved both ICA and PComA were retained in the study to achieve uniform definitions of morphological parameters. SAH patients with multiple aneurysms were excluded to avoid misjudgement of aneurysmal rupture status. Finally, 98 PComA aneurysms in 98 patients were retained, including 62 ruptured and 36 unruptured lesions. Of the 36 patients in the unruptured group, 14 exhibited mild headache or dizziness, 7 suffered from ischaemic events, 3 exhibited symptoms of oculomotor nerve palsy, and the other 12 aneurysms were detected incidentally without symptoms of cerebrovascular disease.

The clinical characteristics were collected as the following: age, sex, hypertension, diabetes mellitus, and current smoking status. Hypertension was defined as taking antihypertensive agents, a systolic blood pressure ≥ 140 mmHg, or a diastolic blood pressure ≥ 90 mmHg. Diabetes mellitus was defined as taking antidiabetic agents, treatment with insulin injections, a fasting plasma glucose level ≥ 126 mg/dL, a random plasma glucose level of > 200 mg/dL, or a haemoglobin A1c level $\geq 6.5\%$. Current smoker was defined as those who had smoked at least 100 cigarettes during their lifetime and reported smoking every day or some days before being admitted.

Radiological findings and morphological calculations

The 3DRA was performed using the Artis zee Biplane angiographic system (VC14; Siemens, Erlangen, Germany). The acquired 3DRA data were transferred to the syngo X Workplace (VB15; Siemens) for reconstruction of the 3D internal carotid artery vessel tree and exported in a stereolithography format to Meshmixer 3.0 software (Autodesk Inc., San Francisco, CA, USA). First, we defined the neck plane as the location where the aneurysmal sac pouched outward from the parent vessel. Afterward, the models were divided into the aneurysm dome and the inlet and outlet planes of the parent artery, and then exported in stereolithography format. These formats were imported into Matlab 7.0 (MathWorks, Natick, Massachusetts, USA), which was used to calculate and visualise the morphological parameters.

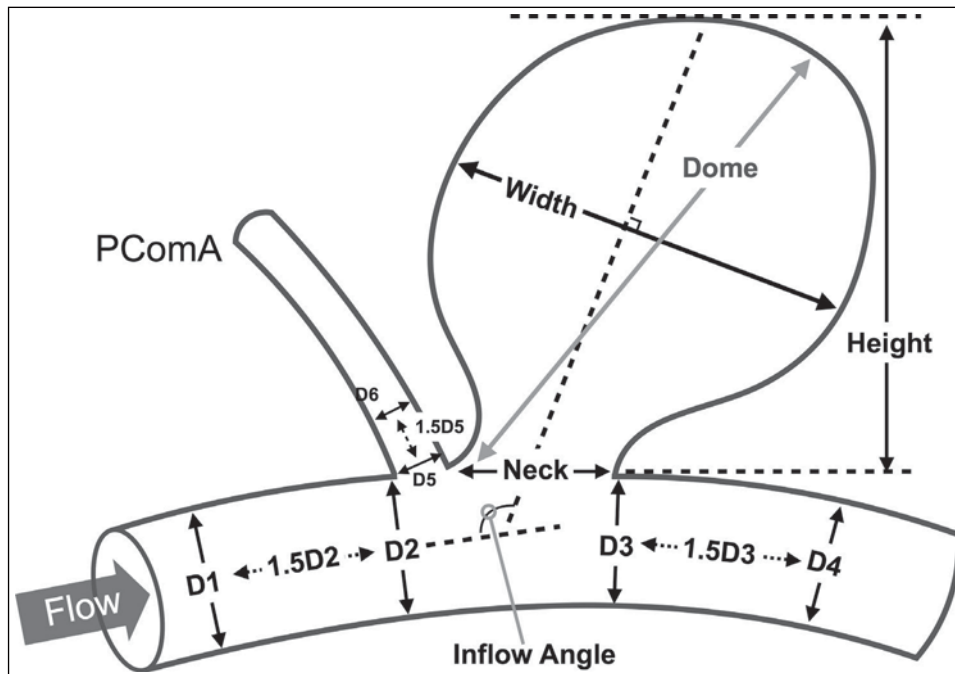


Figure 1. Definitions of morphological parameters; Size = Dome; Aspect Ratio = Height/Neck; Size Ratio = $6\text{Dome}/(\text{D1} + \text{D2} + \text{D3} + \text{D4} + \text{D5} + \text{D6})$; Diameter of PComA = $(\text{D5} + \text{D6})/2$; Dome-to-Neck Ratio = Dome/Neck; Bottle-Neck Factor = Width/Neck; PComA — posterior communicating artery.

Morphological parameters of the PComA aneurysms were derived from these models as described in previously (Fig. 1) [2, 8]. An fPCA variant was defined when PcomA has the same calibre as the P2 segment of the PCA and is associated with an atrophic P1 segment. The size of the aneurysm dome was defined as the maximum diameter of the aneurysm dome. Dome height was the longest dimension from the neck to the dome tip, and the dome width was measured perpendicular to the dome height. Aspect ratio (AR) was computed by dividing the dome height by neck width. Size ratio (SR) was calculated by dividing size by the average diameter of the parent artery and dome-to-neck ratio (DN) by dividing size by neck width. Bottleneck factor (BNF) was defined as the ratio of dome width to neck width. Inflow angle was the angle between inflow and the aneurysm's main axis from the centre of the neck to the tip of the dome.

Statistical analysis

Statistical analyses were performed using Microsoft Excel 2003 and SAS 9.1 (SAS Institute, Cary, North Carolina, USA). Variables were expressed as median (interquartile range) or number of patients (%) as appropriate. Analysis was performed for the total cohort, aneurysms with fPCA, and aneurysms without fPCA to compare the performance of morphological param-

eters in different vascular configurations, respectively. In univariate analysis, a Mann-Whitney U test was used for measurement data, and the chi-square test was performed for cross-tabulation. Multivariate logistic regression (backward elimination) was used to identify the independent risk factors. $P < 0.05$ (two-sided) was the criterion for statistical significance.

RESULTS

Risk factors for PComA aneurysms rupture

The clinical and morphological characteristics of the patients and PComA aneurysms are shown in Table 1. The patients' ages ranged from 42 to 82, with a median age of 61 years. Twenty-three were males and 73 were females. The demographic characteristics and medical history showed no significant differences between the ruptured and unruptured groups (Table 2).

The size of PComA aneurysms ranged from 1.23 to 6.84 mm, with a median size of 4.36 mm. The ruptured PComA aneurysms had a significantly larger size ($p = 0.004$), AR ($p = 0.003$), SR ($p = 0.001$) and inflow angle ($p < 0.001$). Other morphological characteristics, including DN ($p = 0.113$), BNF ($p = 0.089$), and diameter of PComA ($p = 0.206$) did not exhibit statistical significance between the ruptured and unruptured groups.

Table 1. Clinical and morphological characteristics of the patients and aneurysms

	All (n = 98)	Fetal-type PComA (n = 39)	Non-fetal-type PComA (n = 59)	P
Age [years]	61 (52, 66)	62 (52, 69)	60 (52, 65)	0.311
Male	23 (23.5)	8 (20.5)	15 (25.4)	0.574
Hypertension	49 (50.0)	23 (59.0)	26 (44.1)	0.149
Diabetes	11 (11.2)	6 (15.4)	5 (8.5)	0.463
Current smoking	7 (7.1)	2 (5.1)	5 (8.5)	0.819
Size [mm]	4.48 (3.56, 5.57)	4.45 (3.92, 5.56)	4.49 (3.18, 5.60)	0.511
Aspect ratio	1.02 (0.81, 1.35)	1.00 (0.82, 1.36)	1.02 (0.80, 1.32)	0.635
Size ratio	1.69 (1.29, 1.95)	1.61 (1.32, 1.96)	1.70 (1.29, 1.94)	0.752
Dome to neck ratio	1.08 (0.92, 1.37)	1.07 (0.89, 1.47)	1.10 (0.92, 1.37)	0.502
Bottleneck factor	1.16 (0.94, 1.37)	1.27 (0.97, 1.42)	1.11 (0.90, 1.32)	0.176
Inflow angle	113.0 (97.6, 127.9)	114.6 (101.5, 124.2)	108.4 (95.9, 127.9)	0.234
PComA diameter [mm]	1.32 (0.04, 1.95)	1.97 (1.70, 2.50)	0.73 (0.04, 1.35)	< 0.001

Data was expressed as median (25%, 75%); PComA — posterior communicating artery

Table 2. Univariate analysis of rupture-related parameters in aneurysms with or without fetal-type variant

	All		P	Fetal-type PCA		P	Non-fetal-type PCA		P
	Ruptured (n = 62)	Unruptured (n = 36)		Ruptured (n = 25)	Unruptured (n = 14)		Ruptured (n = 37)	Unruptured (n = 22)	
Size [mm]	4.54 (3.97, 5.81)	4.07 (2.74, 4.94)	0.004	4.39 (3.81, 5.77)	4.52 (3.92, 5.58)	0.942	4.61 (4.16, 5.86)	3.05 (2.41, 4.66)	0.001
Aspect ratio	1.13 (0.89, 1.37)	0.85 (0.71, 1.24)	0.003	1.00 (0.81, 1.36)	1.05 (0.83, 1.36)	0.942	1.18 (0.91, 1.49)	0.77 (0.61, 1.02)	< 0.001
Size ratio	1.77 (1.42, 2.17)	1.46 (0.90, 1.80)	0.001	1.61 (1.28, 2.22)	1.60 (1.40, 1.89)	0.942	1.80 (1.59, 2.13)	0.98 (0.79, 1.78)	< 0.001
Dome to neck ratio	1.10 (0.94, 1.40)	1.02 (0.87, 1.24)	0.113	1.07 (0.89, 1.47)	1.14 (0.84, 1.35)	0.919	1.25 (0.99, 1.40)	1.01 (0.89, 1.23)	0.047
Bottleneck factor	1.22 (1.04, 1.40)	1.10 (0.90, 1.32)	0.089	1.27 (0.94, 1.39)	1.25 (1.06, 1.55)	0.633	1.21 (1.04, 1.43)	0.96 (0.83, 1.16)	0.003
Inflow angle	118.5 (105.7, 132.2)	98.7 (89.9, 113.1)	< 0.001	120.5 (109.9, 134.4)	101.0 (93.5, 113.7)	0.001	116.0 (103.9, 130.9)	95.7 (86.6, 111.6)	0.001

Data was expressed as median (25%, 75%); PCA — posterior cerebral artery

Table 3. Multivariate analysis of rupture-related parameters in aneurysms with or without fetal-type variant

Group	Independent risk factor	Odds ratio	95% CI	P
All (n = 98)	Size ratio	1.625	1.034–2.553	0.035
	Inflow angle	2.286	1.417–3.690	0.001
Fetal PCA (n = 39)	Inflow angle	3.223	1.444–7.197	0.004
Non-fetal PCA (n = 59)	Size ratio	2.378	1.216–4.650	0.011
	Inflow angle	2.086	1.082–4.020	0.028

CI — confidential interval; PCA — posterior cerebral artery

Multivariate logistic regression was performed to identify the independent risk factors of PComA aneu-

rysm rupture using a backward elimination process. All significant parameters that were significant in the univariate analysis were included. The result showed that SR (odds ratio [OR]: 1.625; 95% confidence interval [CI]: 1.034–2.553; $p = 0.04$) and inflow angle (OR: 2.286; 95% CI: 1.417–3.690; $p < 0.01$) were independently associated with the rupture status of PComA aneurysms (Table 3).

Impact of fPCA on morphological parameters

Of the total 98 patients, unilateral fPCA with ipsilateral PComA aneurysm was observed in 33 patients and bilateral fPCA in 6 patients. In this group, 25 (64.1%) aneurysms were ruptured and 14 (35.9%)

were unruptured; while in aneurysms without fPCA variant, 37 (62.7%) were ruptured and 22 (37.3%) were unruptured. Between the fPCA and non-fPCA groups, the baseline characteristics and morphological parameters showed no significant differences, except that the diameters of PComA were higher in the fPCA group ($p < 0.01$) (Table 1).

Then the parameters were further analysed to investigate their relationship with aneurysm rupture in both fPCA group and non-fPCA group relatively (Tables 2, 3). In the fPCA group, only the inflow angle was significantly different between ruptured and unruptured lesions, and further logistic regression analysis showed it as an independent risk factor for rupture (OR: 3.223; 95% CI: 1.444–7.197; $p = 0.004$). While in non-fPCA group, all morphological parameters were significantly associated with the rupture status of PComA aneurysms ($p < 0.05$). Logistic regression analysis showed the independent risk factors for rupture were SR (OR: 2.378; 95% CI: 1.216–4.650; $p = 0.011$) and inflow angle (OR: 2.086; 95% CI: 1.082–4.020; $p = 0.028$).

DISCUSSION

In this study, the performances of morphological parameters in discriminating rupture status were compared between PComA aneurysms with and without fetal-type variant of PCA. The results indicated that the arterial variant might have an impact on the morphological analysis for establishing IA rupture risk. Among the parameters included in the study, inflow angle was found to be a statistically significant rupture predictor for PComA aneurysms.

Unruptured intracranial aneurysms are increasingly detected, which emphasizes the necessity of reliable methods for estimating IA rupture risk [17, 18]. Various mechanisms, including morphology, haemodynamics, and wall inflammation, were reported to be associated with IA rupture [4, 8, 10, 11]. Among them, the morphology of IA and its parent arteries might be the most feasible for clinical use because of its simple and quantitative nature. Increasing numbers of morphological parameters have been introduced and may be roughly classified into the following groups: 1) size-related ratios within the aneurysm itself, such as AR, which is the ratio of aneurysm height to neck; 2) size-related ratios of the aneurysm and its parent artery, such as SR; and 3) other spatial relationships between the aneurysms and its parent artery, such as inflow angle. The utility of

these morphological parameters might be affected by other factors not included in the morphological analysis, such as the location of IA [7, 18]. Location-specific designs, such as employed here, are therefore preferred in studies on rupture risk prediction of IAs [8, 10]. Only PComA aneurysms were considered, which are one of the most common types in clinical practice. Although avoiding biases by distinctive vessel wall characteristics and peri-aneurysmal environment of IAs with this approach, the controversial status of IA rupture prediction remains unchanged. Further sensitizing IA rupture risk investigation to the influence of size and configuration of involved arteries, i.e. vascular variants, may serve as a means to address this controversy. The various anatomic configurations of ICA-PComA bifurcations make PComA aneurysms a well-suited model system to study the effect of these vascular variants on the morphological analysis and thus IA rupture risk. fPCAs is one of the most common variants of the circle of Willis, which has been detected in 4–29% of the general population [5, 16]. Although some studies revealed aneurysms occurred more frequently in patients with this type of variant, few evidences have been obtained on its effect on PComA aneurysm rupture prediction [14]. Therefore, we specified our analysis on PComA aneurysms with fPCA to investigate the impact of arterial variants on the performance of morphological parameters. Interestingly, our results show that the size-related parameters (size, AR, SR, DN, BNF) that were significant between ruptured and unruptured aneurysms in non-fPCA group, lost their discriminating power in the fPCA group; and only the inflow angle was significantly related with rupture status of aneurysms of the fPCA variant.

According to the International Study of Unruptured Intracranial Aneurysms (ISUIA), aneurysmal size was closely associated with IA rupture and the rupture rate of IAs smaller than 7 mm was very low [18]. However, we observed in this study that the median size of ruptured aneurysms was even lower than 5 mm. This indicates that size alone might not be adequate for accurate rupture prediction. In addition, other ratio parameters focusing on the aneurysm itself (AR, DN, and BNF) were shown not to be independently associated with IA rupture. Only SR was retained as an independent rupture risk factor in the total cohort and in the non-fPCA group, highlighting the importance of the relationship between aneurysmal sac and its parent artery in aneurysm rupture risk assessment.

Initially introduced by Dhar et al. [2], SR has been one of the most studied parameters and suggested as a reliable discriminant of rupture status. Kashiwazaki et al. [6] demonstrated that SR could highly predict the rupture risk of IAs, especially for small ones (< 5 mm). Rahman et al. [12] also confirmed prospectively the correlation between SR and aneurysm rupture status. According to a haemodynamic study of Tremmel et al. [15] more complex flow, multiple vortices, and lower wall shear stress were observed in aneurysm models with larger SR. SR not being an independent risk factor for IA rupture in the fPCA group may explain the existence of larger PComAs in the fPCA group.

Inflow angle was the only parameter independently associated with aneurysmal rupture status in both fPCA and non-fPCA. This emphasis on the spatial relationship between the aneurysmal sac and its parent arteries in respect to rupture is consistent with several previous studies [1, 8]. Baharoglu et al. [1] related increasing inflow angle to higher inflow velocity and greater wall shear stress magnitude and spatial gradients in the inflow zone and dome, as well as a greater transmission of kinetic energy into the distal portion of the dome. These haemodynamic features may be important factors that increase the risk of rupture. Inflow angle was also revealed to be associated with irregular haemodynamic patterns [9]. The role of the inflow angle for clinical IA rupture prediction should be investigated in future prospective studies with larger sample size.

Limitations of the study

The present study does have several limitations. Firstly, as a retrospect and single-institutional study, there is an inherent bias selection of PComA aneurysms. Secondly, the relatively small and unbalanced sample size of both groups might affect the analysis. Due to this limited sample size, only the most widely studied morphological parameters were studied to ensure the reliability of the multivariate analysis. In addition, we assumed that the morphology of the PComA aneurysm did not change significantly after rupture, which could affect the accuracy of the results [13].

CONCLUSIONS

Performance of morphological parameters in discriminating rupture status is different between PComA aneurysms with and without fPCA variants.

Inflow angle might be a reliable discriminant for the rupture status of PComA aneurysms.

Funding

This study was funded by the National Research and Development Project of Key Chronic Diseases (Grant No. 2016YFC1300700) and National Natural Science Foundation of China (Grant Nos. 81701775 and 81771264).











Conflict of interest: None declared

REFERENCES

1. Baharoglu MI, Schirmer CM, Hoit DA, et al. Aneurysm inflow-angle as a discriminant for rupture in sidewall cerebral aneurysms: morphometric and computational fluid dynamic analysis. *Stroke*. 2010; 41(7): 1423–1430, doi: [10.1161/STROKEAHA.109.570770](https://doi.org/10.1161/STROKEAHA.109.570770), indexed in Pubmed: [20508183](https://pubmed.ncbi.nlm.nih.gov/20508183/).
2. Dhar S, Tremmel M, Mocco J, et al. Morphology parameters for intracranial aneurysm rupture risk assessment. *Neurosurgery*. 2008; 63(2): 185–197, doi: [10.1227/01.neu.0000316847.64140.81](https://doi.org/10.1227/01.neu.0000316847.64140.81).
3. Forget TR, Benitez R, Veznedaroglu E, et al. A review of size and location of ruptured intracranial aneurysms. *Neurosurgery*. 2001; 49(6): 1322–1325, doi: [10.1097/00006123-200112000-00006](https://doi.org/10.1097/00006123-200112000-00006), indexed in Pubmed: [11846931](https://pubmed.ncbi.nlm.nih.gov/11846931/).
4. Frösen J, Piippo A, Paetau A, et al. Remodeling of saccular cerebral artery aneurysm wall is associated with rupture: histological analysis of 24 unruptured and 42 ruptured cases. *Stroke*. 2004; 35(10): 2287–2293, doi: [10.1161/01.STR.0000140636.30204.da](https://doi.org/10.1161/01.STR.0000140636.30204.da), indexed in Pubmed: [15322297](https://pubmed.ncbi.nlm.nih.gov/15322297/).
5. Horikoshi T, Akiyama I, Yamagata Z, et al. Magnetic resonance angiographic evidence of sex-linked variations in the circle of willis and the occurrence of cerebral aneurysms. *J Neurosurg*. 2002; 96(4): 697–703, doi: [10.3171/jns.2002.96.4.0697](https://doi.org/10.3171/jns.2002.96.4.0697), indexed in Pubmed: [11990810](https://pubmed.ncbi.nlm.nih.gov/11990810/).
6. Kashiwazaki D, Kuroda S. Size ratio can highly predict rupture risk in intracranial small (<5 mm) aneurysms. *Stroke*. 2013; 44(8): 2169–2173, doi: [10.1161/STROKEAHA.113.001138](https://doi.org/10.1161/STROKEAHA.113.001138), indexed in Pubmed: [23743979](https://pubmed.ncbi.nlm.nih.gov/23743979/).
7. Korja M, Lehto H, Juvela S, et al. Lifelong rupture risk of intracranial aneurysms depends on risk factors: a prospective Finnish cohort study. *Stroke*. 2014; 45(7): 1958–1963, doi: [10.1161/STROKEAHA.114.005318](https://doi.org/10.1161/STROKEAHA.114.005318), indexed in Pubmed: [24851875](https://pubmed.ncbi.nlm.nih.gov/24851875/).
8. Lv N, Feng Z, Wang C, et al. Morphological risk factors for rupture of small (<7 mm) posterior communicating artery aneurysms. *World Neurosurg*. 2016; 87: 311–315, doi: [10.1016/j.wneu.2015.12.055](https://doi.org/10.1016/j.wneu.2015.12.055), indexed in Pubmed: [26724608](https://pubmed.ncbi.nlm.nih.gov/26724608/).
9. Lv N, Wang C, Karmonik C, et al. Morphological and hemodynamic discriminators for rupture status in posterior communicating artery aneurysms. *PLoS One*. 2016; 11(2): e0149906, doi: [10.1371/journal.pone.0149906](https://doi.org/10.1371/journal.pone.0149906), indexed in Pubmed: [26910518](https://pubmed.ncbi.nlm.nih.gov/26910518/).

10. Matsukawa H, Fujii M, Akaike G, et al. Morphological and clinical risk factors for posterior communicating artery aneurysm rupture. *J Neurosurg.* 2014; 120(1): 104–110, doi: [10.3171/2013.9.JNS13921](https://doi.org/10.3171/2013.9.JNS13921), indexed in Pubmed: [24160476](https://pubmed.ncbi.nlm.nih.gov/24160476/).
11. Miura Y, Ishida F, Umeda Y, et al. Low wall shear stress is independently associated with the rupture status of middle cerebral artery aneurysms. *Stroke.* 2013; 44(2): 519–521, doi: [10.1161/STROKEAHA.112.675306](https://doi.org/10.1161/STROKEAHA.112.675306), indexed in Pubmed: [23223503](https://pubmed.ncbi.nlm.nih.gov/23223503/).
12. Rahman M, Smietana J, Hauck E, et al. Size ratio correlates with intracranial aneurysm rupture status: a prospective study. *Stroke.* 2010; 41(5): 916–920, doi: [10.1161/STROKEAHA.109.574244](https://doi.org/10.1161/STROKEAHA.109.574244), indexed in Pubmed: [20378866](https://pubmed.ncbi.nlm.nih.gov/20378866/).
13. Schneiders JJ, Marquering HA, van den Berg R, et al. Rupture-associated changes of cerebral aneurysm geometry: high-resolution 3D imaging before and after rupture. *AJNR Am J Neuroradiol.* 2014; 35(7): 1358–1362, doi: [10.3174/ajnr.A3866](https://doi.org/10.3174/ajnr.A3866), indexed in Pubmed: [24557706](https://pubmed.ncbi.nlm.nih.gov/24557706/).
14. Songsaeng D, Geibprasert S, Willinsky R, et al. Impact of anatomical variations of the circle of Willis on the incidence of aneurysms and their recurrence rate following endovascular treatment. *Clin Radiol.* 2010; 65(11): 895–901, doi: [10.1016/j.crad.2010.06.010](https://doi.org/10.1016/j.crad.2010.06.010), indexed in Pubmed: [20933644](https://pubmed.ncbi.nlm.nih.gov/20933644/).
15. Tremmel M, Dhar S, Levy E, et al. Influence of intracranial aneurysm-to-parent vessel size ratio on hemodynamics and implication for rupture. *Neurosurgery.* 2009; 64(4): 622–631, doi: [10.1227/01.neu.0000341529.11231.69](https://doi.org/10.1227/01.neu.0000341529.11231.69).
16. van Raamt AF, Mali WP, van Laar PJ, et al. The fetal variant of the circle of Willis and its influence on the cerebral collateral circulation. *Cerebrovasc Dis.* 2006; 22(4): 217–224, doi: [10.1159/000094007](https://doi.org/10.1159/000094007), indexed in Pubmed: [16788293](https://pubmed.ncbi.nlm.nih.gov/16788293/).
17. Vlak MH, Algra A, Brandenburg R, et al. Prevalence of unruptured intracranial aneurysms, with emphasis on sex, age, comorbidity, country, and time period: a systematic review and meta-analysis. *Lancet Neurol.* 2011; 10(7): 626–636, doi: [10.1016/S1474-4422\(11\)70109-0](https://doi.org/10.1016/S1474-4422(11)70109-0), indexed in Pubmed: [21641282](https://pubmed.ncbi.nlm.nih.gov/21641282/).
18. Wiebers D. Unruptured intracranial aneurysms: natural history, clinical outcome, and risks of surgical and endovascular treatment. *Lancet.* 2003; 362(9378): 103–110, doi: [10.1016/s0140-6736\(03\)13860-3](https://doi.org/10.1016/s0140-6736(03)13860-3).

Standard clinical computed tomography fails to precisely visualise presence, course and branching points of deep cerebral perforators

R. Rzepliński¹, M. Sługocki¹, M. Kwiatkowska², S. Tarka², M. Tomaszewski³,
M. Kucewicz³, K. Karczewski⁴, P. Krajewski², J. Małachowski³, B. Cizek¹

¹Department of Descriptive and Clinical Anatomy, Medical University of Warsaw, Poland

²Department of Forensic Medicine, Medical University of Warsaw, Poland

³Institute of Mechanics and Computational Engineering, Faculty of Mechanical Engineering, Military University of Technology, Warsaw, Poland

⁴Institute of Materials Science and Engineering, Faculty of Advanced Technologies and Chemistry, Military University of Technology, Warsaw, Poland

[Received: 29 October 2021; Accepted: 28 November 2021; Early publication date: 15 December 2021]

Background: Standard computed tomography (CT) images have earned a well-established position in neuroimaging. Despite that, CT is somehow limited by its resolution, which does not enable to distinctively visualise structures smaller than 300 µm in diameter. Perforating arteries, most of which measure 100–400 µm in diameter, supply important subcortical structures (thalamus, basal ganglia, internal capsule). Consequently, pathologies affecting these vessels (e.g. lacunar strokes) can have a devastating clinical outcome. The aim of our study was to assess standard CT's ability to visualise perforators and compare it with microscopic and micro-CT pictures.

Materials and methods: We have obtained 6 brainstem and 17 basal ganglia specimens. We infused them with barium sulphate contrast medium administered into either vertebral or internal cerebral artery. After that, the specimens were fixed in formalin and subsequently a series of CT, micro-CT and microscopic examinations were performed.

Results: The median number of visualised perforators in brainstem and basal ganglia specimens was 8 and 3, respectively for CT and 18 and 7 for micro-CT ($p < 0.05$). Standard CT failed to clearly visualise branching points and vessels smaller than 0.25–0.5 mm (1–2 voxels) in diameter. Parallel vessels, like lenticulostriate arteries could not be differentiated in standard CT due to their proximity being smaller than the resolution.

Conclusions: Basing on our results, we infer that CT is a poor modality for imaging of the perforators, presenting both quantitative and qualitative flaws in contrast with micro-CT. (Folia Morphol 2023; 82, 1: 37–41)

Key words: perforating arteries, cerebral perforators, computed tomography, micro-computed tomography, cerebral circulation

Address for correspondence: R. Rzepliński, MD, Department of Descriptive and Clinical Anatomy, Medical University of Warsaw, ul. Chałubińskiego 5, 02–004 Warszawa, Poland, tel/fax: +48 22 629 52 83, e-mail: radoslaw.rzeplinski@wum.edu.pl

This article is available in open access under Creative Common Attribution-Non-Commercial-No Derivatives 4.0 International (CC BY-NC-ND 4.0) license, allowing to download articles and share them with others as long as they credit the authors and the publisher, but without permission to change them in any way or use them commercially.

INTRODUCTION

The clinical significance of the anatomy of cerebral perforating arteries is well known [14]: despite their relatively small diameter of below 1 mm [3, 5], their pathology results in development of serious diseases such as lacunar stroke, intracerebral haemorrhage, vascular dementia, as well as leads to severe ischaemic complications after aneurysmal subarachnoid haemorrhage and neurovascular procedures [1, 2, 8, 9, 11]. Despite advances in neuroimaging techniques, assessment of presence and function of perforating arteries remains challenging.

The aim of the study was to assess suitability of standard contrast enhanced computed tomography (CT) for visualising deep cerebral perforators by comparing its results to microscopic and micro-computed tomography (micro-CT) studies of anatomical specimens.

MATERIALS AND METHODS

Preparation of the specimens

The specimens of basal ganglia and brainstem were prepared by obtaining an unfixed brain from the cadaver, filling the arteries with contrast medium (barium sulphate), and fixing in 10% buffered formalin solution, as precisely described previously [12]. In each case, the pontine branches of the basilar artery (from the vertebrobasilar junction to the superior cerebellar arteries) or the lenticulostriate arteries were counted and measured using a microsurgical microscope.

Scanning of the specimens and radiological analysis

Every specimen was scanned with both standard clinical CT scanner (Toshiba Asteion TSX-034A, voxel size 0.25 mm, 120 kV, 150 mA) and micro-CT scanner (Nikon Metris XT H 225 ST, voxel size 0.0034 mm, 225 kV, 4 million pixels detector). Images were processed in CT Pro 3D software (Metris XT 2.2, Nikon Metrology, Belmont, CA) and Mimics Innovation Suite 24.0 (Materialise, Belgium). The pontine branches or the lenticulostriate arteries were counted in each case. The quality of visualisation of the branching sites and the course of the arteries were also determined. The numbers of arteries visualised in standard and micro-CT were compared with the Wilcoxon signed rank sum test.

Ethical approval

All procedures performed in the study were in accordance with the ethical standards of the institutional research committee and with the 1964 Helsinki declaration and its later amendments. The study protocol was approved by The Ethics Committee of Medical University of Warsaw, Poland (Number 138/2020).

RESULTS

Six specimens of brainstem and 17 specimens of basal ganglia were prepared and scanned by both standard and micro-CT. The median (first–third quartile) number of the pontine branches of the basilar artery amounted to 8 (7–9) and 18 (17–21) in standard and micro-CT, respectively ($p = 0.031$). The median (first–third quartile) number of the lenticulostriate arteries amounted to 3 (3–4) and 7 (7–8) in standard and micro-CT, respectively ($p < 0.0001$). Numbers of arteries counted under microsurgical microscope and visualised in micro-CT were equal in all cases — every artery filled with contrast medium was visible in micro-CT. Diameters of the perforating arteries measured with the use of microsurgical microscope ranged from 0.11 to 0.76 mm and were equal to the diameters measured on micro-CT scans with an accuracy of arterial wall thickness. In standard CT vessels of diameter below 1–2 voxel sizes (0.25–0.5 mm) were either invisible or could not be measured reliably (Fig. 1). Moreover, perforating arteries tend to have parallel course (e.g. lenticulostriate arteries branching from M2 and distal M1 entering the hemisphere in the anterior perforated substance) and standard CT does not allow to differentiate them, because of distance between the arteries being smaller than the resolution. Therefore, counting and measuring perforating arteries in standard CT scans was significantly compromised. In contrast, micro-CT scans provided clear and precise geometry of branching points and course of studied arteries (Figs. 1, 2).

DISCUSSION

The main purpose of the study was to investigate suitability of standard CT for visualising perforating arteries of cerebral circulation. Our work clearly shows that this method is ineffective and unreliable. There are several quantitative and qualitative differences between standard CT scans on the one hand and microscopic and micro-CT studies on the other.

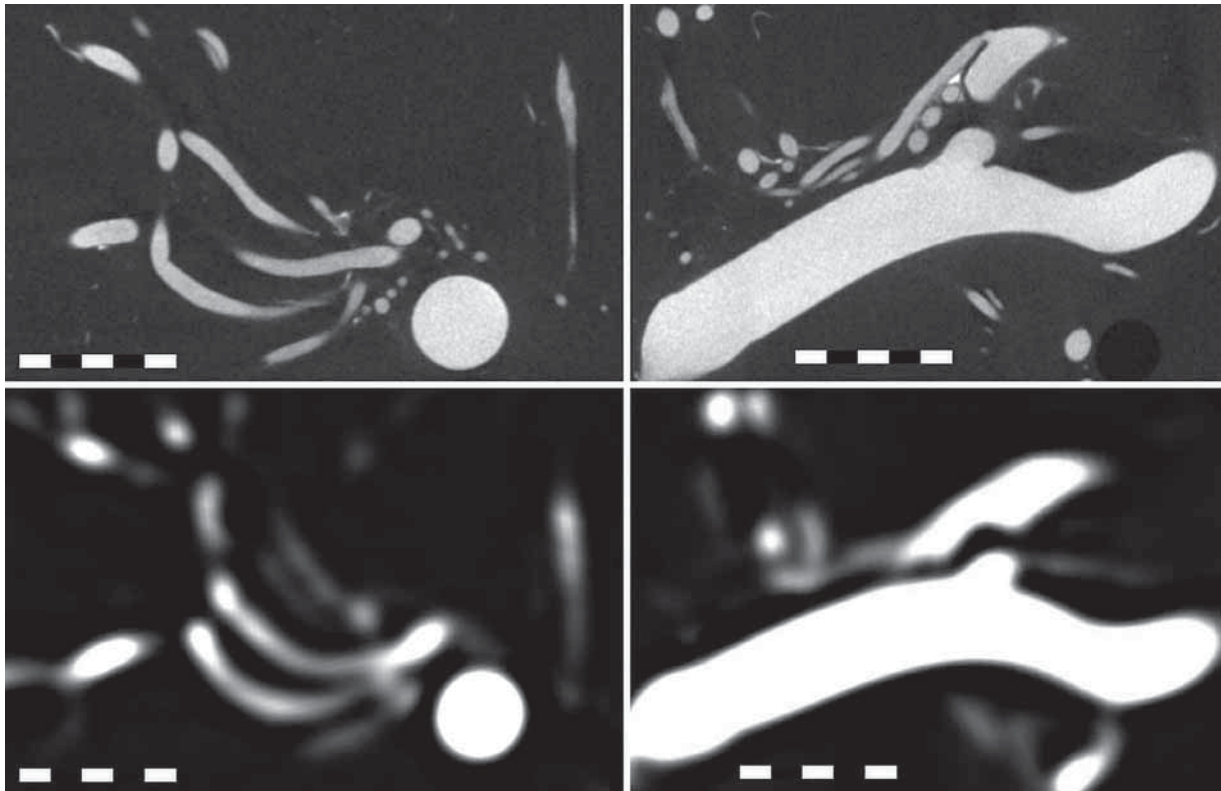


Figure 1. Comparison of micro-computed tomography (CT) (upper row) and standard CT (lower row) images in the same plane of a representative middle cerebral artery. Resolution of the standard CT image does not allow to differentiate parallel lenticulostriate arteries and some perforators are invisible. In standard CT a group of perforators can easily be misinterpreted as one vessel. The diameters of the lenticulostriate arteries cannot be measured accurately because of the lack of a clear border between contrast-enhanced vessel lumen and non-enhanced surrounding tissues. The branching points cannot be identified in the case of standard CT. Length of the ruler is 5 mm.

Quantitative differences between standard and micro-CT scans

The number of visualised pontine and perforating arteries was significantly higher, when counted using microscopic or micro-CT images, which was mainly due to better visualisation of smaller vessels. The resolution of standard CT significantly limited the ability to visualise the perforating arteries, because their diameters usually do not exceed 1–2 sizes of voxel.

Moreover, the number and the diameters of perforators in the micro-CT picture was the same as under the microsurgical microscope, suggesting that these techniques can be utilized interchangeably. This advantage is important especially when studying internal microvasculature as surrounding tissues can be left intact.

Qualitative differences between standard and micro-CT scans

As presented above, the standard CT could visualise only the presence of the biggest perforating arteries. What's more interesting, the resolution was not high

enough to study geometry of branching points or courses of the arteries. The micro-CT has visualised branching points and the courses of the perforating arteries far better than the standard CT. Moreover, standard CT scans could not precisely determine the number and branching points of parallel lenticulostriate arteries or pontine branches, making determination of the parent segment impossible. These properties are crucial to plan intracranial procedures, create reliable three-dimensional models, analyse supply areas, dynamics of blood flow and forces acting on arterial walls. Micro-CT allows studying all of the aforementioned aspects.

Noteworthy, angio-CT of the head usually visualises veins to some extent, which further reduces the quality of image. It is especially important in the case of the lenticulostriate arteries because they are located parallel to the deep middle cerebral vein.

The resolution of digital subtraction angiography and magnetic resonance imaging (even 7T [4]) usually do not reach values below 0.25 mm [6, 7]: therefore, one can anticipate the same problems with visualising the perforators as in the case of CT.

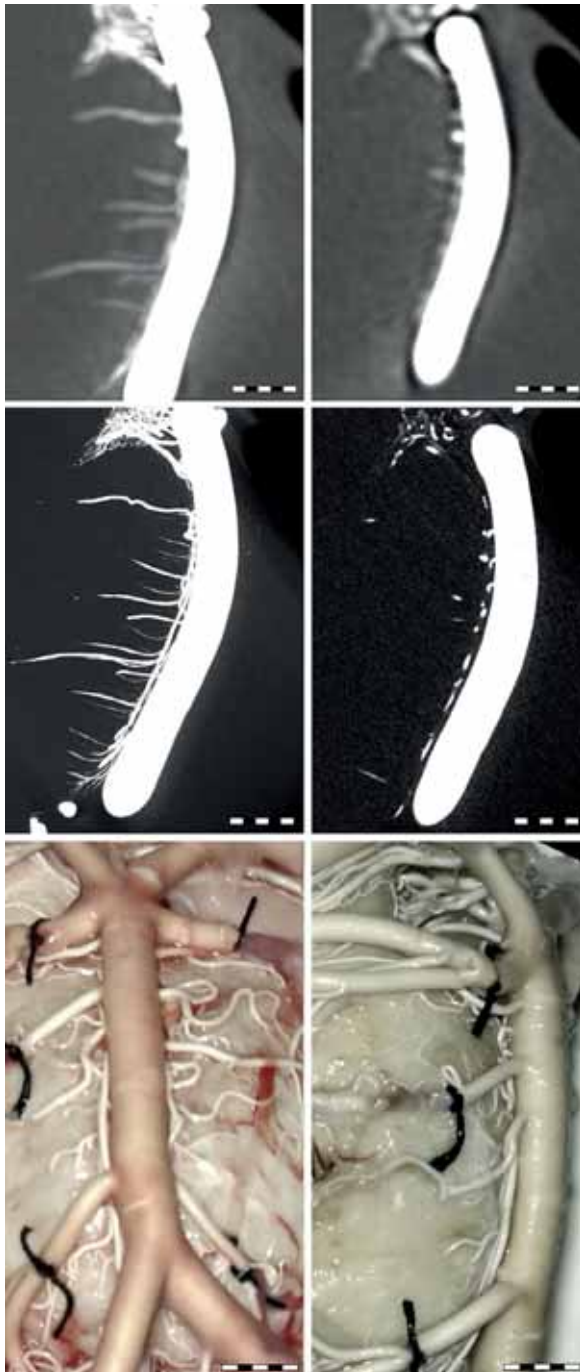


Figure 2. Comparison of standard-computed tomography (CT) (top) and micro-CT (middle) images in the same plane and microscopic images of a fixed brainstem specimen (bottom). The CT images on the left side are maximum intensity projection reconstructions (thickness 6.0 mm), and the CT images on the right side are mid-line sagittal slices. Some of the perforating arteries are invisible in standard CT. Similarly, branching points are not evident. Microscopic images show anterior and lateral view of the basilar artery and pontine branches. Length of the ruler is 5 mm.

Clinical relevance of the study

Our study clearly shows that absence of a structure in imaging studies is not equivalent to non-existence in real life. This conclusion is critical, when studying cerebral vasculature, as the resolution is comparable to the diameters of some arteries (including variants of the circle of Willis with hypoplastic anterior cerebral artery or posterior communicating artery) [10]. Neurosurgeons and neuroradiologists should be aware of that fact when planning and performing intracranial interventions. Micro-CT is a useful tool in preclinical studies [13, 15].

Limitations of the study

The study was specimen-based; however, standard clinical CT scanner was used. Up to date, no micro-CT scanners are admitted to clinical use. It is only possible to study previously prepared anatomical specimens. The volume of the specimen is usually restricted due to technical features of scanners.

CONCLUSIONS

Computed tomography is inappropriate to study presence, course, and geometry of the perforating arteries of cerebral circulation. Micro-CT, in contrast, is a feasible and effective method that allows for precise determination of the number, branching points, and the course of the pontine and perforating arteries. These advantages may be used for several anatomical and haemodynamic studies; however, clinical application is restricted by technical features of micro-CT scanners.

Acknowledgements

The authors sincerely thank those who donated their bodies to science so that anatomical research could be performed. Results from such research can potentially increase mankind's overall knowledge that can then improve patient care. Therefore, these donors and their families deserve our highest gratitude.

Funding

The study was founded by the National Science Centre, Poland (award number 2020/37/B/ST8/03430, Recipient: Jerzy Małachowski). The National Science Centre had no involvement in the study design, in the

collection, analysis and interpretation of data, in the writing of the manuscript, in the decision to submit the manuscript for publication. Michał Tomaszewski is recipient of Foundation for Polish Science scholarship.

Conflict of interest: None declared

REFERENCES

1. Brinjikji W, Murad MH, Lanzino G, et al. Endovascular treatment of intracranial aneurysms with flow diverters: a meta-analysis. *Stroke*. 2013; 44(2): 442–447, doi: [10.1161/STROKEAHA.112.678151](https://doi.org/10.1161/STROKEAHA.112.678151), indexed in Pubmed: [23321438](https://pubmed.ncbi.nlm.nih.gov/23321438/).
2. Cannistraro RJ, Badi M, Eidelman BH, et al. CNS small vessel disease: A clinical review. *Neurology*. 2019; 92(24): 1146–1156, doi: [10.1212/WNL.0000000000007654](https://doi.org/10.1212/WNL.0000000000007654), indexed in Pubmed: [31142635](https://pubmed.ncbi.nlm.nih.gov/31142635/).
3. Ciszek B, Aleksandrowicz R, Zabek M, et al. Classification, topography and morphometry of the early branches of the middle cerebral artery. *Folia Morphol*. 1996; 55(4): 229–230, indexed in Pubmed: [9243859](https://pubmed.ncbi.nlm.nih.gov/9243859/).
4. Hartevelde AA, De Cocker LJJ, Dieleman N, et al. High-resolution postcontrast time-of-flight MR angiography of intracranial perforators at 7.0 Tesla. *PLoS One*. 2015; 10(3): e0121051, doi: [10.1371/journal.pone.0121051](https://doi.org/10.1371/journal.pone.0121051), indexed in Pubmed: [25774881](https://pubmed.ncbi.nlm.nih.gov/25774881/).
5. Kwiatkowska M, Ciszek B. The anatomy of the median branches of the basilar artery. *Folia Morphol*. 2000; 59(4): 323–325, indexed in Pubmed: [11107706](https://pubmed.ncbi.nlm.nih.gov/11107706/).
6. Naidich TP. (ed). *Imaging of the brain*. Saunders/Elsevier, Philadelphia 2013.
7. Osborn AG, Hedlund GL, Salzman KL. *Osborn's brain: imaging, pathology, and anatomy*. 2 ed. Elsevier, Philadelphia 2018.
8. Phillips TJ, Wenderoth JD, Phatouros CC, et al. Safety of the pipeline embolization device in treatment of posterior circulation aneurysms. *AJNR Am J Neuroradiol*. 2012; 33(7): 1225–1231, doi: [10.3174/ajnr.A3166](https://doi.org/10.3174/ajnr.A3166), indexed in Pubmed: [22678845](https://pubmed.ncbi.nlm.nih.gov/22678845/).
9. Regenhardt RW, Das AS, Lo EH, et al. Advances in understanding the pathophysiology of lacunar stroke: a review. *JAMA Neurol*. 2018; 75(10): 1273–1281, doi: [10.1001/jamaneurol.2018.1073](https://doi.org/10.1001/jamaneurol.2018.1073), indexed in Pubmed: [30167649](https://pubmed.ncbi.nlm.nih.gov/30167649/).
10. Rhoton A. The supratentorial arteries. *Neurosurgery*. 2002; 51(suppl_4): S1–53–S1–120, doi: [10.1097/00006123-200210001-00003](https://doi.org/10.1097/00006123-200210001-00003).
11. Rzepliński R, Kostyra K, Skadorwa T, et al. Acute platelet response to aneurysmal subarachnoid hemorrhage depends on severity and distribution of bleeding: an observational cohort study. *Neurosurg Rev*. 2021; 44(5): 2647–2658, doi: [10.1007/s10143-020-01444-7](https://doi.org/10.1007/s10143-020-01444-7), indexed in Pubmed: [33241455](https://pubmed.ncbi.nlm.nih.gov/33241455/).
12. Rzepliński R, Tomaszewski M, Stugocki M, et al. Method of creating 3D models of small caliber cerebral arteries basing on anatomical specimens. *J Biomech*. 2021; 125: 110590, doi: [10.1016/j.jbiomech.2021.110590](https://doi.org/10.1016/j.jbiomech.2021.110590), indexed in Pubmed: [34214861](https://pubmed.ncbi.nlm.nih.gov/34214861/).
13. Skadorwa T, Maślanka M, Ciszek B. The morphology and morphometry of the fetal fallopian canal: a microtomographic study. *Surg Radiol Anat*. 2015; 37(6): 677–684, doi: [10.1007/s00276-014-1395-2](https://doi.org/10.1007/s00276-014-1395-2), indexed in Pubmed: [25480106](https://pubmed.ncbi.nlm.nih.gov/25480106/).
14. Vogels V, Dammers R, van Bilsen M, et al. Deep cerebral perforators: anatomical distribution and clinical symptoms: an overview. *Stroke*. 2021; 52(10): e660–e674, doi: [10.1161/STROKEAHA.120.034096](https://doi.org/10.1161/STROKEAHA.120.034096), indexed in Pubmed: [34311568](https://pubmed.ncbi.nlm.nih.gov/34311568/).
15. Wojciechowski T, Skadorwa T, Nève de Mévergnes JG, et al. Microtomographic morphometry of the stapedius muscle and its tendon. *Anat Sci Int*. 2020; 95(1): 31–37, doi: [10.1007/s12565-019-00490-6](https://doi.org/10.1007/s12565-019-00490-6), indexed in Pubmed: [31111392](https://pubmed.ncbi.nlm.nih.gov/31111392/).

Vitamin D3 promotes oligodendrogenesis and modulates synucleinopathy in lead-induced nigral pars compacta neurotoxicity in rats

R.A. Imam¹ , M.R. Abdel-Hamed²

¹Department of Anatomy and Embryology, Faculty of Medicine, Cairo University, Egypt

²Department of Anatomy and Embryology, Faculty of Medicine, Ain Shams University, Egypt

[Received: 31 July 2021; Accepted: 29 December 2021; Early publication date: 17 January 2022]

Background: Lead-induced neurotoxicity was marked with locomotor and Parkinsonian-like changes. Oligodendrocytes and synucleinopathy were signed to in the pathophysiology of some neurodegenerative diseases. Vitamin D3's (D3) role in substantia nigra pars compacta (SNpc) disorders is debated between neuroscientists. The aim of the study was to investigate lead-induced SNpc neurotoxic changes and explore the possible neuroprotective role of D3 and the possible involvement of oligodendrocytes and α -synuclein.

Materials and methods: This study included 40 adult Wistar rats assigned into four equal groups: control, lead (Pb) (in drinking water, 1,000 mg/L), Pb + D3 (D3 injection, 1,000 IU/kg IM; 3 days/week), and D3. After 8 weeks, the rats were sacrificed, and their midbrain underwent biochemical and immunoblotting analysis. Midbrain paraffin blocks were stained for histological and immunohistochemical assessment.

Results: Lead (Pb) had increased significantly ($p < 0.05$) nigral α -synuclein and caspase-11 by immunoblotting analysis. Histologically, it induced neurodegeneration in SNpc and significantly decreased neuronal cell density by cresyl violet staining. Pb also significantly reduced SNpc tyrosine hydroxylase immunoreaction, significantly elevated glial fibrillary acid protein (GFAP) and α -synuclein immunoreaction associated with a mild but significant increase in caspase-3. In the Pb + D3 group, all the previous deleterious changes were significantly alleviated in addition to significant upregulation of anti-oligodendrocytes immunoexpression.

Conclusions: Lead (Pb) may induce SNpc neurotoxicity presumably via activation of caspase-11 and α -synuclein. D3 may modulate this neurotoxicity probably through an oligodendrogenic effect. (Folia Morphol 2023; 82, 1: 42–52)

Key words: lead (Pb), pars compacta, D3-synucleinopathy, oligodendrocytes

INTRODUCTION

As an environmentally toxic heavy metal, lead (Pb) induced profound clinical changes in most body systems, particularly on the nervous system (the primary

target of the Pb) [1]. It had been evidenced that frequent exposure to lead is linked with Parkinsonism-like motor deficits, suggesting strong evidence for a role of Pb in the development of Parkinson's disease (PD)

Address for correspondence: Dr. R.A. Imam, Department of Anatomy and Embryology, Faculty of Medicine, Cairo University, Cairo, Egypt, tel: +2001006114696; e-mail: redaabdelnasser@cu.edu.eg; abdelnasserreda@gmail.com

This article is available in open access under Creative Common Attribution-Non-Commercial-No Derivatives 4.0 International (CC BY-NC-ND 4.0) license, allowing to download articles and share them with others as long as they credit the authors and the publisher, but without permission to change them in any way or use them commercially.

(the most typical neurobiological motion disorder of old age predominating in 2–3% of ≥ 65 years old worldwide) [14, 18]. Oligodendrocytes, myelin producers of the central nervous system, are involved in the pathophysiology of some neurodegenerative diseases [17]. For example, aggregates of α -synuclein in oligodendrocytes, forming glial cytoplasmic inclusions, were a main neuropathological finding in multiple system atrophy neurodegenerative disease [13]. However, the role of oligodendrocytes in pars compacta neurodegenerative disorders is not yet clear. Inclusion synucleinopathy is a particular pathological feature for some neuronal disorders [21]. Caspase-11 had been early reported to mediate nigral neurotoxicity in 1-Methyl-4-Phenyl-1, 2, 3, 6-Tetrahydropyridine (MPTP)-received mice [7]. Vitamin D3 had been proved to protect against lead-induced adverse changes in some organs like kidneys and testis [4]. However, neuro researchers debate the vitamin D3 role in substantia nigra pars compacta (SNpc) neurodegenerative disorders [6]. Some authors have reported that D3 may protect SNpc neurons against oxidative stress and inflammation in some neuronal conditions [8]. This study aimed to investigate lead-induced SNpc neurotoxicity, explore its relation with α -synuclein, oligodendrocytes and caspases-3, -11, and explore the possible protective role of D3 against this neurotoxicity.

MATERIALS AND METHODS

Materials

Lead acetate was purchased in powder form from El-Gomhouria Company (Cairo, Egypt). D3 was supplied in injection (Devarol S 200,000 IU, 2 mL ampoule; Egypt Memphis Company, Cairo, Egypt). Vitamin D3 kits for serum D3 were purchased as Elisa kits from MyBioSource, USA. ReadyPrep™ protein extraction kit was supplied by Bio-Rad Laboratories Inc. (Hercules, CA, USA). The quantitative protein analysis Bradford Protein Assay Kit was provided by Bio Basic Inc. (Markham, ON, Canada). Polyacrylamide gels were extracted using TGX Stain-Free™ FastCast™ Acrylamide Kit purchased from Bio-Rad Laboratories Inc. Caspase 11 primary antibody (caspase-11; Rat mAb) was purchased from Cell Signaling Technology (Beverly, MA, USA). α -synuclein primary antibody for immunoblotting analysis was purchased from Santa Cruz Biotechnology (Santa Cruz, CA, USA). Immunoblotting technique horseradish peroxidase (HRP)-conjugated secondary antibody was goat anti-rabbit IgG-HRP-1

mg Goat mab (Novus Biologicals, Littleton, CO, USA). The chemiluminescent substrate was Clarity™ Western ECL Substrate (Bio-Rad Laboratories Inc.). Primary antibodies utilised in immunohistochemistry were anti-oligodendrocytes (Olig-2) rabbit polyclonal (GeneTex, Inc., Irvine, CA, USA), glial fibrillary acid protein (GFAP) and anti-D3 were rabbit polyclonal (Dako, Denmark), tyrosine hydroxylase (TH) and α -synuclein were rabbit polyclonal (Abcam, UK), caspase-3 was rabbit, polyclonal (Santa Cruz Biotechnology, USA).

Animals

The present study strictly adhered to animal research ethics and was approved by CU-IACUC (no. III-F-47-20). Forty adult Wistar rats weighing 150–200 g were assigned into four equal groups and housed at the animal house of the Faculty of Medicine, Cairo University, Cairo, Egypt. They were subjected to standard animal conditions 2 weeks before the experiment for acclimatisation, fed ad libitum, and grouped into the control group (I) received intramuscular saline, Pb group (II) received a lead in drinking water, Pb + D3 group (III) received lead concomitant with D3 injection and D3 group (IV) received D3 injection.

Chemicals

Lead. The powder was dissolved in drinking water and given to the rats at a dosage of 1,000 mg/L [4].

Vitamin D3. The vitamin was given at a dosage of 1,000 IU/kg IM (3 days/week) [4].

All rats were weighed, blood samples were obtained to measure serum D3 by Elisa and serum lead by atomic absorption spectrophotometer (model SensAA, Australia). The rats were sacrificed by guillotines method 8 weeks from the experiment to minimize brain injury. Their brains were obtained and subjected to biochemical and histological investigations.

Biochemical analysis

Parts from the ventral midbrain were used for biochemical measurement of lead in tissue and immunoblotting analysis (for caspase-11 and α -synuclein).

Measurement of lead in ventral midbrain. Air-dried ventral midbrain tissue was digested with 8 mL of concentrated sulphuric acid then heated for 5 minutes on a hot plate to remove all fumes with the addition of perchloric acid followed by metal analysis by atomic absorption spectrophotometer (model SensAA, Australia).

Immunoblotting analysis technique. The Ready-Prep™ protein extraction kit (total protein) was added for each homogenized ventral midbrain tissues sample. A Bradford assay was conducted, followed by polyacrylamide gel electrophoresis loading. Protein bands were transferred from the gel to the membrane using BioRad Trans-Blot Turbo. The membrane was blocked in tris-buffered saline with Tween 20 (TBST) buffer and 3% bovine serum albumin (BSA) at room temperature for 1 hour. Primary antibodies of caspase-11 and α -synuclein were diluted in TBST followed by overnight incubation in each primary antibody solution against the blotted target protein at 4°C. Incubation was conducted in the HRP-conjugated secondary antibody solution against the blotted target protein for 1 hour at room temperature. The chemiluminescent substrate was applied to the blot as equal volumes from solutions A (Clarity Western Luminal/Enhancer Solution) and B (peroxidase solution). The chemiluminescent signals were captured, and image analysis software was performed to read the band intensity by protein normalisation on the ChemiDoc MP imager.

Histological assessment

The midbrain was preserved in formalin, processed for paraffin blocking, utilised for histological and immunohistochemical staining. Paraffin blocked sections were processed for staining with haematoxylin and eosin (H&E) and cresyl violet stain. For cresyl violet staining, tissue sections were soaked in paraformaldehyde, washed into Pbs, soaked with cresyl violet solution, then dehydrated using ascending grades of ethanol 70%, 90%, and finally 100%.

Immunohistochemical techniques [3]

Midbrain sections were deparaffinised, underwent heat-induced epitope retrieval and stained with anti-D3 (to evaluate D3; dilution, 1:100), TH (to evaluate for dopaminergic neurons; dilution, 1:100), GFAP (to evaluate for astrocytic activity; dilution, 1:100), caspase-3 (dilution 1:100) (to assess for apoptosis), α -synuclein (to detect synucleinopathy, dilution 1:50) and anti-Olig-2 (to evaluate for oligodendrocytes; dilution, 1:100). The slides were entered into the Dako automated system (EnVision Flex-peroxidase blocked). Moreover, the Dako EnVision Flex/HRP was added as the secondary antibody. Leica ICS150 microscope camera was used to photograph H&E and immunohistochemical slides.

Histomorphometric measurement

The area percentage of the positive immune reaction of anti-D3, TH, GFAP, anti-Olig-2, α -synuclein, and caspase-3 was measured using image J analysis software, ten randomly chosen fields measurements ($\times 400$ magnification) from each group were taken and statistically analysed. Also, neuronal cell density by cresyl violet staining was determined by the number of surviving neurons in each field ($\times 400$ magnification) as measured by image J software. According to Wang et al. 2010 [19], non-viable neurons were determined as those with dense cresyl violet staining and pyknotic nuclei.

Ethical approval

All the study procedures and manipulations were done according to the ARRIVE guidelines and the study was approved by Cairo University Institute of Animal Care and Use Committee (CU-IACUC) under No III-F-47-20.

Statistical analysis

GraphPad Prism 8 was utilized to analyse all gathered data represented as mean \pm standard error of the mean (SEM). Analysis of variance and Tukey's test were conducted for in-between group comparison with a cut-off p-value of ≤ 0.05 for significance.

RESULTS

Clinical data

No mortality had been recorded among rats. The body weight of rats at the end of the experiment in the Pb + D3 and D3 groups was significantly increased compared with the control and Pb groups (Table 1).

Biochemical results

Lead and D3 measurement in blood. Lead (Pb) in blood had increased significantly in Pb and Pb + D3 groups compared to control and D3 groups. It showed a mild significant decrease in the Pb + D3 group compared to the Pb group (Table 1). D3 in blood had increased significantly in Pb + D3 and D3 groups compared to control and Pb groups (Table 1).

Lead measurement in the midbrain. Lead (Pb) in the midbrain had increased significantly in Pb and Pb + D3 groups compared to control and D3 groups (Table 1).

Western blot results. Lead (Pb) significantly raised the protein expressions of α -synuclein in the anterior part of the midbrain (ventral) compared to the control

Table 1. Bodyweight (BW) of rats, serum D3 and Pb, midbrain Pb level, and cell density of substantia nigra pars compacta (SNpc) neurons by cresyl violet among different groups

Groups	BW [g]	Serum Pb [$\mu\text{g/dL}$]	Serum D3 [ng/dL]	Midbrain Pb level [$\mu\text{g/mL}$]	The cell density of SNpc neurons by cresyl violet
Control	222 \pm 3.62	3.2 \pm 0.26	26.42 \pm 3.40	0.1093 \pm 0.021	47.7 \pm 2.35
Lead (Pb)	187 \pm 4.32 ^a	50.9 \pm 2.73 ^a	20.63 \pm 3.02	2.33 \pm 0.192 ^a	23.80 \pm 2.30 ^a
Pb + D3	280 \pm 7.06 ^{a,b}	39.59 \pm 3.44 ^{a,b}	77.35 \pm 3.81 ^{a,b}	1.751 \pm 0.364 ^a	34.70 \pm 2.18 ^{a,b}
Vitamin D3	279.8 \pm 7.31 ^{a,b}	3.08 \pm 0.40 ^{b,c}	82.93 \pm 4.36 ^{a,b}	0.1391 \pm 0.030 ^{b,c}	46.20 \pm 2.66 ^{b,c}

^ap < 0.05 i.e. statistically significant when compared with the control group; ^bp < 0.05 when compared with the Pb group; ^cp < 0.05 when compared with Pb + D3 group (data are represented as mean \pm standard error of the mean)

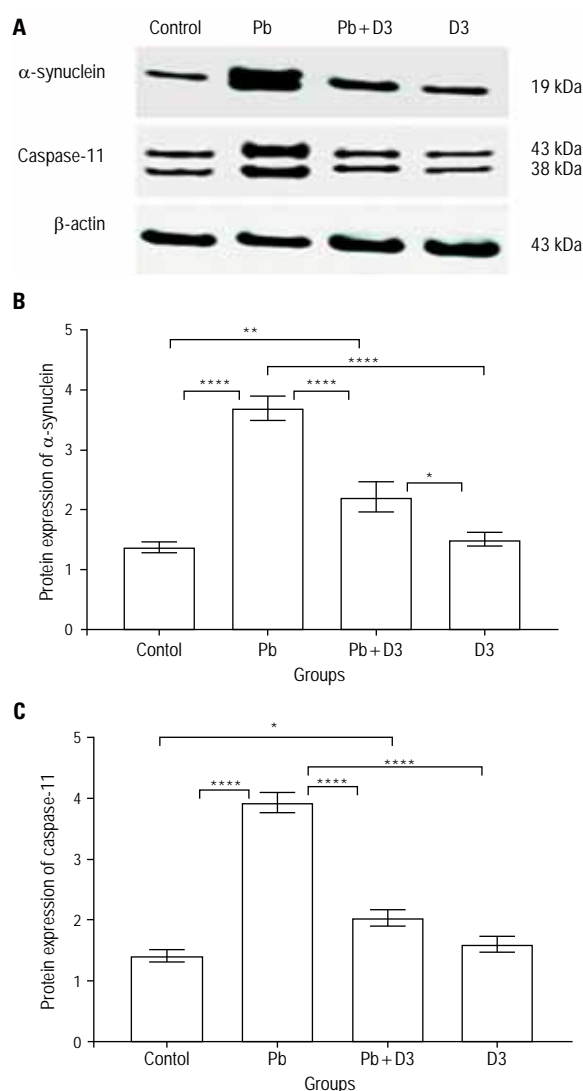


Figure 1. A. Western blot analysis of protein expression of α -synuclein and caspase-11 among the different groups with β -actin as the internal standard. **B, C.** The two graphs show that lead (Pb) had significantly increased α -synuclein and caspase-11 compared with control. In the Pb + D3 group, both proteins were significantly decreased compared with the Pb group; *statistically significant when $p < 0.05$; **when $p < 0.01$; *** when $p < 0.001$; ****when $p < 0.0001$ (error bar = standard error of the mean).

and D3 groups (2.68- and 2.45-fold, respectively). The same was true for caspase-11 in the Pb group compared with the control and D3 groups (2.8- and 2.4-fold, respectively) via Western blot analysis. Compared with the lead group, the simultaneous addition of D3 to lead in group III significantly decreased α -synuclein and caspase-11 (66% and 92%, respectively). However, they were still significantly elevated (60% and 43% for α -synuclein and caspase-11, respectively) compared with the control group (Fig. 1).

Morphological results

The control group, SNpc typical neurons via H&E stain (Fig. 2), appeared with vesicular nuclei and lightly stained cytoplasm. Pb group SNpc exhibited interstitial oedema, darkly stained neurons with pyknotic nuclei, degenerated neurons (karyolysis), lost neurons, and infiltrated glial cells. A few SNpc neurons in the Pb + D3 group were darkly stained, whereas most neurons were preserved. D3 group SNpc exhibited typically appearing neurons.

Via cresyl violet staining (Fig. 3), the control group exhibited standard staining of the nuclei and cytoplasm while Pb group SNpc showed few neurons with dark cresyl violet staining. A few SNpc neurons in the Pb + D3 group were densely stained, whereas most neurons were preserved. The D3 group SNpc exhibited standardly stained neurons. The cell density of SNpc by cresyl violet staining in histomorphometric analysis revealed a significant decrease in the number of viable neurons in the Pb group compared to the control and D3 group (50%, 48%, respectively). The Pb + D3 group showed a significant increase (45%) in the number of viable neurons than the Pb group (Table 1).

Immunohistochemical results

The control and lead SNpc groups exhibited scanty anti-D3 immunostaining (Fig. 4). The Pb + D3

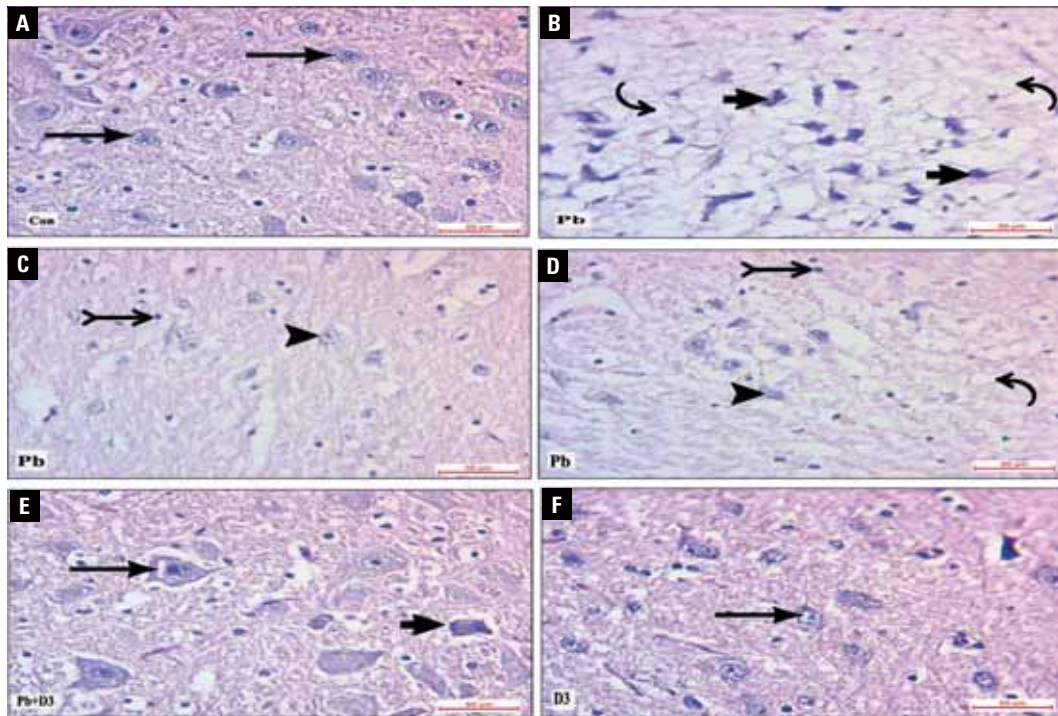


Figure 2. A. The control group (Con) substantia nigra pars compacta (SNpc) exhibits typical neurons with vesicular nuclei and lightly stained cytoplasm (arrows); B, C, D. The lead (Pb) group SNpc with interstitial oedema (curved arrows), darkly stained neurons with pyknotic nuclei (incomplete arrows), degenerated neurons (karyolysis) (arrowheads) and infiltrated glial cells (tailed arrows); E. A few SNpc neurons in the Pb + D3 group are darkly stained, whereas most neurons are preserved; F. Vitamin D3 SNpc group displays typically appearing neurons (H&E $\times 400$, scale bar = 50 μm).

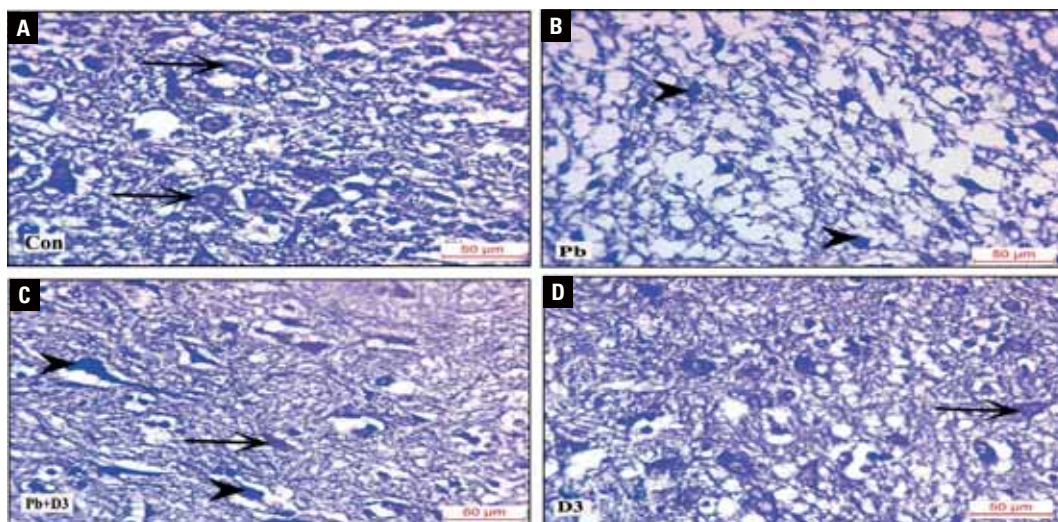


Figure 3. A. The control group (Con) substantia nigra pars compacta (SNpc) with neurons with standard cresyl violet staining of the nuclei and cytoplasm (arrows); B. The lead (Pb) group SNpc shows degenerated neurons with dense cresyl violet staining and pyknotic nuclei (arrowheads); C. A few SNpc neurons in the Pb + D3 group are densely stained, whereas most neurons are preserved; D. The D3 group SNpc with standardly stained neurons (cresyl violet $\times 400$, scale bar = 50 μm).

and D3 groups showed strong anti-D3 immunostaining. Histomorphometric data revealed that the area percentage of positive anti-D3 immunoreaction in the Pb + D3 group significantly increased

compared with both control and Pb groups (11.05- and 12.45-fold, respectively). Additionally, in the D3 group, the area percentage of the positive anti-D3 significantly increased compared with both control

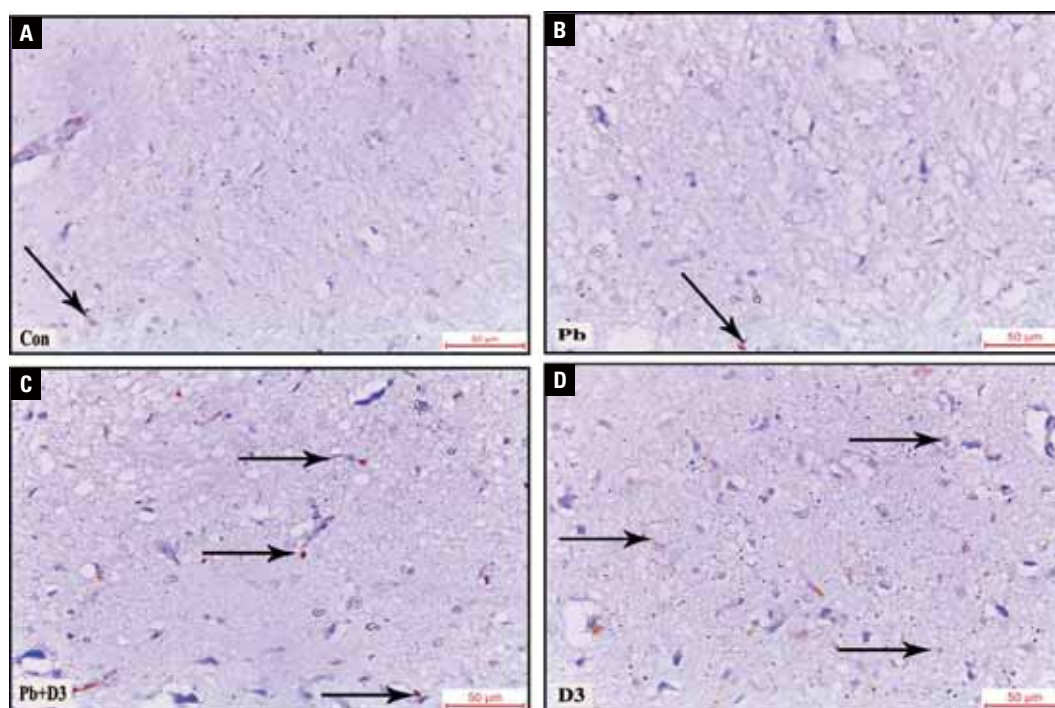


Figure 4. A, B. The control and lead groups respectively (Con, Pb) substantia nigra pars compacta (SNpc) appear with scanty anti D3 immunostaining, whereas the Pb + D3 (C) and D3 (D) groups appear with increased anti-D3 immunostaining (arrows) (anti-D3 $\times 400$, scale bar = 50 μm).

and Pb groups (13.6- and 15.37-fold, respectively; Fig. 5).

Via TH immunostaining (Fig. 6), the control and D3 groups SNpc neurons exhibited a strong TH reaction, whereas the Pb group SNpc appeared with a few neurons and decreased TH reactions. The Pb + D3 SNpc revealed increased reaction compared with the Pb group. Histomorphometric data showed that the area per cent of positive TH immune reaction in the Pb group was significantly decreased compared with control and D3 groups (49%, 43%, respectively). In contrast, it was significantly increased in the Pb + D3 group compared with the Pb group (52%) (Fig. 5).

Via anti-Olig-2 immunostaining (Fig. 7), the control SNpc group appeared with a standard anti-Olig-2 reaction, whereas the lead SNpc group appeared with mildly decreased reaction. The Pb + D3 SNpc group exhibited increased reaction, whereas the D3 group exhibited mild increased reaction. Via histomorphometric analysis, the area percentage of positive anti-Olig-2 significantly increased in the Pb + D3 group compared with that in the control, Pb, and D3 groups (1.96-, 2.11-, and 2.13-fold, respectively) (Fig. 5).

Via GFAP immunostaining (Fig. 8), the lead SNpc group exhibited increased reaction, whereas the Pb + D3 and D3 groups appeared with relatively normal

reactions. Via histomorphometric analysis, the area percentage of the positive GFAP in the Pb group significantly increased compared with the control and D3 groups (3.27- and 2.37-fold, respectively). In contrast, it was significantly decreased (60.6%) in the Pb + D3 group compared with the Pb group, although it was still significantly increased (1.99-fold) compared with the control group (Fig. 5).

Via caspase-3 immunostaining (Fig. 9), the control and D3 group SNpc appeared with a nearly negative reaction, whereas the Pb group SNpc appeared with mildly increased reaction. The Pb + D3 group SNpc exhibited minimally increased reaction. Via histomorphometric analysis, the area percentage of positive caspase-3 reaction has increased mildly although significantly in the Pb group compared with the control and D3 (2.3-, 1.8-fold, respectively). It decreased significantly in the Pb + D3 group (34%) compared to the Pb group (Fig. 5).

Via α synuclein immunostaining (Fig. 10), the control group SNpc showed a nearly negative immune reaction, whereas the lead (Pb group) SNpc appeared with markedly increased reaction (arrows). The Pb + D3 SNpc exhibited a reduced reaction than the Pb group, whereas the D3 group SNpc neurons appeared with scanty α -synuclein reaction. Via histomorphometric analysis, the area percentage of positive α -synuclein

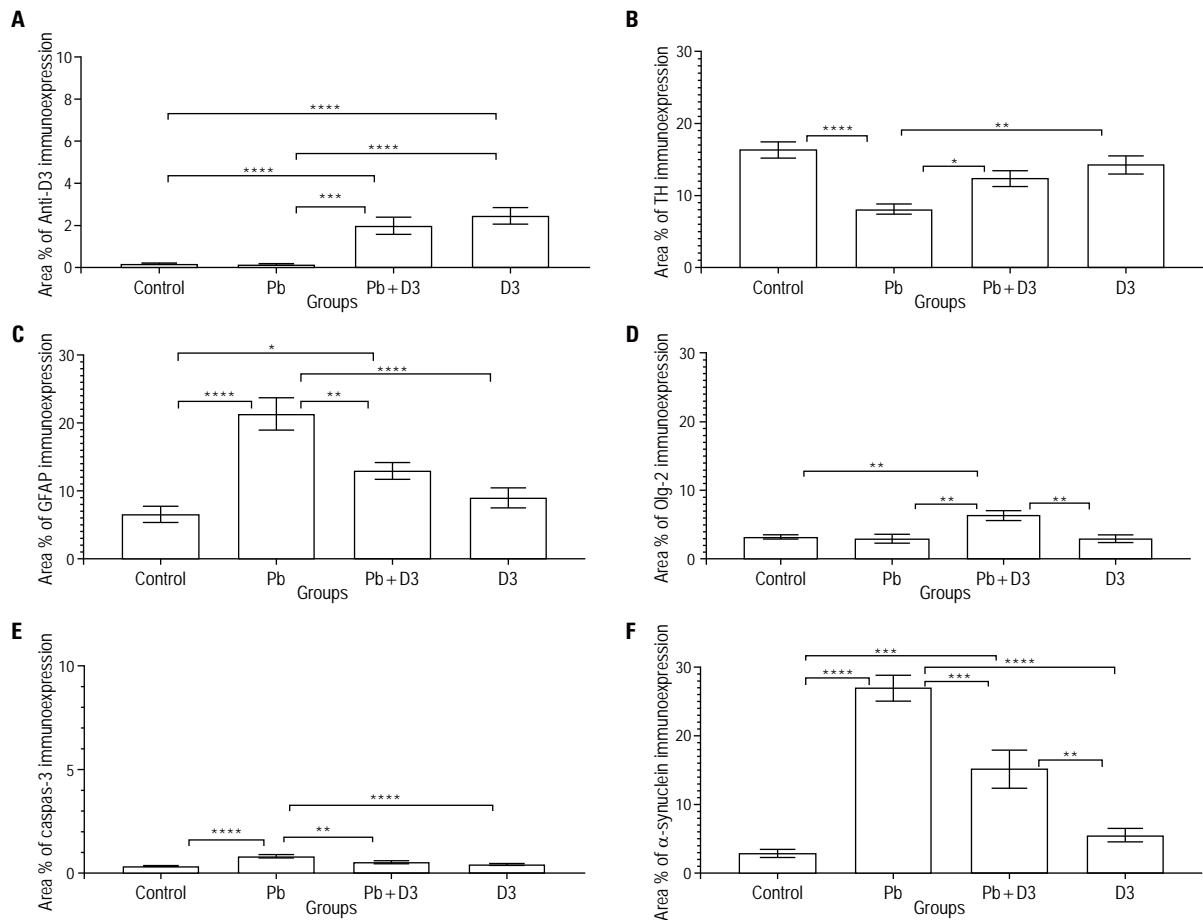


Figure 5. Bar charts of the area percentage of positive anti-D3 (A), tyrosine hydroxylase (TH) (B), glial fibrillary acid protein (GFAP) (C), oligodendrocytes (Olig-2) (D), caspase-3 (E) and α -synuclein (F) immunoreaction in different groups; *statistically significant when $p < 0.05$; **when $p < 0.01$; ***when $p < 0.001$; ****when $p < 0.0001$ (error bar = standard error of the mean).

reaction has increased significantly in the Pb group compared to the control and D3 groups (9.8-, 4.8-fold, respectively). In the Pb + D3 group, it was significantly reduced (44%) as compared to the Pb group.

DISCUSSION

In this study, significantly accumulated lead in the ventral midbrain had induced SNpc neurotoxic changes, as evidenced by activation of α -synuclein, caspase-3 and caspase-11, GFAP, as well as downregulation of TH. Previously proved, lead deteriorated motor functions in rats and degenerated cerebellar neurons via oxidative stress mechanisms [11]. In this work, Pb had significantly elevated nigral α -synuclein levels. Accumulation of misfolded and aggregated α -synuclein in Lewy bodies is a main neurobiological feature for PD resulting in disrupting cellular functions and inducing mitochondria injury as well as synaptic dysfunctions [9]. Additionally, nigral caspase-11 and, to a lesser extent, caspase-3 were

significantly elevated in the Pb group in the present study suggesting their potential mediating role in nigral neuronal cell death. Concordantly, it has been reported that MPTP-induced nigral neurotoxicity was mediated through caspase-11 activation [7]. Studies with caspase-11 blocking agents are still needed to confirm the latter finding of the current work. Strategies monitoring and modifying inflammation and cell death were currently suggested to improve the management of PD, and elevated plasma-borne inflammasome NLRP3 was associated with PD status [2]. Further studies are still warranted to elucidate the role of inflammasomes in the lead-induced SNpc neurotoxicity. Biochemically, lead was significantly increased in the serum and midbrain of this study's Pb group, suggesting its accumulation in SNpc neurons. Morphologically, the accumulated Pb deteriorated the SNpc dopaminergic neurons, significantly decreased cell density by cresyl violet staining, and upregulated GFAP immunoreaction considerably. Additionally,

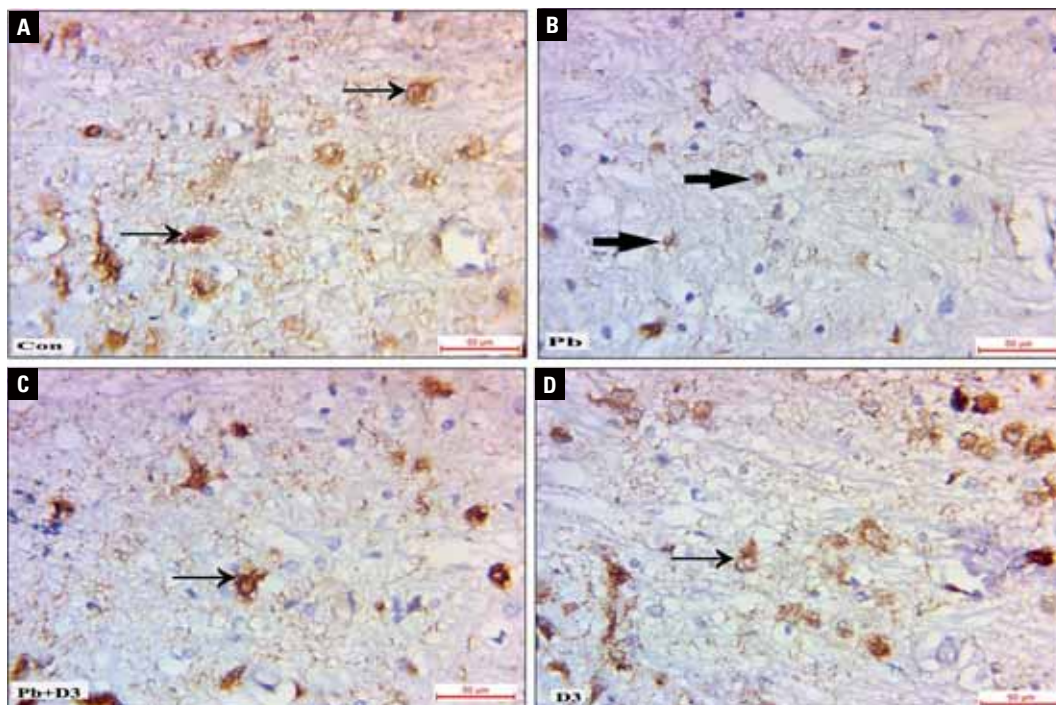


Figure 6. **A.** The control (Con) group substantia nigra pars compacta (SNpc) neurons exhibit a strong tyrosine hydroxylase (TH) reaction (arrows), whereas lead (Pb) group **(B)** SNpc appears with few neurons and decreased TH reactions (incomplete arrow); **C.** The Pb + D3 SNpc shows an increased reaction than the Pb group; **D.** Vitamin D3 group SNpc neurons exhibit a strong TH reaction (TH $\times 400$, scale bar = 50 μm).

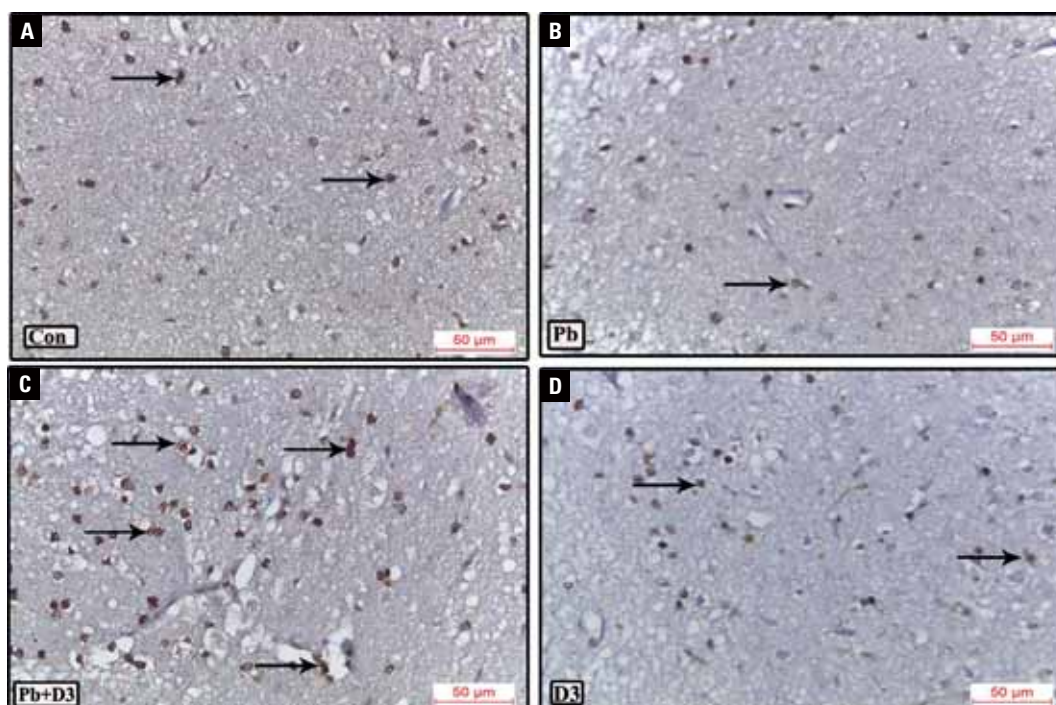


Figure 7. **A, B.** The control (Con) group substantia nigra pars compacta (SNpc) appears with normal anti-oligodendrocytes (Olig-2) reaction (arrows) while lead (Pb) group SNpc appeared with mildly increased reaction; **C.** The Pb + D3 group SNpc exhibits increased reaction; **D.** Vitamin D3 group exhibits mild increased reaction (anti-Olig-2 $\times 400$, scale bar = 50 μm).

Pb significantly reduced the area percentage of TH immunopositive dopaminergic neurons, denoting

its dangerous neurotoxic impacts. Previously, lead disrupted cerebellar neurons [1] and hippocampal

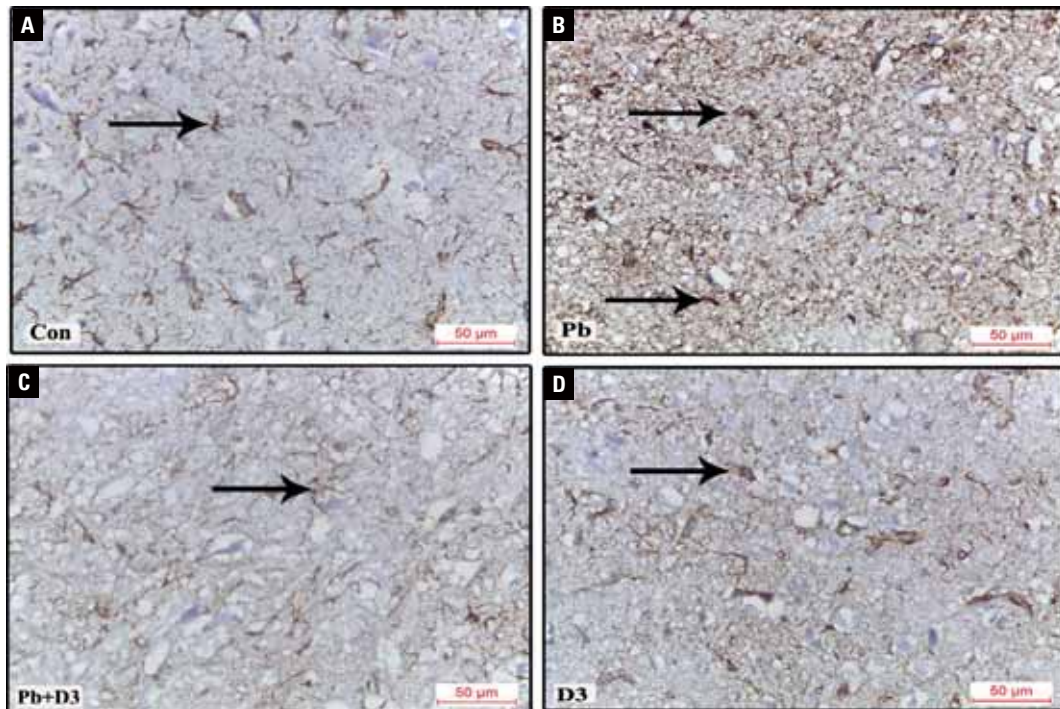


Figure 8. A. The control group (Con) substantia nigra pars compacta (SNpc) appears with a typical glial fibrillary acid protein (GFAP) reaction (arrow), whereas the lead (Pb) group (B) exhibits increased reaction; C, D. The Pb + D3 and D3 groups, SNpc appear with relatively typical reactions (GFAP $\times 400$, scale bar = 50 μm).

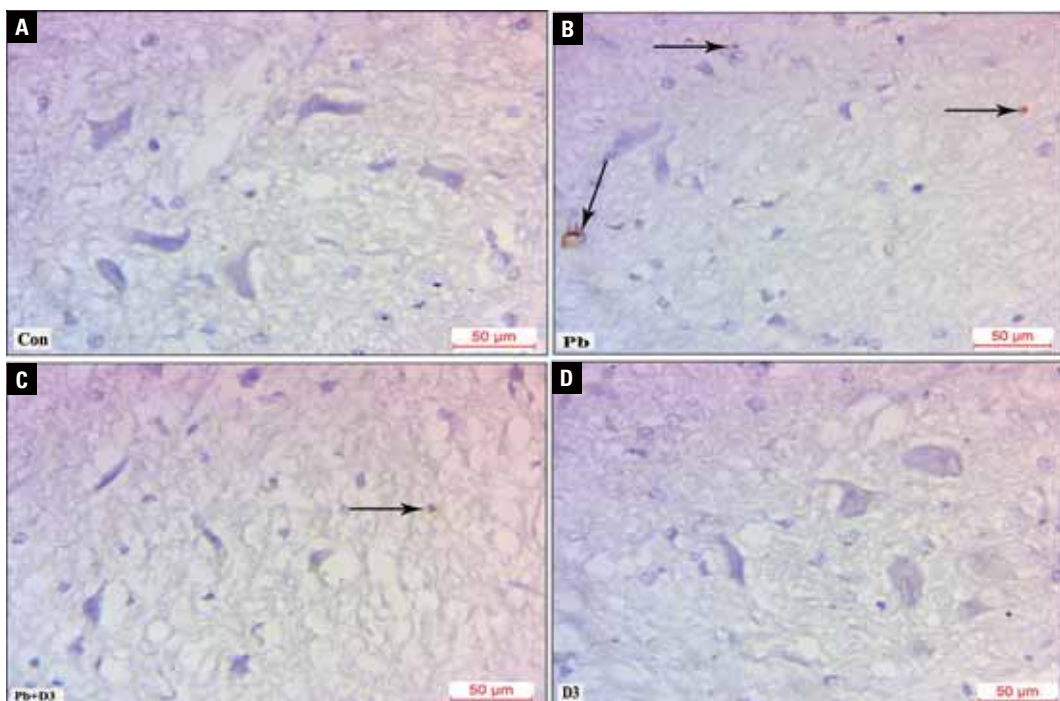


Figure 9. A, B. The control (Con) group substantia nigra pars compacta (SNpc) appears with almost negative caspase-3 immune reaction while the lead (Pb) group SNpc appears with mildly increased reaction (arrows); C, D. The Pb + D3 group SNpc exhibits minimally increased reaction while the D3 group exhibits almost negative reaction (caspase-3 $\times 400$, scale bar = 50 μm).

neurons [20]. Lately, Pb had significantly deteriorated motor functions and coordination in rats. How-

ever, L-DOPA administration did not change these findings, supposing that these Parkinsonian-deficits

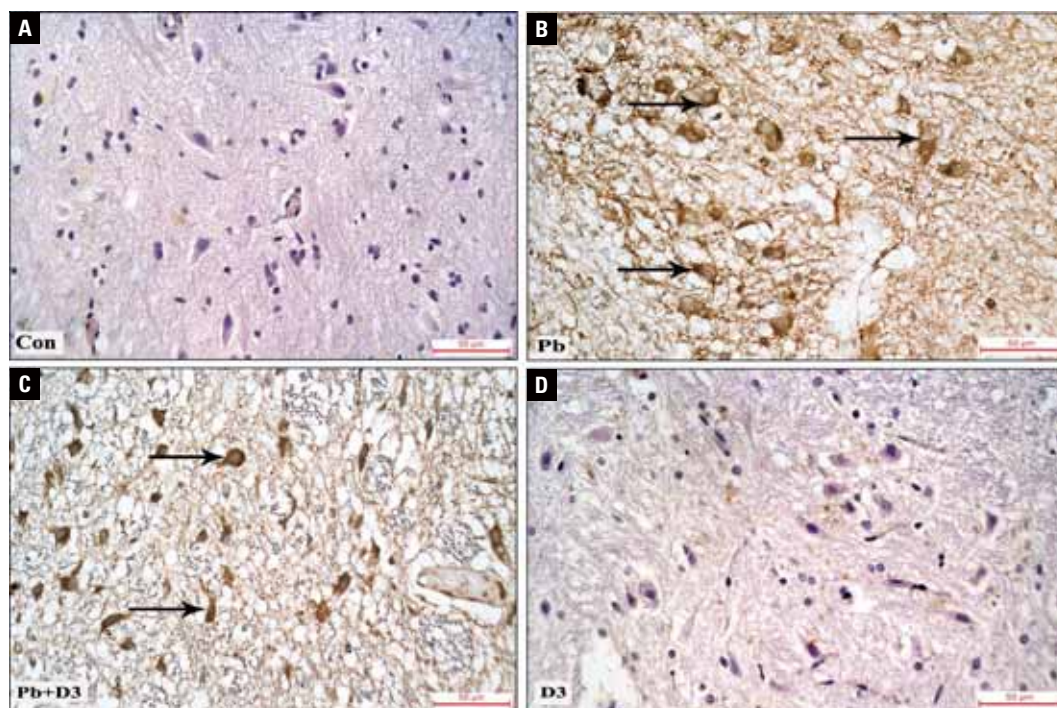


Figure 10. **A.** The control (Con) group substantia nigra pars compacta (SNpc) with negative α -synuclein immune reaction; **B.** The lead (Pb) group SNpc with markedly increased reaction (arrows); **C.** The Pb + D3 SNpc with reduced reaction than the Pb group; **D.** Vitamin D3 group SNpc neurons exhibit scanty α -synuclein reaction (α -synuclein $\times 400$, scale bar = 50 μ m).

may be due to the decline in noradrenaline but not dopamine [18]. A mild but nonsignificant decrease in nigral-positive Olig-2 expression in rats that received Pb had been revealed in this study. However, Olig-2 expression significantly increased in the Pb + D3 group compared with the control and Pb groups. Supporting these results, fish oil and omega 3 injections had been proven to promote oligodendrogenesis in a rat model of post-traumatic brain injury associated with the generation of immature neurons and microvessels and significantly improved cognitive recovery [15]. Contradictory to the later findings of this work, aggregates of α -synuclein in oligodendrocytes were a characteristic pathological feature of multiple systemic atrophy neurodegenerative disease [10], and neurons to oligodendrocytes transfer of α -synuclein had been proven to be the cause of these aggregates [16]. However, the role of oligodendrocytes in lead-induced nigral neurotoxicity is still a candidate for further investigations.

In this study, D3 administration in rats significantly increased their body weight, suggesting its anabolic function, which was a finding that was surprising in the present study. Contradictory to these results, D3 administration in humans during weight loss did not improve weight loss or its related factors [11].

Concomitant D3 administration to lead in group III in this study had significantly improved all nigral biochemical, histological, and immunohistochemical (GFAP, α -synuclein, caspase-3, and TH) markers suggesting its possible neuroprotective role in lead-induced nigral neurotoxicity. This neuroprotective role might be mediated through the significant nigral oligodendrogenesis noticed in the rats that received Pb + D3. Supporting these results, D3 had ameliorated the oxidative stress markers, upregulated TH immunoreaction, and attenuated (tumour necrosis factor- α) immune-reaction in the 6-hydroxydopamine (6-OHDA) exposed striata [8]. However, Lima et al. [8] reported a decrease in anti-D3 immunostaining in 6-OHDA-exposed striata, which was not found in the lead SNpc group in this study. Also, unilateral intrastriatal injections of 6-OHDA in rats demonstrated declined vitamin D levels in their cardiac tissues [12]. The neuroprotective role of D3 in lead-induced nigral neurotoxicity might be attributed to antioxidative stress mechanisms. Presumably, one of the major causes of neuropathological degeneration in SNpc neuronal diseases is the cellular biomolecules oxidative stress injury as detected by the markedly increased or decreased body levels of selenium in PD patients [5]. Further studies in humans are still need-

ed with different doses to match the improvement noticed in animal studies.

CONCLUSIONS

Lead (Pb) may induce SNpc neurotoxicity presumably through activation of caspase-11 and induction of synucleinopathy. D3 may protect against this neurotoxicity probably through an oligodendrogenic effect.

Conflict of interest: None declared

REFERENCES

- Abubakar K, Muhammad Mailafiya M, Danmaigoro A, et al. Curcumin attenuates lead-induced cerebellar toxicity in rats via chelating activity and inhibition of oxidative stress. *Biomolecules*. 2019; 9(9), doi: [10.3390/biom9090453](https://doi.org/10.3390/biom9090453), indexed in Pubmed: [31489882](https://pubmed.ncbi.nlm.nih.gov/31489882/).
- Anderson FL, von Herrmann KM, Andrew AS, et al. Plasma-borne indicators of inflammasome activity in Parkinson's disease patients. *NPJ Parkinsons Dis*. 2021; 7(1): 2, doi: [10.1038/s41531-020-00147-6](https://doi.org/10.1038/s41531-020-00147-6), indexed in Pubmed: [33398042](https://pubmed.ncbi.nlm.nih.gov/33398042/).
- Bancroft JD, Layton C. Connective and other mesenchymal tissues with their stains. In: Suvarna SK, Bancroft JD (eds.). *Bancroft's Theory and Practice of Histological Techniques*. Eighth Ed. Elsevier Limited 2019: 53–175.
- BaSalamah MA, Abdelghany AH, El-Boshy M, et al. Vitamin D alleviates lead induced renal and testicular injuries by immunomodulatory and antioxidant mechanisms in rats. *Sci Rep*. 2018; 8(1): 4853, doi: [10.1038/s41598-018-23258-w](https://doi.org/10.1038/s41598-018-23258-w), indexed in Pubmed: [29556070](https://pubmed.ncbi.nlm.nih.gov/29556070/).
- Ellwanger JH, Franke SIR, Bordin DL, et al. Biological functions of selenium and its potential influence on Parkinson's disease. *An Acad Bras Cienc*. 2016; 88(3 Suppl): 1655–1674, doi: [10.1590/0001-3765201620150595](https://doi.org/10.1590/0001-3765201620150595), indexed in Pubmed: [27556332](https://pubmed.ncbi.nlm.nih.gov/27556332/).
- Fullard ME, Duda JE. A review of the relationship between vitamin d and parkinson disease symptoms. *Front Neurol*. 2020; 11: 454, doi: [10.3389/fneur.2020.00454](https://doi.org/10.3389/fneur.2020.00454), indexed in Pubmed: [32536905](https://pubmed.ncbi.nlm.nih.gov/32536905/).
- Furuya T, Hayakawa H, Yamada M, et al. Caspase-11 mediates inflammatory dopaminergic cell death in the 1-methyl-4-phenyl-1,2,3,6-tetrahydropyridine mouse model of Parkinson's disease. *J Neurosci*. 2004; 24(8): 1865–1872, doi: [10.1523/JNEUROSCI.3309-03.2004](https://doi.org/10.1523/JNEUROSCI.3309-03.2004), indexed in Pubmed: [14985426](https://pubmed.ncbi.nlm.nih.gov/14985426/).
- Lima LAR, Lopes MJ, Costa RO, et al. Vitamin D protects dopaminergic neurons against neuroinflammation and oxidative stress in hemiparkinsonian rats. *J Neuroinflammation*. 2018; 15(1): 249, doi: [10.1186/s12974-018-1266-6](https://doi.org/10.1186/s12974-018-1266-6), indexed in Pubmed: [30170624](https://pubmed.ncbi.nlm.nih.gov/30170624/).
- Mahul-Mellier AL, Burtscher J, Maharjan N, et al. The process of Lewy body formation, rather than simply α -synuclein fibrillization, is one of the major drivers of neurodegeneration. *Proc Natl Acad Sci U S A*. 2020; 117(9): 4971–4982, doi: [10.1073/pnas.1913904117](https://doi.org/10.1073/pnas.1913904117), indexed in Pubmed: [32075919](https://pubmed.ncbi.nlm.nih.gov/32075919/).
- Marmion DJ, Rutkowski AA, Chatterjee D, et al. Viral-based rodent and nonhuman primate models of multiple system atrophy: Fidelity to the human disease. *Neurobiol Dis*. 2021; 148: 105184, doi: [10.1016/j.nbd.2020.105184](https://doi.org/10.1016/j.nbd.2020.105184), indexed in Pubmed: [33221532](https://pubmed.ncbi.nlm.nih.gov/33221532/).
- Mason C, Xiao L, Imayama I, et al. Vitamin D3 supplementation during weight loss: a double-blind randomized controlled trial. *Am J Clin Nutr*. 2014; 99(5): 1015–1025, doi: [10.3945/ajcn.113.073734](https://doi.org/10.3945/ajcn.113.073734), indexed in Pubmed: [24622804](https://pubmed.ncbi.nlm.nih.gov/24622804/).
- Nejm MB, Guimarães-Marques MJ, Oliveira LF, et al. Assessment of vitamin D and inflammatory markers profile in cardiac tissue on Parkinson disease animal model. *Pharmacol Rep*. 2020; 72(2): 296–304, doi: [10.1007/s43440-020-00074-6](https://doi.org/10.1007/s43440-020-00074-6), indexed in Pubmed: [32124387](https://pubmed.ncbi.nlm.nih.gov/32124387/).
- Perry A, Brat DJ. *Practical surgical neuropathology: a diagnostic approach*. 2nd ed. Chapter 27: Biopsy Pathology of neurodegenerative disorders in adults. Philadelphia, PA 2018.
- Poewe W, Seppi K, Tanner CM, et al. Parkinson disease. *Nat Rev Dis Primers*. 2017; 3: 17013, doi: [10.1038/nrdp.2017.13](https://doi.org/10.1038/nrdp.2017.13), indexed in Pubmed: [28332488](https://pubmed.ncbi.nlm.nih.gov/28332488/).
- Pu H, Jiang X, Wei Z, et al. Repetitive and prolonged omega-3 fatty acid treatment after traumatic brain injury enhances long-term tissue restoration and cognitive recovery. *Cell Transplant*. 2017; 26(4): 555–569, doi: [10.3727/096368916X693842](https://doi.org/10.3727/096368916X693842), indexed in Pubmed: [27938482](https://pubmed.ncbi.nlm.nih.gov/27938482/).
- Reyes JF, Rey NL, Bousset L, et al. Alpha-synuclein transfers from neurons to oligodendrocytes. *Glia*. 2014; 62(3): 387–398, doi: [10.1002/glia.22611](https://doi.org/10.1002/glia.22611), indexed in Pubmed: [24382629](https://pubmed.ncbi.nlm.nih.gov/24382629/).
- Ross MH, Pawlina W. *Histology: a text and atlas — with correlated cell and molecular biology*. 7th ed. Chapter 12. Wolters Kluwer Health, Philadelphia 2016: 378.
- Sabbar M, Delaville C, De Deurwaerdère P, et al. Lead-Induced atypical parkinsonism in rats: behavioral, electrophysiological, and neurochemical evidence for a role of noradrenaline depletion. *Front Neurosci*. 2018; 12: 173, doi: [10.3389/fnins.2018.00173](https://doi.org/10.3389/fnins.2018.00173), indexed in Pubmed: [29615861](https://pubmed.ncbi.nlm.nih.gov/29615861/).
- Wang T, Zheng W, Xu He, et al. Cloquinol inhibits zinc-triggered caspase activation in the hippocampal CA1 region of a global ischemic gerbil model. *PLoS One*. 2010; 5(7): e11888, doi: [10.1371/journal.pone.0011888](https://doi.org/10.1371/journal.pone.0011888), indexed in Pubmed: [20686690](https://pubmed.ncbi.nlm.nih.gov/20686690/).
- Xu J, Yan HC, Yang Bo, et al. Effects of lead exposure on hippocampal metabotropic glutamate receptor subtype 3 and 7 in developmental rats. *J Negat Results Biomed*. 2009; 8: 5, doi: [10.1186/1477-5751-8-5](https://doi.org/10.1186/1477-5751-8-5), indexed in Pubmed: [19374778](https://pubmed.ncbi.nlm.nih.gov/19374778/).
- Yachnis AT, Rivera-Zengotita ML. *Neuropathology*. Chapter: Parkinson's Disease and Related Alpha-Synucleinopathies. Saunders, an imprint of Elsevier Inc., Philadelphia 2014: 258–264.

Cisplatin-induced alterations in the blood-nerve barrier: effects of combination of vitamin B1, B6 and B12

A. Tothonglor, P. Kobutree, A. Roumwong, D. Jindatip, S. Agthong 

Department of Anatomy, Faculty of Medicine, Chulalongkorn University, Pathumwan, Bangkok, Thailand

[Received: 24 December 2021; Accepted: 9 January 2022; Early publication date: 21 January 2022]

Background: Cisplatin is a chemotherapeutic agent against solid cancers. However, neuropathy is a major side effect and has no effective treatment so far. Emerging evidence suggests that cisplatin might damage nerve capillaries leading to impaired blood-nerve barrier (BNB). This study aimed to investigate the ultrastructural changes of the BNB in the sciatic nerves and dorsal root ganglia of rats with cisplatin neuropathy and the effects of B₁₋₆₋₁₂.

Materials and methods and Results: The results showed that cisplatin 2 mg/kg injected intraperitoneally twice a week for 5 consecutive weeks caused thermal hypoalgesia and structural abnormalities of nerves and ganglia. Co-treatment with oral B₁₋₆₋₁₂ (100:100:1) 100, 300 and 600 mg/kg/day for 5 weeks reduced the sensory deficit and structural alterations. Electron microscopic analysis demonstrated the higher frequencies and wider distances of pericyte detachment in the capillaries of cisplatin than control groups. Vitamin B1, B6 and B12 especially the medium dose, reversed these abnormalities. Culture of endothelial cells and pericytes with cisplatin demonstrated reduced cell viability, increased caspase-3 activity, lower transendothelial electrical resistance and decreased expression of tight junction proteins, occludin and zonula occluden-2.

Conclusions: Vitamin B1, B6 and B12 could correct these toxic effects of cisplatin. These data confirm that cisplatin causes pathological alterations in the components of BNB which correlate with the severity of neuropathy. Furthermore, B₁₋₆₋₁₂ is effective against these abnormalities and deserves further investigations as potential treatment for cisplatin-induced neuropathy. (Folia Morphol 2023; 82, 1: 53–62)

Key words: pericyte, endothelial cell, cisplatin, nerve, neuropathy

INTRODUCTION

Cisplatin is an antineoplastic agent used to treat cancers of various organs [6]. One of its major side effects is peripheral neuropathy often leading to dose reduction or cessation and thus effectiveness of chemotherapy. Cisplatin-induced neuropathy is mainly characterised by sensory abnormalities in

both animal models and patients [2, 16, 22, 28]. Pathological examination showed degeneration and demyelination of nerve fibres [1, 29]. Although various underlying mechanisms have been identified and relevant agents were tested, no clinically effective drugs were achieved so far [18, 24].

Address for correspondence: Dr. S. Agthong, Department of Anatomy, Faculty of Medicine, Chulalongkorn University, 1873 Rama IV Road, Pathumwan, 10330 Bangkok, Thailand, e-mail: sagthong@hotmail.com

This article is available in open access under Creative Common Attribution-Non-Commercial-No Derivatives 4.0 International (CC BY-NC-ND 4.0) license, allowing to download articles and share them with others as long as they credit the authors and the publisher, but without permission to change them in any way or use them commercially.

Accumulating evidence suggests vascular dysfunction as another potential mechanism. Patients receiving cisplatin-based chemotherapy had arterial occlusion [17] and endothelial damage [5]. In cisplatin-treated rats, reduced nerve blood flow, decreased number of vasa nervorum and endothelial apoptosis were reported [15]. Recently, the lower density and detachment of nerve pericytes have been found in the rats with cisplatin neuropathy [12]. These abnormalities might impair blood-nerve barrier (BNB). This study aimed to further clarify the association of cisplatin neuropathy with BNB defects. In addition, since beneficial effects of vitamin B1, B6 and B12 in combination (B₁₋₆₋₁₂) were seen in the preliminary study, whether this improvement in neuropathy was associated with ameliorated BNB abnormalities was also investigated.

MATERIALS AND METHODS

Animals

The experiment was approved by the institutional ethics committee (Ref. No. 19/58) and carried out in accordance with the Animals for Scientific Purposes Act 2015, Thailand. Thirty female Wistar rats weighing 250 g were divided into five groups: control (C), cisplatin (P), cisplatin + low-dose (P+LB), medium-dose (P+MB) or high-dose B₁₋₆₋₁₂ (P+HB) (n = 6 for each group).

Drug administration

The cisplatin and cisplatin + B₁₋₆₋₁₂ groups received cisplatin (Pfizer, USA) diluted in normal saline to the final concentration of 0.5 mg/mL for intraperitoneal injection. The dose of cisplatin was 2 mg/kg twice a week for 5 continuous weeks (20 mg/kg cumulative dose). This dose regimen has been shown to induce peripheral neuropathy in rats [2, 28]. The control group received normal saline injection with the volume and schedule equivalent to the cisplatin groups. B1, B6 and B12 (all from Sigma) (100:100:1 by weight) were dissolved in normal saline and given by gavage during the cisplatin treatment once daily for 5 weeks. This ratio of B₁₋₆₋₁₂ was selected based on the previous studies [3, 13]. Low-dose, medium-dose and high-dose B₁₋₆₋₁₂ groups received 100, 300 and 600 mg/kg/day, respectively.

Hind-paw thermal nociception

The details of procedure are described elsewhere [29]. Briefly, the test was done at baseline and the

end of 3rd and 5th weeks. Each rat was placed on the hot plate analgesia meter (Harvard Apparatus, UK) maintained at 55°C. When the rat licked its hind paw on either side, elapsed time was recorded as latency. The cut-off duration of 35 s was set to avoid skin burn. The test was repeated at least 3 times with an interval of 15 min and the mean latency was obtained for each rat.

Tissue collection

After the last injection of cisplatin, all the rats were sacrificed by overdose anaesthetics and then transcardially perfused with normal saline. This was followed by 3% glutaraldehyde. L4,5 dorsal root ganglion (DRG) with the proximal and distal parts of sciatic nerves (divided at the trifurcation) were removed, post-fixed in 3% glutaraldehyde and embedded in epoxy resin. These specimens were used for morphometric analysis.

Nerve morphometry

Transverse 1 µm-thick sections of the sciatic nerve were cut, mounted on slides, and stained with pararphenylenediamine. The sections were examined under a light microscope and the cross-sectional areas were chosen using the three-window sampling method [4]. Briefly, under 40× objective lens, three windows of 0.012 mm² were randomly placed, one in the middle and the other two in the periphery of fascicle. Images of these windows were imported into a computer via a digital camera. Morphometric analysis was done to obtain the number of myelinated fibres, axon diameter, myelinated fibre density, myelin thickness and g ratio using the Image-Pro Plus software®. The values derived from the three windows were extrapolated to the whole nerve.

DRG morphometry

The L4 DRG were serially cut into 2 µm-thick sections and stained with toluidine blue. The estimation for total number of neurons in each ganglion was done using the physical dissector method. Details of the procedures were described elsewhere [28]. In brief, every 20th section was selected and the number of neurons with prominent nucleus and nucleolus was counted. Then, this number was extrapolated to the total number for the whole DRG. In addition, at least 300 neurons in each DRG were randomly analysed for areas of the nucleus and nucleolus using the Image-Pro Plus software.

Transmission electron microscopy

Ultrathin sections (70 nm thickness) of the L5 DRG and sciatic nerves were stained with lead citrate and uranyl acetate. Morphology of pericytes and the basement membrane shared with endothelial cells was observed with a transmission electron microscope (JEM-1400PLUS, Japan). In each rat, 20 capillaries were randomly chosen from serial sections of each tissue (DRG, proximal and distal sciatic nerves). Each capillary was evaluated for the presence of pericyte detachment from endothelial cell and vascular basement membrane (VBM) which was classified into two categories: Category 1 pericyte completely attached to the VBM and endothelial cell, category 2 pericyte detached from the VBM and endothelial cell at some points. Then, the distances at the widest detachment between the pericytes and VBM were measured in the capillaries of category 2. In addition, the thickness of VBM at the widest separation point was also measured.

Cell culture

Human umbilical vein endothelial cell (HUVEC) (Invitrogen) and human brain vascular pericyte (HBVP) (ScienCell) were grown according to manufacturers' protocols. Each experiment was performed in triplicate and repeated three times. HUVEC and HBVP were divided into three groups: control, cisplatin, and cisplatin + B₁₋₆₋₁₂. B₁₋₆₋₁₂ was prepared in a ratio of 100:100:1 similar to the animal experiment. In cisplatin and cisplatin + B₁₋₆₋₁₂ groups, HUVEC and HBVP were incubated with 3 µg/mL and 1.5 µg/mL of cisplatin for 24 hours, respectively. For B₁₋₆₋₁₂ treatment, the cells were co-incubated with 1 µg/mL of B₁₋₆₋₁₂ for 24 hours. The above doses were selected according to the preliminary data.

MTT assay

The MTT (3-(4,5-dimethylthiazol-2-yl)-2,5-diphenyltetrazolium bromide) assay was used to evaluate the viability of HUVEC and HBVP. The cells were seeded at 1×10^4 and 5×10^3 cells/well, respectively, in 96-well plates and allowed to attach for 24 hours. The cells were then treated according to the experimental conditions for 24 hours. Finally, the cells were incubated with 100 µL MTT solution (Life technologies, Molecular Probes, USA) for 2 hours. Subsequently, purple formazan crystals were dissolved in 100 µL dimethyl sulfoxide. The absorbance was measured at 570 nm using a microplate reader (Multiskan GO, Thermo Fisher Scientific, USA). The percentage of cell

viability was calculated from the mean absorbance of test samples divided by that of negative control.

Caspase-3 assay

Caspase-3/cpp32 colorimetric assay kit (BioVision, USA) was used to determine the caspase-3 activity. Briefly, the cells were plated at 1×10^6 in the culture vessels. After treatments, the cells were harvested and resuspended in cell lysis buffer. Supernatant of each sample was collected and protein concentration was measured. Then, the sample was diluted with cell lysis buffer to obtain the protein concentration of 1 µg/µL and transferred to a 96-well plate. This was followed by adding working reaction buffer and DEVD-pNA substrate. The plate was incubated at 37°C for 2 hours. The absorbance was measured at 405 nm using a microplate reader (Multiskan GO, Thermo Fisher Scientific, USA). The caspase-3 activity of treated cells was compared with that of controls.

Transendothelial electrical resistance (TEER) study

Human umbilical vein endothelial cell were cultured on the upper chamber of transwell insert (Merck, USA) which was inserted in the 24-well plate at 1×10^4 cells/well. After the cells were grown to confluency, they were treated according to the experimental conditions for 24 hours. Cell resistance (R) was measured using Millicell electrical resistance apparatus (Millicell® ERS-2, Merck, USA). TEER value was calculated using the formula: TEER value (Ωcm^2) = $(R_{\text{sample}} - R_{\text{blank}}) \times \text{membrane area (cm}^2\text{)}$.

Western blot analysis

Human umbilical vein endothelial cell were seeded 2×10^6 cells/mL in a cell culture dish. After being treated according to experimental protocols for 24 hours, the cells were incubated on ice with RIPA lysis buffer (Cell Signaling, USA) containing $1 \times$ protease inhibitor cocktail (Cell Signaling, USA) for 5 min. Subsequently, the cells were scraped, centrifuged and the supernatant collected. Protein concentration of the supernatant was determined using Pierce™ BCA protein assay (Thermo Scientific, USA). Briefly, the sample (1.5 µg/µL) was mixed with the fluorescent dye (4:1 ratio) and denatured at 95°C for 5 min. The marker, samples, antibody diluent, primary antibody (1:200 β-actin [Cell Signaling], 1:200 ZO-1 [Invitrogen], 1:200 ZO-2 [Invitrogen], 1:200 claudin-5 [Invitrogen], and 1:200 occludin [Invitrogen]), rabbit secondary conjugate, streptavidin-HRP, and Luminol-peroxide were

added onto the plate according to the manufacturer's protocol. Subsequently, separation and immunodetection were conducted using WES automated western blotting system (ProteinSimple, USA). Density of digital image was analysed using Compass software (ProteinSimple, USA). Expression of each protein was normalised to that of β -actin.

Statistical analysis

One-way ANOVA followed by Tukey's post hoc test was used for comparing the above parameters between the experimental groups. The test was done using SPSS for Windows version 23. Statistically significant differences were considered when $p < 0.05$.

RESULTS

Body weight

At baseline, the average body weight was similar between groups. However, at the 3rd and 5th weeks, the values of all groups receiving cisplatin were significantly decreased compared with that of the control group (data not shown). Food and water consumption including physical activities were similar between the cisplatin only and cisplatin + B_{1-6-12} groups. There was no mortality in any group during the experiment.

Hind-paw thermal nociception

Before the treatment, the latencies were not significantly different between groups (Fig. 1). However, at the 5th week, the latencies of the cisplatin group were significantly longer than that of the control group, indicating thermal hypoalgesia. In addition, the cisplatin + MB and cisplatin + HB groups had significantly shorter latencies than the cisplatin group and not statistically different from the control group. In contrast, the latency of the cisplatin + LB group was close to that of the cisplatin group and significantly longer than that of the control group.

Nerve morphometry

At the fifth week, morphometric analysis of the sciatic nerve showed that the fibre diameters of the cisplatin including cisplatin + LB and cisplatin + HB groups were significantly lower than those of the control and cisplatin + MB groups (Table 1). There were no significant differences between the cisplatin, cisplatin + LB and cisplatin + HB groups. Furthermore, the fibre densities of the cisplatin and cisplatin + HB groups were significantly higher than those of the control and cisplatin + MB groups. The values of

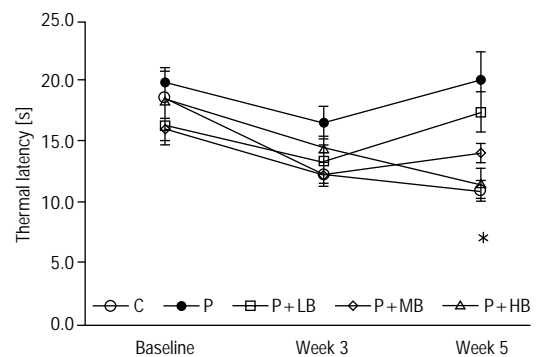


Figure 1. Changes in the thermal latency of hind paw. The graph shows means and standard error of mean; C — control; P — cisplatin; P+LB — cisplatin + low-dose B_{1-6-12} ; P+MB — cisplatin + medium-dose B_{1-6-12} ; P+HB — cisplatin + high-dose B_{1-6-12} ; * $p < 0.01$ P vs. C and P+HB; $p < 0.05$ P vs. P+MB; $p < 0.05$ P+LB vs. C and P+HB.

the cisplatin + MB were not significantly different from those of the control groups. No significant changes were observed between groups in other parameters. However, there were trends toward thinner myelin sheath in all cisplatin-treated groups and higher number of fibres in the cisplatin and cisplatin + HB groups.

DRG morphometry

At the fifth week, the number of DRG neurons and nuclear area were significantly decreased in the cisplatin compared with the control groups (Table 2). However, the nucleolar area was significantly decreased in all cisplatin-treated compared with the control groups. All cisplatin + B_{1-6-12} groups had values between those of the control and cisplatin groups.

Transmission electron microscopic analysis

Separation between the endothelial cell and pericyte or pericyte detachment appeared to be wider and more frequent in the nerve and DRG capillaries from the cisplatin compared with the control groups (Fig. 2). The detachment was less prominent in the cisplatin + B_{1-6-12} groups. When the number of capillaries with detachment was compared with that of total capillaries included, the ratio was significantly higher in the cisplatin than the control groups (Fig. 3). All doses of B_{1-6-12} had the significantly lower ratio than the cisplatin group but remained higher than the control group. However, when considering data of both sciatic nerve and DRG, the ratio of the cisplatin + MB group was the least different from that of the

Table 1. Nerve morphometry

Group	Fibre diameter [μm]	Myelin thickness [μm]	g ratio	Fibre density [$/\mu\text{m}^2$]	Number of fibre
Control (C)	6.52 \pm 0.14	1.29 \pm 0.11	0.61 \pm 0.03	14,583.3 \pm 557.7	8,798 \pm 295
Cisplatin (P)	5.57 \pm 0.09 ^a	1.21 \pm 0.02	0.57 \pm 0.01	20,305.6 \pm 1,073.8 ^b	10,026 \pm 127
Cisplatin + LB	5.77 \pm 0.11 ^b	1.21 \pm 0.02	0.58 \pm 0.01	18,437.5 \pm 681.8	8,680 \pm 596
Cisplatin + MB	6.62 \pm 0.12	1.14 \pm 0.11	0.63 \pm 0.02	13,555.6 \pm 944.6	8,742 \pm 266
Cisplatin + HB	5.55 \pm 0.23 ^a	1.04 \pm 0.04	0.62 \pm 0.00	22,333.3 \pm 1,686.1 ^a	9,673 \pm 244

Data are means \pm standard error of mean; ^a $p < 0.01$ vs. C and MB, ^b $p < 0.05$ vs. C and MB; LB — low-dose B₁₋₆₋₁₂; MB — medium-dose B₁₋₆₋₁₂; HB — high-dose B₁₋₆₋₁₂

Table 2. Dorsal root ganglion morphometry

Group	No. of neuron	Nuclear area [μm^2]	Nucleolar area [μm^2]
Control (C)	21,170 \pm 682	150.43 \pm 5.64	14.28 \pm 0.42
Cisplatin (P)	15,581 \pm 328 ^a	128.18 \pm 4.73 ^b	10.29 \pm 0.62 ^c
Cisplatin + LB	18,113 \pm 511	133.01 \pm 4.67	11.40 \pm 0.46 ^d
Cisplatin + MB	19,024 \pm 766	137.79 \pm 5.46	11.27 \pm 0.14 ^d
Cisplatin + HB	19,730 \pm 1,024	130.26 \pm 4.93	11.16 \pm 0.53 ^d

Data are means \pm standard error of mean; ^a $p < 0.001$ vs. C, ^b $p < 0.05$ vs. MB, ^c $p < 0.01$ vs. HB; ^b $p < 0.05$ vs. C, ^d $p < 0.001$ vs. C, ^d $p < 0.01$ vs. C; LB — low-dose B₁₋₆₋₁₂; MB — medium-dose B₁₋₆₋₁₂; HB — high-dose B₁₋₆₋₁₂

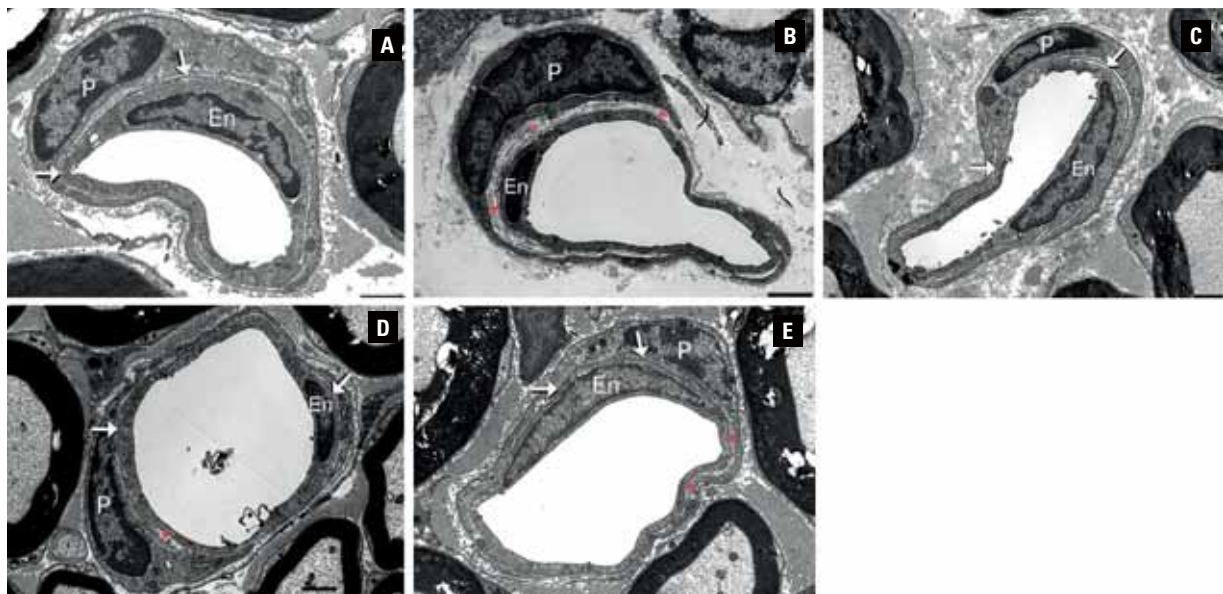


Figure 2. Representative ultrastructural images of capillaries in the sciatic nerves from the control (A), cisplatin (B), cisplatin + low-dose B₁₋₆₋₁₂ (C), cisplatin + medium-dose B₁₋₆₋₁₂ (D) and cisplatin + high-dose B₁₋₆₋₁₂ (E). Arrows indicate the basement membrane shared between the endothelial cell (En) and pericyte (P); *pericyte detachment or separation between the endothelial cells and pericytes; scale bars = 1 μm .

control group. The changes in the proximal and distal parts of nerve were similar.

The separation distance of the cisplatin group was significantly longer than that of the control group in the sciatic nerves but not the DRG (Fig. 4). All cisplatin + B₁₋₆₋₁₂ groups had shorter distances compared with the cisplatin group. The values of the cisplatin + MB group were the closest to those of the control

group. It is worth mentioning that only the cisplatin + HB group had significantly longer distance than the control group in the DRG. As for the thickness of basement membrane at the separation, there were no significant differences between groups (data not shown). Other pathological findings such as accumulation of lysosomes or vacuoles were not detected in the pericytes as well as endothelial cells in any group.

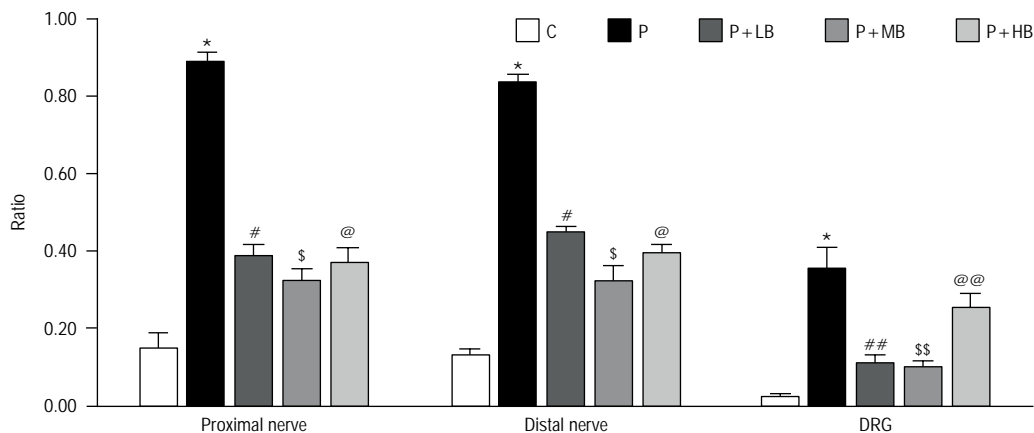


Figure 3. Ratio of the number of capillaries with pericyte detachment from endothelial cells to the total number of capillaries examined in the proximal and distal parts of sciatic nerve including L5 dorsal root ganglion (DRG). The graph shows means and standard error of mean; C — control; P — cisplatin; P+LB — cisplatin + low-dose B_{1-6-12} ; P+MB — cisplatin + medium-dose B_{1-6-12} ; P+HB — cisplatin + high-dose B_{1-6-12} ; * $p < 0.001$ P vs. C, # $p < 0.001$ P+LB vs. P and $p < 0.001$ P+LB vs. C; ## $p < 0.001$ P+MB vs. P; \$ $p < 0.001$ P+MB vs. P and $p < 0.01$ P+MB vs. C; @\$ $p < 0.001$ P+MB vs. P; @ $p < 0.001$ P+HB vs. P and $p < 0.01$ P+HB vs. C; @@ $p < 0.01$ P+HB vs. C.

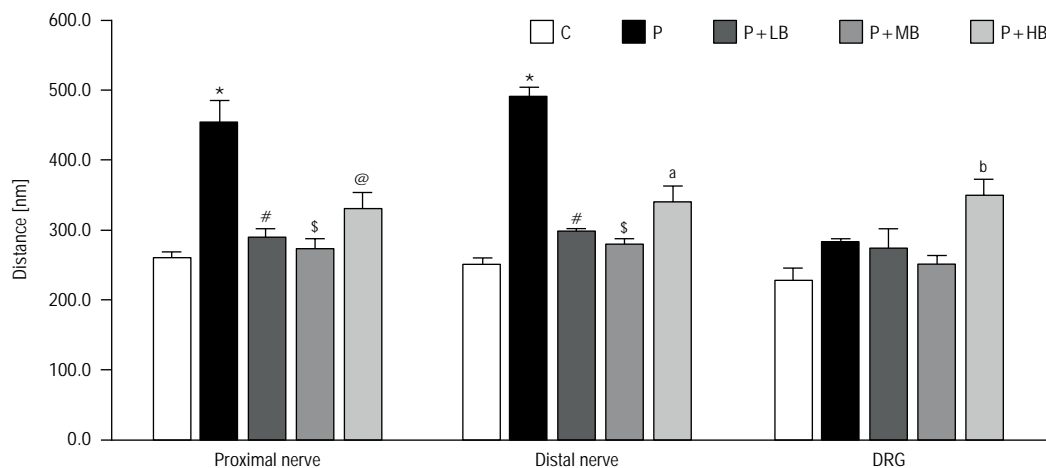


Figure 4. Distance at the widest separation between the endothelial cells and pericytes in the proximal and distal parts of sciatic nerve including L5 dorsal root ganglion (DRG). The graph shows means and standard error of mean; C — control; P — cisplatin; P+LB — cisplatin + low-dose B_{1-6-12} ; P+MB — cisplatin + medium-dose B_{1-6-12} ; P+HB — cisplatin + high-dose B_{1-6-12} ; * $p < 0.001$ P vs. C; # $p < 0.001$ P+LB vs. P; \$ $p < 0.001$ P+MB vs. P; @ $p < 0.001$ P+HB vs. P; ^a $p < 0.001$ P+HB vs. P and $p < 0.01$ P+HB vs. C; ^b $p < 0.05$ P+HB vs. C.

Cell viability and caspase-3 activity

Cell viability of the HUVEC was significantly reduced in the cisplatin group compared with the control group (Fig. 5). This was in agreement with the increased caspase-3 activity after cisplatin treatment. Similarly, cisplatin treatment in the HBVP resulted in lower viability and higher caspase-3 activity (Fig. 5). B_{1-6-12} was able to significantly enhance the viability of both HUVEC and HBVP but yielded only trends toward less caspase-3 activity in both cell types.

TEER

Transendothelial electrical resistance of the cisplatin group was significantly lower than that of the control

group (Fig. 6). Moreover, concomitant addition of B_{1-6-12} with cisplatin caused partial restoration of the resistance.

Expression of tight junction proteins

Expression of occludin and zonula occluden-2 (ZO-2) was significantly decreased in the HUVEC exposed to cisplatin compared with the controls (Fig. 7). However, the expression of claudin-5 and zonula occluden-1 (ZO-1) was not significantly different. Following B_{1-6-12} treatment, the expression of occludin and ZO-2 was completely reversed to those seen in the control group. It is worth mentioning that the ZO-1 expression was significantly enhanced in the cisplatin + B_{1-6-12} group compared with the cisplatin group.

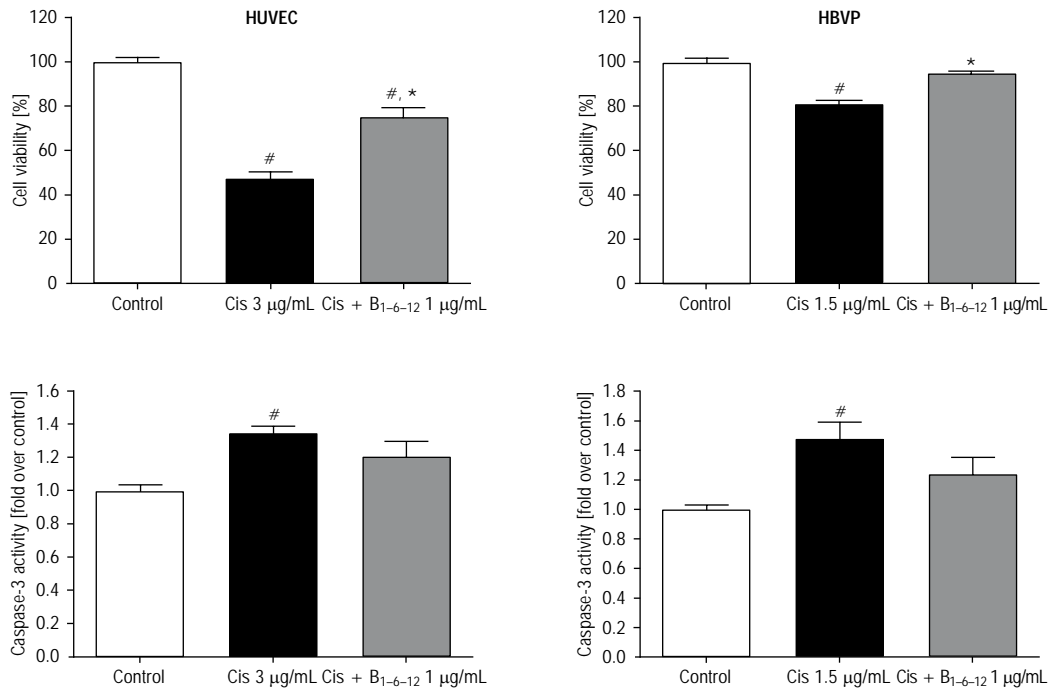


Figure 5. Cell viability and caspase-3 activity of human umbilical vein endothelial cell (HUVEC, left column) and human brain vascular pericyte (HBVP, right column). The graphs show means and standard error of mean; Cis — cisplatin; #*p* < 0.01 vs. control group; **p* < 0.01 vs. cisplatin group.

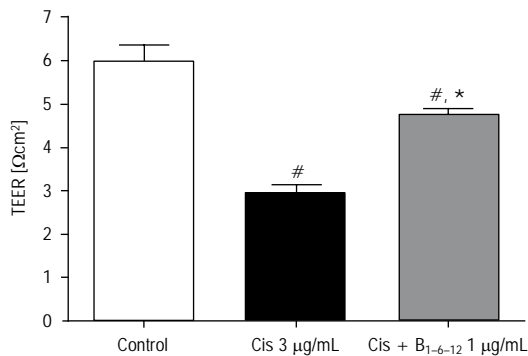


Figure 6. Transendothelial electrical resistance (TEER) of human umbilical vein endothelial cell. The graph shows means and standard error of mean; Cis — cisplatin; #*p* < 0.01 vs. control group; **p* < 0.01 vs. cisplatin group.

DISCUSSION

The rats treated with cisplatin developed neuropathy characterised by thermal hypoalgesia and morphometric changes: reduced fibre diameter, increased fibre density, loss of DRG neurons and shrinkage of nucleus and nucleolus. These features of cisplatin-induced neuropathy were similar to those previously reported [1, 2, 28, 29]. Higher density of nerve fibres was likely due to shrinkage of fibres and slight increase in the number of fibres. Several of these functional and pathological abnormalities were com-

parable to those observed in cancer patients treated with cisplatin [23, 27].

Vitamin B1, B6 and B12 had beneficial effects on thermal sensation and morphometry. High and medium, but not low doses of B₁₋₆₋₁₂ could significantly reduce the prolonged thermal latency seen in the cisplatin group. Furthermore, medium dose was better than low and high doses in restoring the fibre diameter and fibre density toward controls. As for DRG, all doses of B₁₋₆₋₁₂ appeared to have modest effects on the loss of neurons including shrinkage of nucleus and nucleolus caused by cisplatin. It is worth noting that B₁₋₆₋₁₂ did not have any significant effect on the weight loss used to indicate the general toxicity of cisplatin.

The previous study has demonstrated the pericyte detachment from endothelial cells in the nerves from cisplatin-treated rats which was rarely seen in the controls [12]. This study confirmed with quantitative analysis that pericytes detached with significantly higher frequencies and severity in the cisplatin than in the control rats. It is worth mentioning that despite the higher frequencies of detachment in the DRG from all cisplatin-treated compared with the control groups, the distances were not significantly different. More research is required to clarify why the pericytes detach with shorter distances in the DRG than in the nerves.

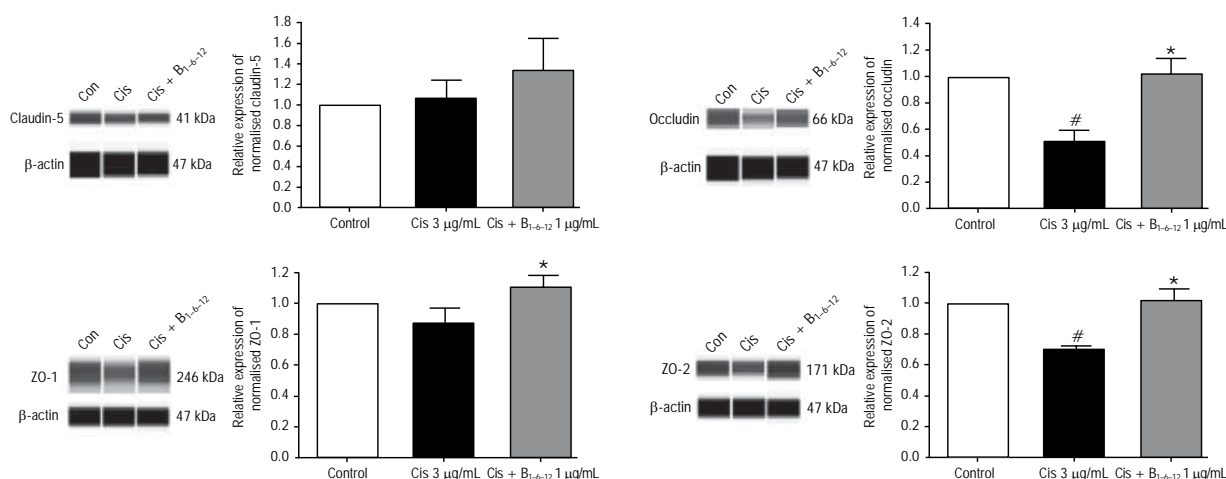


Figure 7. Protein expression of claudin-5, occludin, zonula occluden-1 and -2 (ZO-1 and ZO-2) representative immunoblots are shown. The density of each protein was normalised to that of β-actin. The graphs show means and standard error of mean; Con — control; Cis — cisplatin; #p < 0.05 vs. control group; *p < 0.05 vs. cisplatin group.

Pericyte detachment or migration has been shown in various conditions and organs. Increased migration of pericytes was observed in the retina of diabetic rats [21]. More pericytes in the anterior pituitary gland detached from the capillary walls of the prolactinoma rats than the normal controls [11]. Pericytes migrated from the vascular wall in response to traumatic brain injury [7]. Implications of the pericyte detachment are still unclear. However, since pericytes, endothelial cells and vascular basement membrane co-operate as the BNB to regulate the microvascular functions [20], the detachment is likely deleterious to the nerve. At least in the cisplatin-induced ototoxicity model, ultrastructural changes in the endothelial cells and pericyte migration in the stria vascularis of cochlea were associated with auditory impairment [30].

All doses of B₁₋₆₋₁₂ could alleviate the elevation in cisplatin-induced pericyte detachment in both sciatic nerves and DRG with the best result seen in the medium-dose group. Moreover, both low and medium doses of B₁₋₆₋₁₂ could equally normalise the distances of detachment. Nevertheless, high dose of B₁₋₆₋₁₂ may be less favourable or even harmful, especially in the DRG. The detachment distance in the high-dose group was significantly longer than those in the other groups. This dose-dependent effect of B₁₋₆₋₁₂ will be discussed later.

Due to the effects of cisplatin and B₁₋₆₋₁₂ on the nerve and DRG capillaries described above, the question which cell component of the BNB was affected by the drugs has emerged. This was clarified using separate cultures of endothelial cells (HUVEC) and

pericytes (HBVP). Cisplatin reduced the viability of both cell types at least via activation of caspase-3. This was consistent with the previous reports of endothelial cell apoptosis and enhanced caspase-3 activity following cisplatin treatment [8, 9, 15, 19]. Furthermore, TEER which represents the barrier function, was also reduced by cisplatin. Moreover, the expression of tight junction proteins in the HUVEC was examined. Expression of occludin and ZO-2, but not claudin-5 and ZO-1, was significantly lower in the cisplatin-treated cells compared with the controls. Reduced expression of tight junction proteins was also found in the stria vascularis of cochlea in cisplatin-treated mice [30].

Pericytes as well as endothelial cells are important for the normal functions of BNB and damage in any of these components might cause neuropathy. The above data from cell culture and ultrastructural analysis indicate that cisplatin causes endothelial and pericyte damage including the BNB disruption. The previous studies have already suggested the importance of tight junction proteins in the BNB integrity and nerve functions. Reduced level of claudin-5 was associated with BNB dysfunction in chronic inflammatory demyelinating polyradiculoneuropathy (CIDP) [14]. Shimizu et al. [25] showed that pericytes controlled the expression of claudin-5 in the endothelial cells through secretion of growth factors. Besides claudin-5, nerve pericytes also express other important components of the BNB, for example, fibronectin, collagen type IV [26].

Vitamin B1, B6 and B12 could partially correct the reduced viability of both HUVEC and HBVP after

cisplatin administration. Furthermore, the decreased TEER was also alleviated by B₁₋₆₋₁₂. Regarding the tight junction proteins, B₁₋₆₋₁₂ was able to correct the reduced expression of occludin and ZO-2 and further enhanced the expression of ZO-1 above the control level. All these data suggest that beneficial effects of B₁₋₆₋₁₂ on functional and morphometric parameters of cisplatin neurotoxicity described earlier might be exerted at least via improvement in the BNB functions. This could be due to less cell toxicity and enhanced expression of some tight junction proteins. Although numerous agents targeting various mechanisms were effective in experimental cisplatin neuropathy, they failed to show significant benefits in clinical trials [24]. Vitamin B1, B6 and B12 are water-soluble vitamins essential for normal functions of the nervous system and frequently prescribed for neuropathies from various causes. However, current evidence of efficacy of B vitamins in chemotherapy-induced neuropathy is still inconclusive [18]. The results of this study support the continued effort to develop B₁₋₆₋₁₂ as the potential treatment for cisplatin-induced neuropathy. It is worth noting that less or unfavourable effects of high-dose B₁₋₆₋₁₂ in the morphometric analysis of DRG and sciatic nerves were found in this study. This might be due to toxicity of all or specific B vitamins. Excessive intake of pyridoxine (B₆) can cause neuropathy [10]. Therefore, optimal dose of these B vitamins must be determined to prevent the overdose side effects. Data in this study suggest the medium dose (300 mg/kg/day per oral) of B₁₋₆₋₁₂ as the most suitable.

The results in this study also suggest the BNB impairment as additional important mechanism underlying cisplatin-induced neuropathy. This is in accordance with the previous study showing the BNB abnormalities in CIDP cases [14]. However, it remains to be proved whether these alterations in the BNB occur in the patients with cisplatin neuropathy. Moreover, the BNB integrity should be examined in neuropathies from other chemotherapeutic drugs or other causes. In the future, drugs with beneficial effects on endothelial cells or pericytes can be assessed for potential treatments against peripheral neuropathy with impaired BNB.

CONCLUSIONS

This study has demonstrated the favourable effects of B₁₋₆₋₁₂ on thermal hypoalgesia and abnormal morphometric parameters of the sciatic nerves and DRG induced by cisplatin. Ultrastructural analysis

revealed that cisplatin stimulated pericyte detachment in the capillaries in those tissues. In addition, cell culture experiments showed reduced viability of endothelial cells and pericytes, transendothelial electrical resistance and expression of some tight junction proteins. B₁₋₆₋₁₂, especially the medium dose, could improve the sensory deficit and structural alterations. Moreover, cell viability, barrier function and tight junction proteins were also corrected by B₁₋₆₋₁₂. These data suggest that BNB disruption is one of the pathological mechanisms underlying cisplatin-induced neuropathy and B₁₋₆₋₁₂ are the potential treatment.

Acknowledgements

We are grateful to the Research Affairs, Faculty of Medicine, Chulalongkorn University for assistance regarding transmission electron microscopy. This work was supported by the Faculty of Medicine, Chulalongkorn University under the Ratchadaphiseksomphot Fund (RA62/022 & RA63/030) and the 90th Anniversary of Chulalongkorn University Fund (Ratchadaphiseksomphot Endowment Fund, GCU-GR1125631039D-39).





Conflict of interest: None declared

REFERENCES

1. Al Moundhri MS, Al-Salam S, Al Mahrouqee A, et al. The effect of curcumin on oxaliplatin and cisplatin neurotoxicity in rats: some behavioral, biochemical, and histopathological studies. *J Med Toxicol*. 2013; 9(1): 25–33, doi: [10.1007/s13181-012-0239-x](https://doi.org/10.1007/s13181-012-0239-x), indexed in Pubmed: [22648527](https://pubmed.ncbi.nlm.nih.gov/22648527/).
2. Authier N, Gillet JP, Fialip J, et al. An animal model of nociceptive peripheral neuropathy following repeated cisplatin injections. *Exp Neurol*. 2003; 182(1): 12–20, doi: [10.1016/s0014-4886\(03\)00003-7](https://doi.org/10.1016/s0014-4886(03)00003-7), indexed in Pubmed: [12821373](https://pubmed.ncbi.nlm.nih.gov/12821373/).
3. Bartoszyk GD, Wild A. B-vitamins potentiate the antinociceptive effect of diclofenac in carrageenin-induced hyperalgesia in the rat tail pressure test. *Neurosci Lett*. 1989; 101(1): 95–100, doi: [10.1016/0304-3940\(89\)90447-3](https://doi.org/10.1016/0304-3940(89)90447-3), indexed in Pubmed: [2771158](https://pubmed.ncbi.nlm.nih.gov/2771158/).
4. Chentanez V, Cha-oumphol P, Kaewsema A, et al. Accuracy of the three-window sampling method in morphometric analysis of human sural nerve. *J Neurosci Methods*. 2006; 157(1): 154–157, doi: [10.1016/j.jneumeth.2006.04.001](https://doi.org/10.1016/j.jneumeth.2006.04.001), indexed in Pubmed: [16704879](https://pubmed.ncbi.nlm.nih.gov/16704879/).
5. Dieckmann KP, Struss WJ, Budde U. Evidence for acute vascular toxicity of cisplatin-based chemotherapy in patients with germ cell tumour. *Anticancer Res*. 2011; 31(12): 4501–4505, indexed in Pubmed: [22199322](https://pubmed.ncbi.nlm.nih.gov/22199322/).
6. Dilruba S, Kalayda GV. Platinum-based drugs: past, present and future. *Cancer Chemother Pharmacol*. 2016; 77(6): 1103–1124, doi: [10.1007/s00280-016-2976-z](https://doi.org/10.1007/s00280-016-2976-z), indexed in Pubmed: [26886018](https://pubmed.ncbi.nlm.nih.gov/26886018/).

7. Dore-Duffy P, Owen C, Balabanov R, et al. Pericyte migration from the vascular wall in response to traumatic brain injury. *Microvasc Res.* 2000; 60(1): 55–69, doi: [10.1006/mvre.2000.2244](https://doi.org/10.1006/mvre.2000.2244), indexed in Pubmed: [10873515](https://pubmed.ncbi.nlm.nih.gov/10873515/).
8. Dursun B, He Z, Somerset H, et al. Caspases and calpain are independent mediators of cisplatin-induced endothelial cell necrosis. *Am J Physiol Renal Physiol.* 2006; 291(3): F578–F587, doi: [10.1152/ajprenal.00455.2005](https://doi.org/10.1152/ajprenal.00455.2005), indexed in Pubmed: [16622172](https://pubmed.ncbi.nlm.nih.gov/16622172/).
9. Eguchi R, Fujimori Y, Ohta T, et al. Calpain is involved in cisplatin-induced endothelial injury in an in vitro three-dimensional blood vessel model. *Int J Oncol.* 2010; 37(5): 1289–1296, doi: [10.3892/ijo_00000780](https://doi.org/10.3892/ijo_00000780).
10. Hadtstein F, Vrolijk M. Vitamin B-6-induced neuropathy: exploring the mechanisms of pyridoxine toxicity. *Adv Nutr.* 2021; 12(5): 1911–1929, doi: [10.1093/advances/nmab033](https://doi.org/10.1093/advances/nmab033), indexed in Pubmed: [33912895](https://pubmed.ncbi.nlm.nih.gov/33912895/).
11. Jindatip D, Fujiwara K, Sarachana T, et al. Characteristics of pericytes in diethylstilbestrol (DES)-induced pituitary prolactinoma in rats. *Med Mol Morphol.* 2018; 51(3): 147–155, doi: [10.1007/s00795-018-0180-4](https://doi.org/10.1007/s00795-018-0180-4), indexed in Pubmed: [29344720](https://pubmed.ncbi.nlm.nih.gov/29344720/).
12. Jindatip D, Nopparat W, Kobutree P, et al. Pericyte loss and detachment in experimental cisplatin-induced neuropathy. *Int J Morphol.* 2019; 37(2): 509–514, doi: [10.4067/s0717-95022019000200509](https://doi.org/10.4067/s0717-95022019000200509).
13. Jolivald CG, Mizisin LM, Nelson A, et al. B vitamins alleviate indices of neuropathic pain in diabetic rats. *Eur J Pharmacol.* 2009; 612(1-3): 41–47, doi: [10.1016/j.ejphar.2009.04.028](https://doi.org/10.1016/j.ejphar.2009.04.028), indexed in Pubmed: [19393643](https://pubmed.ncbi.nlm.nih.gov/19393643/).
14. Kanda T, Numata Y, Mizusawa H. Chronic inflammatory demyelinating polyneuropathy: decreased claudin-5 and relocated ZO-1. *J Neurol Neurosurg Psychiatry.* 2004; 75(5): 765–769, doi: [10.1136/jnnp.2003.025692](https://doi.org/10.1136/jnnp.2003.025692), indexed in Pubmed: [15090575](https://pubmed.ncbi.nlm.nih.gov/15090575/).
15. Kirchmair R, Walter DH, Li M, et al. Antiangiogenesis mediates cisplatin-induced peripheral neuropathy: attenuation or reversal by local vascular endothelial growth factor gene therapy without augmenting tumor growth. *Circulation.* 2005; 111(20): 2662–2670, doi: [10.1161/CIRCULATIONAHA.104.470849](https://doi.org/10.1161/CIRCULATIONAHA.104.470849), indexed in Pubmed: [15897348](https://pubmed.ncbi.nlm.nih.gov/15897348/).
16. Krarup-Hansen A, Helweg-Larsen S, Schmalbruch H, et al. Neuronal involvement in cisplatin neuropathy: prospective clinical and neurophysiological studies. *Brain.* 2007; 130(Pt 4): 1076–1088, doi: [10.1093/brain/awl356](https://doi.org/10.1093/brain/awl356), indexed in Pubmed: [17301082](https://pubmed.ncbi.nlm.nih.gov/17301082/).
17. Li SH, Chen WH, Tang Y, et al. Incidence of ischemic stroke post-chemotherapy: a retrospective review of 10,963 patients. *Clin Neurol Neurosurg.* 2006; 108(2): 150–156, doi: [10.1016/j.clineuro.2005.03.008](https://doi.org/10.1016/j.clineuro.2005.03.008), indexed in Pubmed: [16412836](https://pubmed.ncbi.nlm.nih.gov/16412836/).
18. Liu YW, Liu CT, Su YL, et al. A narrative review of complementary nutritional supplements for chemotherapy-induced peripheral neuropathy. *Altern Ther Health Med.* 2020; 26(4): 43–49, indexed in Pubmed: [31634876](https://pubmed.ncbi.nlm.nih.gov/31634876/).
19. Nuver J, De Haas EC, Van Zweeden M, et al. Vascular damage in testicular cancer patients: A study on endothelial activation by bleomycin and cisplatin in vitro. *Oncol Rep.* 2009; 23(1), doi: [10.3892/or_00000630](https://doi.org/10.3892/or_00000630).
20. Peltonen S, Alanne M, Peltonen J. Barriers of the peripheral nerve. *Tissue Barriers.* 2013; 1(3): e24956, doi: [10.4161/tisb.24956](https://doi.org/10.4161/tisb.24956), indexed in Pubmed: [24665400](https://pubmed.ncbi.nlm.nih.gov/24665400/).
21. Pfister F, Feng Y, vom Hagen F, et al. Pericyte migration: a novel mechanism of pericyte loss in experimental diabetic retinopathy. *Diabetes.* 2008; 57(9): 2495–2502, doi: [10.2337/db08-0325](https://doi.org/10.2337/db08-0325), indexed in Pubmed: [18559662](https://pubmed.ncbi.nlm.nih.gov/18559662/).
22. Quasthoff S, Hartung H. Chemotherapy-induced peripheral neuropathy. *J Neurol.* 2002; 249(1): 9–17, doi: [10.1007/pl00007853](https://doi.org/10.1007/pl00007853).
23. Roelofs RI, Hrshesky W, Rogin J, et al. Peripheral sensory neuropathy and cisplatin chemotherapy. *Neurology.* 1984; 34(7): 934–938, doi: [10.1212/wnl.34.7.934](https://doi.org/10.1212/wnl.34.7.934), indexed in Pubmed: [6330613](https://pubmed.ncbi.nlm.nih.gov/6330613/).
24. Santos NA, Ferreira RS, Santos AC. Overview of cisplatin-induced neurotoxicity and ototoxicity, and the protective agents. *Food Chem Toxicol.* 2020; 136: 111079, doi: [10.1016/j.fct.2019.111079](https://doi.org/10.1016/j.fct.2019.111079), indexed in Pubmed: [31891754](https://pubmed.ncbi.nlm.nih.gov/31891754/).
25. Shimizu F, Sano Y, Abe MA, et al. Peripheral nerve pericytes modify the blood-nerve barrier function and tight junctional molecules through the secretion of various soluble factors. *J Cell Physiol.* 2011; 226(1): 255–266, doi: [10.1002/jcp.22337](https://doi.org/10.1002/jcp.22337), indexed in Pubmed: [20665675](https://pubmed.ncbi.nlm.nih.gov/20665675/).
26. Shimizu F, Sano Y, Haruki H, et al. Advanced glycation end-products induce basement membrane hypertrophy in endoneurial microvessels and disrupt the blood-nerve barrier by stimulating the release of TGF- β and vascular endothelial growth factor (VEGF) by pericytes. *Diabetologia.* 2011; 54(6): 1517–1526, doi: [10.1007/s00125-011-2107-7](https://doi.org/10.1007/s00125-011-2107-7), indexed in Pubmed: [21409414](https://pubmed.ncbi.nlm.nih.gov/21409414/).
27. Thompson SW, Davis LE, Kornfeld M, et al. Cisplatin neuropathy. Clinical, electrophysiologic, morphologic, and toxicologic studies. *Cancer.* 1984; 54(7): 1269–1275, doi: [10.1002/1097-0142\(19841001\)54:7<1269::aid-cn-cr2820540707>3.0.co;2-9](https://doi.org/10.1002/1097-0142(19841001)54:7<1269::aid-cn-cr2820540707>3.0.co;2-9), indexed in Pubmed: [6088023](https://pubmed.ncbi.nlm.nih.gov/6088023/).
28. Wongtawatchai T, Agthong S, Kaewsema A, et al. Sex-related differences in cisplatin-induced neuropathy in rats. *J Med Assoc Thai.* 2009; 92(11): 1485–1491, indexed in Pubmed: [19938741](https://pubmed.ncbi.nlm.nih.gov/19938741/).
29. Wongtawatchai T, Agthong S, Kaewsema A, et al. Altered phosphorylation of mitogen-activated protein kinases in dorsal root ganglia and sciatic nerve of rats with cisplatin-induced neuropathy. *Asian Biomed (Res Rev News).* 2012; 6: 397–411.
30. Zhang N, Cai J, Xu L, et al. Cisplatin-Induced stria vascularis damage is associated with inflammation and fibrosis. *Neural Plast.* 2020; 2020: 8851525, doi: [10.1155/2020/8851525](https://doi.org/10.1155/2020/8851525), indexed in Pubmed: [33029120](https://pubmed.ncbi.nlm.nih.gov/33029120/).

Evaluation of cell morphology and adhesion capacity of human gingival fibroblasts on titanium discs with different roughened surfaces: an *in vitro* scanning electron microscope analysis and cell culture study

H. Yıldız¹, E. Sen², H. Dalcik³, S.E. Meseli¹

¹Periodontology Department, Faculty of Dentistry, Istanbul Aydin University, Istanbul, Turkey

²Histology and Embryology Department, Faculty of Medicine, Istanbul Aydin University, Istanbul, Turkey

³Anatomy Department, Faculty of Medicine, Istanbul Aydin University, Istanbul, Turkey

[Received: 8 July 2021; Accepted: 7 August 2021; Early publication date: 17 August 2021]

Background: Implantoplasty is an option in peri-implantitis treatment. What is known about the effects of implantoplasty on peri-implant soft tissue adhesion and cell behaviours is limited. This study aimed to evaluate the morphological features and adhesion capacity of human gingival fibroblast (HGF) cells onto sand-blasted, large-grit, acid-etched (SLA[®]) titanium (Ti) discs surfaces roughened with different implantoplasty protocols.

Materials and methods: The study included a total of 48 Ti discs divided into four groups ($n = 12$ per group): Group I: machined, smooth surface discs; Group II: SLA[®] surface discs; Group III: SLA[®] surface discs roughened with diamond bur sequence (40 and 15- μm grit); Group IV: SLA[®] surface discs roughened with diamond bur sequence (125 and 40- μm grit). Following polishing procedure, the surface roughness value of discs was assessed by a profilometer and scanning electron microscope. HGFs were cultured on Ti discs and cell adhesion was examined after the 24th, 48th, and 72nd hours. Statistical significance was set at the $p \leq 0.05$ level.

Results: Scanning electron microscope analyses of the discs revealed that fibroblasts exhibited well-dispersion and a firm attachment in all groups. The cells in group I and II had thin and long radial extensions from the areas where the nucleus was located to the periphery; however, attached cells in group III and IV showed more spindle-shaped morphology. The surface roughness parameters of the test groups were lower than those of the SLA[®]. The SLA[®] group showed the highest HGF adhesion (group II) ($p \leq 0.05$). HGF adhesion in group IV was greater compared to group III, but less than group I.

Conclusions: This study showed that the characteristics of the burs applied in the implantoplasty protocol are determinant for the surface roughness and fibroblast adhesion occurs on surfaces with decreased roughness following implantoplasty. Consequently, it should be kept in mind that the surface properties of the implant may affect the adherent cell morphology and adhesion. (Folia Morphol 2023; 82, 1: 63–71)

Key words: cell adhesion, cell morphology, human gingival fibroblasts, implantoplasty, surface roughness

Address for correspondence: S.E. Meseli, Asst. Prof., PhD, DDS, Faculty of Dentistry, Periodontology Department, Istanbul Aydin University, Istanbul, Turkey, tel: +905304667471, fax: +902124255759, e-mail: suleymanmeseli@aydin.edu.tr

This article is available in open access under Creative Common Attribution-Non-Commercial-No Derivatives 4.0 International (CC BY-NC-ND 4.0) license, allowing to download articles and share them with others as long as they credit the authors and the publisher, but without permission to change them in any way or use them commercially.

INTRODUCTION

The peri-implant soft tissue encircles the implant in the neck region similar to a tight collar. This structure, which is crucial for osseointegration of the implant, should adhere firmly to the implant surface [18]. The gingival epithelium proliferates along the implant surface without a connective tissue attachment, which is likely due to the proximity of tissue fibres in parallel arrangement along the implant axis [16]. This fundamental phenomenon underlying the mechanism of soft tissue adaptation at the cellular level is still unknown.

Fibroblasts are the primary cells of the soft connective tissue of the periodontium. Inflammation of the periodontal tissue leads to a breakdown of fibroblasts and impaired tissue integrity. As a result of the progressive degenerative changes, a loss of periodontal tissue occurs. This pathogenesis, which manifests itself in periodontal tissues, is also observed in peri-implant tissues. The soft tissues surrounding the implant function as a biological barrier and protect the peri-implant bone from microbiological infections [19].

Human gingival fibroblasts (HGF) exhibit a "filopodial" structure that extends further into grooves and microstructures on rough surfaces [7], which results in increased fibroblast adhesion [38, 41]. On the contrary, HGFs accumulate more randomly on smooth surfaces [22]. Surface texture, such as roughness and topographical changes, influences connective tissue adhesion to the transmucosal section of implants. Various physical, chemical, and biochemical surface modification techniques were introduced to increase roughness and improve cell adhesion [3]. At the same time, these well-designed surface modifications must also minimise microbial colonisation around the implant surface [17].

In vivo studies have shown a positive association between plaque accumulation rate and surface roughness in the supragingival region [9, 37]. To observe bacterial adherence and colonisation in the oral cavity, where surface irregularities such as grooves, pits, perikymata, and abrasion defects are frequently present in scanning electron microscope (SEM) images [12]. Since it is difficult to remove microorganisms from these areas, they colonise and form biofilm structures. In the case of abutment materials with a rough surface, it was found that they contain 25 times more pathogenic bacteria than smooth materials [30]. Moreover, smooth surfaces facilitate oral hygiene procedures performed by patients.

The roughness value (R_a) serves to determine the structural height of the surface and defines the arithmetic mean of the profile values [40]. In a subsequent investigation based on their previous short-term study [29], the researchers concluded that lowering the R_a value well below the $0.2 \mu\text{m}$ threshold had no significant effect on the gingival microbial colonisation [5].

In the treatment of peri-implantitis, surgical treatments are required in addition to conventional treatment methods to ensure complete decontamination [5]. Implantoplasty, also known as mechanical modification of the implant, is recommended as part of surgical treatment to change implant surface topography, reduce microbial colonization, and thus prevent reinfection [1, 4, 32]. While it is not possible to completely eliminate microorganisms using current implantoplasty techniques, a combination of mechanical and chemical techniques is more effective [35]. However, there are still experimental, non-standardised, and non-consensual implantoplasty techniques, so the mechanical or biological outcomes of these treatment approaches are still unknown.

The purpose of this *in vitro* study was to determine and compare the adhesion of HGF to: sand-blasted, large-grit, acid-etched (SLA[®])-surfaced titanium (Ti) discs after applying diamond bur sequences with different implantoplasty protocols. The null hypothesis of the present study was that surface modifications in implantoplasty procedures did not affect HGF growth and adhesion.

MATERIALS AND METHODS

Pre-made cell lines were used in the present 72-hour *in vitro* cell culture study. Therefore, approval from the ethics committee was not necessary.

Sample size and study groups

Based on values from methodologically similar studies [22, 24, 25], the power analysis tool G-POWER calculated a total sample size of 48, with an effect size of 0.65, 95% power, and a margin of error of 0.56%. Groups were evenly distributed, with 12 discs in each group.

A total of 48 commercially available grade 4 pure Ti discs with a diameter of 10 mm and a thickness of 2.5 mm were used (Trias-ixx2, Servo Dental, Hagen, Germany). The discs met the biocompatibility requirements of the "Standard Specification for Unalloyed Titanium for Surgical Implant Applications" (ASTM

F 67/ ISO 5832-2). Four groups each with 12 discs included in the study were:

- Group I: machined discs with smooth surfaces;
- Group II: SLA® discs with roughened surfaces;
- Group III: the SLA® discs were milled for 2 minutes with a round-tipped red diamond bur (40 µm grit, Dimei Royal, China); and for 1-minute with a round-tipped white diamond bur (15 µm grit, Komet Dental, Germany). Subsequently, all discs were polished with Brownie silicone under a 1-minute water rinse;
- Group IV: SLA® discs were milled for 2 minutes with a round-tipped green diamond bur (125 µm grit, Dimei Royal, China); and for 1-minute with a round-tipped white diamond bur (15 µm grit, Komet Dental; Germany). Subsequently, all discs were polished with Brownie silicone under a 1-minute water rinse.

Standardisation was maintained during the surface roughening protocol in groups III and IV with a custom-built stabilisation mechanism. In a controlled environment, one of the researchers (H.Y.) milled each disc clockwise from its centre to its outer periphery for the specified time frame with a separate set of burs, while an external observer recorded the milling times for each disc. H.Y. took a 5-minute break between each disc milling. This *in vitro* approach was used to model the milling process during implantoplasty [25]. As part of the preparation for cell culture, each disc was assigned a unique number. The R_a value of each disc was measured using a mechanical profilometer (MahrSurf M 400, Germany).

Cell culture

Following *in vitro* milling procedures, all discs were agitated for 5 minutes in an ultrasonic cleaner and the samples were cleaned with 20% ethanol for 10 minutes. Discs were then autoclaved at 134°C for 20 minutes under a gauge pressure of 2 kg/cm² (Dri-Tec, Canada).

The human gingival fibroblast cell line (HGF1; ATCC) was used for cell culture. Cells were passaged in flasks containing Dulbecco Modified Eagle Medium culturing media (HyClone, USA) containing 10% fetal bovine serum (Sigma-Aldrich Co., USA, the CAS number: 9014-81-7) and incubated at a temperature of 37°C, relative humidity of 95% (to minimise media evaporation and condensation), and 5% CO₂. Upon reaching 80% confluency, the cells were then subcultured using with phosphate buffered saline

(Sigma-Aldrich Co., USA, the CAS number: 7758-11-4) and a trypsin-ethylenediaminetetraacetic acid solution (0.5 g/L trypsin; 0.2 g/L EDTA, Sigma-Aldrich Co., USA, the CAS number: 9002-07-7). Cells from passages 3 and 4 were used in this study.

Analysis of cell viability, proliferation and adhesion

To determine cell viability and proliferation, 3-(4,5-dimethylthiazol-2-yl)-2,5-diphenyltetrazolium bromide (MTT) (Sigma-Aldrich Co., USA, the CAS number: 57360-69-7) was used as the gold standard for assessing the metabolic activity of the cells. The sterilised discs of each group were placed in 24-well plates. Each well was seeded with 100.000 HGFs at a density of 100.000 cells/mL and incubated at 37°C in a CO₂ incubator. The samples were transferred to a new 24-well plate after 24 hours. The wells were then filled with the MTT solution and placed in the incubator to determine cell viability and proliferation [25]. After 3.5 hours, a dimethyl sulfoxide (DMSO) solution (Sigma-Aldrich Co., USA, the CAS number: 67-68-5) was added to each well. Formazan products were transferred to a 96-well plate and the absorbance was measured at a reference wavelength of 570 nm. Cell proliferation and viability were measured after 24, 48, and 72 hours. The absorbance of formazan accepted that it was linearly correlated with the number of adhered cells and MTT-labelled cells are defined by their adhesion characteristics [6, 14, 27, 42].

Scanning electron microscope analysis

A sample collection from each group was randomised using a computer-generated randomisation table to assess surface topography, cell morphology and fibroblast adhesion by SEM (ZEISS EVO® LS 10, Yildiz Technical University, Turkey). Before the imaging, the samples were coated with a 10 nm thin gold layer.

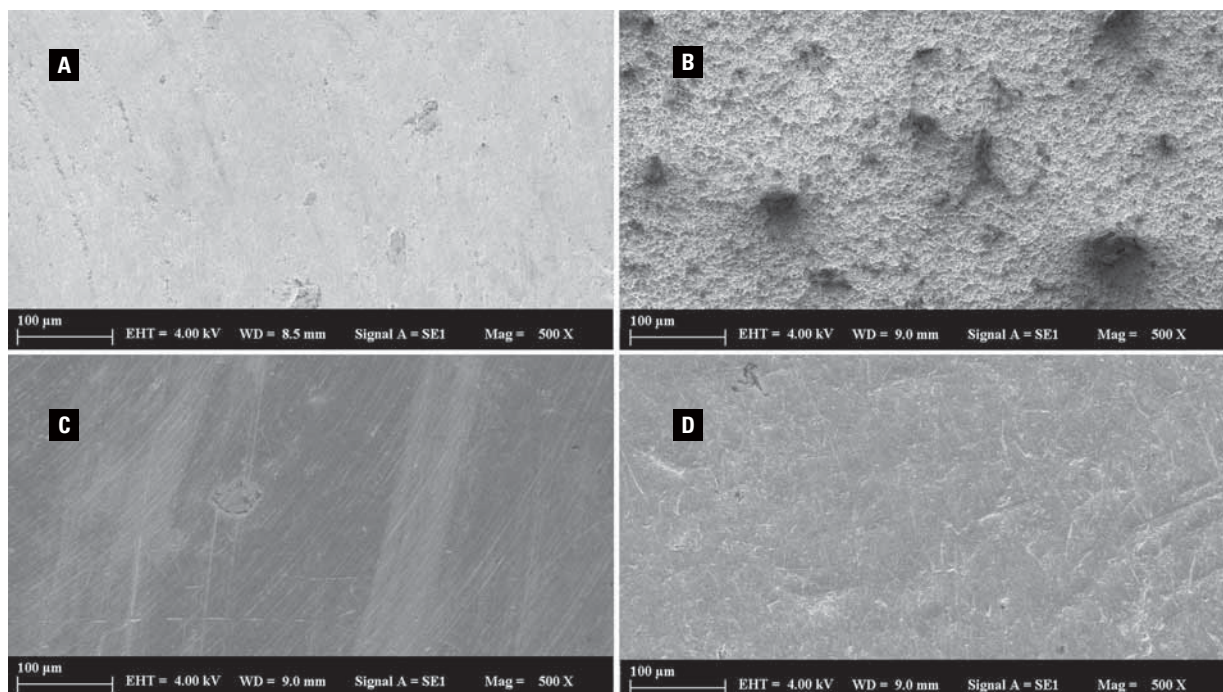
Statistical analysis

Statistical analysis of this study was performed using Statistical Package for Social Sciences version 24.00. The Kolmogorov-Smirnov test was used to assess the normality of the quantitative data. The Kruskal-Wallis test was used for multiple comparisons between groups, while the Mann-Whitney U test was used to compare the mean values of two groups. Repeated measurements of the mean values of the groups were compared with Friedman's test. The Wilcoxon signed-rank test was used to compare the mean values of

Table 1. Discs roughness value (R_a) values

Discs	Group I	Group II	Group III	Group IV
1	0.317	1.099	0.577	1.057
2	0.224	1.418	0.757	0.824
3	0.221	1.360	0.889	1.098
4	0.196	1.532	0.449	0.897
5	0.439	1.087	0.582	0.914
6	0.145	1.093	0.614	0.752
7	0.165	0.908	0.456	0.728
8	0.263	1.538	0.731	0.740
9	0.127	1.282	0.511	0.817
10	0.258	1.480	0.506	0.743
11	0.162	1.712	0.501	0.947
12	0.320	1.714	0.655	0.834
Mean \pm SD	0.236 \pm 0.09	1.351 \pm 0.26	0.602 \pm 0.13	0.862 \pm 0.12

SD — standard deviation

**Figure 1.** Scanning electron microscope images of surface topographies of the Ti discs (500 \times magnification); **A.** Group I; **B.** Group II; **C.** Group III; **D.** Group IV.

variables in any group recorded 2 times in study period, while Friedman test was used to compare the mean values of variables recorded more than 2 times. The level of statistical significance was set at $p \leq 0.05$.

RESULTS

The R_a values of the individual discs in each group are shown in Table 1. The mean R_a value of group II ($p = 0.001$) was found to be the highest, while group I

($p = 0.001$) had the lowest value. There were also significant differences among the mean R_a values of the groups ($p \leq 0.05$).

The SEM analysis of each group showed that the surface topographies varied when the surfaces were treated with different burs. During the surface modification process, irregular structures, multiple grooves and protrusions formed on the SLA[®] surfaces (Fig. 1A–D). Due to the characteristics of the

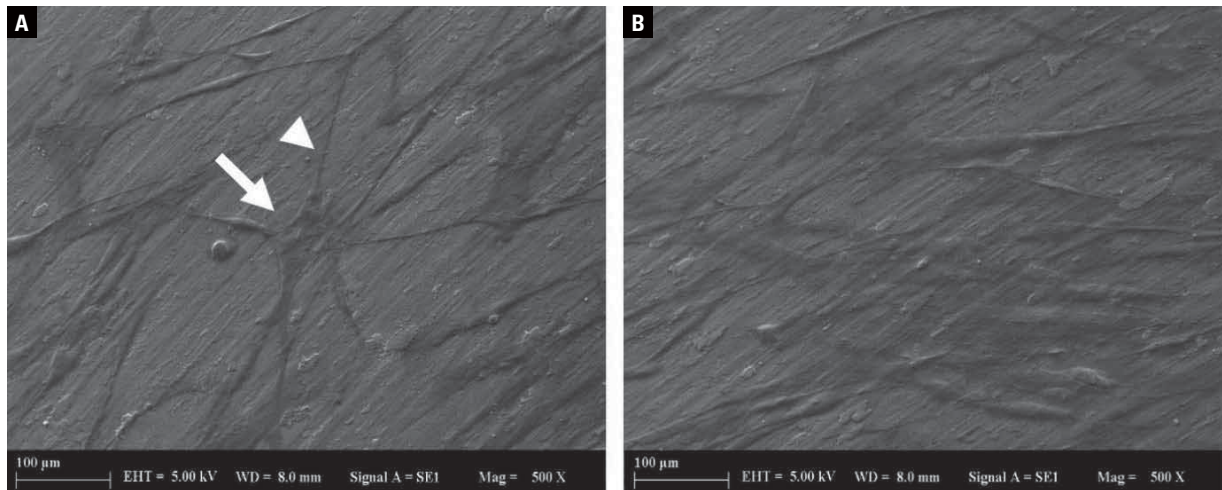


Figure 2. A, B. Scanning electron microscope images of fibroblast group I (24th hour, A, B, 500× magnification) (arrow: cell body; arrow head: cytoplasmic extension).

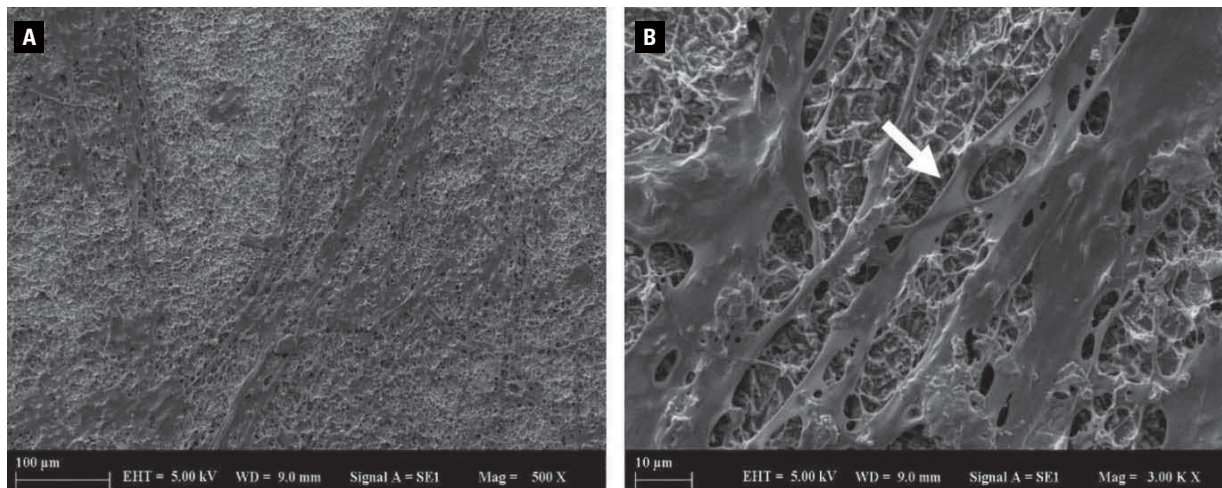


Figure 3. A, B. Scanning electron microscope images of fibroblast group II (24th hour, A, 500×, B, 3000× magnification) (arrow: cytoplasmic extension).

burs, mild surface irregularities occurred in groups III and IV.

Scanning electron microscope-generated morphologic micrographs showed that well-dispersed and evenly distributed cells that were firmly attached to the surfaces in all groups. The morphology of the cultured HGF were in close contact with each other and formed a carpet-like layer that adhered firmly to the Ti discs. The SEM images clearly showed the fibroblasts that exhibited thin and long radial extensions—marked with the arrows in the figures—from the cell nucleus zone to the periphery in groups I and II (Figs. 2, 3). But, considering the proliferation and adhesion areas revealed with the formazan crystals formed as the result of MTT assays, attached cells in

group III and IV showed spindle-shaped morphology that the extensions of cells more closely located to nuclei (Figs. 4, 5).

For each study time point, there were significant differences between groups in terms of cell adhesion ($p = 0.001$) (Table 2). According to the pairwise comparisons, group III had the lowest adhesion rate ($p \leq 0.05$), while group II had the highest rate ($p \leq 0.05$). In addition, cell adhesion was significantly higher in group I than in group IV ($p \leq 0.05$).

When the mean cell adhesion values of the groups evaluated according to study time points, the significant difference was found only in group II ($p = 0.035$). The mean per cent cell adhesion values between groups showed that only the mean value of group II

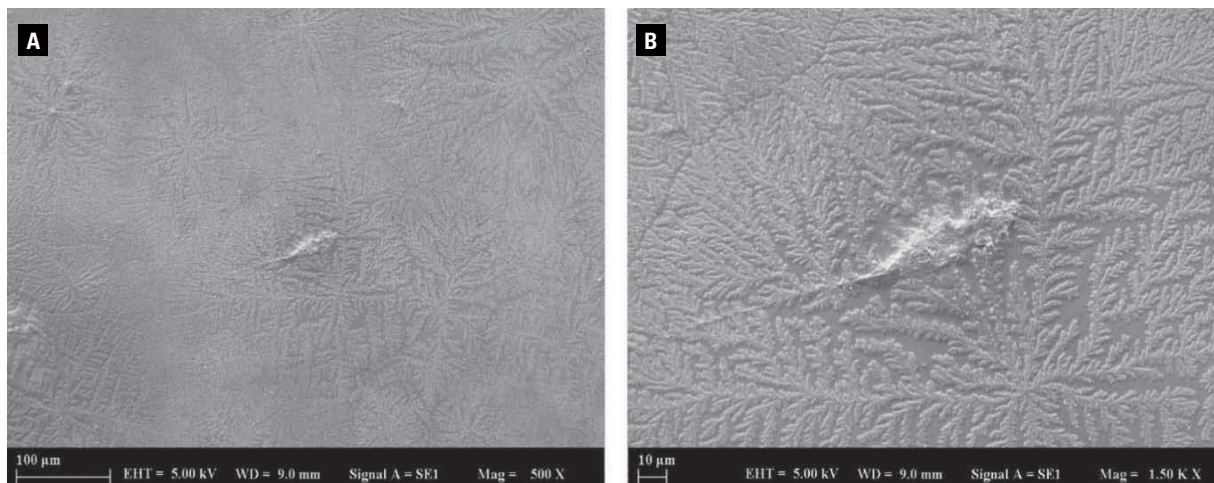


Figure 4. A, B. Scanning electron microscope images of cellular cytoplasmic adhesion areas in group III (24th hour, A. 500×, B. 1500× magnification).

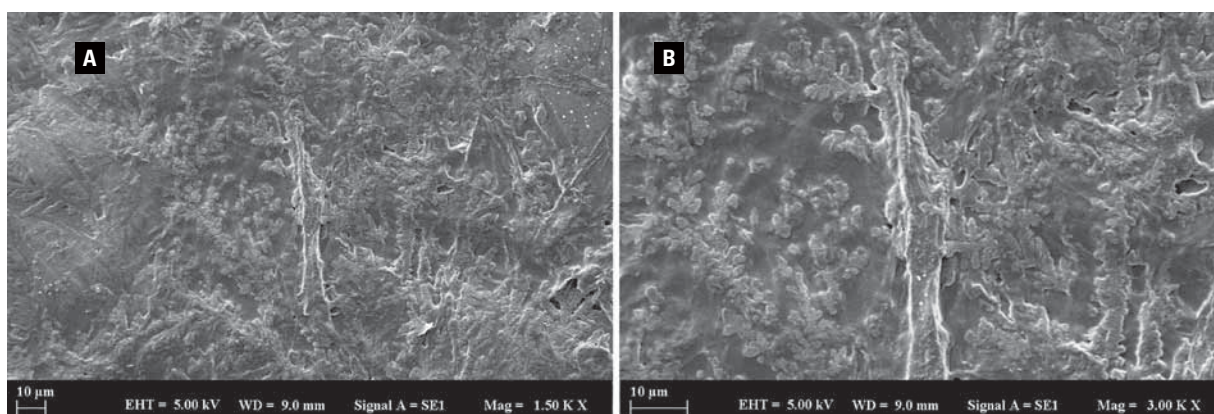


Figure 5. A, B. Scanning electron microscope images of fibroblast group IV (24th hour, A. 1500×, B. 3000× magnification).

Table 2. Inter- and intra-group comparisons of fibroblast adhesion

	Standard	Group I	Group II	Group III	Group IV	P*
24 th hours	100 ± 0.25 99.75–100.32 (99.96)	60.83 ± 0.73 ^{oe} 60–61.54 (60.89)	66.48 ± 0.39 ^{Δ,§} 66.04–66.84 (66.52)	35.58 ± 1.61 [¶] 33.37–37.15 (35.89)	51.78 ± 0.74 51.23–52.87 (51.5)	0.001
48 th hours	100 ± 1.57 98.64–101.58 (99.88)	61.14 ± 2.23 ^{oe} 58.58–63.52 (61.24)	69.54 ± 1.83 ^{Δ,μ} 67.61–71.86 (69.26)	36.25 ± 2.22 [¶] 33.35–38.2 (36.73)	52.61 ± 0.55 51.97–53.24 (52.61)	0.001
72 nd hours	100 ± 5.95 96.08–108.82 (97.54)	63.5 ± 1.38 ^{oe} 62.14–65.24 (63.31)	72.94 ± 5.54 ^Δ 66.81–80.24 (72.27)	35.91 ± 2.45 [¶] 32.3–37.48 (36.93)	54.87 ± 6.37 50.93–64.36 (52.1)	0.001
P [¶]	0.397	0.077	0.035	0.668	0.437	–

Data are shown as mean ± standard deviation, median and percentage (%) and minimum–maximum.
 P < 0.05: *Kruskal-Wallis test; Mann-Whitney U test Δ(Group II–I/III/IV) ¶(Group III–I/IV) œ(Group I–IV)
 P < 0.05: †Friedman test; Wilcoxon Signed Rank test §(24th hour–48th hour/72nd hour) μ(48th hour–72nd hour)

at 48 hours was significantly higher than that at 24 hours (p = 0.029), while it was significantly lower at 72 hours (p ≤ 0.05) (Table 2).

DISCUSSION

Several surface properties, including morphological properties, roughness, surface textures, and hy-

drophilicity, can affect cell adhesion and proliferation [20, 26]. Ti surface modifications improve cell surface adhesion, cell migration, and bone apposition [23]. The goal of surface modifications in dental implants is to achieve a stable implant with enhanced soft tissue adaptation [23]. The adhesion behaviour of fibroblasts is known to differ among materials with varying degrees of surface roughness. Although the rough surfaces of Ti materials may pose a greater challenge to the peri-implant tissue health, the soft tissue adaptation of these surfaces has been shown to improve significantly [28]. The study conducted by Sculean et al. [34] revealed that surface modifications have a significant effect on the surface characteristics of Ti surfaces as well as on biochemical responses and cell adhesion rates.

The results obtained from this *in vitro* study conducted without a bacterial model demonstrates that the adhesion potential of HGF is affected by the surface roughness of Ti. The maximum adhesion of the fibroblasts was observed in the SLA[®]-surface group, which also had the highest surface roughness. Additionally, the findings in implantoplasty groups showed that adhesion rates of group III was less than that of group IV, as a consequence of the less surface roughness in group III. Considering all of them, the null hypothesis was rejected in this presented study.

Several studies evaluating implantoplasty protocols showed widely varying values for surface roughness. Ramel et al. [31] found that the application of a short diamond sequence followed by silicone polishers or Arkansas stone sequences yielded in R_a values between 0.32 and 0.39 μm . In another study, implantoplasty with diamond burs and silicone polishers on roughened surfaces resulted in R_a values of 4.0 μm [31]. Another study examined diamond, tungsten, and multilaminar burs without polishers and the researchers found R_a values between 4.12 to 5.01 μm [36]. Maal et al. [25] demonstrated that carbide burs achieve smoother surfaces than diamond burs. They found that the surface roughness affects initial cell adhesion after implantoplasty and smoother surfaces enhanced fibroblast growth. Similar to previous studies, the present *in vitro* study without a bacterial environment showed that Ti discs with smooth surfaces had the lowest roughness values (group I) while the SLA[®] discs had the highest values and the highest adhesion rates of gingival fibroblasts (group II). Depending on the properties of the dental burs, group IV had a higher roughness value than

group III, suggesting that the adhesion properties of cultured HGFs to Ti discs with different surface morphologies could have significant implications on the milling approaches for implantoplasty.

The findings of an *in vitro* study concluded that a surface roughness of less than 0.2 μm can only be achieved by implementing chairside implantoplasty protocols [11]. Additionally, surface roughness can be reduced by polishing the surface with silicone burs after milling [10]. The mean R_a values in the implantoplasty groups were lower than those in the SLA[®] group in our study; however, they were not close to the cut-off value of 0.2 μm . Despite extensive studies on the effects of surface roughness on the topography of the peri-implant mucosa, there are still conflicting results.

The results of animal model studies demonstrated that surface changes did not have a negative effect on the soft tissue interaction with implant surface [2, 13]. Furthermore, Schwarz et al. [33] found no differences in the probing depth of the peri-implant junction between implants surfaced with plasma sprayed and SLA[®]. On the contrary, human biopsy samples from acidified or oxidised junction areas of implants showed less epithelial downgrowth and longer connective tissues [8, 15]. However, in the current study, the maximum adhesion of the fibroblasts was observed in the SLA[®]-surface group, which also had the highest surface roughness, indicating a positive association between surface roughness and fibroblast adhesion. Based on the data we collected, group III had lower adhesion levels compared to group IV. This finding is consistent with previous studies showing that fibroblasts respond differently to materials with different surface roughness values [25, 39]. Currently, these *in vitro* results without a bacterial environment cannot be directly translated into clinical applications due to the differences between *in vitro* and *in vivo* conditions. In this study, we experimentally designed Ti surfaces with various surface properties. Intraoral Ti surfaces are rare due to their difficult nature, which is why the values of R_a were different from those measured *in vivo*.

To date, implantoplasty research has focused on surface roughness, surface coating, heat dissipation during operation, and fracture resistance [2, 25, 31, 36]. Another issue not addressed in this study was surface corrosion, which requires further investigation to determine its effectiveness. Soft tissue has been tightly adapted to the implant surface as a result of

implantoplasty techniques. Ti residues released during implantoplasty may have detrimental effects on peri-implant tissues [21]. For this reason, implantoplasty should only be performed in situations where implants are supracrestally exposed or gingival recession as a result of peri-implant bone loss.

CONCLUSIONS

The surface roughness has a crucial role in fibroblast morphology and adhesion: however, it is not the only factor affecting them. Therefore; the clinicians should not forget that the surface they create during implantoplasty should have a sufficient smoothness value to prevent microbial colonisation and, at the same time, a sufficient roughness value to allow fibroblast adhesion. It should be considered that the present study has inherent limitations as an *in vitro* cell behaviour study, and should be designed with different implantoplasty protocols. Our study emphasizes the importance of developing a standard implantoplasty protocol that does not compromise fibroblast adhesion while providing predictable outcomes.

Acknowledgements

The authors would like to acknowledge Servo Dental, Germany, for providing Ti discs and Bilim Implant, Turkey, for measuring the surface roughness values of the materials. We also thank M.Sc. Yusuf Iseri for the linguistic support he provided.

Conflict of interest: None declared

REFERENCES

- Albouy JP, Abrahamsson I, Persson LG, et al. Spontaneous progression of ligature induced peri-implantitis at implants with different surface characteristics. An experimental study in dogs II: histological observations. *Clin Oral Implants Res.* 2009; 20(4): 366–371, doi: [10.1111/j.1600-0501.2008.01645.x](https://doi.org/10.1111/j.1600-0501.2008.01645.x), indexed in Pubmed: [19309770](https://pubmed.ncbi.nlm.nih.gov/19309770/).
- Areid N, Willberg J, Kangasniemi I, et al. Organotypic in vitro block culture model to investigate tissue-implant interface. An experimental study on pig mandible. *J Mater Sci Mater Med.* 2021; 32(11): 136, doi: [10.1007/s10856-021-06608-5](https://doi.org/10.1007/s10856-021-06608-5), indexed in Pubmed: [34709465](https://pubmed.ncbi.nlm.nih.gov/34709465/).
- Bagno A, Di Bello C. Surface treatments and roughness properties of Ti-based biomaterials. *J Mater Sci Mater Med.* 2004; 15(9): 935–949, doi: [10.1023/B:JMSM.0000042679.28493.7f](https://doi.org/10.1023/B:JMSM.0000042679.28493.7f), indexed in Pubmed: [15448401](https://pubmed.ncbi.nlm.nih.gov/15448401/).
- Berglundh T, Gottfredsen K, Zitzmann NU, et al. Spontaneous progression of ligature induced peri-implantitis at implants with different surface roughness: an experimental study in dogs. *Clin Oral Implants Res.* 2007; 18(5): 655–661, doi: [10.1111/j.1600-0501.2007.01397.x](https://doi.org/10.1111/j.1600-0501.2007.01397.x), indexed in Pubmed: [17608738](https://pubmed.ncbi.nlm.nih.gov/17608738/).
- Bollen CM, Papaioanno W, Van Eldere J, et al. The influence of abutment surface roughness on plaque accumulation and peri-implant mucositis. *Clin Oral Implants Res.* 1996; 7(3): 201–211, doi: [10.1034/j.1600-0501.1996.070302.x](https://doi.org/10.1034/j.1600-0501.1996.070302.x), indexed in Pubmed: [9151584](https://pubmed.ncbi.nlm.nih.gov/9151584/).
- Chen Y, Lu B, Yang Q, et al. Combined integrin phosphoproteomic analyses and small interfering RNA-based functional screening identify key regulators for cancer cell adhesion and migration. *Cancer Res.* 2009; 69(8): 3713–3720, doi: [10.1158/0008-5472.CAN-08-2515](https://doi.org/10.1158/0008-5472.CAN-08-2515), indexed in Pubmed: [19351860](https://pubmed.ncbi.nlm.nih.gov/19351860/).
- Chou L, Firth JD, Uitto VJ, et al. Substratum surface topography alters cell shape and regulates fibronectin mRNA level, mRNA stability, secretion and assembly in human fibroblasts. *J Cell Sci.* 1995; 108 (Pt 4): 1563–1573, doi: [10.1242/jcs.108.4.1563](https://doi.org/10.1242/jcs.108.4.1563), indexed in Pubmed: [7615675](https://pubmed.ncbi.nlm.nih.gov/7615675/).
- Cochran DL, Buser D, ten Bruggenkate CM, et al. The use of reduced healing times on ITI implants with a sandblasted and acid-etched (SLA) surface: early results from clinical trials on ITI SLA implants. *Clin Oral Implants Res.* 2002; 13(2): 144–153, doi: [10.1034/j.1600-0501.2002.130204.x](https://doi.org/10.1034/j.1600-0501.2002.130204.x), indexed in Pubmed: [11952734](https://pubmed.ncbi.nlm.nih.gov/11952734/).
- Conserva E, Generali L, Bandieri A, et al. Plaque accumulation on titanium disks with different surface treatments: an in vivo investigation. *Odontology.* 2018; 106(2): 145–153, doi: [10.1007/s10266-017-0317-2](https://doi.org/10.1007/s10266-017-0317-2), indexed in Pubmed: [28831602](https://pubmed.ncbi.nlm.nih.gov/28831602/).
- Costa-Berenguer X, García-García M, Sánchez-Torres A, et al. Effect of implantoplasty on fracture resistance and surface roughness of standard diameter dental implants. *Clin Oral Implants Res.* 2018; 29(1): 46–54, doi: [10.1111/clr.13037](https://doi.org/10.1111/clr.13037), indexed in Pubmed: [28736922](https://pubmed.ncbi.nlm.nih.gov/28736922/).
- de Souza Júnior JM, Oliveira de Souza JG, Pereira Neto AL, et al. Analysis of effectiveness of different rotational instruments in implantoplasty: an in vitro study. *Implant Dent.* 2016; 25(3): 341–347, doi: [10.1097/ID.0000000000000381](https://doi.org/10.1097/ID.0000000000000381), indexed in Pubmed: [26840269](https://pubmed.ncbi.nlm.nih.gov/26840269/).
- Engel AS, Kranz HT, Schneider M, et al. Biofilm formation on different dental restorative materials in the oral cavity. *BMC Oral Health.* 2020; 20(1): 162, doi: [10.1186/s12903-020-01147-x](https://doi.org/10.1186/s12903-020-01147-x), indexed in Pubmed: [32493365](https://pubmed.ncbi.nlm.nih.gov/32493365/).
- Englezos E, Cosyn J, Koole S, et al. Resective treatment of peri-implantitis: clinical and radiographic outcomes after 2 years. *Int J Periodontics Restorative Dent.* 2018; 38(5): 729–735, doi: [10.11607/prd.3386](https://doi.org/10.11607/prd.3386), indexed in Pubmed: [30113610](https://pubmed.ncbi.nlm.nih.gov/30113610/).
- Ghorbani FM, Kaffashi B, Shokrollahi P, et al. PCL/chitosan/Zn-doped nHA electrospun nanocomposite scaffold promotes adipose derived stem cells adhesion and proliferation. *Carbohydr Polym.* 2015; 118: 133–142, doi: [10.1016/j.carbpol.2014.10.071](https://doi.org/10.1016/j.carbpol.2014.10.071), indexed in Pubmed: [25542118](https://pubmed.ncbi.nlm.nih.gov/25542118/).
- Glauser R, Schüpbach P, Gottlow J, et al. Periimplant soft tissue barrier at experimental one-piece mini-implants with different surface topography in humans: A light-microscopic overview and histometric analysis. *Clin Implant Dent Relat Res.* 2005; 7 Suppl 1: S44–S51, doi: [10.1111/j.1708-8208.2005.tb00074.x](https://doi.org/10.1111/j.1708-8208.2005.tb00074.x), indexed in Pubmed: [16137087](https://pubmed.ncbi.nlm.nih.gov/16137087/).
- Guy SC, McQuade MJ, Scheidt MJ, et al. In vitro attachment of human gingival fibroblasts to endosseous implant materials. *J Periodontol.* 1993; 64(6): 542–546,

- doi: [10.1902/jop.1993.64.6.542](https://doi.org/10.1902/jop.1993.64.6.542), indexed in Pubmed: [8393107](https://pubmed.ncbi.nlm.nih.gov/8393107/).
17. Hayakawa T, Yoshinari M, Nemoto K, et al. Effect of surface roughness and calcium phosphate coating on the implant/bone response. *Clin Oral Implants Res.* 2000; 11(4): 296–304, doi: [10.1034/j.1600-0501.2000.011004296.x](https://doi.org/10.1034/j.1600-0501.2000.011004296.x), indexed in Pubmed: [11168222](https://pubmed.ncbi.nlm.nih.gov/11168222/).
 18. Ivanovski S, Lee R. Comparison of peri-implant and periodontal marginal soft tissues in health and disease. *Periodontol* 2000. 2018; 76(1): 116–130, doi: [10.1111/prd.12150](https://doi.org/10.1111/prd.12150), indexed in Pubmed: [29193334](https://pubmed.ncbi.nlm.nih.gov/29193334/).
 19. Kawahara H, Kawahara D, Hashimoto K, et al. Morphological studies on the biological seal of titanium dental implants. Report I. In vitro study on the epithelization mechanism around the dental implants. *Int J Oral Maxillofac Imp.* 1998; 13: 457–464.
 20. Keller JC, Draughn RA, Wightman JP, et al. Characterization of sterilized CP titanium implant surfaces. *Int J Oral Maxillofac Implants.* 1990; 5(4): 360–367, indexed in Pubmed: [2094654](https://pubmed.ncbi.nlm.nih.gov/2094654/).
 21. Kim H, Murakami H, Chehroudi B, et al. Effects of surface topography on the connective tissue attachment to subcutaneous implants. *Int J Oral Maxillofac Implants.* 2006; 21(3): 354–365, indexed in Pubmed: [16796277](https://pubmed.ncbi.nlm.nih.gov/16796277/).
 22. Lee SW, Kim SY, Rhyu IC, et al. Influence of microgroove dimension on cell behavior of human gingival fibroblasts cultured on titanium substrata. *Clin Oral Implants Res.* 2009; 20(1): 56–66, doi: [10.1111/j.1600-0501.2008.01597.x](https://doi.org/10.1111/j.1600-0501.2008.01597.x), indexed in Pubmed: [19133333](https://pubmed.ncbi.nlm.nih.gov/19133333/).
 23. Lim YJ, Oshida Y, Andres CJ, et al. Surface characterizations of variously treated titanium materials. *Int J Oral Maxillofac Implants.* 2001; 16(3): 333–342, indexed in Pubmed: [11432653](https://pubmed.ncbi.nlm.nih.gov/11432653/).
 24. Louropoulou A, Slot DE, Van der Weijden FA. Titanium surface alterations following the use of different mechanical instruments: a systematic review. *Clin Oral Implants Res.* 2012; 23(6): 643–658, doi: [10.1111/j.1600-0501.2011.02208.x](https://doi.org/10.1111/j.1600-0501.2011.02208.x), indexed in Pubmed: [21564303](https://pubmed.ncbi.nlm.nih.gov/21564303/).
 25. Maal M, Elingsen SA, Reseland JE, et al. Experimental implantoplasty outcomes correlate with fibroblast growth in vitro. *BMC Oral Health.* 2020; 20(1): 25, doi: [10.1186/s12903-020-1012-1](https://doi.org/10.1186/s12903-020-1012-1), indexed in Pubmed: [32000771](https://pubmed.ncbi.nlm.nih.gov/32000771/).
 26. Martinez MA, Balderrama Íd, Karam PS, et al. Surface roughness of titanium disks influences the adhesion, proliferation and differentiation of osteogenic properties derived from human. *Int J Implant Dent.* 2020; 6(1): 46, doi: [10.1186/s40729-020-00243-5](https://doi.org/10.1186/s40729-020-00243-5), indexed in Pubmed: [32839885](https://pubmed.ncbi.nlm.nih.gov/32839885/).
 27. Miki I, Ishihara N, Otoshi M, et al. Simple colorimetric cell-cell adhesion assay using MTT-stained leukemia cells. *J Immunol Methods.* 1993; 164(2): 255–261, doi: [10.1016/0022-1759\(93\)90318-2](https://doi.org/10.1016/0022-1759(93)90318-2).
 28. Ong JL, Prince CW, Raikar GN, et al. Effect of surface topography of titanium on surface chemistry and cellular response. *Implant Dent.* 1996; 5(2): 83–88, indexed in Pubmed: [9081579](https://pubmed.ncbi.nlm.nih.gov/9081579/).
 29. Quirynen M, Bollen CM, Papaioannou W, et al. The influence of titanium abutment surface roughness on plaque accumulation and gingivitis: short-term observations. *Int J Oral Maxillofac Implants.* 1996; 11(2): 169–178, indexed in Pubmed: [8666447](https://pubmed.ncbi.nlm.nih.gov/8666447/).
 30. Quirynen M, van der Mei HC, Bollen CM, et al. An in vivo study of the influence of the surface roughness of implants on the microbiology of supra- and subgingival plaque. *J Dent Res.* 1993; 72(9): 1304–1309, doi: [10.1177/00220345930720090801](https://doi.org/10.1177/00220345930720090801), indexed in Pubmed: [8395545](https://pubmed.ncbi.nlm.nih.gov/8395545/).
 31. Ramel CF, Lüssi A, Özcan M, et al. Surface roughness of dental implants and treatment time using six different implantoplasty procedures. *Clin Oral Implants Res.* 2016; 27(7): 776–781, doi: [10.1111/clr.12682](https://doi.org/10.1111/clr.12682), indexed in Pubmed: [26355907](https://pubmed.ncbi.nlm.nih.gov/26355907/).
 32. Renvert S, Persson GR, Piri FQ, et al. Peri-implant health, peri-implant mucositis, and peri-implantitis: Case definitions and diagnostic considerations. *J Clin Periodontol.* 2018; 45(Suppl. 20): S278–S285, doi: [10.1186/s12903-020-1012-1](https://doi.org/10.1186/s12903-020-1012-1).
 33. Schwarz F, Ferrari D, Herten M, et al. Effects of surface hydrophilicity and microtopography on early stages of soft and hard tissue integration at non-submerged titanium implants: an immunohistochemical study in dogs. *J Periodontol.* 2007; 78(11): 2171–2184, doi: [10.1902/jop.2007.070157](https://doi.org/10.1902/jop.2007.070157), indexed in Pubmed: [17970685](https://pubmed.ncbi.nlm.nih.gov/17970685/).
 34. Sculean A, Gruber R, Bosshardt DD. Soft tissue wound healing around teeth and dental implants. *J Clin Periodontol.* 2014; 41 (Suppl. 15): S6–S22, doi: [10.1111/jcpe.12206](https://doi.org/10.1111/jcpe.12206), indexed in Pubmed: [24641001](https://pubmed.ncbi.nlm.nih.gov/24641001/).
 35. Stavropoulos A, Wikesjö UME. Growth and differentiation factors for periodontal regeneration: a review on factors with clinical testing. *J Periodontol Res.* 2012; 47(5): 545–553, doi: [10.1111/j.1600-0765.2012.01478.x](https://doi.org/10.1111/j.1600-0765.2012.01478.x), indexed in Pubmed: [22486242](https://pubmed.ncbi.nlm.nih.gov/22486242/).
 36. Tawse-Smith A, Kota A, Jayaweera Y, et al. The effect of standardised implantoplasty protocol on titanium surface roughness: an in-vitro study. *Braz Oral Res.* 2016; 30(1): e137, doi: [10.1590/1807-3107BOR-2016.vol30.0137](https://doi.org/10.1590/1807-3107BOR-2016.vol30.0137), indexed in Pubmed: [28001245](https://pubmed.ncbi.nlm.nih.gov/28001245/).
 37. Teranaka A, Tomiyama K, Ohashi K, et al. Relevance of surface characteristics in the adhesiveness of polymicrobial biofilms to crown restoration materials. *J Oral Sci.* 2018; 60(1): 129–136, doi: [10.2334/josnusd.16-0758](https://doi.org/10.2334/josnusd.16-0758), indexed in Pubmed: [29162785](https://pubmed.ncbi.nlm.nih.gov/29162785/).
 38. Walboomers XF, Monaghan W, Curtis A, et al. Attachment of fibroblasts on smooth and microgrooved polystyrene. *J Biomed Mater Res.* 1999; 46(2): 212–220, doi: [10.1002/\(sici\)1097-4636\(199908\)46:2<212::aid-jbm10>3.0.co;2-y](https://doi.org/10.1002/(sici)1097-4636(199908)46:2<212::aid-jbm10>3.0.co;2-y).
 39. Watzak G, Zechner W, Tangl S, et al. Soft tissue around three different implant types after 1.5 years of functional loading without oral hygiene: a preliminary study in baboons. *Clin Oral Implants Res.* 2006; 17(2): 229–236, doi: [10.1111/j.1600-0501.2005.01217.x](https://doi.org/10.1111/j.1600-0501.2005.01217.x), indexed in Pubmed: [16584420](https://pubmed.ncbi.nlm.nih.gov/16584420/).
 40. Wennerberg A, Albrektsson T. Effects of titanium surface topography on bone integration: a systematic review. *Clin Oral Implants Res.* 2009; 20 (Suppl. 4): 172–184, doi: [10.1111/j.1600-0501.2009.01775.x](https://doi.org/10.1111/j.1600-0501.2009.01775.x), indexed in Pubmed: [19663964](https://pubmed.ncbi.nlm.nih.gov/19663964/).
 41. Zhang F, Huang Y, Li X, et al. Surface modification and its effect on attachment, spreading, and proliferation of human gingival fibroblasts. *Int J Oral Maxillofac Implants.* 2011; 26(6): 1183–1192, indexed in Pubmed: [22167422](https://pubmed.ncbi.nlm.nih.gov/22167422/).
 42. Zheng S, Guan Y, Yu H, et al. Poly-L-lysine-coated PLGA/poly(amino acid)-modified hydroxyapatite porous scaffolds as efficient tissue engineering scaffolds for cell adhesion, proliferation, and differentiation. *New J Chem.* 2019; 43(25): 9989–10002, doi: [10.1039/c9nj01675a](https://doi.org/10.1039/c9nj01675a).

Human lumbosacral root and ligamentum flavum thicknesses: a magnetic resonance study

R. Khasawneh¹ , E. Abu El-Rub¹, M. Allouh^{2, 3}

¹Department of Basic Medical Sciences, Faculty of Medicine, Yarmouk University, Irbid, Jordan

²Department of Anatomy, Faculty of Medicine, Jordan University of Science and Technology, Irbid, Jordan

³Department of Anatomy, College of Medicine and Health Sciences, United Arab Emirates University, Al Ain, United Arab Emirates

[Received: 3 July 2021; Accepted: 18 October 2021; Early publication date: 9 November 2021]

Background: This study investigated the lumbosacral plexus (LSP) nerve root thickness and ligamentum flavum (LF) thickness and correlated them with age and sex. These findings provided a useful data for spinal nerve root micro-anastomosis surgery and lumbar decompression surgery.

Materials and methods: This retrospective study was conducted with 350 individuals with ages ranging from 21 to 80 years under magnetic resonance imaging to evaluate the possible cause of a lower back pain.

Results: According to the morphometric measurements of the LSP root thickness, the diameter gradually increased from L1 to S1. L1 has the thinnest root (3.9 ± 0.81 mm) while S1 has the thickest root (5.45 ± 0.8 mm). The measurements revealed inconsiderable differences in the LSP thickness in relation to age, sex in the study population. Regarding the LF, the thickness of the LF was found to insignificantly increase with age. Besides, the LF thickness was inconsequentially higher in female. The mean thickness of the right LF at different spinal levels was measured (L2–L3 = 3.19 ± 0.27 , L3–L4 = 3.38 ± 0.11 mm, L4–L5 = 3.71 ± 0.29 mm, and L5–S1 = 3.64 ± 0.21 mm). The mean thickness of the left LF was non-significantly higher.

Conclusions: The LSP root and LF thicknesses not related to age or sex. (Folia Morphol 2023; 82, 1: 72–78)

Key words: lumbosacral plexus, ligamentum flavum, spinal nerve root, magnetic resonance image

INTRODUCTION

The lumbosacral plexus (LSP) is a series of nerve convergences and divergences that ultimately combine into larger terminal nerves and supply the pelvis and lower extremities

Disorders affecting the LSP with time may alter root diameter such as lumbosacral radiculopathy which is a damage that caused by compression of

the nerve roots which exit the spine, levels L1–S4 and cause a pain in the lower back and hip which radiates down the back of the thigh into the leg [3]. Determine normal LSP nerve root dimensions can provide valuable structural information that for monitoring any pathological changes of the lumbar nerve root [20]. Moreover, nerve root size may also determine degree of blockade after epidural

Address for correspondence: Assist. Prof. R. Khasawneh, Department of Basic Medical Sciences, Faculty of Medicine, Yarmouk University, Irbid, Jordan, e-mail: ramada@yu.edu.jo

This article is available in open access under Creative Common Attribution-Non-Commercial-No Derivatives 4.0 International (CC BY-NC-ND 4.0) license, allowing to download articles and share them with others as long as they credit the authors and the publisher, but without permission to change them in any way or use them commercially.

or spinal anaesthesia, but good measures of this fundamental anatomic parameter have not been published.

Numerous factors can affect the LSP thickness; these factors can be focal like tumoural factors or can be diffused like diabetes-related factors. Pathological changes pertaining to LSP may alter nerve root thickness [14]. Slightly increased thickness is sometimes difficult to assess specially when changes are diffused and symmetrical in both sides. Furthermore, there are some controversies in defining the normal LSP thickness. To date, few studies addressed the normal LSP root size dimensions and how they are affected by different diseases [8].

In the light of this, the first purpose of the current study is to establish normal LSP nerve root thickness retrospectively by reviewing large series of magnetic resonance imaging (MRI) images, and correlate the LSP thickness with age and gender. Knowing the thickness of the LSP has clinical significance for the surgeons who will undergo surgical intervention for LSP or the surrounding structures. The available literature regarding LSP dimensions has some contradictions regarding the exact thickness of the LSP [12, 20].

Also to make this article more value, we investigated the ligamentum flavum (LF). The LF wraps around the medial aspect of the spinal articulations and has high percentage of elastic fibres which is responsible of its yellowish colour. These elastic characteristics of LF diminish with age, due to remarkable loss of the elastic fibres and a concomitant replacement by collagen fibres [17]. Moreover, LF joints between vertebrae, LF reinforced and supported the vertebrae as it attached to the front of the upper lamina above and to the back of the lower lamina below [27], also, LF maintain a smooth surface of the posterior dural sac, control intervertebral movement, and affect the intrinsic stability of the spine [19].

Many researchers have demonstrated that the LF plays an important role in vertebral disease, more specifically, in spinal stenosis [7, 28]. The LF thickening is considered an important cause of radiculopathy exists in lumbar degenerative disease [23]. The LF is an important anatomical structure, and might be changed in patients suffered from low back or leg pain. Therefore, the thickness of the LF should be measured and evaluated carefully in the case of spinal stenosis. Considering this fact, we studied the LF on each side of different spinal levels, and correlated the measurements with age and sex.

MATERIALS AND METHODS

Sample study

This retrospective study first was performed with the Ethics approval of the institutional research board at Jordan University of science and technology (IRB # 8/134/2020).

The study included participants from King Abdullah University hospital in Irbid, Jordan, who had been referred for MRI imaging to assess the possible causes of low back pain in the past two years. Individuals with a history of fractures, dislocation or surgeries in the vertebral column or spinal cord were excluded from the study. The total study group consisted of 350 individuals with ages ranging from 21 to 80 years. Among the study subjects, 155 were males and 195 were females.

The male and female individuals were further subcategorized into two age groups; the young age group (21–50 years) and the elderly age group (51–80 years).

The control group included in the current study composed of 85 healthy individuals who underwent MRI as a routine procedure of their annual checkup. The subjects in the control group were without structural changes in the vertebral column similar to the study group, but had no pain. This control group was included in the current study to exclude any possible differences that may result from inflammatory or degenerative changes. Among the control group, 41 were females and 44 were males, with age range from 25 to 57 years.

MRI imaging measurements

Images were obtained on a Signa HDxt 3.0T scanner. For the LSP, IDEAL T2 weight images on the coronal plane were acquired for all studied individuals. The T band width: 62.5 kHz, matrix was 320 × 256, with 42 × 42 cm field of view. The slice thickness was 1.5 mm, gap: 0 mm, repetition time: 7680 ms, echo time: 90.8 ms, band width: 62.5 kHz, number of excitations: 3.

Observations were made on the DICOM files using the manufacture's software. The LSP root size was evaluated by two specialised radiologists, who were blind to the study. We measured LSP root diameter from the first lumbar (L1) to the first sacral (S1) nerve on the coronal plane at 5 mm distance from the dorsal root ganglion (Fig. 1).

Regarding LF, T1-sequence axial sections at four levels: L2-L3, L3-L4, L4-L5, and L5-S1 were obtained.

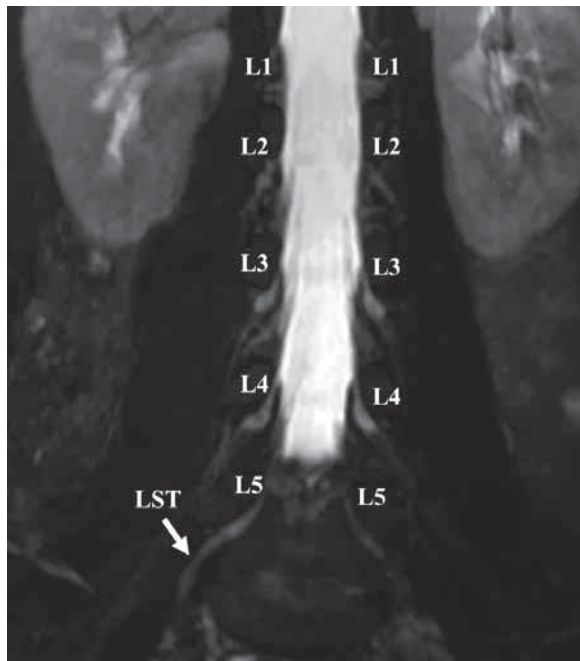


Figure 1. Magnetic resonance image of a coronal section demonstrating the method for determining the lumbosacral plexus roots from L1 to S1; LST — lumbosacral plexus.

The same radiologists who investigated the LSP also assessed the thickening of the LF in all study subjects. The thickness of the LF was measured with an electronic ruler with a resolution of 0.1 mm by means of a line drawn transversally to the facet joint level (Fig. 2) through the middle section of the LF. If the thickness was bilaterally asymmetrical, the measurement of the thickest part was used.

Statistical analysis

After applying the Levene's test to determine the homogeneity of variance, the data were evaluated by independent samples t-test or one-way analysis of variance (ANOVA) at 5% and 1% levels of significance. Fischer's (LSD) post hoc test was performed to examine statistical differences between the groups. The data were presented as mean \pm standard error of the mean (SEM).

RESULTS

Lumbosacral root thickness

The results of MRI images and basic anatomy atlas showed that the conus medullaris terminate at the level of L1-L2 as described by previous study [13].

The results also showed insignificant difference in the thickness of lumbosacral roots between the

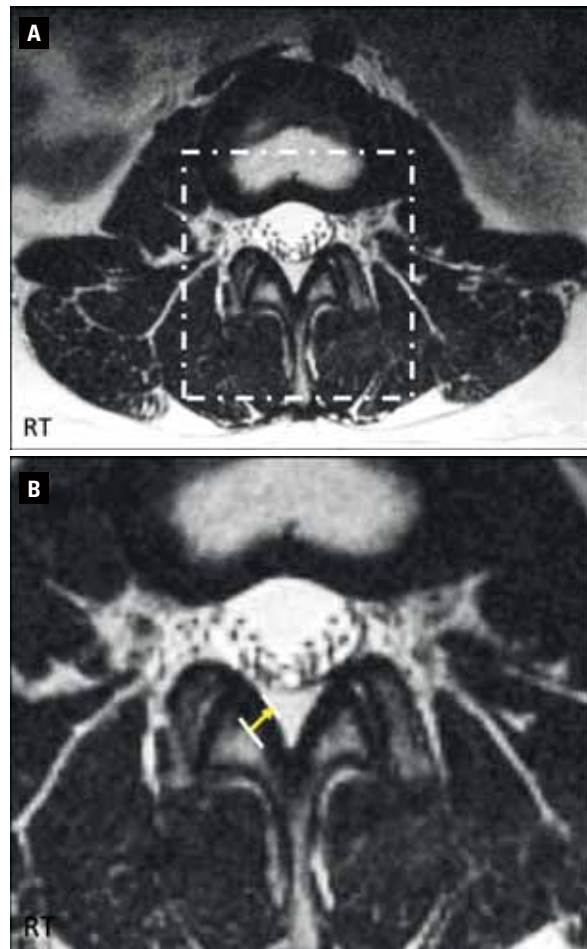


Figure 2. Measurement of the thickness of the ligamentum flavum in T1-weighted magnetic resonance image scan; **A.** The target area was selected for analysis; **B.** The arrow represents the ligamentum flavum thickness at the facet joint level; RT — right side.

right and left side and the mean values of the root thickness in our patients were as follows: L1: 3.9 ± 0.81 mm, L2: 4.17 ± 0.79 mm, L3: 4.3 ± 0.78 , L4: 5.2 ± 0.72 mm, L5: 5.32 ± 0.45 mm and S1: 5.45 ± 0.8 mm. The diameters of each spinal nerve root are shown in Table 1.

The data were collected from patients without structural changes in vertebral column but having pain. In order to exclude any possible effects that may results from pain and inflammation, additional data were collected from 85 healthy individual without structural changes in the vertebral column and having no pain. The results did not show any significant difference in the thickness of lumbosacral root between the study group and the control group. Our data indicated and validated that chronic inflammatory pain does not affect the structure and morphology of the vertebral column.

Table 1. The diameters of lumbosacral nerve roots

Lumbosacral root	Right root thickness [mm]	Left root thickness [mm]	Root thickness [mm]
L1	3.9 ± 0.94	3.9 ± 0.68	3.9 ± 0.81
L2	4.17 ± 0.76	4.17 ± 0.82	4.17 ± 0.79
L3	4.3 ± 0.95	4.31 ± 0.79	4.3 ± 0.87
L4	5.2 ± 0.57	5.25 ± 0.88	5.2 ± 0.72
L5	5.32 ± 0.54	5.32 ± 0.38	5.32 ± 0.45
S1	5.5 ± 0.78	5.4 ± 0.83	5.45 ± 0.8

Data are shown as mean ± standard error of the mean.

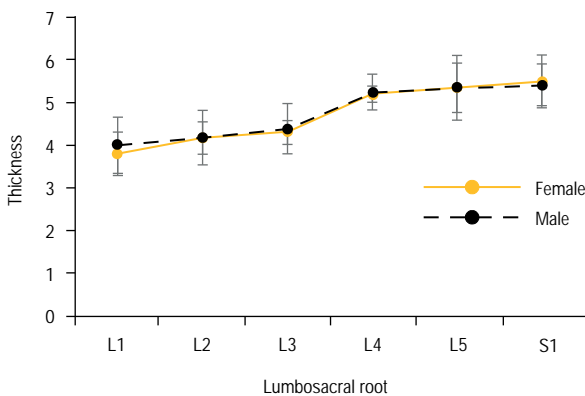


Figure 3. Variation of lumbosacral plexus (LSP) nerve roots thickness with sex. The data revealed a non-significant difference in the LSP nerve roots thickness between males and females. Each column represents the mean LSP nerve root thickness ± standard error of the mean.

Variation of lumbosacral root thickness with sex and age

The subjects were divided according to their gender as follows: male group (n = 155) and female group (n = 195). We found no correlation (p = 0.43) between the lumbosacral root thickness and gender of the participants (Fig. 3).

The subjects were further divided into two different age subgroups as follows: young adults (21–50 years; n = 118), and elderly group (51–80 years, n = 232). There was no noticeable association (p = 0.31) between the thickness of the lumbosacral roots and age of study subjects (Fig. 4).

Variation of ligamentum flavum with sex and age

The thickness of LF was measured at L2-3, L3-4, L4-5 and L5-S levels on both sides. The results are showed in Table 2. The relationship among thickness, age, and spinal level was examined.

There was no significant difference between the two sex groups pertaining to LF thickness at the

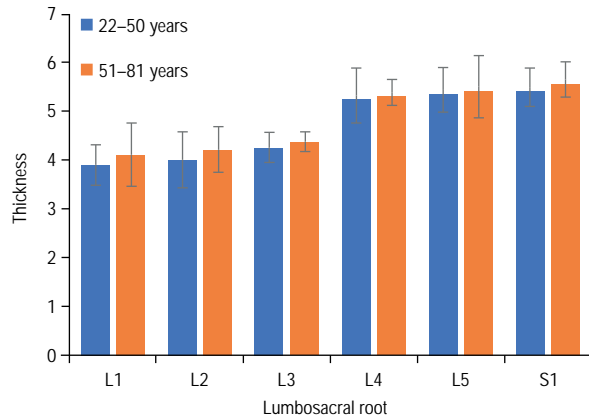


Figure 4. Variation of lumbosacral plexus (LSP) nerve roots thickness with age. The data revealed a non-significant difference in the LSP nerve roots thickness between young and older populations. Each column represents the mean LSP nerve root thickness ± standard error of the mean.

Table 2. Measurement of thickness of the ligamentum flavum (LF) at different spinal levels

LF spinal level	Right side [mm]	Left side [mm]
L2-L3	3.19 ± 0.27	3.47 ± 0.2
L3-L4	3.38 ± 0.11	3.51 ± 0.21
L4-L5	3.71 ± 0.29	3.84 ± 0.15
L5-S1	3.64 ± 0.21	3.73 ± 0.17

Data are shown as mean ± standard error of the mean.

segments L2/3, L3/4, L4/5 and L5/S1 (p > 0.05). On the other hand, females found to have larger average thickness of the right and left LF, and the greater average thickness of the ligament was at L3/L4 (Table 3).

According to age, our results indicated that LF thickness increased with age; but this increase was insignificant. However, the increments at L4-5 and L3-4 were larger than that at L2-3 and L5-S1. Moreover, the results showed that the mean thickness of the left LF was higher in the left side than the right side (Table 4).

In this context, comparing the study group with the control group did not show any significant difference in the thickness of both right and left LF. The data are shown in Supplementary material (see journal website).

DISCUSSION

The LSP is a well-protected structure because of its secure location deep in the retroperitoneum, protected by the pelvic brim, which will give the required support and firmness for LSP [6]. Based on that secured and unique structure of LSP, the injuries of

Table 3. Thickness of ligamentum flavum (LF) at different lumbar spinal levels in different sex groups

LF level	Male	Female	P-value
Right side			
L2-L3	3.19 ± 0.22	3.25 ± 0.24	0.44
L3-L4	3.31 ± 0.17	3.38 ± 0.12	0.28
L4-L5	3.48 ± 0.27	3.4 ± 0.19	0.12
L5-S1	3.67 ± 0.2	3.53 ± 0.34	0.62
Left side			
L2-L3	3.54 ± 0.11	3.6 ± 0.28	0.39
L3-L4	3.59 ± 0.29	3.68 ± 0.17	0.14
L4-L5	3.68 ± 0.14	6.76 ± 0.23	0.52
L5-S1	3.62 ± 0.23	3.7 ± 0.25	0.29

Data are shown as mean ± standard error of the mean.

Table 4. Thickness of ligamentum flavum (LF) at different lumbar spinal levels in different age groups

LF level	RT	LT	P-value
22–50 years			
L2-L3	3.19 ± 0.15	3.37 ± 0.3	0.51
L3-L4	3.3 ± 0.24	3.45 ± 0.17	0.18
L4-L5	3.54 ± 0.31	3.73 ± 0.19	0.25
L5-S1	3.49 ± 0.11	3.64 ± 0.24	0.12
51–80 years			
L2-L3	3.27 ± 0.27	3.46 ± 0.16	0.34
L3-L4	3.36 ± 0.23	3.51 ± 0.32	0.27
L4-L5	3.67 ± 0.15	3.82 ± 0.14	0.15
L5-S1	3.57 ± 0.09	3.7 ± 0.32	0.62

Data are shown as mean ± standard error of the mean. LT — left side; RT — right side

lower extremities are less compared with the upper extremities.

The exact values of human LSP thickness are varied in the literature. The clinical importance of morphometric data on LSP thickness has been emphasized by many studies [4, 11, 12, 15, 20, 29]. In this retrospective study, the thickness of LSP showed a gradual increase from L1 to S1, known as cephalo-caudal pattern (Table 1). Large variations in determining LSP thickness should be taken into consideration when performing morphometric analyses of the spinal cord and the LSP. Based on such morphometric data, the existence of pathological conditions in the LSP such as compression or atrophy can be assessed by comparing these pathological changes with the normal reported values of the affected segment. The present study provides an updated reference of the normal

LSP thickness values and its relation to the most important risk; age and sex. This reference can be used to evaluate any disease affecting the LSP area.

The outcome of this study revealed that the LSP thickness increases by moving downwards, towards the sacrum as previously reported [4, 11, 29]. The only study that contradicts the concept of gradual increase in LSP thickness was conducted by Izci et al. [12] who reported that L1 was the thinnest root of the LSP (4.1 mm) and L4 was the thickest (5.5 mm) root of the LSP. No study so far investigated the effect of age or sex on the thickness of LSP, which has been revealed by our study to have no significant relation to the thickness of the LSP.

In this study we were able to measure the diameters of all lumbosacral spinal nerve roots using the 2-point Dixon deconvolution (IDEAL T2-WI) technique to separate water and lipid resonance signals by phase-sensitive MRI. The IDEAL T2-WI is used to obtain an inhomogeneous map based on only in-phase and out-of-phase image data. The method 2-point Dixon technique is designed for T1- or density-weighted spin-echo imaging while the double-echo scheme is more appropriate for T2-weighted spin-echo imaging [5]. The 2-point Dixon deconvolution technique is considered superior to other techniques, such as short tau inversion recovery (STIR) sequence, in evaluating the nerve structure and distinguish nerve roots from peripheral tissue [25]. T2 Dixon water-only image showed higher mean scores for fat suppression quality and lesion conspicuity than SPAIR [18], moreover, 2-point Dixon fat suppression was significantly more consistent than SPAIR on both T2 and T1 [10].

The LF is a short but thick ligament of elastic fibres that connects the laminae of adjacent vertebrae from the C2 to S1 [1]. The function of LF to maintain the upright posture and to assist the vertebral column in resuming its shape after flexion, and maintains a smooth surface for the dural sac [26]. The results of this study did not show any correlation between age or sex and the LF thickness in both sides. On the other hand, minor changes in LF thickness were beheld at the L4-L5 and L5-S1 spinal levels as age increased. Moreover, LF was thicker in females comparing to males. The finding of this study was in congruence with other studies [16, 26]. The values of LF reported in the current study were similar to those reported by Horwitz [9], who reported that LF thickness were (L3-L4 = 3.5 mm, L4-L5 = 3.8 mm, and L5-S1 = 3.6 mm). The highest

value reported was 6.1 mm by Ramani et al. [24], who explained their findings by suggesting a possible relation to the connection of a hypertrophied ligament with prolapsed disc. As a result, we can conclude that the borderline between normal and pathologic LF thickness should not be set at 4 mm. Hypertrophy of the LF above 4 mm is usually involved in the pathogenesis of lumbar spinal stenosis, which can narrow the diameter of the spinal canal and compress the dural sac and nerve roots, causing many symptoms, even in the absence of a bulging annulus fibrosus or herniated nucleus pulposus or osseous spurs [1, 26].

A strong correlation between the patient age and LF thickness at the L4-L5 level has been reported by Okuda et al. [23] and Altinkaya et al. [2], who showed that the LF increase in thickness with age. On the other hand, Safak et al. [26] found no association between LF thickness and the age. Safak et al. [26] suggested that the degradation and mechanical stress are more important than age or gender as risk factors affecting the thickness of the LF.

When the spine is tilted or bent, the LF extends and the tension increases; despite the elastic and flexible nature of the ligament, at neutral position, the ligament has pretension which prevents the possibility to from buckling or wrinkles. Repeated injury can result in initiating many inflammatory and remodelling changes that cause the degeneration, hyperplasia, and hypertrophy of LF. Moreover, the LF may bulge in the canal space and reduce the diameter of the spinal canal, as a result, it would compress the nearby nerves and cause a disturbance in the local circulatory cycle. Some studies had suggested that the degree of hypertrophy of LF is positively correlated with chronic low back pain, and it is difficult to be cured [21]. This means that LF thickness may be closely related to the pathogenesis of spinal pain processes.

All above mentioned delineated the important of identifying the normal LF thickness, since the thickening or hypertrophy of the LF can lead to spinal stenosis and narrowing the spinal canal, it may compress the intraspinal nerve root or cauda equine. This stenosis, compression and corresponding neural symptoms can even occur in the absence of articular process hyperplasia or nucleus pulposus prolapse. Moreover, this study is of paramount importance due to the significant increase in the incidence of lumbar spinal narrowing, as LF hypertrophy is a common cause of lumbar stenosis and is thought to be de-

generation-driven pathology, which leads to negative impacts on the quality of life of these patients [22] due to lower limb and lower back pain, numbness, and weakness. These above mentioned symptoms will be mitigated after squatting down or resting.

CONCLUSIONS

Exploring the correlation between various factors and LF thickness provides reference for pedicle screw placement and lumbar decompression surgery, the development of individualised surgical programmes, and can effectively reduce the incidence of unnecessary postoperative complications induced by misplacement.

Conflict of interest: None declared

REFERENCES

1. Abbas J, Hamoud K, Masharawi YM, et al. Ligamentum flavum thickness in normal and stenotic lumbar spines. *Spine (Phila Pa 1976)*. 2010; 35(12): 1225–1230, doi: [10.1097/BRS.0b013e3181bfca15](https://doi.org/10.1097/BRS.0b013e3181bfca15), indexed in Pubmed: [20216339](https://pubmed.ncbi.nlm.nih.gov/20216339/).
2. Altinkaya N, Yildirim T, Demir S, et al. Factors associated with the thickness of the ligamentum flavum: is ligamentum flavum thickening due to hypertrophy or buckling? *Spine (Phila Pa 1976)*. 2011; 36(16): E1093–E1097, doi: [10.1097/BRS.0b013e318203e2b5](https://doi.org/10.1097/BRS.0b013e318203e2b5), indexed in Pubmed: [21343862](https://pubmed.ncbi.nlm.nih.gov/21343862/).
3. Berry JA, Elia C, Saini HS, et al. A review of lumbar radiculopathy, diagnosis, and treatment. *Cureus*. 2019; 11(10): e5934, doi: [10.7759/cureus.5934](https://doi.org/10.7759/cureus.5934), indexed in Pubmed: [31788391](https://pubmed.ncbi.nlm.nih.gov/31788391/).
4. Chaves H, Bendersky M, Goñi R, et al. Lumbosacral plexus root thickening: Establishing normal root dimensions using magnetic resonance neurography. *Clin Anat*. 2018; 31(6): 782–787, doi: [10.1002/ca.23073](https://doi.org/10.1002/ca.23073), indexed in Pubmed: [29575220](https://pubmed.ncbi.nlm.nih.gov/29575220/).
5. Coombs BD, Szumowski J, Coshov W. Two-point Dixon technique for water-fat signal decomposition with B0 inhomogeneity correction. *Magn Reson Med*. 1997; 38(6): 884–889, doi: [10.1002/mrm.1910380606](https://doi.org/10.1002/mrm.1910380606), indexed in Pubmed: [9402188](https://pubmed.ncbi.nlm.nih.gov/9402188/).
6. Dyck P, Thaisethawatkul P. Lumbosacral plexopathy. *CONTINUUM: Lifelong Learning in Neurology*. 2014; 20: 1343–1358, doi: [10.1212/01.con.0000455877.60932.d3](https://doi.org/10.1212/01.con.0000455877.60932.d3).
7. Grenier N, Kressel HY, Schiebler ML, et al. Normal and degenerative posterior spinal structures: MR imaging. *Radiology*. 1987; 165(2): 517–525, doi: [10.1148/radiology.165.2.3659376](https://doi.org/10.1148/radiology.165.2.3659376), indexed in Pubmed: [3659376](https://pubmed.ncbi.nlm.nih.gov/3659376/).
8. Halil C, Atilla K, Gulis K, et al. Lumbosacral conjoined root anomaly. anatomical considerations of exiting angles and root thickness, results of 21 patients. *Turkish Neurosurg*. 2015, doi: [10.5137/1019-5149.jtn.16490-15.1](https://doi.org/10.5137/1019-5149.jtn.16490-15.1).
9. Horwitz T. Lesions of the intervertebral disk and ligamentum flavum of the lumbar vertebrae. *Surgery*. 1939; 6: 410–425.
10. Huijgen WHF, van Rijswijk CSP, Bloem JL. Is fat suppression in T1 and T2 FSE with mDixon superior to the frequency

- selection-based SPAIR technique in musculoskeletal tumor imaging? *Skeletal Radiol.* 2019; 48(12): 1905–1914, doi: [10.1007/s00256-019-03227-8](https://doi.org/10.1007/s00256-019-03227-8), indexed in Pubmed: [31154494](https://pubmed.ncbi.nlm.nih.gov/31154494/).
11. Iwanaga J, Simonds E, Patel M, et al. Anatomic study of superior cluneal nerves: application to low back pain and surgical approaches to lumbar vertebrae. *World Neurosurg.* 2018; 116: e766–e768, doi: [10.1016/j.wneu.2018.05.087](https://doi.org/10.1016/j.wneu.2018.05.087), indexed in Pubmed: [29787877](https://pubmed.ncbi.nlm.nih.gov/29787877/).
 12. Izci Y, Gürkanlar D, Ozan H, et al. The morphological aspect of lumbar plexus and roots. *Turkish Neurosurg.* 2005; 15(2): 87–92.
 13. Khasawneh RR. Influence of age, sex, height and lumbar stenosis on the position of the conus medullaris in adults. *Int J Morphol.* 2019; 37: 867–871.
 14. Kirkaldy-Willis WH. The relationship of structural pathology to the nerve root. *Spine (Phila Pa 1976).* 1984; 9(1): 49–52, doi: [10.1097/00007632-198401000-00010](https://doi.org/10.1097/00007632-198401000-00010), indexed in Pubmed: [6719256](https://pubmed.ncbi.nlm.nih.gov/6719256/).
 15. Ko HY, Park JH, Shin YB, et al. Gross quantitative measurements of spinal cord segments in human. *Spinal Cord.* 2004; 42(1): 35–40, doi: [10.1038/sj.sc.3101538](https://doi.org/10.1038/sj.sc.3101538), indexed in Pubmed: [14713942](https://pubmed.ncbi.nlm.nih.gov/14713942/).
 16. Kolte VS, Khambatta S, Ambiyi MV. Thickness of the ligamentum flavum: correlation with age and its asymmetry—an magnetic resonance imaging study. *Asian Spine J.* 2015; 9(2): 245–253, doi: [10.4184/asj.2015.9.2.245](https://doi.org/10.4184/asj.2015.9.2.245), indexed in Pubmed: [25901237](https://pubmed.ncbi.nlm.nih.gov/25901237/).
 17. Kosaka H, Sairyo K, Biyani A, et al. Pathomechanism of loss of elasticity and hypertrophy of lumbar ligamentum flavum in elderly patients with lumbar spinal canal stenosis. *Spine (Phila Pa 1976).* 2007; 32(25): 2805–2811, doi: [10.1097/BRS.0b013e31815b650f](https://doi.org/10.1097/BRS.0b013e31815b650f), indexed in Pubmed: [18246001](https://pubmed.ncbi.nlm.nih.gov/18246001/).
 18. Lee S, Choi DS, Shin HS, et al. FSE T2-weighted two-point Dixon technique for fat suppression in the lumbar spine: comparison with SPAIR technique. *Diagn Interv Radiol.* 2018; 24(3): 175–180, doi: [10.5152/dir.2018.17320](https://doi.org/10.5152/dir.2018.17320), indexed in Pubmed: [29770772](https://pubmed.ncbi.nlm.nih.gov/29770772/).
 19. Liu Lm, Song Ym, Gong Q. [Treatment of lumbar stenosis and root pain resulting from simple hypertrophy of lumbar ligamentum flavum]. *Zhongguo Xiu Fu Chong Jian Wai Ke Za Zhi.* 2003; 17(1): 50–51, indexed in Pubmed: [12916310](https://pubmed.ncbi.nlm.nih.gov/12916310/).
 20. Liu Y, Zhou X, Ma J, et al. The diameters and number of nerve fibers in spinal nerve roots. *J Spinal Cord Med.* 2015; 38(4): 532–537, doi: [10.1179/1079026814Z.000000000273](https://doi.org/10.1179/1079026814Z.000000000273), indexed in Pubmed: [24605949](https://pubmed.ncbi.nlm.nih.gov/24605949/).
 21. Munns JJ, Lee JYB, Espinoza Orías AA, et al. Ligamentum flavum hypertrophy in asymptomatic and chronic low back pain subjects. *PLoS One.* 2015; 10(5): e0128321, doi: [10.1371/journal.pone.0128321](https://doi.org/10.1371/journal.pone.0128321), indexed in Pubmed: [26010138](https://pubmed.ncbi.nlm.nih.gov/26010138/).
 22. Nandi J, Chowdhery A. A randomized controlled clinical trial to determine the effectiveness of caudal epidural steroid injection in lumbosacral sciatica. *J Clin Diagn Res.* 2017; 11(2): RC04–RC08, doi: [10.7860/JCDR/2017/21905.9392](https://doi.org/10.7860/JCDR/2017/21905.9392), indexed in Pubmed: [28384946](https://pubmed.ncbi.nlm.nih.gov/28384946/).
 23. Okuda T, Fujimoto Y, Tanaka N, et al. Morphological changes of the ligamentum flavum as a cause of nerve root compression. *Eur Spine J.* 2005; 14(3): 277–286, doi: [10.1007/s00586-004-0782-5](https://doi.org/10.1007/s00586-004-0782-5), indexed in Pubmed: [15583951](https://pubmed.ncbi.nlm.nih.gov/15583951/).
 24. Ramani PS, Perry RH, Tomlinson BE. Role of ligamentum flavum in the symptomatology of prolapsed lumbar intervertebral discs. *J Neurol Neurosurg Psychiatry.* 1975; 38(6): 550–557, doi: [10.1136/jnnp.38.6.550](https://doi.org/10.1136/jnnp.38.6.550), indexed in Pubmed: [1151422](https://pubmed.ncbi.nlm.nih.gov/1151422/).
 25. Reeder SB, Pineda AR, Wen Z, et al. Iterative decomposition of water and fat with echo asymmetry and least-squares estimation (IDEAL): application with fast spin-echo imaging. *Magn Reson Med.* 2005; 54(3): 636–644, doi: [10.1002/mrm.20624](https://doi.org/10.1002/mrm.20624), indexed in Pubmed: [16092103](https://pubmed.ncbi.nlm.nih.gov/16092103/).
 26. Safak AA, Is M, Sevinc O, et al. The thickness of the ligamentum flavum in relation to age and gender. *Clin Anat.* 2010; 23(1): 79–83, doi: [10.1002/ca.20883](https://doi.org/10.1002/ca.20883), indexed in Pubmed: [19941359](https://pubmed.ncbi.nlm.nih.gov/19941359/).
 27. Sinnatamby C, Last R. *Last's anatomy regional and applied.* Edinb Churchill Livingstone Elsevier 2011.
 28. Yoshida M, Shima K, Taniguchi Y, et al. Hypertrophied ligamentum flavum in lumbar spinal canal stenosis. Pathogenesis and morphologic and immunohistochemical observation. *Spine (Phila Pa 1976).* 1992; 17(11): 1353–1360, doi: [10.1097/00007632-199211000-00015](https://doi.org/10.1097/00007632-199211000-00015), indexed in Pubmed: [1462211](https://pubmed.ncbi.nlm.nih.gov/1462211/).
 29. Yusof MI, Hassan MN, Abdullah MS. The relationship amongst intervertebral disc vertical diameter, lateral foramen diameter and nerve root impingement in lumbar vertebra. *Malays Orthop J.* 2018; 12(1): 21–25, doi: [10.5704/MOJ.1803.004](https://doi.org/10.5704/MOJ.1803.004), indexed in Pubmed: [29725508](https://pubmed.ncbi.nlm.nih.gov/29725508/).

The pattern of branching and intercommunications of the musculocutaneous nerve for surgical issues: anatomical study

M.G. Al-Sobhi¹, A.I. Zaki^{2,3}, F.A. Abd El Hamid^{2,3}, R.A. Alshali², H.N. Mustafa² 

¹Master of Technical Anatomy and Histology, Department of Anatomy, Faculty of Medicine, King Abdulaziz University, Jeddah, Saudi Arabia

²Department of Anatomy, Faculty of Medicine, King Abdulaziz University, Jeddah, Saudi Arabia

³Department of Anatomy, Faculty of Medicine, Alexandria University, Alexandria, Egypt

[Received: 30 September 2021; Accepted: 8 December 2021; Early publication date: 31 December 2021]

Background: The aim of the present work was to provide evidence about the anatomical variations as regard the origin, distribution, and branching pattern of the musculocutaneous nerve (MCN).

Materials and methods: Brachial plexus was dissected in 40 upper limbs of 20 male adult cadavers. The pattern of the MCN was photographed by a digital camera.

Results: The location and length of the nerve branches between left and right arms were recorded and statistically analysed. In 90% of specimens the MCN originates from the lateral cord of the brachial plexus, in 5% it arose from the median nerve (MN), while in the remaining 5% specimen, it was absent. The MCN pierced the coracobrachialis muscle in 90% of specimens, and in the remaining 10% did not pierce it. The motor branches to biceps brachii muscle were categorised into: type 1 (90%): one branch that divides to supply the two heads of biceps; type 2 (5%): double branches, innervating each head of biceps separately. The motor branches to brachialis muscle were categorised into: type 1 (82.9%): one branch; type 2 (14.2%): double branches and type 3 (2.9%): three branches that innervating brachialis muscle. Communications between the MCN and the MN were observed in 35% of specimens.

Conclusions: The knowledge of the common and uncommon MCN variations is important especially to the surgeons for carrying out surgical procedures in axilla and arm. (Folia Morphol 2023; 82, 1: 79–87)

Key words: brachial plexus, musculocutaneous nerve, axilla, median nerve, anatomical variations

INTRODUCTION

The brachial plexus is considered the most important part of the peripheral nervous system in the upper limb that has a wide range of variability in its formation, course, pattern of branches, intercommu-

nications and classifications, its percentage of variations reach 12.8% [28]. It has been studied by many investigators since the ancient ages as its variations have critical clinical significance [19].

Address for correspondence: Dr. H.N. Mustafa, Department of Anatomy, Faculty of Medicine, King Abdulaziz University, PO Box 80205, Jeddah 21589, Saudi Arabia, tel: 00966566764762, e-mail: hesham977@gmail.com

This article is available in open access under Creative Common Attribution-Non-Commercial-No Derivatives 4.0 International (CC BY-NC-ND 4.0) license, allowing to download articles and share them with others as long as they credit the authors and the publisher, but without permission to change them in any way or use them commercially.

The musculocutaneous nerve (MCN) begins at the level of the inferior border of the pectoralis minor muscle. Following the classical manuals, it arises as a terminal branch from the lateral cord of the brachial plexus and passes through the coracobrachialis, then between biceps brachii and brachialis muscles to supply them. After that, it continues as “the lateral cutaneous nerve of the forearm”, which is the cutaneous innervation along the lateral side of the forearm. The branch to brachialis muscle supplies also the elbow joint. So that the MCN is responsible for motor innervations of the muscles of the anterior compartment of the arm and sensory supply to the skin of the lateral side of the forearm [20, 31].

Isolated MCN injuries have been diagnosed and reported in a variety of clinical situations, including direct trauma to the anterior shoulder, fractures of the humerus and clavicle, abundant fracture callous formation, anterior shoulder dislocations, gunshot wounds, lacerations, and intravenous catheterisation, also, some cases of MCN palsy were reported after forceful exercise [21, 34]. The nerve is at risk both with open and arthroscopic procedures (especially anterior shoulder surgery) and can be stretched by retractor placement on the coracobrachialis muscle for exposure [13]. So, attention should be taken in shoulder surgeries (e.g. shoulder joint replacement), before placing a retractor on the medial side of the incision to retract the conjoined muscles and pectoralis major, it is essential to identify the MCN to avoid it injury [22].

Variations of the MCN and its branches are common; these variations have been described in human by many authors [14, 16, 23, 27, 29]. This study was conducted to demonstrate the anatomical variations in the origin, course, distribution, and branching pattern of the MCN in the axilla and arm and to define the intercommunications with the median nerve (MN) in the human male adult cadavers to prevent lesions during surgical procedures.

MATERIALS AND METHODS

This study was conducted after the approval from the Unit of Biomedical Ethics Research Committee in Faculty of Medicine, King Abdulaziz University, Saudi Arabia. All methods and techniques used during carrying out the research were in accordance with the protocol approved above. The present study was carried out on 40 upper limbs of 20 male adult cadavers fixed in 10% formalin. Preserved cadavers



Figure 1. The left axilla and arm showing the normal origin of musculocutaneous nerve (MCN): it arises from the lateral cord of the brachial plexus and piercing the coracobrachialis muscle (cb); MN — median nerve; UN — ulnar nerve; MC — medial cord.

obtained from the dissection room of the Anatomy Department, Faculty of Medicine.

The brachial plexus was dissected carefully with special concern to the exposure and topographic localisation of the MCN regarding the variations of its origin, course, and branching pattern. These findings were photographed using a digital camera (Canon-EOS-650D, made in Japan). In addition, a Vernier calliper was used to measure the length of the MCN and its branches. The MCN was traced from the coracoid process to the lateral epicondyle of the humerus. The MCN was studied as regards its branches, distribution, and communication with other nerves especially the MN. The branches arising from the MCN to innervate the biceps and brachialis muscles were identified and studied regarding their number, site of exit, length, and variations. Various univariate analyses were used to assess each variation, to clarify some of the relationships between the variables. All data were analysed using SPSS version 23.

RESULTS

Forty upper limbs of 20 cadavers were studied, the brachial plexus was dissected, and the MCN was studied on both right and left upper extremities. Several variations in the course and the branching pattern of the MCN were observed.

Origin of musculocutaneous nerve

In 38 (18 right, 20 left) (95%) out of 40 upper limb specimens, the MCN was appearing from the lateral cord of the brachial plexus as described in the classical manuals (Fig. 1), in only one arm (right)



Figure 2. The right axilla and arm showing, the musculocutaneous nerve (MCN) arising from the lateral root (LR) of the median nerve (MN). MCN gives 3 branches; 1 to brachialis (br), 2 to short head of biceps (S), and 3 to long head (L) and then continues as lateral cutaneous nerve of the forearm (LCN). Additional branch to L from nerve to brachialis muscle (arrow).



Figure 3. The right axilla and arm showing, the absence of musculocutaneous nerve. The median nerve (MN) gives 2 branches; 1 supplying biceps (B) muscle and 2 supplying brachialis (bbr) muscle and then continues as lateral cutaneous nerve of the forearm (LCN). Lateral cord (LC) gives (bc) branch to coracobrachialis muscle.

Table 1. Location of branches of musculocutaneous nerve in the arm

	Right arm	Left arm
Coracoid-lateral epicondyle distance [cm]	29.17 ± 2.45	29.31 ± 2.15
Average distance from coracoid process to coracobrachialis muscle [cm]	7.71 ± 1.23	7.78 ± 2.01
Average distance from coracoid process to coracobrachialis muscle as % of coracoid-lateral epicondyle distance	26.39 ± 3.22	26.47 ± 5.88
Average distance from coracoid process to emergence of nerves supplying biceps brachii muscle [cm]	12.14 ± 2.56	12.72 ± 2.18
Average distance from coracoid process to emergence of nerve(s) supplying biceps brachii muscle as % of coracoid-lateral epicondyle distance	41.29 ± 6.24	43.44 ± 6.93
Average distance from coracoid process to emergence of nerves supplying brachialis muscle [cm]	15.38 ± 3.39	17.19 ± 3.93*
Average distance from coracoid process to emergence of nerve(s) supplying brachialis muscle as % of coracoid-lateral epicondyle distance	52.34 ± 8.62	58.15 ± 11.04*
Average distance from coracoid process to emergence of communicating branch to median nerve [cm]	11.73 ± 4.13	13.07 ± 2.79
Average distance from coracoid process to emergence of communicating branch to median nerve as % of coracoid-lateral epicondyle distance	42.22 ± 8.43	44.47 ± 8.36

Data are shown as mean ± standard deviation. Student t-test: *p < 0.05 compared to the right side.

(2.5%) MCN arose from the MN (Fig. 2), while in the remaining arm (right) (2.5%) it was absent (Fig. 3). Regarding the coracoid-lateral epicondyle distance it was approximated in both right (29.17 ± 2.45 cm) and left (29.31 ± 2.15 cm) upper limbs (Table 1).

Relations of musculocutaneous nerve with the muscles of the arm

Coracobrachialis muscle. In 26 (14 right, 12 left) (65%) of the specimens, the MCN entered the upper part of coracobrachialis muscle (Fig. 4), while in four (2 right, 2 left) (10%) it entered its middle part (Figs. 5, 6), in another four (1 right, 3 left) (10%) it entered the lower part of the muscle (Fig. 7), and in two specimens (left) (5%) it entered the upper part of the coracobrachialis muscle and gives a branch to biceps muscle, then the main trunk entered again the lower

part of the muscle (Fig. 8). While in the remaining four specimens (3 right, 1 left) (10%) the MCN did not enter the coracobrachialis muscle, in this case an isolated branch originated from the lateral cord of the brachial plexus and pierced the coracobrachialis muscle to supply it instead of the MCN (Figs. 2, 9). Average distance (cm) from coracoid process to coracobrachialis muscle was approximated in both right (7.71 ± 1.23) and left (7.78 ± 2.01) arms, representing a percentage of coracoid-lateral epicondyle distance equal to 26.39 ± 3.22 in right arm and 26.47 ± 5.88 in left arm (Table 1).

Biceps and brachialis muscles. In 35 (15 right, 20 left) (87.5%) out of 40 specimens, the branches of the MCN that innervate the biceps and brachialis muscles arose from it after it leaves the coracobrachialis muscle (Fig. 4). In 5 specimens (right) (12.5%)



Figure 4. The right axilla and arm showing, the musculocutaneous nerve (MCN) entered the superior part of the coracobrachialis muscle (cb). It gives branch 1 which bifurcates to supply biceps (B) muscle. It gives also communicating branch (arrowhead) with the median nerve (MN).



Figure 7. The left axilla and arm showing, the musculocutaneous nerve (MCN) gives 3 branches (a) to biceps (bs) muscle, to brachialis (b) muscle and communicating (C) with the median nerve (MN); UN — ulnar nerve; Cb — coracobrachialis.



Figure 5. The left axilla and arm showing, the musculocutaneous nerve (MCN) gives a communicating branch (C) which pierces coracobrachialis (cb) muscle to join the median nerve (MN). MCN supplies brachialis muscle (br) by only one branch (arrow).



Figure 8. The left axilla and arm showing, the musculocutaneous nerve (MCN) gives branch 1 to supply biceps (bs) muscle and communicating branch (C) to join the median nerve (MN) which gives (B1) to supply brachialis (br) muscle. The main trunk of MCN gives (B2) to supply also br muscle, then continues as lateral cutaneous nerve of the forearm (LCN); cb — coracobrachialis muscle.



Figure 6. The right axilla and arm showing, the musculocutaneous nerve (MCN) gives (bb) branch which bifurcates into a and b branches to supply short (S) and long (L) heads of biceps muscle and gives also 1, 2, 3 to supply brachialis muscle (br) then continues as lateral cutaneous nerve of the forearm (LCN); cb — coracobrachialis muscle.



Figure 9. The right axilla and arm showing, the musculocutaneous nerve (MCN) joins the median nerve (MN) by a short trunk (arrow). MCN gives branch 1 to biceps (B) and branch to (bbr) brachialis (br) muscle and continues as lateral cutaneous nerve of the forearm (LCN); UN — ulnar nerve.

Table 2. Length of musculocutaneous nerve branches in the arm

Length of motor branch supplying	Right arm	Left arm
Long head of biceps brachii muscle	4.27 ± 1.23	3.88 ± 1.36
Short head of biceps brachii muscle	3.47 ± 0.91	3.22 ± 1.02
Brachialis muscle	5.35 ± 1.86	5.04 ± 1.21

Data are shown as mean ± standard deviation.



Figure 10. The right axilla and arm showing, the musculocutaneous nerve (MCN) gives branch 1 which bifurcates to supply short (S) and long (L) heads of biceps muscle and branches 2 and 3 to supply brachialis (br) muscle; cb — coracobrachialis muscle; LCN — lateral cutaneous nerve of forearm.



Figure 11. The right axilla and arm showing, the musculocutaneous nerve (MCN) divided into two branches: 1 — branch to biceps and 2 — branch continue as lateral cutaneous nerve of forearm (LCN) and give a and b branches to brachialis (br) and communicating branch (C); MN — median nerve.

the branches to both biceps and brachialis muscles, along with the lateral cutaneous nerve of the forearm, arose from the MN itself (Figs. 2, 3).

Distribution of musculocutaneous nerve

Patterns of the branches supplying the biceps brachii muscle (35 specimens). The average distance (cm) from the coracoid process to emergence of motor branches to both short and long heads of biceps brachii

muscle is shorter; statistically non-significance; in the right (12.14 ± 2.56) than the left (12.72 ± 2.18) arms, representing a percentage of coracoid-lateral epicondyle distance which is also shorter; statistically non-significance; the right (41.29 ± 6.24) than that in the left (43.44 ± 6.93) arms (Table 1). Regarding the length of branches to the short head of biceps brachii it is shorter; statistically non-significance; in the left (3.22 ± 1.02) than in the right (3.47 ± 0.91) arms (Table 2). Also, the length of branches to the long head of biceps brachii is shorter; statistically non-significance; in the left (3.88 ± 1.36) than in the right (4.27 ± 1.23) arms (Table 2). So, the length of branches to short head of biceps brachii are shorter than that of long head without statistically significance difference (Table 2).

Two anatomical variations were observed for the innervation of the biceps brachii muscle in this study: — type 1: a solar branch from the musculocutaneous that is divided to supply the two heads of the biceps muscle individually; seen in 33 (14 right, 19 left) (94.3%) of studied arms; — type 2: in two limbs (1 right, 1 left) (5.7%), two separate branches arose from the musculocutaneous, one to supply the long head while the other one to supply the short head of the biceps. There was an additional branch innervating the distal part of the long head of biceps (Fig. 2).

Patterns of the branches supplying the brachialis muscle (35 specimens). The average distance (cm) from the coracoid process to emergence of motor branches innervating the brachialis muscle is shorter; with statistically significant difference $p < 0.05$; in the right (15.38 ± 3.39) than the left (17.19 ± 3.93) arms, representing a percentage of coracoid-lateral epicondyle distance which is also shorter; with statistically significant difference $p < 0.05$; in the right (52.34 ± 8.62) than that in the left (58.15 ± 11.04) arms (Table 1).

Regarding the length of branches to brachialis muscle it is shorter; statistically non-significance; in the left (5.04 ± 1.2) than in the right (5.35 ± 1.86) arms (Table 2).

Three types of anatomical variations were observed: — type I: it is found in 29 specimens (19 right, 10 left) (82.9%) of arms, where there was a single branch innervating the brachialis muscle from the main trunk of MCN (Fig. 9); — type II: in 5 specimens (4 right, 1 left) (14.2%) of arms, there were two branches that innervate the brachialis muscle from the main trunk of MCN (Figs. 10, 11);



Figure 12. The right axilla and arm showing, the musculocutaneous nerve (MCN) gives a communicating branch (C) to join the median nerve (MN) before piercing the coracobrachialis muscle (cb); UN — ulnar nerve.

- type III: in one right specimen (2.9%) of arms, three branches innervating the brachialis muscle, these branches originated also from the main trunk of MCN (Fig. 6).

Patterns of communication between musculocutaneous and median nerves. This communication was observed in 24 (11 right, 13 left) (60%) out of 40 specimens.

The average distance (cm) from the coracoid process to emergence of communicating branch to MN is shorter; statistically non-significance; in the right (11.73 ± 4.13) than the left (13.07 ± 2.79) arms, representing a percentage of coracoid lateral epicondyle distance which is also shorter; statistically non-significance; the right (42.22 ± 8.43) than that in the left (44.47 ± 8.36) arms (Table 1).

The communicating branches were categorised based on their origin from the MCN and its union with the MN:

- There are three different types of communications:
- type A: the proximal part of the MCN sharing a common trunk with the proximal part of the MN. This finding was observed in 4 specimens (3 right, 1 left) (16.7%) (Fig. 9);
- type B: the proximal part of the MCN gives a communicating branch to join the middle part of the MN, it was observed in 6 specimens (2 right, 4 left) (25%) (Fig. 12). In two arms (1 right, 1 left) (8.3%), of the previous specimens, a branch arising from this communication supplying the brachialis muscle (Fig. 8);
- type C: in the remaining 12 specimens (4 right, 8 left) (50%), within the coracobrachialis muscle, a communicating branch arose from the middle part of the MCN to join the middle part of the MN

(in 8 specimens) and joined the distal part of the MN (in other 4 specimens) (Figs. 5, 7, 11).

DISCUSSION

Embryologically, the limb buds are developed from the lateral plate of the mesoderm and the mesenchyme of those buds discriminate into the deep structures of the limbs, whereas the axons of the peripheral nerves develop in a distal direction from the ectoderm to reach the muscles and skin [11]. The somite migration led to formation of the extremities, where they bring their own nerve supply, so every dermatome and myotome keeps the original segmental innervation. During somite migration, some of the nerves come into close proximity and fuse in a particular pattern, forming a plexus early in fetal life [1, 2]. The existence of anatomical neuromuscular variations maybe due to different factors that enhance the pathway of muscle formation in the limbs. Factors guiding nerve growth are chemo-attractive and repellent that control cellular proliferation to proper tissue formation. Butz et al. [6] stated that signalling mechanisms during embryogenesis could have a role during the 5th week of gestation, the axons of spinal nerves propagate distally to reach the mesenchyme of the limb, and insufficient signalling may negatively impact the normal formation of the brachial plexus. This embryological clarification justifies what we observed in our finding.

The anatomical variations from the expected pattern of peripheral nerve course and relations can be a challenge for the surgeons. In the arm, variations of the nerves that innervate the anterior compartment (musculocutaneous, median, and ulnar nerves) are more common than those of the posterior compartment [7, 25].

Musculocutaneous nerve is a terminal branch of the brachial plexus, which provides the chief motor innervation for the arm flexors besides the sensory innervation for the lateral side of the forearm. In the present study, MCN originated from the lateral cord of the brachial plexus in 90% of cases while from the MN in only 5% of cases. These findings were in agreement with Bergman et al. [4], who reported that this nerve arose from the lateral cord in 90.5%, but on the contrary to this study they found that the MCN arose from the MN in only 2% of specimens. Moreover, they reported that it might be doubled, unusually short or absent.

In the present study, the MCN was found to be absent in 5% of cases. The absence of the MCN was reported by many authors in previous studies [27, 29].

In particular, a case study was similar to the present study, in that the motor nerve to the coracobrachialis muscle arose from the lateral cord, while the motor nerve to the biceps brachii and brachialis muscles arose from the MN [15].

Variable pathways and relations of the MCN within the coracobrachialis muscle were described. Ozturk et al. [24] stated that the MCN pierced the coracobrachialis muscle in all studied 42 specimens of upper limb, whereas Pacha Vicente et al. [26] and Eglseder and Goldman [10] observed that the MCN did not enter the coracobrachialis muscle in 29.6% and 6.5% of their samples, respectively. Furthermore, Macchi et al. [19] observed a range of differences in the entry site of the MCN into the coracobrachialis muscle, and that was correlated with a low variability in the exit site of the nerve from the muscle. However, the exit point was positively related to the length of the muscle. Choi et al. [8] stated that the MCN penetrated the coracobrachialis muscle at a lower level in a single arm but did not pierce it in 4.7% of the specimens. Uysal et al. [32] observed that the MCN pierced the upper part of the coracobrachialis muscle in 43% of studied limbs and its middle part in 37% and its lower part in 17%, while it did not pierce it in only 3% of samples. In the present study, the MCN pierced the upper part of coracobrachialis muscle in 65% of the specimens, while in only 10%, it pierced its middle part and in another 10% it pierced its lower part. In only 5% of specimens, it entered the upper part of the coracobrachialis muscle and gives a branch to biceps muscle then the main trunk entered again the lower part of the muscle. While in the remaining 10% of specimens, the MCN did not penetrate the muscle.

These observations demonstrated the relations between the MCN and the coracobrachialis muscle. Furthermore, it shows the probability of nerve injury particularly when the upper and middle parts of the coracobrachialis muscle are exposed to trauma.

Earlier studies revealed the appearance of the MCN using ultrasound. Schafhalter-Zoppoth and Gray [30] observed that if this nerve was not visible in the coracobrachialis muscle, it was probably fused with the MN, later it is separated from it. The MCN innervates the coracobrachialis and the biceps brachii, plus the majority of brachialis muscle. The branch supplying the coracobrachialis arose from the MCN prior to

piercing the muscle, while the branches supplying the biceps and brachialis muscles originating from it after its exit from the muscle [18, 30].

The significance of the nerves supplying the biceps and brachialis in the surgeries of the brachial plexus has been extensively acknowledged [26]. In a previous study on the branches of the MCN to both biceps and brachialis muscles; it was stated that there are three types of the innervation pattern to biceps muscle observed in 24 studied cadavers [35]. Type I, one main branch arose from the main trunk of the MCN distal to the coracobrachialis muscle and consequently divided into two branches to supply each (short and long) heads of the biceps muscle. Type II, two main branches for each head of the biceps separately, the proximal branch for the short head and the distal one for the long head of the muscle. Type III, two main branches; a proximal branch gives two subdivisions, each one to supply a head of the biceps muscle, plus a distal one to supply the common belly. A study found type I in 83.3% of cases while in this study it was found in 95.5% of cases [35], while in Pacha Vicente's findings, it was 60.5% [26]. Types II and III were stated in 8.3% and 8.3% of cases respectively by Yang et al. [35], while it was 27.9% and 11.6% respectively by Pacha Vicente et al. [26]. In 5% of specimens in this study, there was no example found of type III branching pattern to the biceps that was defined by Elgammal et al. [12], which was three isolated main branches: first to long head, second to short head and the third one to the common belly.

The measurements that were carried on the exit point of the first branch to biceps and brachialis muscles are specified in past reports [12]. In this study the methodology described by Yang et al. [35] and Elgammal et al. [12] was applied, which uses the coracoid process of the scapula and the medial epicondyle of the humerus as reference points for these measurements was followed.

Yang et al. [35] observed two innervation patterns of the brachialis muscle (type I showing one main branch, and type II showing two main branches). The type II innervation pattern was demonstrated in 8.4%, in the present study, but it was 4.2% of the samples of Yang et al. [35] while 27.9% of the samples of Pacha Vicente [16, 26, 35]. An additional type to those described by Yang et al. [35] was seen in a single specimen (5%) in this study, where there were three branches innervating the brachialis muscle,

these branches originated also from the main trunk of MCN [9, 14, 35].

Intercommunications between the MCN and MN had an important clinical significance, especially in relative to the accurate explanation of clinical neurophysiology, realizing the anatomy of the anterior shoulder repairs after trauma, and recognizing the dysfunction of median and MCNs [8, 9]. The frequency of these communications has been reported to differ between 5% and 46.4% [23]. Interestingly, a case was reported in a cadaver showing that the MCN gives a third root to form the MN [6]. Although intercommunicating branches most commonly originate from the MCN and joined the MN, both reported incidents where the intercommunicating branch originates from the MN and joined the MCN [18, 26]. In the present study, the reverse was observed; the intercommunicating branch arose from the MCN and joined the MN in 35% of arms.

Similar to Uysal et al. [32], a branch originating from the communicating branch between the MCN and the MN to the brachialis was seen in this study in only a single arm [16, 32].

Choi et al. [8] detected that in 26.4% of cases, there was communicating branches or fusion of the MCN and MN [8, 16]. The communicating branches were classified into three patterns; 1st pattern (19.2%) revealed merging of the MCN and MN, 2nd pattern (74%) had one branch communicating between the MCN and MN, while 3rd pattern (6.8%) had two branches communicating between the two nerves. It has been also described that the communicating branch originated from the MCN proximal to the entry point to the coracobrachialis muscle in 29.4%, through the muscle in 2%, distal to it in 54.9%, and from it as the MCN did not enter the muscle in 13.7% of cases [8, 14].

On the other hand, Venieratos and Anagnostopoulou [33] studied 22 specimens and they categorised the communicating branches into three types: proximal to the entry point of the musculocutaneous nerve into the coracobrachialis in 9 specimens (type I), distal to coracobrachialis in 10 specimens (type II), and beyond coracobrachialis in 3 specimens (type III) [23, 33]. In this work, the communicating branches between the MCN and MN were observed and categorised into three types according to where they arose and merged the respective nerves.

Type A — the proximal part of the MCN sharing a common trunk with the proximal part of the MN

in only one specimen (14.2%), type B — the communicating branch arose from the proximal part of the MCN to merge the middle part of the MN in two (28.4%) specimen and in type C (57.2%), the most observed type, the communicating branch arose from the middle part of the MCN within the coracobrachialis muscle to merge the middle part of the MN, these observation was in agreement with findings of Ballesteros et al. [3]. These finding were in the contrary to Nascimento et al. [21] who stated that the point of joining the MCN with the MN is distal to the coracobrachialis muscle in type II, and type III, where neither the nerve nor the communicating branch pierce the coracobrachialis muscle [3, 5].

The site of nerve communication and the number of branches that originate from the MCN to merge the MN may change the clinical symptoms and case progression along with management. Therefore, these differences should be considered during the clinical examination and treatment of traumatic injuries to upper limb.

CONCLUSIONS

The presented data in our work that demonstrate the branches of the MCN are significant for surgical doctors who perform operational procedures in the axilla and upper arm region.

Acknowledgements

The authors wish to express their gratitude to all those who donated their bodies to medical science so that anatomical research could be performed. Results from such research can potentially increase mankind's overall knowledge that can then improve patient care. Therefore, these donors and their families deserve our highest gratitude [17].

Conflict of interest: None declared

REFERENCES

1. Afshar A. An update on embryology of the upper limb. *J Hand Surg Am.* 2013; 38(11): 2304, doi: [10.1016/j.jhsa.2013.09.018](https://doi.org/10.1016/j.jhsa.2013.09.018), indexed in Pubmed: [24207000](https://pubmed.ncbi.nlm.nih.gov/24207000/).
2. Al-Qattan M, Kozin S. Update on embryology of the upper limb. *J Hand Surg.* 2013; 38(9): 1835–1844, doi: [10.1016/j.jhsa.2013.03.018](https://doi.org/10.1016/j.jhsa.2013.03.018).
3. Ballesteros LE, Forero PL, Buitrago ER. Communication between the musculocutaneous and median nerves in the arm: an anatomical study and clinical implications. *Rev Bras Ortop.* 2015; 50(5): 567–572, doi: [10.1016/j.rboe.2014.08.009](https://doi.org/10.1016/j.rboe.2014.08.009), indexed in Pubmed: [26535190](https://pubmed.ncbi.nlm.nih.gov/26535190/).
4. Bergman RA, Afifi AK, Miyauchi R. *Illustrated Encyclopedia of Human Anatomic Variation. Opus III: Nervous System.* 2015.

5. Budhiraja V, Rastogi R, Kumar Asthana A, et al. Concurrent variations of median and musculocutaneous nerves and their clinical correlation--a cadaveric study. *Ital J Anat Embryol.* 2011; 116(2): 67–72, indexed in Pubmed: [22303635](#).
6. Butz JJ, Shiwochan DG, Brown KC, et al. Bilateral variations of brachial plexus involving the median nerve and lateral cord: An anatomical case study with clinical implications. *Australas Med J.* 2014; 7(5): 227–231, doi: [10.4066/AMJ.2014.2070](#), indexed in Pubmed: [24944720](#).
7. Chelly JE. *Peripheral nerve blocks: a color atlas.* Lippincott Williams & Wilkins 2009.
8. Choi D, Rodriguez-Niedenführ M, Vázquez T, et al. Patterns of connections between the musculocutaneous and median nerves in the axilla and arm. *Clin Anat.* 2002; 15(1): 11–17, doi: [10.1002/ca.1085](#), indexed in Pubmed: [11835538](#).
9. Chrysikos D, Athanasopoulos A, Georgakopoulos P, et al. Anatomical variation of a communicating branch between the musculocutaneous and the median nerve: a case report. *Acta Med Acad.* 2020; 49(1): 71–74, doi: [10.5644/ama2006-124.286](#), indexed in Pubmed: [32738120](#).
10. Eglseider WA, Goldman M. Anatomic variations of the musculocutaneous nerve in the arm. *Am J Orthop (Belle Mead NJ).* 1997; 26(11): 777–780, indexed in Pubmed: [9402212](#).
11. El-Naggar MM, Al-Saggaf S. Variant of the coracobrachialis muscle with a tunnel for the median nerve and brachial artery. *Clin Anat.* 2004; 17(2): 139–143, doi: [10.1002/ca.10213](#), indexed in Pubmed: [14974102](#).
12. Elgammal Y, Frolov A, Martin J. The branching pattern and internal topography of the musculocutaneous nerve. *FASEB J.* 2020; 34(S1): 1–1, doi: [10.1096/fasebj.2020.34.s1.04481](#).
13. Frazer EA, Hobson M, McDonald SW. The distribution of the radial and musculocutaneous nerves in the brachialis muscle. *Clin Anat.* 2007; 20(7): 785–789, doi: [10.1002/ca.20521](#), indexed in Pubmed: [17854055](#).
14. Gelmi C, Pedrini F, Fermi M, et al. Communication between median and musculocutaneous nerve at the level of cubital fossa: a case report. *Transl Res Anat.* 2018; 11: 1–4, doi: [10.1016/j.tria.2018.04.001](#).
15. Gümüşburun E, Adigüzel E. A variation of the brachial plexus characterized by the absence of the musculocutaneous nerve: a case report. *Surg Radiol Anat.* 2000; 22(1): 63–65, doi: [10.1007/s00276-000-0063-x](#), indexed in Pubmed: [10863751](#).
16. Hunter D, Zdilla M. The absent musculocutaneous nerve: A systematic review. *Transl Res Anat.* 2021; 22: 100092, doi: [10.1016/j.tria.2020.100092](#).
17. Iwanaga J, Singh V, Takeda S, et al. Acknowledging the use of human cadaveric tissues in research papers: Recommendations from anatomical journal editors. *Clin Anat.* 2021; 34(1): 2–4, doi: [10.1002/ca.23671](#), indexed in Pubmed: [32808702](#).
18. Krishnamurthy A, Nayak SR, Venkatraya Prabhu L, et al. The branching pattern and communications of the musculocutaneous nerve. *J Hand Surg Eur Vol.* 2007; 32(5): 560–562, doi: [10.1016/J.JHSE.2007.06.003](#), indexed in Pubmed: [17950223](#).
19. Macchi V, Tiengo C, Porzionato A, et al. Musculocutaneous nerve: histotopographic study and clinical implications. *Clin Anat.* 2007; 20(4): 400–406, doi: [10.1002/ca.20402](#), indexed in Pubmed: [17022027](#).
20. Moore KL, Dalley AF. *Clinically oriented anatomy.* Wolters Kluwer india Pvt Ltd 2018.
21. Nascimento SR, Ruiz CR, Pereira E, et al. Rare anatomical variation of the musculocutaneous nerve: case report. *Rev Bras Ortop.* 2016; 51(3): 366–369, doi: [10.1016/j.rboe.2015.08.019](#), indexed in Pubmed: [27274492](#).
22. Occhiboi E, Clement R. Anatomic total shoulder arthroplasty and reverse total shoulder arthroplasty. *JBJS J Orthop Physician Assist.* 2020; 8(1): 0025, doi: [10.2106/jbjs.jopa.19.00025](#).
23. Orellana-Donoso M, Valenzuela-Fuenzalida J, Gold-Semmler M, et al. Neural entrapments associated with musculoskeletal anatomical variations of the upper limb: Literature review. *Transl Res Anat.* 2021; 22: 100094, doi: [10.1016/j.tria.2020.100094](#).
24. Ozturk A, Bayraktar B, Taskara N, et al. Morphometric study of the nerves entering into the coracobrachialis muscle. *Surg Radiol Anat.* 2005; 27(4): 308–311, doi: [10.1007/s00276-005-0326-7](#), indexed in Pubmed: [15968480](#).
25. Oztürk NC, Uzmsanel D, Oztürk H. An unreported pattern of musculocutaneous and median nerve communication with multiple variations of biceps brachii: a case report. *Surg Radiol Anat.* 2010; 32(9): 887–890, doi: [10.1007/s00276-009-0616-6](#), indexed in Pubmed: [20049596](#).
26. Pacha Vicente D, Forcada Calvet P, Carrera Burgaya A, et al. Innervation of biceps brachii and brachialis: Anatomical and surgical approach. *Clin Anat.* 2005; 18(3): 186–194, doi: [10.1002/ca.20057](#), indexed in Pubmed: [15768419](#).
27. Pacholczak R, Klimek-Piotrowska W, Walocha JA. Absence of the musculocutaneous nerve associated with a supernumerary head of biceps brachii: a case report. *Surg Radiol Anat.* 2011; 33(6): 551–554, doi: [10.1007/s00276-010-0771-9](#), indexed in Pubmed: [21225427](#).
28. Pandey SK, Shukla VK. Anatomical variations of the cords of brachial plexus and the median nerve. *Clin Anat.* 2007; 20(2): 150–156, doi: [10.1002/ca.20365](#), indexed in Pubmed: [16795062](#).
29. Parchand MP, Patil ST. Absence of musculocutaneous nerve with variations in course and distribution of the median nerve. *Anat Sci Int.* 2013; 88(1): 58–60, doi: [10.1007/s12565-011-0126-6](#), indexed in Pubmed: [22237923](#).
30. Schafhalter-Zoppoth I, Gray AT. The musculocutaneous nerve: ultrasound appearance for peripheral nerve block. *Reg Anesth Pain Med.* 2005; 30(4): 385–390, doi: [10.1016/j.rapm.2004.12.008](#), indexed in Pubmed: [16032591](#).
31. Snell RS. *Snell's Clinical Anatomy.* Wolters Kluwer India Pvt Ltd. 2018.
32. Uysal II, Seker M, Karabulut AK, et al. Brachial plexus variations in human fetuses. *Neurosurgery.* 2003; 53(3): 676–684, doi: [10.1227/01.neu.0000079485.24016.70](#), indexed in Pubmed: [12943583](#).
33. Venieratos D, Anagnostopoulou S. Classification of communications between the musculocutaneous and median nerves. *Clin Anat.* 1998; 11(5): 327–331, doi: [10.1002/\(SICI\)1098-2353\(1998\)11:5<327::AID-CA6>3.0.CO;2-M](#), indexed in Pubmed: [9725577](#).
34. Vineyard AP, Gallucci AR, Imbus SR, et al. Residents case report: musculocutaneous nerve injury in a collegiate baseball pitcher. *Int J Sports Phys Ther.* 2020; 15(5): 804–813, doi: [10.26603/ijsp20200804](#), indexed in Pubmed: [33110700](#).
35. Yang ZX, Pho R, Kour AK, et al. The musculocutaneous nerve and its branches to the biceps and brachialis muscles. *J Hand Surg Am.* 1995; 20(4): 671–675, doi: [10.1016/s0363-5023\(05\)80289-8](#).

Anatomical description of the perforating cutaneous nerve

K. Shafarenko¹, J.A. Walocha¹, R.S. Tubbs^{2–6}, K. Jankowska¹, A. Mazurek¹

¹Department of Anatomy, Jagiellonian University Medical College, Krakow, Poland

²Department of Neurosurgery, Tulane Centre for Clinical Neurosciences, Tulane University School of Medicine, New Orleans, LA, United States

³Department of Neurosurgery and Ochsner Neuroscience Institute, Ochsner Health System, New Orleans, LA, United States

⁴Department of Neurology, Tulane Centre for Clinical Neurosciences, Tulane University School of Medicine, New Orleans, LA, United States

⁵Department of Anatomical Sciences, St. George's University, Grenada, West Indies

⁶Department of Surgery, Tulane University School of Medicine, New Orleans, LA, United States

[Received: 5 October 2021; Accepted: 12 December 2021; Early publication date: 17 January 2022]

Background: The perforating cutaneous nerve/perforating nerve of the sacrotuberous ligament is rarely observed. It usually arises from the posterior division of the sacral plexus or the pudendal nerve and perforates the sacrotuberous ligament. The anatomy of this nerve and its variants is poorly described in the literature, but there are data indicating its role in pudendal neuralgia.

Materials and methods: Herein, we present an anatomical study of six formalin-fixed cadavers with descriptions of the topography of spinal nerves S2–S4, the pudendal bundle, the perforating cutaneous nerve and the sacrotuberous ligament.

Results: We found three perforating cutaneous nerves and described each of them in detail, with measurements of length and width, and point of perforation of the sacrotuberous ligament.

Conclusions: We distinguished three types of perforating cutaneous nerve on the basis of our findings and previous publications; two of the three types were observed in our study. (Folia Morphol 2023; 82, 1: 88–95)

Key words: perforating cutaneous nerve, sacrotuberous ligament, pudendal nerve, pudendal neuralgia, anatomy

INTRODUCTION

The lumbosacral plexus is the largest plexus in the human body. It is made up of ventral rami of the lumbar, sacral and coccygeal spinal nerves. The sacral plexus (SP) begins with the fourth lumbar and ends with the first coccygeal nerve. The surface of the SP adheres to the anterior surface of the piriformis muscle (PM), while its front adjoins the complex of internal iliac vessels. Each spinal nerve, except the pairs from S4 to Co1, is divided into anterior and posterior divisions, which connect to form the nerves of the SP. The SP

comprises short and long branches; the short branches are predominantly responsible for innervating the periosteum, joints and muscles such as the piriformis. The long branches are the sciatic nerve, the posterior cutaneous nerve of the thigh, the superior and inferior gluteal nerves, the pudendal nerve (PN), variable the perforating cutaneous nerve (PCN) and the coccygeal nerve (Fig. 1). Bochenek et al. (2008) [1]. The PCN has a diverse anatomical topography: it can arise from the PN, be absent, or emerge from the pudendal plexus independently of the PN [10]. According to Termino-

Address for correspondence: Dr. A. Mazurek, Department of Anatomy, Jagiellonian University Medical College, ul. Kopernika 12, 31–034 Kraków, Poland, tel/fax: +48 12 422 95 11, e-mail: agt.mazurek@student.uj.edu.pl

This article is available in open access under Creative Common Attribution-Non-Commercial-No Derivatives 4.0 International (CC BY-NC-ND 4.0) license, allowing to download articles and share them with others as long as they credit the authors and the publisher, but without permission to change them in any way or use them commercially.

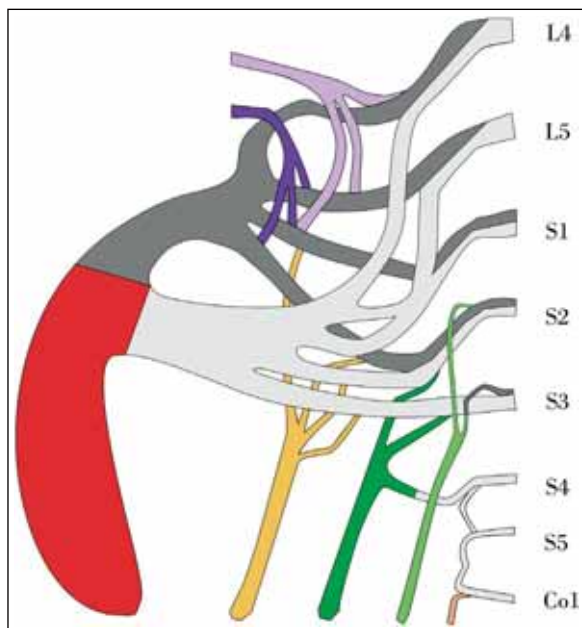


Figure 1. A schematic drawing of the sacral plexus based on “Surgical anatomy of the sacral plexus and its branches”, Preface (Fig. 4) [5]. Each spinal nerve, except the pairs from S4 to Co1, is divided into the anterior (light grey) and posterior (dark grey) divisions, which connect forming the nerves of the SP. The sciatic plexus is composed of the sciatic nerve (red), the posterior cutaneous nerve of the thigh (yellow), the superior (light purple) and inferior (dark purple) gluteal nerves. The pudendal plexus incorporates the pudendal nerve (dark green), which is a constant part, and the varying perforating cutaneous nerve (light green). The coccygeal plexus is comprised of the coccygeal nerve (peach).

logia Anatomica 2019, aforementioned name of the nerve determines only the nerve, which arises from the sacral plexus. Therefore, we decided to use the name “perforating of the STL nerve” in a situation where the nerve arises from the PN. All of the long branches of the SP, except the coccygeal nerve [1] and sometimes the PCN [10], extend from the pelvis through the greater sciatic foramen, which is divided into the suprapiriform and the infrapiriform foramina by the PM. The superior gluteal nerve passes through the suprapiriform foramen; the other aforementioned nerves pass through the infrapiriform foramen [1].

The PN usually arises from the ventral branches (anterior divisions) of the S2-S4 spinal nerves and is accompanied laterally by the internal pudendal vessels. It extends from the pelvis under the inferior border of the PM, crosses the ischial spine posteriorly and reenters the pelvis through the lesser sciatic foramen [1]. Subsequently, it reaches the pudendal canal on the medial surface of the ischial tuberosity, where it divides into its terminal branches: the perineal nerve, the dorsal nerve of the penis or clitoris,

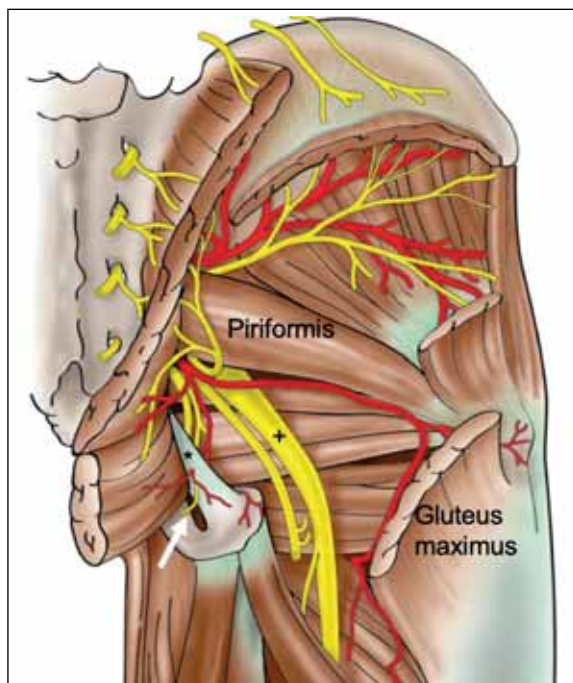


Figure 2. A figure of the perforating cutaneous nerve from “Surgical anatomy of the sacral plexus and its branches”, Chapter 6 (Fig. 6.1) [5]. Posterior view of the gluteal region. The perforating cutaneous nerve (arrow) is seen emanating from the sacrotuberous ligament (asterisk). For reference, note the laterally placed sciatic nerve (+).

and the inferior rectal nerve (IRN). The perineal nerve innervates the muscles of the urogenital triangle and the skin on the posterior part of the scrotum or labia majora. The skin of the penis or clitoris is supplied by dorsal nerve of the penis or clitoris. The IRN supplies the external anal sphincter and the mucous membrane of the inferior half of the anal canal and the skin of the anal area [4, 6]. In 40–56% of cases the IRN does not enter pudendal canal with the PN but instead reaches the ischioanal fossa [3, 7].

In summary, the sensory component of the PN supplies the skin of the pelvic muscles and the genitals except the area around of the mons pubis and the anterior part of the scrotum or labia, whereas the motor component innervates the pelvic muscles and the external genitalia. Moreover, the PN is the only nerve of the SP that carries parasympathetic fibres to the pelvic organs. Its autonomic component is responsible for the processes of urination, defecation and erection. In some cases the PN gives off the perforating of the sacrotuberous ligament (STL) nerve, which most frequently arises in the area surrounding the ischial spine (Fig. 2) [1].

The PN is classified into five types on the basis of the number of its trunks: one-trunked (56.2%), two-trunk-

ed (11%), two-trunked with one trunk as an IRN piercing the sacrospinous ligament (SSL) (11%), two-trunked with one as an IRN not perforating through the SSL (9.5%), and three-trunked (12.3%) [2, 6, 8]. The IRN, which perforates the SSL, is described below.

The aim of this study is to offer a detailed depiction of topography of the PCN, concerning the part between the inferior border of the PM and the inferior border of the STL. The perforating of the STL nerve as a branch of the PN is emphasized. The information is based on dissections of the subgluteal region.

MATERIALS AND METHODS

There are few data describing the PCN/perforating of the STL nerve, so our research was primarily aimed at on gathering and systematizing all possible information about the subject; the anatomical description was based on our dissections.

Structures required for the study were dissected in embalmed female and male cadavers obtained from the Anatomy Department of the Jagiellonian University Medical College. During our research, 6 cadavers (3 female and 3 male) and 12 sacral plexuses were examined through the gluteal approaches. The age, race, weight and cause of death were not provided for scientific purposes.

The gluteal approach was used to expose structures located in front of the gluteus maximus muscle. First, the muscle was cut and the adipose tissue in front of it was removed. The ischial tuberosity was then identified and the STL was separated from the front surface of the gluteus maximus. If the point of perforation through the STL was not found, the dissection was aborted. However, in all cases in the present study the aforementioned point and the PCN/perforating of the STL nerve were found, so the dissections were continued until the pudendal neurovascular bundle, the SSL, and other branches of the PN and nearby structures were displayed. If the PCN/perforating of the STL nerve was present, the ischioanal fossa was additionally dissected in the anteromedial direction to the greatest possible extent of small nerves that branch from PCN/perforating of the STL nerve to determine the range of its innervation. If the PCN arose directly from the SP, as it did in some specimens, part of the sacral bone was removed and the ventral rami of S2-S4 spinal nerves were exposed.

All the steps described below were performed only on cadavers with a PCN/perforating of the STL nerve. The point at which the pudendal neurovascular bundle arose under the inferior border of the PM was documented. The anatomical relationship of the PN

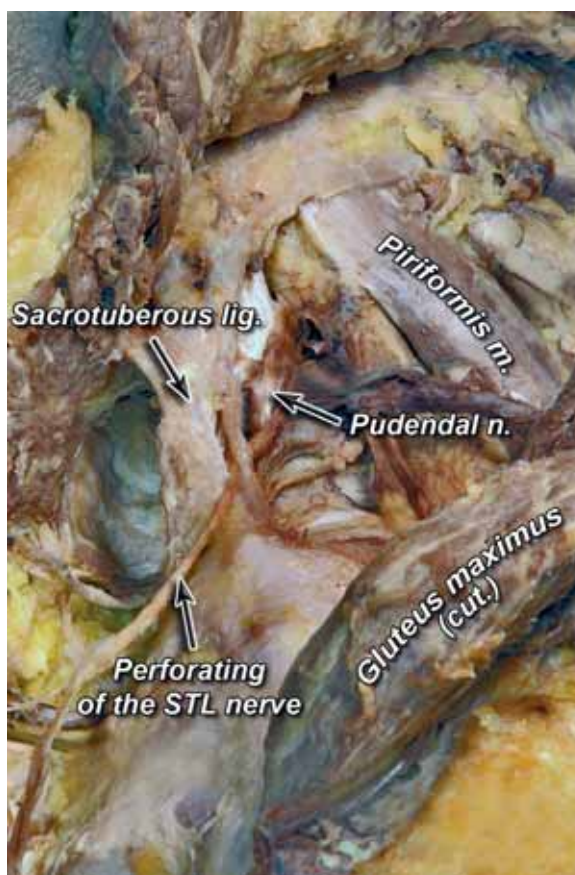


Figure 3. The sacrotuberous ligament (STL) perforated by the right perforating of the STL nerve. The superior view of the right gluteal area shows the perforating of the STL nerve, which arises from the pudendal nerve. It forms a fissure in the ligament during perforation.

to the STL was recorded. The PN, PCN/perforating of the STL nerve, and STL were measured and the anatomical relationship of the PCN/perforating of the STL nerve to the STL was thereby established. The widths and the lengths of the PN, PCN/perforating of the STL nerve, and STL and its fissure, which was formed as a result of perforation, were measured. So were the distances from specifically selected points on the PN to the sacral attachment of the STL, and from the point of origin of the PCN/perforating of the STL nerve to that of the PN under the inferior border of the PM. All measurements were taken 3 times and the median was calculated by the same researcher using the same calliper. Photographs of all cadavers with a PCN/perforating of the STL nerve were obtained.

RESULTS

During our study, three were found, one of them on the right male gluteal area (perforating of the STL nerve) (Fig. 3) and the other two in female cadavers

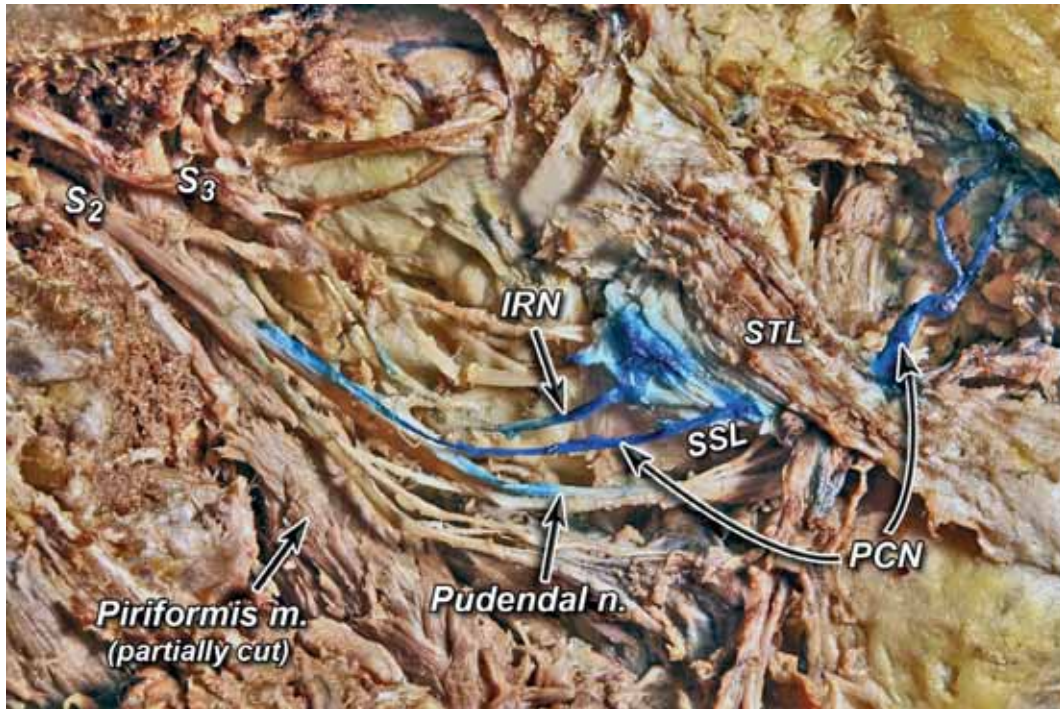


Figure 4. The sacrotuberous ligament (STL) perforated by the left perforating cutaneous nerve (PCN). Two nerves, which perforate the ligaments, were indicated with a bluish tint. The first one perforates the STL and the second one passes through the sacrospinous ligament (SSL); IRN — inferior rectal nerve; S₂ — ventral branch of the second sacral nerve; S₃ — ventral branch of the third sacral nerve.

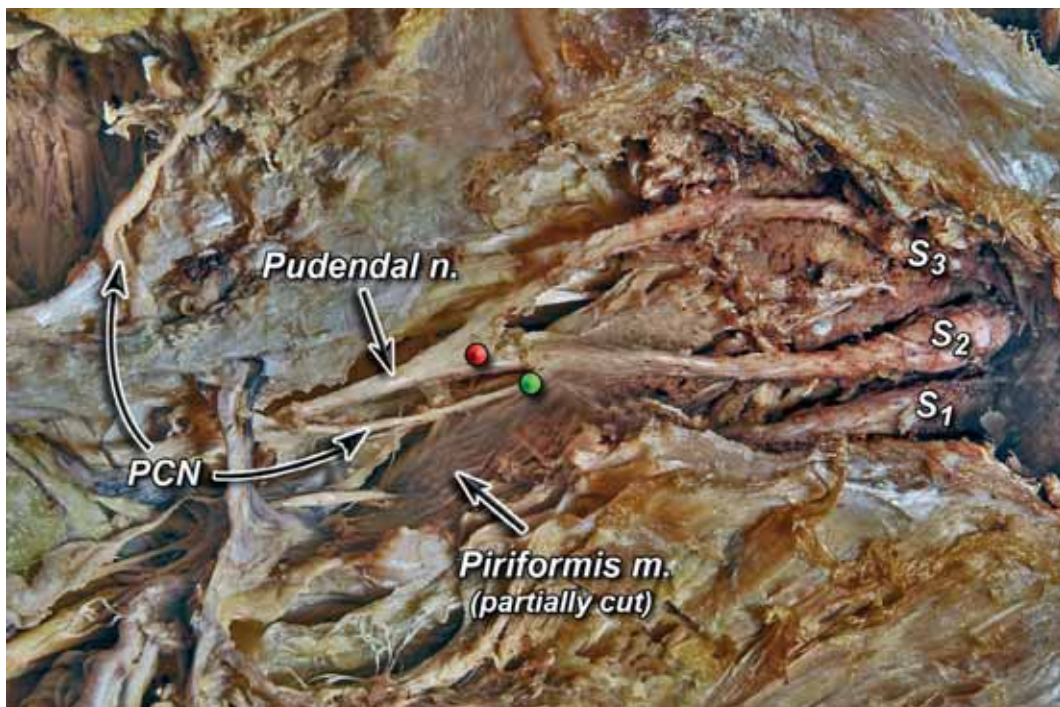


Figure 5. The sacrotuberous ligament perforated by the right perforating cutaneous nerve (PCN). This view shows the PCN above the pudental nerve. The green pin indicates the origin point of the PCN, while the red pin indicates the origin point of the pudental nerve; S₁ — the ventral branch of the first sacral nerve; S₂ — the ventral branch of the second sacral nerve; S₃ — the ventral branch of the third sacral nerve.

bilaterally (PCNs) (Figs. 4, 5). Furthermore, we detected a nerve perforating the left SSL in the female

cadaver. Its terminal nerve fibres reached the lateral wall of the rectum. From these observations and the

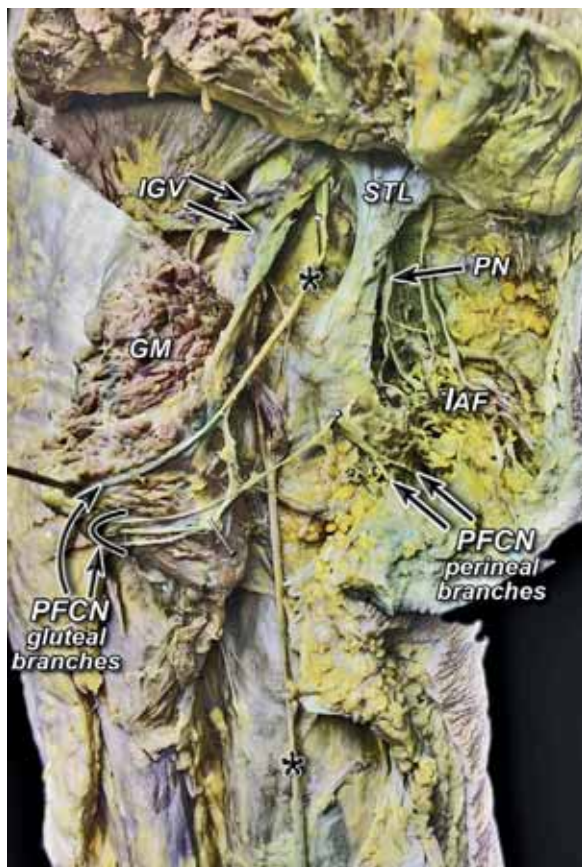


Figure 6. The posterior cutaneous nerve of the thigh with its gluteal and perineal branches; *the posterior cutaneous nerve of the thigh, also known as posterior femoral cutaneous nerve (PFCN); GM — gluteus maximus muscle; IAF — ischioanal fossa; IGV — inferior gluteal vessels; PN — pudendal nerve; STL — sacrotuberous ligament.

classification of the PN in relation to the number of its trunks [6], we concluded that the aforementioned nerve is the IRN (Fig. 4). Considering the specimen with no PCN/perforating of the STL nerves, replacement nerve fibres with the same sensory innervation were found (Fig. 6). These were the gluteal branches from the posterior cutaneous nerve of the thigh.

Our findings show that the PCN/perforating of the STL nerve can arise independently from the ventral branch of the S2 (PCN) or from the PN (perforating of the STL nerve). In 2 cases the nerves arose from the SP (Figs. 4, 5), in 1 case from the PN. In the specimen where the perforating of the STL nerve began as a branch of the PN, the distance between its point of origin and the highest place where the nerve was exposed was 22.38 mm. This means that the perforating of the STL nerve arose at least 22.38 mm lower than if the PCN had arisen independently from the SP. The origin point of the STL, when it arises from the

PN, is located between the SSL and the STL, which is important as it is the most common location of stricture in pudendal neuralgia cases. The median distance between the point where the PCN/perforating of the STL nerve arose, in the SP and the point of origin of the PN was 9.38 mm (range: 7.73–11.03 mm).

The width of the PCN/perforating of the STL nerve at any point ranges from 0.8 mm to 1.65 mm (median 1.10 mm). Thus, the PCN is 2.0–4.6 times thinner than the PN.

We distinguished two courses for the PCN/perforating of the STL nerve: one is characteristic of the perforating of the STL nerve as a PN branch and the other of nerves arising from the SP. Conventionally, the course of the PCN/perforating of the STL nerve can be divided into three parts: the part before perforation, the perforating part and the part after perforation.

The part of the perforating of the STL nerve before perforation is relatively short. It begins from lateral area of the PN, crosses this nerve posteriorly and almost immediately perforates the inferior part of STL at its superolateral border. If the PCN arises from the SP, the aforementioned part of the nerve is considerably longer. In that case the PCN begins from the lateral or posterior area of the ventral branch of S2, first accompanying it and subsequently also the PN, later lying medially or laterally to those structures. About halfway from the point of perforation of the STL, the PCN runs obliquely toward the medial side. If the PCN arises from the posterior area, it does not cross the PN but runs between the PN and IRN (medially of the PN and laterally of the IRN) and perforates the STL near the surface of the SSL. However, if it arises from the lateral area, the PCN crosses the PN posteriorly and perforates the STL perpendicular to the course of its fibres.

Regarding the perforating part of the PCN/perforating of the STL nerve, it is important to identify the topographical relationship of the nerve to the ligament. Since the PCN/perforating of the STL nerve perforates the ligament completely differently in different cases, it is essential to discuss each case individually.

The STL perforated by the right perforating of the STL nerve (Fig. 3)

The median length of the perforating of the STL nerve from its departure point to the point of perforation was 19.95 mm. The median length of the STL from the point of perforation to its ischial attachment was 16.02 mm, whereas its median length from the point

of perforation to the sacral attachment was 65.03 mm. The median width of the STL fibre, which lay laterally from the point of perforation, was 3.08 mm, while the median width of the medial STL fibre was 8.72 mm. After the length and width relationships were calculated, it was concluded that the perforating of the STL nerve perforates the STL around 1/5 lower and 1/3 of its lateral part. The nerve formed a visible fissure, which was 22.75 mm long, about 2/7 of the total length of the ligament.

The STL perforated by the left PCN (Fig. 4)

The median length of the PCN from its departure point to the point of perforation was 43.37 mm. The perforation of the STL differed significantly from the one mentioned above. In the former case, the PCN perforated the ligament from front to back, ran through its entire thickness and left a fissure. In the present case, the PCN perforated the ligament vertically, from the top down, entered between its fibres at the superolateral border and ran through its entire width, exiting from its inferomedial border. The PCN did not form a fissure, but "hid" in the ligament forming a canal. It follows from the above that there was no single point of perforation, but rather two: the entry and exit points from the ligament. The total median length of the STL was 69.55 mm. The entry and the exit points were approximately half-way along the STL, and were almost symmetrically located in relation to its midpoint with a deviation about 8–9 mm. The median length of the STL from the entry point to its sacral attachment was 25.96 mm; its median length from the exit point to its ischial attachment was 26.78 mm. There are respectively 8.81 and 7.99 mm of the distance from the midpoint of the STL (34.77 mm) to the points mentioned above.

The STL perforated by the right PCN (Fig. 5)

The median length of the PCN from its departure point to the point of perforation was 42.39 mm, which is about 0.1 cm less than in the aforementioned case of the nerve in the left buttock. Like, the left PCN, the right PCN perforated the ligament in an inferomedial direction and entered between its fibres at superolateral border. The difference between the courses of these nerves was that in this case the PCN did not pass through the entire width of the STL but exited it at a point roughly corresponding to half its width. It is worth mentioning that in this case the entry and exit points of the nerve were at the same

level in relation to the STL length, in contrast to the left PCN. The total median length of the STL was 64.36 mm. The median length of the STL from the entry and exit points to its sacral attachment was 26.07 mm; its median length from the entry and exit points to its ischial attachment was 38.29 mm. Thus, the PCN perforated the STL at about 2/5 of its upper part.

In summary, the PCN/perforating of the STL nerve can perforate any part of the STL (lower, middle or upper) in the posterior or inferomedial direction by forming a fissure or canal, which may or may not pass the full width of the ligament.

Regarding the part of the PCN after the perforation, the perforating of the STL nerve runs differently from the other two PCNs. After the perforation, it runs on the posterior surface of the STL, heads downwards and medially, crosses the STL attachment to the ischial tuberosity and subsequently runs between the inferior ramus of the ischium and the ischioanal fossa posterior to pudendal canal. Finally, it turns in an anteromedial direction to enter the ischioanal fossa. It is divided into terminal branches that extend to the adipose tissue of the skin and provide sensory innervation to the inferomedial area of the buttock. Moreover, it is possible that the perforating of the STL nerve along with the perineal nerves can innervate a medial area of the perineal skin, since its terminal branches head in that direction. The total median length of the perforating of the STL nerve that arises from the PN is 97.75 mm. The total length of the PCNs, that arise from the ventral branches of the S2 ranges from 82.16 to 84.32 mm. After the perforation, the aforementioned nerves are divided into terminal branches, which enter between the gluteal maximus muscle and the adipose tissue of the skin and subsequently provide sensory innervation to the inferomedial area of the buttock. However, these branches do not reach the anterior area of the perineal skin. It is worth noting that the mentioned innervation area is similar to the one described by Florian-Rodriguez et al. (2016) [3].

All measurements of the PCN/perforating of the STL nerve are presented in Table 1 and the characteristic traits of its course in Table 2.

DISCUSSION

The limitation of our study is the insufficient information about PCN/perforating of the STL nerve anatomy in reports in the literature. Nevertheless, our findings correlate with most of the information about the topic in various sources.

Table 1. Measurements of the perforating cutaneous nerve (PCN)/perforating of the sacrotuberous ligament (STL) nerve

Measure	The right perforating of the STL nerve (Fig. 2)	The left PCN (Fig. 3)	The right PCN (Fig. 4)
The origin point of the nerve in relation to the origin point of the pudendal nerve	At least 22.38 mm below	7.73 mm above	11.03 mm above
The width of the nerve	1.65 mm	0.8 mm	0.87 mm
The median length of the nerve from its departure point to the perforation point	19.95 mm	43.37 mm	42.39 mm
The total length of the nerve	97.75 mm	84.32 mm	82.16 mm

Table 2. The characteristic traits of the perforating cutaneous nerve (PCN)/perforating of the sacrotuberous ligament (STL) nerve course

Trait	The right perforating of the STL nerve (Fig. 2)	The left PCN (Fig. 3)	The right PCN (Fig. 4)
Does the nerve cross the pudendal nerve?	Yes	No	Yes
The direction of the perforation	Posterior direction with forming a fissure	Lower-medial direction with forming a canal	Lower-medial direction with forming a canal
The perforation point	1/5 lower and 1/3 of STL lateral part	Halfway point of the length of the STL	2/5 of STL upper part
The innervation area	Lower-medial area of the buttock and a medial area of the perineal skin	Lower-medial area of the buttock	Lower-medial area of the buttock

Table 3. Difference between publication data and our findings concerning the perforating cutaneous nerve (PCN)/perforating of the sacrotuberous ligament (STL) nerve anatomy

	Publication data	Our findings
The presence of the PCN/perforating of the STL nerve	As a separate unit from S2/S3 with perforation the STL From the pudendal nerve with perforation the STL As a separate unit from S2/S3 without perforation the STL	As a separate unit from S2/S3 with perforation the STL From the pudendal nerve with perforation the STL
The absence of the PCN/perforating of the STL nerve	Gluteal branches of the posterior cutaneous nerve of the thigh (the inferior cluneal nerves) Perforans coccygeus major nerve	Gluteal branches of the posterior cutaneous nerve of the thigh (the inferior cluneal nerves)

First of all, it is worth mentioning that naming of the PCN, which occur in English-language literature, is non-uniform. For example, Tubbs et al. [10] mention the inferior medial cluneal nerve, which is associated with its innervation area. It is also interesting that if this nerve is absent, it is replaced by gluteal branches of the posterior cutaneous nerve of the thigh (Fig. 6). There are reports that the perforans coccygeus major nerve can also replace the PCN, but our findings did not confirm this [10].

Eisler [see 10] found the PCN as a separate unit 22 times in 34 plexuses. He also noted that the PCN can arise from the PN and perforate the STL; this was found three times in the 34 plexuses. Moreover, there are reported cases wherein the PCN does not perforate the STL, instead arising independently from ventral branches of the S2-S3 spinal nerves. If the PCN does not perforate the STL, it will follow the same course as the PN (Table 3) [2, 10].

There is no reliable information about the prevalence of the PCN. Our findings show that it occurred in 25% (3/12) of the plexuses examined. Two of the three aforementioned anatomical variations were found during our study. The predominant type (66.6%; 2/3) was the independently arising PCN; in 33.3% the PCN arose as a branch of the PN. In 16.6% (2/12) of the examined plexuses, which had no PCN, there were inferior medialis cluneal nerves (Fig. 6). Another limitation of our study is the fact that not all anatomical variations of the PCN were noted, probably because of the small number of cadavers examined. There is a high probability that the findings would have differed if more plexuses had been studied.

In the studies by Ploteau et al. (2017) [9], the transligamentous course of the PN was mentioned in patients with pudendal neuralgia. It is possible that such a course predisposes to the development of this disease. There were no reports of transliga-

mentous branches arising from the PN. It is worth mentioning that the target group in this study was quite limited, including only people with pudendal neuralgia, and the symptoms associated with the transligamentous passing of the PN are so rare (5% of nerves including 3% of perforating the STL) that we found no cases [8, 9]. The most common location of entrapment of the nerve in patients with pudendal neuralgia is in the space between the SSL and the STL (74%). It is most often caused by anatomical variants of the STL and the invasion of ligament fibres into this area. The aforementioned space is a place where the PCN can arise from the PN. Commonly, PN decompression-transposition surgery is performed through the transgluteal approach to ensure constant visual control of all nerves from the gluteal area with a transligamentous course (the PCN perforating the STL, the PN perforating the SSL or STL and the IRN perforating the SSL) [9]. It is worth mentioning that the IRN pierces the SSL in 11% of the population [6].

There are also reports of PN and PCN injury as a complication following vaginal prolapse repair surgery. Sensory loss results from entrapment of the neural structures by the sutures after cystocele repair surgery. The symptoms concern the skin innervated by the PCN [2].

Florian-Rodriguez et al. [3] marked previously unidentified branches, which are present in 85% of cases (14 female cadavers). These branches follow different courses from the PCN, but they have the same innervation area. They arise from ventral branches of the S3 or/and S4 sacral nerves and are not associated with the PN or the IRN. Subsequently, they pierce the adipose tissue of the ischioanal fossa (S4 branch) or the inferior border of the gluteus maximus muscle (S3 branch). The branch from S4 passes between the SSL and the STL without perforating, whereas the branch from S3 perforates the STL. It was concluded that these nerves can be an anatomical variation of the PCN [3, 10].

CONCLUSIONS

The PCN/perforating of the STL nerve is a neural structure that does not always occur, but anatomical knowledge of it is very useful owing to its location. Considering the topographical relationships of the STL, SSL and PCN/perforating of the STL nerve, this nerve is often injured for a variety of reasons. Neuralgia is limited mainly to the inferomedial area of the buttock. Anatomical knowledge of the PCN/perforating of the STL nerve facilitates differentiation from PN neuralgia and helps in making a correct diagnosis.

In addition, it is worth remembering that in surgical practice the STL is tightly connected to the PCN/perforating of the STL nerve, so special care is needed before dissection of the area near the ligament.

Acknowledgements

The authors sincerely thank those who donated their bodies to science so that anatomical research could be performed. Results from such research can potentially increase mankind's overall knowledge that can then improve patient care. Therefore, these donors and their families deserve our highest gratitude [5].

Also, we acknowledge Jacenty Urbaniak from the Anatomy Department of the Jagiellonian University Medical College for excellent technical assistance during preparation of the figures used in this manuscript.

Conflict of interest: None declared

REFERENCES

1. Bochenek A, Reicher M. Anatomia człowieka. Tom V. Wydawnictwo Lekarskie PZWL, Warszawa 2008.
2. Bohrer JC, Chen CC, Walters MD. Pudendal neuropathy involving the perforating cutaneous nerve after cystocele repair with graft. *Obstet Gynecol.* 2008; 112(2 Pt 2): 496–498, doi: [10.1097/AOG.0b013e31817f19b8](https://doi.org/10.1097/AOG.0b013e31817f19b8), indexed in Pubmed: [18669778](https://pubmed.ncbi.nlm.nih.gov/18669778/).
3. Florian-Rodriguez ME, Hare A, Chin K, et al. Inferior gluteal and other nerves associated with sacrospinous ligament: a cadaver study. *Am J Obstet Gynecol.* 2016; 215(5): 646.e1–646.e6, doi: [10.1016/j.ajog.2016.06.025](https://doi.org/10.1016/j.ajog.2016.06.025), indexed in Pubmed: [27343565](https://pubmed.ncbi.nlm.nih.gov/27343565/).
4. Gray H. Anatomy of the human body. Bartley.com 2000.
5. Iwanaga J, Singh V, Takeda S, et al. Acknowledging the use of human cadaveric tissues in research papers: Recommendations from anatomical journal editors. *Clin Anat.* 2021; 34(1): 2–4, doi: [10.1002/ca.23671](https://doi.org/10.1002/ca.23671), indexed in Pubmed: [32808702](https://pubmed.ncbi.nlm.nih.gov/32808702/).
6. Mahakkanukrauh P, Surin P, Vaidhayakarn P. Anatomical study of the pudendal nerve adjacent to the sacrospinous ligament. *Clin Anat.* 2005; 18(3): 200–205, doi: [10.1002/ca.20084](https://doi.org/10.1002/ca.20084), indexed in Pubmed: [15768420](https://pubmed.ncbi.nlm.nih.gov/15768420/).
7. Montoya TI, Calver L, Carrick KS, et al. Anatomic relationships of the pudendal nerve branches. *Am J Obstet Gynecol.* 2011; 205(5): 504.e1–504.e5, doi: [10.1016/j.ajog.2011.07.014](https://doi.org/10.1016/j.ajog.2011.07.014), indexed in Pubmed: [21889763](https://pubmed.ncbi.nlm.nih.gov/21889763/).
8. Pirro N, Sielezneff I, Le Corroller T, et al. Surgical anatomy of the extrapelvic part of the pudendal nerve and its applications for clinical practice. *Surg Radiol Anat.* 2009; 31(10): 769–773, doi: [10.1007/s00276-009-0518-7](https://doi.org/10.1007/s00276-009-0518-7), indexed in Pubmed: [19495555](https://pubmed.ncbi.nlm.nih.gov/19495555/).
9. Ploteau S, Perrouin-Verbe MA, Labat JJ. Anatomical variants of the pudendal nerve observed during a transgluteal surgical approach in a population of patients with pudendal neuralgia. *Pain Physician.* 2017; 20(1): E137–E143, doi: [10.36076/2017.1.e137](https://doi.org/10.36076/2017.1.e137).
10. Tubbs RS, Iwanaga J, Loukas M, Dumont AS, Reina MA. Surgical anatomy of the sacral plexus and its branches. Elsevier, Philadelphia 2021.

Are the nerves supplying the anterior sacroiliac joint nociceptive?

E. Yilmaz¹, A.V. D'Antoni², Ł. Olewnik³, J. Iwanaga^{4–6}, T. Saga⁷, M. Loukas⁸, R.S. Tubbs^{4, 5, 8–11}

¹Department of Trauma Surgery, BG University Hospital Bergmannsheil, Ruhr University Bochum, Bürkle-de-la-Camp-Platz, Bochum, Germany

²Wagner College, Staten Island, New York and Division of Anatomy, Department of Radiology, Weill Cornell Medicine, New York, NY, United States

³Department of Anatomical Dissection and Donation, Medical University of Lodz, Poland

⁴Department of Neurology, Tulane University School of Medicine, New Orleans, LA, United States

⁵Department of Neurosurgery, Tulane University School of Medicine, New Orleans, LA, United States

⁶Division of Gross and Clinical Anatomy, Department of Anatomy, Kurume University School of Medicine, Kurume, Fukuoka, Japan

⁷Domain of Anatomy, Kurume University School of Nursing, Kurume, Fukuoka, Japan

⁸Department of Anatomical Sciences, St. George's University, St. George's, Grenada, West Indies

⁹Department of Structural and Cellular Biology, Tulane University School of Medicine, New Orleans, LA, United States

¹⁰Department of Surgery, Tulane University School of Medicine, New Orleans, LA, United States

¹¹Department of Neurosurgery and Ochsner Neuroscience Institute, Ochsner Health System, New Orleans, LA, United States

[Received: 20 December 2021; Accepted: 5 January 2022; Early publication date: 31 January 2022]

Background: Sacroiliac joint (SIJ) pain is often difficult to diagnose. Moreover, while its anatomical characteristics have been well studied, its innervation and the contributions of particular nerves remain controversial, especially in relation to posterior joint innervation. To our knowledge, previous studies have not investigated the presence of nociceptive fibres in the nerves innervating the anterior SIJ. *Materials and methods:* Eight adult cadaveric sides underwent dissection of the anterior SIJ. Adjacent anterior rami were examined for branches to the anterior SIJ. Any branches contributing to the anterior SIJ were measured and then resected. These samples were fixed in formalin and substance P was identified immunohistologically.

Results: On all sides, 1–2 small branches (mean diameter of 0.33 mm) arose from the posterior aspect of the L4 anterior ramus (12.5%), the L5 anterior ramus (62.5%), or simultaneously from both the L4 and L5 anterior rami (25%). These branches had a mean length of 13.5 mm. All histological samples contained nerve tissue. All samples of nerve fibres traveling to the anterior SIJ were positive for diffuse substance P reactivity. There were no histological differences between sides or sex. Each of the branches identified as travelling to the SIJ exhibited similar positivity for substance P.

Conclusions: This cadaveric study demonstrates that the anterior SIJ nerve fibres carry pain fibres. This new knowledge has application to patients with SIJ syndrome and to its various treatments including interventional approaches to SIJ pain. (Folia Morphol 2023; 82, 1: 96–101)

Key words: back pain, sacroiliac joint pain, syndrome, innervation

Address for correspondence: J. Iwanaga, DDS, PhD, Department of Neurosurgery, Tulane Centre for Clinical Neurosciences, Tulane University School of Medicine, 131 S. Robertson St. Suite 1300, New Orleans, LA 70112, United States, tel: 5049885565, fax: 5049885793, e-mail: iwanagajoeca@gmail.com

This article is available in open access under Creative Common Attribution-Non-Commercial-No Derivatives 4.0 International (CC BY-NC-ND 4.0) license, allowing to download articles and share them with others as long as they credit the authors and the publisher, but without permission to change them in any way or use them commercially.

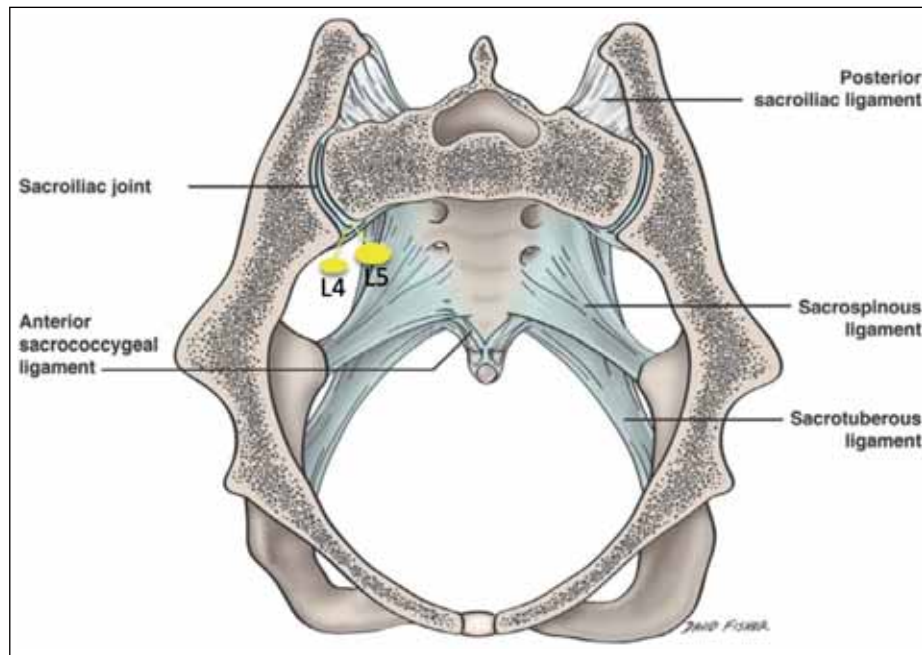


Figure 1. Superior view of the sacroiliac (SI) joint and related ligaments showing contributions from the L4 and L5 anterior rami to SI joint.

INTRODUCTION

The sacroiliac joint (SIJ) connects the sacrum to the ilium and transfers the weight from the spine to the lower extremities. While its anatomical characteristics have been well studied, SIJ innervation and the contributions of particular nerves remain controversial [6]. The SIJ has been identified as a potential cause of low back pain (LBP), and joint degeneration has been shown to be age-related and highly prevalent even in asymptomatic patients [7]. Recently, research on the SIJ as a cause and target of low back pain has intensified. The reported prevalence of SIJ dysfunction as a cause of LBP varies from 15% to 36% [6, 29]. SIJ-related pain is difficult to diagnose, and several different clinical tests and diagnostic blocks are used to confirm a diagnosis [11]. The clinical symptoms range from buttock pain, with or without extension to the posterolateral thigh, to pain in the area of the posterior inferior iliac spine, to lumbar pain, to pain radiating into the groin. There is no real consensus on how to diagnose SIJ-related pain [16, 17, 26, 30]. Furthermore, most clinical tests of the SIJ are limited in their validity and reliability [33]. Therefore, SIJ pain scores have been developed to corroborate a diagnosis. Kurosawa et al. [25] described a score using the following criteria: one-finger test, groin pain, pain while sitting on a chair, SIJ shear test, tenderness of the posterosuperior iliac spine, and tenderness of the sacrotuberous ligament. This score has proven effective

for differentiating SIJ pain from any other cause of buttock pain, and provides moderate accuracy in diagnosing it [35].

Several different treatments such as physical therapy, nerve blocks, steroid injections, denervation, and ablation have been described. Treatment success ranges from 30% to 85% [6]. However, since SIJ innervation is still not fully understood, we recently studied the nerve contribution to the anterior SIJ. Previously, we demonstrated that the vast majority of nerve contributions to the anterior SIJ arise from the anterior rami of L4 or L5 (Fig. 1) [7]. However, to the best of our knowledge, there has been no immunohistological analysis of the fibre type in these branches [2, 27, 32, 36]. Therefore, the purpose of this study was to identify the fibre type of the nerve branches supplying the anterior SIJ using immunohistochemistry.

MATERIALS AND METHODS

We dissected 4 fresh-frozen cadavers (8 sides) for this study. The age at death ranged from 67 to 98 years (mean 75 years). Two cadavers were male and two were female. The cadavers were positioned supine and a midline incision was made from the xiphoid process to the pubic symphysis. We split the linea alba from the subjacent peritoneum. The greater omentum was lifted upwards and the intestines and mesentery were retracted. After the

retroperitoneal space had been carefully opened, the fascia was removed and the psoas major muscle was identified. Next, the lumbar plexus was visualised by retracting the muscle laterally. Using a surgical microscope (OPMI CS NC31, Carl Zeiss, Germany), we identified the lower lumbar anterior rami (e.g., L4, L5) and upper sacral anterior rami (e.g., S1) and the anterior SIJ. Any branches contributing to the anterior SIJ were measured with microcallipers (Mitutoyo, Japan). These samples were fixed in formalin and substance P was identified immunohistologically. Substance P is found in primary sensory neurons; it is a NK1 receptor agonist and belongs to the tachykinin group, which is released in response to noxious stimuli [30].

Tissue preparation

The specimens were fixed by immersion in 0.1 M phosphate-buffered 4% formaldehyde at 4°C. The samples were cryoprotected with 30% sucrose in phosphate buffer containing 0.9% sodium chloride supplemented with 0.15% sodium azide and were then sectioned at 50 μ m intervals. The sections were stored at 4°C pending processing. Following blocking (suppression of non-specific staining) with 2.5% normal horse serum, the sections were incubated with anti-rabbit substance P (Millipore Sigma, Burlington, MA; dilution 1:1000). Following incubation, sections were rinsed with TRIS-HCl buffer, pH 7.6, and treated with 3,3'-diamino-benzidine until the desired colour intensity was reached. Slides were mounted and allowed to dry at room temperature. Once cover-slipped, the slides were examined under a light microscope and representative images photographed.

Statistical analysis between sides and sex was performed using Student t-tests with statistical significance set at $p < 0.05$.

RESULTS

On all sides, 1–2 small branches (Fig. 2) ranging in diameter from 0.28 to 0.47 mm (mean 0.33 mm) arose from the posterior aspect of the L4 anterior ramus ($n = 1$; 12.5%), the L5 anterior ramus ($n = 5$; 62.5%), or simultaneously from both the L4 and L5 anterior rami ($n = 2$; 25%). These branches ranged from 7 mm to 38 mm long (mean 13.5 mm). All histological samples were consistent with nerve tissue. No specimen showed any gross evidence of pathology or previous surgery in the areas dissected. All samples of

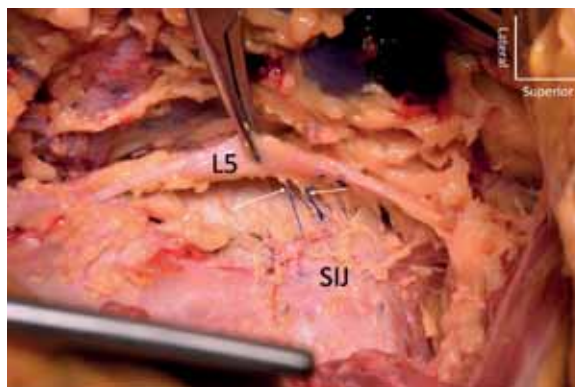


Figure 2. Cadaveric dissection of the left sacroiliac joint (SIJ) and related nerve lumbar anterior rami branches (arrows) to the SIJ.

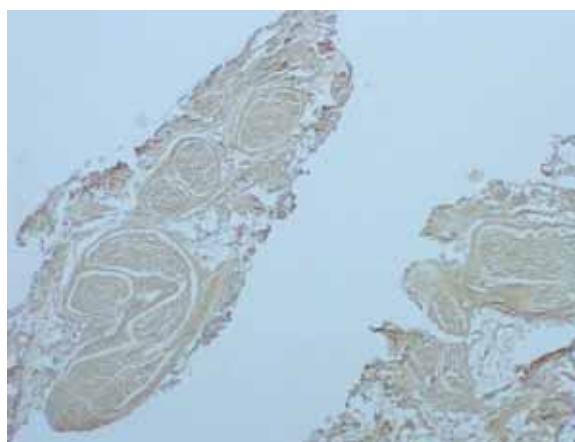


Figure 3. Histological section of two selected sacroiliac joint nerve branches noting positive reactivity for substance P (40 \times).

nerve fibres travelling to the anterior SIJ were positive for substance P (Fig. 3). There were no histological differences or statistical significance between sides or sex. Each of the branches identified as travelling to the SIJ exhibited similar diffuse positivity for substance P. All controls reacted appropriately.

DISCUSSION

The SIJ is a complex and biomechanically little-understood irregularly-shaped joint. According to Jesse et al. [22], three different surface shapes can be distinguished depending on the alpha angle. The SIJ is important in weight-bearing, load transfer and the structural stability of the pelvic girdle, which is provided mainly by the posterior sacroiliac complex ligaments forming the appearance of a suspension bridge [34]. SIJ pain can result from injury to or loosening of the ligamentous complex after trauma or inflammation [23, 24]. Minor movements resulting in

collisions between the articulating surfaces can also regenerate pain [37].

However, innervation of the SIJ is still little understood. It is mostly accepted that the innervation derives from the anterior rami of L4, L5 and the posterior rami of L5-S3 [14, 15]. Ferrante et al. [13] were the first to report radiofrequency ablation to treat SIJ-related pain. They showed that radiofrequency ablation can significantly reduce pain even though only 36% of their patients met the criterion of at least a 50% decrease in the visual analogue pain scale. They denervated the joint by inserting three electrodes at 90° starting at the inferior anterior margin and placing the two other more cephalad at 1 cm distances [13]. Cheng et al. [3] described a modified technique with bipolar radiofrequency by placing a continuous straight strip lesion laterally to the sacral foramina in order to denervate the L5, S1, S2 and S3 posterior rami. They observed a significantly higher rate of pain reduction (> 50%) than with cooled radiofrequency [3]. A randomized prospective study by Dutta et al. [11] compared patients who underwent intraarticular methylprednisolone (n = 15) with those who underwent pulsed radiofrequency (PRF) treatment (n = 15) of the L4 medial branch, L5 posterior rami and the lateral sacral branches. Patients in the PRF group showed more significant pain relief and functional improvement than those in the intraarticular methylprednisolone group [11]. Vallejo et al. [38] reported 22 patients undergoing pulsed radiofrequency of the medial branch of L4, the posterior rami of L5, and the lateral branches of S1 and S2. Sixteen (72.7%) patients reported a "good" result (pain relief > 50% in VAS). However, the duration of pain relief ranged from only 6 to 32 weeks [38]. Ding et al. [8] reported overall efficiencies of 56.3% conventional radiofrequency (CRF) and 31.3% pulsed radiofrequency (PRF) using a continuous lesion lateral to the S1-S3 foramina. Gevargez et al. [18] achieved similar results using computed tomography-guided intervention in 43 patients by applying CRF to the posterior rami of the L5 nerve and to the posterior interosseous sacroiliac ligaments. Significant pain relief was experienced by 31.6% of the patients. Cohen et al. [4] found negative correlations between age, duration of symptoms, and outcome. Patients were subjected to radiofrequency ablation of the L4-L5 posterior rami and S1-S3 lateral branches. Fifty-two per cent were considered successfully treated (pain reduction > 50% for at least 6 months) [4]. Interestingly, van Tilburg et al. [39]

could not reject the hypothesis that there is no difference in pain reduction between patients who underwent radiofrequency ablation of the S1-S4 nerve root lateral branches and L5 posterior branch and patients in the placebo-treatment group. They found 42.1% pain reduction in both groups [39].

The SIJ is closely related to the lumbosacral plexus, and while the posterior SIJ is supplied by the lateral branches of the L3/L4-S3 posterior rami, the anterior joint has been said to be innervated by L2-S2 [6]. However, our more recent cadaveric study narrowed this range to L4 and L5 anterior rami and the findings of the present study support these earlier findings. A randomised placebo-controlled trial with 28 patients by Cohen et al. [5] showed that L4 and L5 posterior rami and S1-S3 lateral branch denervation can lead to pain relief and a functional benefit for up to 6 months post-procedure in selected patients. Different rates of success in pain relief have been reported for radiofrequency ablation, which could be related to the different techniques used, including different denervation processes, locations and targeted nerve branches [1].

Specialised peripheral sensory neurons (nociceptors) detect noxious stimuli and mediate pain [10]. Nociceptive fibres are classified according to their sensitivity to heat, cold and noxious mechanical stimuli. Most nociceptors have unmyelinated axons (C-fibres) with small diameter, which is directly correlated with the transmission speed. In contrast, initial 'fast-onset' pain is mediated not by C-fibres, but by A-fibres with myelinated axons [9]. Debate about innervation of the SIJ continues. However, several studies support the assumption that nociceptive signals originate directly from the SIJ. A histological study of neural elements of the human SIJ (n = 6) by Vilensky et al. [40] revealed mechanoreceptors, nerves and nerve fascicles. Grob et al. [19] found myelinated and unmyelinated fibres in the joint. Ikeda et al. [20] reported nerve diameters ranging from 0.2 to 2.5 μm , which puts the nerve in the range of C- and A-delta fibres [37]. There are substance P and calcitonin gene-related polypeptide positive fibres, associated with nociception, in the SIJ and surrounding ligaments. Szadek et al. [32] revealed substance P and CGRP positive fibre-like structures in their cartilage tissue samples from 10 human cadavers. Sakamoto et al. [28] identified mechanosensitive afferent units in the SIJ and adjacent tissues.

Eno et al. [12] showed that SIJ degeneration is age-related and highly prevalent even in asymptot-

ic patients. Furthermore, Suri et al. [31] observed growth of neurovascular tissue in human knees with advanced osteoarthritis. Whether these results are associated with joint degeneration or are valid for non-degenerated SIJs has yet to be determined.

CONCLUSIONS

This cadaveric study demonstrates that the anterior SIJ nerve fibres carry pain fibres. This new knowledge has application to patients with SIJ syndrome and to its various treatments including interventional approaches to SIJ pain.

Acknowledgements

The authors sincerely thank those who donated their bodies to science so that anatomical research could be performed. Results from such research can potentially increase mankind's overall knowledge that can then improve patient care. Therefore, these donors and their families deserve our highest gratitude [21].

Conflict of interest: None declared

REFERENCES

- Aydin SM, Gharibo CG, Mehnert M, et al. The role of radiofrequency ablation for sacroiliac joint pain: a meta-analysis. *PM R*. 2010; 2(9): 842–851, doi: [10.1016/j.pmrj.2010.03.035](https://doi.org/10.1016/j.pmrj.2010.03.035), indexed in Pubmed: [20869684](https://pubmed.ncbi.nlm.nih.gov/20869684/).
- Castañeda-Corral G, Jimenez-Andrade JM, Bloom AP, et al. The majority of myelinated and unmyelinated sensory nerve fibers that innervate bone express the tropomyosin receptor kinase A. *Neuroscience*. 2011; 178: 196–207, doi: [10.1016/j.neuroscience.2011.01.039](https://doi.org/10.1016/j.neuroscience.2011.01.039), indexed in Pubmed: [21277945](https://pubmed.ncbi.nlm.nih.gov/21277945/).
- Cheng J, Chen SL, Zimmerman N, et al. A new radiofrequency ablation procedure to treat sacroiliac joint pain. *Pain Physician*. 2016; 19(8): 603–615, indexed in Pubmed: [27906939](https://pubmed.ncbi.nlm.nih.gov/27906939/).
- Cohen SP, Strassels SA, Kurihara C, et al. Outcome predictors for sacroiliac joint (lateral branch) radiofrequency denervation. *Reg Anesth Pain Med*. 2009; 34(3): 206–214, doi: [10.1097/AAP.0b013e3181958f4b](https://doi.org/10.1097/AAP.0b013e3181958f4b), indexed in Pubmed: [19587617](https://pubmed.ncbi.nlm.nih.gov/19587617/).
- Cohen SP, Hurley RW, Buckenmaier CC, et al. Randomized placebo-controlled study evaluating lateral branch radiofrequency denervation for sacroiliac joint pain. *Anesthesiology*. 2008; 109(2): 279–288, doi: [10.1097/ALN.0b013e31817f4c7c](https://doi.org/10.1097/ALN.0b013e31817f4c7c), indexed in Pubmed: [18648237](https://pubmed.ncbi.nlm.nih.gov/18648237/).
- Cohen SP, Chen Y, Neufeld NJ. Sacroiliac joint pain: a comprehensive review of epidemiology, diagnosis and treatment. *Expert Rev Neurother*. 2013; 13(1): 99–116, doi: [10.1586/ern.12.148](https://doi.org/10.1586/ern.12.148), indexed in Pubmed: [23253394](https://pubmed.ncbi.nlm.nih.gov/23253394/).
- Cox M, Ng G, Mashriqi F, et al. Innervation of the anterior sacroiliac joint. *World Neurosurg*. 2017; 107: 750–752, doi: [10.1016/j.wneu.2017.08.062](https://doi.org/10.1016/j.wneu.2017.08.062), indexed in Pubmed: [28838880](https://pubmed.ncbi.nlm.nih.gov/28838880/).
- Ding Y, Li H, Yao P, et al. Clinical observation of CT-guided intra-articular conventional radiofrequency and pulsed radiofrequency in the treatment of chronic sacroiliac joint pain. *J Pain Res*. 2018; 11: 2359–2366, doi: [10.2147/JPR.S179712](https://doi.org/10.2147/JPR.S179712), indexed in Pubmed: [30410388](https://pubmed.ncbi.nlm.nih.gov/30410388/).
- Djohri L, Lawson SN. Abeta-fiber nociceptive primary afferent neurons: a review of incidence and properties in relation to other afferent A-fiber neurons in mammals. *Brain Res Brain Res Rev*. 2004; 46(2): 131–145, doi: [10.1016/j.brainresrev.2004.07.015](https://doi.org/10.1016/j.brainresrev.2004.07.015), indexed in Pubmed: [15464202](https://pubmed.ncbi.nlm.nih.gov/15464202/).
- Dubin AE, Patapoutian A. Nociceptors: the sensors of the pain pathway. *J Clin Invest*. 2010; 120(11): 3760–3772, doi: [10.1172/JCI42843](https://doi.org/10.1172/JCI42843), indexed in Pubmed: [21041958](https://pubmed.ncbi.nlm.nih.gov/21041958/).
- Dutta K, Dey S, Bhattacharyya P, et al. Comparison of efficacy of lateral branch pulsed radiofrequency denervation and intraarticular depot methylprednisolone injection for sacroiliac joint pain. *Pain Physician*. 2018; 21(5): 489–496, indexed in Pubmed: [30282393](https://pubmed.ncbi.nlm.nih.gov/30282393/).
- Eno JJT, Boone CR, Bellino MJ, et al. The prevalence of sacroiliac joint degeneration in asymptomatic adults. *J Bone Joint Surg Am*. 2015; 97(11): 932–936, doi: [10.2106/JBJS.N.01101](https://doi.org/10.2106/JBJS.N.01101), indexed in Pubmed: [26041855](https://pubmed.ncbi.nlm.nih.gov/26041855/).
- Ferrante FM, King LF, Roche EA, et al. Radiofrequency sacroiliac joint denervation for sacroiliac syndrome. *Reg Anesth Pain Med*. 2001; 26(2): 137–142, doi: [10.1053/rapm.2001.21739](https://doi.org/10.1053/rapm.2001.21739), indexed in Pubmed: [11251137](https://pubmed.ncbi.nlm.nih.gov/11251137/).
- Forst SL, Wheeler MT, Fortin JD, et al. The sacroiliac joint: anatomy, physiology and clinical significance. *Pain Physician*. 2006; 9(1): 61–67, indexed in Pubmed: [16700283](https://pubmed.ncbi.nlm.nih.gov/16700283/).
- Vilensky JA, O'Connor BL, Fortin JD, et al. Sacroiliac joint innervation and pain. *Am J Orthop (Belle Mead NJ)*. 1999; 28(12): 687–690, indexed in Pubmed: [10614759](https://pubmed.ncbi.nlm.nih.gov/10614759/).
- Fortin JD, Dwyer AP, West S, et al. Sacroiliac joint: pain referral maps upon applying a new injection/arthrography technique. Part I: Asymptomatic volunteers. *Spine (Phila Pa 1976)*. 1994; 19(13): 1475–1482, indexed in Pubmed: [7939978](https://pubmed.ncbi.nlm.nih.gov/7939978/).
- Fortin JD, Aprill CN, Ponthieux B, et al. Sacroiliac joint: pain referral maps upon applying a new injection/arthrography technique. Part II: Clinical evaluation. *Spine (Phila Pa 1976)*. 1994; 19(13): 1483–1489, indexed in Pubmed: [7939979](https://pubmed.ncbi.nlm.nih.gov/7939979/).
- Gevargez A, Groenemeyer D, Schirp S, et al. CT-guided percutaneous radiofrequency denervation of the sacroiliac joint. *Eur Radiol*. 2002; 12(6): 1360–1365, doi: [10.1007/s00330-001-1257-2](https://doi.org/10.1007/s00330-001-1257-2), indexed in Pubmed: [12042940](https://pubmed.ncbi.nlm.nih.gov/12042940/).
- Grob KR, Neuhuber WL, Kissling RO. [Innervation of the sacroiliac joint of the human]. *Z Rheumatol*. 1995; 54(2): 117–122, indexed in Pubmed: [7793158](https://pubmed.ncbi.nlm.nih.gov/7793158/).
- Ikeda R. [Innervation of the sacroiliac joint. Macroscopical and histological studies]. *Nihon Ika Daigaku Zasshi*. 1991; 58(5): 587–596, doi: [10.1272/jnms1923.58.587](https://doi.org/10.1272/jnms1923.58.587), indexed in Pubmed: [1744230](https://pubmed.ncbi.nlm.nih.gov/1744230/).
- Iwanaga J, Singh V, Ohtsuka A, et al. Acknowledging the use of human cadaveric tissues in research papers: recommendations from anatomical journal editors. *Clin Anat*. 2021; 34(1): 2–4, doi: [10.1002/ca.23671](https://doi.org/10.1002/ca.23671), indexed in Pubmed: [32808702](https://pubmed.ncbi.nlm.nih.gov/32808702/).
- Jesse MK, Kleck C, Williams A, et al. 3D morphometric analysis of normal sacroiliac joints: a new classification of

- surface shape variation and the potential implications in pain syndromes. *Pain Physician*. 2017; 20(5): E701–E709, indexed in Pubmed: [28727714](#).
23. Kim YH, Yao Z, Kim K, et al. Quantitative investigation of ligament strains during physical tests for sacroiliac joint pain using finite element analysis. *Man Ther*. 2014; 19(3): 235–241, doi: [10.1016/j.math.2013.11.003](#), indexed in Pubmed: [24378472](#).
 24. Kloppers FJ, van der Merwe JF, van Zyl AA. Sacroiliac screw versus locking square plate fixation in sacroiliac joint disruption on composite bone models: a descriptive comparative biomechanical study. *Transl Res Anat*. 2022; 26: 100156, doi: [10.1016/j.tria.2021.100156](#).
 25. Kurosawa D, Murakami E, Ozawa H, et al. A diagnostic scoring system for sacroiliac joint pain originating from the posterior ligament. *Pain Med*. 2017; 18(2): 228–238, doi: [10.1093/pm/pnw117](#), indexed in Pubmed: [28204687](#).
 26. Murakami E, Aizawa T, Noguchi K, et al. Diagram specific to sacroiliac joint pain site indicated by one-finger test. *J Orthop Sci*. 2008; 13(6): 492–497, doi: [10.1007/s00776-008-1280-0](#), indexed in Pubmed: [19089535](#).
 27. Ruscheweyh R, Forsthuber L, Schoffnegger D, et al. Modification of classical neurochemical markers in identified primary afferent neurons with Abeta-, Adelta-, and C-fibers after chronic constriction injury in mice. *J Comp Neurol*. 2007; 502(2): 325–336, doi: [10.1002/cne.21311](#), indexed in Pubmed: [17348016](#).
 28. Sakamoto N, Yamashita T, Takebayashi T, et al. An electrophysiologic study of mechanoreceptors in the sacroiliac joint and adjacent tissues. *Spine (Phila Pa 1976)*. 2001; 26(20): E468–E471, doi: [10.1097/00007632-200110150-00008](#), indexed in Pubmed: [11598526](#).
 29. Simopoulos TT, Manchikanti L, Gupta S, et al. A systematic evaluation of the therapeutic effectiveness of sacroiliac joint interventions. *Pain Physician*. 2012; 15(3): E247–E278, indexed in Pubmed: [22622913](#).
 30. Slipman CW, Jackson HB, Lipetz JS, et al. Sacroiliac joint pain referral zones. *Arch Phys Med Rehabil*. 2000; 81(3): 334–338, doi: [10.1016/s0003-9993\(00\)90080-7](#), indexed in Pubmed: [10724079](#).
 31. Suri S, Gill SE, Massena de Camin S, et al. Neurovascular invasion at the osteochondral junction and in osteophytes in osteoarthritis. *Ann Rheum Dis*. 2007; 66(11): 1423–1428, doi: [10.1136/ard.2006.063354](#), indexed in Pubmed: [17446239](#).
 32. Szadek KM, Hoogland PV, Zuurmond WWA, et al. Possible nociceptive structures in the sacroiliac joint cartilage: an immunohistochemical study. *Clin Anat*. 2010; 23(2): 192–198, doi: [10.1002/ca.20908](#), indexed in Pubmed: [20014392](#).
 33. Telli H, Telli S, Topal M. The validity and reliability of provocation tests in the diagnosis of sacroiliac joint dysfunction. *Pain Physician*. 2018; 21(4): E367–E376, indexed in Pubmed: [30045603](#).
 34. Tile M. Pelvic ring fractures: should they be fixed? *J Bone Joint Surg Br*. 1988; 70(1): 1–12, doi: [10.1302/0301-620X.70B1.3276697](#), indexed in Pubmed: [3276697](#).
 35. Tonosu J, Oka H, Watanabe K, et al. Validation study of a diagnostic scoring system for sacroiliac joint-related pain. *J Pain Res*. 2018; 11: 1659–1663, doi: [10.2147/JPR.S167033](#), indexed in Pubmed: [30214275](#).
 36. van Rossum D, Hanisch UK, Quirion R. Neuroanatomical localization, pharmacological characterization and functions of CGRP, related peptides and their receptors. *Neurosci Biobehav Rev*. 1997; 21(5): 649–678, doi: [10.1016/s0149-7634\(96\)00023-1](#).
 37. Vleeming A, Schuenke MD, Masi AT, et al. The sacroiliac joint: an overview of its anatomy, function and potential clinical implications. *J Anat*. 2012; 221(6): 537–567, doi: [10.1111/j.1469-7580.2012.01564.x](#), indexed in Pubmed: [22994881](#).
 38. Vallejo R, Benyamin RM, Kramer J, et al. Pulsed radiofrequency denervation for the treatment of sacroiliac joint syndrome. *Pain Med*. 2006; 7(5): 429–434, doi: [10.1111/j.1526-4637.2006.00143.x](#), indexed in Pubmed: [17014602](#).
 39. van Tilburg CWJ, Schuurmans FA, Stronks DL, et al. Randomized sham-controlled double-blind multicenter clinical trial to ascertain the effect of percutaneous radiofrequency treatment for sacroiliac joint pain: three-month results. *Clin J Pain*. 2016; 32(11): 921–926, doi: [10.1097/AJP.0000000000000351](#), indexed in Pubmed: [26889616](#).
 40. Vilensky JA, O'Connor BL, Fortin JD, et al. Histologic analysis of neural elements in the human sacroiliac joint. *Spine (Phila Pa 1976)*. 2002; 27(11): 1202–1207, doi: [10.1097/00007632-200206010-00012](#), indexed in Pubmed: [12045518](#).

A study of coronary dominance and its clinical significance

D.P. Aricatt¹, A. Prabhu², R. Avadhani¹, K. Subramanyam³, A.S. Manzil⁴, J. Ezhilan⁵, R. Das⁶

¹Department of Anatomy, Yenepoya Medical College, Yenepoya University Deralakatte, Mangalore, Karnataka, India

²Yenepoya Research Centre, Yenepoya University Deralakatte, Mangalore, Karnataka, India

³Department of Interventional Cardiology, K.S. Hegde Medical Academy Hospital, Mangalore, Karnataka, India

⁴Department of CardioVascular Sciences, Sahakarana Hrudayalaya, Government Medical College Pariyaram, Kannur, Kerala, India

⁵Department of Cardiology, Madras Medical Mission, Chennai, Tamilnadu, India

⁶Division of Data Analytics, Bioinformatics and Structural Biology (DABS), Mangalore, Karnataka, India

[Received: 23 October 2021; Accepted: 28 November 2021; Early publication date: 17 January 2022]

Background: Coronary artery disease is the most common cause of morbidity and mortality especially in the developing countries. The aim of the study was to find out cardiac dominance percentages and its association with coronary artery stenosis among each pattern of dominance. The objectives were to assess coronary vessel morphology of patients within each pattern of dominance, to find if gender differences exist among dominance patterns and also to find the distribution percentages of stenosis among dominance patterns.

Materials and methods: Four thousand angiograms from patients of Indian origin were studied prospectively after procuring the sanction for the same from the ethical committee of the pre-selected hospitals from four states of South India. Informed consents were obtained. Post coronary artery bypass grafting, post percutaneous coronary intervention patients and patient being diabetic for ≥ 5 years were excluded from the study.

Results: Right cardiac dominance was seen in 85.5%, left in 9.7%, and co-dominant in 4.8% cases. The percentages of dominance were almost similar among both genders except for left dominance which were higher among male samples. The diameter of right coronary artery and left circumflex coronary artery coronary arteries were significantly associated with dominance patterns. The prevalence of stenosis was more for left dominance patterns, followed by right dominance patterns and least for co-dominant patterns.

Conclusions: There is a necessity to see association between dominance patterns with the coronary artery disease which can help the interventional cardiologists. The disease patterns in the present study were predominantly in the left dominant or in the co-dominant hearts. (Folia Morphol 2023; 82, 1: 102–107)

Key words: cardiac dominance, coronary vessel morphology, coronary artery disease

Address for correspondence: Dr. D.P. Aricatt, Yenepoya (Deemed to be) University, Department of Anatomy, Yenepoya Medical College, Deralakatte, 575018 Mangalore, Karnataka, India, e-mail: drdiviamanoj@gmail.com

This article is available in open access under Creative Common Attribution-Non-Commercial-No Derivatives 4.0 International (CC BY-NC-ND 4.0) license, allowing to download articles and share them with others as long as they credit the authors and the publisher, but without permission to change them in any way or use them commercially.

INTRODUCTION

The major arteries supplying the heart are right coronary artery (RCA) and left main coronary arteries (LMCA) with the right posterior descending artery (PDA) for RCA and left anterior descending (LAD) and circumflex artery (LCx) for LMCA as the main branches [27]. Coronary dominance is described by which coronary artery branch gives off the PDA and supplies the inferior wall of heart. Estimates are that 80–85% of the population is right heart dominant with the posterior descending artery originating from the RCA; 7–13% of the population is left heart dominant with the PDA originating from the LCx, and about 2–5% is balanced or codominant with the PDA supplied by both the LCx and RCA [15]. When the branches from both the distal RCA and the distal LCx artery cross the inferior interventricular septum, it was termed as co-dominance. This was reported to have a prevalence of 7–8% [13]. Different studied by various authors confirm that the coronary artery system was right dominant in 85%, left dominant in 8% and co-dominant in 7% of cases [5, 17, 22, 23]. Certain recent studies indicated a high prevalence for left dominance followed by co-dominance pattern (DP) and lower prevalence percentages for right DP. This is contradictory to the previous studies [1, 11, 25].

Ischaemic myocardial infarction and atherosclerotic involvement of LAD ostium were not associated with the left pattern of dominance [12]. The significance between dominance and the extent of coronary artery disease (CAD) were evaluated, by quantitative coronary angiography (QCA) it was found that CAD severity, arterial territory involvement and DP were related to each other [23]. In contrast, few authors reported the significant role of DP in the inferior wall infarcts and associated high mortality rates with left DP [3, 24].

Cardiac DPs with their correlations with atherosclerotic prominence and their clinical significance need to be studied in a broader perspective. Though left DP believed to have significantly higher mortality rate; supporting evidences are lacking due to reduced sample size. In this context, the present study outlooks the incidence of right, left and co-DP in a broader aspect. Present study reports the percentage prevalence of the DP and if gender specificity persists among each pattern of dominance. The present study tries to correlate the association between the diameters of the coronary artery and to the type of coronary vascular distribution.

MATERIALS AND METHODS

Study population

A cross sectional study was conducted in four cities of India. Hospitals were purposely selected according to the number of cardiac patients identified by them. The age of the study subjects was given a cut-off at 75 years due to marginal benefits marked during the follow-ups. Hence, a conservative approach is proven to be appropriate for the above-mentioned age which itself indicates a poor prognosis with an average yearly mortality rate of 33–35% [4]. The inclusion criteria were all patients who undergo percutaneous coronary angiographic procedure due to abnormalities in the normal cardiac parameters after obtaining their informed consent. Exclusion criteria were patients with a previous history of coronary artery bypass grafting and recanalised normal looking coronary arteries with or without in-stent restenosis coronary arteries as well as patients being diabetic for 5 or more than 5 years. The sample size was estimated by consulting a statistician and using the statistical software G* Power 3.0.10 and 4000 subjects were studied by convenience sampling. All ethical principles for human research were followed and ethical approval was obtained from the Institutional Ethics Committee of all the hospitals from where data was collected.

Database pooling

Four thousand angiogram reports were collected and studied. The three main DP are right dominant, left-dominant and balanced or co-dominant depending on the origin of the PDA from RCA or LCx. The origin of the PDA and the posterolateral branches were best evaluated in the left anterior oblique (LAO) cranial or anterior-posterior (AP) cranial view. If the LCx is dominant, the optimal projection for the left PDA was the LAO cranial. Co-dominance can be explained as branches from both the distal RCA and the distal LCx artery crosses the inferior interventricular septum. LAO cranial or AP cranial view can give an optimal projection to observe the same [15]. Normal or diseased segments among each DP were noted down.

Calibration assessments from QCA [14, 19] systems were carried out by the same method in which the coronary catheter was employed for angiography procedure. This was used as calibrating the object by automated edge detection technique resulting in corresponding calibration factors (mm/pixel) and the vessel contour were detected by operator independent edge detection algorithms. Angiographic views were selected for calibration assessment by minimis-

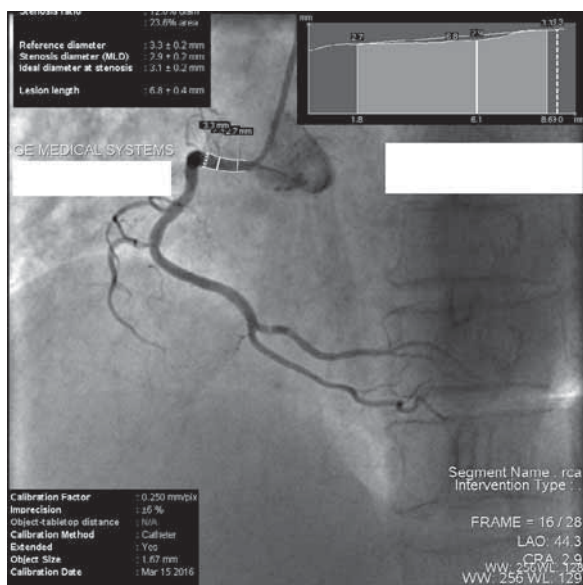


Figure 1. Quantitative coronary angiography image with an arrow pointing right coronary artery by left anterior oblique cranial projections. Image procured from DICOM image output on 100 M bit Ethernet of GE Innova 2100 IQ system with a capability of autosend and background transfer for fast transmission with minimal user interaction.

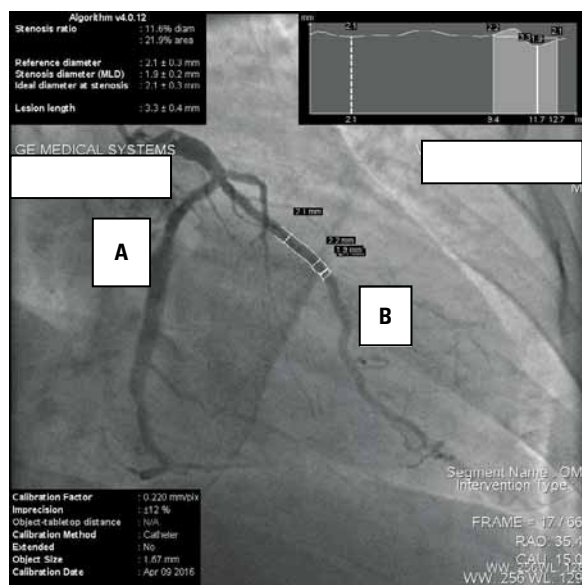


Figure 2. Quantitative coronary angiography images with arrows pointing left circumflex artery (A) and its obtuse marginal branch (B) by right anterior oblique caudal projections. Images procured from DICOM image output on 100 M bit Ethernet of GE Innova 2100 IQ system with a capability of autosend and background transfer for fast transmission with minimal user interaction.

ing the foreshortening of the coronary segments by separating them from adjacent intervening structures.

For LCx ostial and proximal LCx were measured around ostium and before the origin of the first obtuse marginal for the proximal segment calibration assessment. For RCA, the ostium and proximal segments were measured before the origin of first acute marginal (AM1) by stenosis analysis programme using the automated coronary analysis package of the Innova 2100 IQ Cath at an AW4.4 workstation or Siemens QCA — Scientific coronary analysis. QCA were performed for vessel diameters ranging from 0.5 mm – 7 mm at *syngo* X Workplace: VB21 with acquisition at 7.5, 10, 15 and 30 f/s, acquisition for display and storage in original matrix of 12-bit (Figs. 1, 2). Statistical analysis of the present study was done using the SPSS software package for Windows version 22.0 (SPSS Inc., Chicago, IL). Descriptive statistics were used to present the socio-demographic data. Results were tabulated according to the standard format.

RESULTS

Among total sample population (n = 4000), there were 2,696 (67.4%) males and 1,304 (32.6%) females. Non flow limiting coronary arteries were seen in 933 (23.3%) cases and 3,067 (76.7%) had CAD.

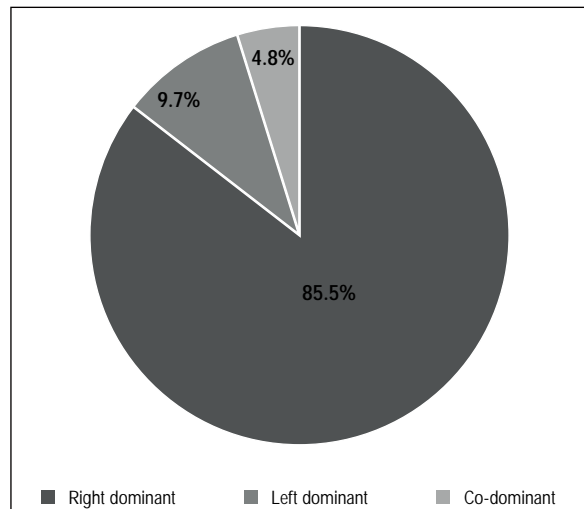
Coronary DP and significance

There was no difference in the DP's of normal and diseased samples. The DP's were right dominant > left dominant > co-dominant. Among genderwise categorised samples DP's were right dominant > left dominant > co-dominant. The percentages of dominance were almost similar among both genders except for left dominance. Left dominance percentages were higher among male samples. These findings were similar to distribution of DP among total samples. The dimensions of coronary artery segments contributing for the DP namely, LCx and RCA were assessed. The coronary artery measurements (CAM) of normal segments were grouped under each DP for total and genderwise categorised samples. In total and genderwise categorised samples the difference in the CAM between LCx proximal part (LCx-p) and RCA proximal part (RCA-p) in the right DP was highly significant ($p < 0.01$), and was very highly significant ($p < 0.001$) in left DP. However, this difference was not significant ($p > 0.05$) in co-DP (Table 1). Multiple comparisons were done for CAM of LCx-p and RCA-p with DP among total and genderwise categorised normal samples. Although, in total samples the difference in the CAM of LCx-p and RCA-p between right DP and left DP was very highly

Table 1. Genderwise comparison of non-indexed coronary artery measurements (CAM) based on cardiac dominance patterns (DP) of normal samples (n = 933)

Samples	DP	LCx-p [mm]	RCA-p [mm]	P-value
Male (n = 521)	Right dominant	3.05 ± 0.62	3.19 ± 0.66	< 0.01**
	Left dominant	3.39 ± 0.58	2.73 ± 0.59	< 0.001***
	Co-dominant	3.19 ± 0.58	2.88 ± 0.69	> 0.05
Female (n = 412)	Right dominant	2.90 ± 0.60	3 ± 0.61	< 0.01**
	Left dominant	3.30 ± 0.56	2.62 ± 0.75	< 0.001***
	Co-dominant	3.04 ± 0.70	2.66 ± 0.39	> 0.05
Total (n = 933)	Right dominant	2.99 ± 0.61	3.10 ± 0.64	< 0.01**
	Left dominant	3.35 ± 0.57	2.69 ± 0.66	< 0.001***
	Co-dominant	3.13 ± 0.63	2.78 ± 0.58	> 0.05

The CAM was taken based on quantitative coronary angiography reports and is represented as mean ± standard deviation for each coronary artery segments in the DP's. Statistical test used: One way ANOVA; ***p < 0.001 indicates very highly significant difference; **p < 0.01 indicates highly significant difference; *p < 0.05 indicates significant difference; p > 0.05 indicates non-significant difference between non-indexed CAM of the segments contributing for the DP's. LCx-p — left circumflex coronary artery (proximal part); RCA-p — right coronary artery (proximal part)

**Figure 3.** Distribution based on dominance patterns among total samples. The data was categorised based on quantitative coronary angiography reports.**Table 2.** Genderwise multiple comparison of non-indexed coronary artery measurements (CAM) based on cardiac dominance patterns (DP) of normal samples (n = 933)

Dependant variable	DP	Male samples		Female samples		Total samples	
		MD	P-value	MD	P-value	MD	P-value
LCX-p	CO L	-0.20395	0.349	-0.25885	0.291	-0.22534	0.112
	CO R	0.13661	0.475	0.13986	0.569	0.14346	0.248
	L R	0.34057*	< 0.01**	0.39871*	< 0.01**	0.36880*	< 0.001***
RCA-p	CO L	0.14324	0.643	0.03476	0.978	0.09608	0.698
	CO R	-0.31142*	< 0.05*	-0.33945*	< 0.05*	-0.32011*	< 0.01**
	L R	-0.45466	< 0.001***	-0.37422	< 0.01**	-0.41620	< 0.001***

The CAM was taken based on quantitative coronary angiography reports for each coronary artery segments in the DP's. Statistical test used: Post Hoc (Tukey's test), p < 0.001*** indicates very highly significant difference, p < 0.01** indicates highly significant difference, p < 0.05* indicates significant difference, p > 0.05 indicates non-significant difference between non-indexed CAM of the segments contributing for the DP's. MD — mean difference; LCX-p — left circumflex coronary artery (proximal part); RCA-p — right coronary artery (proximal part); L — left dominant; R — right dominant; CO — co-dominant

significant (p < 0.001), in genderwise categorised samples, it was only highly significant (p < 0.01). There was also a significant difference (p < 0.05) between co-dominant and right DP in genderwise categorised samples (Table 2).

DISCUSSION

Cardiac dominance and associations with CAD

In the present study there was right cardiac dominance in 85.5%, left in 9.7%, and co-dominant in 4.8% cases (Fig. 3, Table 3). Various authors have also reported the dominance percentages as 83–85% right, 6–8% left and 5–7% cases as co-dominant [2, 6, 10, 15, 21, 23, 27, 28]. There was only slight variation in the co-dominant pattern which was lower in

Table 3. Distribution of normal, diseased and total segments based on dominance patterns (DP)

DP	DP, n (%)		
	Normal (n = 933)	Diseased (n = 3067)	Total (n = 4000)
Right dominant	809 (86.7%)	2610 (85%)	3419 (85.5%)
Left dominant	74 (7.9%)	315 (10.3%)	389 (9.7%)
Co-dominant	50 (5.4%)	142 (4.6%)	192 (4.8%)

The data was categorised based on quantitative coronary angiography reports and is represented as frequency with percentage in parenthesis; n — frequency

the present study. However, the DP seen in other studies have not been consistent, especially in the ones that have looked at only left and right dominance and not the co-DP (Fig. 4). Gebhard et al. (2018) [10]

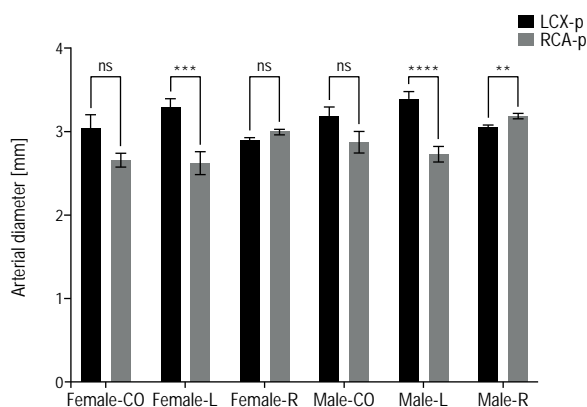


Figure 4. Artery measurements of dominance patterns among genderwise categorised samples. The data was categorised based on quantitative coronary angiography reports; LCx-p — left circumflex coronary artery (proximal part); RCA-p — right coronary artery (proximal part); L — left dominant; R — right dominant; CO — co-dominant; *** $p < 0.001$ indicates very highly significant difference; ** $p < 0.01$ indicates highly significant difference; * $p < 0.05$ indicates significant difference; $p > 0.05$ or ns indicates no significant difference.

denoted right dominance among 91% and left among 9% of the study population in their studies.

Another study found that left dominance was seen in 9.8% cases and non-left dominance in 90.2% samples. Few studies even found an opposite dominant pattern with a high prevalence for left dominance or for co-DP and lower prevalence percentages for right dominance [10, 20, 22, 25, 26]. There is a need to delve further into this aspect of coronary dominance as these variations should not merely be a consequence of different assessment methods used. Besides coronary angiography, the methods used have been 64-slice computed tomography coronary angiography (CTCA), multidetector CTCA, corrosion casting or formalin-fixed human hearts.

In the present study the diameter of RCA-p and LCx-p coronary arteries were significantly associated with DP. The average size of the RCA-p was significantly smaller in the left DP as compared to that of right DP and vice versa for LCx-p dimensions among right dominant cases. Another Indian study conducted by Elangovan et al. (2005) [8] found similar association. Similarly the dimensions of LCx were significantly smaller in co-dominant cases when compared to left DP [7, 16]. Studies conducted in rest of the world have found similar results in relation to RCA-p and LCx-p sizes among the right and left DP. However, contrary to the present study they did not find association between CAM and co dominant patterns [16].

There is a necessity to see association between DP with the CAD as this can help the interventional cardiologist to be more alert. The disease patterns in the present study were predominantly in the left dominant or in the co dominant hearts. These findings are consistent with the studies that also found the similar disease patterns [3, 9, 12]. This left dominant disease pattern is biologically plausible because main origin of blood supply to the left ventricle is from the LCA. So it is regarded as the dominant vessel even in cases with anatomical right dominance.

Perfusion studies have also shown that even in anatomically right dominant hearts, left functional dominance is seen. Target lesions were more frequently found in hearts that had left coronary dominance with a higher incidence of periprocedural myocardial infarction [18]. Ghaffari et al. (2013) [11] have explained that atherosclerotic involvement of LAD was more related with atherosclerotic involvement of LAD ostium and ischemic myocardial infarction than to DP's. Contrary to this theory, few studies have shown more extensive CAD in patients with a right dominant coronary artery system [28] but it is not known whether they are exceptions or indicative of lack of association between DP and CAD. There has to be multi-centric studies with larger sample sizes to make a valid conclusion regarding the same.

CONCLUSIONS

The present study concludes that the prevalence of stenosis was more for left DP, followed by right DP and minimal for co-dominant patterns. A significant association was found between the diameters of the LCx-p and RCA-p and the type of coronary vascular distribution. There is a necessity to see association between DP with the CAD as this can help the interventional cardiologist to be more alert during the interventional procedures.

Conflict of interest: None declared

REFERENCES

1. Adil M, Nadeem M, Hafizullah M, et al. Comparison of left coronary artery diameter among diabetics and non-diabetics. *J Postgrad Med Inst (Peshawar-Pakistan)*. 2012; 26(4): 369–376.
2. Altin C, Kanyilmaz S, Koc S, et al. Coronary anatomy, anatomic variations and anomalies: a retrospective coronary angiography study. *Singapore Med J*. 2015; 56(6): 339–345, doi: [10.11622/smedj.2014193](https://doi.org/10.11622/smedj.2014193), indexed in Pubmed: 25502334.

3. Amin K, Javed M, Mehmood A, et al. Acute inferior wall myocardial infarction: Frequency of AV blocks. *TPMJ*. 2004; 11(1): 31–37.
4. Azad N, Lemay G. Management of chronic heart failure in the older population. *J Geriatr Cardiol*. 2014; 11(4): 329–337, doi: [10.11909/j.issn.1671-5411.2014.04.008](https://doi.org/10.11909/j.issn.1671-5411.2014.04.008), indexed in Pubmed: [25593582](https://pubmed.ncbi.nlm.nih.gov/25593582/).
5. Bordoloi R. An anatomical study of coronary artery dominance in human cadaveric hearts. *J Evid Based Med Healthcare*. 2016; 3(103): 5695–5699, doi: [10.18410/jebmh/2016/1177](https://doi.org/10.18410/jebmh/2016/1177).
6. Cademartiri F, Malagò R, La Grutta L, et al. Coronary variants and anomalies: methodology of visualisation with 64-slice CT and prevalence in 202 consecutive patients. *Radiol Med*. 2007; 112(8): 1117–1131, doi: [10.1007/s11547-007-0210-0](https://doi.org/10.1007/s11547-007-0210-0), indexed in Pubmed: [18080097](https://pubmed.ncbi.nlm.nih.gov/18080097/).
7. Dhakal A, Shrestha R, Maskey A, et al. Coronary artery dimensions in the Nepalese population. *JASI*. 2015; 64(1): 27–31, doi: [10.1016/j.jasi.2015.03.001](https://doi.org/10.1016/j.jasi.2015.03.001).
8. Elangovan C, Jaganathan V, Alageshan R, et al. Clinical and anthropometric correlation of normal Coronary artery dimensions. *Indian Heart J*. 2005; 57(5): 381–425.
9. Gebhard C, Fuchs TA, Stehli J, et al. Coronary dominance and prognosis in patients undergoing coronary computed tomographic angiography: results from the CONFIRM (COronary CT Angiography EvaluationN For Clinical Outcomes: An International Multicenter) registry. *Eur Heart J Cardiovasc Imaging*. 2015; 16(8): 853–862, doi: [10.1093/ehjci/jeu314](https://doi.org/10.1093/ehjci/jeu314), indexed in Pubmed: [25744341](https://pubmed.ncbi.nlm.nih.gov/25744341/).
10. Gebhard C, Gick M, Ferenc M, et al. Coronary dominance and prognosis in patients with chronic total occlusion treated with percutaneous coronary intervention. *Catheter Cardiovasc Interv*. 2018; 91(4): 669–678, doi: [10.1002/ccd.27174](https://doi.org/10.1002/ccd.27174), indexed in Pubmed: [28795482](https://pubmed.ncbi.nlm.nih.gov/28795482/).
11. Ghaffari S, Kazemi B, Dadashzadeh J, et al. The relation between left coronary dominance and atherosclerotic involvement of left anterior descending artery origin. *J Cardiovasc Thorac Res*. 2013; 5(1): 1–4, doi: [10.5681/jcvtr.2013.001](https://doi.org/10.5681/jcvtr.2013.001), indexed in Pubmed: [24251001](https://pubmed.ncbi.nlm.nih.gov/24251001/).
12. Goldberg A, Southern DA, Galbraith PD, et al. Coronary dominance and prognosis of patients with acute coronary syndrome. *Am Heart J*. 2007; 154(6): 1116–1122, doi: [10.1016/j.ahj.2007.07.041](https://doi.org/10.1016/j.ahj.2007.07.041), indexed in Pubmed: [18035084](https://pubmed.ncbi.nlm.nih.gov/18035084/).
13. Helft G, Dambrin G, Zaman A, et al. Percutaneous coronary intervention in anticoagulated patients via radial artery access. *Catheter Cardiovasc Interv*. 2009; 73(1): 44–47, doi: [10.1002/ccd.21758](https://doi.org/10.1002/ccd.21758), indexed in Pubmed: [19089936](https://pubmed.ncbi.nlm.nih.gov/19089936/).
14. Hermiller JB, Cusma JT, Spero LA, et al. Quantitative and qualitative coronary angiographic analysis: review of methods, utility, and limitations. *Cathet Cardiovasc Diagn*. 1992; 25(2): 110–131, doi: [10.1002/ccd.1810250207](https://doi.org/10.1002/ccd.1810250207), indexed in Pubmed: [1544153](https://pubmed.ncbi.nlm.nih.gov/1544153/).
15. Jeffrey JP, Scott K, and De. Coronary arteriography and Intra coronary Imaging. In: Mann DL, Zipes DP, Libby P, Bonow RO. Braunwald's heart disease: a textbook of cardiovascular medicine. Part 1. Elsevier Health Sciences 2017: 392–428.
16. Kim E, Yoo J, Cheon W, et al. Coronary artery size in Korean: normal value and its determinants. *Korean Circ J*. 2005; 35(2): 115, doi: [10.4070/kcj.2005.35.2.115](https://doi.org/10.4070/kcj.2005.35.2.115).
17. Koşar P, Ergun E, Öztürk C, et al. Anatomic variations and anomalies of the coronary arteries: 64-slice CT angiographic appearance. *Diagn Interv Radiol*. 2009; 15(4): 275–283, doi: [10.4261/1305-3825.DIR.2550-09.1](https://doi.org/10.4261/1305-3825.DIR.2550-09.1), indexed in Pubmed: [19957241](https://pubmed.ncbi.nlm.nih.gov/19957241/).
18. Lam MK, Tandjung K, Sen H, et al. Coronary artery dominance and the risk of adverse clinical events following percutaneous coronary intervention: insights from the prospective, randomised TWENTE trial. *EuroIntervention*. 2015; 11(2): 180–187, doi: [10.4244/EIJV11I2A32](https://doi.org/10.4244/EIJV11I2A32), indexed in Pubmed: [24602919](https://pubmed.ncbi.nlm.nih.gov/24602919/).
19. MacAlpin RN, Abbasi AS, Grollman JH, et al. Human coronary artery size during life. A cinearteriographic study. *Radiology*. 1973; 108(3): 567–576, doi: [10.1148/108.3.567](https://doi.org/10.1148/108.3.567), indexed in Pubmed: [4269246](https://pubmed.ncbi.nlm.nih.gov/4269246/).
20. Moore KL, Dalley AF, Agur AM. Clinically oriented anatomy. Lippincott Williams & Wilkins 2013: 151–174.
21. Mowatt G, Cummins E, Waugh N, et al. Systematic review of the clinical effectiveness and cost-effectiveness of 64-slice or higher computed tomography angiography as an alternative to invasive coronary angiography in the investigation of coronary artery disease. *Health Technol Assess*. 2008; 12(17): iii–iv, ix, doi: [10.3310/hta12170](https://doi.org/10.3310/hta12170), indexed in Pubmed: [18462576](https://pubmed.ncbi.nlm.nih.gov/18462576/).
22. Paudel N, Jha GS, Alurkar VM, et al. Coronary dominance and predictors of adverse events during coronary interventional procedures: an observational study. *J Adv Intern Med*. 2017; 6(1): 4–8, doi: [10.3126/jaim.v6i1.18311](https://doi.org/10.3126/jaim.v6i1.18311).
23. Paul A, Avadhani R, Subramanyam K. Anomalous origins and branching patterns in coronary arteries: an angiographic prevalence study. *JASI*. 2016; 65(2): 136–142, doi: [10.1016/j.jasi.2016.09.001](https://doi.org/10.1016/j.jasi.2016.09.001).
24. Reagan K, Buxt LM, Katz J. Introduction to coronary arteriography. *Radiol Clin North Am*. 1994; 32(3): 419–433, indexed in Pubmed: [8184022](https://pubmed.ncbi.nlm.nih.gov/8184022/).
25. Reddy V, Lokanadham S. Coronary dominance in south Indian population. *Int J Med Res Health Sci*. 2013; 2(1): 78–82.
26. Shukri IG, Hawas JM, Karim SH, et al. Angiographic study of the normal coronary artery in patients attending Ulaimani Center for Heart Diseases. *ESJ*. 2014; 10(24): 384–415.
27. Standing S, Borley NR, Collins P, Crossman AR, Gatzoulis MA, Healy JC. Gray's Anatomy. 41 stedn. Churchill Livingstone, London 2008: 978–980.
28. Vasheghani-Farahani A, Kassaian SE, Yaminisharif A, et al. The association between coronary arterial dominance and extent of coronary artery disease in angiography and paraclinical studies. *Clin Anat*. 2008; 21(6): 519–523, doi: [10.1002/ca.20669](https://doi.org/10.1002/ca.20669), indexed in Pubmed: [18698656](https://pubmed.ncbi.nlm.nih.gov/18698656/).

Morphometry and morphological analysis of carotico-clinoid foramen: an anatomical study with clinical implications

A. Priya¹, R.K. Narayan², S.K. Ghosh¹, P. Kumar³

¹Department of Anatomy, All India Institute of Medical Sciences, Patna, India

²Department of Anatomy, Andaman and Nicobar Islands Institute of Medical Sciences, Port Blair, India

³Department of Radiodiagnosis, All India Institute of Medical Sciences, Patna, India

[Received: 13 October 2021; Accepted: 29 October 2021; Early publication date: 16 November 2021]

Background: The dural fold between anterior and middle clinoid processes on mineralisation leads to the formation of caroticoclinoid foramen (CCF). Different morphology of this foramen presents with different clinical features. The present study reports the frequency of CCF in the population of Bihar, while providing an account of assimilated information from previous literature regarding the association of caroticoclinoid ligament ossification with age and human genetics.

Materials and methods: The study was conducted on 100 adult dry human skulls of unknown age and sex, and 50 lateral view radiographs of the head.

Results: Of the 100 dry skull bones, 9 presented with different forms of CCF. Bilateral complete foramina were noticed in 2 (2%) skull bones, while the incomplete foramina were observed bilaterally in 3 (3%) and unilaterally in 4 (4%) skulls. The lateral view radiograph data ($n = 50$) presented with a bilateral foramen in one subject and unilateral complete CCF in two different subjects. On measurements of the diameters of the complete CCF the mean values observed were 4.06 mm and 4.51 mm on the right side, while that on the left side were 5.15 mm and 4.14 mm. For the incomplete foramina, the mean values for the vertical diameter were 4.48 mm on the right and 4.19 mm on the left side, respectively.

Conclusions: The frequency of CCF in the present study population of Bihar was much lesser than that of previously studied populations. However, the variation in frequency of different morphological types of CCF was observed to be the same across populations. The variations in CCF's metric data could help in predicting the morphological changes it causes to the clinoidal segment of the internal carotid artery, as well as in distinguishing its varieties. (Folia Morphol 2023; 82, 1: 108–118)

Key words: caroticoclinoid foramen, human genetics, mineralisation

INTRODUCTION

Henle [see 20] was the first to describe the carotico-clinoid foramen (CCF) formed by the presence of an osseous bridge between the tip of the middle and anterior clinoid processes (Fig. 1A). The anterior

clinoid process (ACP) is prolongation of medial end of lesser wing of sphenoid, whereas the middle clinoid process (MCP) is present on either side of the tuberculum sellae. The dural fold between ACP and MCP (also called as caroticoclinoid ligament [CCL])

Address for correspondence: Dr. R.K. Narayan, Assistant Professor, Department of Anatomy, Andaman and Nicobar Islands Institute of Medical Sciences, Port Blair, India, tel: 9234896343, e-mail: narayanintouch@gmail.com

This article is available in open access under Creative Common Attribution-Non-Commercial-No Derivatives 4.0 International (CC BY-NC-ND 4.0) license, allowing to download articles and share them with others as long as they credit the authors and the publisher, but without permission to change them in any way or use them commercially.

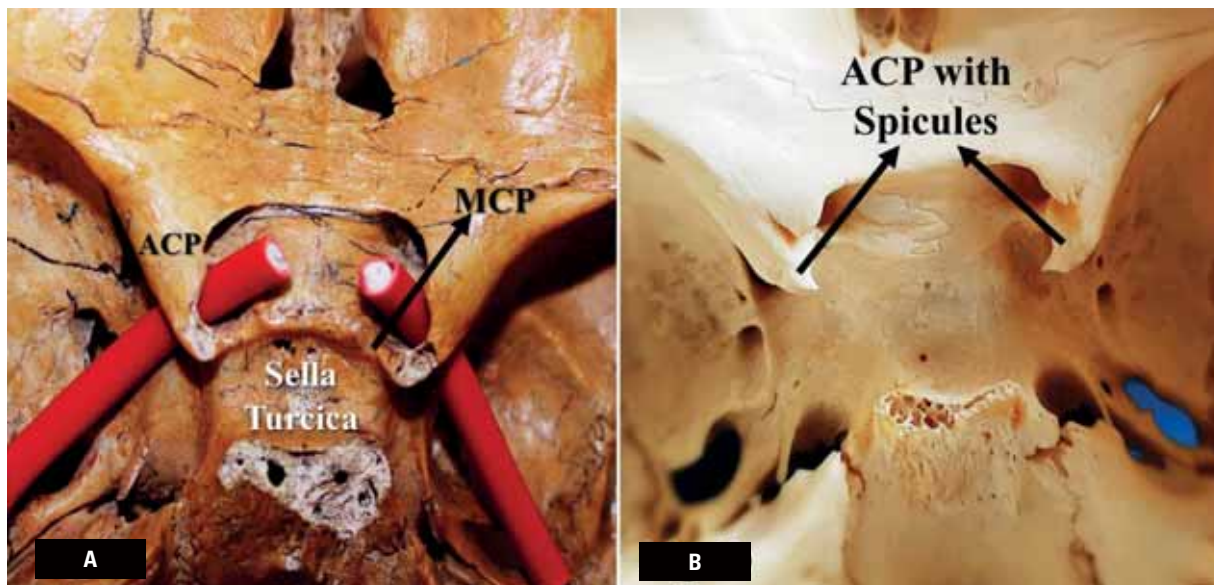


Figure 1. **A.** Specimen of skull base showing sella turcica and bilateral complete caroticoclinoid foramen (CCF) formed between anterior clinoid process (ACP) and middle clinoid process (MCP). Red coloured polyvinyl chloride wire inserted in the CCFs used to measure the diameter of the foramen; **B.** Specimen of skull base showing sella turcica and bilateral incomplete CCF with spicules extending from ACP.

on ossification leads to the formation of CCF, while the ossified fold between ACP and posterior clinoid process (PCP) (also known as interclinoid ligament [ICL]) is termed as the “sella turcica bridge” (STB) and forms the interclinoid foramen (ICF) [5, 47].

The literature mentions multiple classification by different authors regarding the morphology (complete, contact, and incomplete [with or without spicules] types) of CCF. Different morphological patterns of the foramen present with different clinical features. The complete foramen (Fig. 1A) can present with severe headache due to compression and spontaneous rupture of the clinoidal segment of internal carotid artery (ICA) [47]. Incomplete CCF (Fig. 1B) can further be classified into contact type and one with spicules on ACP or MCP. The latter can cause rupture of ICA and may lead to the formation of carotico-cavernous sinus fistula, a direct communication between the ICA and cavernous sinus [5, 21]. The varied clinical presentations raise the query related to the aetio-pathogenesis of the foramen, which indeed is related to the ossification of the dural fold or the ligament.

Mineralisation or ossification physiologically occurs in two types of human tissue, the bone, and tooth. Occurrence of ossification in other tissues is referred to as ectopic calcification. Touska et al. [55] mentioned that ectopic calcification or mineralisation of skull base ligaments occurs later in life as a result of interaction between many factors, including genetic,

mechanical stress, and metabolic [55]. Ossified skull base ligaments have been reported in different age groups, but when observed in children without any evident stimuli as mentioned above may explain the embryological basis, termed as atavistic (i.e., representing evolutionary remnants), on account of the presence of similar ossified structures in non-human species [11].

Since being explained by Henle [see 20], numerous populations based radiographic, autopsy and dry skull bone studies have reported the frequency of CCF, while trying to explain few aetiological associations with age and diseases. None of these findings were reproduced in following studies till date. The present study while reporting the frequency of CCF in the population of Bihar, also provides an account of assimilated information from previous literature regarding the association of frequency of CCF with age and human genetics.

MATERIALS AND METHODS

The multicentric retrospective study was conducted on 100 adult dry human skulls of unknown age and sex, and 50 lateral view radiographs of the head. The present study was done in Department of Anatomy at All India Institute of Medical Sciences, Patna while dry skull bone data were also collected from other major medical institutes of Bihar. The radiological data of those patients whose lateral view of head

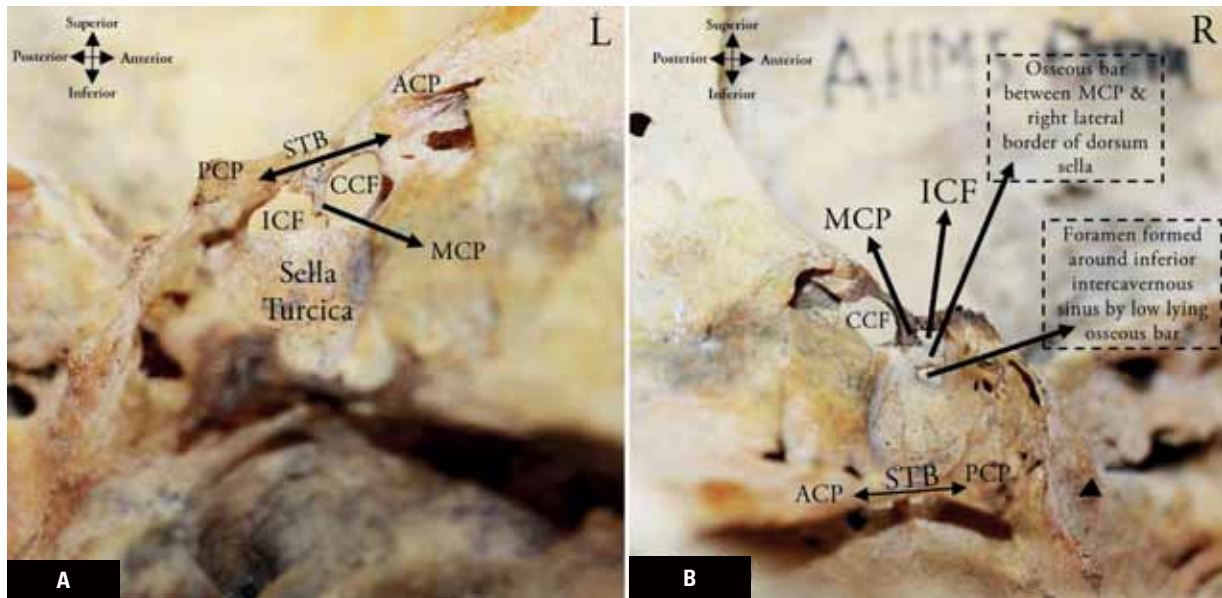


Figure 2. A. Specimen of skull base showing left side of the sella turcica. Sella turcica bridge (STB) is formed by the ossified connection between anterior clinoid process (ACP), middle clinoid process (MCP), and posterior clinoid process (PCP). Caroticoclinoid foramen (CCF) formed underneath the ossified segment connecting ACP and MCP, housing the internal carotid artery. Interclinoid foramen (ICF) formed underneath the segment connecting MCP and PCP; **B.** Right side of the sella turcica in a skull base specimen showing STB, ACP, MCP, PCP, CCF, and ICF. The unique feature of a low lying osseous bar connecting MCP and right lateral border of dorsum sella, theoretically, forming a foramen around the inferior intercavernous sinus; L — left; R — right.

was taken for non-cranial pathologies were collected from archives of Department of Radiodiagnosis at All India Institute of Medical Sciences, Patna. Prior approval from ethics committee of the above mentioned institute was taken to conduct the study, and the requirement of the informed patient consent for utilising stored radiographic data from the departmental archives was waived off.

The following parameters were observed:

- presence or absence of CCF;
- type of foramen (complete/incomplete, unilateral/bilateral);
- shape of the CCF, if present;
- antero-posterior diameter and vertical diameter of CCF, if present.

All the above parameters were observed in dry skull bones, while in the radiographs only the first two parameters were noted. In addition, the frequency of the coexisted ossified variants of the ICF (foramen formed by ossification of STB between ACP-PCP and that formed by ossification of interclinoid ligament between MCP-PCP) were also observed on the dry skull and radiographic specimens. In the radiological data, age, and gender wise frequency for CCF was observed.

The present study comprised of skulls in which the vaults were removed so that the upper surface of sphenoid bone could be visualised. Skulls with broken

sphenoid bone were excluded. The dry skull specimens without any visible deformity in upper surface of sphenoid bone were included. All observations and measurements were taken twice, independently by two observers. Mean value of the measurements by the two observers were taken as the accurate value for each parameter.

Probes of known dimensions (Polyvinylchloride Wire of known calibrated diameter of 5.5 mm) were used to measure the diameter of the CCF. Measurements were also recorded in millimetres (mm) using Mitutoyo digital vernier callipers (precision 0.01 mm; Kawasaki, Japan).

RESULTS

Of the 100 dry skull bones, 9 presented with different forms of CCF. Bilateral complete foramina (Fig. 1A) were noticed in two skull bones, while the incomplete foramina (Fig. 1B) were observed bilaterally in 3, and unilaterally in 4 skulls of which 3 were on the left and one was on the right side.

One of the skulls with bilateral CCF also presented with the “sella turcica bridge” joining the ACP, MCP, and PCP bilaterally (Fig. 2A, B). On the left side, the bridge formed the CCF between the ACP and MCP, while a contact type ICF was formed between MCP and PCP having a thin gap between the extensions

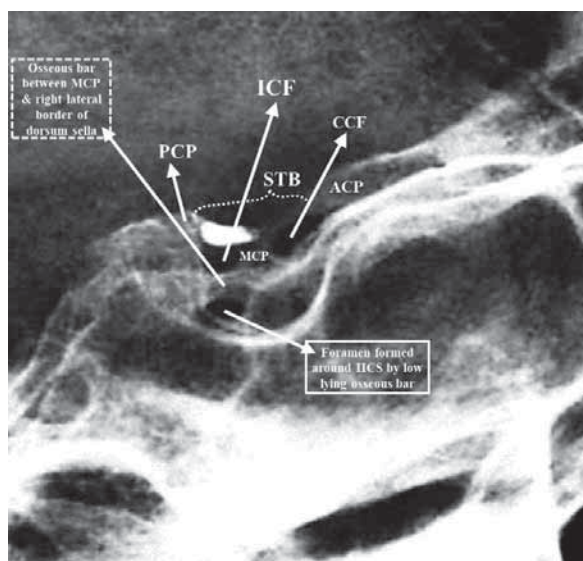


Figure 3. Radiograph of right lateral view of the skull base specimen presenting with sella turcica bridge (STB), anterior clinoid process (ACP), middle clinoid process (MCP), posterior clinoid process (PCP), caroticoclinoid foramen (CCF), interclinoid foramen (ICF), and a foramen around the inferior intercavernous sinus formed by a low-lying osseous bar connecting MCP and right lateral border of dorsum sellae; IICS — inferior inter-cavernous sinus.

of the two processes towards each other respectively (Fig. 2A). On the right side of the sella, the bridge forms a CCF and the ICF. The ICF was divided into two foramina by an osseous bar between the MCP and the midpoint of the right lateral border of the dorsum sellae (Fig. 2B). The right lateral radiographic view of the concerned skull also confirmed the ossification of the bridge and the osseous bar (Fig. 3). The second specimen presenting with bilateral CCF had no “sella turcica bridge”; therefore, the ICF was also absent (Fig. 1A).

Among the dry bone specimens having incomplete foramina ($n = 7$), an extension from the ACP was observed which was distant from the prominent MCP. In three of these specimens, the extensions from the ACP were in the form of pointed spicule, which can be classified as type III (dangerous type) CCF, based on Keyes classification.

On measurements of the antero-posterior and vertical diameter of the complete CCF, the mean values observed were 4.06 mm and 4.51 mm on the right side while that on the left side were 5.15 mm and 4.14 mm. For the incomplete foramina, the mean values for the vertical diameter were 4.48 mm on the right and 4.19 mm on the left side, respectively.

The lateral view radiograph data ($n = 50$) presented with one bilateral and two unilateral complete

CCF. The sample comprised of 25 radiographs from each gender with an age range of 12 to 73 years. The bilateral complete CCF was observed in a 43-year-old male, while the unilateral incomplete ones were observed on the right lateral view radiograph of a 27-year-old male, and a 17-year-old female.

DISCUSSION

The dural folds or the ligamentous structures (CCL) extending between the ACP and MCP on ossification leads to the formation of CCF. The total frequency of CCF in the present study population of Bihar (9%) though varies differently with individual reports of certain population, but when compared to the total reported values of those populations, it is on the lesser side to that of the Caucasian (25.9%), Turkish (20.51%), South Indian (21.06%) and Gujrat region (12.5%) populations (Table 1) [1, 4–7, 9, 15, 18–20, 31, 33, 35, 37, 45, 48–51, 53]. The frequency of CCF is more in Caucasian and Turkish population as compared to the oriental population, which could be explained on the basis of racial differences. Similar patterns were observed when the frequency of CCF was observed in the present study based on the morphological classification given by Keyes [31] (Complete, Contact, Incomplete types) and then was compared with those reported in the previous literature (Table 2) [1, 4, 5, 7, 10, 16, 20, 22, 28–31, 35, 45, 47, 49–51].

Radiographical data reporting the morphological presentation of CCF based on their laterality are collected from the CT scans/angiograms and lateral view radiographs. The CCF observed in present study radiographs had only complete morphological forms with a bilateral frequency of 2% and a unilateral frequency of 4% specimens, respectively. This frequency observed in the present study was slightly higher than that reported for unilateral complete CCF in United Kingdom population (Table 3) [3, 8, 14, 22, 25, 34, 36, 40–42, 46, 54, 55].

The data on morphological types of CCF as per the classification given by Keyes [31] varies similarly in different types of populations being reported over nine decades. Of the three types, the incomplete variety (type III) or the dangerous type is the most common followed by the complete (type I), and then the contact type (type II) (Table 2). Keyes [31] reported the frequency of incomplete CCF to be 19.1% in Caucasian Americans, while the same was observed to be as high as 36.6% by Natsis et al. [45] in the Cau-

Table 1. Comparing the prevalence of caroticoclinoid foramen based on their laterality of occurrence observed in present study with those reported in literature

Study	Population/Region	Number of skulls	Caroticoclinoid foramen [n (%)]			Sella turcica bridge
			Unilateral	Bilateral	Total	
Keyes (1935) [31]	Caucasian American	2187	—	—	600 (27.46%)	189 (8.68%)
Azeredo et al. (1988) [6]	Portuguese	270	6 (2.22%)	11 (4.05%)	17 (6.27%)	9 (3.04%)
Inoue et al. (1990) [28]	Caucasian American	50	11 (22%)	7 (14%)	18 (36%)	2 (4%)
Cireli et al. (1990) [15]	Turkish	50	3 (6%)	—	3 (6%)	1 (2%)
Deda et al. (1992) [18]	Turkish	88	6 (6.82%)	7 (7.95%)	13 (14.77%)	4 (4.54%)
Gurun et al. (1994) [26]	Turkish	198	16 (8.08%)	11 (5.55%)	27 (13.63%)	2 (1.01%)
Lee et al. (1997) [35]	Korean	73	15.7%	1.4%	17.1%	—
Erturk et al. (2004) [20]	Turkish	171	41 (23.98%)	20 (11.69%)	61 (35.67%)	14 (8.18%)
Peker et al. (2006) [48]	Turkish	80	—	—	—	21 (26.6%)
Skrzat et al. (2006) [53]	Polish	80	7 (8.75%)	6 (7.5%)	13 (16.25%)	11 (13.7%)
Archana et al. (2010) [4]	Indian	250	23 (9.2%)	7 (2.8%)	30 (12%)	55 (22%)
Desai et al. (2010) [19]	South India region	223	53 (23.74%)	30 (13.45%)	83 (37.19%)	—
Boyan et al. (2011) [9]	Turkish	34	—	—	4 (11.8%)	—
Kolagi et al. (2011) [33]	South India region	112	6 (5.35%)	3	—	9 (8.04%)
Aggarwal et al. (2011) [1]	Western India	70	—	—	15.72%	—
Freire et al. (2011) [23]	Brazilian	80	7 (8.75%)	2 (2.5%)	5 (6.25%)	—
Fernandez-Miranda et al. (2012) [22]	Caucasian American	50	10 (20%)	3 (6%)	13 (26%)	—
Kanjija et al. (2012) [29]	Gujarat region	200	11 (6.5%)	18 (9%)	29 (14.5%)	15 (7.5%)
Kapur et al. (2012) [30]	Bosnian	200	19 (9.25%)	15 (7.5%)	33 (16.5%)	13 (6.5%)
Magadam et al. (2012) [37]	South India region	50	3 (6%)	—	3 (6%)	—
Shaikh et al. (2013) [51]	Western India	100	10 (10%)	14 (14%)	24 (24%)	—
Archana et al. (2013) [5]	South India region	50	1 (2%)	1 (2%)	2 (4%)	—
Bansode et al. (2017) [7]	South India region	35	2 (5.75%)	5 (14.2%)	7 (20%)	—
Purohit and Singh (2018) [49]	Gujarat region	200	15 (7.5%)	6 (3%)	21 (10.5%)	4 (2%)
Natsis et al. (2018) [45]	Greece	123	39 (31.7%)	35 (28.4%)	74 (60.1%)	24 (19.5%)
Sharma et al. (2018) [50]	Hamann-Todd Osteological collection	2726	—	—	1854 (68%)	224 (8%)
Caucasian*		2960	92 (3.1%)	77 (2.6%)	768 (25.9%)	248 (8.5%)
Turkish population**		621	66 (10.6%)	38 (6.1%)	145 (23.3%)	42 (6.7%)
South India region***		470	65 (13.89%)	39 (8.3%)	99 (21.06%)	9 (1.91%)
Gujrat region****		400	26 (6.5%)	24 (6%)	50 (12.5%)	21 (5.25%)
Present study	Bihar region	100	7 (7%)	2 (2%)	9 (9%)	1 (1%)

*Average results presented for the Caucasian population from Keyes (1935), Azeredo et al. (1988), Inoue et al. (1990), Kapur et al. (2012), Skrzat et al. (2012), and Natsis et al. (2018)

**Average results presented for Turkish population from Cireli et al. (1990), Deda et al. (1992), Gurun et al. (1994), Erturk et al. (2002), Peker et al. (2006), Bopyan et al. (2011)

***Average results presented for South Indian population from Desai et al. (2010), Kolagi et al. (2011), Magadam et al. (2012), Archana et al. (2013), and Bansode et al. (2017)

****Average results for Gujrat region from Kanjija et al. (2012), and Purohit and Singh (2018)

casian population of Greece. Though the frequency of incomplete variety was presented to be 46.6% in Hamann-Todd Osteological Collection by Sharma et al. [50], but the ethnicity of the collection cannot be fixed. Whenever this common variety presents with a pointed spicule it is then referred to as the dangerous type because of its ability to puncture the ICA. The next common variety, the complete CCF, can be

considered as a bony distal dural ring [46]. The contact-type CCFs are rarely reported. The Hamann-Todd Osteological Collection study for CCFs by Sharma et al. [50] reported its frequency in 2.75% samples. Becktor et al. [8] in their cephalometric radiograph study had presented the contact and incomplete STB as a common variety (type B in the study), the STB is responsible for converting the space between the

Table 2. Comparing the prevalence of caroticoclinoid foramen based on their morphology as observed in present study with those reported in literature

Study	Population/Region	Number of skulls	Caroticoclinoid foramen [n (%)]		
			Incomplete	Contact	Complete
Keyes (1935) [31]	Caucasian American	2187	418 (19.15%)	0	155 (7.08%)
Inoue T et al. (1990) [28]	Caucasian American	50	16 (32%)	0	1 (2%)
Lee et al. (1997) [35]	Korean	73	8 (11.60%)	0	3 (4.10%)
Erturk et al. (2004) [20]	Turkish	171	25 (14.91%)	0	6 (4.09%)
Ozdugmus et al. (2003) [47]	Turkish	50	0	0	3 (6%)
Archana et al. (2010) [4]	Indian	250	17 (6.8%)	0	9 (3.6%)
Aggarwal et al. (2011) [1]	Western India	70	9 (12.8%)	0	2 (2.8%)
Kanjija et al. (2012) [29]	Gujarat region	200	5 (2.5%)	0	16 (8%)
Fernandez-Miranda et al. (2012) [22]	Caucasian American	50	—	—	16 (32%)
Kapur et al. (2012) [30]	Bosnian	200	19 (9.5%)	0	9 (4.5%)
Shaikh et al. (2013) [51]	Western India	100	16 (16%)	0	4 (4%)
Archana et al. (2013) [5]	South India region	50	1 (2%)	0	1 (2%)
Dagtekin et al. (2014) [16]	Turkish	40	0	0	2 (5%)
Brahmbhatt et al. (2015) [10]	Gujrat region	50	0	0	1 (2%)
Bansode et al. (2017) [7]	South India region	35	3 (8.5%)	0	2 (5.7%)
Purohit and Singh (2018) [49]	Gujarat region	200	10 (5.0%)	0	11 (5.5%)
Natsis et al. (2018) [45]	Greece	123	45 (36.6%)	0	29 (23.6%)
Sharma et al. (2018) [50]	Hamann-Todd Osteological collection	2726	1275 (46.6%)	75 (2.75%)	504 (18.48%)
Caucasian*		2745	552 (20.4%)	0	226 (8.23%)
Turkish population**		261	25 (9.5%)	0	11 (4.2%)
South India region***		85	4 (4.7%)	0	3 (3.5%)
Gujrat region****		450	15 (3.3%)	0	28 (6.2%)
Present study (2021)	Bihar region	100	7 (7%)	0	2 (2%)

*Average results presented for the Caucasian population from Keyes (1935), Inoue et al. (1990), Leonardi et al. (2006), Kapur et al. (2012), and Natsis et al. (2018)

**Average results presented for Turkish population from Erturk et al. (2002), Ozdogmus et al. (2003), and Dagtekin et al. (2014)

***Average results presented for South Indian population from Archana et al. (2013), and Bansode et al. (2017)

****Average results for Gujrat region from Kanjija et al. (2012), Brahmbhatt et al. (2015), and Purohit and Singh (2018)

clinoid processes into a foramen. Ota et al. [46] mentioned that it is difficult to distinguish between the contact and incomplete variety of CCF intraoperatively and on preoperative computed tomography (CT), forcing them to classify the CCFs into two varieties only. Such reasons add to the limited reporting of the contact type CCF. Though Suprasanna et al. [54] reported the frequency of the contact variety CCF as 9.2% in a CT angiography study of south Indian population. The report included 1.8% frequency for bilateral contact variety CCF and 5.5% frequency for unilateral presence of contact variety CCF (Table 3).

The unilateral CCF are more frequently observed than the bilateral ones in dry skull data reported in literature from different populations (Table 1). The present study too observed a three times higher frequency of the unilateral CCF. Radiographic data from

lateral view cephalometric studies, CT angiograms, and scans of head region presented with observations similar to the dry skull data regarding laterality of CCF, with the exception of the tomographic study data by Touska et al. [55]. They reported higher proportions of bilateral CCF (10.1%) in Caucasians of United Kingdom (Table 3).

Many of the radiological studies based on the ossification of the ICL or CCL have analysed the association of the ligamentous ossification with age and sex [14, 25, 36, 54, 55]. Most of these studies have reported no significant association for the ossification of ICL or CCL in either of the genders [14, 25, 36, 54, 55]. A positive correlation between age and ICL or CCL ossification was reported by Cederberg et al. [14] and Leonardi et al. [36], whereas Suprasanna et al. [54], Gibelli et al. [25], and Touska et al. [55]

Table 3. Comparing the radiological prevalence of caroticoclinoid foramen based on their laterality and morphology as observed in present study with those reported in literature

Study	Population/ /Region	Sample size (n)	Age range [years]	Gender distribu- tion	Caroticoclinoid foramen [n (%)]		
					Incomplete	Complete	Contact
Becktor et al. (2000) [8]	Denmark	177 lateral view cephalometric radiographs	—	—	—	33 (18.6%)	—
Cederberg et al. (2003) [14]	Caucasian American	255 lateral view cephalometric radiographs	8–76	M = 114 F = 141	185 (72.5%)	21 (8.2%)	—
Leonardi et al. (2006) [36]	Italian	135 lateral view cephalometric radiographs	8–16	—	54 (40%)	16 (11.9%)	—
Alkofide (2007) [3]	Saudi Arabian	180 cephalograms	10–26	M = 90 F = 90	—	2 (1.1%)	—
Marsan and Oztas (2009) [40]	Turkish	118 cephalograms	21–32	F = 118	—	14 (11.86%)	—
Meyer-Marcotty et al. (2010) [41]	German	400 cephalograms	16 - 34	—	—	56 (14%)	—
Fernandez-Miranda et al. (2012) [22]	Caucasian American	100 CT angiograms	—	—	—	U/L = 20 (20%); B/L = 6 (6%)	—
Kucia et al. (2014) [34]	Polish	322 lateral view cephalometric radiographs	9–16	—	22 (6.8%)	16 (4.9%)	—
Ota et al. (2015) [46]	Japan	72 CT angiograms for para-clinoid aneurysm	31–78	M = 8 F = 64	9 (6.25%)	9 (6.25%)	—
Miller et al. (2017) [42]	Caucasian American	150 maxillofacial CT	31–68	M = 75 F = 75	—	63 (42%)	—
Suprasanna et al. (2017) [54]	South India	54 CT cerebral angiography studies showing para-clinoid aneurysms	18–70	M = 24 F = 30	11 (20.37%) U/L = 7 (12.96%); B/L = 2 (3.7%)	8 (14.8%) U/L = 4 (7.4%); B/L = 2 (3.7%)	5 (9.2%) U/L = 3 (5.5%); B/L = 1 (1.8%)
Gibelli et al. (2018) [25]	Italian	300 CT head scans	18–99	M = 150 F = 150	—	26 (8.7%)	—
Touska et al. (2019) [55]	United Kingdom	240 CT studies	6–80	M = 119 F = 121	10 (4.1%)	15 (6.2%)	—
Present study (2021)	Bihar	50 lateral view radiographs of the head	12–73	M = 25 F = 25	2 (4%) [U/L]	1 (2%) [B/L]	—

B/L — bilateral; CT — computed tomography; F — female; M — male; U/L — unilateral

mentioned that no significant correlation was found between the entities.

Most of the reported data on CCF is mainly concerned with its frequency in different populations as well as the effects it possesses on the nearby neurovascular structures. The dimensions of CCF are merely documented, and if so, that too only for the complete ones. The vertical diameter of the complete foramen on either side for the present study data is higher than that reported in the literature, while that for the antero-posterior (AP) diameter is lesser than that reported by Freire et al. [23] and Ozdugmus et al. [47] on either side. The vertical diameter measurements for incomplete foramina were not found in the literature, therefore couldn't be compared with the present study findings (Table 4) [23, 38, 47]. The variation in dimensions of CCF could help in predicting the mor-

phological changes it causes to the clinoidal segment of the ICA [17]. Also, the CCF's metric data could be used to advantage in cases where it becomes difficult to distinguish between the varieties of the CCF, as was explained by Ota et al. [46]. These could be vital for neurosurgeons as the measurements could be obtained preoperatively from the digital radiographs or CT scans.

The embryological development of sphenoid bone in mammal occurs from two components: first, the basi-post-sphenoid and the orbito-sphenoid, being derived from cephalic mesoderm, and second, the basi-pre-sphenoid and the ali-sphenoid from neural crest cells. The two primordia have different genetic control which adds to their heterogeneity [13]. The literature cites numerous evidences explaining the development of anomalous structure from the neural

Table 4. Comparing reported data of foraminal parameters with those of present study

	Measurements of caroticoclinoid foramen [mm]					
	RIGHT			LEFT		
	Complete		Incomplete	Complete		Incomplete
	AP	Vertical	Vertical	AP	Vertical	Vertical
Ozdogmus et al. (2003) [47]	5.14	—	—	5.25	—	—
Freire et al. (2011) [23]	5.23	—	—	5.23	—	—
Mallik and Sawant (2015) [38]	4.01	3.64	—	4.12	3.6	—
Present study (2021)	4.06	4.51	4.48	5.15	4.14	4.19

AP — antero-posterior

crest, such as cleft palate, palatal displacement of canines, and neck skeletal elements in cases of ponticulus posticus [25]. This association of the neural crest cells with anomalies might also explain the ectopic ossification of CCL as a developmental anomaly.

The ectopic calcification of the CCLs, which are soft tissue elements, can also be a part of genetic syndromes such as Gorlin-Goltz syndrome, clinically known as Nevoid basal cell carcinoma syndrome (NBCCS) [39] or can be caused due to mutations in genes preventing mineralisation (osteopontin or matrix Gla protein gene) [43, 52].

One of the protected structures underneath the dural fold or ligaments between the clinoid processes is ICA, which at the termination of carotid sulcus passes through an osseo-ligamentous opening bounded superiorly by the ACP, postero-inferiorly by the MCP, anteriorly by the lateral edge of tuberculum sellae, and postero-superiorly by the CCL between the two processes [21]. Clinically, the ossified CCL can present with severe headache due to traction on the ICA [47], and radiographically it may be misdiagnosed as a para-posterior communicating arterial aneurysm on CT angiography [27]. In conditions requiring surgical exposure of ICA and cavernous sinuses, such as clinoidal segment aneurysm or in removal of central skull base tumour (skull base meningiomas, craniopharyngiomas, supra-sellar extended pituitary adenomas), the ossified ligament could warrant excessive manipulation and drilling during anterior clinoidectomy, thus may lead to damage or rupture of the ICA [50]. In endoscopic procedures, the endonasal approach to the pituitary gland can be complicated due to the ossified CCL as it obscures the MCP presentation which acts as a landmark for the anteromedial dome of cavernous sinus and for the progression of ICA from its clinoidal segment to its cavernous part [22]. To diagnose such clinical scenarios, or to clarify the

radiographic confusion, and to foresee the surgical complications presented by the CCF, it is mandatory to have the pertinent knowledge and awareness regarding the occurrence and frequency of the CCF formed due to the ossified CCL.

The clinical implications and intra-op surgical complications of CCF are mainly due to ossification of the CCL which renders the foramen unyielding to the underlying structures and hinders their surgical exposure [44]. Various researchers have tried to associate this ectopic ossification with endocrinological disorders [48], infectious diseases [12, 25], cranio-facial deviations [8], ageing [25, 45], and developmental anomaly [32]. While the literature nullifies the role of endocrinological disorders and infectious diseases in the aetiology of the ossified ligament, it does provide contradicting evidence regarding the role played by ageing in the same where some authors have reported ectopic ossification of the CCL as an age-related change [14, 36] while others have refuted the same with evidence [25, 45, 54, 55]. Also, there have been a few logical scientific explanations (but no experimental proof) indicating that the complex embryology [13], and genetics [25, 43, 52] can play a crucial role in the aetiopathogenesis of CCF.

The present study authors in one of their previous reports have mentioned the unique finding where the ICF was divided into two foramina by an osseous bar between the MCP and the midpoint of the right lateral border of the dorsum sellae (Figs. 2B; 3) [44]. The foramen beneath the osseous bar was supposed to be formed around inferior inter-cavernous sinus, which may pose same radiological and intra-op surgical complications as have been discussed for CCF. Similar finding had been previously reported by Galdames et al. [24] on the left side in an osteological case report but didn't provide any theories about the finding. Localised compression of the inferior inter-cavernous

sinus due to the unyielding foramen around it can be viewed as dilation on sagittal T1-weighted magnetic resonance imaging images, a false positive radiological sign for intracranial hypotension [2].

CONCLUSIONS

Intricate knowledge of the CCF is of paramount importance in treatment of clinoidal segment aneurysm of ICA, arterio-venous malformation, and while approaching the central skull base tumours. Topographically, CCF is crucial because of its vicinity with sphenoidal sinus, cavernous sinus, and pituitary gland. The frequency of CCF in the present study population of Bihar was much lesser than that of the Caucasian, Turkish and other Asian populations. However, the variation in frequency of different morphological types of CCF was observed to be the same across populations. Where the incomplete type of CCF was the most common variety followed by the complete and contact type. The difficulty to distinguish the contact type from the incomplete type on the preoperative CT scans or during operative procedures and being classified together with the incomplete type are a few reasons for the meagre reporting of the contact type. The CCF was observed to be more prevalent as a unilateral entity in both the dry skull and radiological data across populations. The variations in CCF's metric data could help in predicting the morphological changes it causes to the clinoidal segment of the ICA, as well as in distinguishing its varieties. The frequency of CCF depends on various factors such as age, embryology, and genetics. The association of ageing with the ossification of CCL has contradictory evidence in literature, while the embryological theory of sphenoid bone formation from different primordia does explain the ossification as a developmental anomaly. The pre-op radiological examination of the head helps in confirming the extent and morphology of the ligamentous calcification which in turn prevents surgical complications, misinterpretation of para-posterior communicating arterial aneurysm on CT angiography, and intracranial hypotension on sagittal T1-weighted magnetic resonance imaging images. The present study in Bihar region needs more data for both the dry skull and radiological samples, to be compared comprehensively with populations having large data base. Data of different parameters of the CCF along with the points to measure them on radiological entities would help the neurosurgeons to better utilize the morphometric aspect of the fo-

ramina during surgical procedures. As the sensitivity of CT scans in distinguishing the varieties of CCF has emerged as an issue, it provides the scope of further studies on the entity.

Acknowledgements

We are grateful to all the technical staff who contributed to all protocol/project development, data collection or management, data analysis of the study. We also thank all the residents and faculty members of Department of Anatomy and Radiodiagnosis of All India Institute of Medical Science Patna.

Conflict of interest: None declared

REFERENCES

1. Aggrawal B, Gupta M, Kumar H. Ossified caroticoclinoid ligament of sphenoid bone. *Bombay Hosp J.* 2011; 53(4): 743–746.
2. Alcaide-Leon P, López-Rueda A, Coblentz A, et al. Prominent Inferior Intercavernous Sinus on Sagittal T1-Weighted Images: A Sign of Intracranial Hypotension. *AJR Am J Roentgenol.* 2016; 206(4): 817–822, doi: [10.2214/AJR.15.14872](https://doi.org/10.2214/AJR.15.14872), indexed in Pubmed: [27003051](https://pubmed.ncbi.nlm.nih.gov/27003051/).
3. Alkofide EA. The shape and size of the sella turcica in skeletal Class I, Class II, and Class III Saudi subjects. *Eur J Orthod.* 2007; 29(5): 457–463, doi: [10.1093/ejo/cjm049](https://doi.org/10.1093/ejo/cjm049), indexed in Pubmed: [17693429](https://pubmed.ncbi.nlm.nih.gov/17693429/).
4. Archana R, Anita R, Jyoti C, et al. Incidence of osseous interclinoid bars in Indian population. *Surg Radiol Anat.* 2010; 32(4): 383–387, doi: [10.1007/s00276-009-0582-z](https://doi.org/10.1007/s00276-009-0582-z), indexed in Pubmed: [19862467](https://pubmed.ncbi.nlm.nih.gov/19862467/).
5. Archana BJ, Shivaleela C, Kumar GV, et al. An osteological study of incidence, morphometry, and clinical correlations of carotico-clinoid foramen in dried adult human skulls. *RJPBCS.* 2013; 4(3): 347–352.
6. Azeredo RA, Liberti EA, Watanabe IS. Anatomical variations of the clinoid process of the human sphenoid bone. *Arq Cent Estud Curso Odontol Univ Fed Minas Gerais.* 1988; 25-26: 9–11.
7. Bansode S, P D, Vinila B, et al. Study of incidence of the carotico-clinoid foramen in the south Indian dry adult skulls: a cross sectional study. *Int J Anat Res.* 2017; 5(3.1): 4051–4055, doi: [10.16965/ijar.2017.247](https://doi.org/10.16965/ijar.2017.247).
8. Becktor JP, Einersen S, Kjaer I. A sella turcica bridge in subjects with severe craniofacial deviations. *Eur J Orthod.* 2000; 22(1): 69–74, doi: [10.1093/ejo/22.1.69](https://doi.org/10.1093/ejo/22.1.69), indexed in Pubmed: [10721247](https://pubmed.ncbi.nlm.nih.gov/10721247/).
9. Boyan N, Ozsahin E, Kizilkanat E, et al. Surgical importance of the morphometry of the anterior clinoid process, optic strut, caroticoclinoid foramen, and interclinoid osseous bridge. *Neurosurgery Quarterly.* 2011; 21(2): 133–136, doi: [10.1097/wnq.0b013e31820f1929](https://doi.org/10.1097/wnq.0b013e31820f1929).
10. Brahmbhatt RJ, Bansal M, Mehta C, et al. Prevalence and dimensions of complete sella turcica bridges and its clinical significance. *Indian J Surg.* 2015; 77(Suppl 2): 299–301, doi: [10.1007/s12262-012-0800-5](https://doi.org/10.1007/s12262-012-0800-5), indexed in Pubmed: [26730013](https://pubmed.ncbi.nlm.nih.gov/26730013/).

11. Camarda AJ, Deschamps C, Forest D, et al. Stylohyoid chain ossification: a discussion of etiology. *Oral Surg Oral Med Oral Pathol.* 1989; 67(5): 508–514, doi: [10.1016/0030-4220\(89\)90264-8](https://doi.org/10.1016/0030-4220(89)90264-8), indexed in Pubmed: [2497419](https://pubmed.ncbi.nlm.nih.gov/2497419/).
12. Carstens M. Die selladiagnostik. *Fortschr Geb Rontgenstrahlen.* 1949; 71: 257–272.
13. Catala M. [Embryology of the sphenoid bone]. *J Neuroradiol.* 2003; 30(4): 196–200, indexed in Pubmed: [14566186](https://pubmed.ncbi.nlm.nih.gov/14566186/).
14. Cederberg RA, Benson BW, Nunn M, et al. Calcification of the interclinoid and petroclinoid ligaments of sella turcica: a radiographic study of the prevalence. *Orthod Craniofac Res.* 2003; 6(4): 227–232, doi: [10.1034/j.1600-0544.2003.00243.x](https://doi.org/10.1034/j.1600-0544.2003.00243.x), indexed in Pubmed: [14606526](https://pubmed.ncbi.nlm.nih.gov/14606526/).
15. Cireli E, Ustun EE, Yurtseven M, et al. Fossa sella turcica varyasyonlarının degerlendirilmesi I: Morfolojik ve antropolojik kriterlere gre. *Ege Tıp Dergisi.* 1990; 29: 364–367.
16. Dagtekin A, Avci E, Uzansel D, et al. Microsurgical anatomy and variations of the anterior clinoid process. *Turk Neurosurg.* 2014; 24(4): 484–493, doi: [10.5137/1019-5149.JTN.8738-13.1](https://doi.org/10.5137/1019-5149.JTN.8738-13.1), indexed in Pubmed: [25050671](https://pubmed.ncbi.nlm.nih.gov/25050671/).
17. Das S, Suri R, Kapur V. Ossification of caroticoclinoid ligament and its clinical importance in skull-based surgery. *Sao Paulo Med J.* 2007; 125(6): 351–353, doi: [10.1590/s1516-31802007000600009](https://doi.org/10.1590/s1516-31802007000600009), indexed in Pubmed: [18317606](https://pubmed.ncbi.nlm.nih.gov/18317606/).
18. Deda H, Tekdemir I, Kaplan A, et al. Sinus cavernosus mikro anatomisi (bölüm 1) kemik yapılar ve varyasyonlar. *J Faculty Med Univ Ankara.* 1992; 45: 477–486.
19. Desai SD, Sreepadma S. Study of caroticoclinoid foramen in dry human skulls of North Interior Karnataka. *NJBMS.* 2010; 1: 60–64.
20. Erturk M, Kayalioglu G, Govsa F. Anatomy of the clinoidal region with special emphasis on the caroticoclinoid foramen and interclinoid osseous bridge in a recent Turkish population. *Neurosurg Rev.* 2004; 27(1): 22–26, doi: [10.1007/s10143-003-0265-x](https://doi.org/10.1007/s10143-003-0265-x), indexed in Pubmed: [14634836](https://pubmed.ncbi.nlm.nih.gov/14634836/).
21. Evans BT. Infratemporal and pterygopalatine fossae and temporomandibular joint. In: Standring S, Anand N (eds.) *Gray's Anatomy: The Anatomical Basis of Clinical Practice.* Elsevier, Philadelphia 2016: 534–555.
22. Fernandez-Miranda JC, Tormenti M, Latorre F, et al. Endoscopic endonasal middle clinoidectomy: anatomic, radiological, and technical note. *Neurosurgery.* 2012; 71(2 Suppl): 233–239, doi: [10.1227/NEU.0b013e3182690b6b](https://doi.org/10.1227/NEU.0b013e3182690b6b), indexed in Pubmed: [22806082](https://pubmed.ncbi.nlm.nih.gov/22806082/).
23. Freire AR, Rossi A, Prado FB, et al. Caroticoclinoid foramen in human skulls: incidence, morphometry and its clinical implications. *Int J Morphol.* 2011; 29(2): 427–431, doi: [10.4067/s0717-95022011000200021](https://doi.org/10.4067/s0717-95022011000200021).
24. Galdames IS, Matamala DZ, Smith R. Ossification of the sella turcica and clinoid ligaments: case report, morphological study and literature review. *Int J Morphol.* 2008; 26(4): 799–801, doi: [10.4067/s0717-95022008000400002](https://doi.org/10.4067/s0717-95022008000400002).
25. Gibelli D, Cellina M, Gibelli S, et al. Sella turcica bridging and ossified carotico-clinoid ligament: Correlation with sex and age. *Neuroradiol J.* 2018; 31(3): 299–304, doi: [10.1177/1971400917751036](https://doi.org/10.1177/1971400917751036), indexed in Pubmed: [29323624](https://pubmed.ncbi.nlm.nih.gov/29323624/).
26. Gurun R, Magden O, Ertem AD. Foramen corticoclinoidem. *Cerrahpasa Tıp Dergisi.* 1994; 25: 685–691.
27. Gupta V, Khandelwal N, Mathuria SN, et al. Calcified interclinoid ligament: an unusual cause of misinterpretation on cerebral CT angiography. *Clin Radiol.* 2013; 68(7): e426–e428, doi: [10.1016/j.crad.2013.03.019](https://doi.org/10.1016/j.crad.2013.03.019), indexed in Pubmed: [23622793](https://pubmed.ncbi.nlm.nih.gov/23622793/).
28. Inoue T, Rhoton AL, Theele D, et al. Surgical approaches to the cavernous sinus: a microsurgical study. *Neurosurgery.* 1990; 26(6): 903–932, doi: [10.1097/00006123-199006000-00001](https://doi.org/10.1097/00006123-199006000-00001), indexed in Pubmed: [2362670](https://pubmed.ncbi.nlm.nih.gov/2362670/).
29. Kanjiya D. Incidence of ossified interclinoid bars in dry human skulls of Gujarat state. *IJBAR.* 2013; 3(12), doi: [10.7439/ijbar.v3i12.867](https://doi.org/10.7439/ijbar.v3i12.867).
30. Kapur E, Mehić A. Anatomical variations and morphometric study of the optic strut and the anterior clinoid process. *Bosn J Basic Med Sci.* 2012; 12(2): 88–93, doi: [10.17305/bjbm.2012.2502](https://doi.org/10.17305/bjbm.2012.2502), indexed in Pubmed: [22642592](https://pubmed.ncbi.nlm.nih.gov/22642592/).
31. Keyes JEL. Observations on four thousand optic foramina in human skulls of known origin. *Arch Ophthalmol.* 1935; 13(4): 538–568, doi: [10.1001/archophth.1935.00840040026002](https://doi.org/10.1001/archophth.1935.00840040026002).
32. Kjaer I. Ossification of the human fetal basicranium. *J Craniofac Genet Dev Biol.* 1990; 10(1): 29–38, indexed in Pubmed: [2373754](https://pubmed.ncbi.nlm.nih.gov/2373754/).
33. Kolagi S, Herur A, Patil G, et al. Complete sella turcica bridges prevalence and dimensions. *J Anat Soc India.* 2011; 60(1): 22–25, doi: [10.1016/s0003-2778\(11\)80005-5](https://doi.org/10.1016/s0003-2778(11)80005-5).
34. Kucia A, Jankowski T, Siewniak M, et al. Sella turcica anomalies on lateral cephalometric radiographs of Polish children. *Dentomaxillofac Radiol.* 2014; 43(8): 20140165, doi: [10.1259/dmfr.20140165](https://doi.org/10.1259/dmfr.20140165), indexed in Pubmed: [25182120](https://pubmed.ncbi.nlm.nih.gov/25182120/).
35. Lee HY, Chung IH, Choi BY, et al. Anterior clinoid process and optic strut in Koreans. *Yonsei Med J.* 1997; 38(3): 151–154, doi: [10.3349/ymj.1997.38.3.151](https://doi.org/10.3349/ymj.1997.38.3.151), indexed in Pubmed: [9259614](https://pubmed.ncbi.nlm.nih.gov/9259614/).
36. Leonardi R, Barbato E, Vichi M, et al. A sella turcica bridge in subjects with dental anomalies. *Eur J Orthod.* 2006; 28(6): 580–585, doi: [10.1093/ejo/cjl032](https://doi.org/10.1093/ejo/cjl032), indexed in Pubmed: [16954179](https://pubmed.ncbi.nlm.nih.gov/16954179/).
37. Magadam A, Jevoor P, Dixit D, et al. A study of caroticoclinoid foramen in the South Indian skulls: Incidence, morphometry, and its clinical correlations. *BIOMIRROR, An Open Access Journal.* 2012; 3(5): 1–3.
38. Mallik S, Santanu VG. Bilateral “carotico-clinoid foramen” with “sella turcica bridge”: a case report. *Anat Physiol.* 2015; 5(S5), doi: [10.4172/2161-0940.s5-006](https://doi.org/10.4172/2161-0940.s5-006).
39. Manjima S, Naik Z, Keluskar V, et al. Multiple jaw cysts-unveiling the Gorlin-Goltz syndrome. *Contemp Clin Dent.* 2015; 6(Suppl 1): S102–S105, doi: [10.4103/0976-237X.152959](https://doi.org/10.4103/0976-237X.152959), indexed in Pubmed: [25821359](https://pubmed.ncbi.nlm.nih.gov/25821359/).
40. Marsan G, Oztas E. Incidence of bridging and dimensions of sella turcica in Class I and Class III Turkish adult female patients. *World J Orthod.* 2009; 2: 99–103.
41. Meyer-Marcotty P, Reuther T, Stellzig-Eisenhauer A. Bridging of the sella turcica in skeletal Class III subjects. *Eur J Orthod.* 2010; 32(2): 148–153, doi: [10.1093/ejo/cjp081](https://doi.org/10.1093/ejo/cjp081), indexed in Pubmed: [19752019](https://pubmed.ncbi.nlm.nih.gov/19752019/).
42. Miller C, Chamoun R, Beahm D. Morphometric analysis of the middle clinoid process using maxillofacial computed tomography scans. *Oper Neurosurg (Hagerstown).* 2017;

- 13(1): 124–130, doi: [10.1227/NEU.0000000000001310](https://doi.org/10.1227/NEU.0000000000001310), indexed in Pubmed: [28931257](https://pubmed.ncbi.nlm.nih.gov/28931257/).
43. Murshed M, Schinke T, McKee MD, et al. Extracellular matrix mineralization is regulated locally; different roles of two gla-containing proteins. *J Cell Biol.* 2004; 165(5): 625–630, doi: [10.1083/jcb.200402046](https://doi.org/10.1083/jcb.200402046), indexed in Pubmed: [15184399](https://pubmed.ncbi.nlm.nih.gov/15184399/).
 44. Narayan RK, Asghar A, Ghosh SK. Ossification around intercavernous sinus: an osteological finding that can complicate trans-sphenoidal surgery. *Morphologie.* 2020; 104(347): 280–286, doi: [10.1016/j.morpho.2020.06.005](https://doi.org/10.1016/j.morpho.2020.06.005), indexed in Pubmed: [32646846](https://pubmed.ncbi.nlm.nih.gov/32646846/).
 45. Natsis K, Piagkou M, Lazaridis N, et al. Incidence and morphometry of sellar bridges and related foramina in dry skulls: Their significance in middle cranial fossa surgery. *J Craniomaxillofac Surg.* 2018; 46(4): 635–644, doi: [10.1016/j.jcms.2018.01.008](https://doi.org/10.1016/j.jcms.2018.01.008), indexed in Pubmed: [29534911](https://pubmed.ncbi.nlm.nih.gov/29534911/).
 46. Ota N, Tanikawa R, Miyazaki T, et al. Surgical microanatomy of the anterior clinoid process for paraclinoid aneurysm surgery and efficient modification of extradural anterior clinoidectomy. *World Neurosurg.* 2015; 83(4): 635–643, doi: [10.1016/j.wneu.2014.12.014](https://doi.org/10.1016/j.wneu.2014.12.014), indexed in Pubmed: [25527880](https://pubmed.ncbi.nlm.nih.gov/25527880/).
 47. Ozdoğmuş O, Saka E, Tulay C, et al. The anatomy of the carotico-clinoid foramen and its relation with the internal carotid artery. *Surg Radiol Anat.* 2003; 25(3-4): 241–246, doi: [10.1007/s00276-003-0111-4](https://doi.org/10.1007/s00276-003-0111-4), indexed in Pubmed: [12748816](https://pubmed.ncbi.nlm.nih.gov/12748816/).
 48. Peker T, Anil A, Gülekon N, et al. The incidence and types of sella and sphenopetrous bridges. *Neurosurg Rev.* 2006; 29(3): 219–223, doi: [10.1007/s10143-006-0018-8](https://doi.org/10.1007/s10143-006-0018-8), indexed in Pubmed: [16528575](https://pubmed.ncbi.nlm.nih.gov/16528575/).
 49. Purohit BJ, Singh PR. Incidence, anatomy and clinical significance of carotico-clinoid foramen and interclinoid osseous bridge in human skulls in gujarat region. *Int J Anat Radiol Surg.* 2018; 7(2): 33–37, doi: [10.7860/IJARS/2018/35641:2391](https://doi.org/10.7860/IJARS/2018/35641:2391).
 50. Sharma A, Rieth GE, Tanenbaum JE, et al. A morphometric survey of the parasellar region in more than 2700 skulls: emphasis on the middle clinoid process variants and implications in endoscopic and microsurgical approaches. *J Neurosurg.* 2018; 129(1): 60–70, doi: [10.3171/2017.2.JNS162114](https://doi.org/10.3171/2017.2.JNS162114), indexed in Pubmed: [28799880](https://pubmed.ncbi.nlm.nih.gov/28799880/).
 51. Shaikh S, Ukey R, Kawale D, et al. Study of carotico-clinoid foramen in dry human skull of aurangabad district. *Int J Basic Med Sci.* 2013; 5(3): 148–154.
 52. Steitz SA, Speer MY, McKee MD, et al. Osteopontin inhibits mineral deposition and promotes regression of ectopic calcification. *Am J Pathol.* 2002; 161(6): 2035–2046, doi: [10.1016/S0002-9440\(10\)64482-3](https://doi.org/10.1016/S0002-9440(10)64482-3), indexed in Pubmed: [12466120](https://pubmed.ncbi.nlm.nih.gov/12466120/).
 53. Skrzat J, Szewczyk R, Walocha J. The ossified interclinoid ligament. *Folia Morphol.* 2006; 65(3): 242–245, indexed in Pubmed: [16988924](https://pubmed.ncbi.nlm.nih.gov/16988924/).
 54. Suprasanna K, Kumar A. Surgically relevant bony anatomical variations in paraclinoid aneurysms-three-dimensional multi-detector row computed tomography-based study. *J Neurosci Rural Pract.* 2019; 8(3): 330–334, doi: [10.4103/jnpr.jnpr_416_16](https://doi.org/10.4103/jnpr.jnpr_416_16).
 55. Touska P, Hasso S, Oztek A, et al. Skull base ligamentous mineralisation: evaluation using computed tomography and a review of the clinical relevance. *Insights Imaging.* 2019; 10(1): 55, doi: [10.1186/s13244-019-0740-8](https://doi.org/10.1186/s13244-019-0740-8), indexed in Pubmed: [31115710](https://pubmed.ncbi.nlm.nih.gov/31115710/).

Porcine coronary arteries: immunohistochemical profile of TNF-alpha, IL-1beta, TGF-beta1 and ICAM-1

S. Taurone^{1*}, M.T. Santarelli^{1*}, E. De Santis², C. Di Gioia³, E. Pompili², F. Pellegrino⁴, P. Familiari⁵, V. Papa⁶, C. Zanza^{7,8,9}, L. Coppola⁴, G. Familiari^{2*}, M. Artico^{1*}

¹Department of Sensory Organs, Sapienza University of Rome, Italy

²Department of Anatomical, Histological, Forensic Medicine and Orthopaedics Sciences, Sapienza University of Rome, Italy

³Department of Radiological, Oncological and Pathological Sciences, Sapienza University of Rome, Italy

⁴UOC of Pathology, Sandro Pertini Hospital, Rome, Italy

⁵Department of Human Neurosciences, Sapienza University of Rome, Italy

⁶Department of Motor Sciences and Wellness, University of Naples "Parthenope", Naples, Italy

⁷Department of Emergency Medicine, Foundation of Policlinico Agostino Gemelli-IRCCS, Catholic University of Sacred Heart, Rome, Italy.

⁸Department of Anaesthesia and Critical Care, AON SS Antonio e Biagio e Cesare Arrigo, Alessandria, Italy

⁹Foundation Ospedale Alba-Bra and Department of Anaesthesia, Critical Care and Emergency Medicine, Pietro and Michele Ferrero Hospital, Verduno, Italy

[Received: 5 June 2021; Accepted: 27 November 2021; Early publication date: 16 December 2021]

Background: In our study we used immunohistochemical technique to demonstrate the presence of the cytokines tumour necrosis factor alpha (TNF- α), interleukin 1beta (IL-1 β), transforming growth factor beta1 (TGF- β 1) and intercellular adhesion molecule-1 (ICAM-1) in porcine coronaries even in physiological conditions. *Materials and methods:* Inflammatory cytokines are polypeptide mediators which act as a communication signal between immune system cells and other types of cells in different organs and tissues, both in human and pig coronary circulation. *Results:* Our results show that pro-inflammatory cytokines TNF- α , IL-1 β , TGF- β 1 and ICAM-1 are also present in the medium tunica of the coronary arteries under physiological conditions. These results may be compared with those found in coronary atherosclerosis, where the increase in TNF- α has a dramatic effect on the function of the left ventricle, and the high value of IL-1 correlates directly with the extent of myocardial necrosis. In our study we observe the damage and activation of endothelial cells; this induces endothelial dysfunction by accumulation and oxidation of low density lipoproteins (LDL). The formation of oxidized LDL could play a central role in the amplification of the inflammatory response causing an increased expression of pro-inflammatory cytokines which promotes leukocyte recruitment in the intimal layer. These leukocytes, after the adhesion to the endothelium, penetrate the intimate tunic. *Conclusions:* Therefore inflammatory processes promote the onset and evolution of atheroma and the development of thrombotic complications. (Folia Morphol 2023; 82, 1: 119–126)

Key words: porcine coronary arteries, cytokines, IL-1beta, TNF-alpha, TGF-beta1, ICAM-1

Address for correspondence: Dr. S. Taurone, Department of Sensory Organs, Sapienza University of Rome, Policlinico Umberto I, v. le del Policlinico 155, 00161 Rome, Italy, tel: +39 0649976852, e-mail: t.samanta@yahoo.it

*These authors equally contributed

This article is available in open access under Creative Common Attribution-Non-Commercial-No Derivatives 4.0 International (CC BY-NC-ND 4.0) license, allowing to download articles and share them with others as long as they credit the authors and the publisher, but without permission to change them in any way or use them commercially.

INTRODUCTION

Cytokines are proteins produced by various types of cells in response to a stimulus; they have autocrine or paracrine effects and led the cells of the immune system to communicate with each other. Many cytokines are pleiotropic, because they act on a large variety of cells and tissues [5, 25]. Cytokines play an important role in cardiovascular disease by inducing inflammation, cell proliferation and apoptosis. Activated macrophages are known to be a major source of inflammatory cytokines. Previous studies have shown that cells present in the vascular wall, such as vascular smooth muscle and endothelial cells, produce different types of cytokines that are involved in cardiovascular disease [16, 18, 27]. Coronary atherosclerosis represents the main cardiac manifestation of a systemic pathological process initiated and fuelled by cellular and humoral mechanisms of an inflammatory nature [23]. Most cardiac pathologies such as acute myocardial infarction and its complications are the result of the action of a complex inflammatory network that culminates and is concentrated in the event acute but involves the entire body and in particular the cardio-vascular system [35]. The atherosclerotic process begins with the accumulation of low density lipoprotein (LDL)-cholesterol in the intestine with consequent endothelial damage, which favours inflammation, which is responsible for the expression of adhesion molecules on the cell membrane and the secretion of biologically active and chemotactic substances such as cytokines, growth factors and free radicals; these substances favour the recall and subsequent infiltration of leukocytes, with transformation of monocytes into macrophages. The secretion of inflammatory cytokines and some growth factors favour the proliferation and migration towards the intima of the smooth muscle cells (SMC) of the middle layer, promoting the formation of the fibrolipidic plaque [2, 43, 44]. The formation of atherosclerotic plaques determines the onset of coronary heart disease. They form on the inner walls of the cardiac arteries following the migration of SMC and the production of components of the extracellular matrix. These pro-inflammatory events recruit immune cells into the plaques causing severe inflammation and thrombosis [30]. The precise molecular mechanisms responsible for the transformation of an atheroma into an atherosclerotic plaque remain unknown, based on the theory that inflammation is the main trigger we decided to carry out a prelimi-

nary study on porcine coronary arteries. The porcine heart offers really a good resemblance to the human heart, especially about coronary arteries and haemodynamics. Moreover, the wide social acceptance of their use, the similarity of their coronary circulation to that of humans, the approximation of their haemodynamic values and the size of the heart, make this animal model ideal for experimental studies [15, 20]. In the present study we studied the expression of some cytokines that are supposed to be involved in the cascade mechanisms after vascular damage.

Interleukin 1 (IL-1) and tumour necrosis factor alpha (TNF- α) practically act on all cells and tissues and are defined as "primary inflammatory cytokines", because they are capable of setting in motion the entire cascade of mediators of the inflammatory response [26, 39]. Transforming growth factor beta1 (TGF- β 1) is the most widespread cytokine present in endothelial cells, connective tissues and blood. Intercellular adhesion molecule-1 (ICAM-1) is a member of the immunoglobulin super family, including antibodies and T-cell receptors, it is present in low concentrations in the membranes of leukocytes and endothelial cells. ICAM-1 release may be induced by IL-1 and TNF- α and it is expressed by vascular endothelium, macrophages and lymphocytes. Investigation of the mechanisms of atherosclerosis determined that inflammation plays a central role in the development, progression and outcome of acute coronary syndrome. Many scientific works demonstrate the role of some cytokines in acute coronary syndrome: IL-8, IL-10, IL-18, IL-2, TNF- α , interferon γ are involved in this clinical condition [26, 29, 31, 38, 39, 41, 42]. The inflammatory theory of Russell Ross [33] concerns the mechanism by which cardiovascular risk factors evoke a restorative response from the vascular wall. This mechanism consists of a response that begins by endothelial activation, a purely functional alteration, and then it progresses and stabilizes by the formation of an atherosclerotic plaque, a real morphological alteration. This key concept focuses scientific interest in the actors of the inflammatory response, in particular the leukocytes and the mediators that modulate and support this process. This theory is supported by experimental data and simultaneous elevation, in case of coronary atherosclerosis, of the markers of inflammation, including also some inflammatory cytokines with proven implications on prognosis. In various animal models of atherosclerosis, signs of inflammation have been found together with lipid

accumulation in the wall of the arteries. In an experimental diabetic model obtained from pigs with streptozotocin-induced diabetes, an increased production of superoxide in coronary media and adventitia, due to increased nicotinamide-adenine dinucleotide phosphate (NADPH) oxidase activity, has been described [1]. Diabetes-induced oxidative stress resulted in an inflammatory response in the adventitia (increased expression of IL-6, TNF- α , monocyte chemoattractant protein-1, vascular cell adhesion molecule-1 (VCAM-1) and in the media tunic (VCAM-1 only). An enhanced redox state is accompanied by the upregulation of inflammatory cytokines (IL-6 and TNF- α), chemokines (monocyte chemoattractant protein-1 [MCP-1]), and adhesive molecules (VCAM-1). VCAM-1 and ICAM-1 are highly expressed around adventitial vasa vasorum. Expression of proinflammatory cytokines such as IL-6 and IL-8 has been reported to be increased in acute coronary syndromes [4, 37]. This observation suggests additional vascular portals for inflammatory cells. In fact, several inflammatory cells (lymphocytes and mast cells for instance) have been noted in the adventitia after fatal acute coronary syndromes or intractable vasospasm [1, 13]. In our study we demonstrate the presence of cytokines TNF- α , IL-1 β , TGF- β 1 and ICAM-1 in the porcine coronary arteries even in physiological conditions.

MATERIALS AND METHODS

Sampling

A total of 22 swine hearts (*Sus scrofa domestica*, Great white Polish pigs, all males, 18–30 weeks old, 80–140 kg of weight) were dissected up to 1 hour after commercial animal slaughter. No animals were sacrificed deliberately for this study and all samples were originally intended as obtained for use in the food industry. All hearts were normal with no congenital heart defects and were obtained from healthy animals that had no recognizable diseases. The hearts were obtained intact, washed until free of blood and blood clots using a saline solution. Specimens of coronary arteries (left carotid artery, left carotid right and circumflex coronary arteries) have been harvested, fixed in formalin, embedded in paraffin and then cut in serial sections (7 μ m of thickness).

Immunohistochemistry (IHC)

The immunohistochemical analysis was performed using the ABC/HRP technique (avidincomplexed with biotinylated peroxidase) on 7 μ m thick paraffin

sections that were cut using a rotative microtome. These sections were deparaffinised and hydrated through decreasing ethanol series to distilled water, then subjected to microwave irradiation and immersed in citrate buffer (pH = 6) twice for 5 minutes each time. Subsequently, endogenous peroxidase activity was quenched using 0.3% hydrogenous peroxide in methanol for 30 minutes. To evaluate the immunolocalisation of TGF- β 1, IL-1 β , TNF- α and ICAM-1 the following antibodies were employed: i) rabbit anti-TGF- β 1 polyclonal antibody (dilution 1:50; cat no. sc-130348; Santa Cruz, CA, USA); ii) rabbit anti-IL-1 β polyclonal antibody (dilution 1:50; cat no. sc-12742; Santa Cruz Biotechnology, Santa Cruz, CA, USA); iii) mouse anti-TNF- α monoclonal antibody (dilution 1:100; cat no. sc-133192; Santa Cruz Biotechnology); iv) mouse anti-ICAM-1 monoclonal antibody (dilution 1:25; cat no. sc-107; Santa Cruz, CA, USA). Incubation with the primary antibodies was performed overnight at 4°C. Optimal antibody dilution and incubation times were assessed in preliminary experiments. As negative control, the primary antibodies were omitted. After exposure to the primary antibodies all slides were rinsed twice in phosphate buffer (pH = 7.4) and incubated for 1 hour with the appropriate secondary biotinylated antibody at the final dilution of 1:200. The secondary biotinylated antibodies against rabbit and mouse immunoglobulins were purchased from Abcam (biotinylated goat anti-mouse antibody and biotinylated goat anti-rabbit antibody). The slides were then incubated with peroxidase-conjugated avidin (Vector laboratories, Burlingame, CA, USA, Vectastain Elite ABC kit Standard*PK 6-100) for 30 minutes. Slides were washed in phosphate buffer (pH = 7.4) and treated with 0.05% 3,3-diaminobenzidine (DAB) and 0.1% H₂O₂. Finally, sections were counterstained with Mayer's haematoxylin and dehydrated rapidly. The staining assessment was made by three experts. Negative control experiments were carried out: i) by omitting the primary antibody; ii) by substituting the primary antibody with an equivalent amount of non-specific immunoglobulins; iii) by pre-incubating the primary antibody with the specific blocking peptide (antigen/antibody = 5 according to supplier's instructions). The staining assessment was made by two experienced observers in light microscopy. Immunoreactivity of TGF- β 1, IL-1 β , TNF- α and ICAM-1 was assessed in all samples.

The intensity of the immune reaction was assessed microdensitometrically using an IAS 2000 image anal-

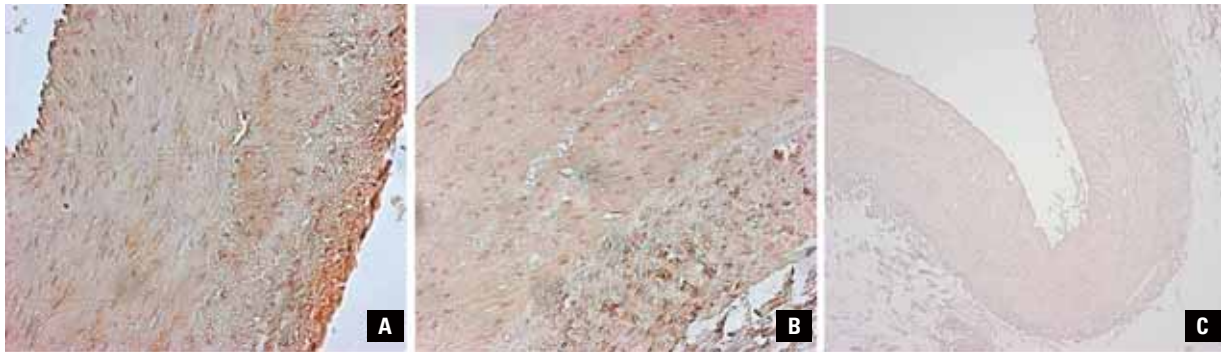


Figure 1. Immunohistochemical staining of porcine coronary arteries for interleukin 1 β . **A, B.** Interleukin 1 β was observed in the endothelial cells and in the nuclei of the smooth muscle cells of the media. No adventitial inflammation was observed, we did not observe any significant neointima formation in all the samples examined; **C.** Negative controls, without antibody (A. $\times 20$; B. $\times 40$; C. $\times 10$).

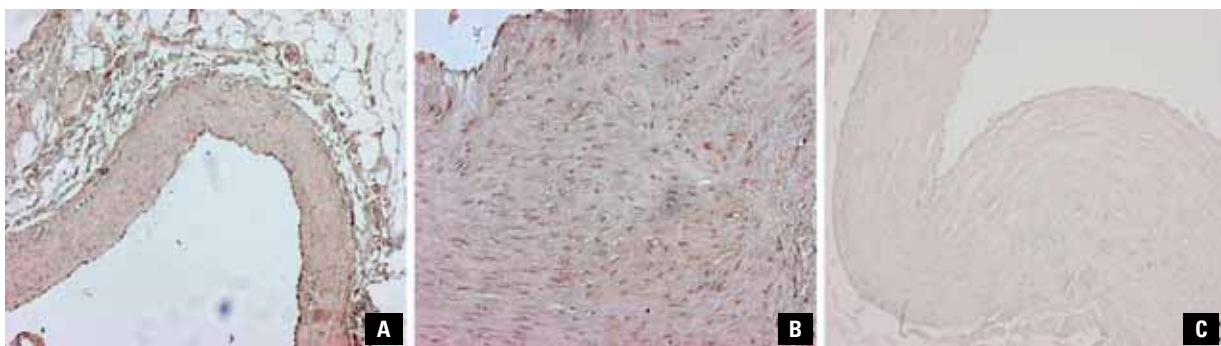


Figure 2. Immunohistochemical staining of porcine coronary arteries for *transforming growth factor* beta (TGF- $\beta 1$). Representative micrographs of vascular wall morphology are shown in panels **A** and **B**. TGF- $\beta 1$ shows positivity of the endothelium and of the nuclei of the smooth muscle cells of the media, we did not observe any significant neointima formation in all the samples examined; **C.** Negative controls, without antibody (A. $\times 10$; B. $\times 40$; C. $\times 20$).

yser (Delta Sistemi, Rome, Italy) connected via a TV camera to the microscope. Twelve $100 \mu\text{m}^2$ areas were delineated in each section by measuring the diaphragm. The system was calibrated taking the background obtained in sections exposed to non-immune serum as zero.

Statistical analysis

All experiments were performed on at least three occasions in duplicate.

We divided the pigs into two groups: group 1 — pigs 18–24 weeks old; group 2 — pigs 24–30 weeks old.

To perform the statistical analysis we compared the percentage of expression of each cytokine analysed in the two groups. Comparisons between the two groups were analysed using the unpaired Student's *t* test. Quantitative data of the intensity of immune staining were analysed statistically by analysis of variance (ANOVA). Data are expressed as mean +

+ standard error of mean. A value of *p*-value < 0.05 was considered significant.

RESULTS

On macroscopic examination, no obvious coronary lesions were found in the analysed segments. Positive areas for each immunohistochemical stain were measured. IL-1 β protein was detected in the adventitial vessel endothelium in 12 of 12 specimens, IL-1 β was present in macrophages (mainly foam cells) of 10 of 11 specimens of coronary arteries. Immunostaining for IL-1 β showed a strong positivity in endothelial cells and in nuclei of the middle tunica SMCs (Fig. 1A, B). The presence of IL-1 β in coronary arterial wall cells was studied by histochemistry to determine the reproducibility of the histological grading, 8 blocks had multiple sections cut. The other cytokines analysed, such as TGF- $\beta 1$, ICAM-1 and TNF- α , also showed positive reaction mainly in the nuclei of the SMCs of the media and in the endothelial cells (Figs. 2A; B,

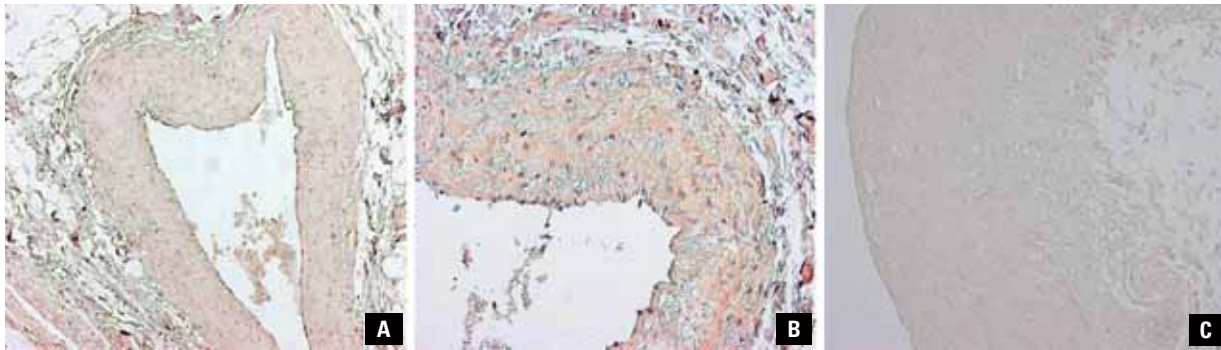


Figure 3. Immunohistochemical staining of porcine coronary arteries for intercellular adhesion molecule-1 (ICAM-1). **A, B.** ICAM-1 shows positivity in the endothelium and in the nuclei of smooth muscle cells of the media. No adventitial inflammation was observed; **C.** Negative controls, without antibody (A. $\times 10$; B. $\times 40$; C. $\times 40$).

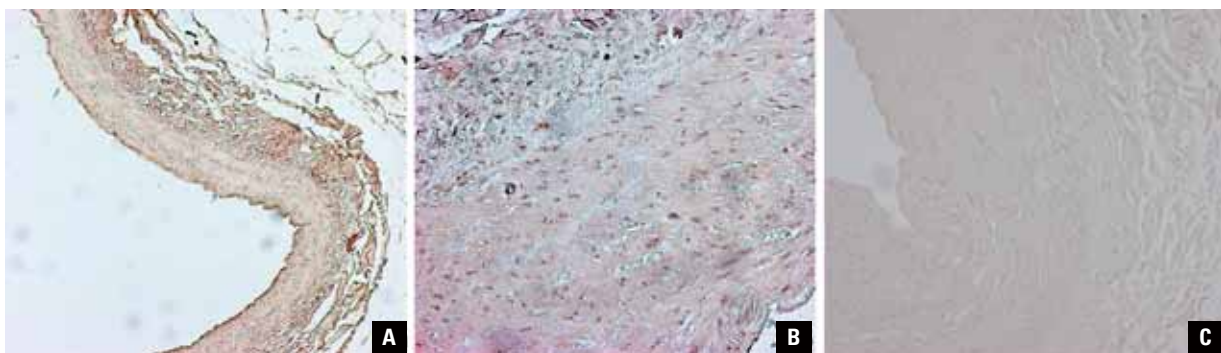


Figure 4. Immunohistochemical staining of porcine coronary arteries for tumour necrosis factor alpha (TNF- α). Representative micrographs of vascular wall morphology are shown in panels **A** and **B**. TNF- α was expressed weak positivity in some nuclei of the smooth muscle cells of the media; **C.** Negative controls, without antibody (A. $\times 10$; B. $\times 40$; C. $\times 40$).

3A, B; 4A, B). Our results show also that, under physiological conditions, the pro-inflammatory cytokines IL-1 β , TGF- β 1, ICAM-1 and TNF- α are already present in the medium tunic of the coronary arteries. In our study high constitutive expression of TGF- β is noted in coronary arteries, however, the *in vivo* relevance of this observation is unclear. Semi-quantitative analysis of inflammation was done by scoring the number of infiltrated inflammatory cells in sections of the vessel wall. In our study we observed that the typical morphology of the coronary arteries was preserved in the entire vessels analysed, in presence of inflammatory cytokines was observed a significant increase in neointimal thickness, neointimal area, the neointima was composed almost entirely of cells with little intercellular matrix.

Quantitative data of the intensity of immune staining, were analysed statistically. We have divided the pigs into two groups, In our analysis, there is no significant difference between the two groups. As shown in Table 1, the immunohistochemical analysis did not

Table 1. Expression levels (%) of TGF- β 1, TNF- α , ICAM-1, IL-1 β in coronary arterial wall of pigs, and respective levels of statistical significance (t-test)

	Group 1, pigs 18–24 weeks old	Group 2, pigs 24–30 weeks old	P-value
TGF- β 1	28.20 \pm 6.28	29.10 \pm 4.15	0.7098
TNF- α	31.70 \pm 6.24	35.10 \pm 4.53	0.1802
ICAM-1	25.70 \pm 5.48	28.00 \pm 4.19	0.3057
IL-1 β	34.70 \pm 4.50	38.20 \pm 3.80	0.0765

The results were considered as statistically significant when p-value < 0.05. TGF- β 1 — transforming growth factor beta1; TNF- α — tumour necrosis factor alpha; ICAM-1 — intercellular adhesion molecule-1; IL-1 β — interleukin 1beta

reveal any significant differences in the expression of the cytokines analysed between the two groups.

DISCUSSION AND CONCLUSIONS

Cytokines play an important role in diseases of the cardiovascular system by inducing inflammation, cell proliferation and apoptosis. It is well known that activated macrophages are a major source of inflam-

matory cytokines [13]. The intimal layer is the site of the earliest vascular atheromatous alterations. The pathogenetic development of these lesions is still not entirely clear today. It is believed that the endothelium plays a fundamental role in the early development of plaque. The most accredited hypothesis places a reaction to intimal layer damage at the basis of this process. In this case, atherosclerosis would represent an inflammatory response of the vascular wall. The location in the intimal layer of low density lipoproteins which, adhering to the proteoglycan layer [11] of this tunica, tend to form aggregates that are more difficult to remove from this site [8], represents a crucial phase of the inflammatory response. Their prolonged accumulation in the tunica intima exposes lipoproteins to the oxidative stress which later induces chemical modifications that are considered crucial for the progression of the atherosclerotic process [22]. Oxidized lipoproteins are able to activate the local production of cytokines that stimulate the expression of adhesion molecules and growth factors from some of the endothelial cells. A functioning endothelium may resist to the adhesion and migration of circulating inflammatory cells. In atherosclerotic endothelial dysfunction, on the other hand, there is an increased expression of molecules such as VCAM-1, ICAM-1 and selectins (E-selectin, P-selectin). It is noteworthy that VCAM-1 is a receptor for an integrin (VLA-4) which is selectively expressed on cells that are early found in the native atheroma as monocytes and T lymphocytes. VCAM-1 and ICAM-1 promote the adhesion and immobilisation of circulating cells [32], while the role of selectins (particularly P-selectin) is related to migration of leukocytes through the endothelial layer [21]. In addition to these adhesion molecules, some chemoattractive factors are important for the intimal migration of leukocytes adhered to the endothelium. Oxidized LDL and other factors expressed in the rising atheroma stimulate the production of MCP-1 which is a great activator of monocyte chemotaxis [12]. The inflammatory cells widely found in the newly formed atheroma are macrophages and T-lymphocytes. Once transformed into foamy cells due to cytoplasmic lipids accumulation, these macrophages are found more frequently in atheroma, where cytokines and growth factors are produced.

The first pathologically relevant atherosclerotic lesion, the so called "lipid streak", begins to form as foamy cells start to accumulate in the intimate layer. This process is still potentially reversible.

The foamy cells of the lipid streak acts as a promoter of the inflammatory process of the vascular wall, which synthesizes and releases cytokines, chemotactic factors and oxidizing radicals. This system of immune cells do not need antigenic stimuli to sustain itself [14]. TNF- α , IL-2, IL-6, interferon- γ , and other pro-inflammatory factors are widely produced by Th1 subpopulation, while Th2 lymphocytes, among other secreted factors, synthesize and release IL-10, the main anti-inflammatory cytokine. The role of acquired immunity, and in particular the T helper mediated one, could therefore orchestrate the inflammatory process triggered in the growing plaque. The cytotoxic T lymphocytes could mediate the release of lipolytic and proteolytic substances, oxidizing and inducing apoptosis of many cell types such as macrophages [36]. Activated SMCs are also capable of secreting factors structurally similar to TGF- β and pro-calcifying molecules as well as calcium binding proteins. These molecules therefore, influence a common phenomenon in advanced atheromatous plaques: the mineralisation. In growing atheroma, SMCs are not the only non-immune cells to migrate and replicate, but even endothelial cells may localise in the plaque and, under the stimulation of molecules such as vascular-endothelial and fibroblast growth factor (VEGF and FGF), can also organize themselves to form microscopic neovascular plexuses rich in adhesion molecules that promote cell migration. These vascular structures also appear to be important for plaque progression, as demonstrated by the fact that anti-neoangiogenic factors can limit their development [10]. When plaque extends beyond remodelling positive capacity of the vessel involved, it begins to produce luminal stenosis, which progressively narrows the internal diameter of the artery and causes a reduction in blood flow. In the specific case of coronary arteries an imbalance between demand and request for oxygen in the myocardium, may lead to the development of a chronic ischaemic heart disease. Activated monocytes are capable of produce cytokines (such as TNF- α and IL-6) that maintain and amplify the inflammatory cascade. The transductive pathway mediated by the transcription factor nuclear factor κ B (NF- κ B) plays a fundamental role in progression of atherosclerosis, and its activation leads to an increase in production of the main pro-inflammatory cytokines, including IL-6 and TNF- α [9, 24, 28]. In our study, we hypothesized that cytokines released by activated macrophages and cells localized in the vas-

cular wall may play an important role in the formation of atherosclerotic lesions, triggering the upregulation of vasoactive substances and growth factors. In fact, previous studies [3, 19] have pointed out that the inflammatory cell infiltrate is more expressed during the early phases of atheromas growth, suggesting that inflammatory cytokines are responsible for the initiation of formation of the atherosclerotic lesions. Neoangiogenesis is a typical feature found in more advanced plaques. Angiogenesis is physiologically regulated by VEGF and its inhibitors. Hypoxia is the major stimulus for the production and cellular release of VEGF. In atherosclerotic lesions there is an expression of VEGF caused by hypoxia and release of molecules by macrophages. Small vessels then form inside the plaque and this phenomenon makes the plaque more unstable, thus facilitating the macrophage recall and a possible internal bleeding. VEGF is expressed by endothelial cells, macrophages and SMCs [6, 17]. The presence of VEGF in the carotid plaque correlates with the presence of a newly formed vascular component, SMCs and inflammation cells [17, 40]. The correlation between the presence of VEGF in the plaque and structural alterations (breaking of the fibrous cap), greater positivity to CD34 (endothelial marker) and expression of VEGFR1 in the present cells has been clearly demonstrated. The evaluation of blood levels of VEGF may be a useful tool to identify atherosclerotic lesions rich in microvessels and therefore more unstable [7, 34]. Monitoring of elements related to the neof ormation of atherosclerotic plaques is the primary objective of numerous new studies which take into consideration the serious consequences that could be caused by the presence of an atherosclerotic plaque in the carotid district, which really represents a high risk condition for the development of cerebrovascular events.


Conflict of interest: None declared

REFERENCES

- Åkerblom A, James SK, Lalic TG, et al. Interleukin-18 in patients with acute coronary syndromes. *Clin Cardiol.* 2019; 42(12): 1202–1209, doi: [10.1002/clc.23274](https://doi.org/10.1002/clc.23274), indexed in Pubmed: [31596518](https://pubmed.ncbi.nlm.nih.gov/31596518/).
- Alexander H, Sprague R, Khalil A. Inflammatory cytokines in vascular dysfunction and vascular disease. *Biochem Pharmacol.* 2009; 78(6): 539–552, doi: [10.1016/j.bcp.2009.04.029](https://doi.org/10.1016/j.bcp.2009.04.029), indexed in Pubmed: [19413999](https://pubmed.ncbi.nlm.nih.gov/19413999/).
- Alexander MR, Owens GK. Epigenetic control of smooth muscle cell differentiation and phenotypic switching in vascular development and disease. *Annu Rev Physiol.* 2012; 74: 13–40, doi: [10.1146/annurev-physiol-012110-142315](https://doi.org/10.1146/annurev-physiol-012110-142315), indexed in Pubmed: [22017177](https://pubmed.ncbi.nlm.nih.gov/22017177/).
- Apostolakis S, Vogiatzi K, Amanatidou V, et al. Interleukin 8 and cardiovascular disease. *Cardiovasc Res.* 2009; 84(3): 353–360, doi: [10.1093/cvr/cvp241](https://doi.org/10.1093/cvr/cvp241), indexed in Pubmed: [19617600](https://pubmed.ncbi.nlm.nih.gov/19617600/).
- Ballou S, Lozanski G. Induction of inflammatory cytokine release from cultured human monocytes by C-reactive protein. *Cytokine.* 1992; 4(5): 361–368, doi: [10.1016/1043-4666\(92\)90079-7](https://doi.org/10.1016/1043-4666(92)90079-7).
- Bianchi E, Artico M, Di Cristofano C, et al. Growth factors, their receptor expression and markers for proliferation of endothelial and neoplastic cells in human osteosarcoma. *Int J Immunopathol Pharmacol.* 2013; 26(3): 621–632, doi: [10.1177/039463201302600306](https://doi.org/10.1177/039463201302600306), indexed in Pubmed: [24067459](https://pubmed.ncbi.nlm.nih.gov/24067459/).
- Bonomini F, Taurone S, Parnigotto P, et al. Role of parnaparin in atherosclerosis. *Int J Exp Pathol.* 2016; 97(6): 457–464, doi: [10.1111/iep.12217](https://doi.org/10.1111/iep.12217), indexed in Pubmed: [28205266](https://pubmed.ncbi.nlm.nih.gov/28205266/).
- Camejo G, Hurt-Camejo E, Wiklund O, et al. Association of apo B lipoproteins with arterial proteoglycans: pathological significance and molecular basis. *Atherosclerosis.* 1998; 139(2): 205–222, doi: [10.1016/s0021-9150\(98\)00107-5](https://doi.org/10.1016/s0021-9150(98)00107-5), indexed in Pubmed: [9712326](https://pubmed.ncbi.nlm.nih.gov/9712326/).
- De Bosscher K, Vanden Berghe W, Haegeman G. The interplay between the glucocorticoid receptor and nuclear factor-kappaB or activator protein-1: molecular mechanisms for gene repression. *Endocr Rev.* 2003; 24(4): 488–522, doi: [10.1210/er.2002-0006](https://doi.org/10.1210/er.2002-0006), indexed in Pubmed: [12920152](https://pubmed.ncbi.nlm.nih.gov/12920152/).
- Devaraj S, Kumaresan PR, Jialal I. Effect of C-reactive protein on chemokine expression in human aortic endothelial cells. *J Mol Cell Cardiol.* 2004; 36(3): 405–410, doi: [10.1016/j.yjmcc.2003.12.005](https://doi.org/10.1016/j.yjmcc.2003.12.005), indexed in Pubmed: [15010279](https://pubmed.ncbi.nlm.nih.gov/15010279/).
- Ding Z, Pothineni NV, Goel A, et al. Impact of hepatitis C seropositivity on the risk of coronary heart disease events. *Am J Cardiol.* 2014; 114(12): 1841–1845, doi: [10.1016/j.amjcard.2014.09.020](https://doi.org/10.1016/j.amjcard.2014.09.020), indexed in Pubmed: [25438910](https://pubmed.ncbi.nlm.nih.gov/25438910/).
- Dong ZM, Chapman SM, Brown AA, et al. The combined role of P- and E-selectins in atherosclerosis. *J Clin Invest.* 1998; 102(1): 145–152, doi: [10.1172/JCI3001](https://doi.org/10.1172/JCI3001), indexed in Pubmed: [9649568](https://pubmed.ncbi.nlm.nih.gov/9649568/).
- Gerdes N, Sukhova GK, Libby P, et al. Expression of interleukin (IL)-18 and functional IL-18 receptor on human vascular endothelial cells, smooth muscle cells, and macrophages: implications for atherogenesis. *J Exp Med.* 2002; 195(2): 245–257, doi: [10.1084/jem.20011022](https://doi.org/10.1084/jem.20011022), indexed in Pubmed: [11805151](https://pubmed.ncbi.nlm.nih.gov/11805151/).
- Gu L, Okada Y, Clinton S, et al. Absence of monocyte chemoattractant protein-1 reduces atherosclerosis in low density lipoprotein receptor-deficient mice. *Mol Cell.* 1998; 2(2): 275–281, doi: [10.1016/s1097-2765\(00\)80139-2](https://doi.org/10.1016/s1097-2765(00)80139-2).
- Hořda MK, Hořda J, Koziej M, et al. Porcine heart interatrial septum anatomy. *Ann Anat.* 2018; 217: 24–28, doi: [10.1016/j.aanat.2018.01.002](https://doi.org/10.1016/j.aanat.2018.01.002), indexed in Pubmed: [29458135](https://pubmed.ncbi.nlm.nih.gov/29458135/).
- Ikeda U, Ohkawa F, Seino Y, et al. Serum interleukin 6 levels become elevated in acute myocardial infarction. *J Mol Cell Cardiol.* 1992; 24(6): 579–584, doi: [10.1016/0022-2828\(92\)91042-4](https://doi.org/10.1016/0022-2828(92)91042-4), indexed in Pubmed: [1518075](https://pubmed.ncbi.nlm.nih.gov/1518075/).

17. Kitagawa T, Yamamoto H, Horiguchi J, et al. Characterization of noncalcified coronary plaques and identification of culprit lesions in patients with acute coronary syndrome by 64-slice computed tomography. *JACC Cardiovasc Imaging*. 2009; 2(2): 153–160, doi: [10.1016/j.jcmg.2008.09.015](https://doi.org/10.1016/j.jcmg.2008.09.015), indexed in Pubmed: [19356549](https://pubmed.ncbi.nlm.nih.gov/19356549/).
18. Kukielka GL, Smith CW, LaRosa GJ, et al. Interleukin-8 gene induction in the myocardium after ischemia and reperfusion in vivo. *J Clin Invest*. 1995; 95(1): 89–103, doi: [10.1172/JCI117680](https://doi.org/10.1172/JCI117680), indexed in Pubmed: [7814650](https://pubmed.ncbi.nlm.nih.gov/7814650/).
19. Lavagno L, Gunella G, Bardelli C, et al. Anti-inflammatory drugs and tumor necrosis factor-alpha production from monocytes: role of transcription factor NF-kappa B and implication for rheumatoid arthritis therapy. *Eur J Pharmacol*. 2004; 501(1-3): 199–208, doi: [10.1016/j.ejphar.2004.07.101](https://doi.org/10.1016/j.ejphar.2004.07.101), indexed in Pubmed: [15464079](https://pubmed.ncbi.nlm.nih.gov/15464079/).
20. Lelovas PP, Kostomitsopoulos NG, Xanthos TT. A comparative anatomic and physiologic overview of the porcine heart. *J Am Assoc Lab Anim Sci*. 2014; 53(5): 432–438, indexed in Pubmed: [25255064](https://pubmed.ncbi.nlm.nih.gov/25255064/).
21. Ley K, Huo Y. VCAM-1 is critical in atherosclerosis. *J Clin Invest*. 2001; 107(10): 1209–1210, doi: [10.1172/JCI13005](https://doi.org/10.1172/JCI13005), indexed in Pubmed: [11375406](https://pubmed.ncbi.nlm.nih.gov/11375406/).
22. Libby P. The vascular biology of atherosclerosis. Chapter in book: Braunwald's Heart disease, 7Th Ed. Elsevier-Saunders, Philadelphia 2005: 921–993.
23. Libby P, Ridker PM, Maseri A. Inflammation and atherosclerosis. *Circulation*. 2002; 105(9): 1135–1143, doi: [10.1161/hc0902.104353](https://doi.org/10.1161/hc0902.104353), indexed in Pubmed: [11877368](https://pubmed.ncbi.nlm.nih.gov/11877368/).
24. Liuzzo G, Crea F, Santamaria M, et al. Persistent activation of nuclear factor kappa-B signaling pathway in patients with unstable angina and elevated levels of C-reactive protein. *J Am Coll Cardiol*. 2007; 49(2): 185–194, doi: [10.1016/j.jacc.2006.07.071](https://doi.org/10.1016/j.jacc.2006.07.071).
25. Marie C, Cavaillon M. Negative feedback in inflammation. The role of anti-inflammatory cytokine. *Bulletin de L Institute Pasteur*. 1997; 95: 141–154.
26. Martínez GJ, Robertson S, Barraclough J, et al. Colchicine acutely suppresses local cardiac production of inflammatory cytokines in patients with an acute coronary syndrome. *J Am Heart Assoc*. 2015; 4(8): e002128, doi: [10.1161/JAHA.115.002128](https://doi.org/10.1161/JAHA.115.002128), indexed in Pubmed: [26304941](https://pubmed.ncbi.nlm.nih.gov/26304941/).
27. Mitsumata M, Fishel RS, Nerem RM, et al. Fluid shear stress stimulates platelet-derived growth factor expression in endothelial cells. *Am J Physiol*. 1993; 265(1 Pt 2): H3–H8, doi: [10.1152/ajpheart.1993.265.1.H3](https://doi.org/10.1152/ajpheart.1993.265.1.H3), indexed in Pubmed: [8342646](https://pubmed.ncbi.nlm.nih.gov/8342646/).
28. Moulton KS, Heller E, Konerding MA, et al. Angiogenesis inhibitors endostatin or TNP-470 reduce intimal neovascularization and plaque growth in apolipoprotein E-deficient mice. *Circulation*. 1999; 99(13): 1726–1732, doi: [10.1161/01.cir.99.13.1726](https://doi.org/10.1161/01.cir.99.13.1726), indexed in Pubmed: [10190883](https://pubmed.ncbi.nlm.nih.gov/10190883/).
29. Mourouzis K, Oikonomou E, Siasos G, et al. Pro-inflammatory cytokines in acute coronary syndromes. *Curr Pharm Des*. 2020; 26(36): 4624–4647, doi: [10.2174/1381612826666200413082353](https://doi.org/10.2174/1381612826666200413082353), indexed in Pubmed: [32282296](https://pubmed.ncbi.nlm.nih.gov/32282296/).
30. Rafieian-Kopaei M, Setorki M, Doudi M, et al. Atherosclerosis: process, indicators, risk factors and new hopes. *Int J Prev Med*. 2014; 5(8): 927–946, indexed in Pubmed: [25489440](https://pubmed.ncbi.nlm.nih.gov/25489440/).
31. Robertson S, Martínez GJ, Payet CA, et al. Colchicine therapy in acute coronary syndrome patients acts on caspase-1 to suppress NLRP3 inflammasome monocyte activation. *Clin Sci (Lond)*. 2016; 130(14): 1237–1246, doi: [10.1042/CS20160090](https://doi.org/10.1042/CS20160090), indexed in Pubmed: [27129183](https://pubmed.ncbi.nlm.nih.gov/27129183/).
32. Rong JX, Rangaswamy S, Shen L, et al. Arterial injury by cholesterol oxidation products causes endothelial dysfunction and arterial wall cholesterol accumulation. *Arterioscler Thromb Vasc Biol*. 1998; 18(12): 1885–1894, doi: [10.1161/01.atv.18.12.1885](https://doi.org/10.1161/01.atv.18.12.1885), indexed in Pubmed: [9848880](https://pubmed.ncbi.nlm.nih.gov/9848880/).
33. Ross R. Atherosclerosis: an inflammatory disease. *N Engl J Med*. 1999; 340(2): 115–126, doi: [10.1056/NEJM199901143400207](https://doi.org/10.1056/NEJM199901143400207), indexed in Pubmed: [9887164](https://pubmed.ncbi.nlm.nih.gov/9887164/).
34. Russell DA, Abbott CR, Gough MJ. Vascular endothelial growth factor is associated with histological instability of carotid plaques. *Br J Surg*. 2008; 95(5): 576–581, doi: [10.1002/bjs.6100](https://doi.org/10.1002/bjs.6100), indexed in Pubmed: [18344184](https://pubmed.ncbi.nlm.nih.gov/18344184/).
35. Sabatine MS, Morrow DA, de Lemos JA, et al. Multimarker approach to risk stratification in non-ST elevation acute coronary syndromes: simultaneous assessment of troponin I, C-reactive protein, and B-type natriuretic peptide. *Circulation*. 2002; 105(15): 1760–1763, doi: [10.1161/01.cir.0000015464.18023.0a](https://doi.org/10.1161/01.cir.0000015464.18023.0a), indexed in Pubmed: [11956114](https://pubmed.ncbi.nlm.nih.gov/11956114/).
36. Sakaguchi H, Takeya M, Suzuki H, et al. Role of macrophage scavenger receptors in diet-induced atherosclerosis in mice. *Lab Invest*. 1998; 78(4): 423–434, indexed in Pubmed: [9564887](https://pubmed.ncbi.nlm.nih.gov/9564887/).
37. Sean PD. Cellular and oxidative mechanisms associated with interleukin-6 signaling in the vasculature. *Int J Mol Sci*. 2017; 18(12), doi: [10.3390/ijms18122563](https://doi.org/10.3390/ijms18122563), indexed in Pubmed: [29186034](https://pubmed.ncbi.nlm.nih.gov/29186034/).
38. Sheth AR, Grewal US, Patel HP, et al. Possible mechanisms responsible for acute coronary events in COVID-19. *Med Hypotheses*. 2020; 143: 110125, doi: [10.1016/j.mehy.2020.110125](https://doi.org/10.1016/j.mehy.2020.110125), indexed in Pubmed: [32763657](https://pubmed.ncbi.nlm.nih.gov/32763657/).
39. Spoletini M, Taurone S, Tombolini M, et al. Trophic and neurotrophic factors in human pituitary adenomas (Review). *Int J Oncol*. 2017; 51(4): 1014–1024, doi: [10.3892/ijo.2017.4120](https://doi.org/10.3892/ijo.2017.4120), indexed in Pubmed: [28902350](https://pubmed.ncbi.nlm.nih.gov/28902350/).
40. Taurone S, Galli F, Signore A, et al. VEGF in nuclear medicine: Clinical application in cancer and future perspectives (Review). *Int J Oncol*. 2016; 49(2): 437–447, doi: [10.3892/ijo.2016.3553](https://doi.org/10.3892/ijo.2016.3553), indexed in Pubmed: [27277340](https://pubmed.ncbi.nlm.nih.gov/27277340/).
41. Ueland T, Aukrust P, Caidahl K. CCL21 and prognosis in acute coronary syndrome. *Aging*. 2019; 11(21): 9225–9226, doi: [10.18632/aging.102443](https://doi.org/10.18632/aging.102443).
42. Vaidya K, Martínez G, Patel S. The role of colchicine in acute coronary syndromes. *Clin Ther*. 2019; 41(1): 11–20, doi: [10.1016/j.clinthera.2018.07.023](https://doi.org/10.1016/j.clinthera.2018.07.023), indexed in Pubmed: [30185392](https://pubmed.ncbi.nlm.nih.gov/30185392/).
43. Yang Ke, Zhang XJ, Cao LiJ, et al. Toll-like receptor 4 mediates inflammatory cytokine secretion in smooth muscle cells induced by oxidized low-density lipoprotein. *PLoS One*. 2014; 9(4): e95935, doi: [10.1371/journal.pone.0095935](https://doi.org/10.1371/journal.pone.0095935), indexed in Pubmed: [24755612](https://pubmed.ncbi.nlm.nih.gov/24755612/).
44. Zohlhöfer D, Richter T, Neumann FJ, et al. Transcriptome analysis reveals a role of interferon-gamma in human neointima formation. *Mol Cell*. 2001; 7(5): 1059–1069, doi: [10.1016/s1097-2765\(01\)00239-8](https://doi.org/10.1016/s1097-2765(01)00239-8).

The different forms of the left brachiocephalic vein visualised during cardiovascular implantable electronic device implantation procedures

R. Steckiewicz¹ , P. Stolarz², B. Lange

¹Department of Cardiology, Central University Hospital in Warsaw, Poland

²1st Department of Cardiology, Medical University of Warsaw, Poland

[Received: 6 October 2021; Accepted: 10 November 2021; Early publication date: 26 November 2021]

Background: Among the factors ensuring successful completion of such minimally invasive procedures as cardiac implantable electronic device (CIED) implantation and central venous catheter (CVC) placement are the morphometry and topography of the vessels used for cardiac lead or catheter advancement. Venous access through the left clavipectoral triangle makes use of the left brachiocephalic vein (BCV). The purpose of this study was to present the radiology images of various individual forms of this vessel observed during CIED implantation procedures.

Materials and methods: Our analysis included 100 venography recordings illustrating the left BCV, obtained during de novo CIED implantation procedures. We assessed the mediastinal course of the left BCV, with its natural angles, including angle α (in the middle section of the vessel) and the two angles created by the left BCV and the left subclavian vein (angle β) and the left BCV and the superior vena cava (angle γ).

Results: The mean values of angle α tended to be higher (approximately 141°) than those of the two remaining angles (γ and β), which were comparable at 123° and 127°, respectively. An increase in mean angle α values were accompanied by increased mean angle γ and β values ($p = 0.05$), with only 5% of β and γ angles, in total, having values close to those of a right angle ($90 \pm 10^\circ$).

Conclusions: Individual variability of left BCV topography and morphology comes from developmental formation of the physiological angle in the middle section of this mediastinal vessel's course. The presence of near-right angles along the course of left BCV may potentially result in injuries to the vessel during intravascular procedures. (Folia Morphol 2023; 82, 1: 127–136)

Key words: left brachiocephalic vein, anatomic variation, venography, cardiac implantable electronic device (CIED), central venous catheter (CVC), risk factors, anatomical factors

Address for correspondence: Dr. R. Steckiewicz, Department of Cardiology, Central University Hospital in Warsaw, ul. Banacha 1A, 02–097 Warszawa, Poland, e-mail: r.steckiewicz@pro.onet.pl

This article is available in open access under Creative Common Attribution-Non-Commercial-No Derivatives 4.0 International (CC BY-NC-ND 4.0) license, allowing to download articles and share them with others as long as they credit the authors and the publisher, but without permission to change them in any way or use them commercially.

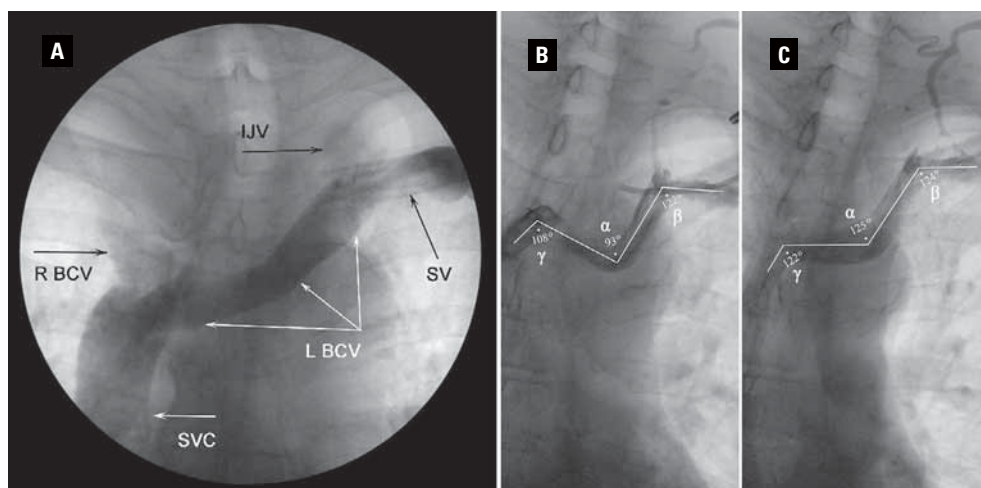


Figure 1. A–C. Radiographic images of the left brachiocephalic vein (BCV) lumen visualised with a contrast medium with respect to the contours of upper mediastinal organs (e.g. the aortic arch, trachea) and bone structures of the chest; **B–C.** Respiratory phase-dependent variability in the shape of left BCV angulations (posteroanterior view, supine position); **B.** Expiratory phase; **C.** Inspiratory phase: angles α , β , and γ increased by 32° , 2° , and 14° , respectively; IJV — internal jugular vein; SV — subclavian vein; SVC — superior vena cava.

INTRODUCTION

Performing minimally invasive transvenous procedures, such as cardiac implantable electronic device (CIED) implantation, facilitates making observations as to the individual differences in vessel layout. These differences can be due to either normal anatomical variations or developmental anomalies [3, 12, 15, 19].

Minimally invasive CIED implantation or central venous catheter (CVC) placement procedures, which make use of mediastinal systemic veins, depend to a large extent on favourable morphometry and topography of the brachiocephalic veins (BCVs), also known as the innominate veins. When the venous system is accessed via the left clavipectoral triangle, the vein used for catheter or cardiac lead advancement within the middle mediastinum is the left BCV — formed by the left jugular vein and the left subclavian vein (SV) merging — which subsequently drains to the superior vena cava (SVC) (Fig. 1A).

Left BCV topography, which depends on the nature and size of the natural anatomical angulations along the course of the vessel, may affect the course of CIED implantation or CVC placement procedures [5, 18]. These natural angulations include: the angle at the middle segment of the left BCV, where its wall is anterior and adjacent to the arteries branching off the aortic arch (angle α , Fig. 1), and two other evaluated angles: one located at the site where the left SV continues into the left BCV (angle β , Fig. 1B, C) and the other located at the site of drainage of the left BCV into the SVC (angle γ , Fig. 1B, C).

The extent of individual variations and the spatial relations of the left BCV to adjacent anatomical structures may contribute to vessel injury during CIED implantation or CVC placement procedures even in the case of a physiological course of the left BCV [11, 13, 14, 16]. There may be direct mechanical injury to some or all the layers of the venous wall, with additional damage to the adjacent arteries in more severe cases; there may also be long-term complications in the form of post-thrombotic lesions at the site of vascular injury [2, 9, 10, 17].

The risk of vascular injury is particularly high in the case of anatomical variations of considerably unusual morphometry and topography. With the angulations along the left BCV course seemingly constituting the most vulnerable sites [5, 18, 22].

The fact that left BCV variations mentioned above are typically asymptomatic means that they are usually detected incidentally during an intravascular procedure [7]. The purpose of this study was to present radiographic data on different forms of the left BCV and the analysis of the types and rates of the individual forms of the vein encountered during CIED implantation procedures over a 6-year period.

MATERIALS AND METHODS

We retrospectively analysed the venography images obtained during de novo CIED implantation procedures performed during the period of 2014–2019. Only the images that definitively and clearly showed the left BCV

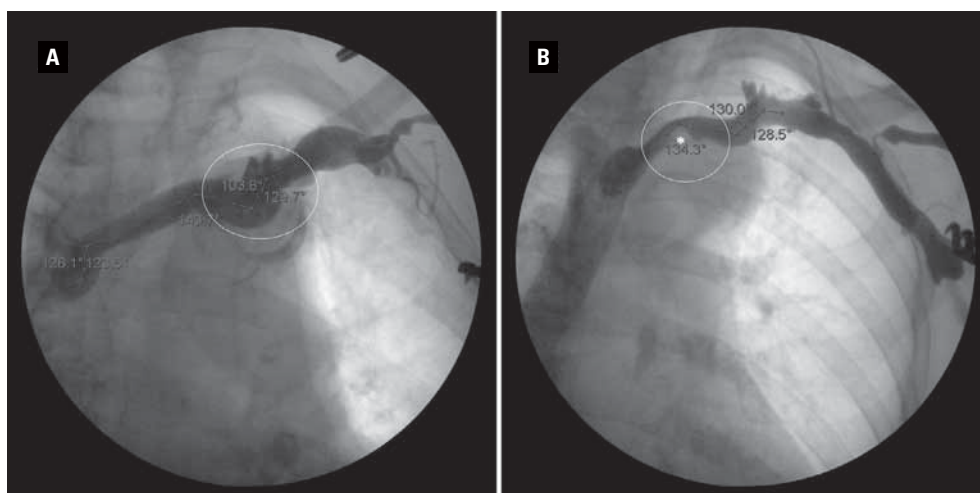


Figure 2. A, B. Radiographic examples of left brachiocephalic vein anomalies (white ovals); **A.** An anomaly with respect to the normal course of the vein at the place where the left subclavian vein drains into the left brachiocephalic vein (the potential location of angle β), most likely due to an additional angulation of the vein in a sagittal plane; **B.** Locally altered morphometry of the vein due to its partial compression via the brachiocephalic trunk (white asterisk).

course, including the entire length of its lumen and the junctions with the left SV and the SVC visualised via a contrast medium, were considered in the analysis (Fig. 1)

The cases where left BCV lumen morphometry had been difficult to interpret or the angles to measure due to such factors as developmental anomalies of the vessel, poorly contrasted images, past cardiothoracic surgeries, or an atypical left BCV course, were excluded from analysis (Fig. 2A, B).

Following the exclusion of some images for the reasons mentioned above, 100 venographic images illustrating the evaluated angulations and the course of the left BCV were ultimately analysed. The images selected for this paper were ones that most clearly show the relevant left BCV forms and angulations. All implantations procedures were performed by operators from the same group of personnel. This limited the effects of potentially diverse levels of operator experience and varying venography techniques on the extent of vein visualisation and the later analysis of left BCV forms.

During the analysed procedures, the cardiac leads were introduced into the cardiovascular system via the veins of the left clavipectoral triangle. The indications for contrast venography were intraoperative situations that required an immediate elucidation of the cause of difficulties in lead advancement.

Selective venographies were used, with the contrast agent administered directly at the site of cephalic vein cutdown or axillary or subclavian vein puncture. This helped effectively visualise the lumina of the veins of the upper mediastinum, while simultaneously

limiting the volume of contrast in comparison to that administered into peripheral veins of the arm. The intravascular flow of contrast was visualised anteroposteriorly via pulsed fluoroscopy at 12 frames per second as well as captured on individual frames.

The evaluated angles were measured at the points where the straight lines drawn along the middle of the contrasted lumina of adjacent venous segments intersected (Fig. 1B, C). In order to ensure data comparability, all venous angle measurements were made on the images obtained during the expiratory phase. We believe that the changes to the left BCV course, including the angles, taking place during that phase may increase the risk of a potential local injury to the vessel during CIED implantation or CVC placement.

Our statistical analysis used: numerical variables in the form of mean values, standard deviations, statistical significance (p -values), tests for normality: the Shapiro–Wilk W test, Kolmogorov–Smirnov D test, Levene’s test for homogeneity of variance, Pearson correlation coefficients. The p -value was 5% if not stated otherwise.

This study had been approved by the Institutional Review Board.

RESULTS

Out of the 2,112 de novo CIED implantation procedures performed over the evaluated period, we initially selected the 391 that had required the use of venography to visualise the vessels through which the cardiac lead was being advanced. Due to our

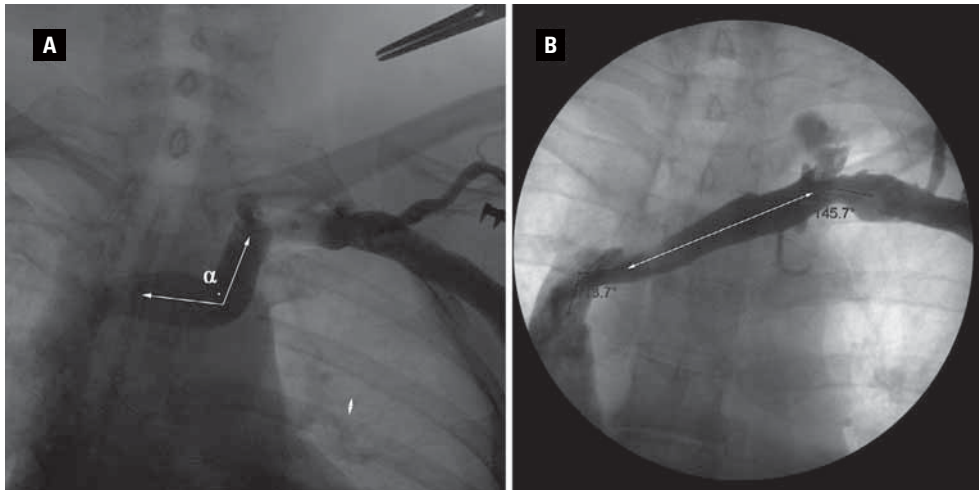


Figure 3. A, B. Interindividual physiological variations of the forms and values of angle α along the left brachiocephalic vein (expiratory phase); **A.** Vein form with angle $\alpha = 100^\circ$; **B.** Vein form with no visible angulation (angle $\alpha = 180^\circ$).

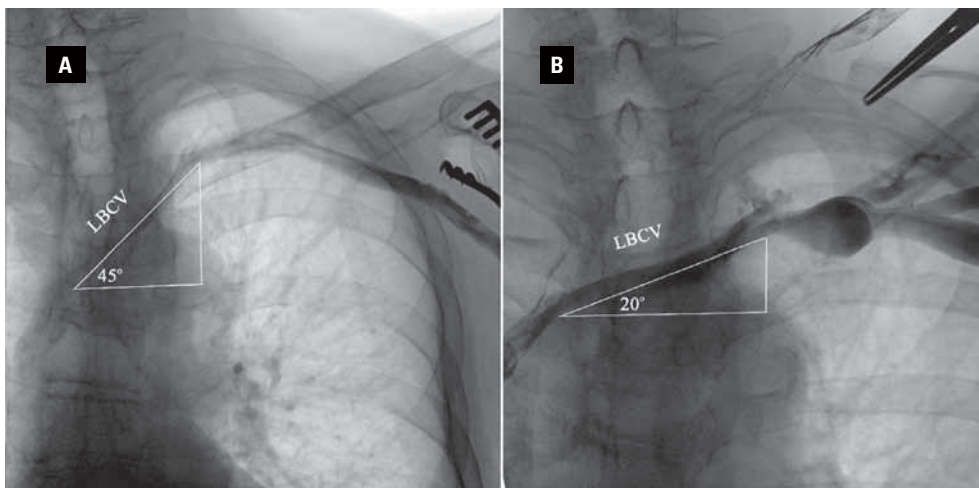


Figure 4. A, B. The extent of interpersonal variations in the slope of the left brachiocephalic vein with respect to the transverse plane (posteroanterior view).

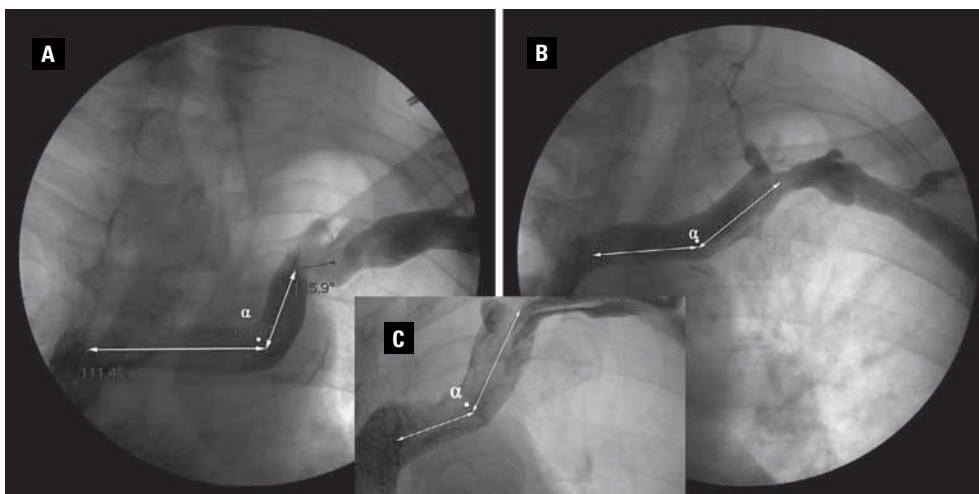


Figure 5. A, B. The location and characteristics of the vertex of left brachiocephalic vein angulation α within the mediastinum, with the angle-forming upstream (oblique) and downstream (horizontal) segments of the vein marked with double-headed arrows; **A.** The downstream segment longer than the upstream segment; **B.** The downstream segment equal to the upstream segment; **C.** The downstream segment shorter than the upstream segment.

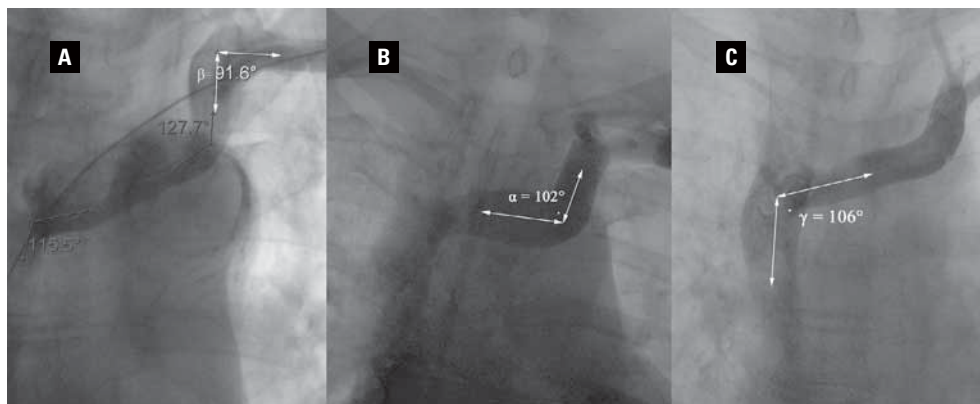


Figure 6. A–C. Examples of the three analysed left brachiocephalic vein angulations that might increase the risk of injury to the vessel during transvenous procedures.

objectives, which required an unequivocal interpretation of the obtained left BCV images, the number of recordings selected for analysis was ultimately pared down to 100. The selection criteria included good visualisation of the entire lumen of the vein's course through the mediastinum, including the SV drainage point and the left BCV drainage point to the SVC, in order to allow the evaluated angles (α , β , and γ) to be measured (Fig. 1B, C).

In the cases with no discernible angulation in the left BCV and the vein's oblique course through the mediastinum (Fig. 3B), the vein's slope with respect to the transverse plane ranged from 20° to 45° (Fig. 4A, B).

The position of the left BCV angle vertex along the vein's length helped distinguish three main types of vein forms in the evaluated material: the predominant form (shown in Fig. 5A) present in 80% of cases, a less common form (shown in Fig. 5B) present in 15% of cases, and the least common form (shown in Fig. 5C) present in only 5% of cases.

Considered collectively, angles β and γ of approximately $90^\circ \pm 10^\circ$ were observed in 5% (Figs. 1B; 6A–C).

Statistical analysis of the results

Basic descriptive statistics

Description: The evaluated angles differ in terms of their mean values, with angle α characterised by the highest value of about 140.6° , and the remaining two angle types characterised by comparable lower values (angles γ of approximately 122.8° and angles β of 126.7°).

The measurements of all angles show similar standard deviations (a range of 15.4–16.1) (Fig. 7).

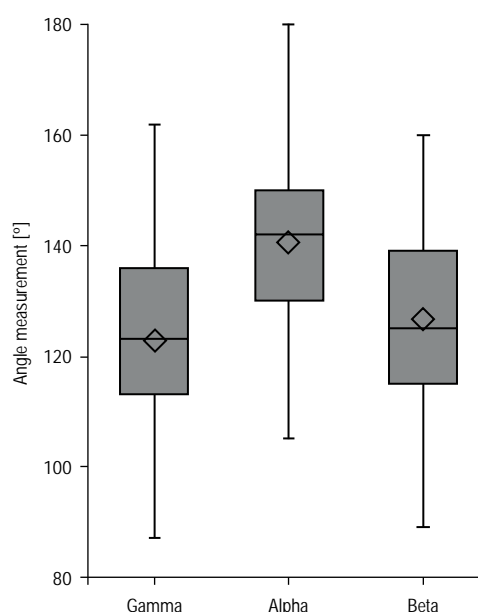


Figure 7. A box-and-whisker plot of the measured values for each angle. The bottom edge of each box represents the first quartile; the line across the box represents the median value; the top edge of each box represents the third quartile. The diamonds mark the mean value, and the whiskers show the minimum and maximum values.

Histogram analysis

Description: The histograms show the proportion of angle values falling within the defined value ranges (Fig. 8A–C).

Gamma angle: The most commonly measured values of angle γ (2/3 of measurements) ranged from 110° to 140° , with values over 140° constituting 15% of all measured values, and values under 100° constituting 6% of measured values.

Alpha angle: Most angle α values (2/3 of all measurements) fell within the 130° – 160° range, which

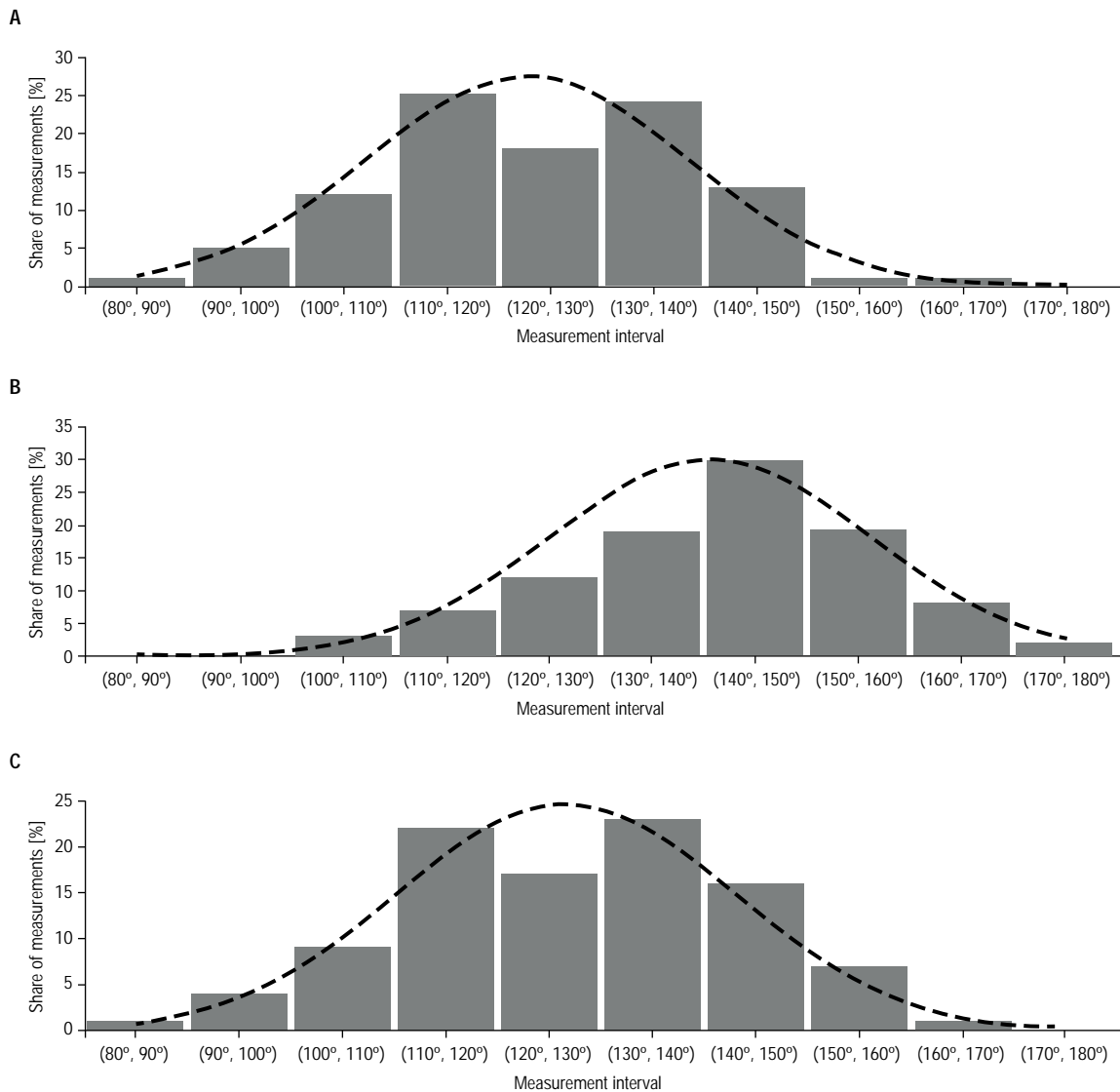


Figure 8. Histograms of the obtained values of angles gamma (A), alpha (B), and beta (C). The dashed lines mark the normal distributions estimated based on the obtained measurements.

made the angle, on average, more obtuse than either β or γ . Values of over 160° constituted 11% of the measurements, and no values under 100° were observed.

Beta angle: The proportion of angles β exceeding 140° was 24% (which was greater than that of angles γ), with values under 100° constituting 5% of the measurements.

The measurements obtained for all angles showed normal distributions (Shapiro–Wilk W test and Kolmogorov–Smirnov D test) and homogeneity of variance (Leven’s test), with the p-value of 0.05.

Comparisons between angles

Comments: The scatter plots show a positive correlation between angles α and β and angles α and γ .

Moreover, there is a slight positive correlation between angles γ and β ; however, it is less pronounced than the other two (Fig. 9A–C).

There was a significant, though weak, positive correlation between angles α and β and angles α and γ . Higher values of angle α may be expected to be associated with higher mean values of angles γ and β . The positive correlation between angles γ and β was not statistically significant; therefore, no conclusions can be drawn as to a correlation between these two angles.

Another confirmation of significant differences between the angles was provided by the results of analysis of variance and Student’s t test for the difference of means (with the Bonferonni correction due to multiple comparisons).

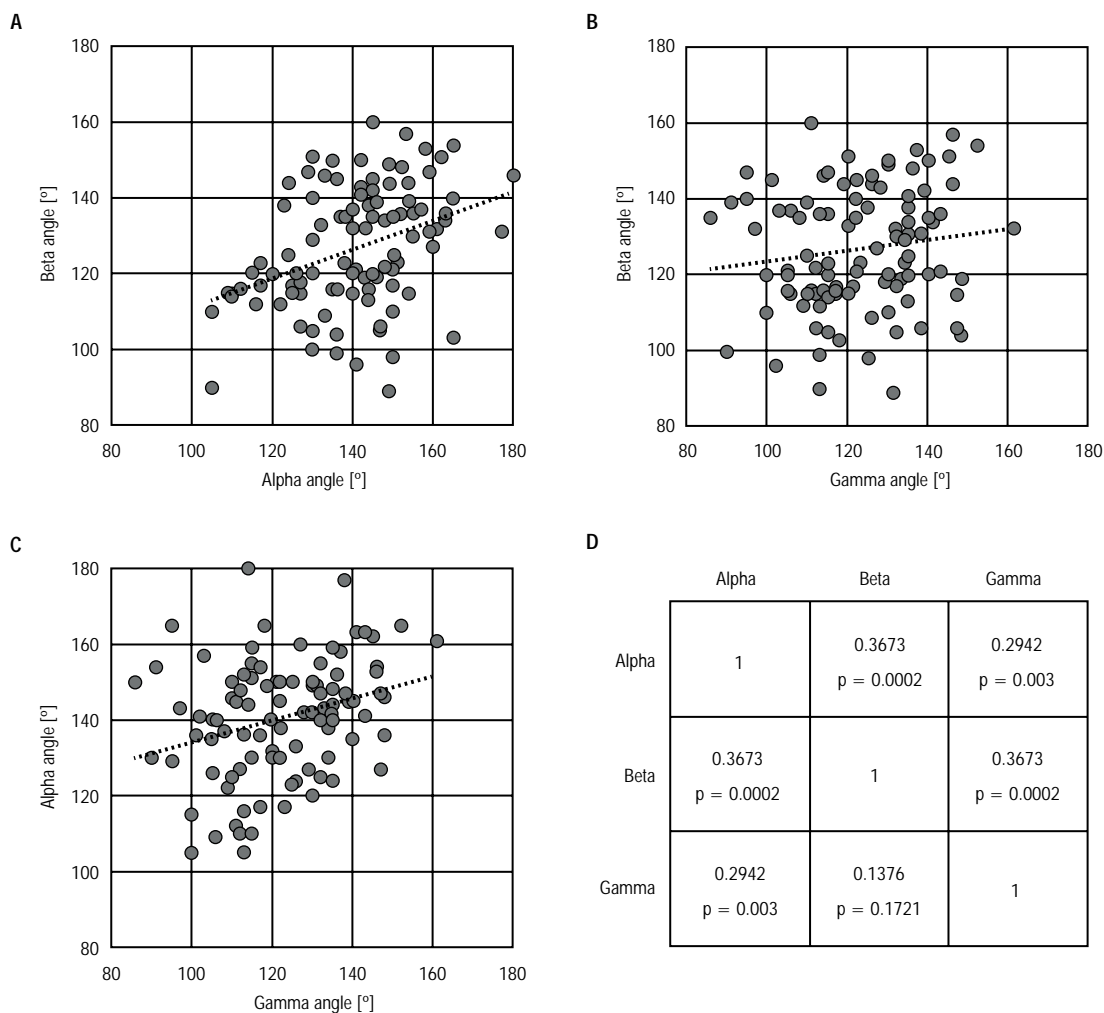


Figure 9. A–C. Scatter graphs of the measurements for each pair of the evaluated angles. The slope of each dotted line of best fit shows the type of correlation; **D.** Pearson correlation coefficients between pairs of angles and their statistical significance.

Analysis of variance results demonstrated significant differences between the evaluated angles ($p < 0.0001$). The results of Student’s t test with $p = 0.05$ showed significant differences between the mean angle values when comparing angles γ and α and angles β and α , with no significant differences between angles γ and β .

Therefore, we can conclude that angles α were significantly more obtuse than the other two types of analysed angles. However, we cannot state that angles γ and β differed significantly in their values.

Drawing conclusions as to the value of a given angle based on the value of another angle

Comments: Upper panel. Based on the value of angle γ in the graph we can draw conclusions as to the likely values of angle α . The graph shows, once again, a positive correlation between the values of angle α

and those of angle γ (this correlation is particularly clear for angle γ values in the 100–170° range). Lower panel: The graph illustrates a positive correlation between the values of angles α and β , with higher values of angle α corresponding to higher expected values of angle β . This positive correlation is visible for the entire range of angle α values. There is no visible correlation between the values of angles γ and β . Moreover, no such correlation was demonstrated in earlier analyses.

DISCUSSION

During normal human embryogenesis, the initially symmetrical venous system consists of two pairs of anterior and posterior cardinal veins, draining the cephalic and caudal areas of the embryo, respectively. These venous pairs anastomose to form the right and left common cardinal veins (ducts of Cuvier). At

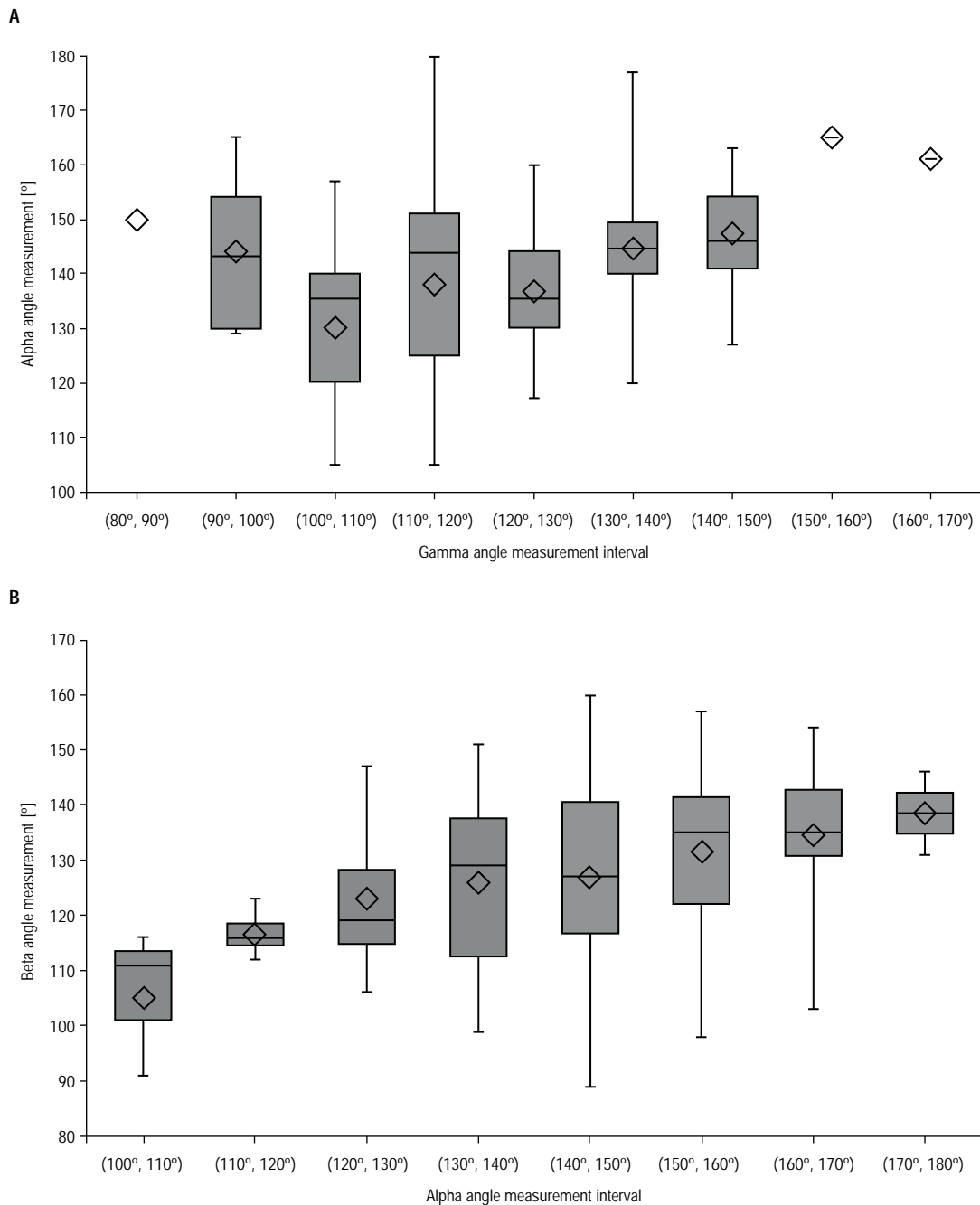


Figure 10. A, B. Box-and-whisker plots showing the ranges of angle measurements; **A.** The relationship between the value of angle α and the value of angle γ ; **B.** The ranges of angle β values with respect to the ranges of angle α values.

8 weeks of gestation, the left and right anterior cardinal veins coalesce to form BCVs. Eventually, the left BCV is nearly 3 times longer than its right counterpart [4]. Each of the BCVs drains its corresponding side of the chest by collecting blood from the ipsilateral internal jugular vein and SV as they join.

The most typical left BCV topography involves the vein coursing above the aortic arch and anterior to its branches (the brachiocephalic trunk, left

common carotid artery, and left subclavian artery). Once it crosses to the right side of the upper mediastinum, the left BCV joins the right BCV to form the SVC [15].

During transvenous CIED implantation procedures, cardiac leads are typically introduced via the veins of the left clavipectoral triangle. In our centre this method is used in approximately 97% of de novo CIED implantation procedures.

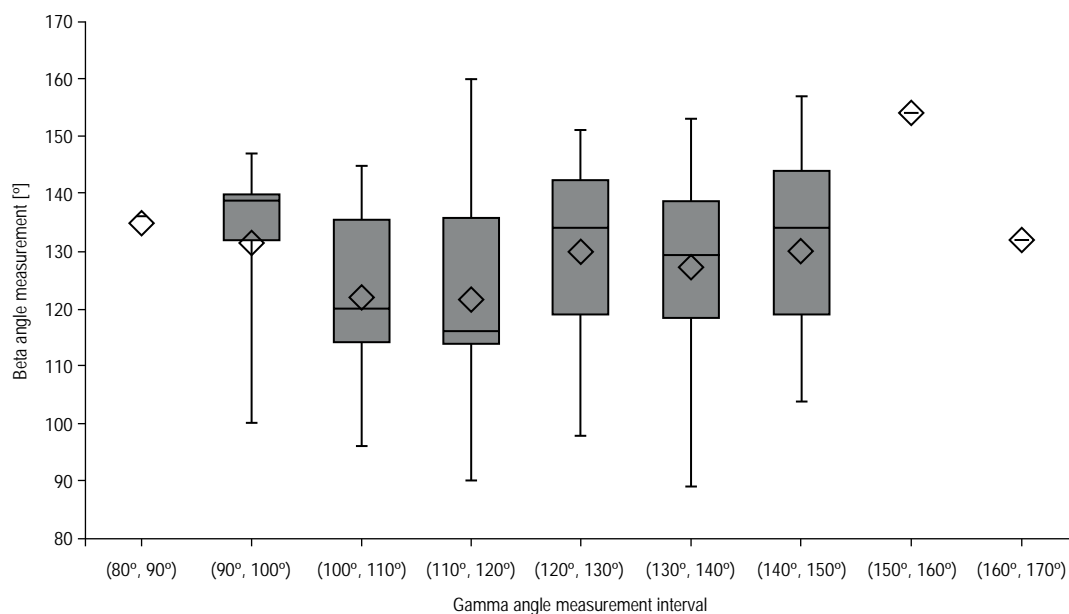


Figure 11. A box-and-whisker plot illustrating the distribution of angle β values with respect to angle γ value ranges.

Radiographic visualisation of the left BCV considerably helps in assessing the vein's morphometry and the nature of its angulations, as well as the position of these angulations with respect to adjacent structures. The nature of the angles along the course of the left BCV through the mediastinum helps observe any relationships between them (Figs. 9, 10). These relationships vary to some extent during chest movements during the expiratory phase of respiration (Fig. 1B, C).

The unique character of venous angulations may predispose to venous wall injuries during CIED implantation or CVC placement procedures. In severe cases, the injury may involve damage to adjacent anatomical structures, producing clinical manifestations. Nonetheless, even an epithelial injury may lead to long-term complications, such as post-thrombotic lesions [1, 9, 18, 21, 22]. The risk of vascular injury is increased by higher numbers of inserted leads, specific structural characteristics of the vein (diameter, wall stiffness, etc.), and any attempts to forcibly overcome potential difficulties in lead advancement [6, 8].

The risk of intraoperative venous injury is also increased in the vascular segments forming right-angle or sharp-angle angulations. In the analysed materials such vulnerable venous segments were: the site where the left SV and the left BCV meet (angle β) and the site of left BCV drainage to the SVC (angle γ) [6, 9, 22]. These angles created such unfavourable conditions in 5–6% of cases, collectively (Fig. 8A, B).

In most cases angle α was an obtuse angle (Fig. 8C), which facilitates lead advancement within the vessel. However, there is always a possibility of accidental lead advancement into the opening of such tributaries as the left superior intercostal vein or the left internal thoracic vein [20].

Limitations of the study

Our assessment of the rates and morphometric parameters of left BCV anatomical variations included a selected group of patients undergoing CIED implantation with the use of venography. Thus, the study population does not reflect the actual prevalence in the general population.

The angles of interest were measured based on contrast-enhanced images of left BCV lumina in posteroanterior views, without considering the potential lateral-view component of angle values.

The method of calculating the values of the angles marked graphically based on the intraluminal flow of the contrast agent may reflect some subjective bias; nonetheless, given the total number of measurements this does not seem to have significantly affected the conclusions, which are mostly based on relative differences.

CONCLUSIONS

The interindividual variations in left BCV topography and morphometry are largely due to the formation of the angulation in the middle of the vein's course through the mediastinum.

Angles whose values were close to 90° were found in 5% of cases and were most commonly at the site where the left SV continues into the left BCV and at the site where the left BCV drains into the SVC.

Conflict of interest: None declared

REFERENCES

1. Abu-El-Haija B, Bhavne PD, Campbell DN, et al. Venous stenosis after transvenous lead placement: a study of outcomes and risk factors in 212 consecutive patients. *J Am Heart Assoc.* 2015; 4(8): e001878, doi: [10.1161/JAHA.115.001878](https://doi.org/10.1161/JAHA.115.001878), indexed in Pubmed: [26231843](https://pubmed.ncbi.nlm.nih.gov/26231843/).
2. Bowdle A. Vascular complications of central venous catheter placement: evidence-based methods for prevention and treatment. *J Cardiothorac Vasc Anesth.* 2014; 28(2): 358–368, doi: [10.1053/j.jvca.2013.02.027](https://doi.org/10.1053/j.jvca.2013.02.027), indexed in Pubmed: [24008166](https://pubmed.ncbi.nlm.nih.gov/24008166/).
3. Chen SJ, Liu KL, Chen HY, et al. Anomalous brachiocephalic vein: CT, embryology, and clinical implications. *AJR Am J Roentgenol.* 2005; 184(4): 1235–1240, doi: [10.2214/ajr.184.4.01841235](https://doi.org/10.2214/ajr.184.4.01841235), indexed in Pubmed: [15788602](https://pubmed.ncbi.nlm.nih.gov/15788602/).
4. Chern MS, Ko JS, Tsai A, et al. Aberrant left brachiocephalic vein: CT imaging findings and embryologic correlation. *Eur Radiol.* 1999; 9(9): 1835–1839, doi: [10.1007/s003300050931](https://doi.org/10.1007/s003300050931), indexed in Pubmed: [10602959](https://pubmed.ncbi.nlm.nih.gov/10602959/).
5. Granata A, Zanolli L, Trezzi M, et al. Anatomical variations of the left anonymous trunk are associated with central venous catheter dysfunction. *J Nephrol.* 2018; 31(4): 571–576, doi: [10.1007/s40620-017-0465-z](https://doi.org/10.1007/s40620-017-0465-z), indexed in Pubmed: [29270845](https://pubmed.ncbi.nlm.nih.gov/29270845/).
6. Gravenstein N, Blackshear RH. In vitro evaluation of relative perforating potential of central venous catheters: comparison of materials, selected models, number of lumens, and angles of incidence to simulated membrane. *J Clin Monit.* 1991; 7(1): 1–6, doi: [10.1007/BF01617891](https://doi.org/10.1007/BF01617891), indexed in Pubmed: [1999693](https://pubmed.ncbi.nlm.nih.gov/1999693/).
7. Guo X, Shi Y, Xie H, et al. Left innominate vein stenosis in an asymptomatic population: a retrospective analysis of 212 cases. *Eur J Med Res.* 2017; 22(1): 3, doi: [10.1186/s40001-017-0243-3](https://doi.org/10.1186/s40001-017-0243-3), indexed in Pubmed: [28115002](https://pubmed.ncbi.nlm.nih.gov/28115002/).
8. Haghjoo M, Nikoo MH, Fazelifar AF, et al. Predictors of venous obstruction following pacemaker or implantable cardioverter-defibrillator implantation: a contrast venographic study on 100 patients admitted for generator change, lead revision, or device upgrade. *Europace.* 2007; 9(5): 328–332, doi: [10.1093/europace/eum019](https://doi.org/10.1093/europace/eum019), indexed in Pubmed: [17369270](https://pubmed.ncbi.nlm.nih.gov/17369270/).
9. Haq AA, Restrepo CS, Lamus D, et al. Thoracic venous injuries: an imaging and management overview. *Emerg Radiol.* 2016; 23(3): 291–301, doi: [10.1007/s10140-016-1386-1](https://doi.org/10.1007/s10140-016-1386-1), indexed in Pubmed: [26965007](https://pubmed.ncbi.nlm.nih.gov/26965007/).
10. Bachleda JP. Iatrogenic injury to the superior vena cava and brachiocephalic vein. *J Infect Dis Ther.* 2014; 2(6): 169, doi: [10.4172/2332-0877.1000169](https://doi.org/10.4172/2332-0877.1000169).
11. Igawa O, Adachi M, Yano A, et al. Brachiocephalic vein perforation on three-dimensional computed tomography. *Europace.* 2007; 9(1): 74–75, doi: [10.1093/europace/eul133](https://doi.org/10.1093/europace/eul133), indexed in Pubmed: [17224430](https://pubmed.ncbi.nlm.nih.gov/17224430/).
12. Kahkouee S, Sadr M, Pedarzadeh E, et al. Anomalous left brachiocephalic vein: important vascular anomaly concomitant with congenital anomalies and heart diseases. *Folia Morphol.* 2017; 76(1): 51–57, doi: [10.5603/FM.a2016.0031](https://doi.org/10.5603/FM.a2016.0031), indexed in Pubmed: [27830886](https://pubmed.ncbi.nlm.nih.gov/27830886/).
13. Ko SF, Huang CC, Ng SH, et al. Imaging of the brachiocephalic vein. *AJR Am J Roentgenol.* 2008; 191(3): 897–907, doi: [10.2214/AJR.07.3552](https://doi.org/10.2214/AJR.07.3552), indexed in Pubmed: [18716126](https://pubmed.ncbi.nlm.nih.gov/18716126/).
14. Ko SF, Ng SH, Fang FM, et al. Left brachiocephalic vein perforation: computed tomographic features and treatment considerations. *Am J Emerg Med.* 2007; 25(9): 1051–1056, doi: [10.1016/j.ajem.2007.06.013](https://doi.org/10.1016/j.ajem.2007.06.013), indexed in Pubmed: [18022501](https://pubmed.ncbi.nlm.nih.gov/18022501/).
15. Mitsuoka H, Arima T, Ohmichi Y, et al. Analysis of the positional relationship between the left brachiocephalic vein and its surrounding vessels via computed tomography scan: A retrospective study. *Phlebology.* 2020; 35(6): 416–423, doi: [10.1177/0268355519898320](https://doi.org/10.1177/0268355519898320), indexed in Pubmed: [31918641](https://pubmed.ncbi.nlm.nih.gov/31918641/).
16. Nakabayashi K. Iatrogenic brachiocephalic vein perforation during pacemaker implantation. *BMJ Case Rep.* 2015; 2015(29), doi: [10.1136/bcr-2015-209369](https://doi.org/10.1136/bcr-2015-209369), indexed in Pubmed: [25634862](https://pubmed.ncbi.nlm.nih.gov/25634862/).
17. Rozmus G, Daubert JP, Huang DT, et al. Venous thrombosis and stenosis after implantation of pacemakers and defibrillators. *J Interv Card Electrophysiol.* 2005; 13(1): 9–19, doi: [10.1007/s10840-005-1140-1](https://doi.org/10.1007/s10840-005-1140-1), indexed in Pubmed: [15976973](https://pubmed.ncbi.nlm.nih.gov/15976973/).
18. Salik E, Daftary A, Tal MG. Three-dimensional anatomy of the left central veins: implications for dialysis catheter placement. *J Vasc Interv Radiol.* 2007; 18(3): 361–364, doi: [10.1016/j.jvir.2006.12.721](https://doi.org/10.1016/j.jvir.2006.12.721), indexed in Pubmed: [17377181](https://pubmed.ncbi.nlm.nih.gov/17377181/).
19. Steckiewicz R, Kosior DA, Rosiak M, et al. The prevalence of superior vena cava anomalies as detected in cardiac implantable electronic device recipients at a tertiary cardiology centre over a 12-year period. *Hellenic J Cardiol.* 2016; 57(2): 101–106, doi: [10.1016/j.hjc.2016.03.003](https://doi.org/10.1016/j.hjc.2016.03.003), indexed in Pubmed: [27445024](https://pubmed.ncbi.nlm.nih.gov/27445024/).
20. Steckiewicz R, Stolarz P, Świętoń E, et al. Tributaries of the left brachiocephalic vein posing problems in central venous catheterization and, potentially, in cardiac implantable electronic device placement. *Folia Cardiologica.* 2020; 15(4): 277–284, doi: [10.5603/fc.a2020.0040](https://doi.org/10.5603/fc.a2020.0040).
21. Teichgräber UK, Gebauer B, Benter T, et al. Central venous access catheters: radiological management of complications. *Cardiovasc Intervent Radiol.* 2003; 26(4): 321–333, doi: [10.1007/s00270-003-0112-z](https://doi.org/10.1007/s00270-003-0112-z), indexed in Pubmed: [14667113](https://pubmed.ncbi.nlm.nih.gov/14667113/).
22. Vertemati M, Rizzetto F, Cassin S, et al. Clinical relevance of the left brachiocephalic vein anatomy for vascular access in dialysis patients. *Clin Anat.* 2020; 33(8): 1120–1129, doi: [10.1002/ca.23549](https://doi.org/10.1002/ca.23549), indexed in Pubmed: [31891199](https://pubmed.ncbi.nlm.nih.gov/31891199/).

Anatomo-topographic and histo-cytological study of dromedary's spleen in Algeria

M.A. Fares¹ , T. Khenenou¹ , D.E. Rahmoun² 

¹Laboratory of Sciences and Technics of the Livings, Institute of Agriculture and Veterinary Sciences, Taoura, University of Souk Ahras, Algeria

²Laboratory of Animal Production, Biotechnologies and Health (PABIOS), Institute of Agriculture and Veterinary Sciences Taoura, University of Souk Ahras, Algeria

[Received: 13 August 2021; Accepted: 5 November 2021; Early publication date: 17 January 2022]

Background: Twenty-five spleens of adult, healthy dromedary of the local breed from the region of El Oued, Algeria, were collected at the slaughterhouse in order to carry out research to determine the macroscopic and microscopic structure of spleen in this species, macroscopic study revealed that the spleen has a rectangular shape with a triangular section, rounded edges, a little bit striated, its surface is smooth in which the aspect of the capsule and the parietal surface is shiny and smooth, the morphometric study was carried out after classifying the sampled spleen in five groups according to the animal's body weight which increases with age.

Materials and methods: Our study revealed that the groups show a different value of mass which declines towards a drop of the index, also the indexes of length and width are following a decreasing order.

Results: The histological study revealed that the zone occupied by stroma did not exceed 26.81% of the total components of the capsule which is composed essentially of connective tissue and an inner layer of smooth muscle cells. Vascular and avascular trabeculae extend from the capsule. The immunohistochemistry study made it possible to visualise T lymphocytes of the splenic parenchyma using monoclonal antibodies where a statistical study was carried out to determine the composition of the various compartments of this organ. The localisation of immunocompetent cells in the splenic parenchyma has been elucidated with antibodies specific for T lymphocytes.

Conclusions: The red pulp occupied a maximum area of the spleen with an average of 68.1% composed of sinusoids venous, the cords extend between the sinuses and the interlobular zone contain many cells: macrophages, plasma cells, red blood cells, white blood cells and platelets. (Folia Morphol 2023; 82, 1: 137–146)

Key words: dromedary, lymphocytes, spleen, peri-arteriolar lymphoid sheath, red pulp, white pulp

INTRODUCTION

The spleen is the largest secondary lymphoid organ in mammals and also the primary site for prolif-

eration and differentiation of immune cells and has been described as a centre of blood filtration [5]. The splenic parenchyma has a crucial role in immune

Address for correspondence: Dr. M.A. Fares, PhD Student, Veterinary Anatomy, Laboratory of Sciences and Techniques of Living, Institute of Agriculture and Veterinary Sciences, Taoura, University of Mohamed Cherif Messaadia Souk Ahras, B.P. 1553, Route de Annaba, 41000, Algeria, tel: +213696490031, e-mail: faresamin1995i@gmail.com

This article is available in open access under Creative Common Attribution-Non-Commercial-No Derivatives 4.0 International (CC BY-NC-ND 4.0) license, allowing to download articles and share them with others as long as they credit the authors and the publisher, but without permission to change them in any way or use them commercially.

responses such as exposure to antigens transmitted by blood according to studies by Kannan et al. [14].

Research by Mahadevan [16] demonstrated that the spleen is an organ deep red to blue-black located in the left cranial abdomen, it is adjacent to the greater curvature of the stomach and the omentum is an elongated organ with an approximately triangular section. According to the results of studies by Masternak and Bartke [17] and Mahadevan [16], the size of the spleen varies according to the species and the degree of distension; nonetheless, the mass of the spleen may be important in its assessment. The splenic weight to body weight ratio remains fairly constant regardless of age in most mammals and is generally around 0.2%.

Researchers such as Paraskevas et al. [25] and Xu et al. [33], have demonstrated that the spleen is composed of two functionally and morphologically distinct compartments, the red pulp and the white pulp, the red pulp is a blood filter that removes foreign bodies, erythrocytes, and damaged material, it is a site of haematopoiesis, especially in fetuses and newborn animals. Almenar et al. [1] also described that the spleen is the largest secondary lymphoid organ, containing about a quarter of the body's lymphocytes and it is the one that initiates immune responses to antigens carried by the blood, this function is charged to the white pulp which surrounds the central arterioles, the white pulp is composed of three sub-compartments, the peri-arteriolar lymphoid sheath (PALS), the follicles and the marginal area, this has been shown by Nolte et al. [22]. Histo-cytometric research by Kage et al. [13] and Almenar et al. [1] shows that the spleen is surrounded by a capsule composed of dense fibrous tissue, elastic fibres, and smooth muscle, the outermost layer of the capsule. Splenic is composed of mesothelial cells, the irregularly spaced trabeculae of smooth muscle and elastic fibre tissues that emerge from the capsule to the splenic parenchyma [28, 30]. On the other hand, Rahmoun et al. [29] showed that these trabeculae also contain blood vessels, lymphatics, and nerves.

Looking at the studies of Mollejo et al. [21] who demonstrated that the red pulp is composed of a three-dimensional mesh of the splenic cords and venous sinuses, the spleen cords are composed of the reticular fibres, reticular cells, and macrophages. The white pulp is subdivided into PALS, follicles, and marginal zone, it is composed of lymphocytes, macrophages, dendritic cells, plasma cells, arterioles, and

capillaries in a reticular framework similar to that found in the red pulp, the arterioles entering the latter is surrounded by PALS which are composed of lymphocytes and layers of reticular fibres and flattened reticular cells concentrated according to Dijkstra et al. [3]. The internal PALS cells are largely CD4 T lymphocytes, although lower numbers of CD8 T lymphocytes may also be present, inter-digitised dendritic cells and migrating B cells according to Johnson [12]. The outer PALS is populated with small and medium-sized lymphocytes (B and T cells), macrophages, and plasma cells according to studies by Matsuno et al. [18] and Johnson [12].

The marginal zone is a unique region of the spleen located at the interface of the red pulp with PALS and the follicles considered by many authors to be a separate compartment rather than part of the white pulp, it is designed to filter the systemic circulation to eliminate antigens and pathogens according to Kuper et al. [15] and Bar-Ephraïm and Mebius [2]. Marginal zone macrophages are a unique subset of macrophages at the inner margin of the marginal zone adjacent to PALS and follicles according to Dijkstra et al. [3] and Nolte et al. [22].

The endothelial cells coating the sinuses according to Bar-Ephraïm and Mebius [2]. At the level of the marginal sinus, according to the research of Kage et al. [13] and McGaha and Karlsson [19] have shown that there is a presence of a thick external crown of the marginal zone, composed of reticular fibroblasts, marginal macrophages, medium-sized dendritic cells, and marginal zone B cells, which merge into the red pulp. Macrophages from marginal areas constitute another population of splenic macrophages which stain with the monoclonal antibody ERTR-9 according to Johnson [12]. Marginal zone macrophages are important in the elimination of microorganisms and viruses; they express several pattern recognition receptors such as toll receptors and macrophage receptors with collagen structure, which play a role important in the absorption of various bacteria. Marginal zone B cells are a unique subset of non-circulating B cells having an IgM/IgD phenotype as opposed to follicular B cells which are IgM/IgD according to the results of studies by Johnson [12] and Middleton et al. [20].

MATERIALS AND METHODS

The studies were carried out in the Laboratory of Science and Technique of Living, Institute of Agronomic and Veterinarian Sciences, University of Mohamed Cherif Messaâdia, Souk Ahras, Algeria. The

research material was clinically healthy, sexually mature dromedary spleens (*Camelus dromedarius*) from the El-Oued region of southern Algeria. The animals have not been vaccinated throughout their lives. Material selection took place at the town's communal slaughterhouse after the animals were slaughtered by bleeding. Before slaughter, the animals underwent a mandatory veterinary examination, weighing, and age determination, the animals were classified according to bodyweight into five groups, The first group composed of animals that had a bodyweight compromised between 328 kg and 353 kg, whereas the animals classified in the second group had a bodyweight compromised between 353 kg and 378 kg, while the animals of the third group had a bodyweight compromised between 378 kg and 393 kg, and the fourth group composed of animals that had a bodyweight between 393 kg and 418 kg, and finally, the animals of the fifth group had a bodyweight compromised between 418 kg and 433 kg.

When selecting the material, the topographic characteristics of the spleens were determined. Absolute organ mass was determined using a Techniprot-WTW scale accurate to 0.002 mg. The relative weight of the spleens concerning the bodyweight of the dromedary was also calculated. The linear measurements (length, width) of each spleen were determined using a centimetre ruler.

Microscopic investigations were carried out after fixing the samples in a 5% solution of neutral formalin for 10 days, then in 10% for 12–16 days, followed by storage of the material in this solution for the entire period of the morphological research. For the preparation of histological sections, the samples were cut perpendicularly, selecting five segments from each group. The fragments were incorporated into paraffin after washing with running water; the dehydration was carried out using ethanol with increasing concentration. The casting has been completed. Histological sections 7–10 μm thick were stained with haematoxylin and eosin, according to Van Gieson, Azure II-eosin. The characteristics of the cytoarchitecture and the lymphoid structure were determined using an MBS-10 biological stereoscopic microscope (8 \times eyepieces, 4 \times objectives, 7 \times) and a B-382PLi-ALC light microscope (10 \times eyepieces, 10 \times objectives, 40 \times , 100 \times). A quantitative (morphometric) analysis of structural components was performed by the "spot count" method using eye test systems (inserts) (3 measurements on 5 preparations obtained from each spleen).

The relative area of connective tissue was determined (trabeculae, capsules, and thickening of the hilum, relative area of lymphoid parenchyma as a whole, and in distinct functional areas [capsule, trabecula, red pulp, peri-arterial lymphoid sheath, total white pulp, inactive and active follicle]). The cytoarchitectonics of the individual functional areas of the spleens of the different areas of the splenic parenchyma was determined on thin sections of paraffin stained with Azure II-eosin. The cell count is the relative amount of the lymphoid line, was performed using an Olympus IX71 Inverted Microscope cytometric microscope with an increase of 10–100 under emersion. Based on the data obtained, the average percentage of each type of cellular element was determined.

An immunohistochemical study was performed to determine the localisation of T and B lymphocyte populations in the functional areas of the lymphoid parenchyma of the spleens. For the study, the segments were fixed in a 10% neutral formalin solution, followed by standard routing through alcohols of increasing concentration, after which they were poured into paraffin, and thin sections of 4 to 5 μm thick were made. Immunohistochemical studies were performed by the direct Koons method according to the method of Matsuno et al. [18] Cells immune systems were differentiated using monoclonal antibodies. Antibodies to the CD3 antigen (T cells were used). Diaminobenzidine (DAB) was used as a chromogen. Sections were further stained with haematoxylin, with additional dehydration, clarification in xylene, and incorporation into polystyrene. The statistical analysis of the results was carried out using Statistica 10.0 (StatSoft Inc., USA), and the differences between samples were determined using ANOVA and were considered significant at ≤ 0.05 , ≤ 0.01 , ≤ 0.001 . The quantitative study for the tissue compartments was carried out using the point S system.

RESULTS

After dissection of the animals, it was found that the spleen presents a semi-lunar shape, of firm consistency, of red-brown colour surrounded by a layer of thick connective tissue, it was found that this organ is composed of two compartments which are the body and extremities, this organ is located under the left hypochondrium behind the stomach cavities above the dorsal bag of the rumen to the posterior part of the kidney. Regarding the spleen mass, it was

found that the minimal absolute mass was 236 g in the first group, whereas the maximal mass was 336 g observed in the fifth group. In the other groups, the mass followed an ascending order from the second to the fourth, in which the observed values were 267 g, 280 g and 297 g, respectively (Fig. 1).

The length of the spleens as a value a variation between groups and followed an ascending order same the mass, in which the minimal length value was 40.10 cm observed in the first group, while the maximal length was 51.30 cm observed in the fifth group. The width also showed a variation following an ascending order from the second to the fourth group in which the values were 47.3 cm, 49.9 cm and 50.6 cm, respectively, the minimal value of width was 17.60 cm found in the first group, whereas the maximal width was 26.40 observed in the fifth group, the other values of the third, fourth and fourth group were respectively 44.1 cm, 44.5 cm and 45.8 cm (Figs. 1, 2).

The outer layer mainly consisted of connective tissue including collagen, rubber bands and fibroblasts and smooth muscle cells (SMC). The inner layer was made up mostly of SMC that appear parallel along the longitudinal cut. Trabeculae extend from the capsule and branch out, so that it divides the area into several parts, are distinguished by the presence of white fibres and smooth muscle fibres. At high magnification, it was observed that the space between the capsule and the parenchyma contained red blood cells, so the surface of the white pulp was large, irregular in shape, the PALS had a clear surface with a branching central artery in several branches, the lymphatic follicles and the marginal zone were very clear.

A large marginal area surrounded the white pulp and it was contained in sheathed arteries and SMC. Also, it was observed that the marginal sinus of the marginal zone infiltrates in the marginal zone in the direction of the red pulp supplying the blood directly in the adjacent venous sinuses whose ends which appear open with the marginal zone and penetrate into the reticular mesh of the red pulp and bypass the reticular mesh of the red pulp. It was found that blood from the red pulp collects in the venous sinuses which enter the trabeculae and merge into the trabecular veins, the trabecular veins then converge at the hilum to form the splenic vein which drains to the exterior of the organ (Fig. 3).

Regarding the red pulp, it was found to be composed of a mesh of splenic cords and venous sinuses. At high magnification, the splenic cords are composed

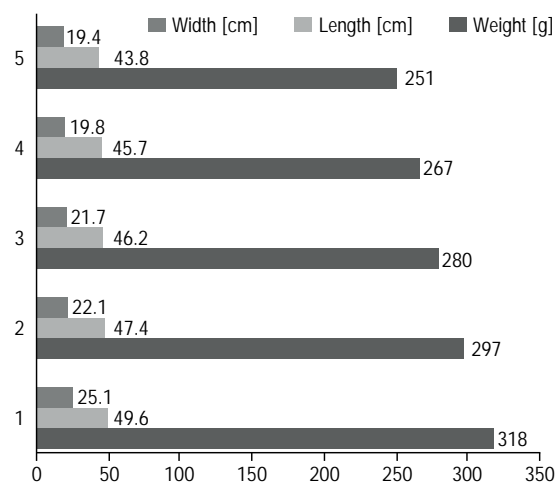


Figure 1. Index of mass, length and width of dromedary spleens according to the groups.

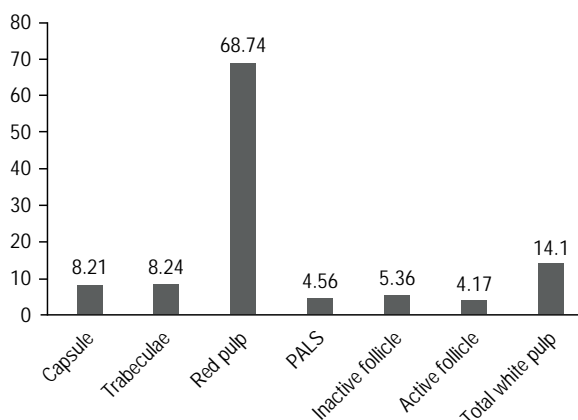


Figure 2. Index of tissue composition of dromedary spleen (%); PALS — peri-arterial lymphoid sheath.

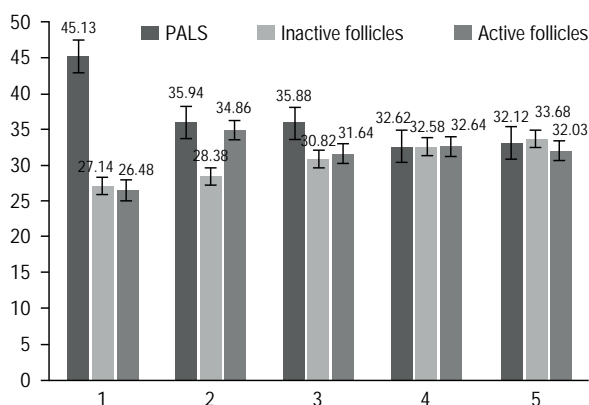


Figure 3. Index of parenchyma composition of dromedary spleen (%); PALS — peri-arterial lymphoid sheath.

of reticular fibres, reticular cells and macrophages. Again, under the microscope it was found that the

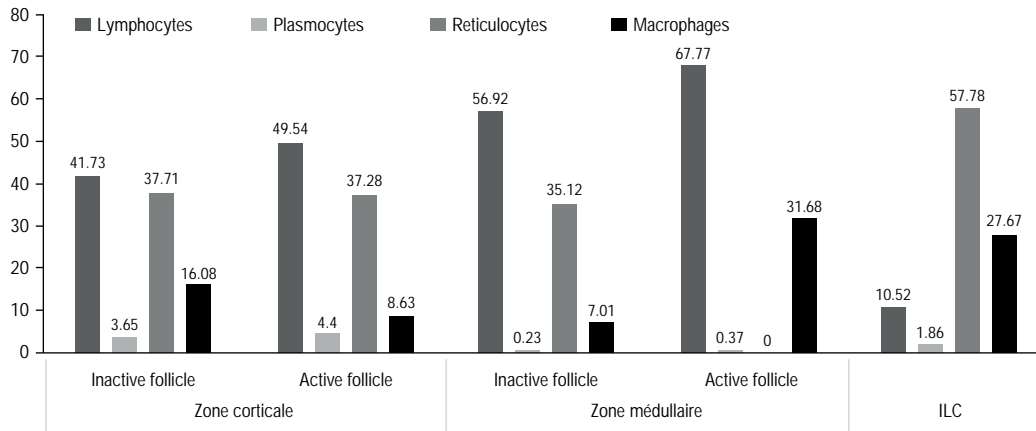


Figure 4. Index of the cellular composition of the dromedary spleen (%); ILC — intralobular connective tissue.

venous sinuses can occupy the entire surface of the red pulp including, they are lined with epithelial tissue and rest on a basement membrane, the periciliary arteries and arteriolar capillaries are also located in the pulp red (Fig. 3).

The statistical study revealed that the stroma which is constituted by capsule and trabecula, the maximal area occupied by the capsule was $13.18 \pm 1.93\%$ observed in the fifth group, with a minimal value of $5.27 \pm 2.53\%$ observed in the second group, while the trabecula occupied an area of $13.54 \pm 1.62\%$ as maximal value observed in the fourth group, while the minimum value was about $4.36 \pm 1.53\%$ observed in the second group, whereas the red pulp occupied a zone with a minimum value of $52.36 \pm 1.72\%$ found in the fourth group, and the maximal value was about $68.09 \pm 0.77\%$ found in the second group (Fig. 4).

The parenchyma and its components were considered as a lymphoid organ integrated into the spleen, for the PALS the minimal value was $32.12 \pm 1.38\%$ observed in the fifth group, whereas the maximal value was $45.13 \pm 1.47\%$ found in the first group, while the zone occupied by the inactive follicles revealed that the minimal value was $27.14 \pm 1.58\%$ observed in the first group, whereas the maximal value was $33.68 \pm 1.17\%$ found in the fifth group. While the area occupied by the active follicles showed a minimum value of $26.48 \pm 1.71\%$ observed in the first group, while the maximal value was $32.64 \pm 1.27\%$ observed in the fourth group (Fig. 5).

Under the high magnification microscope, we could see that the red pulp is formed by blood sinuses

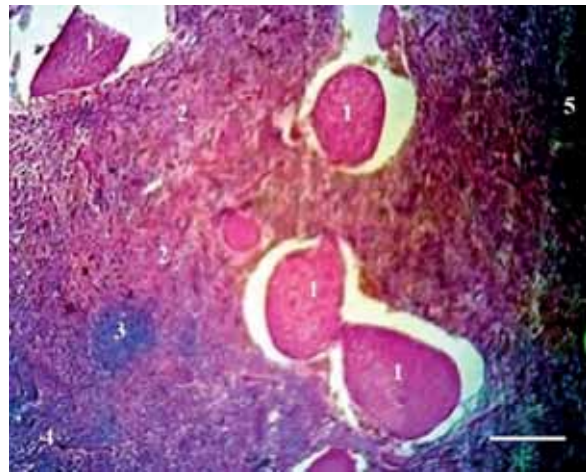


Figure 5. Histological section of the spleen of the dromedary, haematoxylin eosin staining; 1 — red pulp; 2 — white pulp; 3 — follicle; 4 — cortical zone; 5 — medullary zone. Bar = 100 μm .

and Billroth cell cords; the sinus wall is very thick. The cords extend between the sinuses and contain macrophages, plasma cells, erythrocytes, lymphocytes and also platelets. Also, we could see that the white pulp consists of clusters of lymphoid tissue, including Hassall corpuscles, the latter formed a PALS around the central arteries (Fig. 6).

In these areas there are active and inactive lymphoid follicles, which are rich in lymphocytes and plasma cells. A marginal area was found at the junction of the red pulp and the white pulp, which contains lymphoid cells and macrophages. It is separated from the white pulp by the marginal sinus formed by a terminal branch of the central artery. It was also possible to detect the reticular cells which formed a surface in the integrity of the organ's framework (Figs. 6, 7, 8).

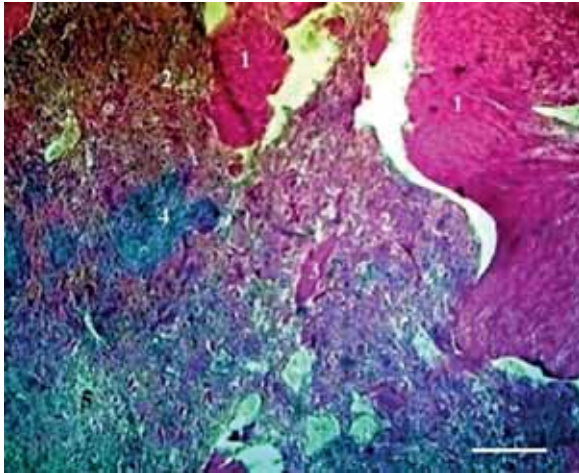


Figure 6. Histological section of the dromedary spleen, haematoxylin-eosin staining; 1 — red pulp; 2 — white pulp; 3 — pulp sinus; 4 — medullary zone. Bar = 100 μ m.

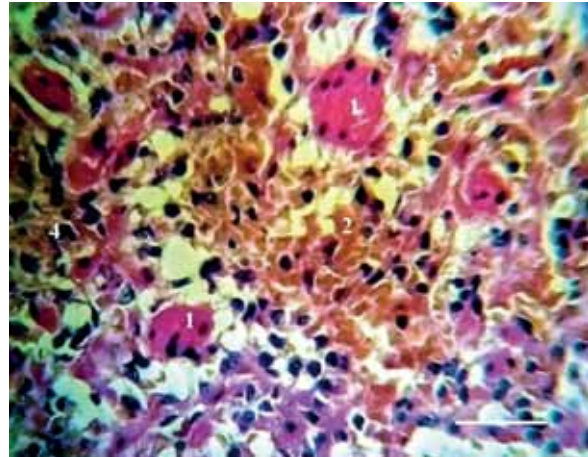


Figure 8. Histological section of the dromedary spleen, Azur II-eosin staining; 1 — red pulp concentration; 2 — reticulocyte; 3 — macrophage; 4 — lymphocyte. Bar = 20 μ m.

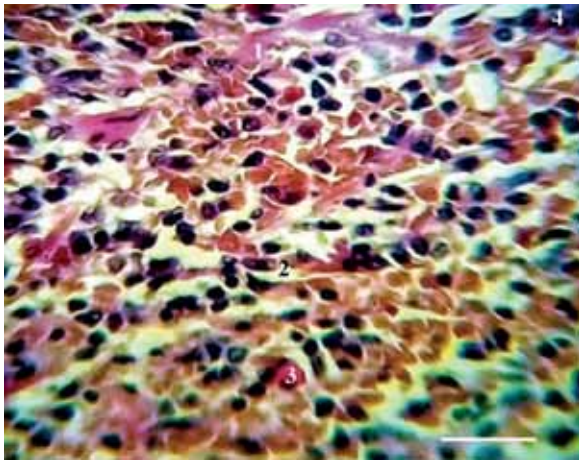


Figure 7. Histological section of the dromedary spleen, Azur II-eosin staining; 1 — reticulocyte; 2 — lymphocyte; 3 — macrophage; 4 — large lymphocyte. Bar = 20 μ m.

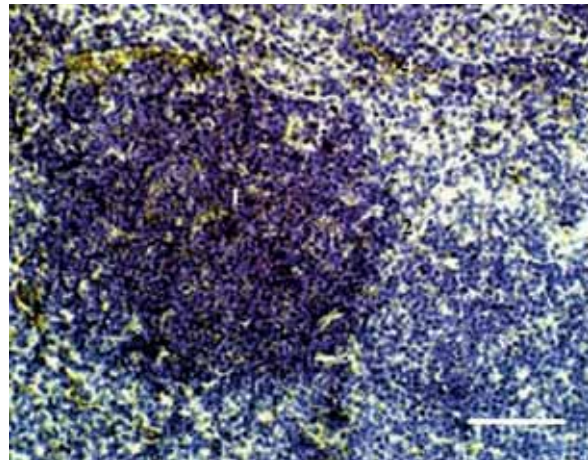


Figure 9. Histological section of the dromedary spleen, immunohistochemical reaction against CD3 T lymphocyte; 1 — follicular centre; 2 — follicular periphery; 3 — cortical zone; 4 — lymphocytic reaction. Bar = 20 μ m.

The use of the immunological translation of lymphocytes at the level of the splenic parenchyma has been identified by the use of anti-CD3 antibodies, their fixations of which are planned at the precisely follicular medullary level, lymphocyte frames clearly visible at the level of the chin of the follicles as well as in the peri-arterial space of the splenic parenchyma of variable density according to the reaction of the lymphocytes (Fig. 9).

On the other hand, we were able to visualise the B lymphocytes with the use of anti-CD3, whose binding appears clearly at the inter follicular level whose mass appears after lymphocyte reaction in general the spleen of the dromedary is in the immunogenic system very active (Fig. 10).

The statistic study of cellular components revealed that the cortical zone components showed different but close values, the lymphocytes occupied a zone of $41.73 \pm 1.48\%$ in the inactive follicles, in contrast, it occupied a zone of $49.54 \pm 1.62\%$ in the active follicles, the reticulocytes occupied a zone of $13.65 \pm 1.29\%$ in the inactive follicles, whereas they occupied an area of $9.4 \pm 1.29\%$ in the active follicles, plasmocytes occupied $25.71 \pm 1.29\%$ of the inactive, while they occupied $22.28 \pm 1.73\%$ in the active follicles, macrophages occupied a zone of $18.08 \pm 1.67\%$ in the inactive follicles, whereas they occupied an area of $18.63 \pm 0.74\%$ in the active follicles. The medullary zone showed a general distribution of

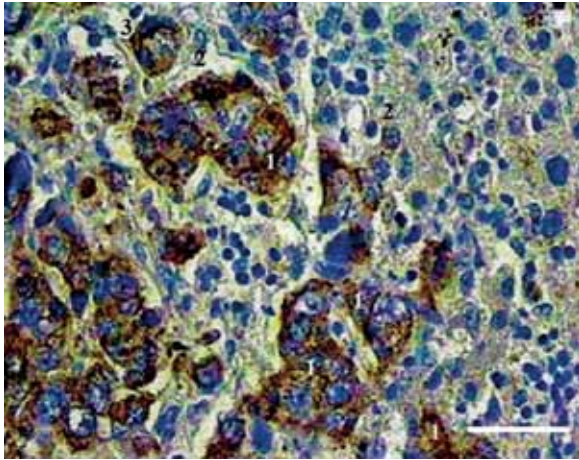


Figure 10. Histological section of the dromedary spleen, immunohistochemical reaction against CD3 T lymphocyte; 1 — lymphocyte; 2 — macrophage; 3 — lymphocyte in reaction. Bar = 20 μm .

values close to the cortical zone, the lymphocytes occupied a zone of $51.92 \pm 1.98\%$ in the inactive follicles, whereas they occupied a zone of $50.77 \pm 1.42\%$ in the active follicles, the reticulocytes occupied an area of $6.23 \pm 1.21\%$ in the inactive follicles, while they occupied an area $4.37 \pm 0.83\%$ in the active ones, plasmocytes occupied $24.12 \pm 1.78\%$ of the inactive follicles, whereas they occupied $25.58 \pm 2.07\%$ in the active follicles, macrophages occupied a zone of $17.01 \pm 1.71\%$ in the inactive follicles, whereas they occupied a zone of $18.68 \pm 2.13\%$ in the active ones. The intralobular connective tissue showed the same organization of values as the cortical and the medullar zone, the lymphocytes occupied an area of $45.52 \pm 1.55\%$, reticulocytes occupied $5.34 \pm 2.73\%$, while plasmocytes and macrophages occupied respectively $22.12 \pm 1.69\%$ and $26.67 \pm 3.18\%$ (Fig. 3).

DISCUSSION

In this study, the spleen of the dromedary was compared with those of other animals. The spleen is an organ of the circulatory and immune systems. It monitors the condition of blood cells and can be used to accumulate blood. In addition, the spleen is involved in lymphopoiesis and can capture and accumulate certain metabolic products. According to researchers [16, 28, 30], the appearance of the spleen of a dog and a cat is similar, it is flat and elongated, with a narrow dorsal end and a wider ventral end. Its parietal surface is smooth, on the visceral surface there are elongated spleen doors, in the hilum area the spleen is relatively loosely connected with a large

omentum. According to Jaji et al. [11], predicts that the spleen is always adjacent to the left abdominal wall, its position largely depends on the fullness of the stomach.

However, the spleen can accumulate up to 16% of all a dog's blood, affecting the displacement of the ventral end to the right half of the abdomen. With an empty stomach, a dog's spleen is completely located in the hypochondrium, while in a cat, in this case, its ventral end is always outside the hypochondrium. With a moderately full stomach and in a dog, the ventral end of the spleen protrudes caudally beyond the edge of the costal arch. When the stomach is full, the spleen is located in the iliac region and sometimes reaches the entrance to the pelvis [4, 7].

Prasad [26] noted that the dorsal end of the spleen is less mobile compared to the ventral one, because in this part of the spleen the gastro-splenic ligament is rather firmly attached to the greater curvature of the stomach. Our results concerning the spleen of the dromedary are almost the same as demonstrated by the researchers; it presents a semi-lunar shape, of firm consistency, of red-brown colour surrounded by a layer of thick connective tissue. It was found that the organ is divided into two compartments: the main body and two extensions at each opposite ends. This organ is located under the left hypochondrium behind the stomach cavities above the dorsal bag of the rumen up to the posterior part of the kidney.

In our research of the mass of the spleen of the dromedary, the maximum value of the absolute mass varied between 318 g and 251 g, with a relative mass between 0.07001% and 0.07470%. The maximum length of the spleen was 49.60 cm, while the minimum length was 43.80 cm; for the width, the maximum value was 25.10 cm, and the minimum value of the width was 19.40 cm.

Regarding the tissue components of the spleen, it was found that the area limited by the stroma is 9.19%, for the first spleen, whose capsule occupies an area of 5.44%, while the trabecula occupies an area of 3.75%, while the area occupied by red pulp was 76.54%, and that occupied by the parenchyma was 13.38%, of which the area occupied by the PALS was 7.54%, and that occupied by inactive follicles was 3.67%, while the area occupied by active follicles was 2.17%, it was also found that the area occupied by the white pulp in total was 13.38%, for the second spleen it was found that the stroma occupied an area of 14.14%, of which the area occupied by the capsule

was 7.57%, and that occupied by the trabecula was 6.57, and the area occupied by the red pulp was 72.87%, and that occupied by the parenchyma was 19.14%, of which the area occupied by the PALS was 5.56%, and that occupied by inactive follicles was 4.37%, while the area occupied by active follicles was 2.42%, and that occupied by total white pulp was by 12.35%. For the third spleen it was found that the area occupied by the stroma was 18.64%, of which the area occupied by the capsule was 8.27%, and that occupied by the trabecula was 10.37%, and the area occupied by the red pulp was 68.27%, and that occupied by the parenchyma was 12.52%, of which the area occupied by the PALS was 3.98%, and that occupied by inactive follicles was 5.28%, while that occupied by active follicles was 3.26%, and the total white pulp occupied an area of 12.52%. For the fourth spleen it was found that the area occupied by the stroma was 23.86%, of which the area occupied by the capsule was 11.57%, and that occupied by the trabecula was 12.29%, and the area occupied by the red pulp was 57.28%, and that occupied by the parenchyma was 18.12%, of which the area occupied by the PALS was 1.18%, and that occupied by inactive follicles was 8.12%, while the area occupied by active follicles was 8.82%, and that occupied by the total white pulp was 18.12%, these data are similar to the results of the researchers [1, 5, 8].

The splenic artery enters the spleen through the hilum, which branches into trabecular arteries, passing into the pulp arteries, which branch into red pulp. An artery passing through a white pulp is called the central. In the red pulp, the central artery branches out in the form of a brush into the cystic arterioles. At the end of cystic arterioles, there is a thickening — an arterial sheath, clearly expressed in pigs [20].

The PALS perform the function of sphincters that block blood flow, as contractile filaments have been found in the endothelium of ellipsoids or arterioles of the PALS. Short arterial capillaries follow, most of which fall into the venous sinuses. Some arterial capillaries open into the reticular tissue of the red pulp (open bloodstream), and then into the venous capillaries. Blood from the venous capillaries is routed to the trabecular veins and then to the splenic vein according to Pabst and Reilmann [23].

According to Papenfuss and Cesta [24], the number of venous sinuses in the spleen of animals of different species is not the same: for example, many of them in rabbits, dogs, guinea pigs, less in cats, cattle

and small cattle. The part of the red pulp between the sinuses is called the splenic strands or pulp. The venous system begins with the venous sinuses. In the areas of sinus transition in the veins, there are similarities between the muscle sphincters, when open, blood flows freely through the sinuses into the veins. On the contrary, the closure (due to the reduction) of the venous sphincter leads to the accumulation of blood in the sinuses. The base of the spleen is the reticular tissue in the form of a sponge filled with parenchyma — white and red pulp as found in our research with silver nitrate impregnation, we have also elucidated almost the same results of other authors [24], also note that the white pulp is constructed from lymphoid tissue collected around the arteries in the form of balls called the spleen lymphatic follicles or spleen body. The number of follicles in different animals is different.

The peri-arterial zone depends on the thymus. It occupies a small area of the follicle near the artery and is formed mainly of T lymphocytes and interdigital cells that adsorb antigens. T cells, which have received information about the state of the microenvironment, migrate to the sinuses of the marginal area through capillaries, as has been described by Vashishtha et al. [32]. The follicle centre reflects the functional state of the follicle and can vary widely with infectious diseases. The reproductive centre is a site independent of the thymus and consists of reticular cells and an accumulation of phagocytes. The mantle zone surrounds the peri-arterial zone, the luminous centre and consists of small, densely localised B lymphocytes and a small number of T lymphocytes, plasma cells and macrophages. The adjacent cells form, so to speak, a crown stratified by circular reticular fibres.

The marginal or marginal zone is a region of transition between the white and red pulps, consisting mainly of T and B lymphocytes and single macrophages, surrounded by marginal or marginal sinusoidal vessels, the results are similar to the author's data [31]. The red pulp of the spleen is 75–78% of the mass of the organ, consists of reticular tissue with cellular blood elements that give the red colour to the parenchyma. The red pulp contains many special arterioles, capillaries, venules and venous sinuses according to the author who found the same results [27].

A variety of cellular elements are deposited in the venous sinus cavity. The sections of red pulp between the sinuses are called pulp cords, which contain many lymphocytes, and the development of plasma cells occurs. In the red pulp there are macrophages — sple-

nocytes, which carry out phagocytosis of destroyed red blood cells. As a result of the breakdown of haemoglobin, bilirubin and iron-containing transferrin are formed and are secreted into the blood. For the histological study of dromedary spleens, the capsule surrounding the organ is very dense thick surrounding the splenic parenchyma, the outermost layer of the splenic capsule was composed of epithelial cells and divided into two layers: outer and inner clearly distinguished, results identical to those of Mollejo et al. [21], Nolte et al. [22], and Eddine Djallal et al. [6].

The outer layer mainly consisted of connective tissue including collagen, rubber bands and fibroblasts and SMC. The inner layer was made up mostly of SMC that appear parallel along the longitudinal cut. Trabeculae extend from the capsule and branch out, so that it divides the area into several parts, are distinguished by the presence of white fibres and smooth muscle fibres. At high magnification, it was observed that the space between the capsule and the parenchyma contained red blood cells, so the surface of the white pulp was large, irregular in shape, the PALS had a clear surface with a branching central artery in several branches, the lymphatic follicles and the marginal zone were very clear. A large marginal area surrounded the white pulp and it was contained in sheathed arteries and SMC. Also, it was observed that the marginal sinus of the marginal zone infiltrates in the marginal zone in the direction of the red pulp supplying the blood directly in the adjacent venous sinuses whose ends which appear open with the marginal zone and penetrate into the reticular mesh of the red pulp and bypass the reticular mesh of the red pulp. It was found that blood from the red pulp collects in the venous sinuses which enter the trabeculae and merge into the trabecular veins, the trabecular veins then converge at the hilum to form the splenic vein which drains to the exterior of the organ, as has been demonstrated by Rahmoun et al. [29].

Regarding the red pulp, it was found to be composed of a mesh of splenic cords and venous sinuses. At high magnification, the splenic cords are composed of reticular fibres, reticular cells and macrophages. Again, under the microscope it was found that the venous sinuses can occupy the entire surface of the red pulp including, they are lined with epithelial tissue and rest on a basement membrane, the periciliary arteries and arteriolar capillaries are also located in red pulp, data similar to research by Gnanadevi et al. [9], Ikegbe et al. [10] and Jaji et al. [11].

CONCLUSIONS

Anatomical and topographical study of the spleen in the dromedary from southern Algeria has revealed that it has dens identical to those of ruminants. Histologically, the structure of the spleen of the dromedary has a similar analogy to those of other mammals, the stroma consists of a capsule that envelops the entire organ with trabecular infiltration throughout the parenchyma of the organ, which separates it in a well-defined lobule of red and white pulp. The white pulp of the spleen shows the PALS and lymphoid follicles, the marginal area separates the red pulp from the white could also be clearly demarcated. In the first group, secondary lymphoid follicles occur in new places along the blood vessels. The tissue components of the dromedary spleen are characterized by primary lymphoid follicles, against the background of significant changes corresponding to the quantitative parameters of immunogenesis, primary lymphoid follicles, accompanied respectively by an increase in the relative area of the stroma and the relationship between stromal and parenchymal components of the organ.

Acknowledgements

The authors wish to thank the team of the histology laboratory of the faculty of veterinary sciences of Taoura, University of Souk-ahras Algeria, for their support and help throughout the research period.

Conflict of interest: None declared

REFERENCES

1. Almenar S, Rios-Navarro C, Ortega M, et al. Anatomy, immunohistochemistry, and numerical distribution of human splenic microvessels. *Ann Anat.* 2019; 224: 161–171, doi: [10.1016/j.aanat.2019.05.004](https://doi.org/10.1016/j.aanat.2019.05.004), indexed in Pubmed: [31121286](https://pubmed.ncbi.nlm.nih.gov/31121286/).
2. Bar-Ephraïm YE, Mebius RE. Innate lymphoid cells in secondary lymphoid organs. *Immunol Rev.* 2016; 271(1): 185–199, doi: [10.1111/imr.12407](https://doi.org/10.1111/imr.12407), indexed in Pubmed: [27088915](https://pubmed.ncbi.nlm.nih.gov/27088915/).
3. Dijkstra CD, Veerman A. Normal anatomy, histology, ultrastructure, rat. *Hemopoietic System.* 1990: 185–193, doi: [10.1007/978-3-642-84110-1_28](https://doi.org/10.1007/978-3-642-84110-1_28).
4. Dos Santos BS, Gomes C, Camargo J, et al. Primary splenic torsion associated with accessory spleen in a dog. *Acta Scientiae Vet.* 2019; 47, doi: [10.22456/1679-9216.97394](https://doi.org/10.22456/1679-9216.97394).
5. Dubey A, Agnihotri D, Jethani SL, et al. Estimation of gestational age using fetal liver morphometry. *Nat J Clin Anat.* 2018; 7(3): 134, doi: [10.4103/2277-4025.294763](https://doi.org/10.4103/2277-4025.294763).
6. Eddine Djallal R, Amine Mohamed F, Manel H, et al. Morpho-histological study of spleen ontogenesis in lambs during antenatal and posnatal period. *J World's Poultry Res.* 2020; 10(1): 12–16, doi: [10.36380/scil.2020.ojafR2](https://doi.org/10.36380/scil.2020.ojafR2).

7. Ernst L. Spleen. Color Atlas of Human Fetal and Neonatal Histology. 2019; 261–268, doi: [10.1007/978-3-030-11425-1_25](https://doi.org/10.1007/978-3-030-11425-1_25).
8. Gavrilin PN, Gavrilina EG, Evert VV. Histoarchitectonics of the parenchyma of lymph nodes of mammals with different structure of intranodal lymphatic channel. Ukrainian J Ecol. 2017; 7(3): 96–107, doi: [10.15421/2017_54](https://doi.org/10.15421/2017_54).
9. Gnanadevi R, Senthilkumar S, Kannan TA, et al. Comparative histoarchitectural study of splenic components in sheep and goat. Int J Curr Microbiol App Sci. 2019; 8(05): 1387–1394, doi: [10.20546/ijcmas.2019.805.158](https://doi.org/10.20546/ijcmas.2019.805.158).
10. Ikpegbu I, Ibe CS, Nlebedum UC, et al. The spleen morphology of the african giant pouch rat (*Cricetomys gambianus*-Waterhouse, 1840) from Eastern Nigeria. J Animal Husbandry Dairy Sci. 2019; 3(1): 20–25, doi: [10.30954/2277-940x.01.2019.2](https://doi.org/10.30954/2277-940x.01.2019.2).
11. Jaji A, Saidu A, Mahre M, et al. Morphology, morphometry and histogenesis of the prenatal dromedary (*camelus dromedarius*) spleen. Macedonian Vet Rev. 2019; 42(2): 141–149, doi: [10.2478/macvetrev-2019-0018](https://doi.org/10.2478/macvetrev-2019-0018).
12. Johnson CD. Spleen. Mayo Clinic Gastrointestinal Imaging Review. 2014; 753–792, doi: [10.1093/med/9780199862153.003.0009](https://doi.org/10.1093/med/9780199862153.003.0009).
13. Kage M, Kondou R, Ogata T. Anatomy of the spleen and pathology of hypersplenism. Clin Invest Portal Hyper. 2019; 25–34, doi: [10.1007/978-981-10-7425-7_3](https://doi.org/10.1007/978-981-10-7425-7_3).
14. Kannan TA, Ramesh G, Ushakumary S, et al. Thymic Hassall's corpuscles in Nandanam chicken — light and electronmicroscopic perspective (*Gallus domesticus*). J Anim Sci Technol. 2015; 57(1): 30, doi: [10.1186/s40781-015-0064-2](https://doi.org/10.1186/s40781-015-0064-2), indexed in Pubmed: 26430516.
15. Kuper H, Marmot M, Hemingway H. Systematic review of prospective cohort studies of psychosocial factors in the etiology and prognosis of coronary heart disease. Semin Vasc Med. 2002; 2(3): 267–314, doi: [10.1055/s-2002-35401](https://doi.org/10.1055/s-2002-35401), indexed in Pubmed: 16222620.
16. Mahadevan V. Anatomy of the pancreas and spleen. Surgery (Oxford). 2016; 34(6): 261–265, doi: [10.1016/j.mpsur.2016.03.014](https://doi.org/10.1016/j.mpsur.2016.03.014).
17. Masternak MM, Bartke A. Growth hormone, inflammation and aging. Pathobiol Aging Age Relat Dis. 2012; 2, doi: [10.3402/pba.v2i0.17293](https://doi.org/10.3402/pba.v2i0.17293), indexed in Pubmed: 22953033.
18. Matsuno K, Ezaki T, Kotani M. Splenic outer periarterial lymphoid sheath (PALS): an immunoproliferative microenvironment constituted by antigen-laden marginal metallophilic and ED2-positive macrophages in the rat. Cell Tissue Res. 1989; 257(3): 459–470, doi: [10.1007/BF00221456](https://doi.org/10.1007/BF00221456), indexed in Pubmed: 2790931.
19. McGaha TL, Karlsson MC. Apoptotic cell responses in the splenic marginal zone: a paradigm for immunologic reactions to apoptotic antigens with implications for autoimmunity. Immunol Rev. 2016; 269(1): 26–43, doi: [10.1111/imr.12382](https://doi.org/10.1111/imr.12382), indexed in Pubmed: 26683143.
20. Middleton DJ, Westbury HA, Morrissy CJ, et al. Experimental Nipah virus infection in pigs and cats. J Comp Pathol. 2002; 126(2-3): 124–136, doi: [10.1053/jcpa.2001.0532](https://doi.org/10.1053/jcpa.2001.0532), indexed in Pubmed: 11945001.
21. Mollejo M, Algara P, Mateo MS, et al. Splenic small B cell lymphoma with predominant red pulp involvement: a diffuse variant of splenic marginal zone lymphoma. Histopathology. 2002; 40(1): 22–30, doi: [10.1046/j.1365-2559.2002.01314.x](https://doi.org/10.1046/j.1365-2559.2002.01314.x).
22. Nolte MA, Hamann A, Kraal G, et al. The strict regulation of lymphocyte migration to splenic white pulp does not involve common homing receptors. Immunology. 2002; 106(3): 299–307, doi: [10.1046/j.1365-2567.2002.01443.x](https://doi.org/10.1046/j.1365-2567.2002.01443.x), indexed in Pubmed: 12100717.
23. Pabst R, Reilmann H. Regeneration of heterotopically transplanted autologous splenic tissue. Cell Tissue Res. 1980; 209(1): 137–143, doi: [10.1007/BF00219930](https://doi.org/10.1007/BF00219930), indexed in Pubmed: 7428023.
24. Papenfuss T, Cesta M. Spleen. Mol Integ Toxicol. 2017; 37–57, doi: [10.1007/978-3-319-47385-7_2](https://doi.org/10.1007/978-3-319-47385-7_2).
25. Paraskevas GK, Koutsouflianiotis KN, Nitsa Z, et al. Knowledge of the anatomy and physiology of the spleen throughout Antiquity and the Early Middle Ages. Anat Sci Int. 2016; 91(1): 43–55, doi: [10.1007/s12565-015-0305-y](https://doi.org/10.1007/s12565-015-0305-y), indexed in Pubmed: 26507317.
26. Prasad A. Ultrasonographic evaluation of fetal gestational age in different trimesters from various anatomical biometric parameters. Indian J Anat. 2018; 7(6): 590–594, doi: [10.21088/ija.2320.0022.7618.3](https://doi.org/10.21088/ija.2320.0022.7618.3).
27. Quesada J, Viilena MI, Agulleiro B. Structure of the spleen of the sea bass (*Dicentrarchus labrax*): A light and electron microscopic study. J Morphol. 1990; 206(3): 273–281, doi: [10.1002/jmor.1052060304](https://doi.org/10.1002/jmor.1052060304), indexed in Pubmed: 29865770.
28. Rahman N, Tandon R, Ghaus F, et al. Comparative anatomy of spleen: histomorphometric study in human, goat, buffalo, rabbit and rat. Acad Anat Int. 2016; 2(1), doi: [10.21276/aaanat.2016.2.1.6](https://doi.org/10.21276/aaanat.2016.2.1.6).
29. Rahmoun DE, Lieshchova MA, Fares MA. Morphological and radiological study of lymph nodes in dromedaries in Algeria. Reg Mech Bios. 2020; 11(2): 330–337, doi: [10.15421/022050](https://doi.org/10.15421/022050).
30. Shringi N. Morphometry of spleen in white Yorkshire pig (*Sus scrofa*). Int J Pure Applied Biosci. 2017; 5(4): 755–757, doi: [10.18782/2320-7051.5555](https://doi.org/10.18782/2320-7051.5555).
31. Silva-O'Hare J, de Oliveira IS, Klevorn T, et al. Disruption of splenic lymphoid tissue and plasmacytosis in canine visceral leishmaniasis: changes in homing and survival of plasma cells. PLoS One. 2016; 11(5): e0156733, doi: [10.1371/journal.pone.0156733](https://doi.org/10.1371/journal.pone.0156733), indexed in Pubmed: 27243459.
32. Vashishtha K, Gaur V, Kapoor K, et al. Morphometric study of human foetal spleen: a study from North-India. Int J Anat Res. 2018; 6(4.3): 5983–5988, doi: [10.16965/ijar.2018.390](https://doi.org/10.16965/ijar.2018.390).
33. Xu M, Li W, Yang S, et al. Morphological characterization of postembryonic development of blood-spleen barrier in duck. Poult Sci. 2020; 99(8): 3823–3830, doi: [10.1016/j.psj.2020.05.012](https://doi.org/10.1016/j.psj.2020.05.012), indexed in Pubmed: 32731968.

Anoctamin 1 and c-Kit immunohistochemical study of interstitial cells of Cajal in the muscularis externa of human gastrointestinal tract

A. Al-Ahmadi¹, R.A. Mohammed², M. Atteya², T.A. Al-Matrafi², M.A. Alfayez²

¹Department of Chemistry, College of Science, King Abdulaziz University, Jeddah, Saudi Arabia

²Department of Anatomy, College of Medicine, King Saud University, Riyadh, Saudi Arabia

[Received: 24 November 2021; Accepted: 20 December 2021; Early publication date: 31 December 2021]

Background: Interstitial cells of Cajal (ICC) are widely distributed in human gastrointestinal (GI) tract, especially in the layer of muscularis externa between neurons and smooth muscles. They play a very important role of coordination of GI tract motility. The aims of this research were to study the morphology and distribution of ICC in the muscularis externa of the GI tract, using immunohistochemistry staining methods, to determine the distribution of immune reactivity of anoctamin 1 (Ano1) compared with c-Kit, and to determine if Ano1 is a reliable marker for ICC in human GI tract.

Materials and methods: Specimens from the wall of stomach, small intestine, and colon were taken from human cadavers and processed for histological and immunohistochemical study using c-Kit and Ano1 primary antibodies.

Results: Interstitial cells of Cajal appeared as bipolar cells, not forming network, in both the circular and longitudinal muscle layers, while in the myenteric area they appeared as multipolar interconnected cells. They were unevenly distributed in and between the muscle layers of the muscularis externa of human GI tract. They were more numerous in the stomach followed by the colon then the small intestine, and more numerous in the myenteric area followed by the circular muscle layer then the longitudinal muscle layer, in the three organs. Our results also showed that Ano1 is a more reliable marker for human ICC than c-Kit.

Conclusions: Interstitial cells of Cajal differed in morphology and were unevenly distributed between muscle layers of muscularis externa and between different parts of human GI tract. (Folia Morphol 2023; 82, 1: 147–157)

Key words: interstitial cells of Cajal, c-Kit, anoctamin 1, stomach, small intestine, colon

INTRODUCTION

Gastrointestinal (GI) tract motility is essential for life and is a highly regulated and coordinated process. Research in motility of GI tract began with the

discovery of spontaneous gastric [3] and colonic [7] contractions. Even after blocking neural activity, Bayliss and Starling [2] discovered that smooth muscle contractions initiating effectual peristalsis still hap-

Address for correspondence: Dr. M. Atteya, Department of Anatomy, College of Medicine, King Saud University, PO Box 2925 (28), Riyadh 11461, Saudi Arabia, tel: +966(11)4699330, mobile: +966502765609, fax: +966(11)4671300, e-mail: mhasan1@ksu.edu.sa

This article is available in open access under Creative Common Attribution-Non-Commercial-No Derivatives 4.0 International (CC BY-NC-ND 4.0) license, allowing to download articles and share them with others as long as they credit the authors and the publisher, but without permission to change them in any way or use them commercially.

pened, indicating the presence of an internal pacemaker in the gut.

Cajal [5] suggested that interstitial cells of Cajal (ICC) play a key role in motility of GI tract by modulating enteric transmission, and later on Keith [28] proposed ICC as pacemakers. According to Yin and Chen [66], ICC provide various important functions in the GI tract involving initiation of slow wave electrical activity, synchronisation of pacemaker activity and effective spread of slow waves, transduction of motor nerve impulses from the GI nervous system, and working as mechanoreceptors to GI muscle stretch [41].

In 1982, Thuneberg [56] surprised GI tract researchers by postulating that ICC in the GI muscles are analogous to the pacemaker cells in the heart, having the potential to function as pacemaker cells and as an impulse conduction system.

Since then, with the accumulation of evidence from morphologic and physiologic studies, this postulate is compatible with experimental observations, and that ICC have the function of either a pacemaker or neuromediator cell in the muscularis of the GI tract [23, 30, 49, 57, 65]. It was revealed to be a distinct mesenchymal cell type [34, 67]. The demonstration of synapse-related proteins in synaptic specializations between ICC and nerves by immunohistochemistry [4] further established the role of ICC as neuromediator cells.

Cajal [6] was the first to recognise ICC as nerve-like cells near ends of more peripheral nerve fibres and classified them as primitive neurons based on their stainability with silver chromate and methylene blue.

Using light and electron microscopy, Taxi [54, 55] named these cells neuronoids to distinguish them from neurons and other cells that were also stained with nerves, such as Schwann cells, fibroblasts, macrophages, and smooth muscle cells. Later on, electron microscopic studies proposed similarity of ICC to either muscle cells [12, 26] or fibroblasts [29, 46]. Langton et al. [33] were the first to report electrical rhythmicity of these cells.

Morphological criteria continued to be the basis of ICC characterisation till Maeda et al. [37] discovered the expression of the tyrosine kinase receptor, c-Kit (CD117), by ICC. This discovery was the landmark in ICC research that has driven it to great progress. To a considerable extent, some ICC do not express c-Kit, such as ICC in the deep muscular plexus in the small intestine of human [59]. Moreover, in addition to ICC,

many other cell types express c-Kit, such as neurons, neuroglia, melanocytes, and mast cells [68].

Recently, a calcium activated chloride channel, anoctamin 1 (Ano1), was identified as a selective marker for all subtypes of ICC in the human and mouse GI tract that allows the immunohistochemical identification of these cells instead of c-Kit [15].

Based on ICC anatomical locations, many morphologic types of ICC were defined [18]. Most of GI ICC occur around the myenteric plexus and are called ICC of the myenteric plexus (ICC-MY or ICC-MP). ICC of the circular muscle (ICC-CM) are those found in the circular muscle. ICC of the longitudinal muscle (ICC-LM) are those in the longitudinal muscle. ICC-CM and ICC-LM are collectively known as intramuscular ICC (ICC-IM). ICC of the deep muscular plexus (ICC-DMP) are those located in the deep muscular plexus [32].

The body and antrum of the stomach are more densely populated by ICC than the fundus, as the antrum has both ICC-MY and ICC-IM, while the fundus has only ICC-IM [21, 38]. In the antrum, ICC-MY are more densely distributed in the greater curvature than in the lesser curvature [21, 38]. Many c-Kit-positive ICC-IM were detected in the circular and longitudinal muscle layers and around the myenteric plexus in the pylorus [61].

According to ICC location in different regions and layers of GI tract, they show specific arrangement, distribution, and cell shape. In the stomach there are regional variations in ICC distribution from cardia to pylorus, while their distribution throughout both the small intestine and colon shows a consistent pattern [32].

Interstitial cells of Cajal show a specific distribution, arrangement and cell shape depending on their location within various regions and tissue layers of the GI tract. Hence, they are classified into several subtypes. The stomach shows distinct regional variations in the distribution of subtypes of ICC from the cardia to pylorus, whereas the small intestine and colon both seem to retain nearly the same distribution pattern of subtypes of ICC throughout each organ.

Most studies on ICC used the animal model and only few studies were done on human samples, and even those were limited to one or two organs of the GI tract, due to difficulty of obtaining samples from different organs of gut of the same person during performing surgeries. Because of the difficulty of collecting amounts of human GI tract tissue enough for research have restricted the understanding of the



Figure 1. Haematoxylin and eosin-stained sections in muscularis externa of stomach, small intestine, and colon, showing inner circular, outer longitudinal, and myenteric plexuses (asterisks) between the circular and longitudinal layers. There is no apparent interstitial cells of Cajal (scale bars 50 μm).

nature of GI tract motility and human ICC in normal or diseased GI tract functions. Therefore, our study was conducted on samples from the three main different GI tract regions (stomach, small intestine, and large intestine) that were obtained from human cadavers.

The study focused on the morphology and distribution of ICC in the muscularis externa that includes the inner circular, outer longitudinal muscle layers and myenteric plexus between them, using immunohistochemistry staining methods. The study also aimed to determine the distribution of immune reactivity of Ano1 compared with c-Kit, and to determine if Ano1 is a reliable marker for ICC in human GI tract.

MATERIALS AND METHODS

Human samples

Samples were obtained from 10 male human cadavers (aged 40–60 years), which were available in the Department of Anatomy, College of Medicine, King Saud University. From each cadaver small specimens about, 1 cm \times 0.5 cm, were excised from the greater curvature of the stomach corpus, first part of duodenum, and proximal colon.

Histological and immunohistochemical study

Full thickness specimens of the wall of stomach, duodenum, and colon were fixed in enough amounts (5–10 times of tissue volume) of 4% paraformaldehyde for 24 hours at room temperature. Fixed tissues were processed for preparation of paraffin blocks. The blocks were cut at 5 μm thickness and sections were mounted onto glass slides to be ready for staining.

Haematoxylin and eosin (H&E) staining. On ordinary glass slides some sections were de-paraffinised to be stained with H&E solutions then mounted with DPX mounting medium.

Immunostaining using anti-c-Kit (CD117) and anti-Ano1 antibodies. Sections from the stomach, small intestine, and colon were immunostained with anti-c-Kit (ab5505) rabbit polyclonal primary antibody (dilution of 1:1000) and anti-Ano1 (ab53212) rabbit polyclonal primary antibody (dilution of 1:1000), according to the manufacturer's data sheets.

Quantification of immune-positive cells. The numbers of c-Kit- and Ano1-positive cells in the circular, myenteric, and longitudinal layers of muscularis externa of stomach, small intestine, and colon were counted at $\times 200$ magnification. Cells in 30 fields from three nonadjacent sections were counted (10 fields per section) [15].

Statistical analysis

All data were expressed as mean \pm standard error of the mean (SEM). Statistical analysis was performed using IBM SPSS Statistics 22 statistical software. One-way analysis of variance (ANOVA) was used for an overall comparison between the study organs and layers of muscularis externa, followed by Bonferroni test for pairwise comparisons. Differences were considered significant when p was equal to or less than 0.05.

RESULTS

Haematoxylin and eosin (Fig. 1)

Histological examination of H&E-stained sections of human stomach, small intestine, and colon showed normal layers of the muscularis externa; circular layer, myenteric layer (neuronal plexuses area), between circular and longitudinal layers, and outer longitudinal layer. ICC were not clearly identified by H&E staining in the three organs (Fig. 1).

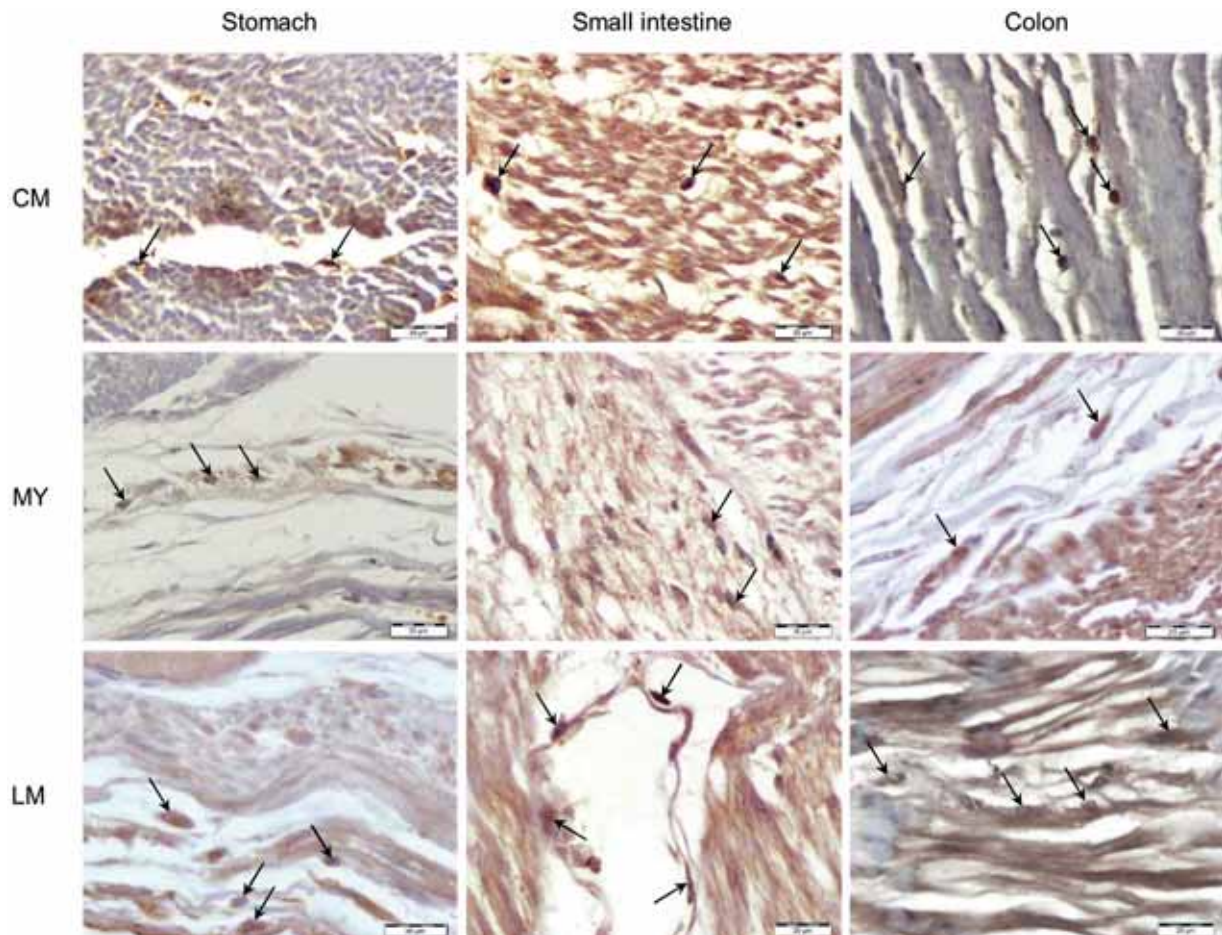


Figure 2. c-Kit immunostaining of muscularis externa of stomach, small intestine, and colon. Most of c-Kit-positive cells (arrows) of the circular (CM) and longitudinal (LM) muscle layers were spindle shaped, while those of the myenteric (MY) area were oval and multipolar cells (scale bars 20 μ m).

Anti-c-Kit immunohistochemistry (Fig. 2, Table 1)

c-Kit immunostaining gave a dark brown coloration of cytoplasm of many types of cells, such as ICC, fibroblasts, and mast cells. Identification of ICC by c-Kit was mainly by their thin processes, but it was difficult to count ICC accurately. Counting c-Kit-positive cells (Table 1) gave higher numbers than counting Ano1-positive cells (Tables 2, 3). ICC of muscularis externa were classified according to their distribution into ICC of the inner circular muscle layer (ICC-CM), ICC of the myenteric plexuses layer (ICC-MY), and ICC of the outer longitudinal muscles layer (ICC-LM).

c-Kit immunostaining of circular layer (ICC-CM). In the stomach, c-Kit-positive ICC appeared spindle shaped with few long processes. They were parallel to the longitudinal axis of the smooth muscle cells surrounding them. They did not form a network. In the small intestine, c-Kit-positive ICC were spindle shaped similar to those of the stomach, but they had special contacts with both neurons and smooth

muscle cells. In the colon, most c-Kit-positive ICC were small, spindle shaped cells with few processes. They ran parallel to the smooth muscle cells.

c-Kit immunostaining of myenteric plexus region (ICC-MY). In the stomach, c-Kit-positive ICC appeared multipolar or stellate shaped. They were connected together by branching processes forming a network around myenteric plexuses. In the small intestine, c-Kit-positive ICC were also multipolar or stellate shaped and formed bundles of up to five cells with overlapping processes. They extended to the circular and longitudinal layers. In the colon, c-Kit-positive ICC were many. They were multipolar with their processes connecting with each other and forming a network around myenteric plexuses.

c-Kit immunostaining of longitudinal muscle layer (ICC-LM). In the stomach, c-Kit-positive ICC were spindle shaped cells scattered in-between the smooth longitudinal muscle cells. In the small intestine, c-Kit-positive ICC appeared as bipolar flat spindle

Table 1. Average counts (mean \pm standard error) of c-Kit-positive cells in the layers of muscularis externa: comparing respective layers between stomach, small intestine, and colon

	Stomach	Small intestine	Colon
CM	47.4 \pm 2.04	36.2 \pm 1.7	39.2 \pm 0.86
P1		0.001*	0.011*
P2	0.001*		0.642
MY	119.2 \pm 5.23	55.0 \pm 1.64	70.4 \pm 1.75
P1		0.000*	0.000*
P2	0.000*		0.02*
LM	45.0 \pm 1.82	34.2 \pm 1.39	38.2 \pm 1.28
P1		0.001*	0.024*
P2	0.001*		0.259

*Significant difference ($p \leq 0.05$); P1 — versus stomach; P2 — versus small intestine; CM — circular muscle layer; MY — myenteric layer; LM — longitudinal muscle layer

Table 2. Average counts (mean \pm standard error) of anoctamin 1-positive interstitial cells of Cajal in the layers of muscularis externa: comparing respective layers between stomach, small intestine, and colon

	Stomach	Small intestine	Colon
CM	41.6 \pm 1.78	31.2 \pm 1.24	37.4 \pm 1.47
P1		0.001*	0.219
P2	0.001*		0.06
MY	104.8 \pm 1.85	45.2 \pm 1.16	59.8 \pm 1.66
P1		0.000*	0.000*
P2	0.000*		0.000*
LM	39.8 \pm 2.46	29.4 \pm 0.87	33.4 \pm 1.63
P1		0.004*	0.077
P2	0.004*		0.412

*Significant difference ($p \leq 0.05$); P1 — versus stomach; P2 — versus small intestine; CM — circular muscle layer; MY — myenteric layer; LM — longitudinal muscle layer

Table 3. Average counts (mean \pm standard error) of anoctamin 1-positive interstitial cells of Cajal in the layers of muscularis externa: comparing layers within each of stomach, small intestine, and colon

	CM	MY	LM
Stomach	41.6 \pm 1.78	104.8 \pm 1.85	40.2 \pm 2.33
P1		0.000*	1.00
P2	0.000*		0.000*
Small intestine	31.2 \pm 1.24	45.2 \pm 1.16	29.4 \pm 0.87
P1		0.000*	0.811
P2	0.000*		0.000*
Colon	37.4 \pm 1.47	59.8 \pm 1.66	33.4 \pm 1.63
P1		0.000*	0.300
P2	0.000*		0.000*

*Significant difference ($p \leq 0.05$); P1 — versus CM; P2 — versus MY; CM — circular muscle layer; MY — myenteric layer; LM — longitudinal muscle layer

cells with a large body and few processes within the fibres of longitudinal smooth muscle layer. In the colon, c-Kit-positive ICC were spindle shaped with few processes.

Anti-Ano1 immunohistochemistry (Fig. 3, Table 2)

Ano1-positive cells were mainly ICC because Ano1 specifically stains their cytoplasm dark brown.

Ano1 immunostaining of ICC in the circular muscle layer (ICC-CM). In the stomach, there were many Ano1-positive ICC between smooth muscle fibres of the circular muscle layer. Most of them were arranged in interconnected groups while others are separately scattered. They had very fine few processes that extended to the surrounding smooth muscle fibres. They were spindle shaped with small rounded or oval nuclei. ICC-CM were significantly more numerous than those of the small intestine and insignificantly more numerous than those of the colon. In the small intestine, Ano1-positive ICC in the circular layer were larger in size and stellate in shape. They had few short processes connected with surrounding muscle fibres. They were significantly fewer than those of the stomach and insignificantly fewer than those of the colon. In the colon, most Ano1-positive ICC were small and spindle shaped. They had few thin processes connecting them with neighbouring muscle fibres and ICCs. They were more numerous than those of the small intestine but less numerous than those of the stomach, with insignificant differences (Fig. 3, Table 2).

Ano1 immunostaining of ICC in the myenteric plexus region (ICC-MY). In the stomach, there were many Ano1-positive ICC in the myenteric plexuses and the connective tissue surrounding them. They were stellate shaped cells with oval nuclei. Some of them formed chain-like structures around plexuses while others were present inside and outside the plexuses. Their number was significantly more numerous than those of the small intestine and colon. In the small intestine, most of Ano1-positive ICC were inside the plexuses. They were small and stellate shape and connected by their processes. They were significantly less numerous than those of the stomach and colon. In the colon, Ano1-positive ICC were mostly small and stellate shaped with oval or rounded nuclei. They had thin processes connecting them, forming chain-like structures around neurons of the plexuses. They were significantly more numerous than those of the small intestine and significantly less numerous than those of the stomach (Fig. 3, Table 2).

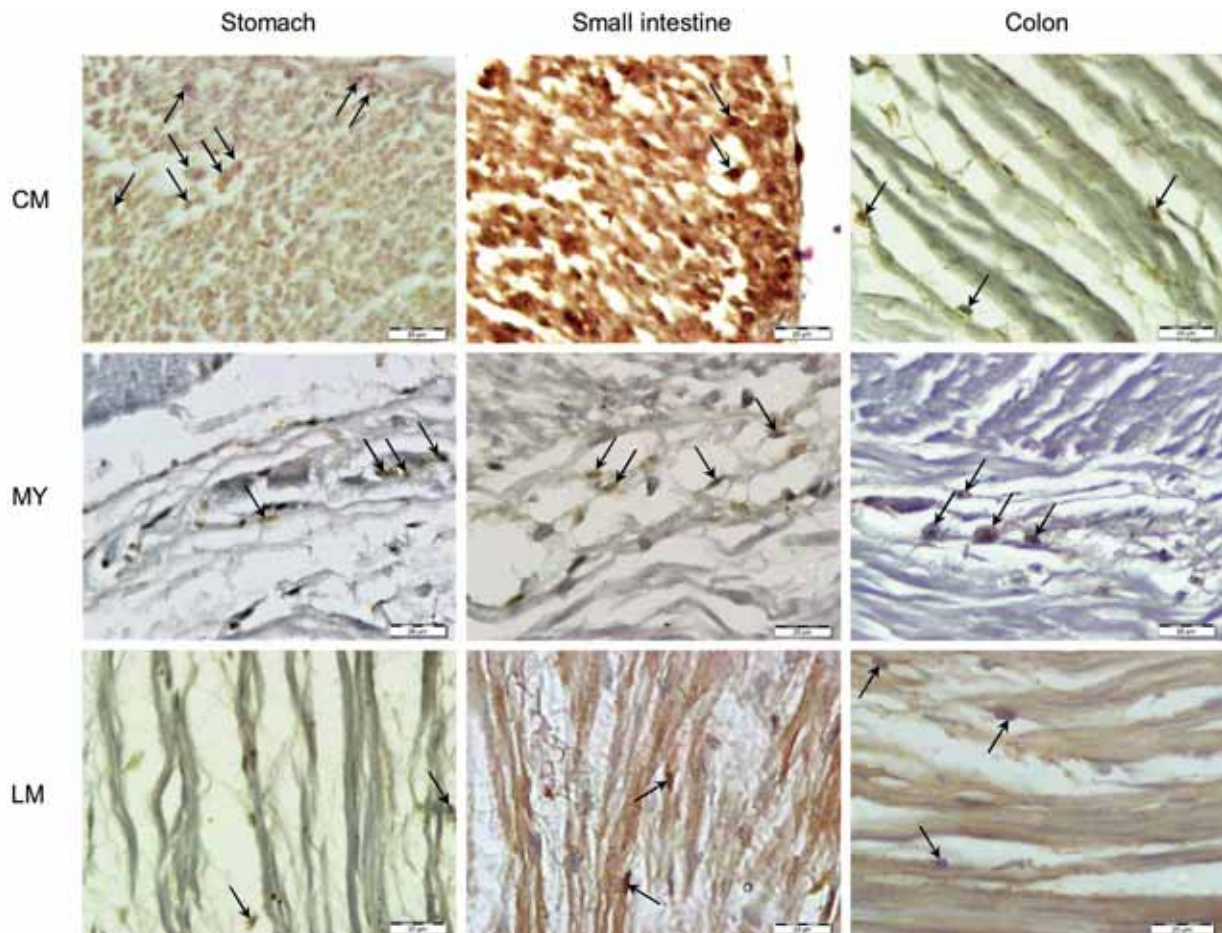


Figure 3. Anoctamin 1 immunostaining of muscularis externa of stomach, small intestine, and colon. Anoctamin 1-positive interstitial cells of Cajal (arrows) of the circular (CM) and longitudinal (LM) muscle layers were spindle shaped, while those of the myenteric (MY) area were stellate multipolar cells (scale bars 20 μm).

Ano1 immunostaining of ICCs in the longitudinal muscle layer (ICC-LM). In the stomach, Ano1-positive ICC between longitudinal smooth muscle fibres were spindle shaped cells with small oval nuclei. They had many long processes that formed a network with the muscle fibres. They were significantly more numerous than those of the small intestine but insignificantly more numerous than those of the colon. In the small intestine, Ano1-positive ICC were scattered between smooth muscle cells of longitudinal muscle layer. They were small and spindle shaped with small flat nuclei. They were significantly fewer than those of the stomach and insignificantly fewer than those of the colon. In the colon, Ano1-positive ICC were spindle shaped cells with oval nuclei. They were scattered between smooth muscle fibres and connected to them by their processes. They were more numerous than those of the small intestine but less numerous than those of the stomach, with insignificant differences (Fig. 3, Table 2).

Ano1-positive ICC distribution in the three layers of muscularis externa of each organ. In each of the three organs, ICC were significantly more numerous in the myenteric area than in either the circular or the longitudinal muscle layers ($p < 0.05$), while the differences in ICC numbers between the circular and the longitudinal muscle layers were statistically insignificant ($p > 0.05$) (Table 3).

DISCUSSION

In the present study, we investigated the distribution and the number of c-Kit and Ano1 immunoreactive cells in the muscularis externa of human stomach, small intestine, and colon. The specimens were examined by using anti-c-kit immunohistochemistry, known to reliably identify the location of ICC and provide information on their distribution and density [43]. However, besides being a marker for ICC, c-Kit have been shown to be expressed also in variety of normal tissues such as brain, placenta and lung [48]

as well as malignant tumours and gastric carcinoma cell line [19, 20]. Additionally, c-Kit has also been shown to be activated by mutations such as in some human cancers such as human gastric carcinomas [14, 19], gastrointestinal stromal tumour (GIST) [31], small cell lung cancer [20], and colorectal cancer [44]. Therefore, ICC seem to have many capabilities, and they might be related to growth of tumours.

Another marker, Anol, considered more reliable than the c-Kit for ICC identification [36], was recently found. It is a Ca^{2+} -activated chloride channel necessary for generation of slow wave and lacking any effect on differentiation of ICC [24]. Anol is thought to be expressed specifically on ICC. Different from c-Kit, Anol plays an important role in pacemaker activity of ICC. For evaluating the ICC network, Anol is better than c-Kit because it is more specific and functionally more important. The abnormal distribution of Anol-positive ICC in the aganglionic colon of Hirschsprung's disease contributes to the persistent bowel symptoms after some pull-through surgeries [3, 10].

In the current study we used samples from human cadavers, because access to enough fresh GI tissue from normal human for research has been a major challenge. Such tissue is frequently restricted to small amounts gained from biopsies. In some situations, larger amounts of human GI tissue can be obtained from sleeve gastrectomy or GI cancer surgeries. Some histological studies have identified c-Kit- and Anol-positive ICC in gastric tissue obtained from sleeve gastrectomy [15, 16, 53] and gastric cancer surgeries [40, 45]. Similar studies have also been done on small intestinal tissue from gastric bypass surgeries [8, 15, 24, 35, 52] and colon tissue from colon cancer surgeries [9, 15, 16, 27]. Although ICC in these GI tissues appeared morphologically normal, still the sources of these tissues were from unhealthy donors (e.g., obesity or cancer patients).

By the end of the last century, ICC were suggested to be regulators of GI motility in animals [13, 17, 59], and the distribution was found to be uneven in the stomach, small intestine and colon, with regional differences. For example, in murine stomach, ICC-MY density was greater at the antrum and corpus than at the fundus while ICC-IM were denser at the fundus and corpus than at the antrum [51]. In addition, ICC-IM density was lower at the lesser curvature than the greater curvature [21, 51]. Therefore, in our study, we preferred to use samples from the greater curvature

of the stomach corpus. According to Vanderwinden et al. [60] who found more concentration of ICC in the muscularis externa of the first part of duodenum, our samples of small intestine were taken from the duodenum. As for the large intestine, our samples were taken from the proximal colon in accordance with Hwang et al. [24] who found much higher density of colonic ICC at the proximal part, where strong haustral contractions begin.

The morphological features of GI tract ICC previously described in the literature were mostly based on observations in laboratory animals using immunohistochemical staining for c-Kit and electron microscopy. In the current research we aimed to study ICC in human muscularis externa using two types of primary antibodies; c-Kit (the most common ICC kit, but non-specific) and Anol (less commonly used but more specific) as the specimens from cadavers were unsuitable for electron microscopic analysis.

Almost all ICC subtypes have similar ultrastructural features, such as numerous mitochondria, intermediate filaments, and gap junctions with each other and with smooth muscle cells. Additionally, according to animal species and anatomical location, some ICC subtypes have features like smooth muscle cells such as an external lamina, dense bodies, caveolae, and subsurface cisterns.

Depending on ICC localisation in the muscularis externa, they have been grouped into submuscular, intramuscular, myenteric, and subserosal. According to their morphology, they were described as either stellate or bipolar. They were also classified based on their function into pacemakers, neuromediators, and mechanoreceptors. Moreover, some authors reported some accordance between morphology, localisation, and function of the various ICC subtypes [50, 66].

In this study, ICC-CM were mainly bipolar cells oriented parallel to the longitudinal axis of the surrounding smooth muscle cells. These cells did not form their own network. However, the distribution and density of ICC-CM differed from one organ to the other. For example, in the small intestine they frequently showed secondary cytoplasmic processes and were scantily distributed in relation to relatively thicker nerve bundles. They did not form their own cellular network. In comparison, ICC-CM of the stomach and colon were elongated and spindle-shaped but were heavily distributed in relation to nerve bundles. Similar finding were reported by Komuro [32].

ICC-MY were multipolar cells that had three to five primary cytoplasmic branches that further gave secondary and tertiary processes that interconnected with their equivalents. These branches formed a network surrounding the myenteric plexus. Similar description was depicted by Komuro [32]. These ICC-MY were found to be closely related to myenteric nerves and have receptors for many neurotransmitters [62] and hormones (e.g., cholecystokinin) [42]. In the small intestine, we noticed that ICC-MY were arranged in bundles of up to five cells, with intersecting processes. These bundles extended between the surrounding muscle cells of the longitudinal and circular layers and into the interlamellar septa, which was in accordance with the description reported by Rumessen et al. [47]. Many researchers referred the function of ICC-MY network to its role as the primary pacemaker region in the stomach and small intestine and to be involved in generating higher frequency activity in the colon [1, 11, 22, 58, 64].

In our study, the morphological features of ICC-LM were similar to that of ICC-CM, but they were usually less numerous than the latter, nearly in the three regions of GI tract examined. Similar findings were reported by Komuro [31].

Our results showed higher numbers of c-Kit-positive cells than Ano1-positive cells. This difference can be attributed to cross staining of some other cells as fibroblasts and mast cells by c-Kit while Ano1 stained ICC only. As ICC Ano1-immunoreactivity was more specific than that of c-Kit [15], we relied on the count of Ano1-positive ICC in each layer of muscularis externa of stomach, small intestine, and colon at $\times 200$ magnification.

Interstitial cells of Cajal were distributed in the three areas of muscularis externa. They were more concentrated in the myenteric area of the three organs. Our results also showed more predominance of ICC in the three layers of the stomach than in the small intestine and colon, while the small intestine showed less numbers of ICC than the stomach and colon.

In general, the number of ICC in muscularis externa of the stomach and colon was more than that of the small intestine, but this difference was not statistically significant for both ICC-CM and ICC-LM, while in myenteric area, ICC-MY of the stomach were significantly more than those of the small intestine and colon, and ICC-MY of the colon were significantly more than those of the small intestine. These findings

can be explained by the slow peristaltic movement of the small intestine (to allow perfect absorption of digested food) if compared with that of the stomach (to digest food and control evacuation of chime) and colon (to control evacuation of waste products).

Regarding the distribution of ICC in the three areas of muscularis externa, we noticed that they were significantly more concentrated in the myenteric area (between circular and longitudinal muscle layers), followed by the circular and then the longitudinal muscle layers. This coincides with the explanation given by Hanani et al. [18], Komuro [32] who found that most ICC in the GI tract occur in the area of the myenteric plexus followed by the circular muscle layer, while ICC were less in the longitudinal muscle layer.

In our study, the density of ICC was significantly higher at the myenteric area than at the circular and longitudinal muscle layers of the muscularis externa. This distinctive regional variation in ICC distribution seemed to be associated with distinctive physiological function of each GI tract layer as reported by Ibba Manneschi et al. [25], Nemeth and Puri [39], Wang et al. [63], who investigated the physiological function of ICC in human stomach, small intestine and colon.

CONCLUSIONS

In conclusion, ICC appeared as bipolar cells, not forming network, in both the circular and longitudinal muscle layers, while in the myenteric area they appeared as multipolar interconnected cells. They were unevenly distributed in and between the muscle layers of the muscularis externa of human GI tract. They were more numerous in the stomach followed by the colon then the small intestine, and more numerous in the myenteric area followed by the circular muscle layer then the longitudinal muscle layer, in the three organs. Our results also showed that Ano1 is a more reliable marker for human ICC than c-Kit.

Acknowledgements

The authors sincerely thank those who donated their bodies to science so that research could be performed. Results from such research can potentially increase mankind's overall knowledge that can then improve patient care. Therefore, these donors and their families deserve our highest gratitude.

Conflict of interest: None declared

REFERENCES

1. Bayguinov PO, Hennig GW, Smith TK. Ca²⁺ imaging of activity in ICC-MY during local mucosal reflexes and the colonic migrating motor complex in the murine large intestine. *J Physiol*. 2010; 588(Pt 22): 4453–4474, doi: [10.1113/jphysiol.2010.196824](https://doi.org/10.1113/jphysiol.2010.196824), indexed in Pubmed: [20876203](https://pubmed.ncbi.nlm.nih.gov/20876203/).
2. Bayliss WM, Starling EH. The movements and innervation of the small intestine. *J Physiol*. 1899; 24(2): 99–143, doi: [10.1113/jphysiol.1899.sp000752](https://doi.org/10.1113/jphysiol.1899.sp000752), indexed in Pubmed: [16992487](https://pubmed.ncbi.nlm.nih.gov/16992487/).
3. Beaumont W. Nutrition Classics. Experiments and observations on the gastric juice and the physiology of digestion. By William Beaumont. Plattsburgh. Printed by F. P. Allen. 1833. *Nutr Rev*. 1977; 35(6): 144–145, doi: [10.1111/j.1753-4887.1977.tb06570.x](https://doi.org/10.1111/j.1753-4887.1977.tb06570.x), indexed in Pubmed: [327355](https://pubmed.ncbi.nlm.nih.gov/327355/).
4. Beckett EAH, Takeda Y, Yanase H, et al. Synaptic specializations exist between enteric motor nerves and interstitial cells of Cajal in the murine stomach. *J Comp Neurol*. 2005; 493(2): 193–206, doi: [10.1002/cne.20746](https://doi.org/10.1002/cne.20746), indexed in Pubmed: [16255030](https://pubmed.ncbi.nlm.nih.gov/16255030/).
5. Cajal SR. Textura del sistema nervioso del hombre y de los vertebrados. Vol. 2. Imprenta y librería de Nicolás Moya, Madrid 1899.
6. Cajal SR. Histologie du système nerveux de l'homme & des vertébrés. Vol. 2. Cervelet, cerveau moyen, rétine, couche optique, corps strié, écorce cérébrale générale & régionale, grand sympathique. A. Maloine, Paris 1911: 891–942.
7. Cannon WB. The movements of the intestines studied by means of the röntgen rays. *Am J Physiol-Legacy Content*. 1902; 6(5): 251–277, doi: [10.1152/ajplegacy.1902.6.5.251](https://doi.org/10.1152/ajplegacy.1902.6.5.251).
8. Chen H, Redelman D, Ro S, et al. Selective labeling and isolation of functional classes of interstitial cells of Cajal of human and murine small intestine. *Am J Physiol Cell Physiol*. 2007; 292(1): C497–C507, doi: [10.1152/ajpcell.00147.2006](https://doi.org/10.1152/ajpcell.00147.2006), indexed in Pubmed: [16943245](https://pubmed.ncbi.nlm.nih.gov/16943245/).
9. Chen ZH, Zhang YC, Jiang WF, et al. Characterization of interstitial Cajal progenitors cells and their changes in Hirschsprung's disease. *PLoS One*. 2014; 9(1): e86100, doi: [10.1371/journal.pone.0086100](https://doi.org/10.1371/journal.pone.0086100), indexed in Pubmed: [24475076](https://pubmed.ncbi.nlm.nih.gov/24475076/).
10. Coyle D, Kelly DAM, O'Donnell AM, et al. Use of anoc-tamin 1 (ANO1) to evaluate interstitial cells of Cajal in Hirschsprung's disease. *Pediatr Surg Int*. 2016; 32(2): 125–133, doi: [10.1007/s00383-015-3822-9](https://doi.org/10.1007/s00383-015-3822-9), indexed in Pubmed: [26510736](https://pubmed.ncbi.nlm.nih.gov/26510736/).
11. Dickens EJ, Hirst GD, Tomita T. Identification of rhythmically active cells in guinea-pig stomach. *J Physiol*. 1999; 514 (Pt 2)(Pt 2): 515–531, doi: [10.1111/j.1469-7793.1999.515ae.x](https://doi.org/10.1111/j.1469-7793.1999.515ae.x), indexed in Pubmed: [9852332](https://pubmed.ncbi.nlm.nih.gov/9852332/).
12. Faussone Pe, Cortesini C, Romagnoli P. [Ultrastructure of the tunica muscularis of the cardiac portion of the human esophagus and stomach, with special reference to the so-called Cajal's interstitial cells]. *Arch Ital Anat Embriol*. 1977; 82(2): 157–177, indexed in Pubmed: [613989](https://pubmed.ncbi.nlm.nih.gov/613989/).
13. Faussone-Pellegrini MS, Cortesini C. Ultrastructural features and localization of the interstitial cells of Cajal in the smooth muscle coat of human esophagus. *J Submicrosc Cytol*. 1985; 17(2): 187–197, indexed in Pubmed: [3999182](https://pubmed.ncbi.nlm.nih.gov/3999182/).
14. Fujiwara T, Motoyama T, Ishihara N, et al. Characterization of four new cell lines derived from small-cell gastrointestinal carcinoma. *Int J Cancer*. 1993; 54(6): 965–971, doi: [10.1002/ijc.2910540617](https://doi.org/10.1002/ijc.2910540617), indexed in Pubmed: [8392984](https://pubmed.ncbi.nlm.nih.gov/8392984/).
15. Gomez-Pinilla PJ, Gibbons SJ, Bardsley MR, et al. Ano1 is a selective marker of interstitial cells of Cajal in the human and mouse gastrointestinal tract. *Am J Physiol Gastrointest Liver Physiol*. 2009; 296(6): G1370–G1381, doi: [10.1152/ajpgi.00074.2009](https://doi.org/10.1152/ajpgi.00074.2009), indexed in Pubmed: [19372102](https://pubmed.ncbi.nlm.nih.gov/19372102/).
16. Gomez-Pinilla PJ, Gibbons SJ, Sarr MG, et al. Changes in interstitial cells of cajal with age in the human stomach and colon. *Neurogastroenterol Motil*. 2011; 23(1): 36–44, doi: [10.1111/j.1365-2982.2010.01590.x](https://doi.org/10.1111/j.1365-2982.2010.01590.x), indexed in Pubmed: [20723073](https://pubmed.ncbi.nlm.nih.gov/20723073/).
17. Hagger R, Gharaie S, Finlayson C, et al. Regional and transmural density of interstitial cells of Cajal in human colon and rectum. *Am J Physiol*. 1998; 275(6): G1309–G1316, doi: [10.1152/ajpgi.1998.275.6.G1309](https://doi.org/10.1152/ajpgi.1998.275.6.G1309), indexed in Pubmed: [9843767](https://pubmed.ncbi.nlm.nih.gov/9843767/).
18. Hanani M, Farrugia G, Komuro T. Intercellular coupling of interstitial cells of cajal in the digestive tract. *Int Rev Cytol*. 2004; 242: 249–282, doi: [10.1016/s0074-7696\(04\)42006-3](https://doi.org/10.1016/s0074-7696(04)42006-3).
19. Hassan S, Kinoshita Y, Kawanami C, et al. Expression of protooncogene c-kit and its ligand stem cell factor (SCF) in gastric carcinoma cell lines. *Dig Dis Sci*. 1998; 43(1): 8–14, doi: [10.1023/a:1018851415704](https://doi.org/10.1023/a:1018851415704), indexed in Pubmed: [9508539](https://pubmed.ncbi.nlm.nih.gov/9508539/).
20. Hibi K, Takahashi T, Sekido Y, et al. Coexpression of the stem cell factor and the c-kit genes in small-cell lung cancer. *Oncogene*. 1991; 6(12): 2291–2296, indexed in Pubmed: [1722571](https://pubmed.ncbi.nlm.nih.gov/1722571/).
21. Hirst GDS, Beckett EAH, Sanders KM, et al. Regional variation in contribution of myenteric and intramuscular interstitial cells of Cajal to generation of slow waves in mouse gastric antrum. *J Physiol*. 2002; 540(Pt 3): 1003–1012, doi: [10.1113/jphysiol.2001.013672](https://doi.org/10.1113/jphysiol.2001.013672), indexed in Pubmed: [11986385](https://pubmed.ncbi.nlm.nih.gov/11986385/).
22. Huizinga JD, Thuneberg L, Klüppel M, et al. W/kit gene required for interstitial cells of Cajal and for intestinal pacemaker activity. *Nature*. 1995; 373(6512): 347–349, doi: [10.1038/373347a0](https://doi.org/10.1038/373347a0), indexed in Pubmed: [7530333](https://pubmed.ncbi.nlm.nih.gov/7530333/).
23. Huizinga JD, Thuneberg L, Vanderwinden JM, et al. Interstitial cells of Cajal as targets for pharmacological intervention in gastrointestinal motor disorders. *Trends Pharmacol Sci*. 1997; 18(10): 393–403, doi: [10.1016/s0165-6147\(97\)01108-5](https://doi.org/10.1016/s0165-6147(97)01108-5).
24. Hwang SJ, Blair PJA, Britton FC, et al. Expression of anoc-tamin 1/TMEM16A by interstitial cells of Cajal is fundamental for slow wave activity in gastrointestinal muscles. *J Physiol*. 2009; 587(Pt 20): 4887–4904, doi: [10.1113/jphysiol.2009.176198](https://doi.org/10.1113/jphysiol.2009.176198), indexed in Pubmed: [19687122](https://pubmed.ncbi.nlm.nih.gov/19687122/).
25. Ibba Manneschi L, Pacini S, Corsani L, et al. Interstitial cells of Cajal in the human stomach: distribution and relationship with enteric innervation. *Histol Histopathol*. 2004; 19(4): 1153–1164, doi: [10.14670/HH-19.1153](https://doi.org/10.14670/HH-19.1153), indexed in Pubmed: [15375758](https://pubmed.ncbi.nlm.nih.gov/15375758/).
26. Imaizumi M, Hama K. An electron microscopic study on the interstitial cells of the gizzard in the love-bird (*Uroloncha domestica*). *Z Zellforsch Mikrosk Anat*. 1969; 97(3): 351–357, doi: [10.1007/BF00968841](https://doi.org/10.1007/BF00968841), indexed in Pubmed: [4906488](https://pubmed.ncbi.nlm.nih.gov/4906488/).

27. Kashyap P, Gomez-Pinilla PJ, Pozo MJ, et al. Immunoreactivity for Ano1 detects depletion of Kit-positive interstitial cells of Cajal in patients with slow transit constipation. *Neurogastroenterol Motil.* 2011; 23(8): 760–765, doi: [10.1111/j.1365-2982.2011.01729.x](https://doi.org/10.1111/j.1365-2982.2011.01729.x), indexed in Pubmed: [21585622](https://pubmed.ncbi.nlm.nih.gov/21585622/).
28. Keith A. The cabendish lecture on a new theory of the causation of enterostasis. *Lancet.* 1915; 186(4799): 371–375, doi: [10.1016/s0140-6736\(01\)53737-x](https://doi.org/10.1016/s0140-6736(01)53737-x).
29. Komuro T. Three-dimensional observation of the fibroblast-like cells associated with the rat myenteric plexus, with special reference to the interstitial cells of Cajal. *Cell Tissue Res.* 1989; 255(2): 343–351, doi: [10.1007/BF00224117](https://doi.org/10.1007/BF00224117), indexed in Pubmed: [2924337](https://pubmed.ncbi.nlm.nih.gov/2924337/).
30. Komuro T. Comparative morphology of interstitial cells of Cajal: Ultrastructural characterization. *Microsc Res Tech.* 1999; 47(4): 267–285, doi: [10.1002/\(sici\)1097-0029\(19991115\)47:4<267::aid-jemt5>3.0.co;2-o](https://doi.org/10.1002/(sici)1097-0029(19991115)47:4<267::aid-jemt5>3.0.co;2-o).
31. Komuro T. Morphological features of interstitial cells of Cajal. In: Kitamura Y, Miettinen M, Hirota S, Kanakura Y (eds.). *Gastrointestinal Stromal Tumor (GIST): from pathology to molecular target therapy*, Gann Monograph on Cancer Research No 53. Japan Scientific Societies Press & Karger, Tokyo, Basel 2004: 109–134.
32. Komuro T. Structure and organization of interstitial cells of Cajal in the gastrointestinal tract. *J Physiol.* 2006; 576(Pt 3): 653–658, doi: [10.1113/jphysiol.2006.116624](https://doi.org/10.1113/jphysiol.2006.116624), indexed in Pubmed: [16916909](https://pubmed.ncbi.nlm.nih.gov/16916909/).
33. Langton P, Ward SM, Carl A, et al. Spontaneous electrical activity of interstitial cells of Cajal isolated from canine proximal colon. *Proc Natl Acad Sci U S A.* 1989; 86(18): 7280–7284, doi: [10.1073/pnas.86.18.7280](https://doi.org/10.1073/pnas.86.18.7280), indexed in Pubmed: [2550938](https://pubmed.ncbi.nlm.nih.gov/2550938/).
34. Lecoin L, Gabella G, Le Douarin N. Origin of the c-kit-positive interstitial cells in the avian bowel. *Development.* 1996; 122(3): 725–733, doi: [10.1242/dev.122.3.725](https://doi.org/10.1242/dev.122.3.725), indexed in Pubmed: [8631250](https://pubmed.ncbi.nlm.nih.gov/8631250/).
35. Lee HT, Hennig GW, Fleming NW, et al. The mechanism and spread of pacemaker activity through myenteric interstitial cells of Cajal in human small intestine. *Gastroenterology.* 2007; 132(5): 1852–1865, doi: [10.1053/j.gastro.2007.02.049](https://doi.org/10.1053/j.gastro.2007.02.049), indexed in Pubmed: [17484879](https://pubmed.ncbi.nlm.nih.gov/17484879/).
36. Loera-Valencia R, Wang XY, Wright GWJ, et al. Ano1 is a better marker than c-Kit for transcript analysis of single interstitial cells of Cajal in culture. *Cell Mol Biol Lett.* 2014; 19(4): 601–610, doi: [10.2478/s11658-014-0214-4](https://doi.org/10.2478/s11658-014-0214-4), indexed in Pubmed: [25338768](https://pubmed.ncbi.nlm.nih.gov/25338768/).
37. Maeda H, Yamagata A, Nishikawa S, et al. Requirement of c-kit for development of intestinal pacemaker system. *Development.* 1992; 116(2): 369–375, doi: [10.1242/dev.116.2.369](https://doi.org/10.1242/dev.116.2.369), indexed in Pubmed: [1283735](https://pubmed.ncbi.nlm.nih.gov/1283735/).
38. Mazet B, Raynier C. Interstitial cells of Cajal in the guinea pig gastric antrum: distribution and regional density. *Cell Tissue Res.* 2004; 316(1): 23–34, doi: [10.1007/s00441-003-0835-9](https://doi.org/10.1007/s00441-003-0835-9), indexed in Pubmed: [14986098](https://pubmed.ncbi.nlm.nih.gov/14986098/).
39. Nemeth L, Puri P. Three-dimensional morphology of c-Kit-positive cellular network and nitrergic innervation in the human gut. *Arch Pathol Lab Med.* 2001; 125(7): 899–904, doi: [10.5858/2001-125-0899-TDMOCK](https://doi.org/10.5858/2001-125-0899-TDMOCK), indexed in Pubmed: [11419974](https://pubmed.ncbi.nlm.nih.gov/11419974/).
40. Park KS, Cho KB, Hwang IIS, et al. Characterization of smooth muscle, enteric nerve, interstitial cells of Cajal, and fibroblast-like cells in the gastric musculature of patients with diabetes mellitus. *World J Gastroenterol.* 2016; 22(46): 10131–10139, doi: [10.3748/wjg.v22.i46.10131](https://doi.org/10.3748/wjg.v22.i46.10131), indexed in Pubmed: [28028361](https://pubmed.ncbi.nlm.nih.gov/28028361/).
41. Pasternak A, Szura M, Gil K, et al. Interstitial cells of Cajal - systematic review. *Folia Morphol.* 2016; 75(3): 281–286, doi: [10.5603/FM.a2016.0002](https://doi.org/10.5603/FM.a2016.0002), indexed in Pubmed: [26806433](https://pubmed.ncbi.nlm.nih.gov/26806433/).
42. Patterson LM, Zheng H, Ward SM, et al. Immunohistochemical identification of cholecystokinin A receptors on interstitial cells of Cajal, smooth muscle, and enteric neurons in rat pylorus. *Cell Tissue Res.* 2001; 305(1): 11–23, doi: [10.1007/s004410100402](https://doi.org/10.1007/s004410100402), indexed in Pubmed: [11512662](https://pubmed.ncbi.nlm.nih.gov/11512662/).
43. Radenkovic G, Savic V, Mitic D, et al. Development of c-kit immunopositive interstitial cells of Cajal in the human stomach. *J Cell Mol Med.* 2010; 14(5): 1125–1134, doi: [10.1111/j.1582-4934.2009.00725.x](https://doi.org/10.1111/j.1582-4934.2009.00725.x), indexed in Pubmed: [19298525](https://pubmed.ncbi.nlm.nih.gov/19298525/).
44. Reed J, Ouban A, Schickor FK, et al. Immunohistochemical staining for c-Kit (CD117) is a rare event in human colorectal carcinoma. *Clin Colorectal Cancer.* 2002; 2(2): 119–122, doi: [10.3816/CCC.2002.n.018](https://doi.org/10.3816/CCC.2002.n.018), indexed in Pubmed: [12453327](https://pubmed.ncbi.nlm.nih.gov/12453327/).
45. Rhee PL, Lee JiY, Son HJ, et al. Analysis of pacemaker activity in the human stomach. *J Physiol.* 2011; 589(Pt 24): 6105–6118, doi: [10.1113/jphysiol.2011.217497](https://doi.org/10.1113/jphysiol.2011.217497), indexed in Pubmed: [22005683](https://pubmed.ncbi.nlm.nih.gov/22005683/).
46. Richardson KC. Electronmicroscopic observations on Auerbach's plexus in the rabbit, with special reference to the problem of smooth muscle innervation. *Am J Anat.* 1958; 103(1): 99–135, doi: [10.1002/aja.1001030105](https://doi.org/10.1002/aja.1001030105), indexed in Pubmed: [13626839](https://pubmed.ncbi.nlm.nih.gov/13626839/).
47. Rumessen J, Mikkelsen H, Qvortrup K, et al. Ultrastructure of interstitial cells of Cajal in circular muscle of human small intestine. *Gastroenterology.* 1993; 104(2): 343–350, doi: [10.1016/0016-5085\(93\)90400-7](https://doi.org/10.1016/0016-5085(93)90400-7), indexed in Pubmed: [8425676](https://pubmed.ncbi.nlm.nih.gov/8425676/).
48. Rygaard K, Nakamura T, Spang-Thomsen M. Expression of the proto-oncogenes c-met and c-kit and their ligands, hepatocyte growth factor/scatter factor and stem cell factor, in SCLC cell lines and xenografts. *Br J Cancer.* 1993; 67(1): 37–46, doi: [10.1038/bjc.1993.7](https://doi.org/10.1038/bjc.1993.7), indexed in Pubmed: [7678980](https://pubmed.ncbi.nlm.nih.gov/7678980/).
49. Sanders KM. A case for interstitial cells of Cajal as pacemakers and mediators of neurotransmission in the gastrointestinal tract. *Gastroenterology.* 1996; 111(2): 492–515, doi: [10.1053/gast.1996.v111.pm8690216](https://doi.org/10.1053/gast.1996.v111.pm8690216), indexed in Pubmed: [8690216](https://pubmed.ncbi.nlm.nih.gov/8690216/).
50. Sanders KM, Ward SM. Kit mutants and gastrointestinal physiology. *J Physiol.* 2007; 578(Pt 1): 33–42, doi: [10.1113/jphysiol.2006.122473](https://doi.org/10.1113/jphysiol.2006.122473), indexed in Pubmed: [17095561](https://pubmed.ncbi.nlm.nih.gov/17095561/).
51. Song G, David G, Hirst S, et al. Regional variation in ICC distribution, pacemaking activity and neural responses in the longitudinal muscle of the murine stomach. *J Physiol.* 2005; 564(Pt 2): 523–540, doi: [10.1113/jphysiol.2004.081067](https://doi.org/10.1113/jphysiol.2004.081067), indexed in Pubmed: [15677686](https://pubmed.ncbi.nlm.nih.gov/15677686/).
52. Strege PR, Ou Y, Sha L, et al. Sodium current in human intestinal interstitial cells of Cajal. *Am J Physiol Gastrointest Liver Physiol.* 2003; 285(6): G1111–G1121, doi: [10.1152/ajpgi.00152.2003](https://doi.org/10.1152/ajpgi.00152.2003), indexed in Pubmed: [12893628](https://pubmed.ncbi.nlm.nih.gov/12893628/).

53. Tang CM, Lee TE, Syed SA, et al. Hedgehog pathway dysregulation contributes to the pathogenesis of human gastrointestinal stromal tumors via GLI-mediated activation of KIT expression. *Oncotarget*. 2016; 7(48): 78226–78241, doi: [10.18632/oncotarget.12909](https://doi.org/10.18632/oncotarget.12909), indexed in Pubmed: [27793025](https://pubmed.ncbi.nlm.nih.gov/27793025/).
54. Taxi J. [On the existence of ciliated neurons in the sympathetic ganglia of certain vertebrates]. *C R Seances Soc Biol Fil*. 1961(155): 1860–1863, indexed in Pubmed: [13919898](https://pubmed.ncbi.nlm.nih.gov/13919898/).
55. Taxi J. Electron microscope study of the innervation of intestinal smooth muscle, compared to that of some other mammalian smooth muscles]. *Arch Biol (Liege)*. 1964(75): 301–328, indexed in Pubmed: [14276581](https://pubmed.ncbi.nlm.nih.gov/14276581/).
56. Thuneberg L. Interstitial Cells of Cajal: Intestinal Pacemaker Cells? *Adv Anat Embryol Cell Biol*. 1982, doi: [10.1007/978-3-642-68417-3](https://doi.org/10.1007/978-3-642-68417-3).
57. Thuneberg L. Interstitial cells of Cajal. In: Wood JD (ed.). *Handbook of Physiology: The Gastrointestinal System*. American Physiological Society, Bethesda, Maryland 1989: 349–386.
58. Torihashi S, Ward SM, Nishikawa S, et al. c-Kit-dependent development of interstitial cells and electrical activity in the murine gastrointestinal tract. *Cell Tissue Res*. 1995; 280(1): 97–111, doi: [10.1007/BF00304515](https://doi.org/10.1007/BF00304515), indexed in Pubmed: [7538451](https://pubmed.ncbi.nlm.nih.gov/7538451/).
59. Torihashi S, Horisawa M, Watanabe Y. c-Kit immunoreactive interstitial cells in the human gastrointestinal tract. *J Auton Nerv Syst*. 1999; 75(1): 38–50, doi: [10.1016/s0165-1838\(98\)00174-x](https://doi.org/10.1016/s0165-1838(98)00174-x).
60. Vanderwinden J, Verslijpe M, De La, et al. Distribution of interstitial cells of Cajal in human duodenum and intestine. *Neurogastroenterol Motil*. 1998; 10: 435.
61. Vanderwinden JM, Liu H, De Laet MH, et al. Study of the interstitial cells of Cajal in infantile hypertrophic pyloric stenosis. *Gastroenterology*. 1996; 111(2): 279–288, doi: [10.1053/gast.1996.v111.pm8690192](https://doi.org/10.1053/gast.1996.v111.pm8690192), indexed in Pubmed: [8690192](https://pubmed.ncbi.nlm.nih.gov/8690192/).
62. Vannucchi M, De Giorgio R, Fausone-Pellegrini M. NK1 receptor expression in the interstitial cells of Cajal and neurons and tachykinins distribution in rat ileum during development. *J Comp Neurol*. 1998; 383(2): 153–162, doi: [10.1002/\(sici\)1096-9861\(19970630\)383:2<153::aid-cne3>3.0.co;2-#](https://doi.org/10.1002/(sici)1096-9861(19970630)383:2<153::aid-cne3>3.0.co;2-#).
63. Wang XY, Paterson C, Huizinga JD. Cholinergic and nitrergic innervation of ICC-DMP and ICC-IM in the human small intestine. *Neurogastroenterol Motil*. 2003; 15(5): 531–543, doi: [10.1046/j.1365-2982.2003.00429.x](https://doi.org/10.1046/j.1365-2982.2003.00429.x), indexed in Pubmed: [14507353](https://pubmed.ncbi.nlm.nih.gov/14507353/).
64. Ward SM, Burns AJ, Torihashi S, et al. Mutation of the proto-oncogene c-kit blocks development of interstitial cells and electrical rhythmicity in murine intestine. *J Physiol*. 1994; 480 (Pt 1): 91–97, doi: [10.1113/jphysiol.1994.sp020343](https://doi.org/10.1113/jphysiol.1994.sp020343), indexed in Pubmed: [7853230](https://pubmed.ncbi.nlm.nih.gov/7853230/).
65. Ward S, Sanders K. Interstitial cells of Cajal: Primary targets of enteric motor innervation. *Anat Rec*. 2001; 262(1): 125–135, doi: [10.1002/1097-0185\(20010101\)262:1<125::aid-ar1017>3.0.co;2-i](https://doi.org/10.1002/1097-0185(20010101)262:1<125::aid-ar1017>3.0.co;2-i).
66. Yin J, Chen JDZ. Roles of interstitial cells of Cajal in regulating gastrointestinal motility: in vitro versus in vivo studies. *J Cell Mol Med*. 2008; 12(4): 1118–1129, doi: [10.1111/j.1582-4934.2008.00352.x](https://doi.org/10.1111/j.1582-4934.2008.00352.x), indexed in Pubmed: [18429936](https://pubmed.ncbi.nlm.nih.gov/18429936/).
67. Young HM, Ciampoli D, Southwell BR, et al. Origin of interstitial cells of Cajal in the mouse intestine. *Dev Biol*. 1996; 180(1): 97–107, doi: [10.1006/dbio.1996.0287](https://doi.org/10.1006/dbio.1996.0287), indexed in Pubmed: [8948577](https://pubmed.ncbi.nlm.nih.gov/8948577/).
68. Zhang SC, Fedoroff S. Cellular localization of stem cell factor and c-Kit receptor in the mouse nervous system. *J Neurosci Res*. 1997; 47(1): 1–15, doi: [10.1002/\(sici\)1097-4547\(19970101\)47:1<1::aid-jnr1>3.0.co;2-n](https://doi.org/10.1002/(sici)1097-4547(19970101)47:1<1::aid-jnr1>3.0.co;2-n).

Evaluation of the angulation of the nasal septum deviation as an anatomical variation for increased frequency of antral pseudocyst: a cone-beam computed tomography study

N. Laçın¹, M. Yalçın², M. Demirkol³

¹Department of Oral and Maxillofacial Surgery, Faculty of Dentistry, Izmir Katip Celebi University, Izmir, Turkey

²Ministry of Health, Istanbul, Turkey

³Department of Oral and Maxillofacial Surgery, Faculty of Dentistry, Gaziantep University, Gaziantep, Turkey

[Received: 5 July 2021; Accepted: 27 October 2021; Early publication date: 16 November 2021]

Background: The aim of the study was to determine whether degree of the nasal septum deviation (NSD) can affect the frequency of antral pseudocyst (AP) formation by cone-beam computed tomography (CBCT).

Materials and methods: This retrospective study was included 466 CBCT images. The NSD were categorised into four groups according to the degree: control group (no NSD, 0°–2°), group A (2°–9°), group B (9°–15°), and group C ($\geq 15^\circ$). The predictor variables were demographic factors (patient's age and gender) and anatomic factors (different degrees of nasal septum angulation). The outcome variable was presence of AP.

Results: Of the 466 cases, 242 (51.9%) had no NSD, 66 (14.2%) had an angle of 2°–9°, 111 (23.8%) had an angle of 9°–15°, and 47 (10.1%) had an angle of over 15°. The prevalence of AP was 2.04 (95% confidence interval [CI] 1.37 to 3.03; $p = 0.001$) times higher in the presence of NSD. Significant increases in presence of AP occurred with NSD in group A (2.37 times higher; $p = 0.003$) and group B (2.07 times higher; $p = 0.003$) compared to control by univariate analysis.

Conclusions: Although there is no sufficient evidence to suggest that NSD is a definitive aetiological factor for AP development, our findings indicated that NSD increased the risk of AP formation. (Folia Morphol 2023; 82, 1: 158–165)

Key words: nasal septum, deviation, antral pseudocyst

INTRODUCTION

Antral pseudocysts (APs) are radiopaque, dome-shaped lesions that do not contain a true epithelial lining and are composed of a serous exudate. APs are predominantly located in the maxillary bone and associated with the Schneiderian membrane [37]. These pathological entities are asymptomatic and can be detected during radiological examination

particularly by plain radiography and/or cone-beam computed tomography (CBCT). APs are considered to be associated with allergic reactions, humidity, temperature, trauma, smoking, odontogenic infection, although its pathogenesis remains controversial [7, 8, 26, 29]. In the sinus elevation procedures through crestal or lateral approach, AP can also be caused by the perforation, trauma and infection of

Address for correspondence: M. Yalçın, DDS, Istanbul Kent University, Faculty of Dentistry, Department of Oral and Maxillofacial Surgery, Istanbul, Turkey, tel: +90 0553 6506065, e-mail: myalcin.omfs@gmail.com

This article is available in open access under Creative Common Attribution-Non-Commercial-No Derivatives 4.0 International (CC BY-NC-ND 4.0) license, allowing to download articles and share them with others as long as they credit the authors and the publisher, but without permission to change them in any way or use them commercially.

the Schneiderian membrane. AP might be unilateral or bilateral in the maxillary bone and the dimension of AP might increase gradually, remain the same, or decrease gradually [16, 38, 39]. AP cannot disrupt the integrity of the cortical plate of the maxillary sinus and of the Schneiderian membrane [16, 39].

Nasal airflow directly affects the development of craniomaxillofacial bones and paranasal sinuses [22]. Obliteration of the nasal passage caused by nasal septum deviation (NSD) prevents optimal nasal breathing and also results in mouth breathing [4]. Nasal septum is defined as a midline structure of the nasal cavity which divides the nasal cavity into halves and supports the external nose structurally [13]. Nasal septum consists of cartilaginous (anteriorly, quadrangular cartilage), bony (posteriorly, vomer and perpendicular plate of the ethmoid bone) and membranous components [13]. NSD is an anatomic variation that affects approximately 80% of adults [36, 43]. In the literature, there are various classifications of NSDs [5, 19]. Cerkes [9] defined five main nasal septum deviation, named as caudal septal deviation, anteroposterior C-shaped deviation, cephalocaudal C-shaped deviation, anteroposterior S-shaped deviation and cephalocaudal S-shaped deviation. Guyuron et al. [19] reported that the most frequent type of NSD was characterised by an inclined septum.

Maxillary sinus pneumatization and airway obstruction in the nose are predisposing factors for pathologies in the maxillary sinus [35]. The maxillary sinus volume might change according to the capacity of the nasal airflow [15, 30]. NSD, concha bullosa, and ostium obstruction might alter the pneumatization of the maxillary sinus, thereby leading to the thickening of the maxillary sinus membrane and chronic sinusitis [23]. NSD is also an aetiological factor affecting the nasal airway and pneumatization of the maxillary sinus [23].

Although possible aetiological factors in the development of AP have been reported in the literature, no study evaluating the relationship between NSD and AP development has been identified. We aimed to investigate whether the presence and degree of NSD has an effect on the development of AP by using CBCT.

MATERIALS AND METHODS

Study sample

Initially, seven hundred CBCT scans obtained between January 2016 and July 2018 and retrieved

from the archives of the Faculty of Dentistry, Izmir Katip Çelebi University were included. CBCT scan were taken for orthodontic treatment, oral and maxillofacial examination and dental implant treatment. The following inclusion criteria were applied: patients older than 18 years, nasal area and both maxillary sinuses entirely visible on the scan with AP present or absent. Exclusion criteria included inadequate scan quality, impacted teeth in the maxillary sinus, nasal and antral sinus infection, cyst and tumour associated with maxillary sinus and/or nasal structure, pseudocyst related to odontogenic infection, age under 18 years, S-shaped septum deviation, multifaceted nasal septum deviation, concha bullosa, previous maxillofacial and/or paranasal surgery, and maxillofacial trauma. After detailed examination, a total of 466 patients with CBCT scan (236 male, 230 female) met our inclusion criteria.

The study was approved by the Ethics Committee of Izmir Katip Çelebi University. (Approval No.: 230), and the study protocol was conducted in accordance with the Helsinki Declaration 1975 as revised in 2000.

CBCT image acquisition, evaluation of the antral pseudocyst and nasal septum

All the images were obtained using a CBCT device (NewTom 5G CBCT machine, QR s.r.l., Verona, Italy). The exposure parameters were as follows: 110 kVp, 1–20 mA, with 15 × 12 cm field of view and resolution mode (voxel size 0.2 mm). The maxillary CBCT scans were obtained from the level of the maxillary teeth crown to the top of the orbit. All CBCT images were evaluated by the same experienced surgeons (NL and MY) on a desktop UltraSharp LED TFT 24-inch monitor (Dell Inc., Round Rock, TX, USA) with appropriate background lighting.

Antral pseudocysts were defined as unilacunar, dome-shaped, radiopaque lesions with no bone resorption on the wall of the maxillary sinus, particularly on the floor of the sinus (Fig. 1) [1, 8, 17, 20, 24, 25, 28, 39, 44]. AP location was classified as right, left and bilateral based on the location of the lesions in the maxillary sinus.

The location of the concavity was determined based on the direction of the deviation [2]. The NSD angle was measured between the two lines drawn on the coronal section of CBCT with the first line drawn from the crista galli to the anterior nasal spine and the second line drawn from the crista galli to the most prominent point of the deviation



Figure 1. Radiographic appearance of antral pseudocysts in the maxillary sinus.



Figure 4. Radiographic appearance of the nasal septum deviated to the right.



Figure 2. The nasal septum deviation angle was measured between the two lines drawn on the coronal section of cone-beam computed tomography, with the first line drawn from the crista galli to the anterior nasal spine and the second line drawn from the crista galli to the most prominent point of the deviation.



Figure 5. Radiographic appearance of the nasal septum deviated to the left.

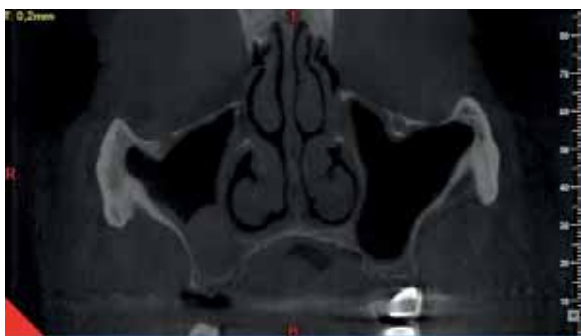


Figure 3. Radiographic appearance of straight nasal septum.

(Fig. 2) [2]. Patients were divided into four groups based on the degree of NSD: i) control group (no NSD, $0^\circ < \text{NSD} \leq 2^\circ$), ii) group A (mild, $2^\circ < \text{NSD} \leq 9^\circ$), iii) group B (moderate, $9^\circ < \text{NSD} \leq 15^\circ$), and iv) group C (severe, $\text{NSD} \geq 15^\circ$) [43]. Directions of NSD were divided into three groups: i) straight nasal septum (control group, $0^\circ < \text{NSD} \leq 2^\circ$), ii) nasal septum deviated to the right, and iii) nasal septum deviated to the left. These measurements were

made in the coronal view and are demonstrated in Figures 3, 4 and 5.

Statistical analysis

Statistical analyses were performed using SPSS for Windows version 22.0 (IBM Corp., Armonk, NY, USA). Binary and multinomial logistic regression analyses were used to estimate the odds ratio (OR) and 95% confidence interval (CI). Gender and age were included in the models to adjust their effects on the dependent variable. Descriptive statistics were expressed as frequencies (n), percentages (%), and mean \pm standard deviation (SD). Intra-operator reliability for each measurement was assessed using the intra-class correlation coefficient (ICC), with an interval of at least 3 weeks between measurements, which yielded a 98% agreement rate. The predictor variables were demographic factors (patient's age and gender) and anatomic factors (different degrees of nasal septum angulation). The outcome variable was presence of AP. The relation between predictors and outcome variable was analysed using binary and multinomial logistic regression analyses, with statistical significance set at a p value less than 0.05.

Table 1. Data of the mean age and nasal septum deviation (NSD) angle

	Number of patients	Minimum	Maximum	Mean	Standard deviation
Age	466	18	83	40.53	18.170
NSD angle	466	.0	33.9	5.819	6.9304

Table 2. Descriptive statistics for 224 cases with nasal septum deviation (NSD)

	Number	Minimum	Maximum	Mean	Standard deviation
NSD angle	224	4.6	33.9	12.106	4.8689

Table 3. Distribution of cases according to the gender, antral pseudocysts (AP) and nasal septum deviation (NSD)

		N	%
Gender	Male	236	50.6
	Female	230	49.4
AP in maxillary sinus	Absence	316	67.8
	Right	55	11.8
	Left	48	10.3
	Bilateral	47	10.1
NSD angle	Absence	242	51.9
	2° < NSD < 9°	66	14.2
	9° ≤ NSD < 15°	111	23.8
	NSD ≥ 15°	47	10.1

RESULTS

According to the ICC test, the concordance index was greater than 0.98, indicating high intra-examiner concordance.

The 466 patients included 50.6% (n = 236) men and 49.4% (n = 230) women with a mean age of 40.53 ± 18.17 (range: 13–83) years and mean NSD angle 5.81 ± 6.93 (Table 1). A straight nasal septum (control group) was detected in 242 (51.9%) images and NSD was detected in 224 (48.1%) images (mean NSD angle, 12.10 ± 4.86) as shown in Table 2. Of the 224 NSD cases, 66 (14.2%) cases had an NSD angle of 2°–9°, 111 (23.8%) of them had an angle of 9°–15°, and 47 (10.1%) of them had an angle of over 15° (Table 3). APs were detected in 150 (32.2%) cases, among whom the lesion was localised on the right side in 55 (11.8%), on the left side in 48 (10.3%), and on both sides in 47 (10.1%) cases (Table 3). Distribution of the AP was shown in Table 4.

Binary logistic regression analysis indicated that the prevalence of AP was 1.82 (95% CI; range: 1.23–2.7) times higher in men than in women (p = 0.003). Moreover, the prevalence of AP was 2.04 (range:

1.37–3.03) times higher in the presence of NSD than in the absence of NSD (p = 0.001) and the age- and gender-adjusted OR was 1.97 (95% CI: 1.32–2.93; p = 0.001). The prevalence of AP was 2.54 (95% CI: 1.60–4.03; p = 0.001) times higher in the right maxillary sinus with NSD compared to the control group and the age- and gender-adjusted OR was 2.44 (95% CI: 1.52–3.89; p = 0.001). However, no significant difference was found between the prevalence of AP in the left maxillary sinus and in the control group (p = 0.069). On the other hand, the prevalence of AP was 2.37 times higher in group A and 2.07 times higher in group B compared to the control group and the age- and gender-adjusted results were statistically significant as well (p = 0.003 and p = 0.005, respectively). Nevertheless, no significant difference was found between group C and the control group (p = 0.190) (Table 5).

DISCUSSION

Aetiological factors of pathological entities or anatomical variations in the maxillary sinus typically include upper respiratory tract infection, trauma, congenital deformities, odontogenic infection/cyst/tumour, adenotonsillar hypertrophy, and chronic nasal airway obstruction [3, 11]. Some of these entities might be symptomatic such as acute sinusitis, odontogenic cyst while some of them might be asymptomatic such as mucocoele, pseudocyst, antral polyps, and mucous retention cyst. The pathologies in the maxillary sinus are generally detected incidentally in routine radiographic and/or clinical examination.

The CBCT enables a three-dimensional examination for the assessment of the anatomic structure and pathologies of the maxillofacial region, thereby allowing a definitive diagnosis. Three-dimensional CBCT images were used in the current study for the detection of the NSD type, measurement of the NSD

Table 4. Distribution of the antral pseudocysts according to the nasal septum deviation (NSD), gender, direction of the NSD and NSD angle

	Location of antral pseudocysts								P-value
	Right		Left		Bilateral		Absence		
	N	%	N	%	N	%	N	%	
NSD									0.05
Absence	23	41.8	18	37.5	19	40.4	182	57.6	
Presence	32	58.2	30	62.5	28	59.6	134	42.4	
Gender									0.007
Male	36	65.5	24	50	31	66	145	45.9	
Female	19	34.5	24	50	16	34	171	54.1	
Direction of NSD									0.009
Straight	23	41.8	18	37.5	19	40.4	183	57.9	
Right	18	32.7	19	39.6	18	38.3	66	20.9	
Left	14	25.5	11	22.9	10	21.3	67	21.2	
NSD angle									0.011
Absence	23	41.8	18	37.5	19	40.4	182	57.6	
2° < NSD < 9°	13	23.6	7	14.6	9	19.1	37	11.7	
9° ≤ NSD < 15°	13	23.6	20	41.7	12	25.5	66	20.9	
NSD ≥ 15°	6	10.9	3	6.3	7	14.9	31	9.8	

Table 5. Multivariate analysis of factors associated with antral pseudocysts

Variables	Antral pseudocysts							
	Presence (n = 150)		Absence (n = 316)		Univariate	Age and gender adjusted results		
	Mean ± SD	Mean ± SD	OR [95% CI]	P	OR [95% CI]	P		
Age	42.14 ± 16.04		39.77 ± 19.08		1.01 [0.97–1.02]	0.188		
	N	%	N	%				
Gender								
Male	91	60.7	145	45.9	1.82 [1.23–2.7]	0.003*		
Female	59	39.3	171	54.1	1 (reference)			
Direction of NSD								
Straight	60	40.0	183	57.9	1 (reference)		1 (reference)	
Right	55	36.7	66	20.9	2.54 [1.60–4.03]	0.001*	2.44 [1.52–3.89]	0.001*
Left	35	23.3	67	21.2	1.59 [0.96–2.63]	0.069	1.56 [0.94–2.59]	0.084
NSD								
Presence	90	60	134	42.4	2.04 [1.37–3.03]	0.001*	1.97 [1.32–2.93]	0.001*
Absence	60	40	182	57.6	1 (reference)		1 (reference)	
NSD angle								
Absence	60	40.0	182	57.6	1 (reference)		1 (reference)	
2° < NSD < 9°	29	19.3	37	11.7	2.37 [1.35–4.19]	0.003*	2.39 [1.35–4.26]	0.003*
9° ≤ NSD < 15°	45	30.0	66	20.9	2.07 [1.28–3.37]	0.003*	2.01 [1.24–3.25]	0.005*
NSD ≥ 15°	16	10.7	31	9.8	1.57 [0.80–3.06]	0.190	1.41 [0.71–2.78]	0.324

*Significant at the 0.05 level; Binary logistic regression model; CI — confidence interval; NSD — nasal septum deviation; OR — odds ratio; SD — standard deviation

angle, detection of AP, and the evaluation of the maxillofacial structure.

Previous studies indicated that the nasal obstruction and impaired intranasal airflow caused by NSD

have an adverse effect on mucociliary activity and the resulting ciliary loss has been shown to increase the incidence of rhinosinusitis [14, 31, 32, 42]. However, although the relationship between NSD and chronic diseases of the sinus has been documented, an exact positive correlation has not yet been established due to inconsistent findings presented by the studies. In a 2009 study, Polat and Dostbil [34] evaluated patients with NSD using rhinoscintigraphy and reported that the administration of septoplasty improved the reduced nasal mucociliary transport rate. Although there have been several studies supporting this finding, Greguric et al. [18] and Collet et al. [10] reported that they found no definitive role of NSD in the pathogenesis of chronic rhinosinusitis [31]. Similarly, Yasan et al. [46] revealed that the mild-to-moderate septal deviation was not a risk factor for chronic sinusitis and only severe septal deviation was found to be a risk factor for the disease. In a confirmatory manner, a systematic review conducted in 2010 found a significant relationship between a septal deviation of $> 10^\circ$ and rhinosinusitis [31]. Although the studies abovementioned have investigated rhinosinusitis, the present study examined the possible effect of NSD on AP associated with inflammatory factors and a comparison was only made with the studies abovementioned since there are a limited number of studies reporting on the relationship between NSD and AP.

In our study, 90 (60%) of the patients were detected with NSD and Binary logistic regression analysis indicated that the prevalence of AP was 2.04 (range: 1.37–3.03) times higher in patients with NSD than in patients without NSD ($p = 0.001$). Additionally, the prevalence of AP was 2.37 (range: 1.35–4.19) times higher in group A (2° – 9°) and 2.07 (range: 1.28–3.37) times higher in group B (9° – 15°) compared to the control group (0° – 2°) ($p = 0.003$ for both). However, although no significant difference was found between group C ($\geq 15^\circ$) and the control group with regard to AP prevalence ($p = 0.190$), this prevalence was 1.41 (range: 0.71–2.78) times higher in group C compared to the control group. These findings are rather consistent with the results of the study by Orlandi [31] who found a significant relationship between a septal deviation of $> 10^\circ$ and rhinosinusitis.

On the other hand, rhinosinusitis, particularly chronic rhinosinusitis, is considered to be associated with allergies, bacteria, viruses, biofilms, osteitis, superantigens, immunological dysregulation, and gastroesophageal reflux [6, 27]. It has also been re-

ported that a single independent factor could not be held responsible and that there could be multiple factors leading to the development of rhinosinusitis [6, 27]. Additionally, although NSD is known to cause ostiomeatal complex narrowing and thereby to aggravate inflammation, the contralateral inflammation in NSD has been reported to be associated with different aetiologies [33]. Perloff et al. [33] suggested that the inflammation spread to the contralateral side through the Haversian system and another hypothesis posited that contralateral inflammation was caused by the nasal secretions pushed into the sinus during nose blowing. Some other studies indicated that the increased airflow on the side contralateral to the deviated septum and the turbulence in the medial meatus lead to ciliary loss in the maxillary sinus and also increase inflammation on both sides [21, 40]. Moreover, NSD has also been radiologically shown to be associated with the presence of contralateral concha bullosa [14, 41].

Antral pseudocysts have been reported to be associated with environmental factors including allergic reactions, smoking, trauma, changes in the air temperature, and humidity [7, 8, 26, 29]. A recent study by de Carvalho et al. [12] reported a significant relationship between the presence of AP and greater height of the maxillary sinus ostium. Another study that was conducted by the two authors of the present study and awaits publication revealed that AP could be associated with the masticatory forces transmitted to the sinus membrane through the protruded healthy maxillary molar roots penetrated into the maxillary sinus [45].

Given that NSD alone could not be held responsible for the development of rhinosinusitis, we consider that NSD alone could not be held responsible for the development of AP as well. This hypothesis could be supported by our finding that indicated that AP was detected in patients with NSD and on the non-deviated (unaffected) side as well, considering that it would be more reasonable to expect that the risk of inflammation on the deviated side would be relatively higher [31]. Accordingly, based on the inflammatory effect of NSD in the pathogenesis of rhinosinusitis reported in the literature, it could be asserted that NSD could have an effective role in the aetiopathogenesis of AP.

Our study was limited in several ways. First, the study only included the clinical symptoms of NSD and the patients with right- or left-side deviation due to

its nature. Accordingly, it did not include the other NSD types and thus included no evaluation on the effect of other NSD types. Secondly, no evaluation was performed on the relationship between AP and the pathologies that could be associated with nasal airway obstruction other than NSD.

CONCLUSIONS

Although there is no sufficient evidence to suggest that NSD is a definitive aetiological factor for AP development, our findings indicated that NSD increased the risk of AP formation.

Conflict of interest: None declared

REFERENCES

- Allard RH, van der Kwast WA, van der Waal I. Mucosal antral cysts. Review of the literature and report of a radiographic survey. *Oral Surg Oral Med Oral Pathol.* 1981; 51(1): 2–9, doi: [10.1016/0030-4220\(81\)90118-3](https://doi.org/10.1016/0030-4220(81)90118-3), indexed in Pubmed: [7007951](https://pubmed.ncbi.nlm.nih.gov/7007951/).
- Al-Rawi NH, Uthman AT, Abdulhameed E, et al. Concha bullosa, nasal septal deviation, and their impacts on maxillary sinus volume among Emirati people: A cone-beam computed tomography study. *Imaging Sci Dent.* 2019; 49(1): 45–51, doi: [10.5624/isd.2019.49.1.45](https://doi.org/10.5624/isd.2019.49.1.45), indexed in Pubmed: [30941287](https://pubmed.ncbi.nlm.nih.gov/30941287/).
- Apuhan T, Yildirim YS, Özasan H. The developmental relation between adenoid tissue and paranasal sinus volumes in 3-dimensional computed tomography assessment. *Otolaryngol Head Neck Surg.* 2011; 144(6): 964–971, doi: [10.1177/0194599811399712](https://doi.org/10.1177/0194599811399712), indexed in Pubmed: [21493325](https://pubmed.ncbi.nlm.nih.gov/21493325/).
- Ballanti F, Baldini A, Ranieri S, et al. Is there a correlation between nasal septum deviation and maxillary transversal deficiency? A retrospective study on prepubertal subjects. *Int J Pediatr Otorhinolaryngol.* 2016; 83: 109–112, doi: [10.1016/j.ijporl.2016.01.036](https://doi.org/10.1016/j.ijporl.2016.01.036), indexed in Pubmed: [26968064](https://pubmed.ncbi.nlm.nih.gov/26968064/).
- Baumann I, Baumann H. A new classification of septal deviations. *Rhinology.* 2007; 45(3): 220–223, indexed in Pubmed: [17956023](https://pubmed.ncbi.nlm.nih.gov/17956023/).
- Benninger MS, Ferguson BJ, Hadley JA, et al. Adult chronic rhinosinusitis: definitions, diagnosis, epidemiology, and pathophysiology. *Otolaryngol Head Neck Surg.* 2003; 129(3 Suppl): S1–32, doi: [10.1016/s0194-5998\(03\)01397-4](https://doi.org/10.1016/s0194-5998(03)01397-4), indexed in Pubmed: [12958561](https://pubmed.ncbi.nlm.nih.gov/12958561/).
- Carter LC, Calamel A, Haller A, et al. Seasonal variation in maxillary antral pseudocysts in a general clinic population. *Dentomaxillofac Radiol.* 1998; 27(1): 22–24, doi: [10.1038/sj.dmfr.4600311](https://doi.org/10.1038/sj.dmfr.4600311), indexed in Pubmed: [9482018](https://pubmed.ncbi.nlm.nih.gov/9482018/).
- Casamassimo PS, Lilly GE. Mucosal cysts of the maxillary sinus: a clinical and radiographic study. *Oral Surg Oral Med Oral Pathol.* 1980; 50(3): 282–286, doi: [10.1016/0030-4220\(80\)90385-0](https://doi.org/10.1016/0030-4220(80)90385-0), indexed in Pubmed: [6932003](https://pubmed.ncbi.nlm.nih.gov/6932003/).
- Cerkes N. The crooked nose: principles of treatment. *Aesthet Surg J.* 2011; 31(2): 241–257, doi: [10.1177/1090820X10394167](https://doi.org/10.1177/1090820X10394167), indexed in Pubmed: [21317122](https://pubmed.ncbi.nlm.nih.gov/21317122/).
- Collet S, Bertrand B, Cornu S, et al. Is septal deviation a risk factor for chronic sinusitis? Review of literature. *Acta Otorhinolaryngol Belg.* 2001; 55(4): 299–304, indexed in Pubmed: [11859650](https://pubmed.ncbi.nlm.nih.gov/11859650/).
- Cooper BC. Nasorespiratory function and orofacial development. *Otolaryngol Clin North Am.* 1989; 22(2): 413–441, indexed in Pubmed: [2664660](https://pubmed.ncbi.nlm.nih.gov/2664660/).
- de Carvalho AB, Ferreira Costa AL, Fuziy A, et al. Investigation on the relationship of dimensions of the maxillary sinus drainage system with the presence of sinusopathies: a cone beam computed tomography study. *Arch Oral Biol.* 2018; 94: 78–83, doi: [10.1016/j.archoralbio.2018.06.021](https://doi.org/10.1016/j.archoralbio.2018.06.021), indexed in Pubmed: [29990588](https://pubmed.ncbi.nlm.nih.gov/29990588/).
- Delaney SW. Evolution of the septoplasty: maximizing functional and aesthetic outcomes in nasal surgery. *MJ Otol.* 2018; 1(1): 004.
- Elahi M, Frenkiel S. Septal deviation and chronic sinus disease. *Am J Rhinol.* 2018; 14(3): 175–180, doi: [10.2500/105065800782102735](https://doi.org/10.2500/105065800782102735).
- Gencer ZK, Ozkırış M, Okur A, et al. The effect of nasal septal deviation on maxillary sinus volumes and development of maxillary sinusitis. *Eur Arch Otorhinolaryngol.* 2013; 270(12): 3069–3073, doi: [10.1007/s00405-013-2435-y](https://doi.org/10.1007/s00405-013-2435-y), indexed in Pubmed: [23512432](https://pubmed.ncbi.nlm.nih.gov/23512432/).
- Giotakis EI, Weber RK. Cysts of the maxillary sinus: a literature review. *Int Forum Allergy Rhinol.* 2013; 3(9): 766–771, doi: [10.1002/alr.21177](https://doi.org/10.1002/alr.21177), indexed in Pubmed: [23677671](https://pubmed.ncbi.nlm.nih.gov/23677671/).
- Gothberg KA, Little JW, King DR, et al. A clinical study of cysts arising from mucosa of the maxillary sinus. *Oral Surg Oral Med Oral Pathol.* 1976; 41(1): 52–58, doi: [10.1016/0030-4220\(76\)90251-6](https://doi.org/10.1016/0030-4220(76)90251-6), indexed in Pubmed: [1061037](https://pubmed.ncbi.nlm.nih.gov/1061037/).
- Gregurić T, Baudoin T, Tomljenović D, et al. Relationship between nasal septal deformity, symptoms and disease severity in chronic rhinosinusitis. *Eur Arch Otorhinolaryngol.* 2016; 273(3): 671–677, doi: [10.1007/s00405-015-3615-8](https://doi.org/10.1007/s00405-015-3615-8), indexed in Pubmed: [25827442](https://pubmed.ncbi.nlm.nih.gov/25827442/).
- Guyuron B, Uzzo C, Scull H. A practical classification of septonasal deviation and an effective guide to septal surgery. *Plast Reconstr Surg.* 1999; 104(7): 2202–2209, doi: [10.1097/00006534-199912000-00041](https://doi.org/10.1097/00006534-199912000-00041).
- Harar RPS, Chadha NK, Rogers G. Are maxillary mucosal cysts a manifestation of inflammatory sinus disease? *J Laryngol Otol.* 2007; 121(8): 751–754, doi: [10.1017/S0022215107005634](https://doi.org/10.1017/S0022215107005634), indexed in Pubmed: [17250779](https://pubmed.ncbi.nlm.nih.gov/17250779/).
- Jang YJu, Myong NH, Park KH, et al. Mucociliary transport and histologic characteristics of the mucosa of deviated nasal septum. *Arch Otolaryngol Head Neck Surg.* 2002; 128(4): 421–424, doi: [10.1001/archotol.128.4.421](https://doi.org/10.1001/archotol.128.4.421), indexed in Pubmed: [11926918](https://pubmed.ncbi.nlm.nih.gov/11926918/).
- Klein JC. Nasal respiratory function and craniofacial growth. *Arch Otolaryngol Head Neck Surg.* 1986; 112(8): 843–849, doi: [10.1001/archotol.1986.03780080043009](https://doi.org/10.1001/archotol.1986.03780080043009), indexed in Pubmed: [3718688](https://pubmed.ncbi.nlm.nih.gov/3718688/).
- Kucybała I, Janik KA, Ciuk S, et al. Nasal septal deviation and concha bullosa: do they have an impact on maxillary sinus volumes and prevalence of maxillary sinusitis? *Pol J Radiol.* 2017; 82: 126–133, doi: [10.12659/PJR.900634](https://doi.org/10.12659/PJR.900634), indexed in Pubmed: [28348652](https://pubmed.ncbi.nlm.nih.gov/28348652/).

24. Lacin N, Tatar B. Evaluation of the frequency of mucous retention cysts in the maxillary sinus in a Turkish population using cone-beam computed tomography. *Makara J Health Res.* 2019; 23(2): 1, doi: [10.7454/msk.v23i2.10711](https://doi.org/10.7454/msk.v23i2.10711).
25. Lilly GE, Cutcher JL, Steiner M. Spherical shadows within the maxillary antrum. *J Oral Med.* 1968; 23(1): 19–21, indexed in Pubmed: [5238722](https://pubmed.ncbi.nlm.nih.gov/5238722/).
26. Mafee MF, Valvassori GE, Becker M. *Imaging of the Head and Neck.* New York, Stuttgart, Thieme 2005.
27. Meltzer EO, Hamilos DL, Hadley JA, et al. Rhinosinusitis: establishing definitions for clinical research and patient care. *J Allergy Clin Immunol.* 2004; 114(6 Suppl): 155–212, doi: [10.1016/j.jaci.2004.09.029](https://doi.org/10.1016/j.jaci.2004.09.029), indexed in Pubmed: [15577865](https://pubmed.ncbi.nlm.nih.gov/15577865/).
28. Myall RW, Eastep PB, Silver JG. Mucous retention cysts of the maxillary antrum. *J Am Dent Assoc.* 1974; 89(6): 1338–1342, doi: [10.14219/jada.archive.1974.0612](https://doi.org/10.14219/jada.archive.1974.0612), indexed in Pubmed: [4529984](https://pubmed.ncbi.nlm.nih.gov/4529984/).
29. Nunes CA, Guedes OA, Alencar AH, et al. Evaluation of periapical lesions and their association with maxillary sinus abnormalities on cone-beam computed tomographic images. *J Endod.* 2016; 42(1): 42–46, doi: [10.1016/j.joen.2015.09.014](https://doi.org/10.1016/j.joen.2015.09.014), indexed in Pubmed: [26521148](https://pubmed.ncbi.nlm.nih.gov/26521148/).
30. Orhan I, Ormeci T, Aydin S, et al. Morphometric analysis of the maxillary sinus in patients with nasal septum deviation. *Eur Arch Otorhinolaryngol.* 2014; 271(4): 727–732, doi: [10.1007/s00405-013-2617-7](https://doi.org/10.1007/s00405-013-2617-7), indexed in Pubmed: [23832260](https://pubmed.ncbi.nlm.nih.gov/23832260/).
31. Orlandi RR. A systematic analysis of septal deviation associated with rhinosinusitis. *Laryngoscope.* 2010; 120(8): 1687–1695, doi: [10.1002/lary.20992](https://doi.org/10.1002/lary.20992), indexed in Pubmed: [20564661](https://pubmed.ncbi.nlm.nih.gov/20564661/).
32. Passali D, Ferri R, Becchini G, et al. Alterations of nasal mucociliary transport in patients with hypertrophy of the inferior turbinates, deviations of the nasal septum and chronic sinusitis. *Eur Arch Otorhinolaryngol.* 1999; 256(7): 335–337, doi: [10.1007/s004050050158](https://doi.org/10.1007/s004050050158), indexed in Pubmed: [10473825](https://pubmed.ncbi.nlm.nih.gov/10473825/).
33. Perloff JR, Gannon FH, Bolger WE, et al. Bone involvement in sinusitis: an apparent pathway for the spread of disease. *Laryngoscope.* 2000; 110(12): 2095–2099, doi: [10.1097/00005537-200012000-00023](https://doi.org/10.1097/00005537-200012000-00023), indexed in Pubmed: [11129028](https://pubmed.ncbi.nlm.nih.gov/11129028/).
34. Polat C, Dostbil Z. Evaluation of the nasal mucociliary transport rate by rhinoscintigraphy before and after surgery in patients with deviated nasal septum. *Eur Arch Otorhinolaryngol.* 2010; 267(4): 529–535, doi: [10.1007/s00405-009-1116-3](https://doi.org/10.1007/s00405-009-1116-3), indexed in Pubmed: [19816701](https://pubmed.ncbi.nlm.nih.gov/19816701/).
35. Poorey VK, Gupta N. Endoscopic and computed tomographic evaluation of influence of nasal septal deviation on lateral wall of nose and its relation to sinus diseases. *Indian J Otolaryngol Head Neck Surg.* 2014; 66(3): 330–335, doi: [10.1007/s12070-014-0726-2](https://doi.org/10.1007/s12070-014-0726-2), indexed in Pubmed: [25032124](https://pubmed.ncbi.nlm.nih.gov/25032124/).
36. Roblin DG, Eccles R. What, if any, is the value of septal surgery? *Clin Otolaryngol Allied Sci.* 2002; 27(2): 77–80, doi: [10.1046/j.1365-2273.2002.00531.x](https://doi.org/10.1046/j.1365-2273.2002.00531.x), indexed in Pubmed: [11994109](https://pubmed.ncbi.nlm.nih.gov/11994109/).
37. Rodrigues C, Arruda J, Silva L, et al. Antral pseudocysts of the maxillary sinus: relationship between radiographic and clinical features. *JORDI Journal of Oral Diagnosis.* 2017; 2: 1–7, doi: [10.5935/2525-5711.20170042](https://doi.org/10.5935/2525-5711.20170042).
38. Rodrigues CD, Freire GF, Silva LB, et al. Prevalence and risk factors of mucous retention cysts in a Brazilian population. *Dentomaxillofac Radiol.* 2009; 38(7): 480–483, doi: [10.1259/dmfr/48774803](https://doi.org/10.1259/dmfr/48774803), indexed in Pubmed: [19767520](https://pubmed.ncbi.nlm.nih.gov/19767520/).
39. Ruprecht A, Batniji S, El-Newehi E. Mucous retention cyst of the maxillary sinus. *Oral Surg Oral Med Oral Pathol.* 1986; 62(6): 728–731, doi: [10.1016/0030-4220\(86\)90271-9](https://doi.org/10.1016/0030-4220(86)90271-9).
40. Shin SH, Heo WW. Effects of unilateral naris closure on the nasal and maxillary sinus mucosa in rabbit. *Auris Nasus Larynx.* 2005; 32(2): 139–143, doi: [10.1016/j.anl.2005.01.015](https://doi.org/10.1016/j.anl.2005.01.015), indexed in Pubmed: [15917170](https://pubmed.ncbi.nlm.nih.gov/15917170/).
41. Stallman JS, Lobo JN, Som PM. The incidence of concha bullosa and its relationship to nasal septal deviation and paranasal sinus disease. *AJNR Am J Neuroradiol.* 2004; 25(9): 1613–1618, indexed in Pubmed: [15502150](https://pubmed.ncbi.nlm.nih.gov/15502150/).
42. Tawakir K, Yilmaz T, Surucu S, et al. Scanning electron microscopy of ciliae and saccharine test for ciliary function in septal deviations. *Laryngoscope.* 2006; 116(4): 586–590, doi: [10.1097/01.MLG.0000205608.50526.28](https://doi.org/10.1097/01.MLG.0000205608.50526.28), indexed in Pubmed: [16585863](https://pubmed.ncbi.nlm.nih.gov/16585863/).
43. van Egmond MM, Rovers MM, Hendriks CTM, et al. Effectiveness of septoplasty versus non-surgical management for nasal obstruction due to a deviated nasal septum in adults: study protocol for a randomized controlled trial. *Trials.* 2015; 16: 500, doi: [10.1186/s13063-015-1031-4](https://doi.org/10.1186/s13063-015-1031-4), indexed in Pubmed: [26537948](https://pubmed.ncbi.nlm.nih.gov/26537948/).
44. Wang JH, Jang YJu, Lee BJ. Natural course of retention cysts of the maxillary sinus: long-term follow-up results. *Laryngoscope.* 2007; 117(2): 341–344, doi: [10.1097/01.mlg.0000250777.52882.7a](https://doi.org/10.1097/01.mlg.0000250777.52882.7a), indexed in Pubmed: [17277631](https://pubmed.ncbi.nlm.nih.gov/17277631/).
45. Yalçın M, Laçin N. Is the relationship of maxillary molar roots to the floor of the maxillary sinus associated with antral pseudocysts? A retrospective study using cone beam computed tomography. *Oral Surg Oral Med Oral Pathol Oral Radiol.* 2020; 130(5): 574–582, doi: [10.1016/j.oooo.2020.05.003](https://doi.org/10.1016/j.oooo.2020.05.003), indexed in Pubmed: [32546427](https://pubmed.ncbi.nlm.nih.gov/32546427/).
46. Yasan H, Doğru H, Baykal B, et al. What is the relationship between chronic sinus disease and isolated nasal septal deviation? *Otolaryngol Head Neck Surg.* 2005; 133(2): 190–193, doi: [10.1016/j.otohns.2005.04.013](https://doi.org/10.1016/j.otohns.2005.04.013), indexed in Pubmed: [16087012](https://pubmed.ncbi.nlm.nih.gov/16087012/).

Anatomical characteristics and significance of the metopism and Wormian bones in dry adult-Chinese skulls

J.-H. Li^{1*}, Z.-J. Chen^{1*}, W.-X. Zhong^{1*}, H. Yang¹, D. Liu^{1, 2}, Y.-K. Li¹

¹School of Traditional Chinese Medicine, Southern Medical University, Guangzhou, Guangdong, P.R. China

²Department of Rehabilitation Medicine, the Third Affiliated Hospital, Southern Medical University, Guangzhou, Guangdong, P.R. China

[Received: 28 October 2021; Accepted: 29 December 2021; Early publication date: 21 January 2022]

Background: This study aimed to investigate the incidence, topographical distribution, morphology, and interrelationship of the metopism and Wormian bones (WBs) in dry adult-Chinese skulls.

Materials and methods: In this study, 285 dried adult-Chinese skull specimens from the Department of Anatomy at the Southern Medical University were examined. The incidence of different types of metopism and WBs were recorded. The length of the metopic suture was measured using a flexible ruler. Additionally, the lengths and widths of the WBs were measured using a vernier calliper.

Results: The incidence of metopism and WBs in Chinese adults were estimated at 10.18% (29/285) and 63.86% (182/285), respectively. The metopism always accompanied WBs (26/29, 89.66%), but the WBs did not necessarily accompany metopism (26/182, 14.29%). The locations of the WBs in the order of decreasing incidence were the lambdoid suture (78.57%, 143/182), pterion (34.62%, 63/182), asterion (12.09%, 22/182), lambda (8.24%, 15/182), sagittal suture (4.95%, 9/182), and Inca bone (3.85%, 7/182). These locations differed in topographical distribution and morphological patterns.

Conclusions: Chinese adults differ in incidence of metopism and WBs from adults of other races, indicating racial differences. The characteristics of WBs vary depending on the cranial site of occurrence. The metopism always accompanies WBs, but the WBs do not necessarily accompany metopism. (Folia Morphol 2023; 82, 1: 166–175)

Key words: Chinese, skull, metopic suture, metopism, Wormian bones, anatomical characteristics

INTRODUCTION

The skull is the most complex skeletal structure in the human body. The skull of a young adult consists of 28 separate flat and irregular bones, most of which are connected by “cranial sutures” [39]. The metopic

suture (MS) is an important cranial suture connecting the bregma to the nasion in the cranial vault. It presumably helps the fetus pass smoothly through the birth canal and assists in brain development, along with the coronal, sagittal, and lambdoid sutures [7, 16].

Address for correspondence: Dr. Y.-K. Li, School of Traditional Chinese Medicine, Southern Medical University, No. 1838, North of Guangzhou Great Road, BaiYun District, Guangzhou, Guangdong Province, 510515, China, e-mail: ortho@smu.edu.cn

*These authors contributed equally to this work. J.-H. Li is the first author, Z.-J. Chen and W.-X. Zhong are the co-first.

This article is available in open access under Creative Common Attribution-Non-Commercial-No Derivatives 4.0 International (CC BY-NC-ND 4.0) license, allowing to download articles and share them with others as long as they credit the authors and the publisher, but without permission to change them in any way or use them commercially.

Closure of the MS typically occurs in infancy or early childhood, but the exact timing is controversial. Most researchers believe that this process is completed by the age of 7 years [40–42]. Incomplete closure of the MS leads to a persistent metopic suture (also known as the metopism or median frontal suture) in adults [3, 26, 44]. Metopism is usually considered a normal anatomical variant, but several researchers believe it is associated with clinically significant findings [41, 44].

Wormian bones (WBs, also known as the isolated sutural bones or supernumerary bones) are irregularly shaped bones formed from additional ossification centres and almost always located in or near the cranial sutures and fontanelles [9, 27]. The isolated bone at the lambda is often referred to as Goethe's ossicle, or the Inca bone due to its prevalence in the skulls of the Incas (South American Indians) [39]. These WBs are present as one or more pterion ossicles or epipteric bones in the pterion and as os Kerckring in bregma [8]. As with metopism, WBs have pathological and diagnostic implications, and their incidence varies among different populations [27]. WBs distinguished normal variation or pathology from its number, arrangement pattern, and size as important factors [17, 22].

Although metopism and WBs have been reported in various ethnic populations, few related large-scale studies on Chinese adults have been performed. Therefore, this study aimed to investigate the incidence, number, morphology, and topographical distribution of the metopism and WBs and the interrelationships among these characteristics in Chinese adults.

MATERIALS AND METHODS

Materials

For this study, 285 dried skull specimens of Chinese adults with unknown age and sex were obtained from the Department of Anatomy of the Southern Medical University in China (the exclusion criteria were damaged skulls, such as those with trauma or pathology affecting the measurement parameters, and skulls of children). All the specimens were from cadaver donations, and written informed consent had been obtained from the donors. To precisely identify the cranial sutures and assess their structural integrity, all the skull specimens were cleaned and dried.

Methods

Firstly, we assessed the incidence, number, and shape of the metopism and WBs in the specimens.

Metopism can be partial (incomplete) or complete. The partial type extends upward from the nasion or downward from the bregma; the complete type connects the bregma to the nasion [44]. Following a previously described method, only the small bones surrounded by the suture were recorded as WBs [27]. Then, the length of the metopic suture was measured (accuracy ± 0.1 mm) using a soft ruler (Martin measure instrument). The lengths and widths of the WBs were measured using a digital vernier calliper (accuracy ± 0.01 mm) (Wuxi Kaibaoding Tool Co., Ltd., China).

The above measurements were independently performed by 2 researchers, each researcher taking 3 measurements (6 measurements in total) per parameter to calculate the mean \pm standard deviation (SD). The researchers who performed the measurements had > 2 years of experience in measurements and were uniformly trained to reduce systematic errors. Digital image acquisition (D610 type camera, Nikon) and processing (Photoshop 2020; Adobe Illustrator 2020, Adobe) were performed after the measurements were completed.

All the methods in this study followed the guidelines of the Helsinki Declaration. Ethical approval for this study was obtained from the Chinese Ethics Committee of Registering Clinical Trials (Reference number: ChiECRCT20210191).

Statistical analysis

The IBM SPSS Statistics 26.0 software for Windows was used to perform statistical analyses. The measurements were expressed as mean \pm SD ($\bar{x} \pm s$). The normality of the data was assessed using the Kolmogorov-Smirnov test. The paired samples t-test or Wilcoxon signed-rank test was used to determine whether the length and width of the bone were consistent. Statistical significance was determined by $p < 0.05$ for all the analyses.

Inter- and intra-observer reliability was determined by calculating the intra-class correlation coefficient (ICC) with a confidence interval (CI) of 95%. $ICC \leq 0.4$, $0.41 \leq ICC \leq 0.60$, $0.61 \leq ICC \leq 0.80$, and $0.81 \leq ICC < 1$ were considered to indicate poor, moderate, good, and very good agreement among the measurements, respectively. The ICC value of 1 indicates perfect reliability [43]. The ICCs of all the measurements were > 0.90 , indicating very good inter- and intra-observer agreement.

Consent to participate

All the methods in the study were carried out following the Helsinki guidelines and declaration.

Table 1. Incidence of metopism in different ethnic groups (in descending order of incidence)

No.	Author(s)	Year	Population	Specimen number (n)	Incidence (%)
1	Zdilla et al. [44]	2018	East Asian	13	15.38%
			European	62	8.06%
			Bengali	35	2.86%
			Egyptian	91	2.20%
2	Present study	2021	Chinese	285	10.18%
3	Brothwell [11]	1981	Iron Age Romano-British	NA	9.91%
			London (17 th C.)	NA	9.09%
			Lachish	NA	8.81%
			German	NA	8.37%
			Anglo-Saxon	NA	8.30%
			Chinese	NA	8.17%
			Ancient Egyptian	NA	3.87%
			Peruvian	NA	2.56%
			Melanesian	NA	2.02%
			N. American Indian	NA	1.45%
			Polynesian	NA	1.33%
			African Negro	NA	1.23%
			Australian	NA	0.63%
			Eskimo	NA	0.28%
4	Bilgin et al. [10]	2013	NA	631	9.7%
5	Çalışkan et al. [13]	2018	Turkish	185	8.1%
6	Cirpan et al. [14]	2016	Turkish	160	7.5%
7	Aksu et al. [4]	2014	West Anatolian	160	7.5%
8	Guerram et al. [20]	2014	European	143	4.41%
9	Ajmani et al. [3]	1983	Nigerian	206	3.4%
10	Agarwal et al. [1]	1979	Indian	1276	2.66%
11	Baaten et al. [5]	2003	Lebanese	NA	1.75%
12	Murlimanju et al. [26]	2011	Indian	81	1.2%

NA — not available

Ethical approval for this study was obtained from the Chinese Ethics Committee of Registering Clinical Trials (Reference number: ChiECRCT20210191).

RESULTS

The incidence and characteristics of the metopism

Among all the specimens, 29 metopism cases were detected, corresponding to 10.18% (29/285) incidence, which differs from the incidence in other ethnic populations (Table 1) [1, 3–5, 10, 11, 13, 14, 20, 26, 44]. Of them, 27 and 2 cases were the complete and partial types (downward from the bregma), respectively. The mean length of the complete type was 12.13 ± 0.62 cm (range: 11.25–13.34 cm), and the partial type was 9.3 cm long on average (8.72 and 9.88 cm) (Fig. 1).

The incidence of WBs

Among the specimens, 182 had WBs, corresponding to 63.86% (182/285) incidence, which differs from the incidence in other ethnic populations (Table 2) [8, 11, 14, 15, 18, 23, 27, 32]. The locations of the WBs in the order of decreasing prevalence were as follows: the lambdoid suture (78.57%, 143/182), pterion (34.62%, 63/182), asterion (12.09%, 22/182), lambda (8.24%, 15/182), sagittal suture (4.95%, 9/182), and Inca bone (3.85%, 7/182).

The characteristics of the WBs in lambdoid, sagittal, and coronal sutures

The WBs in the lambdoid sutures showed unilateral distribution in 51 (35.66%) cases and bilateral

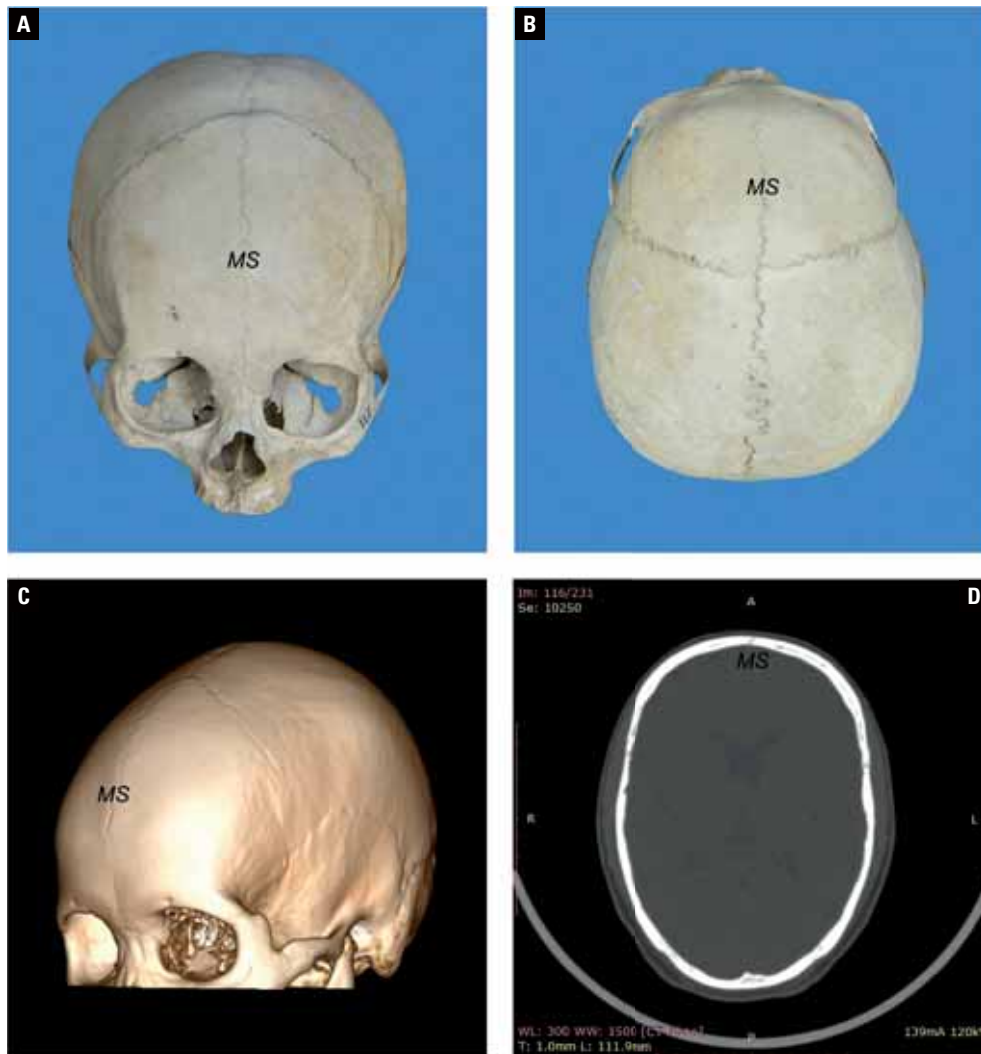


Figure 1. The anterior, superior, lateral, and cross-sectional views of the metopic suture (MS) (or metopism); **A.** Anterior view; **B.** Superior view; **C.** Three-dimensional visualisation of metopism via computer tomography (CT) (RadiAnt DICOM Viewer for windows); **D.** Metopism in a cranial CT cross-section.

in 92 (64.34%) cases. Of the lambdoid-suture WB cases, 29 had only 1 WB, 105 cases had 2–10 WBs, and 9 cases had > 10 WBs. There was no statistically significant difference in the number of WBs at the lateral level (right: 2.05 ± 2.24 ; left: 2.22 ± 2.17 ; $p > 0.05$). The majority of the WBs were parallel-fingered (with tentacles) (48.17%), elliptical (without tentacles) (24.08%), or single-fingered (with tentacles) (17.8%); the remaining minority was polygonal, round, triangular, or in another shape. The mean length and width of these bones were 1.37 ± 0.54 cm (range: 0.27–3.11 cm) and 0.79 ± 0.63 cm (range: 0.15–6.23 cm), respectively; the mean length was significantly greater than the mean width ($p < 0.001$).

We also detected 9 cases of WBs in the sagittal suture, which were located in the pars obelica and

pars lambdica of the suture. They were quadrilateral (44.44%), oval (33.33%), or finger-shaped (22.23%). The mean length and width of these WBs were 1.70 ± 0.30 cm (range: 1.35–1.91 cm) and 1.46 ± 0.79 cm (range: 0.6–2.15 cm), respectively; there was no statistical significance between the mean length and width. No WB was detected in the coronal suture (Fig. 2).

The characteristics of the WBs at the pterion and asterion

Of the cases with WBs around the pterion, 37 (58.73%) and 26 (41.27%) had unilaterally and bilaterally distributed WBs relative to the pterion, respectively. Of the bilateral cases, 20 were symmetrical in number and position. Most of the pterion WBs were

Table 2. Incidence of Wormian bones in different ethnic groups (In descending order of incidence)

No.	Author(s)	Year	Population	Specimen number (n)	Incidence (%)
1	Basnet et al. [8]	2019	Nepalese	70	88.57%
2	Natsis et al. [27]	2019	Greek	166	74.7%
3	Present study	2021	Chinese	285	63.86%
4	Cirpan et al. [15]	2015	West Anatolian	150	59.3%
5	Cirpan et al. [14]	2016	Turkish	160	59.3%
6	Ghosh et al. [18]	2017	Eastern part of India	120	45%
7	Khan et al. [23]	2011	Malaysian	25	24%
8	Ratnaningrum [32]	2020	Indonesian	69	15.9%
9	Brothwell [11]	1981	Chinese	NA	80.32%
			German	NA	75%
			Australian	NA	72.58%
			Iron Age Romano-British	NA	71.03%
			Melanesian	NA	64.15%
			Lachish	NA	63.41%
			Anglo-Saxon	NA	55.56%
			Ancient Egyptian	NA	55.56%
			Peruvian	NA	51.85%
			African Negro	NA	45.05%
			London (17 th C.)	NA	36.02%
			Polynesian	NA	29.92%
			N. American Indian	NA	28.18%
			Eskimo	NA	25%

NA — not available

epipteric (71.74%) (i.e. located at the intersection of the frontal, parietal, sphenoid, and temporal bones). However, some pterion WBs were around the squamosoparietal suture (13.04%), between the sphenotemporal and squamosoparietal (6.52%) or coronal and sphenoparietal (4.35%) sutures, or around the sphenofrontal (4.35%) or sphenotemporal (2.17%) suture. The pterion WBs were mostly quadrilateral (including rectangular, square, and rhombic; 69.7%), followed by triangular (21.2%), polygonal (6.06%), and circular (3.04%). The mean length and width of the pterion WBs were 1.87 ± 0.93 cm (range: 0.63–5.04 cm) and 1.07 ± 0.42 cm (range: 0.48–2.3 cm); their mean length was significantly greater than their mean width ($p < 0.001$).

The WBs at the asterion were mostly bilateral (66.64% vs. 33.36%, bilateral vs. unilateral, respectively). WBs were often found with the lambdoid suture (40.91%), squamosoparietal suture (27.27%), Inca bone (22.73%), or lambda bone (9.09%) (Fig. 3).

The characteristics of the Inca and lambda bones

We found that the lambda and Inca bones were distributed on the posterior side of the skulls. Among the cases with Inca bones, 4 had one bone mass, and 3 had two separated bones. Most of the Inca bones were triangular (4/7, 57.14%), but a significant fraction was polygonal (3/7, 42.86%). The mean length and width of these bones were 4.99 ± 0.57 cm (range: 4.5–5.8 cm) and 5.77 ± 4.46 cm (range: 2.7–12.4 cm), respectively; there was no statistical difference between the mean length and width ($p > 0.05$).

All the lambda bones were found in the posterior fontanelle and were single bones. They were triangular (42.86%, 3/7), circular (28.58%, 2/7), quadrilateral (14.28%, 1/7), or irregularly shaped (14.28%, 1/7). The mean length and width of these bones were 2.25 ± 1.31 cm (range: 0.56–4.08 cm) and 2.52 ± 1.62 cm (range: 0.4–5.02 cm), respectively; there was no statistical difference between the mean length and width ($p > 0.05$) (Fig. 4).

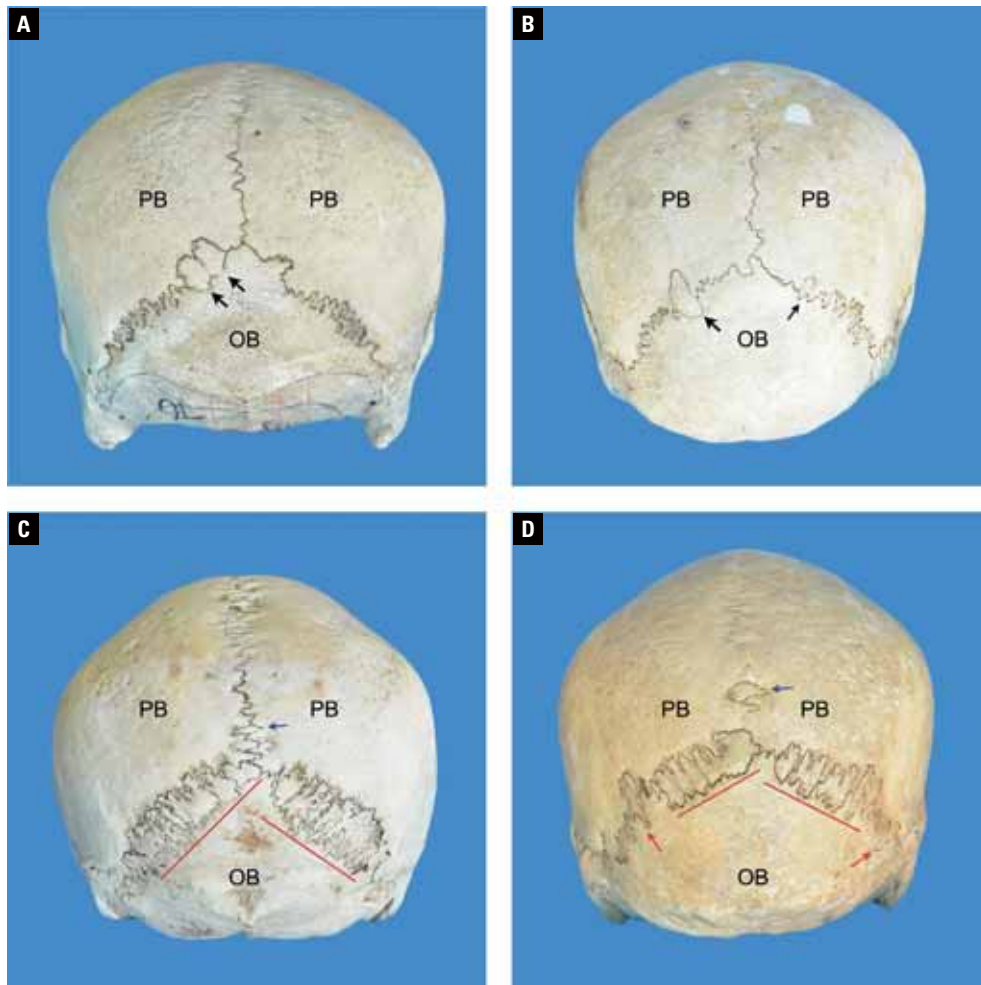


Figure 2. The Wormian bones (WBs) around the lambdoid and sagittal sutures; **A.** The two WBs are located on the same side of the lambdoid suture (black arrows); **B.** The two WBs are symmetrically located relative to the lambdoid suture and both oval-shaped (black arrows); **C, D.** The complex WBs bilaterally located relative to the lambdoid suture were in a parallel-fingered (red line) shape or single-fingered with tentacles (red arrows). WBs were also found around the sagittal suture (blue arrows); PB — parietal bone; OB — occipital bone.

The interrelationship between the metopism and WBs

Among the 29 cases of metopism, 26 concurrently had WBs (89.66%). These cases were only a sub-fraction (14.29%) of all the cases with WBs (182 cases).

DISCUSSION

In this study, we evaluated the number, shape, and size of the WBs in different cranial locations and summarized the anatomical characteristics of these bones. The WBs in the lambdoid suture were relatively small and numerous, with a wide range of variation in morphology; most of them were narrow finger-shaped or oval-shaped. The WBs at the pterion were more prominent in size and less in number compared with other location, they were mostly regular in shape and mainly epipteric bones. Unilaterally and bilaterally

distributed WBs were both observed at the lambdoid suture and pterion. However, the number of unilateral WBs at the lambdoid suture was lower than that of the bilateral ones. The bilateral WBs at the lambdoid suture was asymmetrical in number and location, whereas those at the pterion were mostly symmetrical. The WBs at the sagittal suture (lambda bone) were small in size, fixed in number and position, and mostly quadrilateral (small triangular) or oval (circular). The Inca bones were large, and primarily triangular. The WBs at the star point often concurred with WBs at other positions. The anatomical characteristics of WBs vary depending on the cranial site of occurrence.

The exact mechanism of WB formation remains unknown, and there are two major hypotheses. The first hypothesis suggests that formation of WBs is influenced by genetic factors [18]. The second hy-

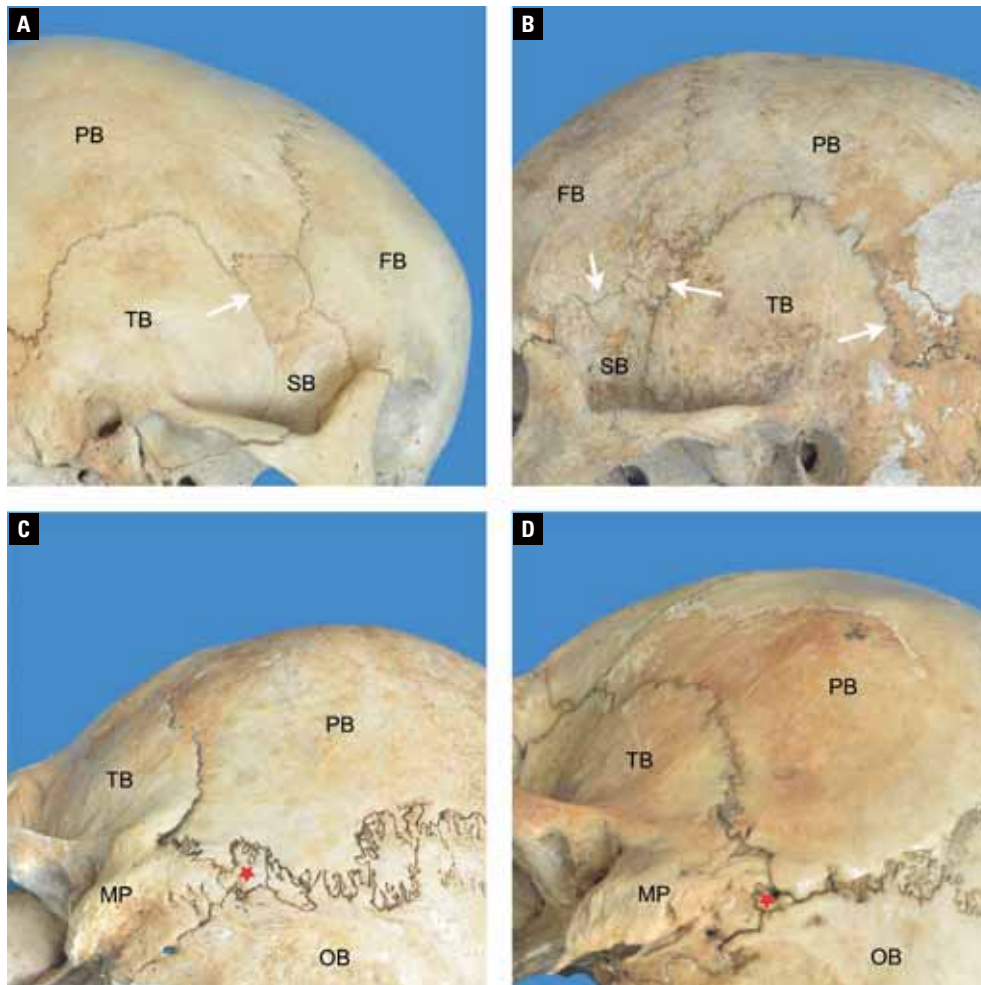


Figure 3. The Wormian bones (WBs) at the pterion and asterion; **A, B.** The WBs located at various locations near the pterion (white arrow); **C, D.** The WBs located at the asterion (red pentacle) appear together with the WBs around the lambdoid suture; FB — frontal bone; PB — parietal bone; TB — temporal bone; SB — sphenoid bone; OB — occipital bone; MP — mastoid process.

pothesis suggests that environmental factors (e.g. artificial cranial deformation) cause WBs to form. The higher occurrence of WBs in the occipital region than in the frontal region may be due to environmental factors [29, 34]. However, multiple scholars believe that genetic and environmental factors influence the locations and number of WBs formed, respectively.

As a normal variant, metopism does not have any medical or morphological implications. However, multiple researchers believe that it is usually associated with malformations in the frontal region (e.g. cranium bifidum, suprasellar teratoma, cleidocranial dysostosis, hypertelorism, and facial cleft) [41]. WBs are common in adults and are also often considered a normal anatomical variant. Kozerska et al. [24] have used microcomputed tomography to examine interseptal bones and found that these bones, like other cranial bones, have both dense and cancellous bone

tissues. However, occurrence of interseptal bones in children can be associated with numerous pathological conditions [27]. The presence of WBs in children is associated with developmental abnormalities in the central nervous system [31] (e.g. hydrocephalus [39], craniosynostosis [2], microcephaly, macrocephaly, cerebral palsy, epilepsy, and learning difficulties). Thus, the presence of WBs in children may serve as a marker for early diagnosis and treatment of paediatric central nervous system abnormalities. The presence of WBs can also be associated with certain types of congenital disorders (e.g. osteogenesis imperfecta [17, 36], Hajdu-Cheney syndrome [37], cleidocranial dysostosis [28], congenital hypothyroidism, rickets [25], limbic callosal syndrome [33] and Enlarged parietal foramina [30]).

During diagnosis or forensic identification, knowledge of metopism, WBs and craniosynostosis is es-

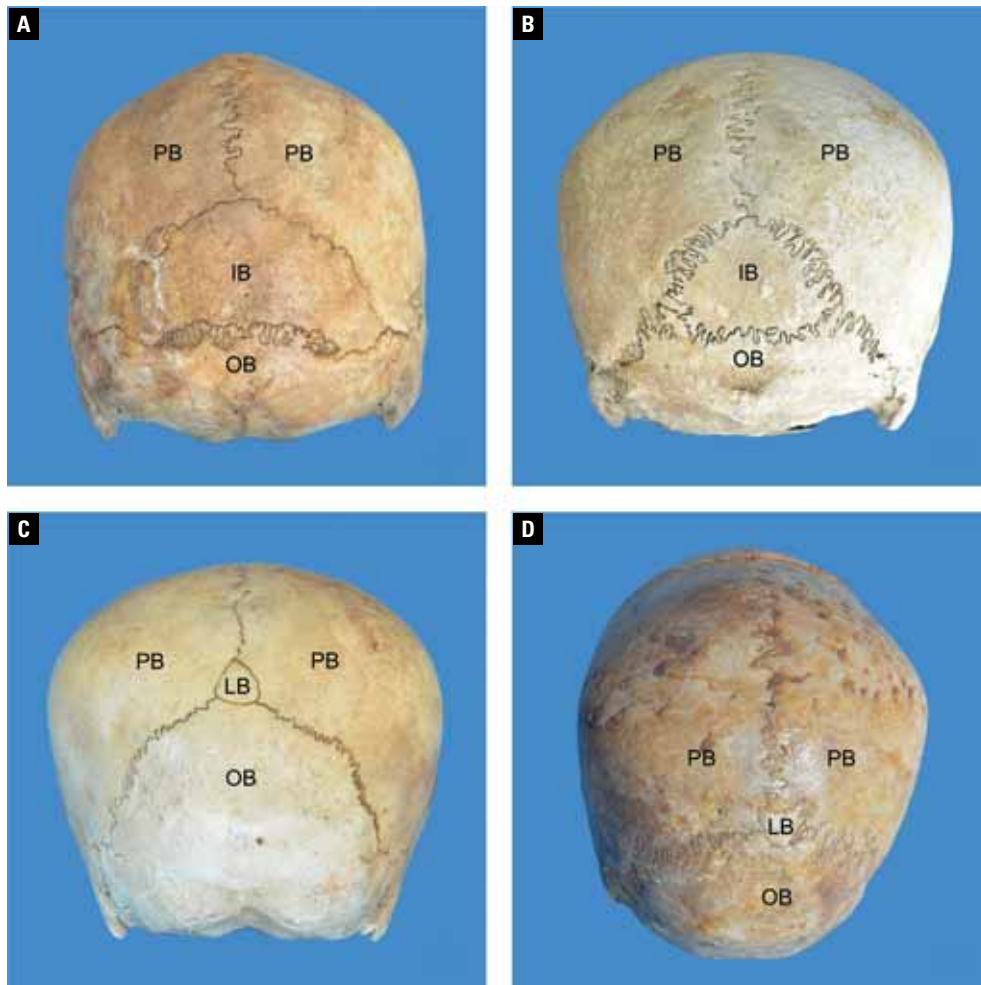


Figure 4. The Inca and lambda bones; **A, B.** Inca bones in the shape of large triangles; **C.** A lambda bone with a small triangular shape; **D.** An irregularly shaped lambda bone; PB — parietal bone; OB — occipital bone; IB — Inca bone; LB — lambda bone.

sential. Their presence may interfere with radiological assessment and forensic identification (easily confused with fractures or gunshot wounds) [6, 12, 19, 38]. Additionally, brain surgeons should always be cautious during a surgical operation because WBs may move and damage surrounding tissues, leading to complications [21, 35].

CONCLUSIONS

Chinese adults differ in incidence of metopism and WBs from adults of other races, indicating racial differences. The characteristics of WBs vary depending on the cranial site of occurrence. The metopism always accompanies WBs, but the WBs do not necessarily accompany metopism. These results may provide an anatomical basis for teaching, clinical practice, and forensic work.

Acknowledgements

The authors are grateful to the donors for donating their bodies to science and making anatomical research possible. Results from such research can potentially increase the overall knowledge of mankind and consequently improve patient care. Therefore, these donors and their families deserve our highest gratitude.

Funding

Supported by Sanming Project of Medicine in Shenzhen (No. SZZYSM202108013); Innovation Team and Talents Cultivation Program of National Administration of Traditional Chinese Medicine. (No: ZYY-CXTD-C-202003).

Conflict of interest: None declared

REFERENCES

- Agarwal SK, Malhotra VK, Tewari SP. Incidence of the metopic suture in adult Indian crania. *Acta Anat (Basel)*. 1979; 105(4): 469–474, doi: [10.1159/000145154](https://doi.org/10.1159/000145154), indexed in Pubmed: [552786](https://pubmed.ncbi.nlm.nih.gov/552786/).
- Agrawal D, Steinbok P, Cochrane DD. Pseudoclosure of anterior fontanelle by wormian bone in isolated sagittal craniosynostosis. *Pediatr Neurosurg*. 2006; 42(3): 135–137, doi: [10.1159/000091854](https://doi.org/10.1159/000091854), indexed in Pubmed: [16636612](https://pubmed.ncbi.nlm.nih.gov/16636612/).
- Ajmani ML, Mittal RK, Jain SP. Incidence of the metopic suture in adult Nigerian skulls. *J Anat*. 1983; 137 (Pt 1): 177–183, indexed in Pubmed: [6630031](https://pubmed.ncbi.nlm.nih.gov/6630031/).
- Aksu F, Cirpan S, Mas NG, et al. Anatomic features of metopic suture in adult dry skulls. *J Craniofac Surg*. 2014; 25(3): 1044–1046, doi: [10.1097/SCS.0000000000000564](https://doi.org/10.1097/SCS.0000000000000564), indexed in Pubmed: [24699103](https://pubmed.ncbi.nlm.nih.gov/24699103/).
- Baaten PJJ, Haddad M, Abi-Nader K, et al. Incidence of metopism in the Lebanese population. *Clin Anat*. 2003; 16(2): 148–151, doi: [10.1002/ca.10050](https://doi.org/10.1002/ca.10050), indexed in Pubmed: [12589670](https://pubmed.ncbi.nlm.nih.gov/12589670/).
- Bademci G, Kendi T, Agalar F. Persistent metopic suture can mimic the skull fractures in the emergency setting? *Neurocirugia (Astur)*. 2007; 18(3): 238–240, indexed in Pubmed: [17622463](https://pubmed.ncbi.nlm.nih.gov/17622463/).
- Barbeito-Andrés J, Bonfili N, Nogué JM, et al. Modeling the effect of brain growth on cranial bones using finite-element analysis and geometric morphometrics. *Surg Radiol Anat*. 2020; 42(7): 741–748, doi: [10.1007/s00276-020-02466-y](https://doi.org/10.1007/s00276-020-02466-y), indexed in Pubmed: [32266441](https://pubmed.ncbi.nlm.nih.gov/32266441/).
- Basnet LM, Shrestha S, Sapkota S. Prevalence of wormian bones in dried adult human skulls: an osteo-morphometric study in Nepal. *Anat Sci Int*. 2019; 94(1): 101–109, doi: [10.1007/s12565-018-0454-x](https://doi.org/10.1007/s12565-018-0454-x), indexed in Pubmed: [30109567](https://pubmed.ncbi.nlm.nih.gov/30109567/).
- Bellary SS, Steinberg A, Mirzayan N, et al. Wormian bones: a review. *Clin Anat*. 2013; 26(8): 922–927, doi: [10.1002/ca.22262](https://doi.org/10.1002/ca.22262), indexed in Pubmed: [23959948](https://pubmed.ncbi.nlm.nih.gov/23959948/).
- Bilgin S, Kantarcı UH, Duymus M, et al. Association between frontal sinus development and persistent metopic suture. *Folia Morphol*. 2013; 72(4): 306–310, doi: [10.5603/fm.2013.0051](https://doi.org/10.5603/fm.2013.0051), indexed in Pubmed: [24402751](https://pubmed.ncbi.nlm.nih.gov/24402751/).
- Brothwell DR. *Digging Up Bones: The Excavation, Treatment, and Study of Human Skeletal Remains*. 3rd ed. Cornell University Press, New York 1981.
- Budinich M, Burgess B, Fisahn C, et al. A previously unreported variant of the synostotic sagittal suture: Case report and review of salient literature. *Transl Res Anat*. 2016; 5: 12–14, doi: [10.1016/j.tria.2016.12.001](https://doi.org/10.1016/j.tria.2016.12.001).
- Çalışkan S, Oğuz KK, Tunali S, et al. Morphology of cranial sutures and radiologic evaluation of the variations of intersutural bones. *Folia Morphol*. 2018; 77(4): 730–735, doi: [10.5603/FM.a2018.0030](https://doi.org/10.5603/FM.a2018.0030), indexed in Pubmed: [29569704](https://pubmed.ncbi.nlm.nih.gov/29569704/).
- Cirpan S, Aksu F, Mas N, et al. Coexistence of wormian bones with metopism, and vice versa, in adult skulls. *J Craniofac Surg*. 2016; 27(2): 493–495, doi: [10.1097/SCS.0000000000002370](https://doi.org/10.1097/SCS.0000000000002370), indexed in Pubmed: [26845093](https://pubmed.ncbi.nlm.nih.gov/26845093/).
- Cirpan S, Aksu F, Mas N. The incidence and topographic distribution of sutures including wormian bones in human skulls. *J Craniofac Surg*. 2015; 26(5): 1687–1690, doi: [10.1097/SCS.0000000000001933](https://doi.org/10.1097/SCS.0000000000001933), indexed in Pubmed: [26114515](https://pubmed.ncbi.nlm.nih.gov/26114515/).
- Cornelissen MJ, Söfteland M, Apon I, et al. Perinatal complications in patients with unsutural craniosynostosis: An international multicentre retrospective cohort study. *J Cranio-maxillofac Surg*. 2017; 45(11): 1809–1814, doi: [10.1016/j.jcms.2017.08.012](https://doi.org/10.1016/j.jcms.2017.08.012), indexed in Pubmed: [28935489](https://pubmed.ncbi.nlm.nih.gov/28935489/).
- Cremin B, Goodman H, Spranger J, et al. Wormian bones in osteogenesis imperfecta and other disorders. *Skeletal Radiol*. 1982; 8(1): 35–38, doi: [10.1007/BF00361366](https://doi.org/10.1007/BF00361366), indexed in Pubmed: [7079781](https://pubmed.ncbi.nlm.nih.gov/7079781/).
- Ghosh SK, Biswas S, Sharma S, et al. An anatomical study of wormian bones from the eastern part of India: is genetic influence a primary determinant of their morphogenesis? *Anat Sci Int*. 2017; 92(3): 373–382, doi: [10.1007/s12565-016-0342-1](https://doi.org/10.1007/s12565-016-0342-1), indexed in Pubmed: [27038026](https://pubmed.ncbi.nlm.nih.gov/27038026/).
- Govsa F, Ozer MA, Bayraktaroglu S, et al. Anatomoradiological identification of intrasutural bones for importance of cranial fracture. *Turk Neurosurg*. 2014; 24(3): 357–362, doi: [10.5137/1019-5149.JTN.8380-13.2](https://doi.org/10.5137/1019-5149.JTN.8380-13.2), indexed in Pubmed: [24848174](https://pubmed.ncbi.nlm.nih.gov/24848174/).
- Guerram A, Le Minor JM, Renger S, et al. Brief communication: The size of the human frontal sinuses in adults presenting complete persistence of the metopic suture. *Am J Phys Anthropol*. 2014; 154(4): 621–627, doi: [10.1002/ajpa.22532](https://doi.org/10.1002/ajpa.22532), indexed in Pubmed: [24888448](https://pubmed.ncbi.nlm.nih.gov/24888448/).
- Guerrero Jazo FJ, Tovar Spinoza Z, Esparza Gutiérrez SV, et al. Rupture or traumatic dislocation of cranial suture on infants, involvement of the lambdoidal accessory bones (Wormian bones): case presentation and analysis. *Childs Nerv Syst*. 2019; 35(11): 2233–2236, doi: [10.1007/s00381-019-04153-9](https://doi.org/10.1007/s00381-019-04153-9), indexed in Pubmed: [31037423](https://pubmed.ncbi.nlm.nih.gov/31037423/).
- Kaplan SB, Kemp SS, Oh KS. Radiographic manifestations of congenital anomalies of the skull. *Radiol Clin North Am*. 1991; 29(2): 195–218, indexed in Pubmed: [1998047](https://pubmed.ncbi.nlm.nih.gov/1998047/).
- Khan AA, Asari MA, Hassan A. Unusual presence of Wormian (sutural) bones in human skulls. *Folia Morphol*. 2011; 70(4): 291–294, indexed in Pubmed: [22117248](https://pubmed.ncbi.nlm.nih.gov/22117248/).
- Kozerska M, Skrzat J, Walocha J, et al. Imaging of the Wormian bones using microcomputed tomography. *Folia Med Cracov*. 2013; 53(4): 21–28, indexed in Pubmed: [25556508](https://pubmed.ncbi.nlm.nih.gov/25556508/).
- Marti B, Sirinelli D, Maurin L, et al. Wormian bones in a general paediatric population. *Diagn Interv Imaging*. 2013; 94(4): 428–432, doi: [10.1016/j.diii.2013.01.001](https://doi.org/10.1016/j.diii.2013.01.001), indexed in Pubmed: [23352712](https://pubmed.ncbi.nlm.nih.gov/23352712/).
- Murlimanju BV, Prabhu LV, Pai MM, et al. Median frontal sutures — incidence, morphology and their surgical, radiological importance. *Turk Neurosurg*. 2011; 21(4): 489–493, indexed in Pubmed: [22194105](https://pubmed.ncbi.nlm.nih.gov/22194105/).
- Natsis K, Piagkou M, Lazaridis N, et al. Incidence, number and topography of Wormian bones in Greek adult dry skulls. *Folia Morphol*. 2019; 78(2): 359–370, doi: [10.5603/FM.a2018.0078](https://doi.org/10.5603/FM.a2018.0078), indexed in Pubmed: [30155873](https://pubmed.ncbi.nlm.nih.gov/30155873/).
- Nikolova SY, Toneva DH, Yordanov YA, et al. Multiple Wormian bones and their relation with definite pathological conditions in a case of an adult cranium. *Anthropol Anz*. 2014; 71(3): 169–190, doi: [10.1127/0003-5548/2014/0355](https://doi.org/10.1127/0003-5548/2014/0355), indexed in Pubmed: [25065115](https://pubmed.ncbi.nlm.nih.gov/25065115/).
- O’Loughlin VD. Effects of different kinds of cranial deformation on the incidence of wormian bones. *Am J Phys Anthropol*. 2004; 123(2): 146–155, doi: [10.1002/ajpa.10304](https://doi.org/10.1002/ajpa.10304), indexed in Pubmed: [14730648](https://pubmed.ncbi.nlm.nih.gov/14730648/).

30. Piagkou M, Skotsimara G, Repousi E, et al. Enlarged parietal foramina: a rare finding in a female Greek skull with unusual multiple Wormian bones and a rich parietal vascular network. *Anat Sci Int.* 2013; 88(3): 175–180, doi: [10.1007/s12565-013-0173-2](https://doi.org/10.1007/s12565-013-0173-2), indexed in Pubmed: [23543411](https://pubmed.ncbi.nlm.nih.gov/23543411/).
31. Pryles CV, Khan AJ. Wormian bones. *Am J Dis Child.* 1979; 133(4): 380–382, doi: [10.1001/archpedi.1979.02130040034007](https://doi.org/10.1001/archpedi.1979.02130040034007), indexed in Pubmed: [433853](https://pubmed.ncbi.nlm.nih.gov/433853/).
32. Ratnaningrum S. Identification of sutural bones in Indonesian skulls. *Transl Res Anat.* 2020; 18: 100061, doi: [10.1016/j.tria.2019.100061](https://doi.org/10.1016/j.tria.2019.100061).
33. Reid TH, Tam A, Antoniou G, et al. Anterior fontanelle Wormian bone with exomphalos major and dysmorphic facial features: a previously unseen association? *J Craniofac Surg.* 2016; 27(7): 1799–1801, doi: [10.1097/SCS.0000000000002962](https://doi.org/10.1097/SCS.0000000000002962), indexed in Pubmed: [27513767](https://pubmed.ncbi.nlm.nih.gov/27513767/).
34. Sanchez-Lara PA, Graham JM, Hing AV, et al. The morphogenesis of wormian bones: a study of craniosynostosis and purposeful cranial deformation. *Am J Med Genet A.* 2007; 143A(24): 3243–3251, doi: [10.1002/ajmg.a.32073](https://doi.org/10.1002/ajmg.a.32073), indexed in Pubmed: [18000970](https://pubmed.ncbi.nlm.nih.gov/18000970/).
35. Saylisoy S. Is there a coexistence of peritemporal wormian bone and congenital aural atresia? *J Comput Assist Tomogr.* 2020; 44(4): 559–561, doi: [10.1097/RCT.0000000000001047](https://doi.org/10.1097/RCT.0000000000001047), indexed in Pubmed: [32697526](https://pubmed.ncbi.nlm.nih.gov/32697526/).
36. Semler O, Cheung MS, Glorieux FH, et al. Wormian bones in osteogenesis imperfecta: Correlation to clinical findings and genotype. *Am J Med Genet A.* 2010; 152A(7): 1681–1687, doi: [10.1002/ajmg.a.33448](https://doi.org/10.1002/ajmg.a.33448), indexed in Pubmed: [20583157](https://pubmed.ncbi.nlm.nih.gov/20583157/).
37. Shah AB, Tisano BK, Elattar O, et al. Foot deformities in hajdu-cheney syndrome: a rare case report and review of the literature. *J Orthop Case Rep.* 2017; 7(5): 11–15, doi: [10.13107/jocr.2250-0685.876](https://doi.org/10.13107/jocr.2250-0685.876), indexed in Pubmed: [29242787](https://pubmed.ncbi.nlm.nih.gov/29242787/).
38. Sidpra J, Jeelani NU, Ong J, et al. Skull fractures in abusive head trauma: a single centre experience and review of the literature. *Childs Nerv Syst.* 2021; 37(3): 919–929, doi: [10.1007/s00381-020-04870-6](https://doi.org/10.1007/s00381-020-04870-6), indexed in Pubmed: [32935234](https://pubmed.ncbi.nlm.nih.gov/32935234/).
39. Standring S. *Gray's Anatomy E-Book: The Anatomical Basis of Clinical Practice.* 42. Elsevier Health Sciences 2020.
40. Teager SJ, Constantine S, Lottering N, et al. Physiologic closure time of the metopic suture in South Australian infants from 3D CT scans. *Childs Nerv Syst.* 2019; 35(2): 329–335, doi: [10.1007/s00381-018-3957-9](https://doi.org/10.1007/s00381-018-3957-9), indexed in Pubmed: [30218142](https://pubmed.ncbi.nlm.nih.gov/30218142/).
41. Vinchon M. The metopic suture: Natural history. *Neurochirurgie.* 2019; 65(5): 239–245, doi: [10.1016/j.neuchi.2019.09.006](https://doi.org/10.1016/j.neuchi.2019.09.006), indexed in Pubmed: [31562880](https://pubmed.ncbi.nlm.nih.gov/31562880/).
42. Vu HL, Panchal J, Parker EE, et al. The timing of physiologic closure of the metopic suture: a review of 159 patients using reconstructed 3D CT scans of the craniofacial region. *J Craniofac Surg.* 2001; 12(6): 527–532, doi: [10.1097/00001665-200111000-00005](https://doi.org/10.1097/00001665-200111000-00005), indexed in Pubmed: [11711818](https://pubmed.ncbi.nlm.nih.gov/11711818/).
43. Walter SD, Eliasziw M, Donner A. Sample size and optimal designs for reliability studies. *Stat Med.* 1998; 17(1): 101–110, doi: [10.1002/\(sici\)1097-0258\(19980115\)17:1<101::aid-sim727>3.0.co;2-e](https://doi.org/10.1002/(sici)1097-0258(19980115)17:1<101::aid-sim727>3.0.co;2-e).
44. Zdilla MJ, Russell ML, Koons AW, et al. Metopism: a study of the persistent metopic suture. *J Craniofac Surg.* 2018; 29(1): 204–208, doi: [10.1097/SCS.0000000000004030](https://doi.org/10.1097/SCS.0000000000004030), indexed in Pubmed: [29049140](https://pubmed.ncbi.nlm.nih.gov/29049140/).

Morphological classification and clinical significance of medial malleolus based on computed tomography three-dimensional reconstruction

L. Xin¹*, K. Liu²*, B. He¹*, M. Chen³*, B. Tang¹, C. Tang¹, L. Zhang^{4, 5, 6, 7}*

¹Department of Orthopaedics, Jiang'an Hospital of Traditional Chinese Medicine, Yibin Sichuan, China

²Department of Radiology, Yibin Third People's Hospital, Yibin Sichuan, China

³Department of Internal Medicine, Jiang'an Hospital of Traditional Chinese Medicine, Yibin Sichuan, China

⁴Department of Orthopaedics, Affiliated Traditional Chinese Medicine Hospital of Southwest Medical University, Luzhou Sichuan, China

⁵Centre for Orthopaedic Diseases Research, Affiliated Traditional Chinese Medicine Hospital of Southwest Medical University, Luzhou Sichuan, China

⁶Expert Workstation in Luzhou, Luzhou Sichuan, China

⁷Clinical Base of Affiliated Traditional Chinese Medicine Hospital of Southwest Medical University, Guangdong Province Medical 3D Printing Application Transformation Engineering Technology Research Centre, Luzhou Sichuan, China

[Received: 5 September 2021; Accepted: 10 December 2021; Early publication date: 16 December 2021]

Background: Internal malleolus fractures and postoperative functional limitations are serious complications of deltoid ligament repair, reconstruction, while studies on conducting beak. Anatomical structure classification of medial malleolus at home and abroad is reported rarely. Hence, this morphological study is mainly designed to investigate the anatomical morphological classification and clinical significance of medial malleolus based on computed tomography (CT) three-dimensional reconstruction.

Materials and methods: From October 2018 to January 2021, 373 patients who underwent CT examination of malleolus medialis joint in the Jiang'an Hospital of Traditional Chinese Medicine were observed. The medial malleolus was observed and classified; then, geometric parameters were measured according to different medial malleolus types.

Results: According to the results of 373 cases, medial malleolus can be divided into four types: omega type (66%), radical sign type (16%), inverted triangle type (14%), and wave type (4%).

Conclusions: There are four main shapes: omega, inverted triangle, radical sign, and wave in the medial malleolus of all normal ankles. The measurement of medial malleolus parameters according to medial malleolus in different shapes was of importance to guide smooth operation of medial malleolus fixation and deltoid ligament reconstruction and epidemiological. (Folia Morphol 2023; 82, 1: 176–182)

Key words: medial malleolus, deltoid ligament, anatomical morphology, computed tomography three-dimensional reconstruction

Address for correspondence: Dr. L. Zhang, Department of Orthopaedics, Affiliated Traditional Chinese Medicine Hospital of Southwest Medical University, Luzhou, China, e-mail: zhanglei870722@126.com; Dr. L. Xin, Department of Orthopaedics, Jiang'an Hospital of Traditional Chinese Medicine, Yibin Sichuan, China, e-mail: 1258356206@qq.com

*These authors contributed equally to this work.

This article is available in open access under Creative Common Attribution-Non-Commercial-No Derivatives 4.0 International (CC BY-NC-ND 4.0) license, allowing to download articles and share them with others as long as they credit the authors and the publisher, but without permission to change them in any way or use them commercially.

INTRODUCTION

The deltoid ligament, originates from the lower margin of the medial malleolus, splits and terminates at the scaphoid, talus and anteromedial calcaneus. It is divided into deep and superficial layers [5, 25]. The superficial ligament consists of 4 bundles that are tibial navicular ligament, tibial spring ligament, tibial calcaneal ligament and tibial talus ligament in sequence. The deep layer consists of the anterior and posterior tibial talus ligaments [8, 15], and the construction is to keep the joint stable by limiting hyperpronation of the talus. The deltoid ligament is the main medial stabilizer of the ankle joint, preventing valgus and anterior talus displacement, and it is also the most important structure to prevent lateral displacement [2, 19, 23]. Overall, the deltoid ligament provides stability for the tibial talo-calcaneal complex. After injuries of deltoid ligament, the stability is weakened, as time goes by, gradually leading to a decrease in contact with the articular surface of the talus to the contralateral, also leading to an increase in contralateral stress on the articular surface [12, 13, 17] and an increase in joint wear. Studies have shown that the displacement of 1 mm will lose 42% of the relative contact area and increase 30% of the stress [2, 7, 16, 22]. Therefore, the triangular ligament should be repaired according to the anatomical and biomechanical characteristics in order to maximise the recovery of its biomechanical structure and tensile strength, and consequently the stability of the ankle, and to improve patient satisfaction after surgery.

The incidence of simple medial malleolus fracture accounts for 7% of all ankle fractures, about 3 times that of the lateral malleolus fractures [1, 14], while the deltoid ligament injury accounts for 6.6–15% of ankle injuries [9]. In clinical practice, fracture reduction and internal fixation is one of the most frequently surgery methods used for medial malleolus fracture at present. In the case of deltoid ligament injury, deltoid ligament reconstruction is the most common choice in foreign countries [10, 21], and repair of the triangular ligament is the most common choice in China [3, 11]. In recent years, reconstruction of the triangular ligament has been used in the treatment of flat foot [20] and has received good clinical results. During the fracture reduction and internal fixation reconstruction of the deltoid ligament, it is necessary to recovery the medial malleolus, and the selection of the location, size and internal thickness of the tunnel determines the success of the operation [18]. Superficial ligament is

visible intraoperatively, and the hole location is easy to be determined, which has been studied at home and abroad; because of the smaller malleolus medialis and complex surrounding anatomical structures, the deep ligaments itself is difficult to be positioned accurately [24], especially in the case of minimally invasive surgery in which the vision is limited. When drilling easy position offset internal malleolus fracture and postoperative functional limitations has become serious complications of deltoid ligament repair and reconstruction, and literatures conducting on beak. Anatomical structure classification of medial malleolus at home and abroad is reported rarely.

Therefore, the purpose of this study is to observe the anatomy of malleolus medialis, and to discuss the indications and contraindications of deltoid ligament reconstruction based on computed tomography (CT) three-dimensional (3D) reconstruction. It can also provide the effective anatomy basis for the deltoid ligament reconstruction, in order to reduce the risk of operation and to lower the incidence of postoperative complications.

MATERIALS AND METHODS

Materials

All patients undergoing 3D CT scan were screened from October 2018 to January 2021. A total of 373 subjects aged between 19 and 66 years were included in this study. There were 198 males and 175 females. There were 177 cases on the left side and 196 cases on the right side, with a mean age of 46.04 ± 10.35 years.

Inclusion criteria: (1) The development of tibia, medial malleolus and deltoid ligament was normal; (2) There was no history of medial malleolus or tibia fracture, and no history of deltoid ligament injury.

Exclusion criteria: (1) malformation of medial malleolus, talus or deltoid ligament; (2) A history of ankle surgery.

Methods

Scans of mid-lower tibia to calcaneus were obtained using a 16-row 128-slice spiral Siemens CT scanner, with patients lying in supine position. The scanned images were transferred to simulation software for 3D reconstruction and 1 mm thin sections.

Patients because of own or external damage, such as car accident sprain, no obvious cause of pain and other reasons below the knee and leg pain related symptoms need the CT scans. Then preliminary screening of the medial malleolus of all patients

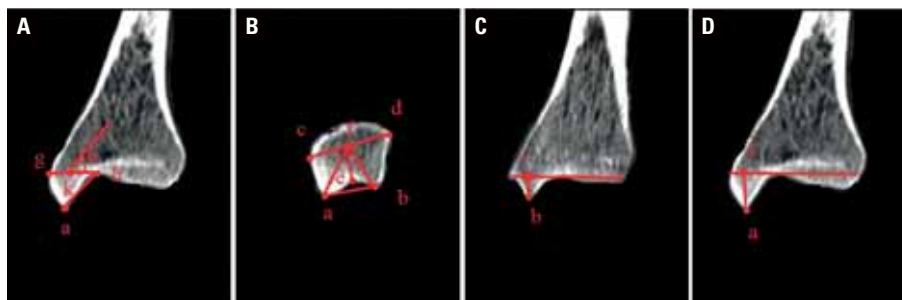


Figure 1. A–D. Morphological measurements were described as follows; ab — sagittal view, medial malleolus, distance between anterior and posterior colliculus (point a is the medial malleolus anterior colliculus, point b is the medial malleolus posterior colliculus); cd — medial malleolus anteroposterior to lips farthest distance (point c is the anterior labial protrusion of the medial malleolus; point d is the most protruding point of the posterior lip of the medial malleolus); ef — the distance from the anteriorly hump point of the medial malleolus to the midpoint of the anteriorly lip of the medial malleolus (point e is the anterior and posterior dune depression of the medial malleolus, point f is the midpoint of the distance between the front and back lips); bf — distance from posterior colliculus of medial malleolus to centre of anterior and posterior labial margin of medial malleolus; af — distance between medial malleolus anterior colliculus and medial malleolus anterior labial margin centre; bi — on the sagittal plane, the distance from posterior colliculus to tibial (point i is the point from point B where it intersects the vertical line of the articular surface of the tibial talus); $\angle\alpha$ — the angle between the midline and the horizontal line of the internal ankle joint; aj — distance from anterior colliculus to tibial joint surface (point j is the point from point a where it intersects the vertical line of the articular surface of the tibial talus).



Figure 2. A–D. The types of the medial malleolus.

undergoing 3D reconstruction was performed by two radiologists. Patients with fractures, malformations, surgical history, or whose age was not in the range of 19–66 years were excluded from the analysis. The medial malleolus was then carefully observed for any other inconspicuous symptoms. Any doubts regarding the classification were discussed and a joint decision was made. Then, geometric parameters were measured, taking the average of the final results. Otherwise, doubts were resolved by the director of radiology department. All the observers have worked in professional imaging for more than 10 years.

The shape of the medial malleolus was first observed and classified on the CT 3D reconstruction. Second, the clearest and most complete medial malleolus layer in the coronal and sagittal planes was selected by means of CT to measure geometric parameters and their adjacent structures, as it was shown in Figure 1.

Statistical analyses

Statistical analyses were performed using SPSS (version 20.0; IBM Corp.). All the measured data were showed by mean \pm standard deviation. The measured geometric parameters corresponding to the type of medial malleolus were analysed by one-way analysis of variance (LSD-t). $P < 0.05$ was considered to indicate a statistically significant difference.

RESULTS

According to the shape of the medial malleolus, it can be divided into omega type, inverted triangle type, wave type and radical sign type, as shown in Figure 2.

In the 3D reconstruction of adult medial malleolus, 248 (66%) cases were omega type, 52 (14%) cases were inverted triangle type, 12 (4%) cases were wave type and 61 (16%) cases were radical sign type. The measured geometric parameters corresponding to each type of medial malleolus were as shown in Table 1. There were significant differences in the af ($p = 0.000$)

Table 1. Measured values of the medial malleolus based on sides of the body and sexes

Distribution	Male	Female	Left	Right
Numbers	198 (53.08%)	175 (46.92%)	183 (49.06%)	190 (50.94%)
ab [cm]	14.73 ± 2.90	15.04 ± 3.15	14.97 ± 3.06	14.78 ± 2.98
cd [cm]	27.11 ± 3.87	27.60 ± 3.84	27.53 ± 3.87	27.16 ± 3.85
ef [cm]	11.04 ± 3.44	11.51 ± 3.21	11.06 ± 3.32	11.45 ± 3.36
af [cm]	16.45 ± 3.62	16.67 ± 3.45	16.36 ± 3.52	16.74 ± 3.58
bf [cm]	14.79 ± 3.51	14.66 ± 3.14	14.92 ± 2.34	14.73 ± 3.26
aj [cm]	12.71 ± 1.15	11.97 ± 1.61	12.63 ± 1.45	12.11 ± 1.86
bi [cm]	5.97 ± 2.05	5.79 ± 1.93	5.75 ± 1.95	6.03 ± 2.04
∠α [°]	45.04 ± 7.14	45.59 ± 7.21	45.12 ± 7.13	45.47 ± 7.23

Table 2. Morphological measurements in four types

	Inverted triangle type	Omega type	Radical sign type	Wave type
Numbers	52 (14%)	248 (66%)	61 (16%)	12 (4%)
ab [cm]	15.23 ± 3.87 ^{bc}	14.73 ± 2.89 ^c	16.50 ± 2.35 ^c	11.42 ± 0.61
cd [cm]	27.45 ± 3.86 ^{bc}	25.82 ± 3.98 ^b	29.44 ± 2.22	27.59 ± 3.64
ef [cm]	11.19 ± 3.73 ^{bc}	11.26 ± 3.36 ^{bc}	12.51 ± 2.62 ^c	8.31 ± 3.14
af [cm]	18.31 ± 2.54 ^{ac}	16.39 ± 3.63 ^b	17.94 ± 2.47 ^c	14.44 ± 4.51
bf [cm]	14.73 ± 3.33 ^c	14.99 ± 3.45 ^{bc}	13.59 ± 2.34 ^c	11.35 ± 4.35
aj [cm]	12.39 ± 1.85 ^c	12.61 ± 1.78	12.25 ± 1.63 ^c	8.15 ± 2.12
bi [cm]	5.21 ± 2.26 ^{ac}	6.06 ± 1.91	5.57 ± 2.06 ^c	6.98 ± 1.14
∠α [°]	45.36 ± 8.09 ^c	45.93 ± 6.43 ^{bc}	43.43 ± 8.30 ^c	38.07 ± 5.55

^ap < 0.05 vs. omega type, ^bp < 0.05 vs. radical sign type, ^cp < 0.05 vs. wave type

and bi ($p = 0.005$) between omega type and inverted triangle type. There were statistical differences in the ab ($p = 0.022$), cd ($p = 0.005$), and ef ($p = 0.035$) between inverted triangle type and radical sign type ($p < 0.05$). There were statistical differences in the ab ($p = 0.000$), ef ($p = 0.007$), af ($p = 0.000$), bf ($p = 0.002$), aj ($p = 0.000$), bi ($p = 0.005$), and $\angle\alpha$ ($p = 0.001$) between inverted triangle type and wave type. There were statistical differences in the cd ($p = 0.000$), ef ($p = 0.008$), af ($p = 0.001$), bf ($p = 0.003$), and $\angle\alpha$ ($p = 0.013$) between omega type and radical sign type ($p < 0.05$). There were statistical differences in the ab ($p = 0.000$), ef ($p = 0.003$), bf ($p = 0.000$), and $\angle\alpha$ ($p = 0.000$) between omega type and wave type. There were statistical differences in the cd ($p = 0.000$), ef ($p = 0.008$), af ($p = 0.001$), bf ($p = 0.003$), and $\angle\alpha$ ($p = 0.013$) between omega type and radical sign type ($p < 0.05$). There were statistical differences in the ab ($p = 0.000$), ef ($p = 0.000$), af ($p = 0.001$), bf ($p = 0.032$), aj ($p = 0.000$), bi ($p = 0.024$), and $\angle\alpha$ ($p = 0.016$) between wave type and radical sign type. The measured geometric

parameters corresponding to each type of medial malleolus were not significantly different between left and right, as shown in Table 2.

DISCUSSION

Ankle is the weight-bearing joint closest to the ground and the most important weight-bearing joint in the body [4]. The stability of the ankle joint plays a very important role in daily exercise and life. With the development of society and the improvement of people's living standard, ankle joint injury mostly occurs in people with strong athletic ability. Eighty five per cent of patients suffer from ankle sprain, which is one of the most common sports injuries; 40% of patients may have residual chronic symptoms, and approximately 5% of ankle injuries are associated with deltoid ligament injuries. However, recent studies have found that 40% to 73% of patients with chronic lateral ankle instability may suffer from deltoid ligament injuries [6]. The deltoid ligament is the strongest ligament in the ankle joint, and its main function is to prevent the ankle from valgus. It starts from the

medial malleolus, fanning down into a bundle and terminates in the scaphoid, talus, and calcaneus. For patients with ligament injury, ligament reconstruction can restore the stability of the ankle joint [10, 21].

Therefore, the treatment of deltoid ligament injury is the key to restore the function of the ankle joint. At present, the treatment of deltoid ligament injury in China mainly uses the suture anchor to repair the ligament [3, 11]. In foreign countries, ligament reconstruction is the main therapeutic method [10, 21]. Whether it is transosseous suture or wire repair, suture with suture anchors or newly developed ligament reconstruction, a borehole is required to establish the hole. The key to reconstruction lies in the diameter and location of the bone tunnel [18]. Improper pore size, position or drilling location can easily lead to unbecoming fixation of postoperative implants, resulting in surgical failure, redislocation, clavicle and coracoid process clefts, and bone fractures. At present, there are few clinical studies on indications and contraindications of the deltoid ligament repairing or reconstruction under different coracoid process shapes, which is also one of the reasons for the high risk of surgical failure and multiple postoperative complications. Therefore, the anatomical morphology of medial malleolus and the anatomical parameters related to the repair or reconstruction of the deltoid ligament need to be studied urgently.

The purpose of this study was to investigate the morphology of the medial malleolus and provide anatomic basis and predictive value for the treatment and surgical guidance of ankle joint injuries. In this study, the medial malleolus could be divided into four different types, among which the omega type accounted for the highest proportion. Most of the geometrical parameters and the anatomical parameters of their attachment points are different under diverse medial malleolus. Therefore, for the ankle injury patients with different medial malleolus shapes, individualised treatment should be paid attention to, so as to improve the success rate of internal fixation of medial malleolus fracture reduction, deltoid ligament repair or reconstruction, and reduce postoperative complications, especially the incidence of medial malleolus fracture. In addition, the attachment points of the deltoid ligament were studied to guide clinicians in selecting the location of bone tunnel drilling.

Among the four shapes of medial malleolus, af was the longest and aj was longer while bi was shorter corresponding to type v. It showed that the anterior

and posterior colliculus were diagonal, so the contact area between the V-shaped deltoid ligament and the medial malleolus was minor or even narrower, preventing excessive movement and other injuries of deltoid ligament caused by unbalanced factors or medial malleolus fractures. The anterior colliculus of the inverted-triangle medial malleolus is quite narrow, and theoretically the drilling location should be far away from the anterior colliculus, but the bi of the four types of medial malleolus is also shorter. Failure to drill in front of the medial malleolus when the bone tunnel is drilled may result in changes in biomechanics after deltoid ligament repair. Therefore, the inverted-triangle medial malleolus should not be fixed with the deltoid ligament of the tunnel, and the medial malleolus upward wire anchor should be considered. The corresponding ab, cd and ef of the radical sign type are the longest, while the aj, bi and $\angle\alpha$ are minor. The radical sign type is similar to the inverted triangle type, and the two joints are oblique and the distance is large. The corresponding population should take protective measures to avoid deltoid ligament injury and medial malleolus fracture caused by imbalanced factors or strenuous exercise. Therefore, when the deltoid ligament corresponding to the radical sign type is broken or the medial malleolus fractures, and the bone volume of medial malleolus of the radical sign type is small, the probability of medial malleolus fractures increases during drilling. In addition, the anterior colliculus is short and the annular structure is prone to slippage. Therefore, when the deltoid ligament corresponding to the medial malleolus of radical sign type is broken or the medial malleolus fractures, it is not appropriate to use deltoid ligament reconstruction, but suture anchor fixation can be adopted. Except the cd and bi, medial malleolus of the wave type are the longest, while the ab, ef, af, bf, aj and $\angle\alpha$ are the smallest. The distance between the two colliculi is short, showing a relatively horizontal line. The distance between the two mounds, the upper and lower lips of the medial malleolus, is the smallest, and the overall height between the two lips, the upper and lower mounds, is the smallest. Theoretically, the contact area between the medial malleolus and the deltoid ligament of the wave type is relatively wide, and there is more bone in the medial malleolus hilum, and the amount of bone in the hilum of the medial malleolus is more, and the anatomical structure is appropriate. Therefore, deltoid ligament reconstruction can be recommend-

ed for the treatment of deltoid ligament injury. Of the omega type, aj and bi were the largest, but the distance was small, cd was the smallest, ab and ef were smaller. Theoretically, the distance between the two colliculi and grooves to the two lips is small, and the volume of the medial malleolus bone is larger, so the anatomical structure is appropriate. Therefore, it is recommended to carry out deltoid ligament reconstruction to treat the deltoid ligament injury. The ef of inverted triangle type was 11.19 ± 3.73 cm, and that of the omega type was 11.26 ± 3.36 cm. For deltoid ligament reconstruction or internal fixation, the locations of inverted triangle type and omega type tunnels were approximately the same. The measure of $\angle\alpha$ of wave type was $38.07 \pm 5.55^\circ$, omega type was $45.93 \pm 6.43^\circ$, inverted triangle type was $45.36 \pm 8.09^\circ$, radical sign type was $43.43 \pm 8.30^\circ$. The measures of $\angle\alpha$ of wave type and radical sign type were smaller. The medial malleolus was slightly horizontal, and the $\angle\alpha$ of omega type and inverted triangle type were larger, which were more vulnerable to external force injury and fracture. Wear high heels less in daily life, because the external force collision can affect the selection of fixation angle and direction of clinical internal fixators. Above all, different treatment plans and materials should be used to repair medial malleolus fractures and deltoid ligaments of different shapes.

Limitations of the study

There are some limitations in this study. Only patients from southwest China were collected, mostly from rural areas, and the sample size was small. In this study, further biomechanical studies could be performed to investigate whether the geometric parameters corresponding to the w-shaped and v-shaped deltoid ligament are shorter, thinner or easier to break. In this study, only the relevant classification and anatomical data of the medial malleolus and the possible mechanism of related diseases were discussed, and further data tracking and improvement are needed.

CONCLUSIONS

The medial malleolus of all normal ankles has four main shapes: omega, inverted triangle, radical sign, and wave. Medial malleolus of omega type and wave type are more suitable for internal fixation, ligament repair and reconstruction, while inverted triangle type and radical sign type have the narrowest

colliculi. Therefore, deltoid ligament reconstruction is generally not appropriate, and internal fixation with thread anchors is preferred. Wave-shaped and radical-sign-shaped medial malleolus have a smaller angle, and the medial malleolus is slightly inclined and horizontal. Omega and inverted triangle have a larger medial malleolus angle, which is more vulnerable to external force and violence injury resulting in fracture. Determining the corresponding measurement parameters according to medial malleolus in different shapes is of significance to guide smooth operation of medial malleolus fixation and deltoid ligament reconstruction surgery.

Acknowledgements

The authors wanted to show their gratitude to the imaging department in Jiang'an Hospital of Traditional Chinese Medicine that provided the samples.

Funding

The study received grants from the National Natural Science Foundation of China (No. 82004458); Traditional Chinese Medicine Research Project of Sichuan Traditional Chinese Medicine Administration (No. 2020JC0138); Health Commission of Sichuan Province Science and Research Project (No. 20PJ143); Luzhou People's Government-Southwest Medical University Shi-zhen Zhong Academician Talent Team Sub-project (2018zszysrctdxm), and Southwest Medical University Research Project (2020ZRQNA045).

Conflict of interest: None declared

REFERENCES

1. Aitken SA, Johnston I, Jennings AC, et al. An evaluation of the Herscovici classification for fractures of the medial malleolus. *Foot Ankle Surg.* 2017; 23(4): 317–320, doi: 10.1016/j.fas.2016.10.003, indexed in Pubmed: 29202995.
2. Alshalawi S, Galhoum AE, Alrashidi Y, et al. Medial ankle instability: the deltoid dilemma. *Foot Ankle Clin.* 2018; 23(4): 639–657, doi: 10.1016/j.fcl.2018.07.008, indexed in Pubmed: 30414658.
3. Bastias GF, Filippi J. Acute deltoid ligament repair in ankle fractures. *Foot Ankle Clin.* 2020; 25(4): 597–612, doi: 10.1016/j.fcl.2020.08.009, indexed in Pubmed: 33543718.
4. Bruno F, Arrigoni F, Palumbo P, et al. Weight-bearing MR imaging of knee, ankle and foot. *Semin Musculoskelet Radiol.* 2019; 23(6): 594–602, doi: 10.1055/s-0039-1697940, indexed in Pubmed: 31745949.
5. Campbell KJ, Michalski MP, Wilson KJ, et al. The ligament anatomy of the deltoid complex of the ankle: a qualitative and quantitative anatomical study. *J Bone Joint Surg Am.*

- 2014; 96(8): e62, doi: [10.2106/JBJS.M.00870](https://doi.org/10.2106/JBJS.M.00870), indexed in Pubmed: [24740670](https://pubmed.ncbi.nlm.nih.gov/24740670/).
6. Cao Y, Hong Y, Xu Y, et al. Surgical management of chronic lateral ankle instability: a meta-analysis. *J Orthop Surg Res.* 2018; 13(1): 159, doi: [10.1186/s13018-018-0870-6](https://doi.org/10.1186/s13018-018-0870-6), indexed in Pubmed: [29940985](https://pubmed.ncbi.nlm.nih.gov/29940985/).
 7. Clanton TO, Williams BT, Backus JD, et al. Biomechanical analysis of the individual ligament contributions to syndesmotic stability. *Foot Ankle Int.* 2017; 38(1): 66–75, doi: [10.1177/1071100716666277](https://doi.org/10.1177/1071100716666277), indexed in Pubmed: [27681857](https://pubmed.ncbi.nlm.nih.gov/27681857/).
 8. Crim J. Medial-sided ankle pain: deltoid ligament and beyond. *Magn Reson Imaging Clin N Am.* 2017; 25(1): 63–77, doi: [10.1016/j.mric.2016.08.003](https://doi.org/10.1016/j.mric.2016.08.003), indexed in Pubmed: [27888852](https://pubmed.ncbi.nlm.nih.gov/27888852/).
 9. Debieux P, Wajnsztein A, Mansur N. Epidemiology of injuries due to ankle sprain diagnosed in an orthopedic emergency room. *Einstein (São Paulo).* 2019; 18, doi: [10.31744/einstein_journal/2020ao4739](https://doi.org/10.31744/einstein_journal/2020ao4739).
 10. Hajewski CJ, Duchman K, Goetz J, et al. Anatomic syndesmotic and deltoid ligament reconstruction with flexible implants: a technique description. *Iowa Orthop J.* 2019; 39(1): 21–27, indexed in Pubmed: [31413670](https://pubmed.ncbi.nlm.nih.gov/31413670/).
 11. Hardy MA, Connors JC, Zulauf EE, et al. Acute deltoid ligament repair in ankle fractures: five-year follow-up. *Clin Podiatr Med Surg.* 2020; 37(2): 295–304, doi: [10.1016/j.cpm.2019.12.004](https://doi.org/10.1016/j.cpm.2019.12.004), indexed in Pubmed: [32146985](https://pubmed.ncbi.nlm.nih.gov/32146985/).
 12. Hartford JM, Gorczyca JT, McNamara JL, et al. Tibiotalar contact area. Contribution of posterior malleolus and deltoid ligament. *Clin Orthop Relat Res.* 1995(320): 182–187, indexed in Pubmed: [7586825](https://pubmed.ncbi.nlm.nih.gov/7586825/).
 13. Kobayashi T, Suzuki E, Yamazaki N, et al. In vivo talocrural joint contact mechanics with functional ankle instability. *Foot Ankle Spec.* 2015; 8(6): 445–453, doi: [10.1177/1938640015585967](https://doi.org/10.1177/1938640015585967), indexed in Pubmed: [25956876](https://pubmed.ncbi.nlm.nih.gov/25956876/).
 14. Kusnezov NA, Eisenstein ED, Diab N, et al. Medial malleolar fractures and associated deltoid ligament disruptions: current management controversies. *Orthopedics.* 2017; 40(2): e216–e222, doi: [10.3928/01477447-20161213-02](https://doi.org/10.3928/01477447-20161213-02), indexed in Pubmed: [27992638](https://pubmed.ncbi.nlm.nih.gov/27992638/).
 15. Lee S, Lin J, Hamid KS, et al. Deltoid Ligament Rupture in Ankle Fracture: Diagnosis and Management. *J Am Acad Orthop Surg.* 2019; 27(14): e648–e658, doi: [10.5435/JAAOS-D-18-00198](https://doi.org/10.5435/JAAOS-D-18-00198), indexed in Pubmed: [30475279](https://pubmed.ncbi.nlm.nih.gov/30475279/).
 16. Liu C, Wang Y, Li Z, et al. Tibiofemoral joint contact area and stress after single-bundle anterior cruciate ligament reconstruction with transtibial versus anteromedial portal drilling techniques. *J Orthop Surg Res.* 2018; 13(1): 247–255, doi: [10.1186/s13018-018-0956-1](https://doi.org/10.1186/s13018-018-0956-1), indexed in Pubmed: [30286774](https://pubmed.ncbi.nlm.nih.gov/30286774/).
 17. Macko VW, Matthews LS, Zwirkoski P, et al. The joint-contact area of the ankle. The contribution of the posterior malleolus. *J Bone Joint Surg Am.* 1991; 73(3): 347–351, indexed in Pubmed: [2002072](https://pubmed.ncbi.nlm.nih.gov/2002072/).
 18. Michels F, Guillo S, Vanrietvelde F, et al. How to drill the talar tunnel in ATFL reconstruction? *Knee Surg Sports Traumatol Arthrosc.* 2016; 24(4): 991–997, doi: [10.1007/s00167-016-4018-0](https://doi.org/10.1007/s00167-016-4018-0), indexed in Pubmed: [26856316](https://pubmed.ncbi.nlm.nih.gov/26856316/).
 19. Milner CE, Soames RW. The medial collateral ligaments of the human ankle joint: anatomical variations. *Foot Ankle Int.* 1998; 19(5): 289–292, doi: [10.1177/107110079801900504](https://doi.org/10.1177/107110079801900504), indexed in Pubmed: [9622418](https://pubmed.ncbi.nlm.nih.gov/9622418/).
 20. Nery C, Lemos AV, Raduan F, et al. Combined spring and deltoid ligament repair in adult-acquired flat-foot. *Foot Ankle Int.* 2018; 39(8): 903–907, doi: [10.1177/1071100718770132](https://doi.org/10.1177/1071100718770132), indexed in Pubmed: [29658814](https://pubmed.ncbi.nlm.nih.gov/29658814/).
 21. Pisanu F, Ortu S, Corda M, et al. Deltoid ligament reconstruction with autologous gracilis tendon in chronic medial ankle instability after ankle fracture surgery: A case report. *Foot (Edinb).* 2021; 49: 101714, doi: [10.1016/j.foot.2020.101714](https://doi.org/10.1016/j.foot.2020.101714), indexed in Pubmed: [33036835](https://pubmed.ncbi.nlm.nih.gov/33036835/).
 22. Ramsey PL, Hamilton W. Changes in tibiotalar area of contact caused by lateral talar shift. *J Bone Joint Surg Am.* 1976; 58(3): 356–357, indexed in Pubmed: [1262367](https://pubmed.ncbi.nlm.nih.gov/1262367/).
 23. Salameh M, Alhammoud A, Alkhatib N, et al. Outcome of primary deltoid ligament repair in acute ankle fractures: a meta-analysis of comparative studies. *Int Orthop.* 2020; 44(2): 341–347, doi: [10.1007/s00264-019-04416-9](https://doi.org/10.1007/s00264-019-04416-9), indexed in Pubmed: [31776609](https://pubmed.ncbi.nlm.nih.gov/31776609/).
 24. Savage-Elliott I, Murawski CD, Smyth NA, et al. The deltoid ligament: an in-depth review of anatomy, function, and treatment strategies. *Knee Surg Sports Traumatol Arthrosc.* 2013; 21(6): 1316–1327, doi: [10.1007/s00167-012-2159-3](https://doi.org/10.1007/s00167-012-2159-3), indexed in Pubmed: [22878436](https://pubmed.ncbi.nlm.nih.gov/22878436/).
 25. Stufkens SAS, van den Bekerom MPJ, Knupp M, et al. The diagnosis and treatment of deltoid ligament lesions in supination-external rotation ankle fractures: a review. *Strategies Trauma Limb Reconstr.* 2012; 7(2): 73–85, doi: [10.1007/s11751-012-0140-9](https://doi.org/10.1007/s11751-012-0140-9), indexed in Pubmed: [22767333](https://pubmed.ncbi.nlm.nih.gov/22767333/).

Accessory anterior ethmoidal nerve and artery: a cadaveric case report

D. Hage¹, J. Iwanaga^{1–4}, A. Danaei⁵, A. Sadr⁶, R.S. Tubbs^{1, 2, 7–11}

¹Department of Neurosurgery, Tulane Centre for Clinical Neurosciences, Tulane University School of Medicine, New Orleans, LA, United States

²Department of Neurology, Tulane Centre for Clinical Neurosciences, Tulane University School of Medicine, New Orleans, LA, United States

³Dental and Oral Medical Centre, Kurume University School of Medicine, Kurume, Fukuoka, Japan

⁴Division of Gross and Clinical Anatomy, Department of Anatomy, Kurume University School of Medicine, Kurume, Fukuoka, Japan

⁵University of British Columbia, Vancouver, Canada

⁶Department of Restorative Dentistry, University of Washington School of Dentistry, Seattle, WA, United States

⁷Department of Anatomical Sciences, St. George's University, St. George's, Grenada, West Indies

⁸Department of Structural and Cellular Biology, Tulane University School of Medicine, New Orleans, LA, United States

⁹Department of Surgery, Tulane University School of Medicine, New Orleans, LA, United States

¹⁰Department of Neurosurgery and Ochsner Neuroscience Institute, Ochsner Health System, New Orleans, LA, United States

¹¹University of Queensland, Brisbane, Australia

[Received: 2 December 2021; Accepted: 5 January 2022; Early publication date: 31 January 2021]

The anterior ethmoidal artery (AEA) is an important surgical landmark for procedures involving the anterior cranial fossa. Many variations in the location and branching pattern of the AEA have been reported throughout the literature. These anatomical variations are important for surgeons to be familiar with as injury to the AEA can lead to massive haemorrhage, orbital haematomas, and cerebrospinal fluid rhinorrhoea. Anatomical landmarks such as the ethmoidal foramen can be used to identify the location of the AEA; however, it is also important to consider that the foramen may have variable presentations. If there is ever difficulty with identification of the AEA, surgeons should pursue a high-resolution computed tomography to minimise the risk of surgical complications. In this report, we present a rare case of a variant accessory anterior ethmoidal artery and nerve, and variations in the ethmoidal foramen found during cadaveric dissection. (Folia Morphol 2023; 82, 1: 183–186)

Key words: anterior ethmoidal artery, anterior ethmoidal nerve, anatomy, variations, orbit

INTRODUCTION

The anterior ethmoidal artery (AEA) is an important landmark to identify when performing surgeries that involve the anterior cranial fossa [3]. Injury to the AEA may cause the proximal segment to retract into

the orbit resulting in an expanding bleeding within the intracanal space [9]. While variations have been reported, the AEA typically branches from the ophthalmic artery (OA) lateral to the anterior ethmoidal foramen in the superomedial interconal space and the

Address for correspondence: J. Iwanaga, DDS, PhD, Department of Neurosurgery, Tulane Centre for Clinical Neurosciences, Tulane University School of Medicine, 131 S. Robertson St. Suite 1300, New Orleans, LA 70112, United States, tel: 5049885565, fax: 5049885793, e-mail: iwanagajoeca@gmail.com

This article is available in open access under Creative Commons Attribution-Non-Commercial-No Derivatives 4.0 International (CC BY-NC-ND 4.0) license, allowing to download articles and share them with others as long as they credit the authors and the publisher, but without permission to change them in any way or use them commercially.

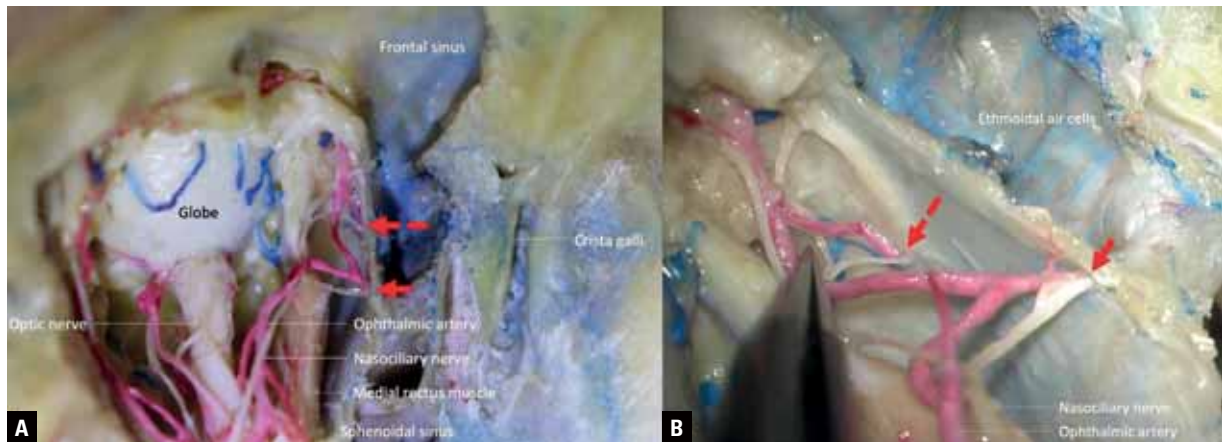


Figure 1. Normal and accessory ethmoidal arteries and nerves. Note that the anterior ethmoidal artery and nerve (both approximately 0.8 mm in diameter, arrow) and accessory ethmoidal artery and nerve (both approximately 0.4 mm in diameter, dotted arrow) enter the ethmoidal cells; **A.** Superior view of the left globe; **B.** Magnified oblique view of the left orbit.

anterior ethmoidal nerve branches from the nasociliary nerve [2]. These both exit the orbit through the anterior ethmoidal foramen [10] and follow a medial course along the anterior cranial fossa toward the cribriform plate [5]. Eventually, the AEA reaches the olfactory fossa and gives off its meningeal artery [16]. Additionally, the posterior ethmoidal artery runs between the superior oblique and the levator superioris muscles and supplies the posterior ethmoid cells, the upper nasal mucosa, and the meninges of the anterior cranial fossa [14]. Herein, we present a rare case of a variant accessory artery and nerve found during cadaveric dissection.

CASE REPORT

During the routine dissection of a cadaveric head of a Caucasian 72-year-old female at the time of death, a variant accessory artery and nerve (dotted arrow) were found anterior to the anterior ethmoidal foramen (arrow) in the left orbit (Fig. 1). The accessory nerve arose from the nasociliary nerve, and the accessory artery branched off the OA. The OA, nasociliary nerve, and their branches travelled superior to the medial rectus muscle. Both foramina connected to the ethmoidal cells. Neither one entered the sphenoidal sinus. There was no posterior ethmoidal foramen. The variant accessory foramen was not found on the right side. There were no previous surgical scars or other anatomical variations in the region dissected.

DISCUSSION

The AEA is at risk of injury from blunt trauma, endoscopic sinus surgery, and surgical interventions

involving the inner wall of the orbit due to its course along the roof of the ethmoid from the orbit to the anterior cranial fossa [1, 4, 11]. Injury to the anterior and posterior ethmoid canals can lead to massive haemorrhage, orbital haematoma, or cerebrospinal fluid rhinorrhoea [4]. The AEA also plays an important role in the management of recurrent epistaxis as the septal branches are often implicated in cases of persistent epistaxis [16]. To quantify this, Turri-Zanoni et al. [16] performed endoscopic endonasal coagulation on 30 patients with epistaxis suspected to originate from the septal branches of the AEA. Among these patients, 16 did not have prior episodes of epistaxis, while 14 had an extensive history of refractory epistaxis [16]. The patients were followed up for a total of 19 months and only two of them were noted to have recurrent epistaxis; one of whom occurred at the 1-month follow-up and resolved following coagulation of the new site of the bleeding [16]. Surgeons need to be familiar with the location of the AEA and its branches as variations in its location and branching patterns may increase the risk of surgical complications.

Several anatomical studies have been conducted to better understand the variations of the ethmoidal arteries. Erdogmus et al. [4] analysed the orbits of 19 cadavers and were able to classify the branching patterns of the AEA into four different categories based on their anatomic relationship to the superior oblique muscle. They determined that the AEA could either branch medial (type 1) or lateral (type 2) to the lower segment of the superior oblique muscle, or branch medial (type 3) or lateral (type 4) to the

upper segment of the superior oblique muscle [4]. In all 38 orbits analysed, the ethmoidal arteries originated from the OA and eventually exited through the anterior ethmoidal foramen [4]. Similarly, Li et al. [10] demonstrated the AEA coursing beneath the superior oblique muscle and branching off the OA lateral to the anterior ethmoidal foramen on all 16 sides of their 8 cadavers. However, in our current case, the accessory AEA and nerve were found anterior to the anterior ethmoidal foramen, rather than lateral to it. Additionally, the posterior ethmoidal artery is also susceptible to variation as Semmer et al. [14] reported that the posterior ethmoidal artery was absent in 15% of specimens where the OA crosses under the optic nerve and 19% of specimens when the OAs cross over the optic nerve. In our case, the clinical significance of the accessory AEA and nerve is unclear due to a lack of available literature. Alternative case reports, however, have documented examples of complications that can arise if there is an unknown variation in the anatomy of the AEA. For example, Wong et al. [17] reported the AEA emerging anteriorly to the bulla ethmoidalis rather than posterior to it in a patient with Waardenburg's syndrome. This only became evident after an inadvertent surgical injury to the AEA resulted in haemorrhage and retraction of the AEA into the orbit, leading to the development of a retrobulbar haematoma [17].

Furthermore, the ethmoidal foramina are also susceptible to variability. In our current case, the posterior ethmoidal foramen was absent, and the variant accessory foramen was not found on the right. Several studies have attempted to quantify the variability of the accessory ethmoidal foramen including Takahasi et al. [15] who investigated 54 orbits, across 27 Japanese cadavers. Among the orbits they analysed, 36 (66.7%) had two ethmoidal foramina, 17 (31.5%) had three foramina, and 1 (1.9%) had one foramen [15]. They labelled the foramen based on their position between the anterior lacrimal crest and the optic canal (anterior, middle, deep middle, and, posterior) [15]. They found that 18 orbits (11 cadavers) were notable for the presence of an accessory foramen, with 17 of those orbits having one accessory foramen and 1 orbit having two accessory foramina [15]. Of the 11 cadavers, 4 (males) had unilateral foramen, 6 (3 males, 3 females) had bilateral foramen, and 1 (male) had one accessory foramen on the right and

two accessory foramen on the left [15]. None of the cadavers included was notable for an absent anterior or posterior foramen as in our case. Similarly, Piagkou et al. [13] conducted a study analysing 249 orbits, across 137 Greek-Caucasian cadavers. Among their samples, 249 (100%) orbits were notable for an anterior ethmoidal foramen, 245 (98.4%) had a posterior ethmoidal foramen, and 68 (27.3%) had a middle ethmoidal foramen [13]. They observed 4 (1.6%) having an accessory foramen to the anterior ethmoidal foramen, 41 (16.5%) with an accessory to the posterior ethmoidal foramen, and 3 (1.2%) with an accessory to the middle ethmoidal foramen [13]. They further classified their cadavers into four categories based on the number of foramina observed: type 1 (4 orbits, 1.6%) — a single anterior ethmoidal foramen, type 2 (152 orbits, 61%) — an anterior and posterior ethmoidal foramina, type 3 (71 orbits, 28.5%) — either an anterior, middle, and posterior foramina (46 orbits, 18.5%), or an anterior and posterior foramina with an accessory to either (25 orbits, 10%), and type 4 (19 orbits, 7.6%) — with a range of 4–6 ethmoidal foramen [13].

CONCLUSIONS

Early identification and awareness of the anatomical variations in the AEA and ethmoidal foramen is important for surgeons to be aware of to reduce the risk of surgical complications. The use of landmarks to aid in the identification of the AEA has been extensively researched and several landmarks have been suggested such as the supraorbital ethmoid cells, nasal beak, nasal crest, and axilla of the middle turbinate [7, 12]. Additionally, if the AEA is unidentifiable on a computed tomography scan, surgeons should pursue a repeat preoperative CT scan with a higher resolution, as this has been shown to better elucidate the location of the AEA [8].

Acknowledgements

The authors sincerely thank those who donated their bodies to science so that anatomical research could be performed. Results from such research can potentially increase mankind's overall knowledge that can then improve cadaver care. Therefore, these donors and their families deserve our highest gratitude [6].

Conflict of interest: None declared

REFERENCES

1. Abdullah B, Lim EH, Husain S, et al. Anatomical variations of anterior ethmoidal artery and their significance in endoscopic sinus surgery: a systematic review. *Surg Radiol Anat.* 2019; 41(5): 491–499, doi: [10.1007/s00276-018-2165-3](https://doi.org/10.1007/s00276-018-2165-3), indexed in Pubmed: [30542930](https://pubmed.ncbi.nlm.nih.gov/30542930/).
2. Dallan I, Seccia V, Lenzi R, et al. Transnasal approach to the medial intraconal space: anatomic study and clinical considerations. *Minim Invasive Neurosurg.* 2010; 53(04): 164–168, doi: [10.1055/s-0030-1263106](https://doi.org/10.1055/s-0030-1263106).
3. de Almeida JR, Snyderman CH, Gardner PA, et al. Nasal morbidity following endoscopic skull base surgery: a prospective cohort study. *Head Neck.* 2011; 33(4): 547–551, doi: [10.1002/hed.21483](https://doi.org/10.1002/hed.21483), indexed in Pubmed: [20824807](https://pubmed.ncbi.nlm.nih.gov/20824807/).
4. Erdogmus S, Govsa F. The anatomic landmarks of ethmoidal arteries for the surgical approaches. *J Craniofac Surg.* 2006; 17(2): 280–285, doi: [10.1097/00001665-200603000-00014](https://doi.org/10.1097/00001665-200603000-00014), indexed in Pubmed: [16633176](https://pubmed.ncbi.nlm.nih.gov/16633176/).
5. Hwang SH, Joo YH, Seo JH, et al. Endoscopic endonasal approach of the medial intraconal space: CT analysis of the anatomic relation between paranasal structures and orbital contents. *J Craniofac Surg.* 2012; 23(4): 966–969, doi: [10.1097/SCS.0b013e31824e5c7f](https://doi.org/10.1097/SCS.0b013e31824e5c7f), indexed in Pubmed: [22777448](https://pubmed.ncbi.nlm.nih.gov/22777448/).
6. Iwanaga J, Singh V, Ohtsuka A, et al. Acknowledging the use of human cadaveric tissues in research papers: recommendations from anatomical journal editors. *Clin Anat.* 2021; 34(1): 2–4, doi: [10.1002/ca.23671](https://doi.org/10.1002/ca.23671), indexed in Pubmed: [32808702](https://pubmed.ncbi.nlm.nih.gov/32808702/).
7. Jang DW, Lachanas VA, White LC, et al. Supraorbital ethmoid cell: a consistent landmark for endoscopic identification of the anterior ethmoidal artery. *Otolaryngol Head Neck Surg.* 2014; 151(6): 1073–1077, doi: [10.1177/0194599814551124](https://doi.org/10.1177/0194599814551124), indexed in Pubmed: [25257902](https://pubmed.ncbi.nlm.nih.gov/25257902/).
8. Lannoy-Penissou L, Schultz P, Riehm S, et al. The anterior ethmoidal artery: radio-anatomical comparison and its application in endonasal surgery. *Acta Otolaryngol.* 2007; 127(6): 618–622, doi: [10.1080/00016480600987826](https://doi.org/10.1080/00016480600987826), indexed in Pubmed: [17503231](https://pubmed.ncbi.nlm.nih.gov/17503231/).
9. Lenzi R, Bleier BS, Felisati G, et al. Purely endoscopic trans-nasal management of orbital intraconal cavernous haemangiomas: a systematic review of the literature. *Eur Arch Otorhinolaryngol.* 2016; 273(9): 2319–2322, doi: [10.1007/s00405-015-3733-3](https://doi.org/10.1007/s00405-015-3733-3), indexed in Pubmed: [26210157](https://pubmed.ncbi.nlm.nih.gov/26210157/).
10. Li L, London NR, Prevedello DM, et al. Intraconal anatomy of the anterior ethmoidal neurovascular bundle: implications for surgery in the superomedial orbit. *Am J Rhinol Allergy.* 2020; 34(3): 394–400, doi: [10.1177/1945892420901630](https://doi.org/10.1177/1945892420901630), indexed in Pubmed: [31973546](https://pubmed.ncbi.nlm.nih.gov/31973546/).
11. Ohnishi T, Tachibana T, Kaneko Y, et al. High-risk areas in endoscopic sinus surgery and prevention of complications. *Laryngoscope.* 1993; 103(10): 1181–1185, doi: [10.1288/00005537-199310000-00020](https://doi.org/10.1288/00005537-199310000-00020), indexed in Pubmed: [8412459](https://pubmed.ncbi.nlm.nih.gov/8412459/).
12. Pernas FG, Coughlin AM, Hughes SE, et al. A novel use of a landmark to avoid injury of the anterior ethmoidal artery during endoscopic sinus surgery. *Am J Rhinol Allergy.* 2011; 25(1): 54–57, doi: [10.2500/ajra.2011.25.3541](https://doi.org/10.2500/ajra.2011.25.3541), indexed in Pubmed: [21711980](https://pubmed.ncbi.nlm.nih.gov/21711980/).
13. Piagkou M, Skotsimara G, Dalaka A, et al. Bony landmarks of the medial orbital wall: an anatomical study of ethmoidal foramina. *Clin Anat.* 2014; 27(4): 570–577, doi: [10.1002/ca.22303](https://doi.org/10.1002/ca.22303), indexed in Pubmed: [24000039](https://pubmed.ncbi.nlm.nih.gov/24000039/).
14. Semmer AE, McLoon LK, Lee MS. Orbital vascular anatomy. In: *Encycloedia of the eye.* Dartt DA (ed.). Academic Press, Oxford 2010: 241–251.
15. Takahashi Y, Kakizaki H, Nakano T. Accessory ethmoidal foramina: an anatomical study. *Ophthalmic Plast Reconstr Surg.* 2011; 27(2): 125–127, doi: [10.1097/IOP.0b013e318201c8fd](https://doi.org/10.1097/IOP.0b013e318201c8fd), indexed in Pubmed: [21224747](https://pubmed.ncbi.nlm.nih.gov/21224747/).
16. Turri-Zanoni M, Arosio AD, Stamm AC, et al. Septal branches of the anterior ethmoidal artery: anatomical considerations and clinical implications in the management of refractory epistaxis. *Eur Arch Otorhinolaryngol.* 2018; 275(6): 1449–1456, doi: [10.1007/s00405-018-4964-x](https://doi.org/10.1007/s00405-018-4964-x), indexed in Pubmed: [29600317](https://pubmed.ncbi.nlm.nih.gov/29600317/).
17. Wong DKC, Shao A, Campbell R, et al. Anterior ethmoidal artery emerging anterior to bulla ethmoidalis: An abnormal anatomical variation in Waardenburg's syndrome. *Allergy Rhinol (Providence).* 2014; 5(3): 168–171, doi: [10.2500/ar.2014.5.0094](https://doi.org/10.2500/ar.2014.5.0094), indexed in Pubmed: [25565054](https://pubmed.ncbi.nlm.nih.gov/25565054/).

Concomitant completely ossified trigeminal pore and Dorello's canal

M.C. Rusu¹ , A.D. Vrapciu¹, P.M. Rădoi², C. Toader²

¹Division of Anatomy, Faculty of Dental Medicine, "Carol Davila" University of Medicine and Pharmacy, Bucharest, Romania

²Faculty of General Medicine, "Carol Davila" University of Medicine and Pharmacy, Bucharest, Romania

[Received: 30 December 2021; Accepted: 9 January 2022; Early publication date: 21 January 2022]

Commonly, the trigeminal and abducens nerve course to the middle cranial fossa, beneath the tentorial border (posterior petroclinoid dural ligament) and, respectively, beneath Grüber's petrosphenoidal ligament, in Dorello's canal. It is hereby reported a rare unilateral association of anatomic variants which was found when the brain computed tomography angiography of a 56-year-old male patient was observed. On the left side, the tentorial border was ossified above the petrous apex, resulting in a tentorial bar 1.96 cm long that transformed the trigeminal pore into a completely ossified one. On that side was also found an ossified petrosphenoidal ligament determining a completely ossified Dorello's canal. On the opposite side a 2.9 mm long clinoid bar extended from the posterior clinoid process to the anterior one. Although these bars are not common in humans they should be documented in computed tomography in cases with associated trigeminal neuralgia and abducens nerve palsy. (Folia Morphol 2023; 82, 1: 187–189)

Key words: trigeminal nerve, abducens nerve, trigeminal neuralgia, petrous apex

INTRODUCTION

Commonly, the trigeminal nerve courses from the posterior fossa to the middle fossa through the trigeminal notch on the superior border of the petrous apex. The abducens nerve courses towards the parasellar region through a notch on the lateral border of the dorsum sellae. The tentorial border (posterior petroclinoid dural ligament) over the trigeminal notch transforms it into the porus trigeminus. The petrosphenoidal ligament over the abducens nerve transforms the respective notch into Dorello's canal.

Ossified ligaments of the skull base, such as the posterior petroclinoid and petrosphenoidal ligaments, have been associated with neural impingement syndromes [6]. An ossified ligament becomes an osseous bar, or a bony bridge.

CASE REPORT

A 56-year-old male was evaluated for possible brain vascular malformations by computed tomography (CT) angiography. A 32-slice CT scanner (Siemens Multislice Perspective Scanner) was used, as previously [4]. The anatomical details were observed using the Horos Project software for iOS. The research was conducted in accordance with the Declaration of Helsinki.

The endocranial details of the sphenoid and temporal bones were observed on three-dimensional renderings. The dorsum sellae and petrous apices were identified. On the right side were found the trigeminal notch, on the petrous apex, and the abducens nerve notch, in the infero-lateral angle of the dorsum sellae (Fig. 1). From the right posterior clinoid process

Address for correspondence: M.C. Rusu, MD, PhD (Med.), PhD (Biol.), Dr. hab., Prof., "Carol Davila" University of Medicine and Pharmacy, 8 Eroilor Sanitari Blvd., RO-050474, Bucharest, Romania, tel: +40722363705, e-mail: anatomon@gmail.com

This article is available in open access under Creative Commons Attribution-Non-Commercial-No Derivatives 4.0 International (CC BY-NC-ND 4.0) license, allowing to download articles and share them with others as long as they credit the authors and the publisher, but without permission to change them in any way or use them commercially.

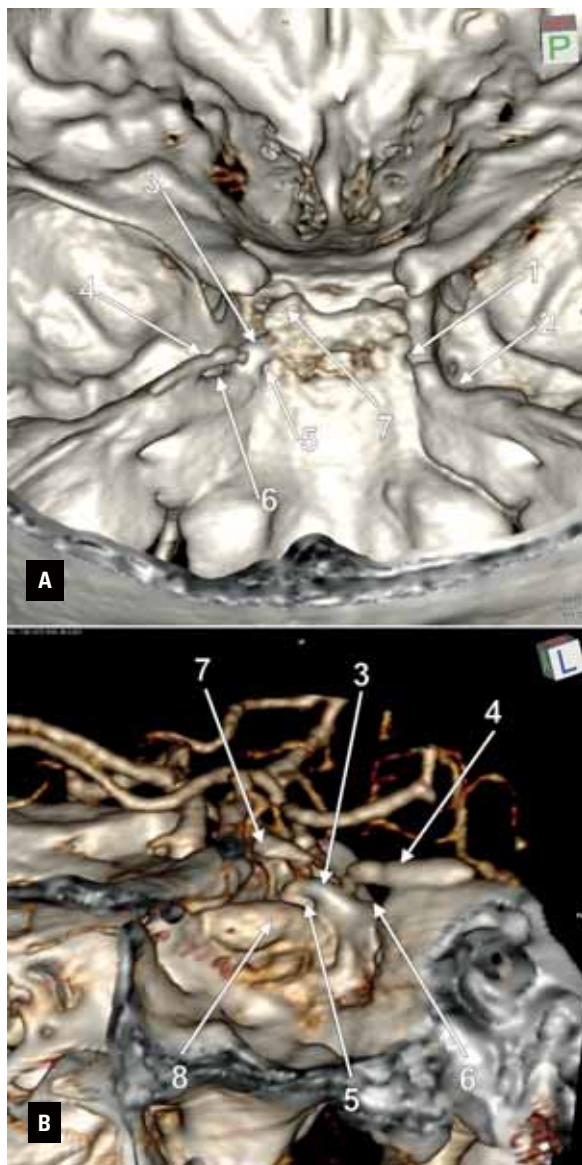


Figure 1. Three-dimensional volume renderings of the cranial fossae depicting the concomitant ipsilateral complete ossification of the left porus trigeminus and Dorello's canal; **A.** Non-contrast, postero-superior view; **B.** Computed tomography angiography, right antero-lateral view; 1 — notch of the right abducens nerve; 2 — trigeminal notch of the right petrous apex; 3 — left ossified petrosphenoidal ligament (petrosphenoidal bar); 4 — left tentorial bar; 5 — ossified left porus trigeminus; 6 — ossified left Dorello's canal; 7 — left posterior clinoid process; 8 — cavernous portion of the left internal carotid artery.

a 2.9 mm long bar extended anteriorly towards the left anterior clinoid process, at 1.9 mm from it. This right clinoid bar was located 3.1 mm inferior to the left posterior communicating artery.

On the opposite side, the passages for the trigeminal and, respectively, abducens nerve, were completely ossified. Above the left petrous apex trigeminal notch a complete tentorial bar of 1.96 cm length and

thick of 2.9 mm was found in the upper border of the trigeminal pore. On that side an ossified petrosphenoidal bar thick of 3.9 mm was closing Dorello's canal superiorly. The left superior cerebellar artery was located at 2.2 mm above the petrosphenoidal bar and at 4.1 mm above the tentorial bar, and contacted the right posterior clinoid process. The lateral end of that clinoid process was projected at 1.9 mm above the petrosphenoidal bar.

DISCUSSION

The tentorial and, respectively, petrosphenoidal bars, are scarcely presented in the anatomical literature. To the best of the authors' knowledge these were not reported to occur concomitantly, such as in the hereby reported case.

The tentorial bar

The porus trigeminus allows passage of the trigeminal nerve above the petrous apex, from the posterior fossa to the middle one. The trigeminal nerve passes beneath the posterior petroclinoid dural fold (ligament, PPCL) [2]. Completely ossified PPCLs were found in 20% of 15 adult microdissected head halves [2]. Such ossified PPCLs transform the osteofibrous trigeminal pore into a bony foramen [2] that is occasionally found in dry skulls [7]. Bony lamellae within the tentorial border and the PPCS were found in close contact with the oculomotor, trochlear, trigeminal and abducens nerves [5]. According to Bergman, Afifi and Miyauchi, "A bar of bone in the dura over the trigeminal nerve has been interpreted as a vestige of the primitive cranial wall as present in reptilia" [1]. The tentorial bar has a dural origin [6].

The petrosphenoidal bar

Dorello's canal is an osteofibrous canal located at the inferior angle of the sellar dorsum. It is traversed by the abducens nerve, the inferior petrosal sinus, and a branch of the meningohypophyseal trunk [8]. Dorello's canal is bounded superiorly by the petrosphenoidal ligament (PSL), or the ligament of Grüber [8]. The PSL is amongst the least commonly mineralised skull base ligaments, with a published prevalence of 5–25%, as documented by Tubbs et al. [6]. The ossified canal of Dorello is found in nonhuman primates [3]. The prevalence of ossification of the PSL for each side was found 6.5% in the right side and 5.1% in the left side [3]. In 31/523 (5.9%) cases the petrosphenoidal bar was unilateral, and in 15/523 (2.8%) cases it was bilateral [3].

CONCLUSIONS

Commonly, trigeminal neuralgia is determined by different skull base masses, or after neurovascular conflicts. This is equally true for the abducens nerve palsy. However, concomitant trigeminal and abducens deficits could be just the result of concomitantly occurring tentorial and petrosphenoidal bars. A computed tomographic anatomic evaluation of the skull base is of help to elucidate the neuropathic picture, or to guide a narrow neurosurgical approach.

Conflict of interest: None declared

REFERENCES

1. Bergman RA, Afifi Ak, Miyauchi R. Illustrated encyclopedia of human anatomic variation: Opus v: Skeletal systems: Cranium. 1995. 2021. <https://www.anatomyatlases.org/AnatomicVariants/SkeletalSystem/Regions/Cranium.shtml>.
2. Kimball D, Kimball H, Matusz P, et al. Ossification of the posterior petroclinoid dural fold: a cadaveric study with neurosurgical significance. *J Neurol Surg B Skull Base*. 2015; 76(4): 272–277, doi: [10.1055/s-0034-1396598](https://doi.org/10.1055/s-0034-1396598), indexed in Pubmed: [26225315](https://pubmed.ncbi.nlm.nih.gov/26225315/).
3. Özgür A, Esen K. Ossification of the petrosphenoidal ligament: multidetector computed tomography findings of an unusual variation with a potential role in abducens nerve palsy. *Jpn J Radiol*. 2015; 33(5): 260–265, doi: [10.1007/s11604-015-0410-9](https://doi.org/10.1007/s11604-015-0410-9), indexed in Pubmed: [25749833](https://pubmed.ncbi.nlm.nih.gov/25749833/).
4. Rădoi PM, Rusu MC, Dincă D, et al. Combined rare anatomic variants: persistent primitive olfactory artery and azygos pericallosal artery. *Surg Radiol Anat*. 2021; 43(8): 1305–1308, doi: [10.1007/s00276-021-02687-9](https://doi.org/10.1007/s00276-021-02687-9), indexed in Pubmed: [33496800](https://pubmed.ncbi.nlm.nih.gov/33496800/).
5. Rusu MC, Ivaşcu RV, Cergan R, et al. Typical and atypical neurovascular relations of the trigeminal nerve in the cerebellopontine angle: an anatomical study. *Surg Radiol Anat*. 2009; 31(7): 507–516, doi: [10.1007/s00276-009-0472-4](https://doi.org/10.1007/s00276-009-0472-4), indexed in Pubmed: [19214365](https://pubmed.ncbi.nlm.nih.gov/19214365/).
6. Touska P, Hasso S, Oztek A, et al. Skull base ligamentous mineralisation: evaluation using computed tomography and a review of the clinical relevance. *Insights Imaging*. 2019; 10(1): 55, doi: [10.1186/s13244-019-0740-8](https://doi.org/10.1186/s13244-019-0740-8), indexed in Pubmed: [31115710](https://pubmed.ncbi.nlm.nih.gov/31115710/).
7. Tubbs RS, Salter EG, Oakes WJ. Bony anomaly of Meckel's cave. *Clin Anat*. 2006; 19(1): 75–77, doi: [10.1002/ca.20163](https://doi.org/10.1002/ca.20163), indexed in Pubmed: [16283637](https://pubmed.ncbi.nlm.nih.gov/16283637/).
8. Tubbs RS, Sharma A, Loukas M, et al. Ossification of the petrosphenoidal ligament: unusual variation with the potential for abducens nerve entrapment in Dorello's canal at the skull base. *Surg Radiol Anat*. 2014; 36(3): 303–305, doi: [10.1007/s00276-013-1171-8](https://doi.org/10.1007/s00276-013-1171-8), indexed in Pubmed: [23877841](https://pubmed.ncbi.nlm.nih.gov/23877841/).

Splitting of the distal median nerve

W.L. Smith¹, Ł. Olewnik², J. Iwanaga^{3–5}, A.S. Dumont³, R.S. Tubbs^{3, 4, 6–10}

¹Tulane University School of Medicine, New Orleans, LA, United States

²Department of Anatomical Dissection and Donation, Medical University of Lodz, Poland

³Department of Neurosurgery, Tulane University School of Medicine, New Orleans, LA, United States

⁴Department of Neurology, Tulane Centre for Clinical Neurosciences, Tulane University School of Medicine, New Orleans, LA, United States

⁵Division of Gross and Clinical Anatomy, Department of Anatomy, Kurume University School of Medicine, Kurume, Fukuoka, Japan

⁶Department of Structural and Cellular Biology, Tulane University School of Medicine, New Orleans, LA, United States

⁷Department of Neurosurgery and Ochsner Neuroscience Institute, Ochsner Health System, New Orleans, LA, United States

⁸Department of Anatomical Sciences, St. George's University, St. George's, Grenada, West Indies

⁹Department of Surgery, Tulane Centre for Clinical Neurosciences, Tulane University School of Medicine, New Orleans, LA, United States

¹⁰University of Queensland, Brisbane, Australia

[Received: 12 September 2021; Accepted: 29 October 2021; Early publication date: 26 November 2021]

Variations of the nerves of the forearm can lead to unexpected clinical findings during physical examination. Additionally, surgery in this region might encounter and potentially damage the nerve in such patients. Here, we present a case of a high split of the median nerve and discuss the findings of the case as well as review salient reports in the literature. Knowledge of such a variation can be important in patient diagnosis and treatment. (Folia Morphol 2023; 82, 1: 190–193)

Key words: anatomy, variation, upper limb, hand, forearm

INTRODUCTION

The median nerve travels through the anterior compartments of the arm and forearm and is often involved in pathological condition, e.g., carpal tunnel syndrome. Variations of the median nerve in the carpal tunnel have been documented and such variations increase the risk of injury during treatment. The median nerve in the forearm can vary: it can pierce the humeral head of the pronator teres or pass deep to the two heads; it may split with the ulnar artery, palmaris longus, flexor pollicis longus, or variant muscle tendons traversing it; and it may travel on the superficial surface of the flexor digitorum superficialis (FDS) instead of deep to it [1–3, 5–8].

Here, we present a case in which the median nerve split in the forearm through the FDS.

CASE REPORT

During the routine dissection of a 42-year-old at death female cadaver, an unusual variant of the median nerve was observed in the right upper limb. At 10.5 cm distal to the medial epicondyle, the nerve forked into two unequal branches. The smaller medial branch (3 mm diameter) travelled 6.5 cm distally to enter the musculotendinous junction of the FDS to the fourth digit, entered the carpal tunnel superficial to all of the long flexor tendons to then terminate as the digital nerve to the lateral side of the fourth digit (Fig. 1). No additional branches were seen from

Address for correspondence: J. Iwanaga, DDS, PhD, Department of Neurosurgery, Tulane Centre for Clinical Neurosciences, Tulane University School of Medicine, 131 S. Robertson St. Suite 1300, New Orleans, LA 70112, United States, tel: 5049885565, fax: 5049885793, e-mail: iwanagajoeca@gmail.com

This article is available in open access under Creative Commons Attribution-Non-Commercial-No Derivatives 4.0 International (CC BY-NC-ND 4.0) license, allowing to download articles and share them with others as long as they credit the authors and the publisher, but without permission to change them in any way or use them commercially.

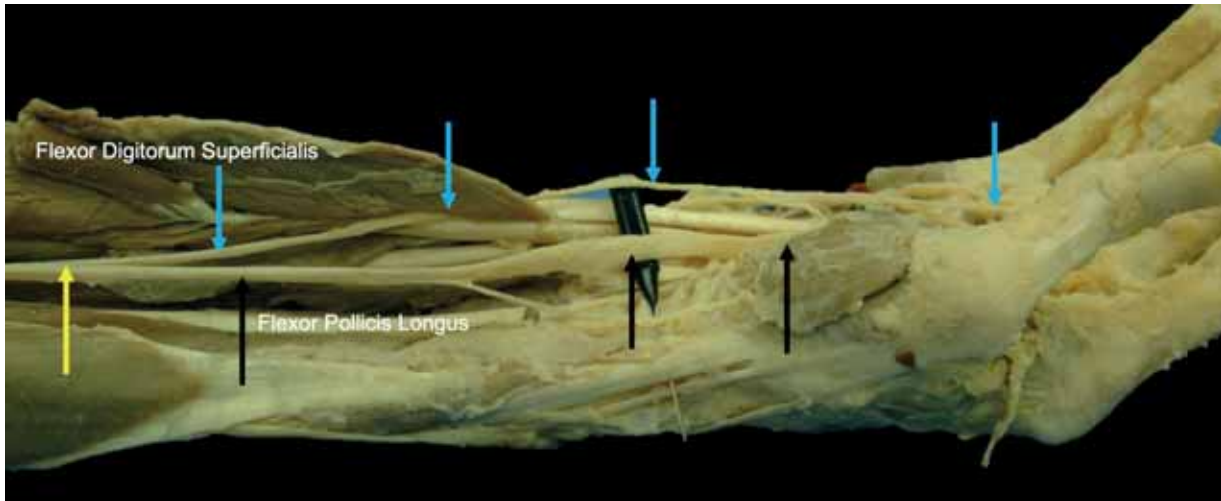


Figure 1. Lateral view of the forearm and hand of the specimen described herein. The lateral edge of the flexor digitorum superficialis is reflected up. The pre-split part of the median nerve is seen at the yellow arrow and the medial and lateral branches seen at the blue and black arrows, respectively.

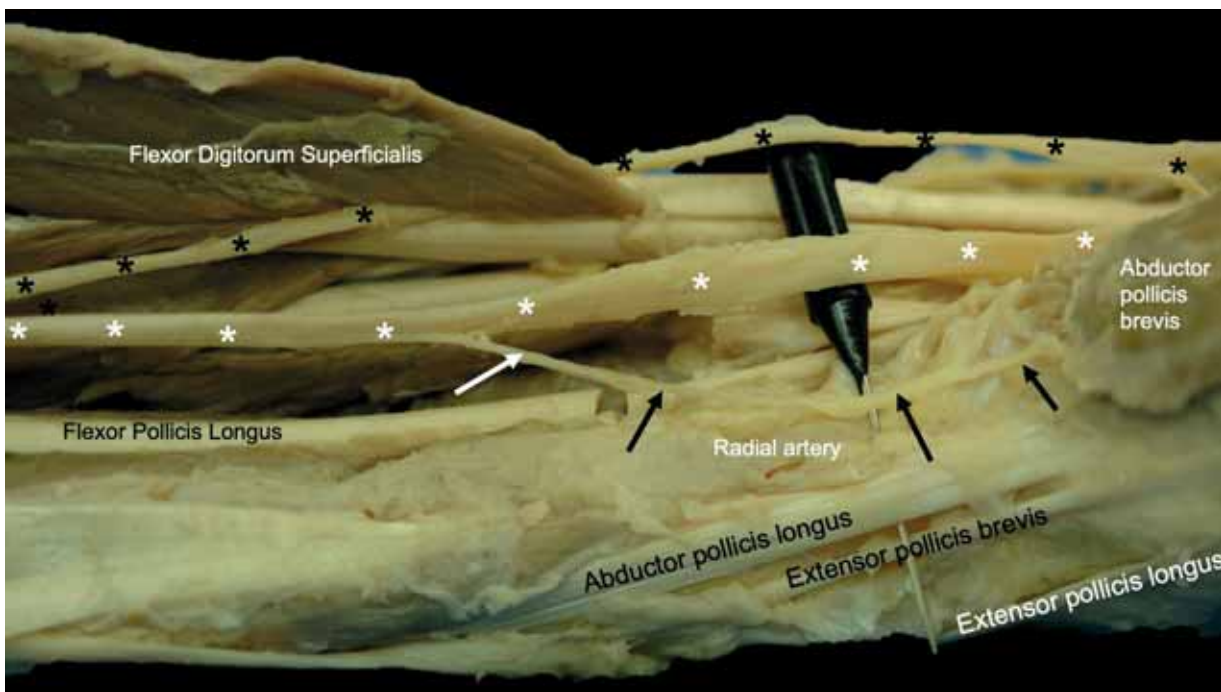


Figure 2. Zoomed in view of Figure 1. Note the medial (black asterisk) and lateral (white asterisk) branches of the split median nerve. The arrows note the palmar cutaneous branch of the nerve arising from the lateral branch.

this branch. The larger lateral branch (5 mm diameter) continued from the split distally between the FDS and flexor digitorum profundus and about the same level as the medial branch pierced the FDS; it gave rise to the palmar cutaneous branch (Fig. 2). This branch continued distally through the carpal tunnel just lateral to the medial branch of the split median nerve. In the hand, this part of the median

nerve gave rise to the recurrent branch, branches to the first and second lumbricals, and terminated as digital nerve branches to the lateral three digits. No communicating branches were identified between the medial and lateral branches of the split median nerve in the forearm or hand. The contralateral median nerve was found to have a typical pathway with no splitting through the FDS.

DISCUSSION

Incidence of a split (bifid, bipartite, bifurcated) just proximal to the flexor retinaculum is reported 2.8% and is usually coexistent with a persistent and often enlarged median artery although this was not seen in our specimen [10, 15, 20]. More proximal splits or "high" divisions, such as presented here, that occur more proximal to the wrist have been described but this is much more uncommon [13, 14, 17, 18, 21]. These high divisions can typically be separated into branching with no associated muscle or artery or branching with an associated lumbrical muscle between the branches [12, 16]. A handful of cases of median nerves being split by a tendon of the FDS have been reported [4, 9, 12, 24]. A case has been reported where the median nerve in the proximal forearm was split by a band between the FDS and flexor pollicis longus, but reunited proximal to the flexor retinaculum was identified [24]. Kadar et al. [12] identified two cases in which the median nerve was split into medial division and lateral divisions by the FDS. In one case, the medial division terminated as the third interspace common digital nerve and was separated by the tendon of palmaris longus and FDS tendon to the fourth finger. In the other case, both divisions provided fibres to the third interspace common digital nerve. In both of these cases no persistent median artery was present [12].

In a similar case to ours, Winkleman and Spinner [23] identified a median nerve that split 9.5 cm distal to the medial epicondyle and travelled separately into the carpal tunnel accompanied by a persistent median artery. A communicating branch from the main median nerve rejoined the split portions distal to the flexor retinaculum. In another case, Tubbs and Salter [22] identified a median nerve that split 6 cm distal to the medial epicondyle. The medial and lateral branches of the split median nerve travelled separately through the carpal tunnel and communicated in the palm. However, the present case did not have a persistent median artery or a communicating branch between to the parts of the split. In both cases, however, the medial branch of the split median nerves penetrated the FDS.

CONCLUSIONS

In case of unusual presentations of median nerve entrapment, the clinician should include in their differential diagnosis that the patient has a proximally split nerve. These variations might cause nerve com-

pression with contraction of the FDS and produce pain suggestive of carpal tunnel syndrome or other entrapment syndromes of the forearm [12, 19]. As found in our case, signs or symptoms of median nerve compression where sensation is normal in the palm but compromised along the lateral aspect of the fourth digit, the lateral branch of the split median nerve might be considered to be compressed by the FDS proximal to the wrist. Lastly, surgery of the anterior forearm could potentially injure such a split median nerve, especially the medial branch of the split as it traverses the FDS and is in a more superficial position in the distal forearm more proximally.

Acknowledgements

The authors sincerely thank those who donated their bodies to science so that anatomical research could be performed. Results from such research can potentially increase mankind's overall knowledge that can then improve patient care. Therefore, these donors and their families deserve our highest gratitude [11].



Conflict of interest: None declared

REFERENCES

1. Amadio PC. Bifid median nerve with a double compartment within the transverse carpal canal. *J Hand Surg Am.* 1987; 12(3): 366–368, doi: [10.1016/s0363-5023\(87\)80005-9](https://doi.org/10.1016/s0363-5023(87)80005-9), indexed in Pubmed: [3584882](https://pubmed.ncbi.nlm.nih.gov/3584882/).
2. Anson B. Morris' Human Anatomy. 12th Ed. McGraw-Hill, Blakiston Division 1966.
3. Artico M, De Santis S, Cavallotti D, et al. Anatomical variations of the ulnar and median nerves in the upper limb. *Ital J Anat Embryol.* 2000; 105(3): 189–200, indexed in Pubmed: [11103856](https://pubmed.ncbi.nlm.nih.gov/11103856/).
4. Baruch A, Hass A. Anomaly of the median nerve. *J Hand Surg Am.* 1977; 2(4): 331–332, doi: [10.1016/s0363-5023\(77\)80143-3](https://doi.org/10.1016/s0363-5023(77)80143-3), indexed in Pubmed: [893990](https://pubmed.ncbi.nlm.nih.gov/893990/).
5. Bergman RA, Afifi AK, Saadeh FA. Compendium of human anatomic variation. Urban & Schwarzenberg, Baltimore 1988.
6. Cavallo AV, Slattery PG, Barton RJ. Endoscopic carpal tunnel release and congenital anomalies of the median nerve. *Hand Surg.* 2003; 8(2): 265–270, doi: [10.1142/s0218810403001753](https://doi.org/10.1142/s0218810403001753), indexed in Pubmed: [15002109](https://pubmed.ncbi.nlm.nih.gov/15002109/).
7. Crandall RC, Hamel AL. Bipartite median nerve at the wrist. Report of a case. *J Bone Joint Surg Am.* 1979; 61(2): 311, doi: [10.2106/00004623-197961020-00034](https://doi.org/10.2106/00004623-197961020-00034).
8. Eiken O, Carstam N, Eddeland A. Anomalous distal branching of the median nerve. Case reports. *Scand J Plast Reconstr Surg.* 1971; 5(2): 149–152, doi: [10.3109/02844317109042956](https://doi.org/10.3109/02844317109042956), indexed in Pubmed: [5136058](https://pubmed.ncbi.nlm.nih.gov/5136058/).
9. Fernandez-Garcia S, Pi-Folguera J, Estallo-Matino F. Bifid median nerve compression due to a musculotendinous

- anomaly of FDS to the middle finger. *J Hand Surg.* 2016; 19(5): 616–617, doi: [10.1016/0266-7681\(94\)90128-7](https://doi.org/10.1016/0266-7681(94)90128-7).
10. Gutowski KA, Olivier WA, Mehrara BJ, et al. Arteriovenous malformation of a persistent median artery with a bifurcated median nerve. *Plast Reconstr Surg.* 2000; 106(6): 1336–1339, doi: [10.1097/00006534-200011000-00016](https://doi.org/10.1097/00006534-200011000-00016), indexed in Pubmed: [11083565](https://pubmed.ncbi.nlm.nih.gov/11083565/).
 11. Iwanaga J, Singh V, Takeda S, et al. Acknowledging the use of human cadaveric tissues in research papers: Recommendations from anatomical journal editors. *Clin Anat.* 2021; 34(1): 2–4, doi: [10.1002/ca.23671](https://doi.org/10.1002/ca.23671), indexed in Pubmed: [32808702](https://pubmed.ncbi.nlm.nih.gov/32808702/).
 12. Kadar IA, Virág TH, Matei IR, et al. High division of the median nerve with unusually high origin of the 3rd space common digital nerve. *Injury.* 2020; 51 Suppl 4: S96–S102, doi: [10.1016/j.injury.2020.03.024](https://doi.org/10.1016/j.injury.2020.03.024), indexed in Pubmed: [32197831](https://pubmed.ncbi.nlm.nih.gov/32197831/).
 13. Kessler I. Unusual distribution of the median nerve at the wrist. A case report. *Clin Orthop Relat Res.* 1969; 67: 124–126.
 14. Kitayama Y, Tsukada S, Kurokawa M. High division of the median nerve: unusual anatomical variation. *Ann Plast Surg.* 1985; 14(1): 74–76, doi: [10.1097/00000637-198501000-00013](https://doi.org/10.1097/00000637-198501000-00013), indexed in Pubmed: [3977243](https://pubmed.ncbi.nlm.nih.gov/3977243/).
 15. Król A, Palczak A, Jedrzejewski KS. Split median nerve. A report of two cases. *Folia Morphol.* 2005; 64(4): 341–344, indexed in Pubmed: [16425164](https://pubmed.ncbi.nlm.nih.gov/16425164/).
 16. Lanz U. Anatomical variations of the median nerve in the carpal tunnel. *J Hand Surg Am.* 1977; 2(1): 44–53, doi: [10.1016/s0363-5023\(77\)80009-9](https://doi.org/10.1016/s0363-5023(77)80009-9), indexed in Pubmed: [839054](https://pubmed.ncbi.nlm.nih.gov/839054/).
 17. Matini K. Abnormal distribution of the median nerve at the wrist and forearm. *Plast Reconstr Surg.* 1983; 71(5): 711–713, doi: [10.1097/00006534-198305000-00025](https://doi.org/10.1097/00006534-198305000-00025), indexed in Pubmed: [6836068](https://pubmed.ncbi.nlm.nih.gov/6836068/).
 18. Moneim M. Unusually high division of the median nerve. *J Hand Surg.* 1982; 7(1): 13–14, doi: [10.1016/s0363-5023\(82\)80005-1](https://doi.org/10.1016/s0363-5023(82)80005-1).
 19. Orellana-Donoso M, Valenzuela-Fuenzalida J, Gold-Semmler M, et al. Neural entrapments associated with musculoskeletal anatomical variations of the upper limb: Literature review. *Transl Res Anat.* 2021; 22: 100094, doi: [10.1016/j.tria.2020.100094](https://doi.org/10.1016/j.tria.2020.100094).
 20. Propeck T, Quinn TJ, Jacobson JA, et al. Sonography and MR imaging of bifid median nerve with anatomic and histologic correlation. *AJR Am J Roentgenol.* 2000; 175(6): 1721–1725, doi: [10.2214/ajr.175.6.1751721](https://doi.org/10.2214/ajr.175.6.1751721), indexed in Pubmed: [11090410](https://pubmed.ncbi.nlm.nih.gov/11090410/).
 21. Thompson I. Anomaly of median nerve and flexor digitorum sublimis muscle. *The Anatomical Record.* 1922; 23(7): 375–379, doi: [10.1002/ar.1090230706](https://doi.org/10.1002/ar.1090230706).
 22. Tubbs RS, Salter EG. A rare finding of the median nerve in the forearm. *Clin Anat.* 2006; 19(8): 704–705, doi: [10.1002/ca.20310](https://doi.org/10.1002/ca.20310), indexed in Pubmed: [16838289](https://pubmed.ncbi.nlm.nih.gov/16838289/).
 23. Winkelman NZ, Spinner M. A variant high sensory branch of the median nerve to the third web space. *Bull Hosp Joint Dis.* 1973; 34(2): 161–166.
 24. Won HS, Oh CS, Chung IH. A split and conjoined median nerve in the forearm. *Anat Sci Int.* 2010; 85(2): 115–117, doi: [10.1007/s12565-009-0040-3](https://doi.org/10.1007/s12565-009-0040-3), indexed in Pubmed: [19337785](https://pubmed.ncbi.nlm.nih.gov/19337785/).

Unusual sensory innervation of the dorsal hand and why we should bear this variation in mind

G.P. Georgiev¹ , B. Landzhov², Ł. Olewnik³, N. Zielinska³, Y. Kartelov², I.N. Dimitrova⁴ , R.S. Tubbs^{5–9}

¹Department of Orthopaedics and Traumatology, University Hospital Queen Giovanna – ISUL, Medical University of Sofia, Bulgaria

²Department of Anatomy, Histology and Embryology, Medical University of Sofia, Bulgaria

³Department of Anatomical Dissection and Donation, Chair of Anatomy and Histology, Medical University of Lodz, Poland

⁴Department of Cardiology, University Hospital 'Prof. Al. Tschirkov', Medical University of Sofia, Bulgaria

⁵Department of Anatomical Sciences, St. George's University, Grenada, West Indies

⁶Department of Neurosurgery, Tulane University School of Medicine, New Orleans, LA, United States

⁷Department of Neurology, Tulane University School of Medicine, New Orleans, LA, United States

⁸Department of Structural and Cellular Biology, Tulane University School of Medicine, New Orleans, LA, United States

⁹Department of Neurosurgery, and Ochsner Neuroscience Institute, Ochsner Health System, New Orleans, LA, United States

[Received: 30 September 2021; Accepted: 29 October 2021; Early publication date: 26 November 2021]

Detailed knowledge of the anatomy and different variations of the superficial branch of the radial nerve could be of great importance not only to anatomists but also to clinicians. A predominant radial nerve supply to the dorsum of the hand is rare. Herein, we present an unusual case of unilateral sensory innervation of the dorsal hand found during routine anatomical dissection of a 72-year-old at death male Caucasian cadaver. We also present a brief discussion of the reported variation and emphasize its potential clinical implications. (Folia Morphol 2023; 82, 1: 194–197)

Key words: radial nerve, variation, dorsal hand, clinical significance

INTRODUCTION

Classically, sensory innervation of the dorsal aspect of the hand is ensured by the superficial branch of the radial nerve (SBRN), the dorsal branch of the ulnar nerve (DBUN), and the lateral antebrachial cutaneous nerve (LABCN) [12, 17].

The SBRN commonly curves around the wrist under the tendon of brachioradialis muscle and then divides into four or five dorsal digital branches. Usually, the first of these ensures sensory innervation of the lateral part of the thumb and the thenar eminence; it could connect with the LABCN. The second branch innervates the medial side of the thumb; the third

supplies the lateral skin area of the second finger; the fourth ensures sensory innervation of the adjacent skin areas of the second and third fingers; the fifth connects to the ramus of the DBUN and supplies the neighbouring sides of the third and fourth fingers, but is often replaced by the DBUN. The dorsal digital nerves reach the root of the thumb nail, the middle phalanx of the index finger, the proximal interphalangeal joints of the third, and the lateral parts of the fourth finger. The remaining dorsal areas of the fingers are supplied by the terminal branches of the ulnar and median nerves [15].

Address for correspondence: G.P. Georgiev, MD, PhD, DSc, Department of Orthopaedics and Traumatology, University Hospital Queen Giovanna – ISUL, Medical University of Sofia, 8, Bialo More Str., BG1527 Sofia, Bulgaria, tel: +359884 493523, e-mail: georgievgp@yahoo.com

This article is available in open access under Creative Common Attribution-Non-Commercial-No Derivatives 4.0 International (CC BY-NC-ND 4.0) license, allowing to download articles and share them with others as long as they credit the authors and the publisher, but without permission to change them in any way or use them commercially.

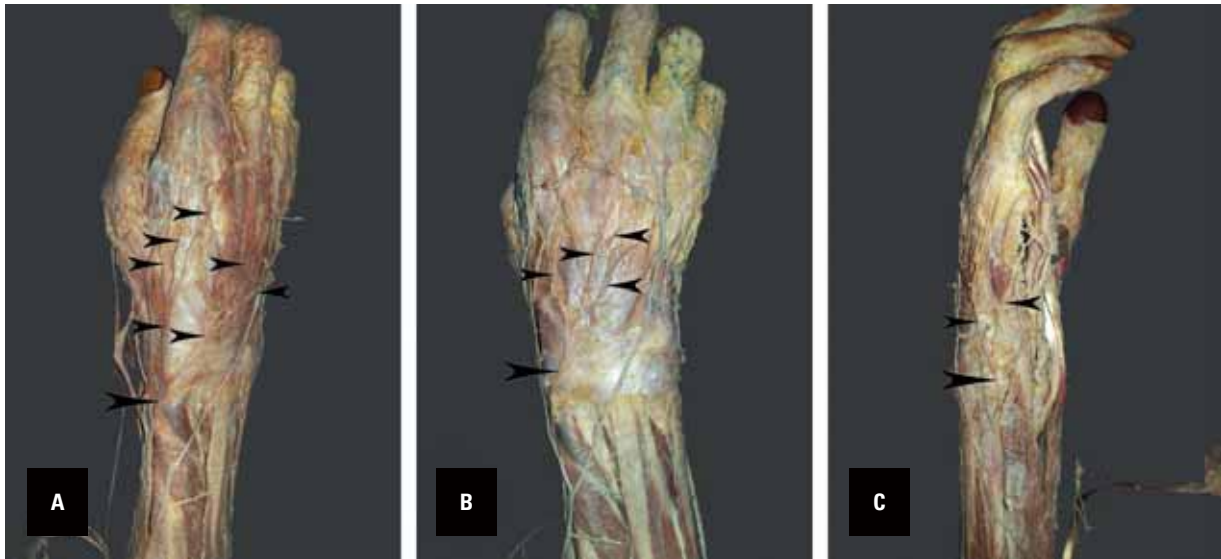


Figure 1. A–C. The lower limb of a 72-year-old at death male Caucasian cadaver showing variation of the superficial branch of the radial nerve (SBRN) and the dorsal branch of the ulnar nerve (DBUN), **A, B.** The large arrowhead indicates the SBRN, the small arrowhead its branches; **C.** The large arrowhead indicates the DBUN, the small arrowhead its branches.

The DBUN appears near the distal part of the flexor carpi ulnaris muscle and then, after piercing the fascia, it is located on the dorsal ulnar side of the wrist and hand. Finally, it splits into two or three terminal branches; the first innervates the medial side of the fifth finger and the second the opposite sides of the fifth and fourth fingers; when there is a third branch, it ensures sensory innervation of the opposite sides of the third and fourth fingers [15].

The LABCN is a cutaneous branch of the musculocutaneous nerve. Distally, it reaches the base of the thenar area and some of its terminal branches can connect with the terminal branch of the radial nerve and the palmar cutaneous branch of the median nerve [15].

Precise knowledge of the dorsal sensory innervation of the hand is not only interesting to anatomists but also has clinical implications for hand surgeons during dorsal flaps and approaches, for regional anaesthetic blocks, and for neurological practice to avoid misinterpretation of nerve pathology [5, 17].

Herein, we present an unusual case of unilateral variation of the SBRN in the right hand.

CASE REPORT

During a routine anatomical dissection of the right upper limb of a 72-year-old male Caucasian cadaver a rare SBRN variation was observed.

After curving around the wrist under the tendon of the brachioradialis muscle, 8.7 cm from the radial

styloid process (RS), and passing over the tendons of the abductor pollicis longus and extensor pollicis brevis muscles, the SBRN divides into two branches. The smaller branch supplies the skin of the medial and lateral sides of the thumb and reaches the root of the nail. The larger branch divides into three smaller branches: the first supplies the skin of the dorsal hand and adjoining sides of the index finger (the medial branch of the nerve to the finger was damaged during the dissection course); the second divides into a further two branches, and the medial one also divides into two, so the major branch ensures innervation of the middle and ring fingers to the proximal interphalangeal joints; and the third supplies the lateral surface of the little finger (Fig. 1A, B; 2).

The DBUN appears near the flexor carpi ulnaris muscle in the distal direction, and after piercing the fascia passes to the ulnar side on the dorsal part of the wrist and hand and finally divides into two branches: the first innervates the medial side of the little finger and the second communicates with a ramus of the superficial branch of the ulnar nerve and thus supplies the skin of the medial palmar side of the fifth finger (Fig. 1C; 2).

DISCUSSION

Several previous articles have presented different innervation variants of the dorsal part of the hand [12].

Mok et al. [12] observed that the common innervation distribution pattern in more than half of all

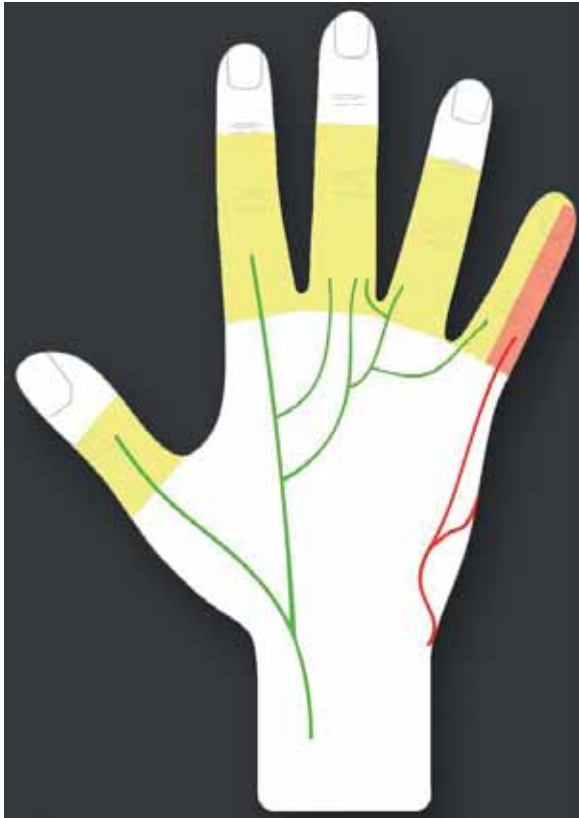


Figure 2. Scheme showing variation of the superficial branch of the radial nerve (green line) and the dorsal branch of the ulnar nerve (red line).

cases was distributed equally between the SBRN and the DBUN. Vergara-Amador and Nieto (2010) [19] described similar results in 56% of cases. Linell [9] reported that in 68.8%, the DBUN supplies the dorsal parts of the medial two and a half digits. According to Mok et al. [12] the nerve territories overlapped significantly among different specimens. This agrees with the findings of other authors [2, 6, 11, 13].

Sulaiman et al. [17] established that the SBRN innervated the thumb and index finger in 63.6% of cases. The DBUN was described as extending the innervation zone more laterally, ensuring the supply to the skin of the ulnar part of the second finger in 3 cases. The usual innervation pattern of the dorsal hand was found in only 12.86% of the hands examined. Sulaiman et al. [17] established that the radial nerve is the sole supplier to the dorsum of the hand in 6.62% of cases when the DBUN is absent. Similar results were reported by Botte et al. [3] in 4.2%, Mok et al. [12] in 3.3%, Robson et al. [14] in 8% and Tiznado et al. [18] in 5.6%. Kuruvilla et al. [7] noted an autosomal dominant inheritance of a variant SBRN

that predominantly innervated the dorsal aspect of the hand. They reported a patient with such a bilateral variation and a similar one in one of the two children.

Sulaiman et al. [17] also reported that the ulnar part of the fifth finger was supplied by the DBUN in all cases when the nerve was established. The DBUN supplied the lateral side of the little finger in 97.9% and the medial side of the ring finger in 96.4%. It provided the sole innervation of the lateral side of the ring finger in 63.6%. The reported variation, if it compressed or injured the ulnar nerve, could present as loss of sensation on the dorsal surface of the medial part of the fifth finger.

Mok et al. [12] proposed a classification of the nerve distribution of the dorsal hand, termed the radial/ulnar/lateral antebrachial cutaneous nerve (RUL) classification system. They accept the normal anatomical pattern as classically described: the SBRN innervates the radial two and a half digits, the DBUN, the ulnar two and a half, and the LABCN innervates no digits and is used for the term Rn/Un/Ln ("n" for normal). When presented in different variants, each nerve is described separately. The described nerve is assigned +1 or -1 for each half of the finger that has additional or less innervation [12].

The sensory innervation differs between the two hands. The symmetry in innervation of the dorsal hand ranges between 29% [16] and 43.2% [17]. Therefore, Sulaiman et al. [17] considered that clinicians should be very careful when they compare healthy with diseased hands in nerve conduction studies.

Clinically, variations of the SBRN involving all or most of the supply to the dorsal part of the hand could impede hand and reconstructive surgeons, and cause difficulty for neurologists interpreting electromyograms or evaluating abnormal symptoms. The presented variation could cause problems for hand and wrist surgery through the dorsal approach, and no safe zone could be defined. In addition, in the event of local block of the SBRN and anaesthesia of the fifth finger, a surgeon should be suspicious for possible SBRN variations, and precise operative technique is mandatory [1, 7, 12, 17, 18]. Moreover, in the event of traumatic injury to the ulnar nerve, such a SBRN variation could lead to misdiagnosis [8].

Auerbach et al. [2] established that the SBRN appeared 8.6 cm proximal to the RS between the tendons of the branchioradialis and extensor carpi radialis longus. This nerve then appeared 6.0 cm

above the fascia from the RS. In the series of Vergara-Amador and Nieto [19] it appeared subcutaneously 8.45 cm from the RS. Mok et al. [12] established that the SBRN pierced the fascia between the tendons of the aforementioned muscles 8.7 cm from the RS. These authors recommend that block of the SBRN should be 7 cm proximal to the radial styloid, where all its branches perforate the fascia and the nerve is widest. However, Mackinnon and Dellon [10] point out that the supply from the LABCN also needs to be borne in mind because it could overlap with these nerves.

CONCLUSIONS

The possibility of a variant total or predominant supply of the dorsal skin by the radial nerve, as reported, could explain atypical symptoms in entrapment neuropathies or acute nerve injury, and could impede electrophysiological tests and dorsal approaches to the hand. As stated by Żytkowski et al. [20] the analysis of such a variation contributes for obtaining an actual, not idealized image of the inside of the human body, which is of crucial importance in everyday clinical practice.

Acknowledgements


The authors wish to express their gratitude to all those who donated their bodies to medical science [4].

Conflict of interest: None declared

REFERENCES

- Abrams RA, Brown RA, Botte MJ. The superficial branch of the radial nerve: an anatomic study with surgical implications. *J Hand Surg Am.* 1992; 17(6): 1037–1041, doi: [10.1016/s0363-5023\(09\)91056-5](https://doi.org/10.1016/s0363-5023(09)91056-5), indexed in Pubmed: [1430933](https://pubmed.ncbi.nlm.nih.gov/1430933/).
- Auerbach DM, Collins ED, Kunkle KL, et al. The radial sensory nerve. An anatomic study. *Clin Orthop Relat Res.* 1994(308): 241–249, indexed in Pubmed: [7955689](https://pubmed.ncbi.nlm.nih.gov/7955689/).
- Botte MJ, Cohen MS, Lavernia CJ, et al. The dorsal branch of the ulnar nerve: an anatomic study. *J Hand Surg Am.* 1990; 15(4): 603–607, doi: [10.1016/s0363-5023\(09\)90022-3](https://doi.org/10.1016/s0363-5023(09)90022-3), indexed in Pubmed: [2380524](https://pubmed.ncbi.nlm.nih.gov/2380524/).
- Iwanaga J, Singh V, Ohtsuka A, et al. Acknowledging the use of human cadaveric tissues in research papers: Recommendations from anatomical journal editors. *Clin Anat.* 2021; 34(1): 2–4, doi: [10.1002/ca.23671](https://doi.org/10.1002/ca.23671), indexed in Pubmed: [32808702](https://pubmed.ncbi.nlm.nih.gov/32808702/).
- Keplinger M, Marhofer P, Moriggl B, et al. Cutaneous innervation of the hand: clinical testing in volunteers shows high intra- and inter-individual variability. *Br J Anaesth.* 2018; 120(4): 836–845, doi: [10.1016/j.bja.2017.09.008](https://doi.org/10.1016/j.bja.2017.09.008), indexed in Pubmed: [29576124](https://pubmed.ncbi.nlm.nih.gov/29576124/).
- Kosinski C. L'innervation cutanée de la face dorsale de la main, basée sur l'examen de 300 pièces anatomiques, avec quelques notions d'anatomic comparée. *Assoc Anatom Compt Rend.* 1927; 22: 121–133.
- Kuruville A, Laaksonen S, Falck B. Anomalous superficial radial nerve: a patient with probable autosomal dominant inheritance of the anomaly. *Muscle Nerve.* 2002; 26(5): 716–719, doi: [10.1002/mus.10239](https://doi.org/10.1002/mus.10239), indexed in Pubmed: [12402296](https://pubmed.ncbi.nlm.nih.gov/12402296/).
- Leis AA, Wells KJ. Radial nerve cutaneous innervation to the ulnar dorsum of the hand. *Clin Neurophysiol.* 2008; 119(3): 662–666, doi: [10.1016/j.clinph.2007.11.045](https://doi.org/10.1016/j.clinph.2007.11.045), indexed in Pubmed: [18164664](https://pubmed.ncbi.nlm.nih.gov/18164664/).
- Linell EA. The distribution of nerves in the upper limb, with reference to variabilities and their clinical significance. *J Anat.* 1921; 55(Pt 2-3): 79–112, indexed in Pubmed: [17103922](https://pubmed.ncbi.nlm.nih.gov/17103922/).
- Mackinnon SE, Dellon AL. The overlap pattern of the lateral antebrachial cutaneous nerve and the superficial branch of the radial nerve. *J Hand Surg Am.* 1985; 10(4): 522–526, doi: [10.1016/s0363-5023\(85\)80076-9](https://doi.org/10.1016/s0363-5023(85)80076-9), indexed in Pubmed: [4020063](https://pubmed.ncbi.nlm.nih.gov/4020063/).
- Mogi E. Untersuchung über die sensible innervation der handrücken bei den japanischen feten. *Redaktion Der Okijimas Folia Anat Jap.* 1937; 15: 675.
- Mok D, Nikolis A, Harris PG. The cutaneous innervation of the dorsal hand: detailed anatomy with clinical implications. *J Hand Surg Am.* 2006; 31(4): 565–574, doi: [10.1016/j.jhsa.2005.12.021](https://doi.org/10.1016/j.jhsa.2005.12.021), indexed in Pubmed: [16632049](https://pubmed.ncbi.nlm.nih.gov/16632049/).
- P'an MT. The cutaneous nerves of the Chinese hand. *Am J Phys Anthropol.* 1939; 25(3): 301–309, doi: [10.1002/ajpa.1330250326](https://doi.org/10.1002/ajpa.1330250326).
- Robson AJ, See MS, Ellis H. Applied anatomy of the superficial branch of the radial nerve. *Clin Anat.* 2008; 21(1): 38–45, doi: [10.1002/ca.20576](https://doi.org/10.1002/ca.20576), indexed in Pubmed: [18092362](https://pubmed.ncbi.nlm.nih.gov/18092362/).
- Standing S. *Gray's anatomy: the anatomical basis of clinical practice.* Churchill Livingstone/Elsevier, Edinburgh 2008.
- Stappaerts KH, Van Hees J, Van den Broeck EA. Peripheral cutaneous nerve distribution to the fingers. *Physiother Res Int.* 1996; 1(1): 41–49, doi: [10.1002/pri.46](https://doi.org/10.1002/pri.46), indexed in Pubmed: [9238722](https://pubmed.ncbi.nlm.nih.gov/9238722/).
- Sulaiman S, Soames R, Lamb C. The sensory distribution in the dorsum of the hand: anatomical study with clinical implications. *Surg Radiol Anat.* 2015; 37(7): 779–785, doi: [10.1007/s00276-014-1416-1](https://doi.org/10.1007/s00276-014-1416-1), indexed in Pubmed: [25572036](https://pubmed.ncbi.nlm.nih.gov/25572036/).
- Tiznado G, Sousa-Rodrigues C, Olave E. Superficial branch of the radial nerve: large distribution in the dorsum of hand. *Int J Morphol.* 2012; 30(2): 374–378.
- Vergara-Amador E, Nieto JL. Estudio anatómico de la rama superficial del nervio radial, implicaciones quirúrgicas. *Rev Fac Med.* 2010; 58(3): 214–220.
- Żytkowski A, Tubbs R, Iwanaga J, et al. Anatomical normality and variability: Historical perspective and methodological considerations. *Transl Res Anat.* 2021; 23: 100105, doi: [10.1016/j.tria.2020.100105](https://doi.org/10.1016/j.tria.2020.100105).

Rare left colic artery variation of the gut arterial system

S.A. Memar¹, A.M. Taylor², S. Ahuja², D.T. Daly² , Y. Tan²

¹A.T. Still University Kirksville College of Osteopathic Medicine, Kirksville, MO, United States

²Centre for Anatomical Science and Education, Department of Surgery, Saint Louis University School of Medicine, Saint Louis, MO, United States

[Received: 6 October 2021; Accepted: 15 November 2021; Early publication date: 26 November 2021]

Most variations of the abdominal blood supply are related to branching of the coeliac trunk and superior mesenteric artery. This case details a remarkable variation in the branching pattern of the left colic artery (LCA) observed during routine cadaveric dissection of an 84-year-old male donor. An anomalous common trunk, originating from the common hepatic artery, gave rise to three branches: 1) an accessory posterior pancreaticoduodenal artery to the head of the pancreas and adjacent duodenum, 2) the dorsal pancreatic artery anastomosing with branches of the splenic artery, and 3) the LCA. The LCA descended between the splenic vein and superior mesenteric artery to supply the left colic flexure and form a collateral route with the middle colic artery by contributing to the marginal artery of Drummond. Knowledge of this variation is clinically relevant for surgical and radiological procedures in the abdomen. (Folia Morphol 2023; 82, 1: 198–204)

Key words: left colic artery, variation, inferior mesenteric artery, coeliac trunk, common hepatic artery, anomaly, anomalous, anastomosis, collateral, colon, liver, pancreas

INTRODUCTION

The coeliac trunk (CT), superior mesenteric artery (SMA), inferior mesenteric artery (IMA), and their collateral pathways are commonly subjected to anatomical variations of both origin and course due to their embryological development pattern [13–15, 18]. Of these three major aortic branches, the CT and SMA display higher rates of variation due to their development from the embryological celiac complex while the IMA is less prone to variation [11, 19]. Variations of the left colic artery (LCA), which is normally the first branch from the IMA, are rare and the few reported instances often include an accessory LCA originating from the SMA or an absent LCA [2, 4, 13, 16]. Knowledge of less commonly observed abdominal arterial

variations, such as these, is clinically important for surgical and radiological interventions.

Normal anatomy of the CT

The CT is the first unpaired vessel arising from the ventral surface of abdominal aorta and it typically gives off three main branches: the left gastric artery (LGA), the splenic artery (SA), and the common hepatic artery (CHA).

The LGA travels cranially toward the oesophagus where it provides oesophageal branches before diving inferiorly along the lesser curvature of the stomach to anastomose with the right gastric artery. The SA immediately travels to the left after arising from the CT. The SA supplies blood to the pancreas as it travels

Address for correspondence: D.T. Daly, Assistant Professor, Centre for Anatomical Science and Education, Department of Surgery, Saint Louis University School of Medicine, Saint Louis, MO 63104, United States, tel.: 314-977-8027, fax: 314-977-5127, e-mail: daniel.daly@health.slu.edu

This article is available in open access under Creative Commons Attribution-Non-Commercial-No Derivatives 4.0 International (CC BY-NC-ND 4.0) license, allowing to download articles and share them with others as long as they credit the authors and the publisher, but without permission to change them in any way or use them commercially.

along the organ's posterosuperior border. The SA then provides the short gastric arteries to the fundus of the stomach and the left gastroepiploic artery before reaching the spleen.

The third branch of the CT is the CHA which travels to the right to supply the liver, gallbladder, pancreas, and the proximal duodenum. Along its course, this artery changes its name to the proper hepatic artery after providing the gastroduodenal artery [15]. The right gastric artery may arise from either the common or proper hepatic artery to travel along the lesser curvature of the stomach and anastomose with the LGA. The proper hepatic artery then bifurcates into right and left hepatic arteries to supply the liver. This normal branching pattern of the CHA has been observed in 80% of the general population [14].

Normal anatomy of the SMA

The second major unpaired vessel originating from the ventral aspect of the abdominal aorta, approximately 1–2 cm below the origin of the CT, is the SMA. The inferior pancreaticoduodenal artery is typically the first branch off the SMA, followed by the middle colic, the right colic and the ileocolic arteries. From the left aspect of the SMA, numerous jejunal and ileal branches supply the small intestine [5].

Normal anatomy of the IMA

The IMA is the last major unpaired vessel of the abdominal aorta, originating from its left anterolateral aspect at the level of the third lumbar vertebra. The first branch of the IMA, the LCA, anastomoses with the middle colic and sigmoid arteries to provide circulation to the distal one-third of the transverse colon and the descending colon. Along its course, the IMA also gives off several sigmoidal arteries to supply the sigmoid colon before terminating as the superior rectal artery and supplying the superior rectum [5, 13, 16].

Purpose

This report details a unique abdominal vascular variation of the hindgut in which the LCA originated from a common trunk arising from the CHA, thereby creating an anastomotic connection between the CT and the IMA. Additional variations in the arterial supply to the duodenum and pancreas were observed in conjunction with this LCA variation. Knowledge of variations within the gut arterial system is relevant for diagnostic and interventional procedures of the

abdominal viscera, especially the pancreas, duodenum, liver, and colon [14].

CASE REPORT

An 84-year-old male cadaver was received through the Saint Louis University Gift Body Programme of the Centre for Anatomical Science and Education (CASE) with signed, informed consent from the donor. The CASE Gift Body Programme abides by all the rules set forth by the Uniform Anatomical Gift Act.

Common trunk from CHA

During routine dissection, variations in the arterial supply to the pancreas, duodenum and hindgut-derivatives were observed. The CHA first provided an inferior branch which served as a common trunk for three arteries: an accessory posterior pancreaticoduodenal artery, the dorsal pancreatic artery, and the LCA (Fig. 1). This trifurcation occurred superior to the splenic vein, just to the left of the hepatic portal vein. Distal to the anomalous common trunk, the CHA displayed a typical branching pattern.

First branch of the common trunk: accessory posterior pancreaticoduodenal artery

The first branch from the common trunk, described as an accessory posterior pancreaticoduodenal artery, travelled rightward along the posterosuperior border of the splenic vein before running deep to the left gastric vein and hepatic portal vein (Fig. 1). After traversing the width of the hepatic portal vein, the artery continued to the right along the posterior surface of the head of the pancreas before splitting into three branches to supply the duodenum and the head of the pancreas. The two superior branches anastomosed with the posterior superior pancreaticoduodenal artery, which originated from the gastroduodenal artery, as expected. The third branch was the largest and most inferior and anastomosed directly with the posterior inferior pancreaticoduodenal artery, which originated from the SMA, as expected. It was also noted the left gastric vein drained directly to the splenic vein instead of the hepatic portal vein as normally seen.

Second branch of the common trunk: dorsal pancreatic artery

The second branch, described as the dorsal pancreatic artery, coursed leftward, anterior to the splenic vein, before continuing as the inferior pancreatic

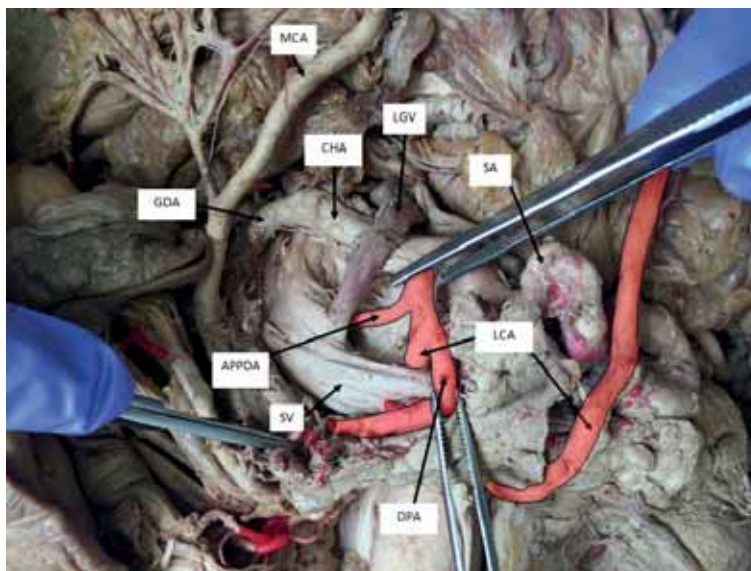


Figure 1. Anomalous common trunk branching from common hepatic artery. A common trunk (red) originated from the common hepatic artery and travelled inferiorly before trifurcating into an accessory posterior pancreaticoduodenal artery, the dorsal pancreatic artery, and the left colic artery. The trifurcation occurred superior to the splenic vein. The left colic artery travelled posterior to the splenic vein before continuing towards the splenic flexure to anastomose with the middle colic artery; APPDA — accessory posterior pancreaticoduodenal artery; CHA — common hepatic artery; DPA — dorsal pancreatic artery; GDA — gastroduodenal artery; LCA — left colic artery; LGV — left gastric vein; MCA — middle colic artery; SA — splenic artery; SV — splenic vein.

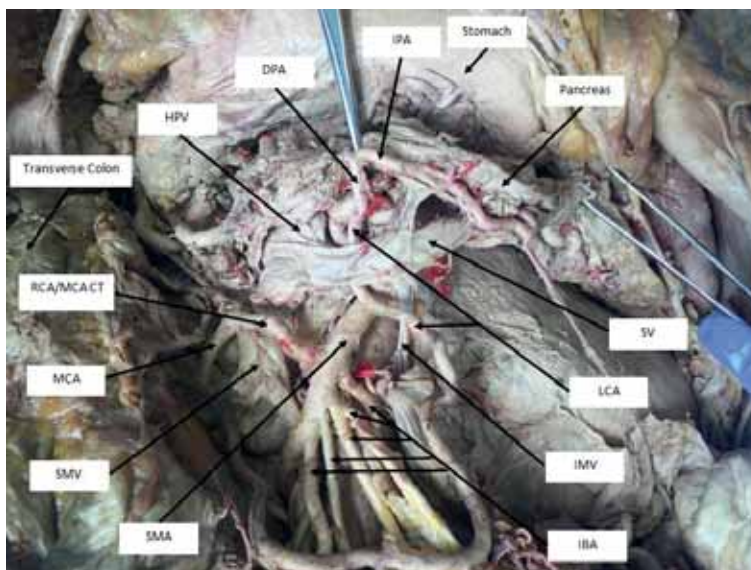


Figure 2. Courses of the dorsal pancreatic and left colic arteries. The dorsal pancreatic artery travelled leftward before continuing as the inferior pancreatic artery and anastomosing with branches of the splenic artery to supply the pancreas. The left colic artery travelled inferiorly between the splenic vein and superior mesenteric artery and was positioned to the right of the junction between the inferior mesenteric vein and the splenic vein before crossing over the inferior mesenteric vein. In this image, the transverse colon is pulled inferiorly and to the right, such that the middle colic artery is at the right of the image and the left colic artery is travelling inferiorly to anastomose with it; DPA — dorsal pancreatic artery; HPV — hepatic portal vein; IBA — intestinal branch arteries; IMV — inferior mesenteric vein; IPA — inferior pancreatic artery; LCA — left colic artery; MCA — middle colic artery; RCA/MCA CT — common trunk of the right and middle colic arteries; SMA — superior mesenteric artery; SMV — superior mesenteric vein; SV — splenic vein.

artery along the posteroinferior border of the pancreas (Fig. 2). While travelling toward the tail of the pancreas, it looped superiorly at two different points

in the middle of the pancreatic body, thereby forming two anastomotic connections with branches of the SA within the pancreas.

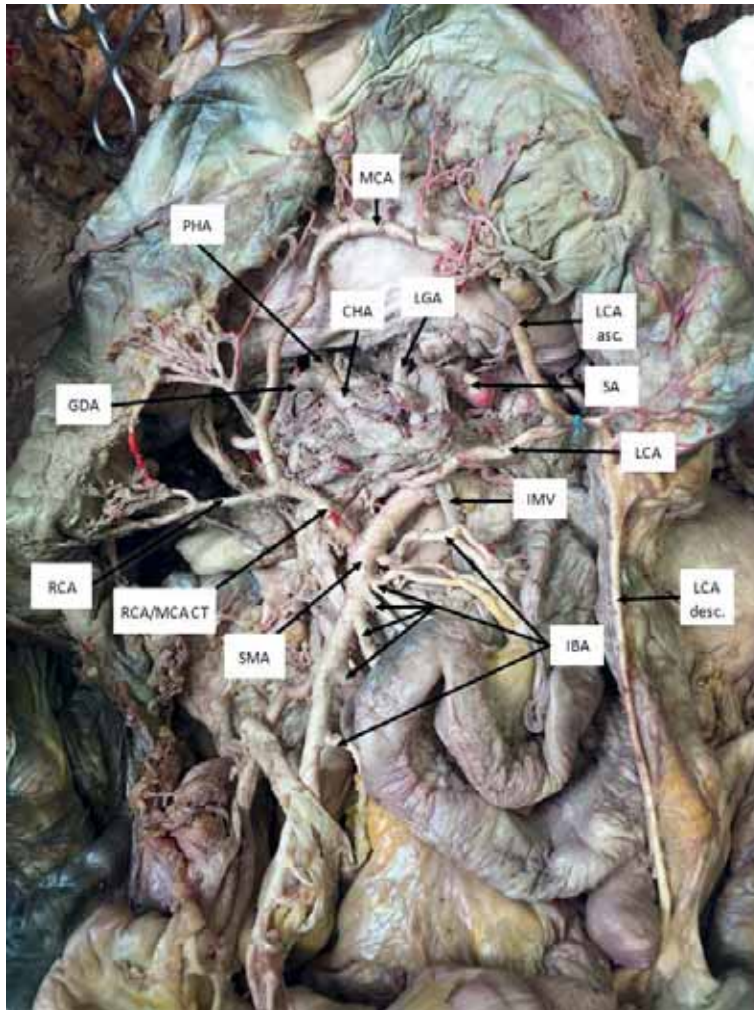


Figure 3. Left colic artery supplying hindgut with view of midgut. The left colic artery was positioned to the right of the junction between the inferior mesenteric vein and the splenic vein after coursing anterior to the superior mesenteric artery. It then passed anterior to the inferior mesenteric vein as it travelled leftward toward the splenic flexure, where it divided into ascending and descending branches. The ascending branch formed an anastomosis with the middle colic artery, which originated from a common trunk with the right colic artery. The descending branch continued inferiorly along the descending colon before anastomosing with the sigmoid branches of the inferior mesenteric artery (not pictured); CHA — common hepatic artery; GDA — gastroduodenal artery; IBA — intestinal branch arteries; IMV — inferior mesenteric vein; LGA — left gastric artery; LCA — left colic artery; LCA asc. — ascending branch of the left colic artery; LCA desc. — descending branch of the left colic artery; MCA — middle colic artery; PHA — proper hepatic artery; RCA — right colic artery; RCA/MCA CT — common trunk of the right and middle colic arteries; SA — splenic artery; SMA — superior mesenteric artery.

Third branch of the common trunk: left colic artery

The most distal branch from the common trunk was the LCA, which travelled inferiorly, posterior to the splenic vein and anterior to the SMA (Figs. 1, 2). After passing over the inferior mesenteric vein, just below its junction with the splenic vein, the LCA coursed leftward towards the splenic flexure and divided into ascending and descending branches (Figs. 3, 4). The ascending branch, which had the larger diameter of the two branches, formed an anastomosis with the middle colic artery, which shared a common trunk with right colic artery from the SMA. The descending

branch continued inferiorly along the descending colon before anastomosing with the sigmoid arteries. The sigmoid and superior rectal arteries originated from the IMA as expected. In this case, the marginal artery of Drummond was formed by the branches from the CT and the SMA and IMA instead of solely the SMA and IMA, as seen normally.

DISCUSSION

Embryological causes and established categorisation of gut arterial variations

The CT, SMA, and IMA are derived from a series of ventral vitelline arteries arising from the embryo-

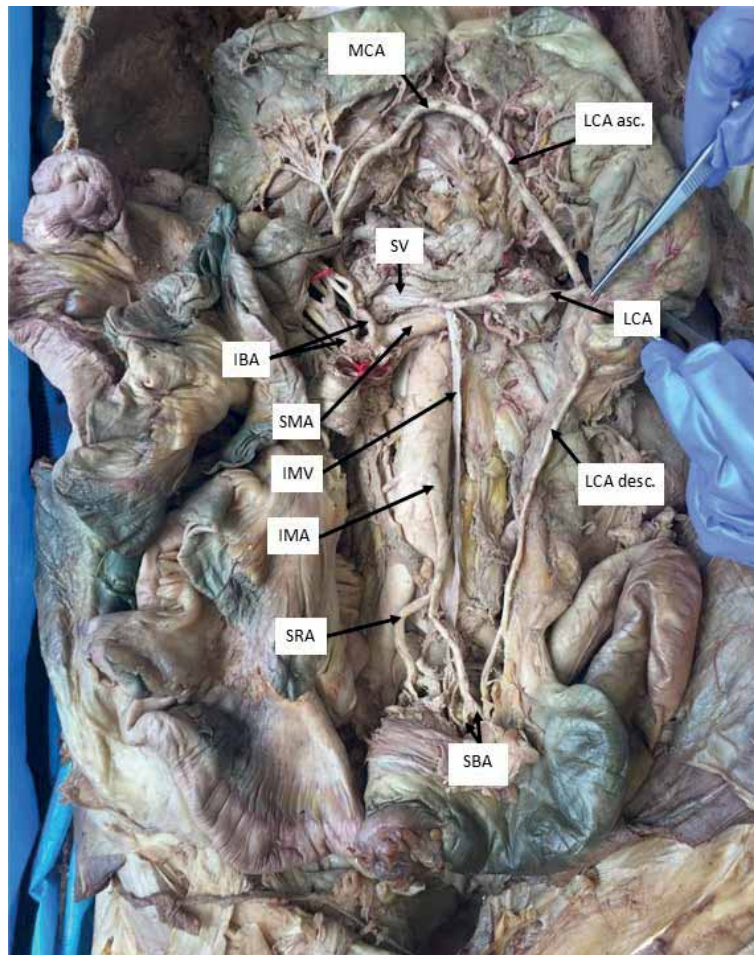


Figure 4. Left colic artery supplying hindgut. The ascending branch of the left colic artery anastomosed with the middle colic artery. The descending branch of the left colic artery anastomosed with the sigmoid branches of the inferior mesenteric artery. In this case, the marginal artery of Drummond was uniquely formed by the branches from the celiac trunk and the superior and inferior mesenteric arteries; IBA — intestinal branch arteries; IMA — inferior mesenteric artery; IMV — inferior mesenteric vein; LCA — left colic artery; LCA asc. — ascending branch of the left colic artery; LCA desc. — descending branch of the left colic artery; MCA — middle colic artery; SBA — sigmoid branch arteries; SMA — superior mesenteric artery; SRA — superior rectal artery; SV — splenic vein.

logical dorsal aortae to supply the fetal abdominal viscera [17]. The vitelline arteries are connected by an anastomotic channel that should regress to promote the development of the unpaired visceral arteries, though the persistence of vitelline remnants may explain variations in the vascular supply to this region [8, 17]. Most abdominal vascular variations in the subdiaphragmatic aorta are related to the liver and kidneys through variations of the CT and SMA [17].

There are several classification systems used to describe intestinal arterial variations. Lipschutz, Adachi, and Morita independently classified the origins of the left gastric, splenic, common hepatic and superior mesenteric arteries [1, 6, 10]. Gamo et al. [6] observed cadaveric specimens and computed tomography images to categorize SMA branching patterns [6]. However, the current case cannot be analysed using

the previous methods, as it either does not fit into the defined categories or it does not involve the mentioned branches.

Most relevant to the current case, Cirocchi et al. [4] conducted a systematic literature review of LCA anomaly case studies from 1953 until 2019 and categorised the LCA branching pattern from the IMA according to Latarjet's work: the LCA either originated independently or from a common trunk with sigmoidal branches [4, 20]. However, in both cases, the LCA was observed to originate from the IMA, which differs from the current variation.

Potential associated pathologies

The anatomical variants observed in the current case could potentially be related to a number of pathological presentations. The LCA as observed in

this case can be associated with compression of the splenic vein and resulting left-sided portal hypertension, which is a rare but life-threatening cause of upper gastrointestinal bleeding. Conversely, portal hypertension may compress the LCA in this unique case and block the blood supply to the distal colon. Additionally, the described vasculature could complicate procedures including pancreatectomy, pancreaticoduodenectomy, cholecystectomy, colectomy and hepatectomy [12]. Arteries supplying the abdominal viscera have also been investigated regarding their efficacy in bypass procedures, so an understanding of gut arterial anastomoses is necessary to determine if such a procedure is possible [3].

While the aforementioned complications are unique to this anatomical presentation, the common surgical concerns associated with any abdominal procedure remain. Examples include nephrectomy procedures which may be jeopardised by the LCA passing in close proximity to supply the left colic flexure and the potential for watershed ischemia at Griffith's point (which is the point of anastomosis between the middle and left colic arteries) [7, 9, 13]. In general, surgical procedures involving the aorta, liver, gallbladder, stomach, duodenum, pancreas, kidneys or lymph nodes may all be impacted by variations like the one presented in this case study.

CONCLUSIONS

This case study involves an anomalous common trunk branching from the CHA and providing the following three branches: an accessory posterior pancreaticoduodenal artery, the dorsal pancreatic artery, and the LCA. While arterial variations of the gut have been recorded in the past, such a connection between the CT and IMA has rarely been reported. Knowledge of atypical gut arterial supply, specifically to the duodenum, pancreas, and distal colon, is beneficial for clinicians to determine the feasibility of surgical procedures, thereby appropriately caring for patients.

Acknowledgements

We would like to thank the Gift Body Programme at the Centre for Anatomical Science and Education, Department of Surgery at Saint Louis University School of Medicine. This case report was presented in part at the 2021 Virtual AACA Annual Meeting of the American Association of Clinical Anatomists.

Conflict of interest: None declared

REFERENCES

1. Adachi B, Hasebe K, Daigaku K. *Das Arteriensystem der Japaner*. Kyoto, Kaiserlich-Japanische Universität zu Kyoto. Maruzen Co., Kyoto and Tokyo 1928.
2. Amonoo-Kuofi HS, el-Badawi MG, el-Naggar ME. Anomalous origins of colic arteries. *Clin Anat*. 1995; 8(4): 288–293, doi: [10.1002/ca.980080408](https://doi.org/10.1002/ca.980080408), indexed in Pubmed: [7552967](https://pubmed.ncbi.nlm.nih.gov/7552967/).
3. Calafiore A, Giammarco GDi, Teodori G, et al. Myocardial revascularization with multiple arterial grafts. *Asian Cardiovasc Thoracic Ann*. 2016; 3(3-4): 95–102, doi: [10.1177/021849239500300402](https://doi.org/10.1177/021849239500300402).
4. Cirocchi R, Randolph J, Cheruiyot I, et al. Systematic review and meta-analysis of the anatomical variants of the left colic artery. *Colorectal Dis*. 2020; 22(7): 768–778, doi: [10.1111/codi.14891](https://doi.org/10.1111/codi.14891), indexed in Pubmed: [31655010](https://pubmed.ncbi.nlm.nih.gov/31655010/).
5. De Martino RR. *Normal and variant mesenteric anatomy*. Springer, New York 2015.
6. Gamo E, Jiménez C, Pallares E, et al. The superior mesenteric artery and the variations of the colic patterns. A new anatomical and radiological classification of the colic arteries. *Surg Radiol Anat*. 2016; 38(5): 519–527, doi: [10.1007/s00276-015-1608-3](https://doi.org/10.1007/s00276-015-1608-3), indexed in Pubmed: [26728989](https://pubmed.ncbi.nlm.nih.gov/26728989/).
7. Ke J, Cai J, Wen X, et al. Anatomic variations of inferior mesenteric artery and left colic artery evaluated by 3-dimensional CT angiography: Insights into rectal cancer surgery. A retrospective observational study. *Int J Surg*. 2017; 41: 106–111, doi: [10.1016/j.ijssu.2017.03.012](https://doi.org/10.1016/j.ijssu.2017.03.012), indexed in Pubmed: [28323157](https://pubmed.ncbi.nlm.nih.gov/28323157/).
8. Kosaka M, Horiuchi K, Nishida K, et al. Hepatopancreatic arterial ring: bilateral symmetric typology in human celiaco-mesenteric arterial system. *Acta Med Okayama*. 2002; 56(5): 245–253.
9. Mann M, Kawzowicz M, Komosa A, et al. The marginal artery of Drummond revisited: a systematic review. *Transl Res Anat*. 2021; 24: 100118, doi: [10.1016/j.tria.2021.100118](https://doi.org/10.1016/j.tria.2021.100118).
10. Morita M. *Sekimen kyōfu no ryōhō*. Jinbun, Kyōto 1935.
11. Murakami T, Mabuchi M, Giuvarasteanu I, et al. Coexistence of rare arteries in the human celiaco-mesenteric system. *Acta Med Okayama*. 1998; 52(5): 239–244.
12. Nayak S, Shetty S, Sirasanagandla S, et al. Anomalous origin and vulnerable course of left colic artery in relation to the pancreas: a case report. *Forensic Med Anat Res*. 2013; 01(04): 83–86, doi: [10.4236/fmar.2013.14018](https://doi.org/10.4236/fmar.2013.14018).
13. Nayak S, Sr S, George B, et al. Unusual origin of left colic artery from the superior mesenteric artery and its course across the left kidney. *Open Access Case Reports*. 2014; 3(4).
14. Noussios G, Dimitriou I, Chatzis I, et al. The main anatomic variations of the hepatic artery and their importance in surgical practice: review of the literature. *J Clin Med Res*. 2017; 9(4): 248–252, doi: [10.14740/jocmr2902w](https://doi.org/10.14740/jocmr2902w), indexed in Pubmed: [28270883](https://pubmed.ncbi.nlm.nih.gov/28270883/).
15. Olewnik Ł, Wyśiadecki G, Polgaj M, et al. A rare anastomosis between the common hepatic artery and the superior mesenteric artery: a case report. *Surg Radiol Anat*. 2017; 39(10): 1175–1179, doi: [10.1007/s00276-017-1859-2](https://doi.org/10.1007/s00276-017-1859-2), indexed in Pubmed: [28432408](https://pubmed.ncbi.nlm.nih.gov/28432408/).
16. Rusu MC, Vlad M, Voinea LM, et al. Detailed anatomy of a left accessory aberrant colic artery. *Surg Radiol Anat*.

- 2008; 30(7): 595–599, doi: [10.1007/s00276-008-0362-1](https://doi.org/10.1007/s00276-008-0362-1), indexed in Pubmed: [18483690](https://pubmed.ncbi.nlm.nih.gov/18483690/).
17. Shaikh H, Wehrle CJ, Khorasani-Zadeh A. Anatomy, abdomen and pelvis, superior mesenteric artery. StatPearls, Treasure Island 2021.
 18. Stimec BV, Terraz S, Fasel JHD. The third time is the charm-anastomosis between the celiac trunk and the left colic artery. Clin Anat. 2011; 24(2): 258–261, doi: [10.1002/ca.21081](https://doi.org/10.1002/ca.21081), indexed in Pubmed: [21322049](https://pubmed.ncbi.nlm.nih.gov/21322049/).
 19. Tandler J. Über die Varietäten der Arteria coeliaca und deren Entwicklung. Anat Hefte. 1904; 25(2): 473–500, doi: [10.1007/bf02300762](https://doi.org/10.1007/bf02300762).
 20. Testut L, Latarjet A. Traité d'anatomie humaine. Doin, Paris 1948.

Ascending palatine branch from the lingual artery with multiple other variations of the external carotid artery

C. Escoffier¹, D. Hage², T. Tanaka³, R.S. Tubbs^{3-7, 10}, J. Iwanaga^{2, 4, 8, 9}

¹College of Dentistry, University of Florida, Gainesville, FL, United States

²Department of Neurosurgery, Tulane Centre for Clinical Neurosciences, Tulane University School of Medicine, New Orleans, LA, United States

³Department of Periodontology, College of Dentistry, University of Florida, Gainesville, FL, United States

⁴Department of Neurology, Tulane Centre for Clinical Neurosciences, Tulane University School of Medicine, New Orleans, LA, United States

⁵Department of Anatomical Sciences, St. George's University, St. George's, Grenada, West Indies

⁶Department of Structural and Cellular Biology, Tulane University School of Medicine, New Orleans, LA, United States

⁷Department of Neurosurgery and Ochsner Neuroscience Institute, Ochsner Health System, New Orleans, LA, United States

⁸Dental and Oral Medical Centre, Kurume University School of Medicine, Kurume, Fukuoka, Japan

⁹Division of Gross and Clinical Anatomy, Department of Anatomy, Kurume University School of Medicine, Kurume, Fukuoka, Japan

¹⁰Department of Surgery, Tulane University School of Medicine, New Orleans, LA, United States

[Received: 25 August 2021; Accepted: 20 October 2021; Early publication date: 16 November 2021]

The external carotid artery (ECA) is the major blood supply for structures in the head and neck. Typically, it has 8 separate branches; but there are many anatomical variations, making it difficult to predict surgical outcomes and complications without 3-dimensional imaging. This case study focuses on a cadaver with multiple anatomical variations in the ECA, i.e., lingual, facial, occipital, ascending pharyngeal, and posterior auricular arteries, found during routine dissection of the right cadaveric neck. We also discuss the incidences of several other anatomical variations of the ECA branches and their surgical implications and potential complications. (Folia Morphol 2023; 82, 1: 205–210)

Key words: lingofacial trunk, external carotid artery, anatomy, variation, cadaver

INTRODUCTION

The external carotid artery (ECA) forms at the bifurcation of the common carotid artery (CCA) at the level of the fourth cervical vertebra. It has eight major branches that supply areas around the head, neck, and face. It terminates as it bifurcates into the maxillary artery, which supplies the maxillary region and several adjacent regions such as the oral cavity, and the superficial temporal artery,

which supplies the area of the scalp overlying the temporal region [12, 13].

The ascending palatine artery is a branch of the facial artery, diverging soon after the facial artery branches off the ECA. It runs along the superior pharyngeal constrictor muscle and travels between the styloglossus and stylopharyngeus muscles. As it arrives at the levator veli palatini muscle it divides into two branches [12, 13]. One continues along the

Address for correspondence: J. Iwanaga, DDS, PhD, Department of Neurosurgery, Tulane Centre for Clinical Neurosciences, Tulane University School of Medicine, 131 S. Robertson St. Suite 1300, New Orleans, LA 70112, United States, tel: 5049885565, fax: 5049885793, e-mail: iwanagajoeca@gmail.com

This article is available in open access under Creative Commons Attribution-Non-Commercial-No Derivatives 4.0 International (CC BY-NC-ND 4.0) license, allowing to download articles and share them with others as long as they credit the authors and the publisher, but without permission to change them in any way or use them commercially.

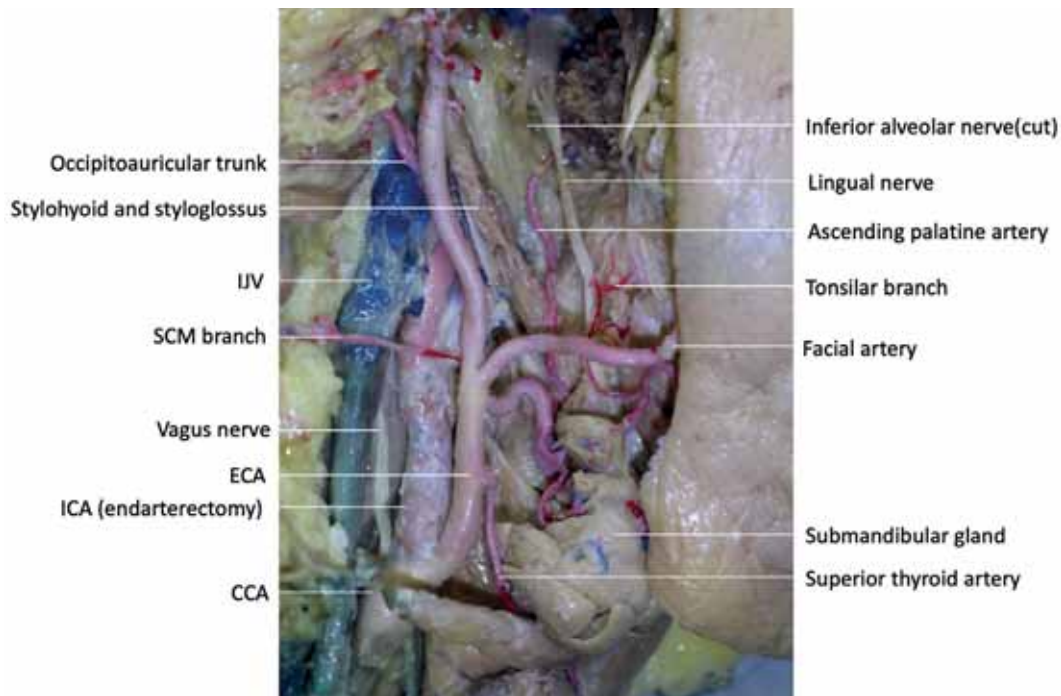


Figure 1. Right external carotid artery (ECA) with multiple variant branches; CCA — common carotid artery; ICA — internal carotid artery; IJV — internal jugular vein; SCM — sternocleidomastoid muscle.

pharynx to supply the palatine glands and the muscles of the soft palate, eventually anastomosing with the descending palatine branch of the maxillary artery. The other immediately pierces the pharynx to supply the palatine tonsil and auditory tube and later anastomoses with the tonsillar branch of the facial artery and the ascending pharyngeal artery [6].

The purpose of this case presentation is to discuss an anatomical variation found during a routine dissection that has important clinical implications for surgeries at the level of the angle of the mandible.

CASE REPORT

During routine dissection of the right cadaveric neck of a 72-year-old at death female, multiple anatomical variations of the ECA were noted (Figs. 1, 2). The cadaver had a history of endarterectomy of the right internal carotid. There was adhesion of the common facial vein and the hypoglossal nerve.

Lingual and facial arteries

A small branch arose from the lingual artery at the depth of the submandibular gland and bifurcated into the ascending palatine artery and a branch to the submandibular gland (Fig. 3). The ascending palatine artery ran laterally to the stylohyoid and styloglossus muscles. This is an atypical presentation, as the as-

ending palatine artery and the branch to the submandibular gland did not arise from the facial artery.

Ascending pharyngeal artery

The sternocleidomastoid branch arose from the ascending pharyngeal artery instead of the occipital artery (Fig. 4).

Occipital and posterior auricular arteries

The occipitoauricular trunk arose from the ECA at the level where the stylohyoid and styloglossus crossed it (Fig. 5).

DISCUSSION

Embryology of the ECA

The development of the ECA begins at weeks 3–5 in utero. The aortic sac gives rise to the aortic arches and the third aortic arch gives rise to the CCA, which later bifurcates into the internal and external carotid arteries. Most branches of the ECA originate from the third arch except for the maxillary artery, which arises from the first aortic arch [5].

Other anatomical variations of the branches of the ECA

There have been many studies aimed at identifying the incidences of different ECA variations. In an ana-

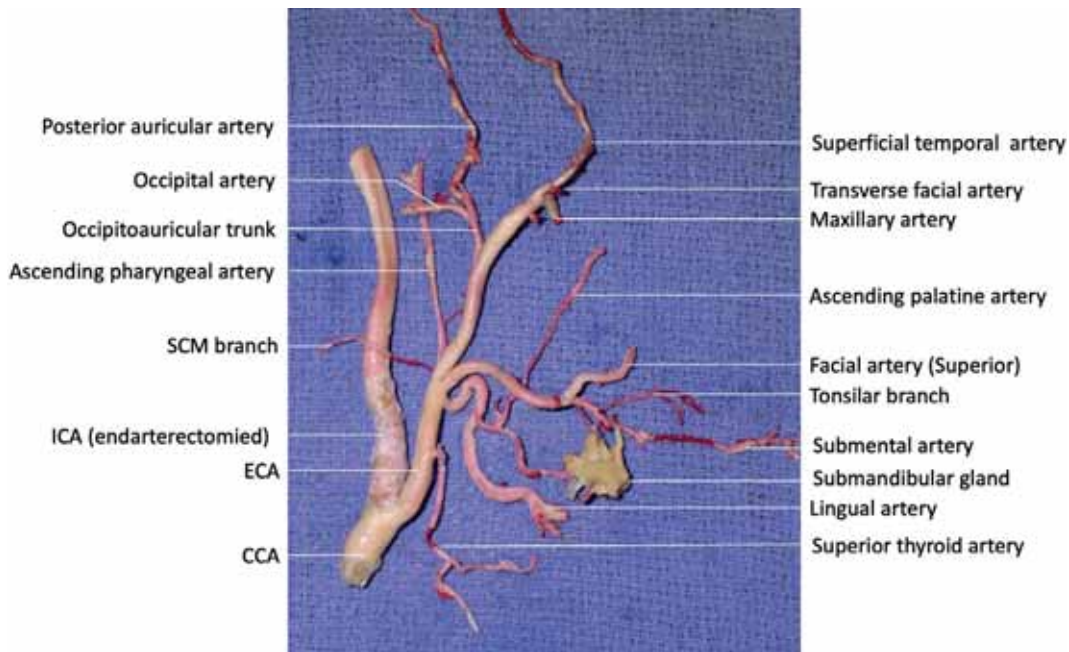


Figure 2. Right external carotid artery (ECA) with multiple variant branches after resection; CCA — common carotid artery; ICA — internal carotid artery; SCM — sternocleidomastoid muscle.

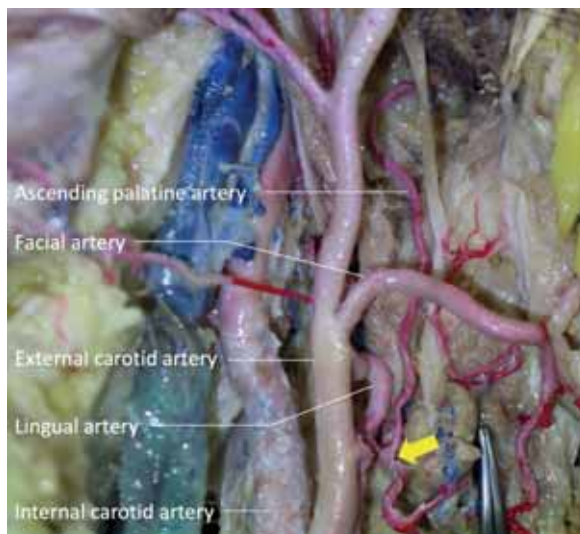


Figure 3. Ascending palatine artery arising from the lingual artery (arrow).

tomical study of 40 cadavers, Devadas et al. [4] identified and quantified various anatomical variations of ECA branching. They observed that only 75% of their specimens had an ECA origin at the level of the upper border of the thyroid cartilage, where it is expected. A higher-than-expected ECA origin was present in 25% cases; there were no cases with a lower-than-expected origin. It was noted that 78.75% of cases displayed separate origins for the anterior branches.

On the other hand, the linguofacial trunk was seen in 16% of the specimens, making it the most commonly observed variation, while a thyrolinguofacial trunk was seen in 1 (1.25%) case; no thyrolingual trunks were present. Notably, a case with a thyrolinguofacial trunk was also reported by Baxla et al. [1]. The ascending pharyngeal artery was normal in 97.5% of their cases, but 1 (1.25%) case had an unusually high origin above the carotid bifurcation, and another (1.25%) displayed double pharyngeal arteries at the posteromedial aspect of the ECA. Other notable variations were a muscular branch to the masseter muscle from the ECA in the parotid region, a slender branch to the internal jugular veins from the ECA above the superior thyroid artery origin, and a superior laryngeal artery emerging directly from the ECA in 3.75% of cases [4].

Several anatomical variations of ECA branching patterns have also been described by Navakalyani et al. [10]. In their report, the facial and lingual arteries arose from a common linguofacial trunk in 8% of cases, and the superior thyroid and the lingual arteries arose from a common thyrolingual trunk in 1%. They also observed the superior thyroid artery originating from the bifurcation of the CCA instead of the ECA in 8% of cases, and the ascending pharyngeal artery emerging from the occipital artery instead of the ECA in 1%. In 5% of cases there was a variation in which the posterior auricular artery branched off the

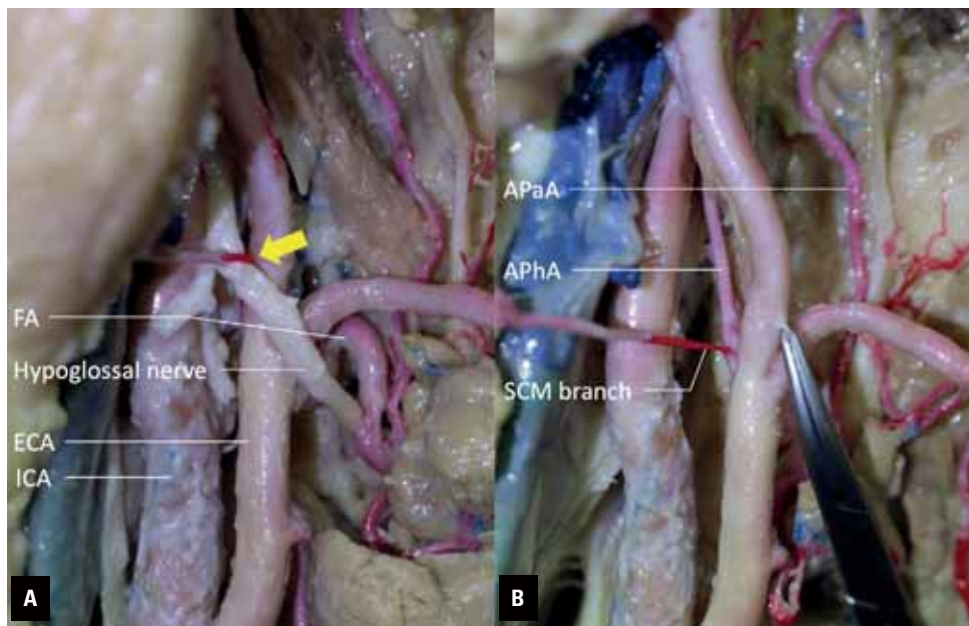


Figure 4. Sternocleidomastoid (SCM) branch arising from the ascending pharyngeal artery (APhA); **A.** SCM branch goes over the hypoglossal nerve (arrow); **B.** After resection of the hypoglossal nerve. The origin of the SCM is seen clearly; APaA — ascending palatine artery; ECA — external carotid artery; FA — facial artery; ICA — internal carotid artery.

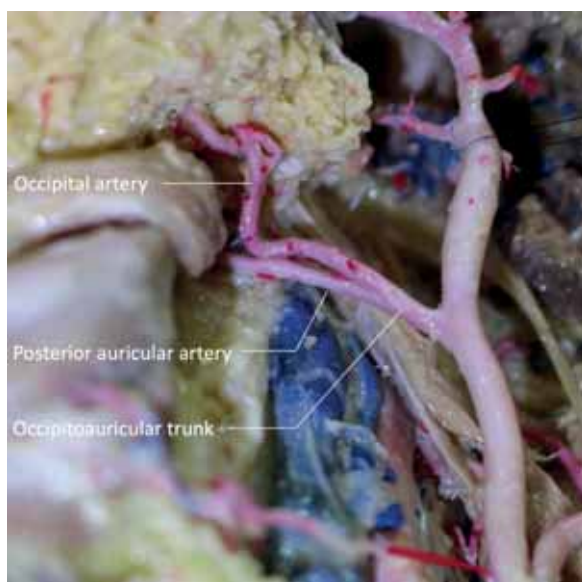


Figure 5. Occipitoauricular trunk.

occipital artery instead of branching separately off the ECA. They found no variations in the origin of the ECA, but like Devadas et al. [10] they noted the origin at a higher level than expected in 2% of cases.

In a study of 302 patients, Yamamoto et al. [14] determined the incidences of ECA branching patterns by analysing 532 ECAs using digital subtraction angiography. They classified these arteries into three categories (A, B, C) based on the number of

branches (two, three, four or more) emerging from the proximal ECA at a common point, the distal ECA counting as 1 branch [14]. Using this criterion, type A (2 branches) is defined as all individual branches arising separately from the proximal ECA. They observed type A in 344 (64.6%) ECAs in 237 (78.5%) patients, type B in 134 (25.2%) ECAs in 110 (36.4%) patients, and type C in 54 (10.2%) ECAs in 49 (16.2%) patients. Although type C was the least prevalent, it had a shorter distance (14.7 ± 6.6 mm) between the CCA and the bifurcation of the first branch of the ECA than type A (21.8 ± 15.6 mm) or type B (20.6 ± 8.9 mm). They also found that 96.3% of type C ECAs had a CCA bifurcation at the level of the third-fourth cervical vertebrae or higher, which was significantly higher than the bifurcation in type A or B. Because there are several anatomical variations, it is imperative that surgeons be aware of the type C variation to avoid unexpected complications [14].

An anatomical variation of the ascending palatine artery, branching from the lingual artery instead of the facial artery, has been noted in previous literature. Unfortunately, we could find no more details of this variation [11].

Our present case contains several variations that have not yet been reported and are not the most commonly encountered. While variations such as the linguofacial, thyrolinguofacial, and thyrolingual

trunks are gaining more exposure amongst surgeons, many others are possible. Each variant has important implications for surgeries of the head and neck such as thyroidectomies or reconstruction of a cervical aneurysm, so increasing our knowledge of these variations is imperative for reducing risks associated with head and neck surgery.

Blood supply to the posterior palate

The ascending palatine artery provides the main source of perfusion to the soft palate, specifically supplying the uvula, palatoglossus, palatopharyngeus, and the levator veli palatini muscle. This artery splits into two branches, the anterior and the posterior ascending palatine arteries. However, some studies have shown that the two branches do not always supply the soft palate simultaneously, which could be surgically significant [3]. The ascending pharyngeal artery also has another role; it has been found to supply the palatopharyngeus muscle [7]. Other arteries to note are the lesser palatine, the palatal branch of the ascending pharyngeal, and the tonsillar, which emerge beneath the mucosal layer and anastomose with the branches of the ascending palatine artery. This rich and interconnected blood supply reduces the risk of necrosis during palatoplasty surgeries [7].

Clinical relevance

The lingual and facial arteries are located in delicate regions of the head and neck, putting them at risk of causing life-threatening haemorrhages in the setting of trauma. Haemorrhages on the floor of the mouth can obstruct the airway and require emergency tracheostomy to maintain airway patency, so anatomical variations are important for physicians to consider when they plan for surgery or treat trauma cases [9]. Although the main complication of submandibulectomies is sialadenitis, it is imperative that surgeons be wary of vessels emerging from the lingual nerve at the level of the sublingual gland [6]. In our case study, the anatomical variation of the ascending palatine vessel emerging from the lingual artery at the submandibular gland would result in necrosis of the palate if it were severed during surgery.

CONCLUSIONS

Anatomical variations in the arteries supplying the palate can affect the outcome of surgeries such as palatoplasty in cleft palate patients and Le Fort I

osteotomies. A study of the risk of palatal necrosis in Le Fort I osteotomies showed that 90% of patients had normal anatomy in which both the ascending palatine and ascending pharyngeal arteries supplied the area, while 10% were dependent on the ascending pharyngeal artery alone for a blood supply to the palate. This reduction in vascular supply can pose a huge risk if the ascending pharyngeal artery is ligated in a patient with the variation, whereas in patients with normal anatomy the ascending palatine artery simply provides a supplement [2].

Acknowledgements

The authors sincerely thank those who donated their bodies to science so that anatomical research could be performed. Results from such research can potentially increase mankind's overall knowledge that can then improve patient care. Therefore, these donors and their families deserve our highest gratitude [8].

Conflict of interest: None declared

REFERENCES

1. Baxla M, Kumari C, Kaler S. Bilateral thyrolinguofacial trunk: unusual and rare branching pattern of external carotid artery. *Anat Cell Biol.* 2018; 51(4): 302–304, doi: [10.5115/acb.2018.51.4.302](https://doi.org/10.5115/acb.2018.51.4.302), indexed in Pubmed: [30637166](https://pubmed.ncbi.nlm.nih.gov/30637166/).
2. Bruneder S, Wallner J, Weiglein A, et al. Anatomy of the Le Fort I segment: Are arterial variations a potential risk factor for avascular bone necrosis in Le Fort I osteotomies? *J Craniomaxillofac Surg.* 2018; 46(8): 1285–1295, doi: [10.1016/j.jcms.2018.04.023](https://doi.org/10.1016/j.jcms.2018.04.023), indexed in Pubmed: [29805066](https://pubmed.ncbi.nlm.nih.gov/29805066/).
3. Cho JH, Kim JW, Park HW, et al. Arterial supply of the human soft palate. *Surg Radiol Anat.* 2017; 39(7): 731–734, doi: [10.1007/s00276-016-1798-3](https://doi.org/10.1007/s00276-016-1798-3), indexed in Pubmed: [28138793](https://pubmed.ncbi.nlm.nih.gov/28138793/).
4. Devadas D, Pillay M, Sukumaran TT. A cadaveric study on variations in branching pattern of external carotid artery. *Anat Cell Biol.* 2018; 51(4): 225–231, doi: [10.5115/acb.2018.51.4.225](https://doi.org/10.5115/acb.2018.51.4.225), indexed in Pubmed: [30637155](https://pubmed.ncbi.nlm.nih.gov/30637155/).
5. Hanneman K, Newman B, Chan F. Congenital variants and anomalies of the aortic arch. *Radiographics.* 2017; 37(1): 32–51, doi: [10.1148/rg.2017160033](https://doi.org/10.1148/rg.2017160033), indexed in Pubmed: [27860551](https://pubmed.ncbi.nlm.nih.gov/27860551/).
6. Hernando M, Echarri R, Taha M, et al. Surgical complications of submandibular gland excision. *Acta Otorinolaringologica.* 2012; 63(1): 42–46, doi: [10.1016/j.otoeng.2012.01.009](https://doi.org/10.1016/j.otoeng.2012.01.009).
7. Huang MH, Lee ST, Rajendran K. Clinical implications of the velopharyngeal blood supply: a fresh cadaveric study. *Plast Reconstr Surg.* 1998; 102(3): 655–667, doi: [10.1097/00006534-199809030-00007](https://doi.org/10.1097/00006534-199809030-00007), indexed in Pubmed: [9727428](https://pubmed.ncbi.nlm.nih.gov/9727428/).

8. Iwanaga J, Singh V, Takeda S, et al. Acknowledging the use of human cadaveric tissues in research papers: Recommendations from anatomical journal editors. *Clin Anat.* 2021; 34(1): 2–4, doi: [10.1002/ca.23671](https://doi.org/10.1002/ca.23671), indexed in Pubmed: [32808702](https://pubmed.ncbi.nlm.nih.gov/32808702/).
9. Mawaddah A, Goh BS, Kew TY, et al. Isolated blunt lingual artery injury secondary to a road traffic accident: diagnostic and therapeutic approach. *Malays J Med Sci.* 2012; 19(2): 77–81.
10. Navakalyani T, Janaki V, Sumalatha Dr. Variant branching patterns of external carotid artery – pharyngo-occipital trunk and occipito - auricular trunk. *IOSR J Dental Med Sci.* 2016; 15(08): 44–47, doi: [10.9790/0853-1508064447](https://doi.org/10.9790/0853-1508064447).
11. Tubbs RS, Shoja MM, Loukas M. ed. *Bergman's Comprehensive Encyclopedia of Human Anatomic Variation.* John Wiley Sons 2016.
12. Uflacker R. ed. *Arteries of the head and neck. Atlas of Vascular Anatomy: An Angiographic Approach* 2007.
13. von Arx T, Tamura K, Yukiya O, et al. The face – a vascular perspective. A literature review. *Swiss Dent J.* 2018; 128(5): 382–392.
14. Yamamoto D, Koizumi H, Ishima D, et al. Angiographic characterization of the external carotid artery: special attention to variations in branching patterns. *Tohoku J Exp Med.* 2019; 249(3): 185–192, doi: [10.1620/tjem.249.185](https://doi.org/10.1620/tjem.249.185), indexed in Pubmed: [31761818](https://pubmed.ncbi.nlm.nih.gov/31761818/).

An unusual variant of the atlantomastoid muscle

N.O. Blackwood¹, Ł. Olewnik², G.P. Georgiev³, G. Wysiadeci⁴, A. Aysenne¹,
J. Iwanaga^{1, 5}, R.S. Tubbs^{1, 5–8}

¹Department of Neurosurgery, Tulane University School of Medicine, New Orleans, LA, United States

²Department of Anatomical Dissection and Donation, Chair of Anatomy and Histology, Medical University of Lodz, Poland

³Department of Orthopaedics and Traumatology, University Hospital Queen Giovanna – ISUL, Medical University of Sofia, Bulgaria

⁴Department of Normal and Clinical Anatomy, Chair of Anatomy and Histology, Medical University of Lodz, Poland

⁵Department of Neurology, Tulane University School of Medicine, New Orleans, LA, United States

⁶Department of Anatomical Sciences, St. George's University, St. George's, Grenada, West Indies

⁷Department of Structural and Cellular Biology, Tulane University School of Medicine, New Orleans, LA, United States

⁸Department of Neurosurgery, and Ochsner Neuroscience Institute, Ochsner Health System, New Orleans, LA, United States

[Received: 20 July 2021; Accepted: 3 November 2021; Early publication date: 16 November 2021]

Knowledge of anatomical variations can be of use to clinicians and surgeons when, for example, viewing images of a patient or performing operations. Such knowledge can minimise the risk of iatrogenic complications. Herein, we present a case of a variant atlantomastoid muscle. The muscle was identified on the left side in an adult cadaver. The muscle's measurements and anatomical relationships are presented as well as a review of salient literature. We hope that increased knowledge of anatomical variants in the suboccipital region can improve patient care. (Folia Morphol 2023; 82, 1: 211–215)

Key words: anatomical variation, atlantomastoid muscle, suboccipital muscles, suboccipital region

INTRODUCTION

The atlantomastoid muscle is a muscle variant in the suboccipital region. It originates from the transverse process of the atlas and inserts on the posterior aspect of the mastoid process of the temporal bone [2, 5, 6, 8, 9, 11]. It is innervated by the dorsal ramus of C1 and supplied by the occipital artery [9]. The clinical relevance of this muscle variant arises from its proximity to important cervical and suboccipital neurovasculature, including the occipital artery, the vertebral artery, and the dorsal ramus of C1 [2, 4, 6, 9]. This paper reports a case of a variant atlantomastoid muscle found in a cadaver and describes its relationships to surrounding anatomical structures.

CASE REPORT

During the routine dissection at the Tulane University School of Medicine, New Orleans, Louisiana, United States of an 88-year-old at death male cadaver, a variant muscle of the suboccipital region was identified. This finding was determined to be the atlantomastoid muscle (Figs. 1, 2). The muscle joined the posterolateral aspect of the transverse process of the atlas to the mastoid part of the temporal bone medial to the mastoid notch. The muscle was more or less positioned halfway between the mastoid notch laterally and the occipitomastoid suture medially. Using microcallipers (Mitutoyo, Japan) to measure the muscle, it was found to be 1.1 cm

Address for correspondence: J. Iwanaga, DDS, PhD, Department of Neurosurgery, Tulane Centre for Clinical Neurosciences, Tulane University School of Medicine, 131 S. Robertson St. Suite 1300, New Orleans, LA 70112, United States, tel: 5049885565, fax: 5049885793, e-mail: iwanagajoecca@gmail.com

This article is available in open access under Creative Common Attribution-Non-Commercial-No Derivatives 4.0 International (CC BY-NC-ND 4.0) license, allowing to download articles and share them with others as long as they credit the authors and the publisher, but without permission to change them in any way or use them commercially.

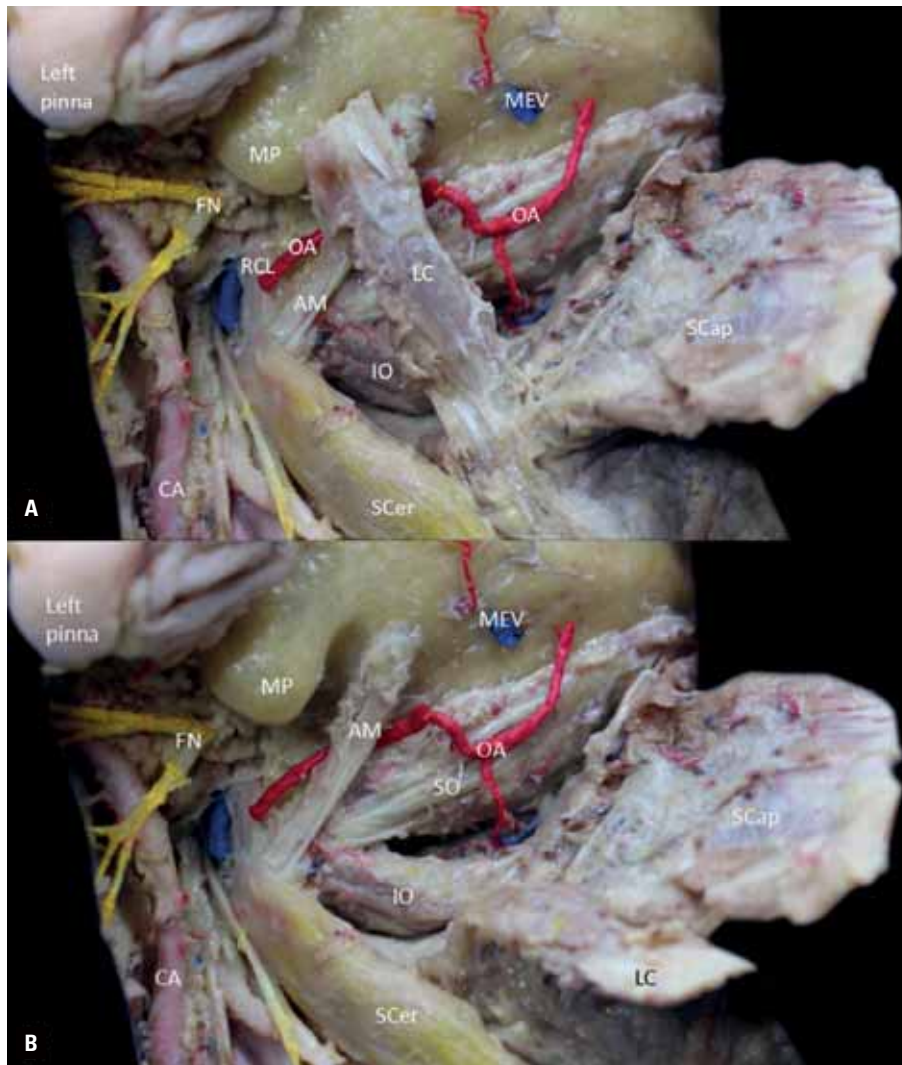


Figure 1. A. Left atlantomastoid muscle (AM) as described in the present case report. The upper fibres of the muscle are covered here by the attachment of the longissimus capitis muscle (LC) onto the mastoid process (MP); **B.** Following the reflection of the LC; CA — external carotid artery; FN — facial nerve; IO — obliquus capitis inferior muscle; MEV — mastoid emissary vein; OA — occipital artery; RCL — rectus capitis lateralis; SCap — splenius capitis muscle; SCer — splenius cervicis muscle; SO — obliquus capitis superior muscle.

in width and 5.3 cm long. Its innervation was via a small branch from the suboccipital nerve. Its blood supply was via a branch from the occipital artery, which travelled deep to the muscle at the junction of its upper third to lower two thirds. The muscle was deep to the longissimus capitis and splenius capitis muscles and in the same plane as the suboccipital triangle muscles, e.g. obliquus capitis superior muscle. As the muscle attached onto the mastoid part of the temporal bone, it was positioned just posterior to the digastric muscle's posterior belly. The mastoid emissary vein was seen medial to the muscle's attachment onto the temporal bone (Fig. 3). No atlantomastoid muscle was identified on the right side, and no additional anatomical variations were

observed on the left side. No medical or surgical history of the cadaver was available.

DISCUSSION

The atlantomastoid muscle has been reported through primary observation in 7 studies (Table 1). The first report was in a description by Winslow in 1732 [11]. Bankart published observations of 158 cadavers in 1869 and included reports of the muscle variant [1]. Gruber [2] remarked on it in a report on 50 cadavers in 1876. Knott [5] studied the atlantomastoid muscle in 33 cadavers. Le Double [6] published a summary of previous reports of the atlantomastoid muscle in addition to his own observations of this muscle in 52 cadavers. Mori [9] published a study of

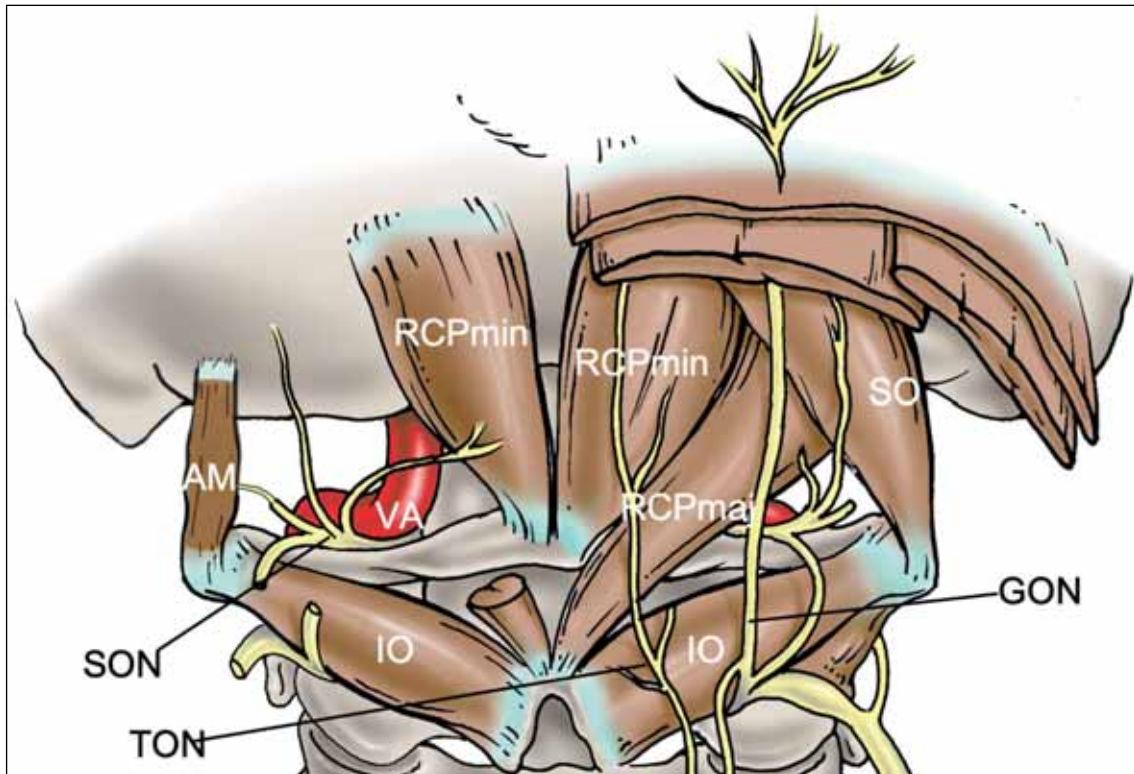


Figure 2. Schematic drawing of the atlantomastoid muscle (AM) noting its innervation from a small branch of the suboccipital nerve (SON). For clarity, the rectus capitis lateralis, which was anterior to the AM is not shown but in this view would have been just anterior to the AM; RCPmin — rectus capitis posterior minor; RCPmaj — rectus capitis posterior major; SO — obliquus capitis superior muscle; IO — obliquus capitis inferior muscle; VA — vertebral artery; greater GON — occipital nerve; TON — third occipital nerve.

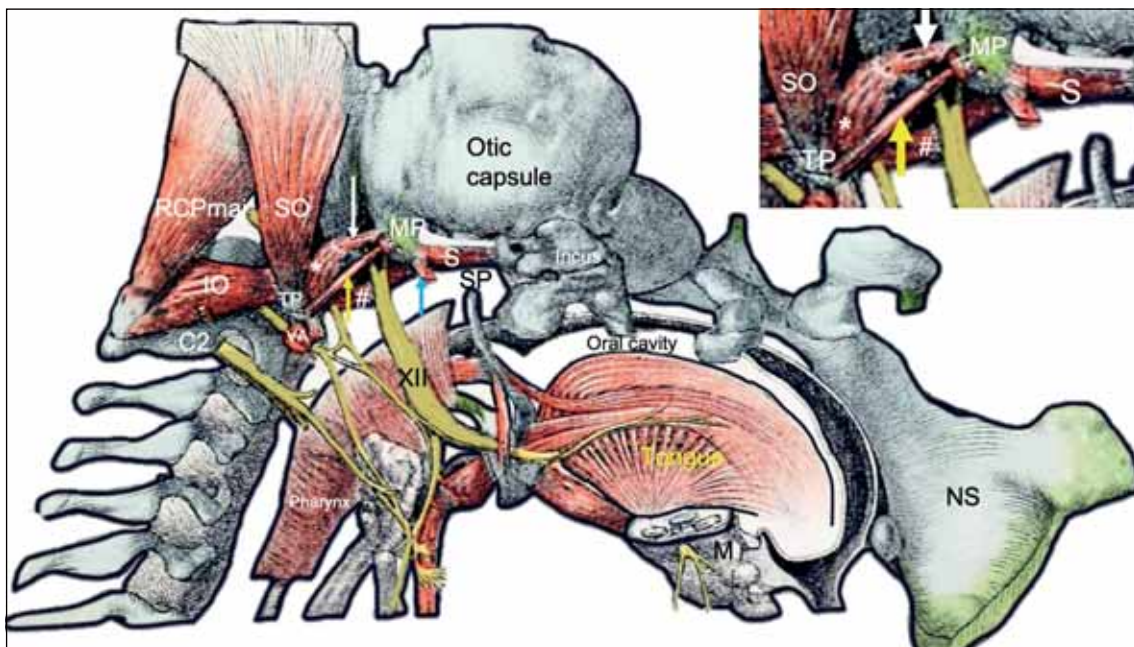


Figure 3. Schematic drawing of a 21 mm long embryo. The atlantomastoid (yellow arrow) and related muscles are noted. Related muscles include the occipitomastoid (white arrow), rectus capitis lateralis (*), rectus capitis anterior (#), posterior belly of the digastric (blue arrow), stapedius (S), obliquus capitis inferior (IO), obliquus capitis superior (SO), and the rectus capitis posterior major (RCPmaj). Bony landmarks include the transverse process (TP) of the C1, styloid process (SP), and the C2 vertebra (C2). The cut vertebral artery (VA) and hypoglossal nerve (XII) are also shown. Anteriorly, the mandible (M) and nasal septum (NS) are seen; MP — mastoid process. (After Lewis, 1920 [8]). The inset is a zoomed in view of the region of the atlantomastoid muscle and its surrounding anatomy.

Table 1. Sex, side, and country of reports of the atlantomastoid muscle

	Number	Sex	Laterality	Country
Gruber [2]	11/50	45M/5F*	4B/L7	Germany
Knott [5]	4/33	Unknown	Unknown	Unknown
Le Double [6]	9/52	6M/3F	4B/L2/R4	France
Mori [9]	14/54	Unknown	5B/L4/R5	Japan

M — males; F — females; B — bilateral; L — left side only; R — right side only. The number column is the reported number of muscles found out of the total number of cadavers dissected. Note that LeDouble states that he identified the atlantomastoid muscle in 9 specimens, he goes on to describe 4 of these as being found bilaterally, and 2 on left sides only and 4 on right sides only which adds up to ten. *Also note that although Gruber listed that he dissected 45 males and 5 females, we are not told the sex of the 11 specimens found to have the muscle and that only LeDouble specified that 6 males and 3 females were found to have the muscle.

this variant in 54 Japanese cadavers in 1964. To our knowledge, since Mori's study, no additional reports of this muscle have been published. There has been no published cadaveric image of the atlantomastoid muscle. Therefore, the current case is of archival value.

Four studies provide information about the frequency of the atlantomastoid muscle. Gruber [2] reported finding the muscle variant in 11 (22%) of 50 cadavers and 15 of 100 sides (15%). Knott [5] observed it in four of 33 (12.1%) subjects. Le Double [6] observed the atlantomastoid muscle in 9 of 52 (17.3%) cadavers. Mori [9] discovered the muscle in 14 (25.9%) of 54 cadavers and 19 (17.6%) of 108 sides. Overall, the muscle has been reported in 15.7% (49/312) of sides and 20.1% (38/189) of cadavers [7].

Questions regarding sex, age, and nationality/ethnicity differences in the atlantomastoid muscle frequency, along with differences between sides, remain valid. Of the 7 primary reports of the muscle, only 4 provided quantitative frequency data [2, 5, 6, 9]. Only the study of 54 Japanese cadavers provided information about the population of origin for samples [9]. LeDouble's report was the only one to relate frequency to sex [6]. Only 3 studies reported laterality differences in the frequency of the atlantomastoid muscle [2, 6, 9]. No observations of age differences in the atlantomastoid muscle among specimens have been published.

The muscle has been reported in the gorilla, chimpanzee, and seminopithecus [2, 10]. Although the exact function is unknown, we posit that it could, in concert with other regional muscles, rotate the skull ipsilaterally.

Most have described the atlantomastoid muscle as attaching onto the mastoid process of the temporal bone. However, as seen in our case, Gruber [2] did

depict 1 case of a more medial attachment of the muscle away from the mastoid process. These attachments of the muscle seem to be a rare variation.

Classifications

Based on reports in the literature and our present case, the atlantomastoid can be classified into two broad categories — attachment onto the mastoid process or attachment to surrounding parts of the temporal bone. We would propose these be considered as types 1 and 2, respectively, with the later, as seen in our present case, being much less common. Within these two categories are smaller variations. The muscle can be anterior or posterior to the rectus capitis lateralis [2]. Gruber [2] added that the atlantomastoid might have accessory slips with the middle scalene, levator scapulae, splenius capitis, or longissimus cervicis muscles. Mori [9] also added that the muscle can have slips to the longissimus capitis, transverse process of C2, and splenius capitis muscle. We propose that such additional slips could be classified as types 1a or 2a depending on the primary bony attachment, i.e. on or adjacent to the mastoid process.

Embryology

The development of the muscles of the suboccipital region has not been well studied. Mori [9] suggested that the atlantomastoid muscle, obliquus capitis superior, and longissimus capitis muscles might share the same embryological derivation due to their innervation by the suboccipital nerve. Lewis [8] described and depicted the atlantomastoid muscle in a 21 mm embryo as being attached to the mastoid blastema and as being long and slender (Fig. 3). He also described the adjacent occipitomastoid (Fig. 3) and believed it might be related to the intertransversarii muscles although he also suggested this muscle could be derived from the pharyngeal arches. Both muscles were considered rudimentary muscles by Lewis who also stated they were not found in adults.

Clinical/Surgical applications

We hope that increased knowledge of anatomical variants in the suboccipital region can improve patient care. Repeated observations on anatomical variations deepen existing knowledge, can help to overcome the subjective aspect in the description made by individual researchers, and can also be useful for clinicians in their daily practice [12]. Procedures that might encounter or specialities that need to know details

about this muscle include neurosurgical approaches to the skull base such as suboccipital craniectomy and exposure of the occipital artery for occipital artery to posterior cerebral artery bypass and interventional procedures that target the occipital region in treating patients with, for example, pain related to muscle spasm or muscle compression of surrounding nerves, i.e. occipital neuralgia migraine and require botulinum toxin injection to the suboccipital musculature. Lastly, although small, the atlantomastoid muscle, with the continued improvement in imaging techniques, e.g. magnetic resonance imaging might be appreciated by radiologist viewing the skull base. Therefore, knowledge of the atlantomastoid can improve interpretation of images and prevent misdiagnosis if it is identified.

CONCLUSIONS

We present a variant of the atlantomastoid muscle. Based on our proposed classification of the muscle, this would be a type 2 muscle. Such a muscle attaching medial to the mastoid notch might be encountered during craniotomies in this region. For example, this is the location of a retrosigmoid craniotomy for access to the cerebellopontine angle. Additionally, surgeons who are localising the occipital artery would need to know that the atlantomastoid muscle, when present, can travel superficially to the artery and lie deep to the longissimus capitis muscle, which normally covers it posteriorly.

Acknowledgements

The authors sincerely thank those who donated their bodies to science so that anatomical research could be performed. Results from such research can potentially increase humankind's overall knowledge


that can then improve patient care. Therefore, these donors and their families deserve our highest gratitude [3].

Conflict of interest: None declared

REFERENCES

1. Bankart J, Pye-Smith P, Phillips J. Notes of abnormalities observed in the dissecting room during the winter sessions of 1866–7 and 1867–8. *Guy's Hospital Reports*. 1869; 14(3): 436–455.
2. Gruber W. Über den Musculus atlantico-mastoideus. *Arch Anat Physiol Wissen Med*. 1876: 733–738.
3. Iwanaga J, Singh V, Ohtsuka A, et al. Acknowledging the use of human cadaveric tissues in research papers: Recommendations from anatomical journal editors. *Clin Anat*. 2021; 34(1): 2–4, doi: [10.1002/ca.23671](https://doi.org/10.1002/ca.23671), indexed in Pubmed: [32808702](https://pubmed.ncbi.nlm.nih.gov/32808702/).
4. Jenkins S, Iwanaga J, Dumont AS, et al. What is the suboccipital nerve? Tracking this confusing historical nomenclature. *Morphologie*. 2021; 105(348): 10–14, doi: [10.1016/j.morpho.2020.09.002](https://doi.org/10.1016/j.morpho.2020.09.002), indexed in Pubmed: [33172783](https://pubmed.ncbi.nlm.nih.gov/33172783/).
5. Knott JF. On abnormalities in human myology. *Proceedings of the Royal Irish Academy*. 1883; 3: 407–427.
6. Le Double AF. Atloïdo-mastôïdien. *Traité des variations du système musculaire de l'homme et de leur signification au point de vue de l'anthropologie zoologique*. 1897; 1: 240–241.
7. Lee RA. What is known about the atlantomastoid muscle: a scoping review. *Queen's University*. 2021: 16–40.
8. Lewis WH. The cartilaginous skull of a human embryo twenty-one millimeters in length. *Contributions to Embryology*. 1920; 9: 299–324.
9. Mori M. Statistics on the musculature of the Japanese. *Okajimas Folia Anat Jap*. 1964; 40(3): 195–300, doi: [10.2535/ofaj1936.40.3_195](https://doi.org/10.2535/ofaj1936.40.3_195).
10. Tubbs RS, Shoja M, Loukas M. *Bergman's Comprehensive Encyclopedia of Human Anatomic Variation*. Wiley 2016.
11. Winslow JB. *Exposition anatomique de la structure du corps humain*. G Desprez & J Desessartz 1732.
12. Żytkowski A, Tubbs R, Iwanaga J, et al. Anatomical normality and variability: Historical perspective and methodological considerations. *Trans Res Anat*. 2021; 23: 100105, doi: [10.1016/j.tria.2020.100105](https://doi.org/10.1016/j.tria.2020.100105).

Presence of accessory abductor digiti minimi muscle in two cadavers

C.D. Hamacher¹, B.J. Browning¹, J.C. Barton¹, N.F. Chase¹, R.E. Larson^{1,2}, D.J. Green^{1,2} 

¹Campbell University School of Osteopathic Medicine, Buies Creek, United States

²Department of Anatomy, Buies Creek, United States

[Received: 25 October 2021; Accepted: 23 December 2021; Early publication date: 17 January 2022]

During routine cadaveric dissection, accessory hypothenar muscles were incidentally discovered in two cadavers, both males, aged 86 and 92. Both muscles originated from the palmaris longus tendon in the distal portion of the forearm and were identified as accessory abductor digiti minimi (AADM) muscles, based on their association with abductor digiti minimi. While AADM is a common variant in the antebrachium, it is less typical for them to originate from the palmaris longus tendon. The presence of such an AADM could complicate surgical procedures requiring resection of the palmaris longus tendon. Moreover, the surrounding neurovasculature — namely the ulnar nerve as it passes through the ulnar canal between the pisiform and hook of the hamate — could be compressed by contractions of an AADM with such a proximal origin. This can manifest as ulnar neuropathies resulting in pain, weakness, or protracted flexion of the fourth and fifth digits (ulnar claw). Our description of these muscles adds to previous accounts of variation of the palmaris longus and abductor digiti minimi muscles while considering potential clinical implications. (Folia Morphol 2023; 82, 1: 216–220)

Key words: anatomy, dissection, variation, forearm, wrist, hand, palm, medicine

INTRODUCTION

The hypothenar muscles of the hand include abductor digiti minimi, flexor digiti minimi, and opponens digiti minimi. All are innervated by the ulnar nerve, take origin from the medial carpus or flexor retinaculum, and serve to abduct, flex, and oppose the fifth digit, respectively (Table 1). Here, we report on two separate cases of accessory abductor digiti minimi (AADM) muscles discovered incidentally during routine cadaveric dissection. Previous discussion of AADM describe the muscle as originating from the flexor retinaculum, pisiform, flexor carpi radialis, or antebrachial fascia, with the latter being the most common origin site [5]. In contrast, both AADM

muscles described in this report originated from the palmaris longus tendon. Palmaris longus is a slender muscle located in the superficial portion of the anterior antebrachium. It shares a common muscle belly of origin — from the medial epicondyle of the humerus — with other superficial flexors of the elbow and wrist: pronator teres, flexor carpi radialis, flexor carpi ulnaris, and flexor digitorum superficialis; its insertion tendon joins the palmar aponeurosis after passing superficial to the flexor retinaculum. The AADM muscles described in this report followed a more extensive course than other such variants [12] and given their more proximal origin site relative to the other hypothenar muscles, passed superficially to

Address for correspondence: Mr. B.J. Browning and Dr. D.J. Green, Campbell University School of Osteopathic Medicine, PO Box 4280, 27506 Buies Creek, United States, e-mail: b_browning0620@email.campbell.edu and dgreen@campbell.edu

This article is available in open access under Creative Commons Attribution-Non-Commercial-No Derivatives 4.0 International (CC BY-NC-ND 4.0) license, allowing to download articles and share them with others as long as they credit the authors and the publisher, but without permission to change them in any way or use them commercially.

Table 1. Origins, insertions, and actions of hypothenar muscles and the accessory abductor digiti minimi (AADM) variant discussed in this report, which are all innervated by the ulnar nerve

Muscle	Origin	Insertion	Action
Abductor digiti minimi	Pisiform; flexor carpi ulnaris tendon	Medial aspect of base of 5 th proximal phalanx	Abduction of the 5 th digit
AADM	Variable: palmaris longus tendon*; flexor retinaculum; pisiform; flexor carpi radialis; antebrachial fascia	Abductor digiti minimi muscle belly	Abduction of the 5 th digit
Flexor digiti minimi	Hook of hamate; flexor retinaculum	Medial aspect of base of 5 th proximal phalanx	Flexion of the 5 th digit
Opponens digiti minimi	Hook of hamate; flexor retinaculum	Medial aspect of 5 th metacarpal	Lateral rotation and opposition of 5 th digit

*Indicates the origin of the AADMs described in this report.

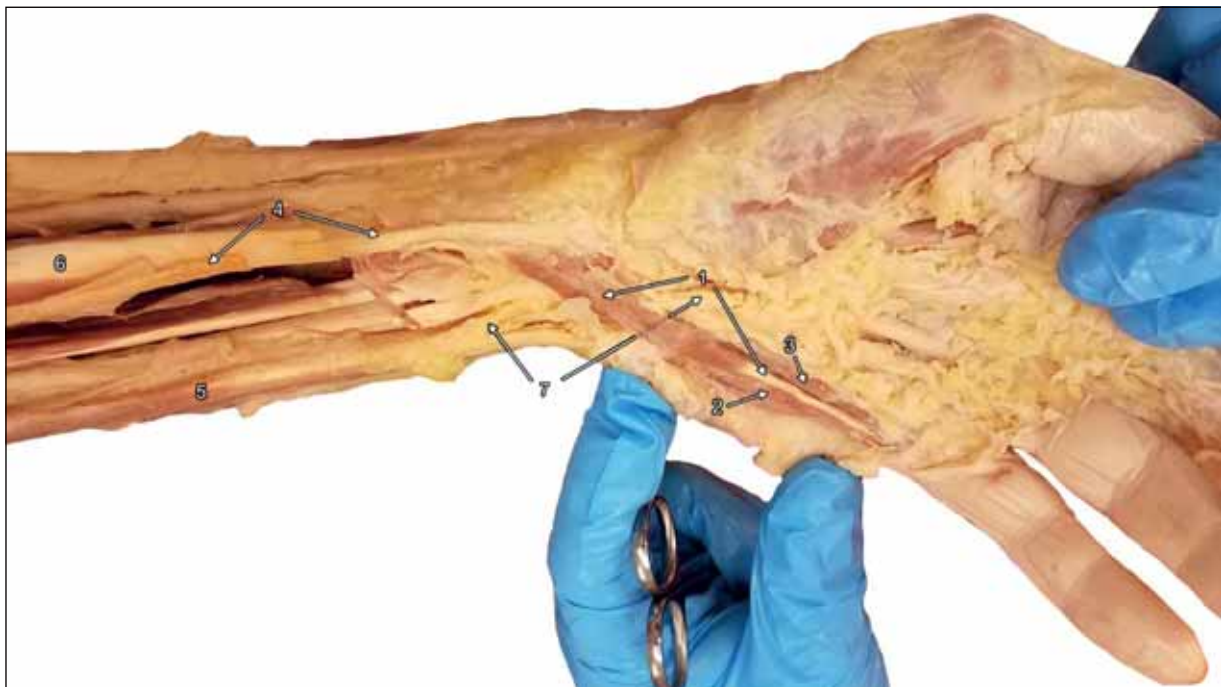


Figure 1. Distal forearm, wrist, and hand of a 92-year-old male cadaver. Note the presence of the accessory abductor digiti minimi (label no. 1) originating from the palmaris longus tendon (no. 4), which crosses medially towards digit five while passing superficial to the ulnar artery and nerve (no. 7). Labels: 1 — accessory abductor digiti minimi; 2 — abductor digiti minimi; 3 — flexor digiti minimi; 4 — palmaris longus (sectioned); 5 — flexor carpi ulnaris; 6 — flexor carpi radialis; 7 — ulnar artery and nerve.

the ulnar nerve and artery. In reviewing the antebrachial anatomy presented in these two cadavers, we consider the potential clinical implications of these muscle variants.

CASE REPORT

During routine anatomical dissection, nearly identical, anomalous forearm musculature was discovered bilaterally in both 92- and 86-year-old male cadaveric specimens (Figs. 1, 2, respectively). These muscles both originated from the palmaris longus tendons in the anterior forearm and passed superficially to the ulnar canal to insert on the fifth proximal phalanx.

Based largely on their proximity to abductor digiti minimi and pattern of insertion, we determined that the anomalous muscles are best classified as AADM [3–5, 9, 11, 12, 14]. AADM is the most common variant of the hypothenar muscles; however, having this variant arise from the palmaris longus tendon is somewhat rare [5]. More typically, the AADM arises from either the flexor retinaculum, pisiform, flexor carpi radialis, or the antebrachial fascia, which is the most common origin site [5]. As with the rest of the hypothenar musculature, the neurovascular supply is distributed through branches of the ulnar nerve and artery [11]. The majority of AADM variants are thin,

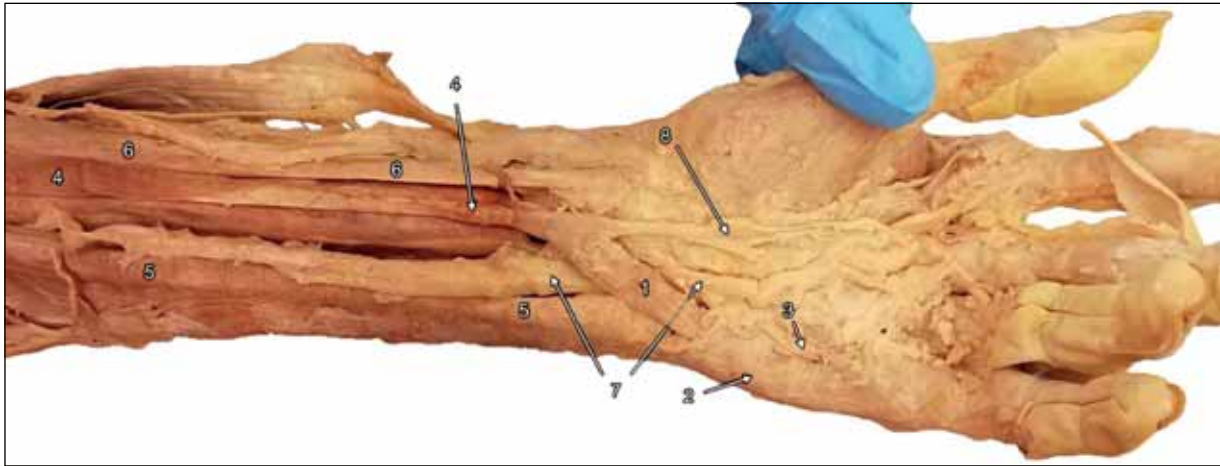


Figure 2. Distal forearm, wrist, and hand of an 86-year-old male cadaver. Just as in Figure 1, note how the accessory abductor digiti minimi (label no. 1) originates from the palmaris longus tendon (no. 4) and crosses superficial and proximal to where the ulnar artery and nerve (no. 7) enter the ulnar tunnel. Labels: 1 — accessory abductor digiti minimi; 2 — abductor digiti minimi; 3 — flexor digiti minimi; 4 — palmaris longus; 5 — flexor carpi ulnaris; 6 — flexor carpi radialis; 7 — ulnar artery and nerve; 8 — palmar aponeurosis.

with a fascial-like appearance [10]. In contrast, both examples of AADM in the cadavers discussed here presented with distinct muscle fascicles and discernible bellies (Figs. 1, 2). Such a large muscle variant in the superficial forearm could lead to pathological compression of nearby neurovascular tissues. In extreme cases this might require its surgical removal [e.g., 4, 11], yet its typically membranous presentation likely limits the necessity of such interventions in most cases.

DISCUSSION

This report documents the discovery of two cadavers (out of 27 specimens dissected during the 2019–2020 academic year) presenting with similar versions of the AADM muscle variant during a routine medical school anatomical dissection course. Such a finding implies that these types of muscular variants are not uncommon. Dodds et al. [5] reported a 22.4% incidence of anomalous muscles associated with the ulnar canal. In fact, these authors note several different presentations of AADM with divergent origin sites: pisiform, antebrachial fascia, palmaris longus tendon, investing fascia of flexor carpi radialis, intermuscular fascia, flexor carpi ulnaris, and flexor retinaculum. Other noted variants include fusion with flexor digiti minimi, and two or more heads of origin, each of which may arise from any of the anatomical structures listed above [11].

Both AADM muscle variants described here originated from the palmaris longus tendon. The modest size of palmaris longus provides limited contri-

butions to elbow and wrist flexion; however, given its absence in approximately 11.7% of forearms, its functional role may be redundant; consequently, it is commonly harvested for use as a tendon graft, and in the treatment of mallet finger, ptosis, and other reconstructive surgeries [2, 7, 8, 13]. While it is unclear how functionally active the AADMs identified in these two cadavers would have been relative to the rest of the hypothenar musculature, their substantial size and visible muscle striations suggest they had a reasonably significant role. Furthermore, had either of these individuals required surgical harvest of the palmaris longus tendon, they may have experienced weakness or other undesirable effects on hand function resulting from potential loss of AADM. Given the prevalence of this variant and the potential for its origin from the antebrachial fascia or palmaris longus, diagnostic imaging using ultrasound or magnetic resonance imaging (MRI) would be critical to reduce the risk of complications prior to the surgical resection of palmaris longus.

In contrast to the potential functional role of AADM, variability of musculature in the volar wrist could lead to neuropathy if the ulnar nerve is compressed along its course. The ulnar canal, formed by the volar carpal ligament, transverse carpal ligament, pisiform, and the hook of the hamate, provides a relatively small passageway for the ulnar nerve and associated vasculature to reach the hand [1]. Patients with ulnar canal syndrome typically present with a combination of sensory symptoms and/or motor symptoms of the fourth and fifth digits, in-

cluding burning, tingling, weakness, or numbness [6]. The role of muscle variants like AADM should be a consideration in patients presenting with otherwise indeterminate neuropathy of the wrist or forearm [9]. There are many well-documented reports of accessory muscles compressing the ulnar nerve or even the median nerve as it enters the carpal tunnel [9, 11, 12]. These accessory muscles may contribute to nerve damage with symptoms including handgrip weakness, wrist and/or hand pain, or “ulnar claw” [9]. In some instances, resection of the anomalous AADM has been shown to relieve symptoms [4, 5, 11, 12]. For example, a recent surgical case noted the presence of an AADM ultimately resulting in surgical intervention to treat bilateral carpal and ulnar tunnel syndromes [11]. Imaging modalities like ultrasound or MRI could identify an AADM either incidentally or prior to surgical decompression of an ulnar or median nerve neuropathy [4, 9, 11]. While many AADM muscles are asymptomatic, injury or hypertrophy occurring in individuals with manual labour occupations may increase the risk for neuropathies like ulnar canal syndrome [9]. With pronounced nerve compression, arterial supply is also likely to be compromised, impacting several intrinsic muscles of the hand and potentially leading to “ulnar claw” deformities [7, 12]. Comorbidities like ulnar artery thrombosis or fibrosis, fractures, Dupuytren’s contracture, or rheumatoid arthritis may amplify these drastic complications. Detailed medical records (beyond cause of death) were unavailable to us, however, so we cannot assess if these AADM muscles presented the donors with any of the musculoskeletal issues listed above.

CONCLUSIONS

During routine cadaveric dissection, the presence of two AADM muscles was identified in two separate individuals. While the discovery of these muscles is not unusual in and of itself, the fact that they both originated from palmaris longus is noteworthy [5]. AADM variants are common, and in the cases we described above, may complicate wrist or hand surgeries for compression neuropathy or when surgical harvesting of the palmaris longus tendon is required. Diagnostic imaging like ultrasound or MRI may limit the risk of such complications, but AADMs are often thin and fascial (unlike the two variants described above) and may be hard to discern using lower resolution imaging modalities.

The ulnar nerve and artery are most commonly compressed by location of typical AADM variants, though the median nerve is also known to be affected, albeit less extensively [5]. To this end, in patients presenting with clinical evidence of ulnar neuropathy, such as medial forearm or hand neuralgia, hand grip weakness, “ulnar claw” syndrome or other indeterminate hand or forearm symptoms, ultrasound or MRI may be used to determine if a muscle variant like AADM may be exacerbating the condition. In cases where an AADM variant becomes symptomatic, surgical resection has been shown to provide long term resolution.

Acknowledgements

We wish to thank these two donors and their families, in particular, and all of the donors who contributed to our anatomical education. We are grateful for the assistance of Dr. Bonnie Brenceke and Mrs. Ashley Valley. We appreciate the encouragement of our editor, Prof. Janusz Moryś, and an anonymous Reviewer. Finally, we wish to acknowledge the Faculty and Administration of the Campbell University School of Osteopathic Medicine for their support of this project.

Conflict of interest: None declared

REFERENCES

1. Aleksenko D, Varacallo M. 2021 [Updated Jul 18]. Guyon Canal Syndrome. In: StatPearls [Internet]. Treasure Island (FL): StatPearls Publishing. <https://www.ncbi.nlm.nih.gov/books/NBK431063/>.
2. Berger P, Duerinckx J. Flexor pollicis longus tendon rupture after volar wrist plating: reconstruction with palmaris longus interposition graft. *Acta Orthop Belg.* 2017; 83(3): 467–472, indexed in Pubmed: [30423650](https://pubmed.ncbi.nlm.nih.gov/30423650/).
3. Coraci D, Luchetti R, Paolasso I, et al. Intermittent ulnar nerve compression due to accessory abductor digiti minimi muscle: Crucial diagnostic role of nerve ultrasound. *Muscle Nerve.* 2015; 52(3): 463–464, doi: [10.1002/mus.24660](https://doi.org/10.1002/mus.24660), indexed in Pubmed: [25808715](https://pubmed.ncbi.nlm.nih.gov/25808715/).
4. Dimitriou C, Natsis K. Accessory abductor digiti minimi muscle causing ulnar nerve entrapment at the Guyon’s canal: a case report. *Clin Anat.* 2007; 20(8): 974–975, doi: [10.1002/ca.20518](https://doi.org/10.1002/ca.20518), indexed in Pubmed: [17583589](https://pubmed.ncbi.nlm.nih.gov/17583589/).
5. Dodds GA, Hale D, Jackson WT. Incidence of anatomic variants in Guyon’s canal. *J Hand Surg Am.* 1990; 15(2): 352–355, doi: [10.1016/0363-5023\(90\)90122-8](https://doi.org/10.1016/0363-5023(90)90122-8), indexed in Pubmed: [2324469](https://pubmed.ncbi.nlm.nih.gov/2324469/).
6. Doherty, T.J. 2021. Ulnar neuropathy at the elbow and wrist. Shefner JM, Goddeau Jr. RP, eds. UpToDate. Waltham, MA: UpToDate Inc. <https://www.uptodate.com/lookup/ulnar-neuropathy-at-the-elbow-and-wrist>.

- [com/contents/ulnar-neuropathy-at-the-elbow-and-wrist](https://www.folia-morphologica.com/contents/ulnar-neuropathy-at-the-elbow-and-wrist) (Accessed on October 18, 2021).
7. Lam DS, Ng JS, Cheng GP, et al. Autogenous palmaris longus tendon as frontalis suspension material for ptosis correction in children. *Am J Ophthalmol.* 1998; 126(1): 109–115, doi: [10.1016/s0002-9394\(98\)00072-5](https://doi.org/10.1016/s0002-9394(98)00072-5), indexed in Pubmed: [9683156](https://pubmed.ncbi.nlm.nih.gov/9683156/).
 8. Liu Z, Ma K, Huang D. Treatment of mallet finger deformity with a modified palmaris longus tendon graft through a bone tunnel. *Int J Burns Trauma.* 2018; 8(2): 34–39, indexed in Pubmed: [29755840](https://pubmed.ncbi.nlm.nih.gov/29755840/).
 9. Lokanathan TH, Surendra M, Ajay N, et al. Unusual co-existence of biaponeurotic palmaris longus and accessory abductor digiti minimi in man. *J Clin Diagn Res.* 2014; 8(1): 146–147, doi: [10.7860/JCDR/2014/7220.3968](https://doi.org/10.7860/JCDR/2014/7220.3968), indexed in Pubmed: [24596749](https://pubmed.ncbi.nlm.nih.gov/24596749/).
 10. Rixey A, Wenger D, Baffour F, et al. Accessory abductor digiti minimi muscle, less muscular than thought: an update on prevalence, morphology, and review of the literature. *Skeletal Radiol.* 2021; 50(8): 1687–1695, doi: [10.1007/s00256-021-03728-5](https://doi.org/10.1007/s00256-021-03728-5), indexed in Pubmed: [33533963](https://pubmed.ncbi.nlm.nih.gov/33533963/).
 11. Slavchev S, Georgiev G. Aberrant abductor digiti minimi muscle found during open surgical decompression of the carpal tunnel: case report. *Revista Argentina de Anatomía Clínica.* 2016; 5(2): 88–91, doi: [10.31051/1852.8023.v5.n2.14063](https://doi.org/10.31051/1852.8023.v5.n2.14063).
 12. Soldado-Carrera F, Vilar-Coromina N, Rodríguez-Baeza A. An accessory belly of the abductor digiti minimi muscle: a case report and embryologic aspects. *Surg Radiol Anat.* 2000; 22(1): 51–54, doi: [10.1007/s00276-000-0051-1](https://doi.org/10.1007/s00276-000-0051-1), indexed in Pubmed: [10863748](https://pubmed.ncbi.nlm.nih.gov/10863748/).
 13. Yong MW, Yusof N, Rampal L, et al. Prevalence of absence of palmaris longus and its association with gender, hand dominance and absence of FDS tendon to little finger among malay population. *J Hand Surg Asian Pac Vol.* 2017; 22(4): 484–489, doi: [10.1142/S021881041750054X](https://doi.org/10.1142/S021881041750054X), indexed in Pubmed: [29117832](https://pubmed.ncbi.nlm.nih.gov/29117832/).
 14. Zeiss J, Jakab E, Khimji T, et al. The ulnar tunnel at the wrist (Guyon's canal): normal MR anatomy and variants. *AJR Am J Roentgenol.* 1992; 158(5): 1081–1085, doi: [10.2214/ajr.158.5.1566671](https://doi.org/10.2214/ajr.158.5.1566671), indexed in Pubmed: [1566671](https://pubmed.ncbi.nlm.nih.gov/1566671/).

Previously unreported variant of the rectus femoris muscle

V.A. Moore¹, L. Xu¹, Ł. Olewnik², G.P. Georgiev³, J. Iwanaga^{4, 5}, R.S. Tubbs^{1, 4–9}

¹Department of Structural and Cellular Biology, Tulane University School of Medicine, New Orleans, LA, United States

²Department of Anatomical Dissection and Donation, Medical University of Lodz, Poland

³Department of Orthopaedics and Traumatology, University Hospital Queen Giovanna – ISUL, Medical University of Sofia, Bulgaria

⁴Department of Neurosurgery, Tulane University School of Medicine, New Orleans, LA, United States

⁵Department of Neurology, Tulane Centre for Clinical Neurosciences, Tulane University School of Medicine, New Orleans, LA, United States

⁶Department of Neurosurgery and Ochsner Neuroscience Institute, Ochsner Health System, New Orleans, LA, United States

⁷Department of Anatomical Sciences, St. George's University, St. George's, Grenada, West Indies

⁸Department of Surgery, Tulane Centre for Clinical Neurosciences, Tulane University School of Medicine, New Orleans, LA, United States

⁹University of Queensland, Brisbane, Australia

[Received: 1 December 2021; Accepted: 13 January 2022; Early publication date: 31 January 2022]

Although uncommon, variant muscular variations can occur related to the quadriceps femoris. Such variations might be encountered in the clinical setting so these should be documented. Here, we report three additional heads related to the rectus femoris muscle identified during routine dissection of the right thigh. To our knowledge, such a variation has not been previously reported. (Folia Morphol 2023; 82, 1: 221–224)

Key words: anatomy, lower limb, quadriceps femoris, anatomical variations, rectus femoris

INTRODUCTION

The anterior compartment of the thigh contains the iliacus, psoas major, sartorius, and the quadriceps femoris. The quadriceps femoris is typically described as being formed by the rectus femoris and the three vastus muscles: vastus medialis, vastus lateralis, and vastus intermedius which all converge and connect to the common quadriceps tendon, which continues as the patellar ligament, which attaches to the tibial tuberosity [1, 9]. Each of the four muscles of the quadriceps femoris are innervated by branches of the femoral nerve [3, 7].

The rectus femoris crosses the hip and thus assists with flexion of the thigh as well as extension of the knee along with the other three parts of the quadri-

ceps femoris. Specifically, the straight head of the rectus femoris originates from the anterior inferior iliac spine and its reflected head from the ilium just superior to the acetabulum [6]. The vastus medialis and vastus lateralis begin at the intertrochanteric line and greater trochanter, respectively and both continue their attachment down the medial and lateral lips of the linea aspera, while the vastus intermedius originates from the anterior and lateral surfaces of the femur [6]. In general, anatomical variations of the quadriceps femoris is uncommon. Here, we report the details of a cadaver found to have a, to our knowledge, previously unreported variant of the rectus femoris muscle.

Address for correspondence: J. Iwanaga, DDS, PhD, Department of Neurosurgery, Tulane Centre for Clinical Neurosciences, Tulane University School of Medicine, 131 S. Robertson St. Suite 1300, New Orleans, LA 70112, United States, tel: 5049885565, fax: 5049885793, e-mail: iwanagajoecca@gmail.com

This article is available in open access under Creative Common Attribution-Non-Commercial-No Derivatives 4.0 International (CC BY-NC-ND 4.0) license, allowing to download articles and share them with others as long as they credit the authors and the publisher, but without permission to change them in any way or use them commercially.

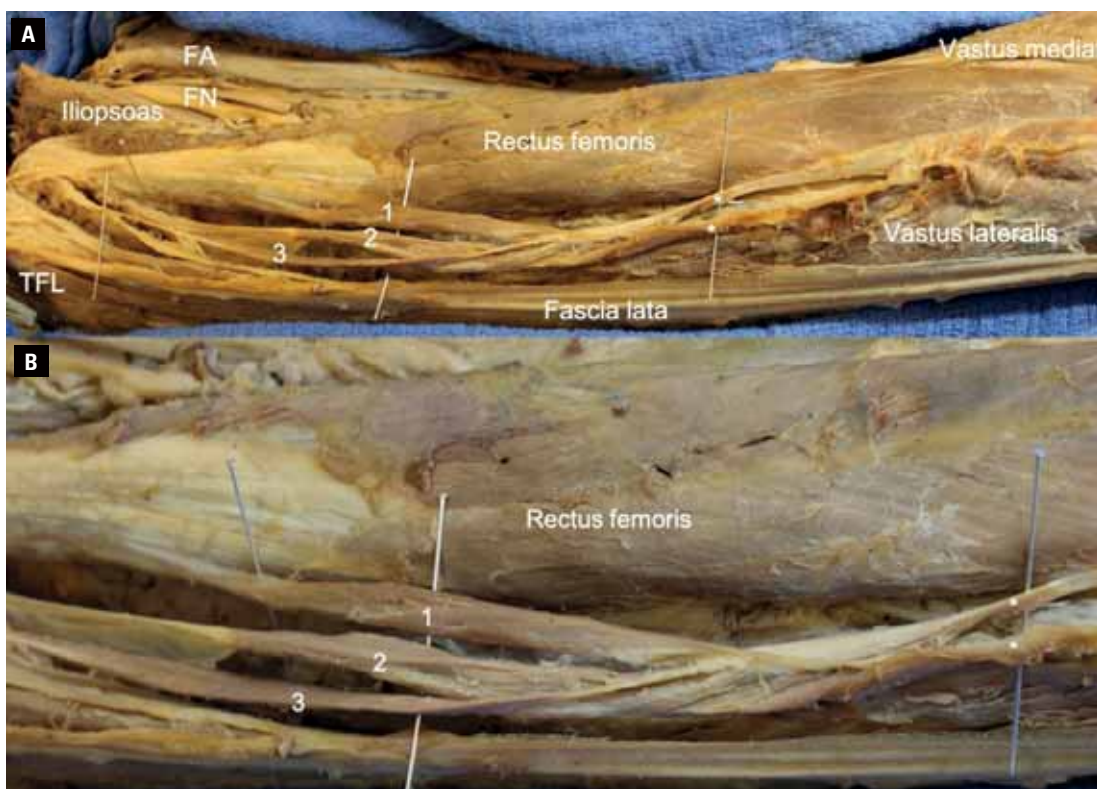


Figure 1. Right anterior thigh in the cadaver presented herein; **A.** Note the three additional heads (1–3) related to the rectus femoris. Also, note the tensor fasciae latae (TFL), femoral nerve (FN), and femoral artery (FA); **B.** Zoomed in view of Figure 1 noting the three additional heads (1–3).

The quadriceps femoris is important in, for example, sports owing to its potential for injury, which can be painful and debilitating. Tears, strains, and contusions are not uncommon and require recovery time. The quadriceps femoris can also be weakened by anterior cruciate ligament ruptures and reconstructions, resulting in atrophy of the vastus medialis and vastus intermedius. Therefore, knowledge of its anatomical variations is important.

CASE REPORT

During the routine dissection of the right anterior thigh in an 82-year-old at death male cadaver, a muscular variation of the quadriceps femoris was observed. Three additional heads were found related to the rectus femoris muscle (Fig. 1). The more medial of these extra heads travelled from the distal part of the proximal tendon of origin of the rectus femoris (near the musculotendinous junction) and coursed distally to attach to a second and more laterally placed variant head that arose from the deep layer of fascia lata (Fig. 2). This intermediate head had two tendons of origin from the deep layer of fascia lata and dis-

tally, prior to fusing with the other two additional muscular heads, split into two more or less equal muscle bellies that took on an oval shape (see Fig. 2). A most lateral variant head of the rectus femoris that was slightly posteriorly rotated fused with the other two variant heads arose from the deep surface of the deep layer of the fascia lata via a broad tendon that also attached into the proximal tendon of origin of the rectus femoris at about the level of the inguinal ligament. The three additional heads came together distally to form a roughly chiasmatic structure that then sent a tendinous band to end in the medial surface of the distal vastus lateralis muscle just proximal to the junction between the rectus femoris and vastus lateralis muscles and a tendinous band that ended in lateral aspect of the distal rectus femoris just proximal to its fusion with the vastus lateralis. Each additional muscle belly was approximately 6 cm in length and 1 cm in width. The contralateral rectus femoris and anterior thigh, in general, was found to be normal with no muscular or other obvious anatomical variations. No distinct nerve or arterial supply was found for any of the additional heads of the rectus femoris

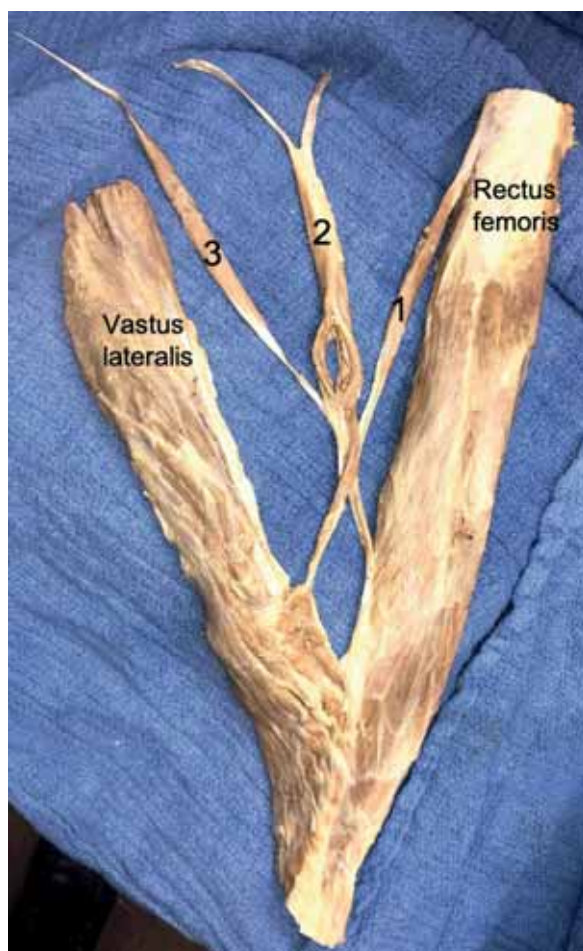


Figure 2. Variant muscle arrangement of the cadaver shown in Figure 1 after removal. The medial (1), intermediate (2), and lateral (3) variant muscles.

muscle. No medical or surgical history of the cadaver was available.

DISCUSSION

Although uncommon, variants to the quadriceps femoris have been identified in previous studies highlighting the complexity of this muscle group. Embryologically, the lower extremity develops opposite to the fifth lumbar and first sacral somites and as the bud develops, it lengthens and extends towards the sacral myotomes. The quadriceps femoris, developed from the myotomic portions of the somites, originally appears as a single mass that later differentiates into the four parts of the quadriceps femoris.

In 2020, Ruzik et al. [9] reported variants of the quadriceps femoris including accessory muscle bellies around the knee. Golland et al. [2] found an accessory head of the quadriceps femoris in 29%

of thighs and identified a fifth head in 36% of thighs. Olewnik et al. [8] reported that in several previous studies there were additional heads in the quadriceps femoris ranging from three to possibly 8 additional heads. Bonnechère et al. [1] identified three to 5 muscle heads in the quadriceps femoris raising the question of nomenclature for the quadriceps femoris.

While there have been several anatomical variants to the quadriceps femoris heads, 2020 Murdock et al. [5] reported the rectus femoris has previously been reported to have variations in the origin, ranging from upper anterior iliac spine to the lower anterior iliac spine or not having any acetabular origin and a muscle slip from the acetabulum directly into the vastus lateralis has been observed. We previously reported a femoral head of the rectus femoris that attached to the femur anteriorly at about the mid length of the rectus femoris muscle [10]. The case presented herein revealed 3 additional heads of the rectus femoris that attached into the distal vastus lateralis and rectus femoris.

CONCLUSIONS

Knowledge of the possibility of additional heads of the rectus femoris as reported here is important to not only anatomists but also clinicians who might observe such a variant on imaging or during surgical procedures.

Acknowledgements

The authors sincerely thank those who donated their bodies to science so that anatomical research could be performed. Results from such research can potentially increase mankind's overall knowledge that can then improve patient care. Therefore, these donors and their families deserve our highest gratitude [4].

Conflict of interest: None declared

REFERENCES

1. Bonnechère B, Louryan S, Feipel V. Triceps, quadriceps or penticeps femoris? Need for proper muscle definition. *Morphologie*. 2020; 104(345): 77–84, doi: [10.1016/j.morpho.2019.06.001](https://doi.org/10.1016/j.morpho.2019.06.001), indexed in Pubmed: [31296371](https://pubmed.ncbi.nlm.nih.gov/31296371/).
2. Golland JA, Mahon M, Willan PL. Anatomical variations in human quadriceps femoris muscles. *J Anat*. 1986; 146: 263–264.
3. Grob K, Gilbey H, Manestar M, et al. The anatomy of the articularis genus muscle and its relation to the extensor

- apparatus of the knee. *JB JS Open Access*. 2017; 2(4): e0034, doi: [10.2106/JBJS.OA.17.00034](https://doi.org/10.2106/JBJS.OA.17.00034), indexed in Pubmed: [30229230](https://pubmed.ncbi.nlm.nih.gov/30229230/).
4. Iwanaga J, Singh V, Takeda S, et al. Acknowledging the use of human cadaveric tissues in research papers: Recommendations from anatomical journal editors. *Clin Anat*. 2021; 34(1): 2–4, doi: [10.1002/ca.23671](https://doi.org/10.1002/ca.23671), indexed in Pubmed: [32808702](https://pubmed.ncbi.nlm.nih.gov/32808702/).
 5. Murdock CJ, Mudreac A, Agyeman K. Anatomy, Abdomen and Pelvis, Rectus Femoris Muscle. [Updated 2020 Aug 10]. In: StatPearls [Internet]. Treasure Island (FL): StatPearls Publishing. <https://www.ncbi.nlm.nih.gov/books/NBK539897/> (2021 Jan).
 6. Netter FH. Atlas of human anatomy. 7th ed., Elsevier 2019: 538–539.
 7. Ogami-Takamura K, Saiki K, Endo D, et al. Gross anatomical investigation of the muscular head between the vastus lateralis and intermedius in the Japanese population: a cadaver study. *Anat Sci Int*. 2021; 96(2): 231–238, doi: [10.1007/s12565-020-00579-3](https://doi.org/10.1007/s12565-020-00579-3), indexed in Pubmed: [33219435](https://pubmed.ncbi.nlm.nih.gov/33219435/).
 8. Olewnik Ł, Tubbs RS, Ruzik K, et al. Quadriceps or multiceps femoris?—Cadaveric study. *Clin Anat*. 2021; 34(1): 71–81, doi: [10.1002/ca.23646](https://doi.org/10.1002/ca.23646), indexed in Pubmed: [32644202](https://pubmed.ncbi.nlm.nih.gov/32644202/).
 9. Ruzik K, Waśniewska A, Olewnik Ł, et al. Unusual case report of seven-headed quadriceps femoris muscle. *Surg Radiol Anat*. 2020; 42(10): 1225–1229, doi: [10.1007/s00276-020-02472-0](https://doi.org/10.1007/s00276-020-02472-0), indexed in Pubmed: [32318799](https://pubmed.ncbi.nlm.nih.gov/32318799/).
 10. Tubbs RS, Salter G, Oakes WJ. Femoral head of the rectus femoris muscle. *Clin Anat*. 2004; 17(3): 276–278, doi: [10.1002/ca.10186](https://doi.org/10.1002/ca.10186), indexed in Pubmed: [15042578](https://pubmed.ncbi.nlm.nih.gov/15042578/).

The ulnar head of the pronator teres muscle originating from the third head of the biceps brachii: a very rare case

Ł. Olewnik¹, N. Zielinska¹, B. Szewczyk¹, R.S. Tubbs^{2–7}

¹Department of Anatomical Dissection and Donation, Medical University of Lodz, Poland

²Department of Anatomical Sciences, St. George's University, Grenada, West Indies

³Department of Neurosurgery, Tulane University School of Medicine, New Orleans, LA, United States

⁴Department of Neurology, Tulane University School of Medicine, New Orleans, LA, United States

⁵Department of Structural and Cellular Biology, Tulane University School of Medicine, New Orleans, LA, United States

⁶Department of Surgery, Tulane University School of Medicine, New Orleans, LA, United States

⁷Department of Neurosurgery, Ochsner Medical Centre, New Orleans, LA, United States

[Received: 2 October 2021; Accepted: 14 October 2021; Early publication date: 9 November 2021]

The biceps brachii is located in the anterior compartment of the arm, which can show numerous morphological variations. During anatomical dissection, an interesting additional muscle was found: the third head of the biceps brachii originated from the short head of the same muscle. The 97.77 mm long muscle belly was directed medially over the arm and then passed into the common tendon (15.97 mm), which thereafter split into aponeurosis and tendon. The 26.33 mm aponeurosis passed and joined the fascia of the forearm. The tendon of the third head of the biceps brachii then gave rise to the ulnar head of the pronator teres muscle. Such an accessory structure could cause neurovascular compression involving the brachial artery and median nerve. Knowledge of the morphological variability of this region is essential not only for anatomists but also for clinicians. (Folia Morphol 2023; 82, 1: 225–230)

Key words: anatomical variations, biceps brachii, third head

INTRODUCTION

It seems that the biceps brachii (BB), next to the plantaris or palmaris longus, is one of the most morphologically variable muscles [29, 30]. Standard anatomy books describe it as consisting of two heads, short and long [27].

There are frequent morphological variations of the BB involving both the proximal and distal attachments, and also additional heads [2, 6, 9, 10, 15, 17, 19, 21–23, 36, 38, 39, 44, 48]. Arguably the greatest degree of morphological variation concerns the number of supernumerary heads, which can range

from three to five [2, 17]. Accessory heads can also arise from the deltoid muscle, the pectoralis major, the coracoid process or the humerus [4, 6, 8, 9, 12, 16, 17, 22]. The supernumerary heads of the BB have functional and clinical implications arising from their potential to influence certain muscle functions or induce symptoms of neurovascular compression [6].

The present case report describes a very rare variant of the third head of the BB, the tendon of which gives origin to the ulnar head of the pronator teres. The brachial artery and the median nerve (MN) could be compressed between the tendon and the aponeurosis.

Address for correspondence: Ł. Olewnik, DPT, PhD, Ass. Prof., Department of Anatomical Dissection and Donation, Medical University of Lodz, ul. Żeligowskiego 7/9, 90–136 Łódź, Poland, e-mail: lukasz.olewnik@umed.lodz.pl

This article is available in open access under Creative Commons Attribution-Non-Commercial-No Derivatives 4.0 International (CC BY-NC-ND 4.0) license, allowing to download articles and share them with others as long as they credit the authors and the publisher, but without permission to change them in any way or use them commercially.

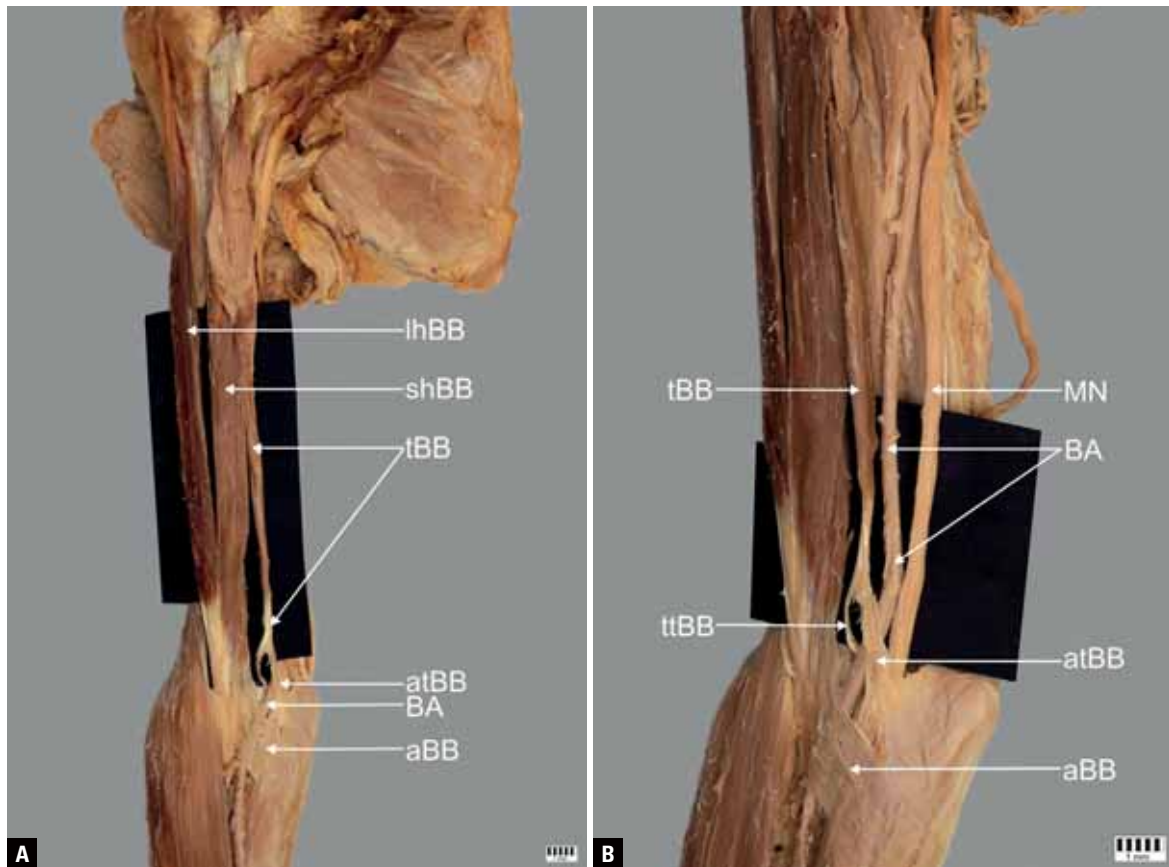


Figure 1. A, B. A third head of the biceps brachii; lhBB — long head of the biceps brachii; shBB — short head of the biceps brachii; tBB — third head of the biceps brachii; atBB — aponeurosis of the third head of the biceps brachii; BA — brachial artery, aBB — aponeurosis of the biceps brachii; ttBB — tendon of the third head of the biceps brachii; MN — median nerve.

Ethical approval and consent to participate

The cadavers belonged to the Department of Anatomical Dissection and Donation, Medical University of Lodz, Poland.

CASE REPORT

A female cadaver, 77 years old at death, was subjected to routine anatomical dissection for research and teaching purposes at the Department of Anatomical Dissection and Donation, Medical University of Lodz, Poland. The right upper limb underwent traditional anatomical dissection and a morphological variant of the third head of the BB was found [33–35, 45–47]. The next stage of the investigation involved a detailed assessment of this structure. The third head of the BB originated from the shBB. The 97.77 mm long muscle belly was directed medially over the arm and then passed into the common tendon (15.97 mm), which then split into aponeurosis and tendon (Fig. 1). The myotendinous junction was 3.72 mm wide and 1.19 mm thick. The 26.33 mm

aponeurosis passed and joined the fascia of the forearm (Fig. 1).

The brachial artery and the MN ran between the aponeurosis and the tendon. The diameter of the brachial artery between the aponeurosis and the tendon was 4.78 mm, and the diameter of the MN was 5.03 mm. The 69.29 mm tendon then gave rise to the ulnar head of the pronator teres muscle (Fig. 2).

An electronic calliper (Mitutoyo Corporation, Kawasaki-shi, Kanagawa, Japan) was used for these measurements. Each measurement was repeated twice with an accuracy of up to 0.1 mm.

No other morphological variations were found.

DISCUSSION

The BB is characterised by numerous morphological variations that concern both its proximal and distal attachments, and the number of bellies [2, 4–6, 17, 22, 29, 37].

Knowledge of the embryological development of the muscle elucidates the occurrence of accessory

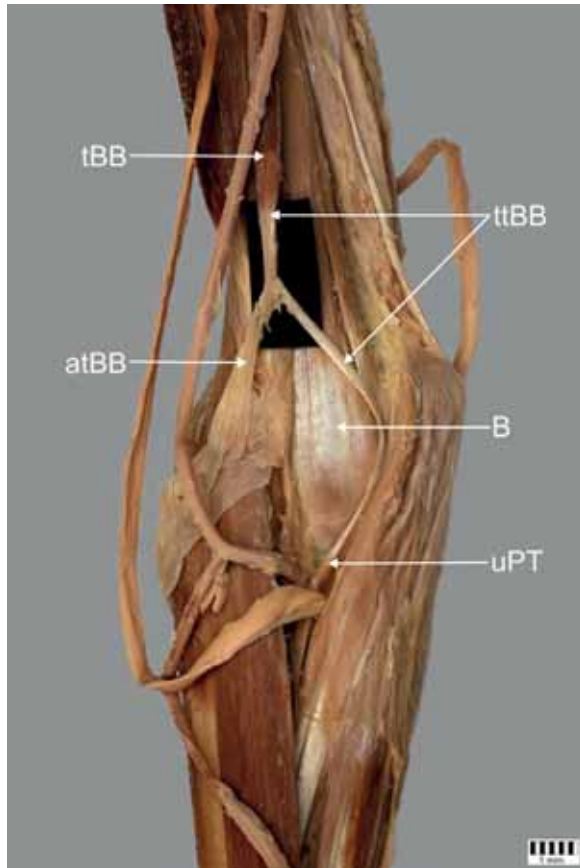


Figure 2. Distal part of the third head of the biceps brachii and proximal part of the anterior compartment of the forearm; tBB — third head of the biceps brachii; ttBB — tendon of the third head of the biceps brachii; atBB — aponeurosis of the third head of the biceps brachii; B — brachialis muscle, uPT — ulnar head of the pronator teres muscle.

heads of the BB. The BB, coracobrachialis, and brachialis muscles are intimately fused during very early stages and probably arise from a common pre-muscular mass. At this early stage, the two heads of the BB are close together and only become separated by the later growth of the scapula. The three muscles can be recognised in embryos measuring 14–16 mm in length, and the long tendon of the caput longum can be recognised in embryos 14 mm long. The distal end of the common muscle mass differentiates later than the proximal end [7]. The third, fourth and fifth heads of the BB are believed to arise from the brachialis muscle. In such instances, the distal attachment is translocated from the ulna and radius [40].

The third head of the BB was first described by Theile [41], Wood [42] and Macalister [26]. Many subsequent authors have reported cases and the incidence of additional heads. The most common variation of

the BB is a third head, occurring in 4.2% to 19.8% [2, 5, 6, 12, 22, 29, 37, 40, 42]. Many cases of third heads have been described. Both Macalister [26] and Wood [42] described a separate slip from the coracobrachialis continuous with the short head of the BB. Macalister [26] also found a third head arising directly from the brachialis muscle and this head crossed the brachial artery; the third head also originated from the deltoid muscle and from the outer tuberosity. Testut [40] reported acromial, labial and pectoral supernumerary heads of the BB. Kosugi et al. [22] found three- and four-headed BB muscles and created a classification system. Type I, three heads, was divided into distinct subtypes. Subtype a was characterised by an origin on the shaft of the humerus (between the coracobrachialis and brachialis muscles). Subtype b was proximally attached to the medial brachial intermuscular septum. Subtype c included cases with different locations of origin, for example from the tendinous part of the pectoralis major, deltoid muscle, or greater tubercle.

Rodriguez-Niedenfuhr et al. [37] distinguished three various origins of the third head of the BB. The first type, originating from the antero-medial surface of the humerus, was the most common (frequency 9%). It was characterised by an inferomedial head distally fused with the insertion of the coracobrachialis muscle. The second type occurred in 1.5% of the population; the superior humeral head was attached to the surface of the humerus between the lesser tubercle and the proximal attachment of the brachialis and coracobrachialis muscles. The third type, occurring in only 0.3% of cases, was an infero-lateral humeral head. Its origin was located on the lateral intermuscular septum between the proximal attachment of the brachioradialis muscle and the insertion of the deltoid muscle [38].

In the third head of the BB we have described, a proximal attachment on the short head of the BB headed towards the medial side of the arm and the muscle belly turned into a common tendon and then split into two parts: the aponeurosis, which connected to the fascia of the forearm, and the tendon, which passed directly into the ulnar head of the pronator teres muscle. A similar case was described by Macalister [25], where the accessory third head originated from the upper border of the pronator teres.

The atypical course of the aponeurosis and tendons could cause pressure on the brachial artery and

the MN. Entrapment of the brachial artery between the aponeurosis and the tendon of the BB could cause acute or chronic intraluminal arterial thrombosis, further leading to acute distal embolisation.

Other pathologies could result from compression the MN [3, 27]. For example, when the MN is compressed by the pronator teres heads, ulnar and humeral, the result is pronator teres syndrome [32] manifested by pain in the volar forearm region and weakness. Another pathology, referred to as the most common, is carpal tunnel syndrome characterised by pain, numbness and paraesthesia's, especially in the fingers, though it can also radiate up the affected arm [11, 27]. MN compression in the arm region is much less frequent. It can be associated with Struthers' ligament and is known as supracondylar process syndrome [20, 32]. Additional structures such as a third head of the biceps brachii can also lead to MN neuropathy [43]. An accessory head of the coracobrachialis muscle is another example, but it occurs at the level of the lateral cord of the brachial plexus [13, 14, 24, 34, 35].

In this case, we are dealing with an even higher likelihood of pressure, which could perturb the innervation of most of the forearm muscles. A typical symptom is pain in forearm reversal movement and sensory disturbances in the fingers and the inner surface of the hand.

A fourth head is much rarer than a third head [1, 12, 22, 37]. Kosugi et al. [22] report that the fourth head of the BB can originate from the pectoralis major tendon or the greater tubercle or articular capsule. A fifth head of the BB has very rarely been described [37].

Accessory heads of the BB can increase the risk of pathologies such as bicipital injury. Moreover, such morphological variations are clinically significant for surgeons, especially for orthopaedics. A possible change in the biomechanical forces applied to the humerus should be considered among patients with humeral fracture with bone displacement. It is worth mentioning that additional structures usually entail some neurovascular compression. An accessory head of the BB can potentially compress the brachial artery, musculocutaneous nerve, and MN, leading to pain and various nerve compression syndromes.

CONCLUSIONS

The BB is highly morphologically variable. The case described is unique in that it gives origin to the

ulnar head of the pronator teres and could also cause pressure on the brachial arteries.

Acknowledgements

The authors sincerely thank those who donated their bodies to science so that anatomical research could be performed. Results from such research can potentially increase mankind's overall knowledge that can then improve patient care. Therefore, these donors and their families deserve our highest gratitude (Iwanaga et al. [18]).

Conflict of interest: None declared

REFERENCES

1. Adachi B. Beitrage zur anatomie der Japaner. XII. Die statistik der muskelvarietten. *Z Morphol Anthr.* 1909; 261–312.
2. Al-Kushi G. Anatomical study of the third head of biceps brachii muscle and its innervation by median nerve in human dissection. *J Clin Med Res.* 2013; 5(4): 47–52, doi: [10.5897/jcmr12.017](https://doi.org/10.5897/jcmr12.017).
3. Andreisek G, Crook DW, Burg D, et al. Peripheral neuropathies of the median, radial, and ulnar nerves: MR imaging features. *Radiographics.* 2006; 26(5): 1267–1287, doi: [10.1148/rg.265055712](https://doi.org/10.1148/rg.265055712), indexed in Pubmed: [16973765](https://pubmed.ncbi.nlm.nih.gov/16973765/).
4. Anson B. *An Atlas of Human Anatomy*, 2nd ed. WB Saunders Company, Philadelphia 1963.
5. Asvat R, Candler P, Sarmiento EE. High incidence of the third head of biceps brachii in South African populations. *J Anat.* 1993; 182 (Pt 1): 101–104, indexed in Pubmed: [8509293](https://pubmed.ncbi.nlm.nih.gov/8509293/).
6. Ballesteros LE, Forero PL, Buitrago ER. Evaluation of additional head of biceps brachii: a study with autopsy material. *Folia Morphol.* 2014; 73(2): 193–198, doi: [10.5603/FM.2014.0028](https://doi.org/10.5603/FM.2014.0028), indexed in Pubmed: [24902098](https://pubmed.ncbi.nlm.nih.gov/24902098/).
7. Bardeen C. Development and variation of the nerves and the musculature of the inferior extremity and of the neighboring regions of the trunk in man. *Am J Anat.* 1906; 6(1): 259–390, doi: [10.1002/aja.1000060108](https://doi.org/10.1002/aja.1000060108).
8. Bergman R, Afifi A, Miyauchi R. *Illustrated encyclopedia of human anatomic variations.* Anatomy Atlas 2017.
9. Blasi M, de la Fuente J, Martinoli C, et al. Multidisciplinary approach to the persistent double distal tendon of the biceps brachii. *Surg Radiol Anat.* 2014; 36(1): 17–24, doi: [10.1007/s00276-013-1136-y](https://doi.org/10.1007/s00276-013-1136-y), indexed in Pubmed: [23708377](https://pubmed.ncbi.nlm.nih.gov/23708377/).
10. Cucca YY, McLay SVB, Okamoto T, et al. The biceps brachii muscle and its distal insertion: observations of surgical and evolutionary relevance. *Surg Radiol Anat.* 2010; 32(4): 371–375, doi: [10.1007/s00276-009-0575-y](https://doi.org/10.1007/s00276-009-0575-y), indexed in Pubmed: [19847376](https://pubmed.ncbi.nlm.nih.gov/19847376/).
11. Dong Q, Jacobson JA, Jamadar DA, et al. Entrapment neuropathies in the upper and lower limbs: anatomy and MRI features. *Radiol Res Pract.* 2012; 2012: 230679, doi: [10.1155/2012/230679](https://doi.org/10.1155/2012/230679), indexed in Pubmed: [23125929](https://pubmed.ncbi.nlm.nih.gov/23125929/).
12. Le Double A. *Traité des variations du système musculaire de l'homme et de leur signification au point de vue de l'anthropologie zoologique.* Schleicher frères, Paris 1897.

13. El-Naggar MM, Al-Saggaf S. Variant of the coracobrachialis muscle with a tunnel for the median nerve and brachial artery. *Clin Anat.* 2004; 17(2): 139–143, doi: [10.1002/ca.10213](https://doi.org/10.1002/ca.10213), indexed in Pubmed: [14974102](https://pubmed.ncbi.nlm.nih.gov/14974102/).
14. Garbelotti SA, Marques SR, Rocha PR, et al. An unusual case of accessory head of coracobrachialis muscle involving lateral cord of brachial plexus and its clinical significance. *Folia Morphol.* 2017; 76(4): 762–765, doi: [10.5603/FM.a2017.0033](https://doi.org/10.5603/FM.a2017.0033), indexed in Pubmed: [28353299](https://pubmed.ncbi.nlm.nih.gov/28353299/).
15. Greig HW, Anson BJ, Budinger JM. Variations in the form and attachments of the biceps brachii muscle. *Q Bull Northwest Univ Med Sch.* 1952; 26(3): 241–244, indexed in Pubmed: [14957982](https://pubmed.ncbi.nlm.nih.gov/14957982/).
16. Gruber W. Die Musculi subscapulares (major et minor) und die neuen supernumären Schultermuskel des Menschen. *Máemoires de l'Acadéemie Impériale des Sciences de Saint Pétersbourg par Divers Savans et Lus dans ses Assemblées*, 4th ed, Sankt Petersburg 1859.
17. Ilayperuma I, Nanayakkara G, Palahepitiya N. Incidence of humeral head of biceps brachii muscle: anatomical insight. *Int J Morphol.* 2011; 29(1): 221–225, doi: [10.4067/s0717-95022011000100037](https://doi.org/10.4067/s0717-95022011000100037).
18. Iwanaga J, Singh V, Ohtsuka A, et al. Acknowledging the use of human cadaveric tissues in research papers: Recommendations from anatomical journal editors. *Clin Anat.* 2021; 34(1): 2–4, doi: [10.1002/ca.23671](https://doi.org/10.1002/ca.23671), indexed in Pubmed: [32808702](https://pubmed.ncbi.nlm.nih.gov/32808702/).
19. Jeong JY, Park SM, Park YE, et al. Morphological classification of anatomical variants of the intra-articular portion of the long head of the biceps brachii tendon and analysis of the incidence and the relationship with shoulder disease for each subtype. *J Orthop Surg (Hong Kong).* 2017; 25(3): 1–6, doi: [10.1177/2309499017742207](https://doi.org/10.1177/2309499017742207), indexed in Pubmed: [29157108](https://pubmed.ncbi.nlm.nih.gov/29157108/).
20. De Jesus R, Dellon AL. Historic origin of the “Arcade of Struthers”. *J Hand Surg Am.* 2003; 28(3): 528–531, doi: [10.1053/jhsu.2003.50071](https://doi.org/10.1053/jhsu.2003.50071), indexed in Pubmed: [12772116](https://pubmed.ncbi.nlm.nih.gov/12772116/).
21. Kopuz C, Sancak B, Ozbenli S. On the incidence of third head of biceps brachii in Turkish neonates and adults. *Acta Anat Nippon.* 1999; 74(3): 301–305, indexed in Pubmed: [10429374](https://pubmed.ncbi.nlm.nih.gov/10429374/).
22. Kosugi K, Shibata S, Yamashita H. Supernumerary head of biceps brachii and branching pattern of the musculocutaneous nerve in Japanese. *Surg Radiol Anat.* 1992; 14(2): 175–185, doi: [10.1007/BF01794898](https://doi.org/10.1007/BF01794898), indexed in Pubmed: [1641744](https://pubmed.ncbi.nlm.nih.gov/1641744/).
23. Landa J, Bhandari S, Strauss EJ, et al. The effect of repair of the lacertus fibrosus on distal biceps tendon repairs: a biomechanical, functional, and anatomic study. *Am J Sports Med.* 2009; 37(1): 120–123, doi: [10.1177/0363546508324694](https://doi.org/10.1177/0363546508324694), indexed in Pubmed: [19029314](https://pubmed.ncbi.nlm.nih.gov/19029314/).
24. Loukas M, Aqueelah H. Musculocutaneous and median nerve connections within, proximal and distal to the coracobrachialis muscle. *Folia Morphol.* 2005; 64: 101–108.
25. Macalister A. Additional observations on muscular anomalies in human anatomy. *Transcations R Irish Acad.* 1875; 25: 1–134.
26. Macalister A. Observations on the muscular variations in the human anatomy. Third series with a catalogue of the principal muscular variations hitherto published. *Trans Rov Irish Acad Sci.* 1875; 25: 1–134.
27. Meyer P, Lintingre PF, Pesquer L, et al. The median nerve at the carpal tunnel ... and elsewhere. *J Belg Soc Radiol.* 2018; 102(1): 17, doi: [10.5334/jbsr.1354](https://doi.org/10.5334/jbsr.1354), indexed in Pubmed: [30039031](https://pubmed.ncbi.nlm.nih.gov/30039031/).
28. Moore K, Arthur F, Dalley I. *Clinically Oriented Anatomy*, 7th ed. Lippincott Williams&Wilkins 2013.
29. Nayak SR, Prabhu LV, Sivanandan R. Third head of biceps brachii: A rare occurrence in the Indian population. *Ann Anat.* 2006; 188(2): 159–161, doi: [10.1016/j.aanat.2005.10.004](https://doi.org/10.1016/j.aanat.2005.10.004), indexed in Pubmed: [16551013](https://pubmed.ncbi.nlm.nih.gov/16551013/).
30. Olewnik Ł, Karauda P, Gonera B, et al. Impact of plantaris ligamentous tendon. *Sci Rep.* 2021; 11(1): 4550, doi: [10.1038/s41598-021-84186-w](https://doi.org/10.1038/s41598-021-84186-w), indexed in Pubmed: [33633305](https://pubmed.ncbi.nlm.nih.gov/33633305/).
31. Olewnik Ł, Kurtys K, Gonera B, et al. Proposal for a new classification of plantaris muscle origin and its potential effect on the knee joint. *Ann Anat.* 2020; 231: 151506, doi: [10.1016/j.aanat.2020.151506](https://doi.org/10.1016/j.aanat.2020.151506), indexed in Pubmed: [32173563](https://pubmed.ncbi.nlm.nih.gov/32173563/).
32. Olewnik Ł, Podgórski M, Polguy M, et al. Anatomical variations of the pronator teres muscle in a Central European population and its clinical significance. *Anat Sci Int.* 2018; 93(2): 299–306, doi: [10.1007/s12565-017-0413-y](https://doi.org/10.1007/s12565-017-0413-y), indexed in Pubmed: [28849397](https://pubmed.ncbi.nlm.nih.gov/28849397/).
33. Olewnik Ł, Zielinska N, Golek Ł, et al. Is it the coracobrachialis superior muscle, or is it an unidentified rare variant of coracobrachialis muscle? *Surg Radiol Anat.* 2021; 43(10): 1581–1586, doi: [10.1007/s00276-021-02773-y](https://doi.org/10.1007/s00276-021-02773-y), indexed in Pubmed: [34037825](https://pubmed.ncbi.nlm.nih.gov/34037825/).
34. Olewnik Ł, Zielinska N, Karauda P, et al. The co-occurrence of a four-headed coracobrachialis muscle, split coracoid process and tunnel for the median and musculocutaneous nerves: the potential clinical relevance of a very rare variation. *Surg Radiol Anat.* 2021; 43(5): 661–669, doi: [10.1007/s00276-020-02580-x](https://doi.org/10.1007/s00276-020-02580-x), indexed in Pubmed: [32979058](https://pubmed.ncbi.nlm.nih.gov/32979058/).
35. Olewnik Ł, Paulsen F, Tubbs RS, et al. Potential compression of the musculocutaneous, median and ulnar nerves by a very rare variant of the coracobrachialis longus muscle. *Folia Morphol.* 2021; 80(3): 707–713, doi: [10.5603/FM.a2020.0085](https://doi.org/10.5603/FM.a2020.0085), indexed in Pubmed: [32844391](https://pubmed.ncbi.nlm.nih.gov/32844391/).
36. Podgórski M, Olewnik Ł, Rusinek M, et al. ‘Superior biceps aponeurosis’: Morphological characteristics of the origin of the short head of the biceps brachii muscle. *Ann Anat.* 2019; 223: 85–89, doi: [10.1016/j.aanat.2019.01.014](https://doi.org/10.1016/j.aanat.2019.01.014), indexed in Pubmed: [30797975](https://pubmed.ncbi.nlm.nih.gov/30797975/).
37. Rodríguez-Niedenführ M, Vázquez T, Choi D, et al. Supernumerary humeral heads of the biceps brachii muscle revisited. *Clin Anat.* 2003; 16(3): 197–203, doi: [10.1002/ca.10060](https://doi.org/10.1002/ca.10060), indexed in Pubmed: [12673814](https://pubmed.ncbi.nlm.nih.gov/12673814/).
38. Schwerdtfeger L, Pascoe M, Clapp T. High incidence of a third head of biceps brachii in females. *Transl Res Anat.* 2018; 12: 25–27, doi: [10.1016/j.tria.2018.08.001](https://doi.org/10.1016/j.tria.2018.08.001).
39. Snoeck O, Lefèvre P, Sprio E, et al. The lacertus fibrosus of the biceps brachii muscle: an anatomical study. *Surg Radiol Anat.* 2014; 36(7): 713–719, doi: [10.1007/s00276-013-1254-6](https://doi.org/10.1007/s00276-013-1254-6), indexed in Pubmed: [24414231](https://pubmed.ncbi.nlm.nih.gov/24414231/).
40. Testut L. Les anomalies musculaires chez l' Homme, expliquées par la anatomie comparée. Leur importance en anthropologie. G Masson, Paris 1884.

41. Theile F. *Traité de Myologie*. Baillière, Paris 1843.
42. Wood J. On human muscular variations and their relation to comparative anatomy. *J Anat Physiol*. 1867; 44–59.
43. Yershov D, Hudák R. Unusual variation of the biceps brachii with possible median nerve entrapment. *Prague Med Rep*. 2015; 116(2): 167–172, doi: [10.14712/23362936.2015.55](https://doi.org/10.14712/23362936.2015.55), indexed in Pubmed: [26093671](https://pubmed.ncbi.nlm.nih.gov/26093671/).
44. Zhou M, Ishizawa A, Akashi H, et al. Bilateral accessory heads of biceps brachii muscle coexisting with brachioradial artery passing between two layers of atypical bicipital aponeurosis. *Transl Res Anat*. 2021; 25: 100134, doi: [10.1016/j.tria.2021.100134](https://doi.org/10.1016/j.tria.2021.100134).
45. Zielinska N, Olewnik Ł. Six-headed coracobrachialis muscle. *Folia Morphol*. 2022; 81(3): 809–813, doi: [10.5603/FM.a2021.0082](https://doi.org/10.5603/FM.a2021.0082), indexed in Pubmed: [34608984](https://pubmed.ncbi.nlm.nih.gov/34608984/).
46. Zielinska N, Olewnik Ł, Karauda P, et al. A very rare case of an accessory subscapularis muscle and its potential clinical significance. *Surg Radiol Anat*. 2021; 43(1): 19–25, doi: [10.1007/s00276-020-02531-6](https://doi.org/10.1007/s00276-020-02531-6), indexed in Pubmed: [32656573](https://pubmed.ncbi.nlm.nih.gov/32656573/).
47. Zielinska N, Tubbs RS, Podgórski M, et al. The subscapularis tendon: A proposed classification system. *Ann Anat*. 2021; 233: 151615, doi: [10.1016/j.aanat.2020.151615](https://doi.org/10.1016/j.aanat.2020.151615), indexed in Pubmed: [33068734](https://pubmed.ncbi.nlm.nih.gov/33068734/).
48. Żytkowski A, Tubbs R, Iwanaga J, et al. Anatomical normality and variability: Historical perspective and methodological considerations. *Transl Res Anat*. 2021; 23: 100105, doi: [10.1016/j.tria.2020.100105](https://doi.org/10.1016/j.tria.2020.100105).

Porcine coronary arteries: immunohistochemical profile of TNF-alpha, IL-1beta, TGF-beta1 and ICAM-1	119
S. Taurone, M.T. Santarelli, E. De Santis, C. Di Gioia, E. Pompili, F. Pellegrino, P. Familiari, V. Papa, C. Zanza, L. Coppola, G. Familiari, M. Artico	
The different forms of the left brachiocephalic vein visualised during cardiovascular implantable electronic device implantation procedures	127
R. Steckiewicz, P. Stolarz, B. Lange	
Anatomo-topographic and histo-cytological study of dromedary's spleen in Algeria	137
M.A. Fares, T. Khenenou, D.E. Rahmoun	
Anoctamin 1 and c-Kit immunohistochemical study of interstitial cells of Cajal in the muscularis externa of human gastrointestinal tract	147
A. Al-Ahmadi, R.A. Mohammed, M. Atteya, T.A. Al-Matrafi, M.A. Alfayez	
Evaluation of the angulation of the nasal septum deviation as an anatomical variation for increased frequency of antral pseudocyst: a cone-beam computed tomography study	158
N. Laçin, M. Yalçin, M. Demirkol	
Anatomical characteristics and significance of the metopism and Wormian bones in dry adult-Chinese skulls	166
J.-H. Li, Z.-J. Chen, W.-X. Zhong, H. Yang, D. Liu, Y.-K. Li	
Morphological classification and clinical significance of medial malleolus based on computed tomography three-dimensional reconstruction	176
L. Xin, K. Liu, B. He, M. Chen, B. Tang, C. Tang, L. Zhang	
CASE REPORTS	
Accessory anterior ethmoidal nerve and artery: a cadaveric case report	183
D. Hage, J. Iwanaga, A. Danaei, A. Sadr, R.S. Tubbs	
Concomitant completely ossified trigeminal pore and Dorello's canal	187
M.C. Rusu, A.D. Vrapciu, P.M. Rădoi, C. Toader	
Splitting of the distal median nerve	190
W.L. Smith, Ł. Olewnik, J. Iwanaga, A.S. Dumont, R.S. Tubbs	
Unusual sensory innervation of the dorsal hand and why we should bear this variation in mind	194
G.P. Georgiev, B. Landzhov, Ł. Olewnik, N. Zielinska, Y. Kartelov, I.N. Dimitrova, R.S. Tubbs	
Rare left colic artery variation of the gut arterial system	198
S.A. Memar, A.M. Taylor, S. Ahuja, D.T. Daly, Y. Tan	
Ascending palatine branch from the lingual artery with multiple other variations of the external carotid artery	205
C. Escoffier, D. Hage, T. Tanaka, R.S. Tubbs, J. Iwanaga	
An unusual variant of the atlantomastoid muscle	211
N.O. Blackwood, Ł. Olewnik, G.P. Georgiev, G. Wysiadecki, A. Aysenne, J. Iwanaga, R.S. Tubbs	
Presence of accessory abductor digiti minimi muscle in two cadavers	216
C.D. Hamacher, B.J. Browning, J.C. Barton, N.F. Chase, R.E. Larson, D.J. Green	
Previously unreported variant of the rectus femoris muscle	221
V.A. Moore, L. Xu, Ł. Olewnik, G.P. Georgiev, J. Iwanaga, R.S. Tubbs	
The ulnar head of the pronator teres muscle originating from the third head of the biceps brachii: a very rare case	225
Ł. Olewnik, N. Zielinska, B. Szewczyk, R.S. Tubbs	

CONTENTS

ORIGINAL ARTICLES

How to write an umbrella review? A step-by-step tutorial with tips and tricks	1
M. Bonczar, P. Ostrowski, A.V. D'Antoni, R.S. Tubbs, J. Iwanaga, S.K. Ghosh, I. Klejbor, M. Kuniewicz, J. Walocha, J. Moryś, M. Koziej	
Anatomy of the occipital lobe using lateral and posterior approaches: a neuroanatomical study with a neurosurgical perspective on intraoperative brain mapping	7
T.A. Dziedzic, A. Bala, A. Balasa, A. Olejnik, A. Marchel	
Safety window for the transsphenoidal approach for pituitary tumours: a computed tomographic angiography study	17
F.J. Arrambide-Garza, P.P. Zarate-Garza, K. Aguilar-Morales, I.S. Villarreal-del-Bosque, A. Quiroga-Garza, A. Gómez-Sánchez, R. Pinales-Razo, R.E. Elizondo-Omaña, S. Guzmán-López	
Circle of Willis: anatomical variations of configuration. A magnetic resonance angiography study	24
M. Enyedi, C. Scheau, R.O. Baz, A.C. Didilescu	
Performance of rupture-related morphological parameters in posterior communicating artery aneurysms with fetal-type variant	30
S. Chen, C. Li, C. Karmonik, Y. Cheng, N. Lv	
Standard clinical computed tomography fails to precisely visualise presence, course and branching points of deep cerebral perforators	37
R. Rzepliński, M. Slugocki, M. Kwiatkowska, S. Tarka, M. Tomaszewski, M. Kucewicz, K. Karczewski, P. Krajewski, J. Mafachowski, B. Ciszek	
Vitamin D3 promotes oligodendrogenesis and modulates synucleinopathy in lead-induced nigral pars compacta neurotoxicity in rats	42
R.A. Imam, M.R. Abdel-Hamed	
Cisplatin-induced alterations in the blood-nerve barrier: effects of combination of vitamin B1, B6 and B12	53
A. Tothonglor, P. Kobutree, A. Roumwong, D. Jindatip, S. Agthong	
Evaluation of cell morphology and adhesion capacity of human gingival fibroblasts on titanium discs with different roughened surfaces: an <i>in vitro</i> scanning electron microscope analysis and cell culture study	63
H. Yildiz, E. Sen, H. Dalcik, S.E. Meseli	
Human lumbosacral root and ligamentum flavum thicknesses: a magnetic resonance study	72
R. Khasawneh, E. Abu El-Rub, M. Allouh	
The pattern of branching and intercommunications of the musculocutaneous nerve for surgical issues: anatomical study	79
M.G. Al-Sobhi, A.I. Zaki, F.A. Abd El Hamid, R.A. Alshali, H.N. Mustafa	
Anatomical description of the perforating cutaneous nerve	88
K. Shafarenko, J.A. Walocha, R.S. Tubbs, K. Jankowska, A. Mazurek	
Are the nerves supplying the anterior sacroiliac joint nociceptive?	96
E. Yilmaz, A.V. D'Antoni, Ł. Olewnik, J. Iwanaga, T. Saga, M. Loukas, R.S. Tubbs	
A study of coronary dominance and its clinical significance	102
D.P. Aricatt, A. Prabhu, R. Avadhani, K. Subramanyam, A.S. Manzil, J. Ezhilan, R. Das	
Morphometry and morphological analysis of carotico-clinoid foramen: an anatomical study with clinical implications	108
A. Priya, R.K. Narayan, S.K. Ghosh, P. Kumar	



INDEXED in: BIOSIS Previews, CAS, CINAHL, CrossRef, Dental Abstracts, EBSCO, Elsevier BIOBASE, EMBIOLOGY, FMJ, Google Scholar, Index Copernicus (159.83), Index Medicus/MEDLINE, Index Scholar, Polish Ministry of Education and Science (70), NCBI/National Center for Biotechnology Information, Polish Medical Bibliography, Scopus, SJR, Thomson Reuters, Thomson Scientific Products — Biological Abstracts, Ulrich's Periodicals Directory, Veterinary Bulletin, WorldCat and Zoological Record.

Cover picture: The left axilla and arm showing the normal origin of musculocutaneous nerve (MCN): it arises from the lateral cord of the brachial plexus and piercing the coracobrachialis muscle (cb); MN — median nerve; UN — ulnar nerve; MC — medial cord. For details see: M.G. Al-Sobhi et al., *Folia Morphol* 2023; 82, 1: 79–87.